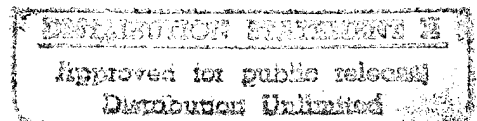Final Technical Report to the Office of Naval Research

ONR Grant Reference N00014-88-J-1017

Classification of Oceanic Light Disruptors Using an Intelligent Remote Imaging System

COLD IRIS

Submitted by:

Kendall L. Carder
David K. Costello
Marine Science Department, University of South Florida
140 7th Avenue South, St. Petersburg, FL 33701-5016
Email: kcarder@monty.marine.usf.edu

Distribution List:

Scientific Officer Code: 322
Steven Ackleson
Office of Naval Research
Ballston Tower One
800 North Quincy Street
Arlington, VA 22217-5660

Administrative Grants Officer
Office of Naval Research
Regional Office
101 Marietta Street, Suite 2805
Atlanta, GA 30323-0008

Director, Naval Research Laboratory
ATTN: Code 2627
Washington, DC 20375

Defense Technical Information Center
Building 5, Cameron Station
Alexandria VA 22304-6045

19960819 012

REPORT DOCUMENTATION PAGE

FORM APPROVED
OMB No. 0704-0188

1. AGENCY USE ONLY (Leave blank)

2. REPORT DATE
03/28/96

3. REPORT TYPE AND DATES COVERED
Final Technical Report, 10/01/87–09/30/95

4. TITLE AND SUBTITLE OF REPORT
Classification of Oceanic Light Disrupters Using an Intelligent Remote Imaging.

5. FUNDING NUMBERS
N00014-88-J-1017

6. AUTHOR(S)
Kendall L. Carder and David K. Costello

7. PERFORMING ORGANIZATION NAME(S) AND ADDRESS(ES)
Marine Science Department
University of South Florida
140 Seventh Avenue South
St. Petersburg, FL 33701-5016

8. PERFORMING ORGANIZATION REPORT NUMBER:
N/A

9. SPONSORING/MONITORING AGENCY NAME(S) AND ADDRESS(ES)
Office of Naval Research
Dr. Steven Ackleson Code: 322
800 N. Quincy Street
Arlington, VA 22217-5660

10. SPONSORING/MONITORING AGENCY REPORT NUMBER:
N/A

11. SUPPLEMENTARY NOTES:
NONE

12a. DISTRIBUTION/AVAILABILITY STATEMENT

DISTRIBUTION STATEMENT A
Approved for public release
Distribution Unlimited

Unlimited

12b. DISTRIBUTION CODE

13. ABSTRACT (Maximum 200 words)

This project explored the automatic enumeration and classification of marine particulates and their effect on the underwater lightfield. Methodologies investigated utilized structed HeCd (442 nm) and visible diode (670 and 685 nm) laser illumination, confocal video cameras, and a pattern recognition algorithm rooted in the theory of Moment Invariant Functions. An Instrument system, the Marine Aggregated Particle Profiling and enumerating Rover (MAPPER) was developed and deployed in Monterey Bay and East Sound, San Juan Islands. The MAPPER system rapidly enumerates marine particulates in large water volumes with data presented as particle size distributions which include particles ranging from tens of micrometers to ten of millimeters equivalent spherical diameter.

14. SUBJECT TERMS
Marine aggregation, underwater visibility, particle enumeration, particle indentification, robotics, target recognition, underwater video, structured illumation.

15. NUMBER OF PAGES:
400

16. PRICE CODE

17. SECURITY CLASSIFICATION OF REPORT:

18. SECURITY CLASSIFICATION OF THIS PAGE

19. SECURITY CLASSIFICATION OF ABSTRACT

20. LIMITATION OF ABSTRACT

DISCLAIMER NOTICE

UNCLASSIFIED

Technical Report
distributed by

DEFENSE
TECHNICAL
INFORMATION
CENTER

DTIC

UNCLASSIFIED

THIS DOCUMENT IS BEST QUALITY AVAILABLE. THE COPY FURNISHED TO DTIC CONTAINED A SIGNIFICANT NUMBER OF PAGES WHICH DO NOT REPRODUCE LEGIBLY.

Final Report to the Office of Naval Research

Classification of Oceanic Light Disruptors using an Intelligent Remote Imaging System (COLD IRIS)

ONR Reference N00014-88-J-1017

Kendall L. Carder and David K. Costello
University of South Florida
Marine Science Department

PREFACE

Toward Readability

A primary objective of this final report is that it be read. Toward that end, we have attempted to write the body of the report to provide the reader with a comprehensive overview of the background, methodology, and results of the COLD IRIS project in a very short (less than five pages) and, relatively non-technical document which can be read in less than 15 minutes. Supplementary material is provided in order to allow the reader to delve deeper into those particular aspects of our work which may stimulate the reader's interest. It is of considerable credit to the ONR Optics program funding strategy, we believe, that this supplementary material consists entirely of technical and scientific publications which were either generated directly by this project or as a prelude or follow up to this project.

Organization

The report is presented in two major sections; **COLD IRIS - Phase I** and **COLD IRIS - Phase II**, which reflect the nature of the funding cycle for the project. Within each section, the scientific justification for the work, the methodology developed, and the results are presented. The **Scientific Justification** and **Methodology** subsections are presented in a narrative manner while the **Results** subsection is presented in a direct, concise manner, and consists of "bullets" stating findings along with citations of our publications which support/develop those findings An additional section, **Relation to Current Work**, briefly notes the applicability of the fruits of this project to our current ONR-sponsored work. An Appendix, **Publications and Presentations**, is for the benefit of the statisticians within ONR and summarizes only those publications and presentations which have arisen directly from this funding.

COLD IRIS - Phase I (FY88-89)

Background

The COLD IRIS project was rooted in our early work involving *in situ* measurement of marine particle physical and optical characteristics (Betzer et al. 1987, 1988a, 1988b; Carder, 1979; Carder et al. 1982, 1986a, 1986b,1986c; Costello, 1988; Costello et al. 1986, 1988; Doyle et al. 1983; Payne et al. 1984). Succinctly, the

sources, sinks, and optical properties of marine particles were poorly understood and their measurement was problematic not only because of time and space considerations but also often because of the friable nature of the particles.

Methodology

To address these problems, we realized that an *in situ*, automatic quantification/classification system must be developed. The friable and labile nature of the particles required an *in situ* system and spatial and temporal considerations (very large sample volumes, extensive data analysis) demanded that the system be automatic, that is, function without human involvement. Fortunately, when this project was conceived, several technological areas (computing, artificial intelligence, neural networks, solid-state optics, miniature sensors, etc.) were beginning to expand exponentially.

The *in situ* system was originally conceived as an expansion of the dual-axis, holographic techniques described in Costello et al. 1989b enhanced with both photographic and video cameras. Laboratory work primarily involved narrow-band-pass and long-pass imagery of laser stimulated fluorescence (HeCd @ 443 nm) and dark-field and Fourier-plane photographic and video imagery (Costello et al. 1989c). Theoretical work concentrated in the area of automated pattern recognition. The approach investigated is rooted in the Theory of Moment Invariants and uses formulations proposed for automated pattern recognition of targets ranging from alphanumeric characters to aircraft (see Costello et al. 1989c, 1994a).

Results

- Moment Invariant Functions were shown to be effective classifiers by providing significant feature vectors for alphanumeric characters, computer-generated images, and marine particle images acquired *in situ* (Carder and Costello, 1994; Costello 1990; Costello et al. 1988, 1989a, 1989c).

- Video spectroscopy was shown to provide feature vectors useful in automated particle identification (Costello, et al. 1989a, Costello, 1990, 1991).

- Eolian mineral particles were shown to be potentially significant for both marine primary productivity and marine optics even in oligotrophic waters (Betzer et al. 1988a, Carder et al. 1991; Carder and Costello, 1994; Costello, 1990; Costello et al. 1989b; Young et al. 1991).

COLD IRIS - Phase II (FY90-95)

Background

In this phase of the COLD IRIS project, funding was provided under the ONR Accelerated Research Initiative, Significant Interactions Governing Marine Aggregation (SIGMA). Initially, the goals of the SIGMA effort did not appear consistent with our interests in individual-particle, and bulk, large-particle optics. However, our primary responsibility in SIGMA, the enumeration of fragile, marine micro- and macro-aggregates, was best met using optical techniques so our experiments during phase I could be put to the task. A considerable challenge arose, however, from the fact that

marine aggregates are, almost by definition, structurally amorphous, nearly transparent, and not amenable to traditional pattern recognition techniques.

Methodology

In this phase of the project, we surveyed traditional *in situ* optical measurement techniques and instrumentation and found that, in many cases, they could not adequately measure the optical effects of large particles and, in no cases, could adequately identify nor provide a particle size distribution for those particles (Carder and Costello, 1994). This required the development of a new methodology which could unambiguously measure nearly-transparent particles in a large, known volume of water. It was also desirable that the instrument be able to utilize light near the wavelength of the traditional transmissometer (660 nm) and be able to function during daylight as well as during night hours.

The result of numerous trials with different imaging configurations was the Marine Aggregated Particle Profiling and Enumerating Rover (MAPPER). References describing the various stages of MAPPER development are cited below. Succinctly, MAPPER uses structured, diode laser illumination (675 nm) to produce a thin (1 mm) sheet of light which is coincident with the image planes of three, synchronized video cameras of differing magnificati.. Particles are illuminated and imaged as they pass through the sheet during the M/ PER free-fall descent through the water column. Maximum horizontal pixel resolution was 17.5 μm with a vertical resolution of less than 1 mm. Vertical resolution is a function of the MAPPER descent velocity (controllable via ballast) divided by the NTSC video rate of 30 frames/sec.

Ancillary optical measurements acquired during MAPPER deployments included beam transmissometry at 660 nm and 512-channel filter pad transmissiometry (350-900 nm).

Results

- The MAPPER prototype structured light module was successfully field tested in Tampa Bay and the concept presented to the optics community (Costello et al. 1991).

- The structured light module was further refined in order to provide quantitative underwater imaging, that is, unambiguous particle sizing combined with individual particle albedo (Costello et al. 1992).

- An Image Control and Examination (ICE) system was developed which provides for frame-by-frame, automated processing of the video imagery from MAPPER systems (Costello et al. 1991, Hou et al. 1994).

- Extensive deployments in Monterey Bay provided very high spatial resolution, 3-dimensional particle size distributions covering nearly three orders of magnitude, circa 100 μm to several cm (Costello et al. 1994a, 1994b, 1994d; Costello and Carder 1994a, 1994b, and *In Prep*; Hou et al. 1994; Jackson et al. 1996 and *In Prep*).

- Optical measurements during the SIGMA mesocosm experiment yielded particle single scattering albedo as well as a multi-component model based on optical attenuation and absorption which predicted particulate organic carbon, particulate

organic nitrogen, and chlorophyll concentrations during the experiment with coefficients of multiple determination in excess of 0.95 (Costello et al. 1994c, 1995a).

- Extensive deployments in East Sound, San Juan Islands, WA expanded upon the database acquired in Monterey Bay with the acquisition of individual-particle light scattering at discrete angles (Costello et al. 1995d; Hou, *In Prep*).

-A formulation of the moment invariant pattern recognition technique was developed to adjust the apparent (perceived) size of a target by imaging systems of differing magnification. The method accounts for the two-dimensional fractal dimension (image porosity) of the particle (Costello et al. 1994a).

- In an examination of the information content of the higher-order Zernike moment invariant functions, it was found that the resolution of the MAPPER imaging systems could be degraded by a factor of about 16 and still yield viable information for pattern recognition applications while resolution could be degraded by about a factor of 32 and still yield reasonable optical attenuation calculations (Hou, *In Prep.*)

- Using MAPPER's hyper-stereo mirror module, light scatter by individual particles at discrete angles near 40-55, 80-100, and 135-150 was measured in order to estimate individual-particle scattering phase functions for marine aggregates and zooplankton. Preliminary results indicate that traditional particle phase functions would underestimate backscattering efficiency for large particles (Costello et al. 1991, Hou, *In Prep.*).

- Essentially all image processing methodologies require that the target be delineated via edge detection or some other intensity thresholding in order to separate the image (the signal) from the background (the noise). We have found however that the inclusion of background noise into moment-based pattern recognition improves target recognition agreement for systems of various resolution. This infers that true background noise is "white" noise while noise associated with a degraded target image (and rejected in traditional processing schemes) still contains useful information (Hou et al. *In Prep.*).

Relation to Current Work

Our current ONR sponsored work involves sea bottom classification in turbid waters and the determination of the components which affect the underwater light field and, hence, the water-leaving radiance, in coastal waters.

The elements of the COLD IRIS project which are directly applicable to current work follow:

- *Video Spectroscopy* is an essential element in interpreting imagery from our Xybion IMC-301 multi-spectral bottom cameras
- *Automated Video Image Processing* is required for processing the video data stream
- *Pattern Recognition* is the basis of our target recognition strategy
- *Laser Stimulated Fluoresence*, along with solar-stimulated fluorescence, provides additional veature vectors for target recognition, furthermore, inelastic processes warrant inclusion in coastal optical modeling

- *Structured Diode Laser Illumination* is utilized for precise under water vehicle altitude ranging and bottom 3-D topography
- *Biochemical/Optical Modeling* is important in predicting water visibility
- *Eolian Mineral Particle Concentration* is analogous to suspended sediment concentration in coastal areas with similar optical effects
- *Large Biological Particle Size Distribution* is an important element in coastal optics which has, heretofore, been largely unaddressed
- *Scattering Phase Function for Large Particles* is intrinsic to the interpretation of water leaving radiance in coastal areas. Aggregates (large particles composed of many microscopic particles) have phase functions similar to a collection of small particles, not to that of a large particle (e.g. zooplankter).

APPENDIX

**Publications and Presentations Directly Originating from This Funding
(ONR Support Acknowledged, * indicates inclusion in Supplementary Material)**
(page 1 of 3)

*Carder, K.L., W.W. Gregg, D.K. Costello, K. Haddad and J.M. Prospero. 1991.
Determination of Saharan dust radiance and chlorophyll from CZCS imagery. Journal of
Geophysical Research 96, D3, 5369-5378.

*Carder, K.L., D.K. Costello, and R.G. Steward. 1986. State of the art instrumentation for
measuring ocean aggregates. Aggregate Dynamics in the Sea Workshop Report, E.
Hartwig and A. Alldredge (eds). Office of Naval Research, Asilomar Ca. 131-181.

*Carder, K.L. and D.K. Costello. 1994. Optical effects of large particles. In Ocean Optics.
R.W. Spinrad, K.L. Carder and M.J. Perry (eds). Oxford University Press, New York,
N.Y. pp 243-257.

Costello, D.K., K.L. Carder and R.G. Steward. (in prep for submission to Deep-Sea
Research). Design and performance of the Marine Aggregated Particle Profiling and
Enumerating Rover (MAPPER).

Costello, D.K. and K.L. Carder. (in prep. for submission to Journal of Geophysical
Research). Underwater light attenuation by the 3-dimensional distribution of large marine
particles in Monterey Bay.

*Costello, D.K., K.L. Carder, and W. Hou. 1995. Aggregation of a diatom bloom in a
mesocosm: bulk and individual-particle optical measurements. Deep-Sea Research II,
(42)1, 29-45.

*Costello, D.K., K.L. Carder, R.F. Chen, T.G. Peacock, and N.S. Nettles. 1995. Multi-spectral
Imagery, hyper-spectral radiometry, and unmanned underwater vehicles: Tools for the
assessment of natural resources in coastal waters. In: Visual Communications and
Image Processing '95. SPIE. Taipei, Taiwan.

*Costello, D.K., W. Hou and K.L. Carder. 1995. Bulk and individual-particle optical
measurements. April 14-22, 1994, East Sound, San Juan Islands, WA. In: SIGMA Data
Report #3 to the Office of Naval Research under the Accelerated Research Initiative,
Significant Interactions Governing Marine Aggregation. 46 pp.

Costello, D.K. and I.I. Kaminer 1995. Joint underwater/air vehicle missions: Scenarios for the
21st century. Plenary presentation, International Program Development in Undersea
Robotics & Intelligent Control. Lisbon, Portugal. Invited.

*Costello, D.K., I.I. Kaminer, K.L. Carder and R. Howard. 1995. The use of unmanned vehicle systems for coastal ocean surveys: Scenarios for joint underwater and air vehicle missions. Proc. International Program Development in Undersea Robotics & Intelligent Control. Lisbon, Portugal. Invited.

*Costello, D.K., W. Hou and K.L. Carder. 1994. Some effects of the sensitivity threshold and spatial resolution of a particle imaging system on the shape of the measured particle size distribution. In: Ocean Optics XII, Jules S. Jaffe, Editor, Proc. SPIE 2258, Bergen, Norway.

*Costello, D.K. and K.L. Carder. 1994. New instrumentation and platforms for subsurface optical measurements. In: Ocean Optics XII, Jules S. Jaffe, Editor, Proc. SPIE 2258, Bergen, Norway.

Costello, D.K., K.L. Carder, R.G. Steward and A. Alldredge. 1994. The Distribution and Optical Properties of Large Marine Particles: Data From a Culture Tank and Field Experiments. EOS AGU/ASLO (75), 3, 35.

*Costello, D.K., K.L. Carder, and R.G. Steward. 1994. Particle size spectra and optical properties. In: Mesocosm Experiment Data Report to the Office of Naval Research under the Accelerated Research Initiative, Significant Interactions Governing Marine Aggregation (SIGMA). 51 pp.

*Costello, D.K., K.L. Carder, W. Hou and R.G. Steward. 1994. 3-dimensional particle size spectra, transmissometry and temperature profiles, and filter pad absorption data. In: Monterey Bay Field Experiment Data Report to the Office of Naval Research under the Accelerated Research Initiative, Significant Interactions Governing Marine Aggregation (SIGMA). 24 pp.

*Costello, D.K., K.L. Carder and W. Hou. 1992. Structured visible diode laser illumination for quantitative underwater imaging. Ocean Optics XI. Gary D. Gilbert, Editor, Proc. SPIE 1750, 95-103.

*Costello, D.K., K.L. Carder and R.G. Steward. 1991. Development of the Marine Aggregated Particle Profiling and Enumerating Rover (MAPPER). Underwater Imaging, Photography, and Visibility, Richard W. Spinrad, Editor, Proc. SPIE 1537, 161-172.

Costello, D.K. 1991. The use of structured visible diode laser illumination and video spectroscopy for marine particle enumeration and identification. Underwater Optics: Engineering Problems and Solutions Workshop. SPIE, San Diego, CA.

Costello, D.K. 1990. In situ collection and imaging of marine particles: Results from the ADIOS program and strategies under investigation in the COLD IRIS program. National University of Taiwan, Institute of Oceanography, Republic of China. Invited.

Costello, D.K., K.L. Carder, and R.G. Steward. 1989. Stategies for automatic classification of marine particles. Optical Society of America. Technical Digest V(18),79. Invited.

*Costello, D.K., K.L. Carder, P.R. Betzer, and R.W. Young. 1989. In-situ holographic imaging of settling particles: Applications for Individual Particle Dynamics and Oceanic Flux Measurements. Deep-Sea Research, 36, 10, 1989.

*Costello, D.K., K.L. Carder, and R.G. Steward.1989. Classification of Oceanic Light Disruptors using an Intelligent Remote Imaging System, Phase I, Year 2. Annual Report to the Office of Naval Research. 16 pp.

Costello, D.K., K.L. Carder, and R.G. Steward. 1988. Computer enhancement of in situ holographic images with preliminary algorithms for marine particle pattern recognition. EOS, 69, 1124.

Hou, W. (In Prep.) Characteristics of large particles and their effects on the submarine light field. Dissertation, University of South Florida, Marine Science Department.

Hou, W., D.K. Costello, K.L. Carder and R.G. Steward. 1994. High-resolution Marine Particle data from MAPPER, a new, in situ optical ocean instrument. EOS AGU/ASLO (75), 3, 21.

Jackson, J.A., R. Maffione, D.K. Costello, A.A. Alldredge, B.E. Logan, H.G. Dam. (in prep for submission to Deep-Sea Research) Particle size spectra, from 1 m to 1 cm, at Monterey Bay as determined by multiple instruments.

Jackson, J.A., R. Maffione, D.K. Costello, A.A. Alldredge, B.E. Logan, H.G. Dam. 1996. Particle size distributions and coagulation rates in Monterey Bay. EOS AGU/ASLO. ·

Lee, Z.P., K.L. Carder, T.G. Peacock, C.O. Davis, and J.L. Mueller. 1996. Method to derive ocean absorption coefficents from remote-sensing reflectance. Applied Optics V35, 3, 453-462.

Lee, Z.P., K.L. Carder, J. Marra, R.G. Steward. and M.J. Perry. 1996. Estimating primary production at depth from remote sensing. Applied Optics V35, 3, 453-462.

SUPPLEMENTARY
MATERIAL

Final Technical Report to the Office of Naval Research

ONR Grant Reference N00014-88-J-1017

Classification of Oceanic Light Disruptors Using an Intelligent Remote Imaging System

COLD IRIS

Kendall L. Carder
David K. Costello
Marine Science Department, University of South Florida
140 7th Avenue South, St. Petersburg, FL 33701-5016
Email: kcarder@monty.marine.usf.edu

SUPPLEMENTARY MATERIAL

Final Report to ONR - COLD IRIS - N00014-88-1017 - Carder & Costello - USF Marine Science

References Cited
(* Indicates Manuscript or Abstract Attached)

*Betzer, P.R., K.L. Carder, R.A. Duce, J.T. Merrill, N.W. Tindale, M. Uematsu, D.K. Costello, R.W. Young, R.A. Feely, J.A. Breland, R.E. Bernstein and A.M. Greco. 1988a. Long-range transport of giant mineral aerosol particles. Nature, 336, 54-56.

Betzer, P.R., R.H. Byrne, K.L. Carder and D.K. Costello. 1988b. In situ and shipboard approaches to physical/chemical transformation in the oceanic water column. U. S. Global Ocean Flux Study, Upper Ocean Processes. Planning report #7 of U. S. GOFS Working Group, Woods Hole, Mass.

Betzer, P.R., K.L. Carder and D.K. Costello. 1987. In situ laser holography: Insights for basic processes/applications for global ocean flux. EOS. Invited.

*Carder, K.L. and D.K. Costello. 1994. Optical effects of large particles. In Ocean Optics. R.W. Spinrad, K.L. Carder and M.J. Perry (eds). Oxford University Press, New York, N.Y. pp 243-257.

*Carder, K.L., W.W. Gregg, D.K. Costello, K. Haddad and J.M. Prospero. 1991. Determination of Saharan dust radiance and chlorophyll from CZCS imagery. Journal of Geophysical Research 96, D3, 5369-5378.

Carder, K.L., D.K. Costello, R.W. Young and P.R. Betzer. 1986a. Dynamics and composition of holographically recorded particles from ADIOS. EOS 67, 899. Invited.

*Carder, K.L., D.K. Costello, and R.G. Steward. 1986b. State of the art instrumentation for measuring ocean aggregates. Aggregate Dynamics in the Sea Workshop Report, E. Hartwig and A. Alldredge (eds). Office of Naval Research, Asilomar Ca. 131-181.

*Carder, K.L., R.G. Steward, P.R. Betzer, D.L. Johnson, and J.M. Prospero. 1986c. Dynamics and composition of particles from an aeolian input event to the Sargasso Sea. Journal of Geophysical Research 91, D1, 1055-1066.

*Carder, K.L. 1979. Holographic microvelocimeter for use in studying ocean particle dynamics. Optical Engineering. V18, N5, 524-526.

Costello, D.K., K.L. Carder and R.G. Steward. (in prep for submission to Deep-Sea Research). Design and performance of the Marine Aggregated Particle Profiling and Enumerating Rover (MAPPER).

Costello, D.K. and K.L. Carder. (in prep. for submission to <u>Journal of Geophysical Research</u>). Underwater light attenuation by the 3-dimensional distribution of large marine particles in Monterey Bay.

Costello, D.K.and I.I. Kaminer 1995. Joint underwater/air vehicle missions: Scenarios for the 21st century. Plenary presentation, <u>International Program Development in Undersea Robotics & Intelligent Control</u>. Lisbon, Portugal. Invited.

*Costello, D.K., K.L. Carder, and W. Hou. 1995a. Aggregation of a diatom bloom in a mesocosm: bulk and individual-particle optical measurements. <u>Deep-Sea Research II</u>, (42)1, 29-45.

*Costello, D.K., K.L. Carder, R.F. Chen, T.G. Peacock, and N.S. Nettles. 1995b. Multi-spectral Imagery, hyper-spectral radiometry, and unmanned underwater vehicles: Tools for the assessment of natural resources in coastal waters. In: <u>Visual Communications and Image Processing '95.</u> SPIE. Taipei, Taiwan.

*Costello, D.K., I.I. Kaminer, K.L. Carder and R. Howard. 1995c. The use of unmanned vehicle systems for coastal ocean surveys: Scenarios for joint underwater and air vehicle missions. Proc. <u>International Program Development in Undersea Robotics & Intelligent Control</u>. Lisbon, Portugal. Invited.

*Costello, D.K., W. Hou and K.L. Carder. 1995d. Bulk and individual-particle optical measurements. April 14-22, 1994, East Sound, San Juan Islands, WA. In: SIGMA Data Report #3 to the Office of Naval Research under the Accelerated Research Initiative, Significant Interactions Governing Marine Aggregation. 46 pp.

*Costello, D.K. and K.L. Carder. 1994a. New instrumentation and platforms for subsurface optical measurements. In: <u>Ocean Optics XII</u>, Jules S. Jaffe, Editor, Proc. SPIE 2258, Bergen, Norway.

*Costello, D.K. and K.L. Carder. 1994b. Using unmanned vehicle systems for ground-thruthing oceanographic satellite data. <u>AUVS '94 - Intelligent Vehicle Systems and Technology</u>, Proc. Asso. for Unmanned Vehicle Systems, Detroit, MI. Invited.

*Costello, D.K., W. Hou and K.L. Carder. 1994a. Some effects of the sensitivity threshold and spatial resolution of a particle imaging system on the shape of the measured particle size distribution. In: <u>Ocean Optics XII</u>, Jules S. Jaffe, Editor, Proc. SPIE 2258, Bergen, Norway.

Costello, D.K., K.L. Carder, R.G. Steward and A. Alldredge. 1994b. The Distribution and Optical Properties of Large Marine Particles: Data From a Culture Tank and Field Experiments. <u>EOS</u> AGU/ASLO (75), 3, 35.

*Costello, D.K., K.L. Carder, and R.G. Steward. 1994c. Particle size spectra and optical properties. In: Mesocosm Experiment Data Report to the Office of Naval Research under the Accelerated Research Initiative, Significant Interactions Governing Marine Aggregation (SIGMA). 51 pp.

*Costello, D.K., K.L. Carder, W. Hou and R.G. Steward. 1994d. 3-dimensional particle size spectra, transmissometry and temperature profiles, and filter pad absorption data. In: Monterey Bay Field Experiment Data Report to the Office of Naval Research under the Accelerated Research Initiative, Significant Interactions Governing Marine Aggregation (SIGMA). 24 pp.

*Costello, D.K., K.L. Carder and W. Hou. 1992. Structured visible diode laser illumination for quantitative underwater imaging. Ocean Optics XI. Gary D. Gilbert, Editor, Proc. SPIE 1750, 95-103.

*Costello, D.K., K.L. Carder and R.G. Steward. 1991. Development of the Marine Aggregated Particle Profiling and Enumerating Rover (MAPPER). Underwater Imaging, Photography, and Visibility, Richard W. Spinrad, Editor, Proc. SPIE 1537, 161-172.

Costello, D.K. 1991. The use of structured visible diode laser illumination and video spectroscopy for marine particle enumeration and identification. Underwater Optics: Engineering Problems and Solutions Workshop. SPIE, San Diego, CA.

Costello, D.K. 1990. In situ collection and imaging of marine particles: Results from the ADIOS program and strategies under investigation in the COLD IRIS program. National University of Taiwan, Institute of Oceanography, Republic of China. Invited.

Costello, D.K., K.L. Carder, and R.G. Steward. 1989a. Stategies for automatic classification of marine particles. Optical Society of America. Technical Digest V(18),79. Invited.

*Costello, D.K., K.L. Carder, P.R. Betzer, and R.W. Young. 1989b. In-situ holographic imaging of settling particles: Applications for Individual Particle Dynamics and Oceanic Flux Measurements. Deep-Sea Research, 36, 10, 1989.

*Costello, D.K., K.L. Carder, and R.G. Steward. 1989c. Classification of Oceanic Light Disruptors using an Intelligent Remote Imaging System, Phase I, Year 2. Annual Report to the Office of Naval Research. 16 pp.

Costello, D.K., K.L. Carder, and R.G. Steward. 1988. Computer enhancement of in situ holographic images with preliminary algorithms for marine particle pattern recognition. EOS, 69, 1124.

Costello, D.K. 1988. Multiple-sample sediment trap with holographic imaging capability: design and function of the ADIOS laser trap. Master's thesis, University of South Florida. 40 pp.

Costello, D.K., R.W. Young, K.L. Carder and P.R. Betzer. 1986. Multiple-sample sediment
traps with in situ holographic imaging of settling particles. EOS 67, 899 Invited

*Doyle, L.J., K.L. Carder, and R.G. Steward. 1983. The hydralic equivalence of mica. Journal
of Sedimentary Petrology, V53, N2, 0643-0648.

Hou, W. (*In Prep.*) Characteristics of large particles and their effects on the submarine light field.
Dissertation, University of South Florida, Marine Science Department.

Hou, W., D.K. Costello, K.L. Carder and R.G. Steward. 1994. High-resolution Marine Particle
data from MAPPER, a new, in situ optical ocean instrument. EOS AGU/ASLO (75), 3,
21.

Jackson, J.A., R. Maffione, D.K. Costello, A.A. Alldredge, B.E. Logan, H.G.
Dam. (in prep for submission to Deep-Sea Research) Particle size spectra, from 1
m to 1 cm, at Monterey Bay as determined by multiple instruments.

Jackson, J.A., R. Maffione, D.K. Costello, A.A. Alldredge, B.E. Logan, H.G.
Dam. 1996. Particle size distributions and coagulation rates in Monterey Bay. EOS
AGU/ASLO.

*Payne, P.R., K.L. Carder, and R.G. Steward. 1984. Image analysis techniques for holograms of
dynamic oceanic particles. Applied Optics, V23, 204-210.

Young, R.W., K.L. Carder, P.R. Betzer, D.K. Costello, R.A. Duce, G.R. Ditullio, N.W.
Tindale, E.A. Laws, M. Uematsu, J.T. Merril, and R.A. Feely. 1991. Atmospheric
iron inputs and primary productivity: phytoplankton responses in the North Pacific. Global
Biogeochemical Cycles. V(5), 2. 119-134.
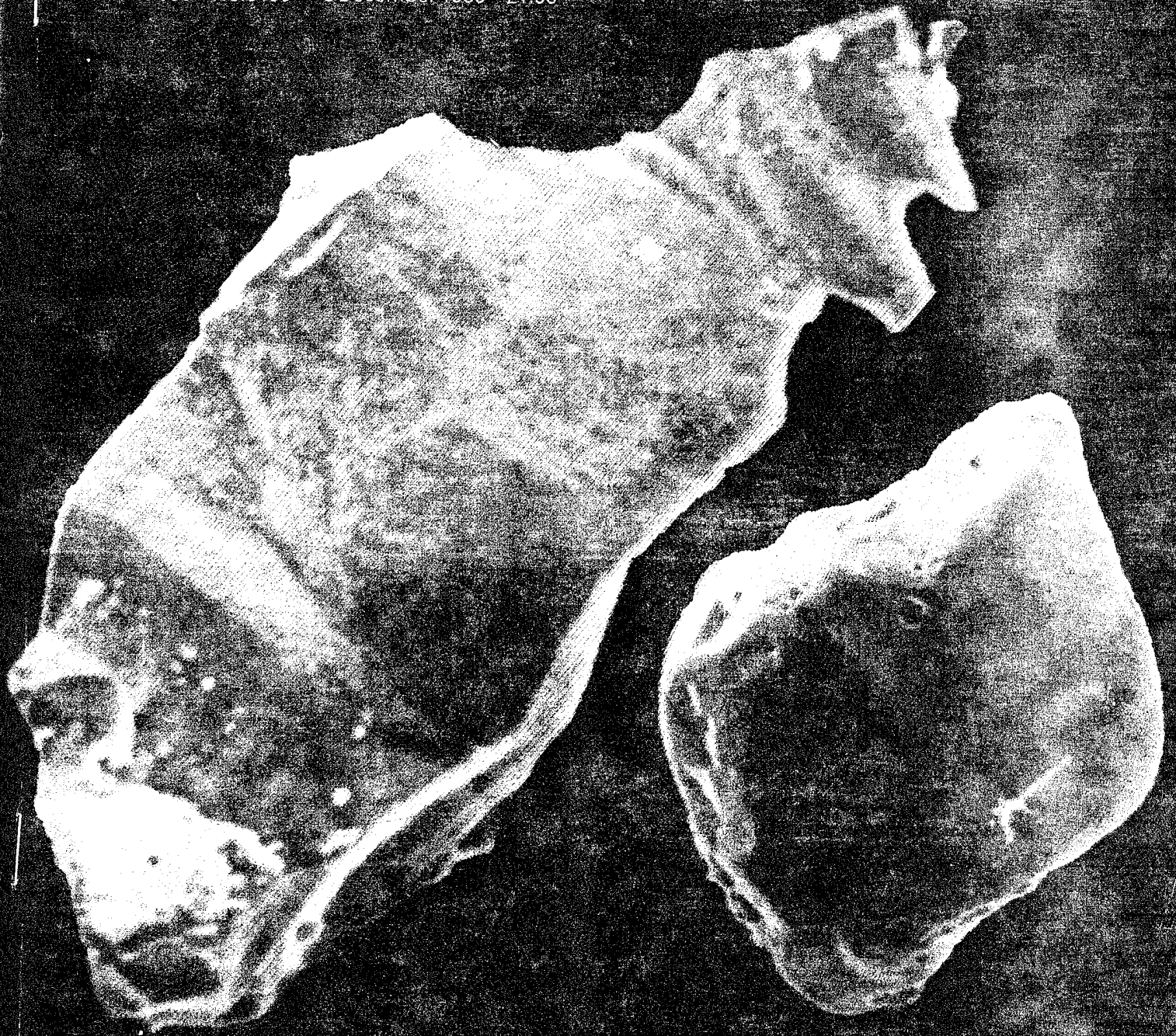
WIND TRANSPORT OF 'GIANT' DUST PARTICLES

Long-range transport of giant mineral aerosol particles

P. R. Betzer*, K. L. Carder*, R. A. Duce†,
J. T. Merrill†, N. W. Tindale†, M. Uematsu†§,
D. K. Costello*, R. W. Young*, R. A. Feely‡,
J. A. Breland*, R. E. Bernstein* & A. M. Greco*

* Department of Marine Science, University of South Florida,
St Petersburg, Florida 33701, USA
† Center for Atmospheric Chemistry Studies, Graduate School of
Oceanography, University of Rhode Island, Narragansett,
Rhode Island 02882, USA
‡ National Oceanic and Atmospheric Administration,
Pacific Marine Environmental Laboratory, 7600 Sand Point Way NE,
Seattle, Washington 98115, USA

Several recent studies have shown that large quantities of mineral dust from eastern Asia are transported through the atmosphere to the North Pacific each spring[1-5]. The paucity of information on mineral fluxes during individual dust events prompted a coordinated effort, Asian Dust Input to the Oceanic System (ADIOS), which simultaneously measured mineral fluxes in the atmosphere and upper water column during such an event. In March 1986 a major dust outbreak in China moved over the North Pacific Ocean and was detected downstream using changes in particle number, size and composition. Most striking was the presence of 'giant' (>75-μm) silica minerals found in atmospheric as well as water-column samples at the ADIOS sampling site (26° N, 155° W). Their appearance more than 10,000 km from their source cannot be explained using currently acknowledged atmospheric transport mechanisms. Furthermore, the large wind-blown minerals that dominated our samples are extremely rare in the long-term sedimentary record in the North Pacific.

Concentrations and fluxes of mineral particles were determined in the atmosphere and upper water column for a 27-day period in March/April 1986 at a station in the North Pacific (26 °N, 155 °W) aboard the R/V *Moana Wave*. Atmospheric sampling was also undertaken from platforms on the windward coasts of Oahu and Midway (Fig. 1). Procedures for collection and analysis of atmospheric aerosol and total-deposition samples for total aluminium, an indicator of aluminosilicate minerals, have been described previously[4,5]. Mineral fluxes in the water column were estimated with free-drifting sediment traps[6], some of which were fitted with programmable sample changers which isolated a sample every four hours[7]. Traps were deployed at depths of 37, 127, 400, 900, 2,200 and 3,500 metres.

§ Present address: Department of Marine Sciences and Technology, Hokkaido Tokai University, Minami-sawa, Minami-ku, Sapporo, 005 Japan.

Atmospheric and water-column samples were analysed using computer-controlled scanning electron microscopy (SEM) and energy-dispersive X-ray analysis (EDXA)[8]. In brief, each of the particles was sized (length/width) and then analysed for 5 s. Based on the proportion of key elements such as Si, Al, Fe, Ti, Mg and Ca, the particles were sorted into chemical macroclasses as a function of size.

According to routine surface meteorological reports from China, a major dust outbreak occurred in 1986 between 15 and 17 March. Relatively low atmospheric aluminium concentrations were observed initially at the ADIOS site on 23 March, but were followed by substantial increases. At Midway our sampling was initiated during and/or after the arrival of the dust from Asia (Fig. 1). The dust pulse reached the ADIOS Station on 25 March, at which time atmospheric aluminium concentrations increased tenfold. A similar concentration change was observed at Oahu one day later. Isentropic back trajectories at 300 K (ref. 9) for air reaching the ADIOS Station on 25 March are consistent with the movement of material from Asia to the ADIOS Station in the open Pacific Ocean with a transit time of 9-11 days.

Atmospheric total-deposition samples collected at the ADIOS site during this dust event showed considerable increases in the particle number flux and mass flux for particles of diameter >75 μm compared with the pre-dust input values (Table 1). Associated with the increased flux was a marked change in the particle size distribution of the material deposited. Before the arrival of the dust pulse, materials deposited at sea were dominated both numerically (>99%) and by mass (>97%) by particles of <75 μm in area-equivalent diameter (equal to $2\sqrt{\text{cross-sectional area}/\pi}$). Although the dust pulse that appeared on 25 March at our open-ocean station was characterized by a small increase in the total mass flux, there was a distinctive change in the particle size distribution resulting from the presence of 'giant' particles. These were primarily quartz grains, several of which had area-equivalent diameters >200 μm. The enhanced total mass flux and input of giant particles continued through the next two atmospheric sampling periods (Table 1).

A corresponding increase in mineral fluxes was detected in the upper water column by the drifting sediment traps. Two sequential 4-h samples collected from a single trap at the 37-m horizon between 25 and 26 March showed distinct changes in the abundance, size and chemical character of particulate material (Table 2). Initially, the particulate material isolated in the trap consisted of relatively small, calcium-dominated particles. The latter sample also had a large number of calcium-dominated particles, but, in sharp contrast to the earlier sample, also contained large silica-bearing particles and increased amounts of various clays and iron-rich materials (Table 2). Four representative giant quartz grains isolated from this trap are

Fig. 1 Map of the sampling region and dust trajectory. Triangles represent sampling stations in the North Pacific Ocean. Atmospheric aluminium concentrations observed during the late March 1986 Asian dust event are shown on the right. An isentropic trajectory at 300 K, reaching the ADIOS station on 26 March 1986, is also shown. The air mass crossed the central-northern North Pacific, moving towards the east at ~4 km altitude, and then descended as it moved into the marine boundary layer. Dots along this trajectory represent 24-h travel times, with open circles at 5-day intervals.
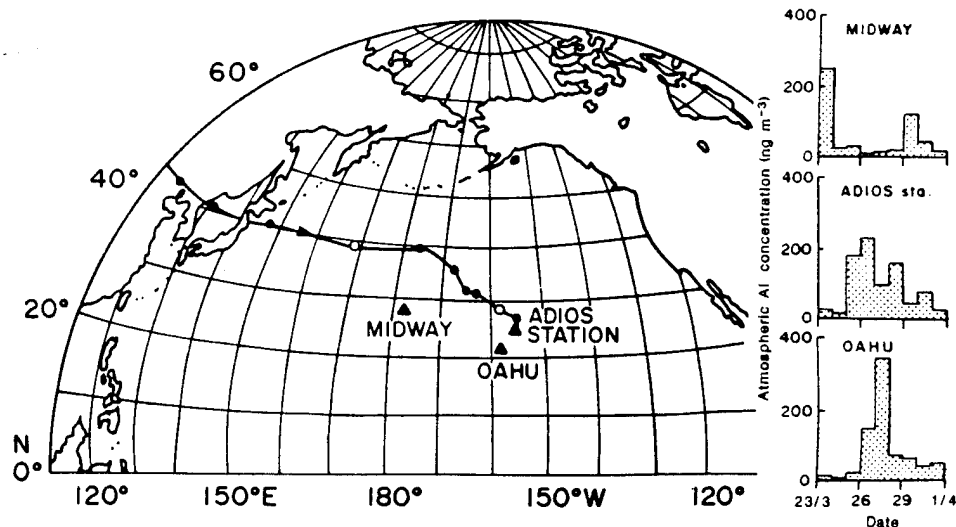
Sample	Area-equivalent diameter range (μm)					
	20–50	50–75	75–100	100–200	>200	Total
08:00, 23/3–08:10, 24/3						
Total particle no. flux	9,776	716	44	0	0	10,536
Quartz particle no. flux	186	22	0	0	0	208
Total mass flux	135	112	8	0	0	255
Quartz mass flux	1	4	0	0	0	5
08:10, 24/3–08:30, 26/3						
Total particle no.flux	1175	171	123	68	6	1543
Quartz particle no. flux	243	132	97	68	6	546
Total mass flux	16	31	76	159	16	298
Quartz mass flux	5	26	63	159	16	269
08:30, 26/3–08:30, 28/3						
Total particle no. flux	3,645	458	156	119	8	4,386
Quartz particle no. flux	1,138	350	156	111	8	1,763
Total mass flux	55	76	96	225	109	561
Quartz mass flux	21	66	96	218	109	510
08:30, 28/3–08:30, 30/3						
Total particle no. flux	5,658	979	518	305	38	7,498
Quartz particle no. flux	2,462	808	499	286	38	4,093
Total mass flux	91	185	285	791	482	1,834
Quartz mass flux	53	161	283	775	482	1,754

Particle number flux in particles $m^{-2} d^{-1}$; mass flux in $\mu g\, m^{-2} d^{-1}$. The figures consider only particles >15 μm in area-equivalent diameter, and do not include sea-salt aerosol particles, specifically particles enriched in NaCl. The number of single particles analysed in each sample (not including sea-salt particles): 23/3–24/3 1,729; 24/3–26/3 897; 26/3–28/3 2,050; 28/3–30/3 2,046.

shown in Fig. 2. The large silica, clay and iron-rich particles noted in the water column were similar both in size and in composition to the atmospheric input material. The flux of non-biogenic material during the latter collection period ($447\ \mu g\, m^{-2} d^{-1}$) is significantly greater than that noted in the earlier period ($43\ \mu g\, m^{-2} d^{-1}$) and is also in good agreement with the range of values from the coincident two-day atmospheric-deposition samples ($300–560\ \mu g\, m^{-2} d^{-1}$).

We stress that the detection of large mineral particles at the ADIOS Station did not result from sample contamination during collection or processing. The giant, chemically distinct particles appeared simultaneously in atmospheric and shallow marine samples. Furthermore, in the water column they were detected in two different sediment traps, deployed several kilometres apart, which were sampling the 37-m horizon on 25 and 26 March, and also in other separate sediment traps sampling at 900, 2,200 and 3,500 m; they were also isolated from 30-litre Niskin bottles and collected from in situ filtrations of suspended matter[10]. In addition, the calculated settling times of the giant silica-bearing materials trapped at 900, 2,200 and 3,500 m also indicate that the arrival of the dust event at our open-ocean location lies somewhere between 20:00, 25 March and 00:18, 26 March. It is highly unlikely that such a consistent pattern would result from artefacts or random contamination. Finally,

Fig. 2 Scanning electron micrographs of four giant quartz particles collected from a sediment trap deployed at a depth of 37 m. The white bar in each photograph represents a distance of 50 μm. Energy-dispersive X-ray analysis of these particles is consistent with their being classified as quartz. These particles have length:width ratios ranging from nearly spherical to 2.5:1, and their topographies suggests that these grains have substantial thickness. In combination, their size and shape are indicative of rapid settling velocities.
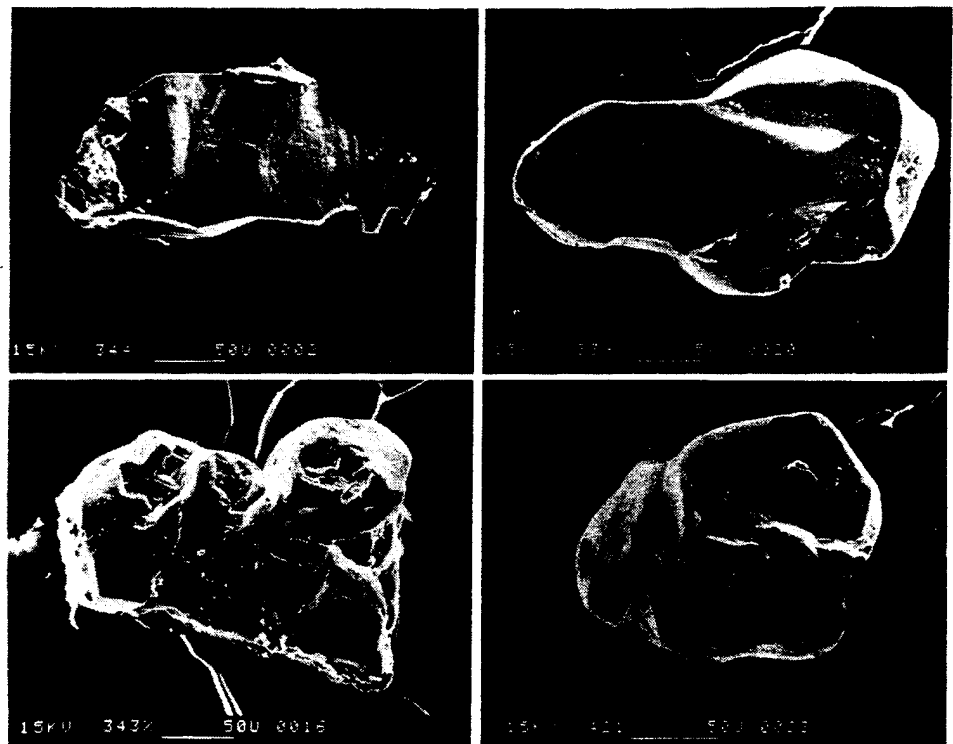
Table 2 Transition in particle fluxes in the upper water column of the North Pacific Ocean

Response to input of atmospheric mineral debris
Sampling period: 16:00 to 20:09 on 25 March
Total non-biogenic mass flux = 43 $\mu g\, m^{-2}\, d^{-1}$

Chemical category	Particle fluxes* by area-equivalent diameter ranges (μm)					Total number	Mass flux†
	10-25	25-50	50-100	100-200	>200		
Ca-rich	863	592	197	73	0	1,725	128
Ca only	246	98	271	122	24	791	410
Ca/Si	123	24	0	0	0	147	1
Al/Si/Ca	24	0	24	0	0	48	3
Al/Si/Fe	0	0	0	0	0	0	0
Al/Si/Mg/Fe	127	148	24	0	0	244	8
Al/Si/K/Fe	24	73	0	0	0	97	3
Al/Si/clay	73	24	0	0	0	97	0
Ti-rich	0	0	0	0	0	0	0
Fe-rich	196	49	0	0	0	245	7
Fe only	295	49	24	0	0	368	12
Si-rich	123	49	0	0	0	172	3
Si only	345	74	24	0	0	443	6
Particle number flux	2,439	1,180	564	195	24	4,447	581
Non-biogenic mass flux	7	18	18	0	0		43

Sampling period: 20:09 to 00:18 on 25/26 March
Total non-biogenic mass flux = 447 $\mu g\, m^{-2}\, d^{-1}$

Chemical category	Particle fluxes* by area-equivalent diameter ranges (μm)					Total number	Mass flux†
	10-25	25-50	50-100	100-200	>200		
Ca-rich	806	339	84	0	0	1,229	29
Ca only	1,103	764	169	0	0	2,036	42
Ca/Si	508	254	84	0	0	846	15
Al/Si/Ca	42	0	42	0	0	84	1
Al/Si/Fe	1,187	254	42	0	0	1,483	18
Al/Si/Mg/Fe	3,013	2,122	763	127	0	6,025	205
Al/Si/K/Fe	1,695	465	42	0	0	2,202	16
Al/Si/clay	1,526	467	0	0	0	1,993	11
Ti-rich	84	84	0	0	0	168	3
Fe-rich	508	382	42	0	0	932	23
Fe only	593	339	126	0	0	1,058	67
Si-rich	933	297	42	42	0	1,314	57
Si only	1,188	467	42	0	0	1,697	31
Particle number flux	13,186	6,234	1,478	169	0	21,067	518
Non-biogenic mass flux	45	112	217	73	0		447

Number of particles analysed in each sample: 16:00–20:09 on 25/3: 719; 20:09–00:18 on 25-26/3: 1,917. Local times are used. Masses calculated as the sum of individual particle masses derived from size and chemical composition data obtained from SEM-EDXA analyses. The two-day atmospheric deposition samples indicate a mineral aerosol flux of 300–560 $\mu m^{-2}\, d^{-1}$.

* Particle number flux in particles $m^{-2}\, d^{-1}$.

† Mass flux in $\mu g\, m^{-2}\, d^{-1}$. The first two chemical categories represent the biogenic contribution.

the composition and size ranges of these giant particles are consistent with their proposed source, specifically China's extensive deserts and/or loess deposits[11,12].

Nonetheless, it is extremely difficult to account for the appearance of giant particles over 10,000 km from their source region. The atmospheric-deposition velocity estimates of Windom[13] allow 20-μm diameter quartz particles to travel ~7,000 km if their initial injection height is 8 km. Gillette[14] invokes a re-suspension probability in which an exponentially decreasing fraction of particles in each settling velocity interval can be carried further and further; however, the parameters he uses are for the atmospheric boundary layer and are not germane to long-range transport. Even with the use of sophisticated meteorological models, including full aerosol microphysics, it is not possible to account for even 30-μm diameter particles from the Sahara travelling a distance of 1,000 km (ref. 15). Although some workers have invoked agglomeration near the sampling location to explain the presence of large particles[15,16], Prospero et al.[17] and Carder et al.[18] detected individual large (>20-μm diameter) particles that were carried more than 4,000 km from their Saharan source. The individual large particles reported here are considerably larger than those detected in refs 17 and 18, and require a re-suspension mechanism. It is

our hypothesis that isolated convective storms along the particles' path provide the required uplift.

Although we are unable to specify the physical mechanisms involved in their transport, the data show the considerable importance of the giant particles to the total mass flux in this event (Tables 1 and 2). In our atmospheric samples, over 83% of the mass flux for particles larger than 20 μm was due to giant (>75-μm diameter) particles during 24–30 March (Table 1). Quartz particles alone comprise 95% of the mass influx in the >75-μm particle range during the dust event (24–26 March). This can be contrasted with the pre-dust data (23–24 March), where less than 4% of the mass input is due to giant particles. During this same period, quartz particles of diameter >20 μm account for only ~2% of the mass input.

When considered in the context of data from the SEAREX Asian Dust Network and routine meteorological observations, the event discussed here appears unremarkable. For example, the peak atmospheric concentrations of dust observed for this event were well within the usual range for dust events observed at North Pacific island sites[4]. The transport meteorology follows the pattern usually observed[9], and the number of routine meteorological reports of dust during the source event, although higher than the seasonal average peak value by ~20%, are not

exceptional. Furthermore, the estimated atmospheric deposition for the entire event (3,000 μg m^{-2}) is less than 1% of the annual average aerosol flux measured in this area[5]. What is clearly remarkable about this event is the presence of such large mineral debris which was carried over 10,000 km from the Asian continent to our open-ocean sampling site. Evidence from other events encountered during the 1986 ADIOS expedition indicates that this event is not unique. That is, although the flux of particles with diameters >75 μm is greater in this event than in others, particles with diameters >50 μm are common in all these events. Large-diameter quartz particles of aeolian origin are found in bottom sediments over large portions of the Central North Pacific Ocean[19], but their proportions are far smaller than those noted in this work. Furthermore, in contrast to our data for both atmosphere and water column, surface sediments from two different sites near the ADIOS Station show no quartz particles of >55-μm diameter[19]. Thus, when viewed in the context of the long-term sedimentary record (~2,000 yr) at the bottom of an ocean whose non-biogenic sedimentary materials are essentially

all of aeolian origin[20], this event is certainly not typical.

It is possible that the actions of man have altered wind erodibility and have thereby modified the size distribution of the mineral aerosol particles at the source; anthropogenic alterations in dust characteristics have been noted elsewhere[21]. Additional research is needed to understand the mechanisms responsible for the long-range transfer of giant mineral aerosols.

1. Duce, R. A., Unni, C. K., Ray, B. J., Prospero, J. M. & Merrill, J. T. *Science* **209**, 1522-1524 (1980).
2. Darzi, M. & Winchester, J. W. *J. geophys. Res.* **87**, 1251-1258 (1982).
3. Parrington, J. R., Zoller, W. H. & Aras, N. K. *Science* **220**, 195-197 (1983).
4. Uematsu, M. *et al. J. geophys. Res.* **88**, 5343-5352 (1983).
5. Uematsu, M., Duce, R. A. & Prospero, J. M. *J. atmos. Chem.* **3**, 123-138 (1985).
6. Betzer, P. R. *et al. Deep Sea Res.* **31**, 1-11 (1984).
7. Costello, D. K., Young, R. W., Carder, K. L. & Betzer, P. R. *Eos* **67**, 899 (1986).
8. Johnson, D. L. in *Proc. Conf. Toxic Hazardous Chemicals* (ed. Pilon, K.) 161-169 (Central New York Water Quality Program, New York, 1980).
9. Merrill, J. T., Bleck, R. & Avila, L. *J. geophys. Res.* **90**, 12927-12936 (1985).
10. Schatzberg, P., Adema, C. M., Thomas, W. M. & Mangum, S. R. in *Oceans '86 Conference Record: Science-Engineering-Adventure* Organotin Symposium, Mar. Tech. Soc., Washington, DC, Vol. 4, 1155-1159 (IEEE Publ. Ser., New York, 1986).
11. Sheng, L. T., Fei, G. X., Sheng, A. Z. & Xiang, F. Y. in *Desert Dust: Origin, Characteristics,*
and Effect on Man (ed. Péwé, T. L.) Spec. Paper 186, 149-157 (Geol. Soc. Am., Boulder, 1981).
12. *Loess in China* (eds Wang, Y.-y. & Zhang, Z.-h.) (Shaanxi People's Art Publishing House, Xian, China, 1980).
13. Windom, H. L. *Bull. geol. Soc. Am.* **80**, 761-782 (1969).
14. Gillette, D. A. in *Desert Dust: Origin, Characteristics, and Effects on Man* (ed. Péwé, T. L.) Spec. Paper 187, 11-26 (Geol. Soc. Am., Boulder, 1981).
15. Westphal, D. L., Toon, O. B. & Carlson, T. N. *J. geophys. Res.* **92**, 3027-3049 (1987).
16. Schutz, L. in *Saharan Dust* (ed. Morales, C.) 267-277 (Wiley, New York, 1979).
17. Prospero, J. M., Bonatti, E., Schubert, C. & Carlson, T. N. *Earth planet. Sci. Lett.* **9**, 287-293 (1970).
18. Carder, K. L., Steward, R. G. & Betzer, P. R. *J. geophys. Res.* **91**, 1055-1066 (1986).
19. Dauphin, J.- P. thesis, (Univ. Rhode Island, 1983).
20. Blank, M., Leinen, M. & Prospero, J. M. *Nature* **314**, 84-86 (1985).
21. Middleton, N. J. *Nature* **316**, 431-434 (1985).

For remote sensing the effect of Raman scattering on reflectance is not apt to be a problem, since the values are probably too small.

The implications of Raman scattering on biological oceanography are potentially exciting. Figure 12-7 is a plot of direct and Raman scattered light at 0 m depth in clear water. The total light field is the sum of these two. In the red region of the spectrum there are some six orders of magnitude more light than would be present without Raman scattering. This may be a critical factor in the process of photomorphogenesis: the response of organisms to light signals that regulate changes in structure and form. In this process the red photons act as a switching mechanism. Photomorphogenesis is a switching mechanism based on very small amounts of red light. The Raman light may be playing a role in gametogenesis.

13

OPTICAL EFFECTS OF LARGE PARTICLES

Kendall L. Carder and David K. Costello
University of South Florida

Introduction

Two important problems facing the ocean optics research community in the coming decade concern optical model *closure* and *inversion* (see Chapter 3). We obtain model *closure* if we can describe the measured light environment by combining elementary measurements of the optical properties of the medium with radiative transfer theory. If we can accurately deduce the concentration of various constituents from a combination of measures of the submarine light field and inverse model calculations, we term this process model *inversion*.

The most elementary measurements of the optical properties of the sea are those that are independent of the geometry of the light field, the *inherent* optical properties (Preisendorfer, 1961). Optical properties that are dependent on the geometry of the light field are termed *apparent* optical properties (AOP). Models of the submarine light field typically relate apparent optical properties to inherent optical properties (see Chapter 2). Examples include the relationship between the AOP irradiance reflectance R and a combination of inherent optical properties (backscattering coefficient b_b and absorption coefficient a), and the relationship between the AOP downwelling diffuse attenuation coefficient k_d and a combination of the absorption coefficient, backscattering coefficient, and downwelling average cosine μ_d (e.g., Gordon et al., 1975; Morel and Prieur, 1977; Smith and Baker, 1981; Morel, 1988; Kirk, 1984a).

Under some circumstances these relationships work well enough that the absorption coefficient can be derived indirectly. This is important since measurement of the absorption coefficient by direct means has been difficult. Derived values for the absorption coefficient by model inversion methods are not easily verified by independent measurements, however, because of the difficulty of measuring the absorption coefficient.

Model closure and model inversion both become more tenuous when the following phenomena are present:

1. Transspectral or inelastic scattering such as fluorescence (e.g., Gordon, 1979; Carder and Steward, 1985; Mitchell and Kiefer, 1988a; Spitzer and Dirks, 1985; Hawes and Carder, 1990) or water Raman scattering (Marshall and Smith, 1990; Stavn, 1990; Stavn and Weidemann, 1988a,b; Peacock et al., 1990; Chapter 12 this volume).

2. Particles that are large relative to the measurement volume for inherent optical property meters such as beam transmissometers, light-scattering photometers, fluorometers, and absorption meters.

The effects of these phenomena are not accounted for in most optical models and may be present in measurements when testing for model closure. They will typically be present in AOP data but not always in inherent optical property data. The transspectral phenomena affecting model closure are being actively pursued as a research topic. However, the effects of large particles on model closure and model inversion have been less vigorously studied and are the focus of this study.

Background

A difficulty inherent in addressing the effect of large particles on the light field results from the difference in the scales of measurement typical for apparent optical properties and inherent optical properties. The apparent optical properties derive from measures of the light field associated with water volumes of order one to hundreds of cubic meters, whereas inherent optical properties derive from very local measurements, with sample volumes ranging from of order cubic millimeters to cubic centimeters. This closure problem can be illustrated by using an example case.

A beam-attenuation or c-meter measures the loss of light from a narrow, collimated light beam of length dl. This loss is due to absorption by water, a_w, by particles, a_p, by colored dissolved organic matter, a_{cdom}, and due to scattering by water molecules, b_w, and by particles, b_p (e.g., see Jerlov, 1968; Petzold, 1972; Kirk, 1984a). In order to minimize the error resulting from the collection of near-forward-scattered light by the sensor and thus underestimating the contributions to c due to $b_w + b_p$, c-meters must be well-collimated with beams that are narrow relative to their length. Minimizing the near-forward-scattering acceptance angle does not, however, allow one to quantify this error unless the nature of the scatterers is known. For example, Baker and Lavelle (1984) showed that spheres of 10 μm and 40 μm diameter, both with refractive indices of 1.2 relative to water, would scatter, respectively, 15% and 43% of the incident light into a near-forward cone with half-angle of 1.03°. For much larger particles that approach the size of the beam itself, this effect worsens. Ultimately, the beam may be blocked entirely or the particles may be only partially illuminated, rendering meaningless any interpretation of their effect on c. When present, these large particles are clearly represented in AOP measurements, however, because of the large volumes of water contained in their measurement fields.

Light-scattering photometers, which measure the radiant intensity scattered in various directions by a small, irradiated volume of water, can be saturated by scattering from a particle occupying a significant cross-section of the source beam. An additional problem arises for measurements of the total scattering coefficient and backscattering coefficient. Since most measurements of these variables derive from integrating volume scattering function measurements, $\beta(\theta)$, over 4π or 2π steradians (e.g., see Kullenberg, 1968; Petzold, 1972), and these θ-dependent measurements are typically not synoptic, the optical properties of the sample volume must remain constant during the time required to obtain the entire suite of $\beta(\theta)$ measurements. To obtain data consistency, average values are typically used for each angle after carefully eliminating "aberrant" data points caused at times by "motes," large particles falling or swimming temporarily through the sample volume. These "moteless" volume scattering functions produce "moteless" b_b and b data when integrated over the appropriate solid angles, data no longer consistent with the actual particle size distribution, c value, or the AOPs. The effects of small motes are not problematic for c-meter data and are not removed. As a result, absorption coefficient data derived from the difference, $c - b$, can be too large.

If it were possible to remove mote effects from c-meter data in a way that was consistent with the method used for deriving "moteless" b data, reasonably accurate absorption coefficients could be derived for "moteless" water. These moteless data include all particles statistically represented in the data used in the averaging process, but they ignore the most erratic effects of motes on the inherent optical properties c, $\beta(\theta)$, b, b_b, and "derived" a. It is not expected that closure between model predictions based on "moteless" inherent optical property data will be achieved with AOP measurements that include the optical effects of motes.

When "moteless" inherent optical properties are used to drive model calculations that simulate apparent optical properties and the submarine light field (which do include the effects of motes), closure is not achievable if the motes play a statistically significant optical role. The focus of this chapter is to examine the optical role played by large particles and to present a method for sizing, classifying, and enumerating them in order to assess their effect upon the optical properties of the ocean and the submarine light field.

Approach

The effect of large particles on apparent optical properties is a function of their concentration relative to smaller particles and, therefore, will vary geographically. High concentrations of large particles are generally associated with near-shore or near-bottom environments. However, significant concentrations of optically "large" particles can be found in the open ocean. In the oligotrophic north central Pacific gyre (26°N, 155°W), Betzer et al. (1988) found an influx of optically large (due to size and high relative index of refraction) eolian particles that amounted to some 10 000 particles m^{-2} day^{-1}. Although the concentrations

from such an influx would likely affect a remotely sensed signal that is dependent on b_b, it is estimated that a typical c-meter with a 1-m pathlength, for example, may measure in these waters a significant perturbation in its background signal due to such eolian particles only 1–2% of the time. A typical scattering meter, because of its small sample volume, would have a probability approaching zero of detecting these particles. Hence, an optically significant portion of the particle population could go essentially undetected.

When particles are present with cross sections that are significant relative to that of the measurement volume, and they are sampled on an infrequent basis or not at all, the inherent optical properties will diverge from those derived from apparent optical properties using inverse models. To estimate the sample volumes required to adequately represent some given particle suite, one must first assume a size distribution function, and also that the particles are evenly dispersed in time and space. A commonly used form for particle size distribution functions is a power-law function of the particle diameter:

$$\frac{dN(D)}{dD} = AD^{-n} \quad (13.1)$$

expressed as particles cm^{-3} μm^{-1} where $N(D)$ is the cumulative number of particles larger than D, $dN(D)$ is the number of particles within size range dD, A is a constant of dimensions particles cm^{-3} μm^{n-1}, and D is in μm.

Using an open-ocean example, and assuming a power-law size distribution with $n = 4$ [used by Hunt (1980) for inorganic particles between 2 and 40 μm diameter and by Sheldon et al. (1972) for organic particles from phytoplankton to whales], and considering the size range from 1 μm to 1 cm, one would expect roughly the same amount of particulate volume to be found in the size ranges (diameters) 1–10 μm, 10–100 μm, 100-1000 μm, and 1–10 mm.

Figure 13-1 shows particle frequency as a function of size with this size distribution assumption and the Sheldon et al. (1972) estimate for surface Sargasso Sea particle volume concentration of 0.01 p.p.m. per log-size class. It also illustrates the number of sample volumes for different instruments required in order to reasonably expect to see even a single particle of a given size. Figure 13-1 suggests that for a typical 25-cm pathlength c-meter with a sample volume of about 50 ml, the 1–10 μm diameter size class in this volume would be well represented. There would, however, be only one 100-μm diameter particle present on average. Continuing this analysis, one would have to look at one thousand 25-cm pathlength c-meter sample volumes in order to expect to see even a single 1-mm diameter particle and one million sample volumes in order to see a single 1-cm diameter particle.

The question then arises whether these "rare-event" large particles are optically significant enough to attempt to measure since, using the above approach, their numbers diminish by a factor of 10^3 for each larger log-size class. However, even though particle numbers are reduced by a factor of 10^3, individual particle cross-sectional area, a significant optical parameter (van de Hulst, 1957), increases by a factor of 10^2 per log-size class. This results in a reduction of total
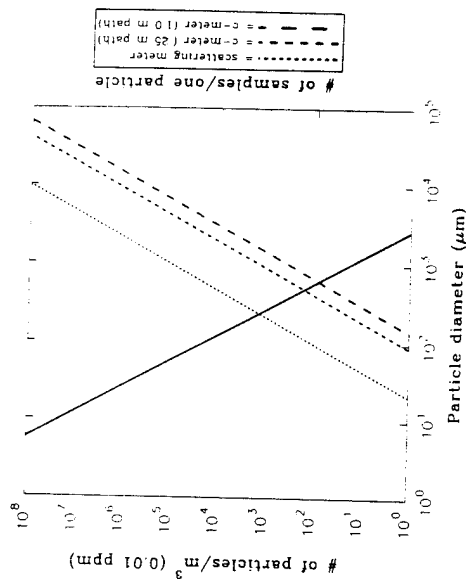

Fig. 13-1. Number of particles m^{-3} (solid line, left ordinate) using Sheldon et al. (1972) estimate for particle volume/water volume ratio (right ordinate) to expect to capture one particle of a given size: ⋯⋯, scattering matter; ----, c-meter (0.25 m path); -----, c-meter (1.0 m path).

particle cross-sectional area per increasing log-size class of only one order of magnitude. One can postulate, then, that at whatever particle size a particular instrument sample volume becomes statistically inadequate (perhaps, 10 μm diameter or less for a scattering meter and 100 μm diameter or less for a c-meter), the next largest log-size class could represent an additional 10% of the potential instrument signal that would not be measured.

While this sampling error may not seem great, the larger size-class particles may have optical effects disproportionate to their spherical-equivalent cross-sectional areas. Larger marine particles, especially large aggregates or marine snow (Alldredge and Silver, 1988) tend to be more complex in shape than smaller particles. This greater degree of complexity would tend to increase the ratio of surface area to volume and change the shape of the volume scattering function, $\beta(\theta)$. In microwave analog experiments Greenberg et al. (1971) found that a "roughened" sphere versus a smooth sphere demonstrated enhanced scattering in all orientations. Furthermore, Zerull and Weiss (1974) found, in a comparison of scattering intensities at angles greater than 10°, that "fluffy" particles scattered nearly an order of magnitude more effectively than smooth particles. This would be especially important for backscattering and reflectance measurements. Hence, despite the reduction of particle numbers by a factor of 10^3 in increasing log-size class and the reduction of total cross-sectional area by an order of magnitude, the optical contribution to c, through b, of the 10–100-μm diameter and the 100-1000 μm diameter size classes could approach the same order of magnitude if "fluffy," marine snow types of aggregates were present in the larger size classes.

must necessarily work in an automated image processing/analysis environment. One approach is discussed later.

Many researchers are involved in the acquisition of image-based data at many different scales. For example, Hammer et al. (1987) describe a system for a three-dimensional (time-multiplexed stereo video) study of fish schooling. Carder et al. (1986) and Costello et al. (1989) describe holographic systems for the study of eolian particles. Honjo et al. (1984) and Asper (1987) describe photographic systems for investigating marine snow. Various aspects of these and other efforts are discussed in Alldredge and Silver (1988). To date, the only selective, intelligent in situ particle observation/collection has been performed by humans utilizing equipment ranging from diving gear to remotely operated vehicles (ROVs) and deep-diving manned submersibles. This is simply because autonomous underwater vehicles (AUVs) optimized for particle research do not, as yet, exist.

We are in the process of modifying a small ROV for large-particle observation and selective collection to act as a test bed for a first-generation AUV, tentatively dubbed the Marine Aggregated Particle Profiling and Enumerating Rover (MAPPER). MAPPER will be a "semi-smart" machine (i.e., programmable and able to respond to external stimuli) and a step toward an eventual artificially intelligent AUV.

Figure 13-2 shows a schematic of the envisioned sample volume for MAPPER as a light-sheet configuration (hence, 90° scattering). Elements of materials of

Fig. 13-2. Marine Aggregated Particle Profiling and Enumerating Rover (MAPPER) optical sample volume configuration (see text).

Under such circumstances, the optical contribution from neither class would generally be adequately measured by a scattering meter, while the latter class would not be adequately measured by a c-meter. Furthermore, because of the nature of these types of instrumentation, there would be zero probability of identifying the large particles, a valuable step when performing model inversions. This would also be the case even for regions having high concentrations of large particles. Hence, even though traditional in situ optical instrumentation may adequately measure the numerically and, generally, optically dominant marine particle classes, the pursuit of model closure and inversion suggests the development of new approaches, especially when considering environments containing large aggregates and animals effecting patchy, schooling types of behavior.

New instrumentation

It is unlikely that existing instrumentation can be simply "scaled up" because of physical limitations, technical considerations, and the critical resultant loss of resolution in measuring the dominant smaller sized particles. This would also not assist in the desired identification of the larger particles. Imaging the large particles, whether it be through photography, holography, video, or some other method, would assist in particle identification and allow the measurement and/or inference of particle optical properties. For example, to first order, the attenuation due to large simple particles can be estimated if the large-particle size distribution is known, since for large particles the attenuation efficiency factor $Q_c \approx 2$ (van de Hulst, 1957). An advantage of continuous, sequential imaging (i.e., video) is that it provides for the behavioral classifications of swimming versus settling and allows the determination of swimming speed for the former and settling speed for the later. For settling particles, if the size and settling speed are known, the dynamic density (which should have some correlation with optical density) can be inferred by inverting the appropriate, shape-dependent, Stokes settling equation (e.g., see Carder et al., 1986; Costello et al., 1989).

Imaging systems

An inherent difficulty in any imaging approach lies in the reduction of massive amounts of information (the images) in order to extract useful data (the particle attributes). A scattering meter or a c-meter, for example, will have two discrete "numbers" corresponding to an instantaneous sample volume (the signal and the reference), while a modest two-dimensional video image, digitized in an image processing environment at a typical $512 \times 512 \times 1$ pixels (low resolution compared to photography and very low resolution compared to three-dimensional holography) will have over 250 000 "numbers" corresponding to an instantaneous sample volume. At normal video frame rates (30 frames/second) this generates nearly one-half billion "numbers" per minute. Thus, any attempt to extract a body of statistically meaningful information from an image data base

$$m_{ij} = \int_{-\infty}^{\infty}\int_{-\infty}^{\infty} x^i y^j \rho(x,y)\, dx\, dy \qquad i,j = 1,2,3\ldots \qquad (13.2)$$

The low-order ordinary moments are especially useful to the extent that m_{10}/m_{00}, m_{01}/m_{00} locate the (x,y) coordinate position for the centroid of the image intensity distribution. Sequential centroid locations, then, can be used in a first-order classification scheme for particles since inanimate particle centroid trajectories would follow the gravitational vector at a constant velocity (settling) relative to water motion, while animated particles would demonstate non-nadir and/or accelerated velocities (swimming).

For this approach to be useful in pattern recognition strategies, however, the sample-space vectors generated must be invariant with object position and/or orientation within the image field. Translational invariance can be achieved by the determination of object centroid (from the first- and zero-order ordinary moments) and then the ordinary moments can be recalculated with the origin of the coordinate field coincident with the object image centroid. This first step toward both translational and rotational invariance, however, can be achieved (and computational time minimized) by transforming the ordinary moments (m_{ij}) into central moments (μ_{ij}), moments relative to the centroid of the object image. Using the notation of Hu (1962):

$$\mu_{00} = m_{00} = \mu \qquad (13.3)$$

$$\mu_{10} = \mu_{01} = 0 \qquad (13.4)$$

$$\mu_{20} = m_{20} - \mu\bar{x}^2 \qquad (13.5)$$

$$\mu_{11} = m_{11} - \mu\bar{x}\,\bar{y} \qquad (13.6)$$

$$\mu_{02} = m_{02} - \mu\bar{y}^2 \qquad (13.7)$$

$$\mu_{30} = m_{30} - 3m_{20}\bar{x} + 2\mu\bar{x}^3 \qquad (13.8)$$

$$\mu_{21} = m_{21} - m_{20}\bar{y} - 2m_{11}\bar{x} + 2\mu\bar{x}^2\bar{y} \qquad (13.9)$$

$$\mu_{12} = m_{12} - m_{02}\bar{x} - 2m_{11}\bar{y} + 2\mu\bar{x}\bar{y}^2 \qquad (13.10)$$

$$\mu_{03} = m_{03} - 3m_{02}\bar{y} + 2\mu\bar{y}^3 \qquad (13.11)$$

where $\bar{x} = m_{10}/m_{00}$, $\bar{y} = m_{01}/m_{00}$.

It is notable that the first-order central moments μ_{10}, μ_{01} are equal to zero under this transformation. This follows intuitively since the first-order "spread" of an object relative to any axis of a coordinate system drawn through its centroid would center about the origin.

---

known reflectance (Spectralon, Labsphere Inc., not shown) and a traditional c-meter are embedded within the light sheet. The light sheet is at the focal plane in the field-of-view of the two large-field video cameras. A third, higher-spatial-resolution video camera focal plane is embedded within the larger image volume to evaluate particles as small as 50 μm diameter that are observed in the c-meter beam within the high resolution field-of-view. In the lower-resolution, large-area camera fields, the pixel resolution is 250 μm.

Depicted in Fig. 13-2 is a large particle in the coincident sample volumes of the c-meter and one of the large-field video cameras. In this scenario, the c-meter would measure some unknown combination of increased/decreased attenuation relative to the small-particle, background level due to a mix of the following mechanisms: (1) absorption, (2) scattering out of the beam, and (3) enhanced scattering in the near-forward direction within the acceptance angle of the instrument. This scattering would contribute to attenuation if this were an "ideal" c-meter. The video image would record the intensity of the 90° side-scatter from the particle (relative to the reference reflector), the size and shape of the particle, and any textural intensity variations caused by particle internal or surface structure. This will enable not only the enumeration of particles by size and shape but also allows an in situ multi-instrument investigation of the optical properties of individual large particles.

MAPPER development is enhanced by utilizing the ROV as a testbed. A light sheet module mounted on the ROV allows experimentation with various lens and camera combinations in different spatial configurations. The ROV is also being utilized in the development of MAPPER control instrumentation (discussed in Costello et. al., 1991) via bidirectional communication multiplexed on the existing ROV video channel. Additionally, the ROV is being used as an independent instrument for the study of large particles. For example, large particles can be actively tracked and stereo views can be acquired using a mirror module and reflected light (near 180° backscatter). This allows an accurate volume determination and an estimate (relative to a standard) of particle reflectivity.

The analysis of the imagery from this or any other large-base imaging system requires an automated image-processing/analysis approach. Furthermore, the inevitable artificially intelligent AUV of the future will require that particle imagery be reduced in near real-time for selective capture to be efficiently implemented. Due to the diversity that marine particles exhibit, the image analysis approach must quickly provide a high degree of information. One method that we have been investigating follows.

Pattern recognition

To describe the distribution of radiance from a particle within an x–y field (i.e., an image), we utilize the method of moment invariants. The two-dimensional (i + j)th order moments of a density distribution function $\rho(x,y)$ are defined in terms of Riemann integrals (proper, bounded) as (Hu, 1962)

These central moments can then be utilized to produce moment functions that possess the desired invariance with rotation and translation. Seven such functions were first formulated by Hu (1962) and are presented here following the form of Dudani et al. (1977):

$$M_1 = (\mu_{20} + \mu_{02}) \tag{13.12}$$

$$M_2 = (\mu_{20} - \mu_{02})^2 + 4\mu_{11}^2 \tag{13.13}$$

$$M_3 = (\mu_{30} - 3\mu_{12})^2 + (3\mu_{21} - \mu_{03})^2 \tag{13.14}$$

$$M_4 = (\mu_{30} + \mu_{12})^2 + (\mu_{21} + \mu_{03})^2 \tag{13.15}$$

$$M_5 = (\mu_{30} - 3\mu_{12})(\mu_{30} + \mu_{12})\left[(\mu_{30} + \mu_{12})^2 - 3(\mu_{21} + \mu_{03})^2\right]$$
$$+ (3\mu_{21} - \mu_{03})(\mu_{21} + \mu_{03})\left[3(\mu_{30} + \mu_{12})^2 - (\mu_{21} + \mu_{03})^2\right] \tag{13.16}$$

$$M_6 = (\mu_{20} - \mu_{02})\left[(\mu_{30} + \mu_{12})^2 - (\mu_{21} + \mu_{03})^2\right]$$
$$+ 4\mu_{11}(\mu_{30} + \mu_{12})(\mu_{21} + \mu_{03}) \tag{13.17}$$

$$M_7 = (3\mu_{21} - \mu_{03})(\mu_{30} + \mu_{12})\left[(\mu_3 + \mu_{12})^2 - 3(\mu_{21} + \mu_{03})^2\right]$$
$$- (\mu_{30} - 3\mu_{12})(\mu_{21} + \mu_{03})\left[3(\mu_{30} - \mu_{12})^2 - (\mu_{21} + \mu_{03})^2\right] \tag{13.18}$$

It is interesting to note that M_7 is a psuedo-invariant function that undergoes a sign change under reflection and, hence, would be useful for recognition of a mirror-image of a cataloged pattern. M_7 would recognize the "front" or "back" of a cataloged pattern and would also be useful for recognition of spatial features such as a right-hand versus a left-hand spiral structure.

Size invariance is more subtle, however, since for the purposes of estimating particle volume, the knowledge of the discrete size of a target particle is not only desirable but necessary. With discrete size and settling speed information, particle dynamic density can be calculated through the inversion of the appropriate (shape-dependent) Stokes settling equation. Since the sample space will necessarily be three dimensional, however, the apparent size (solid angle) of an object will change with a change in position along the axis between the particle and the sensor (optical axis). What is required is "apparent size" invariance, with retention of discrete size information.

The desired "apparent size" invariance can be effected, however, by normalizing M_1 through M_7 in the manner proposed by Dudani et al. (1977). Here, the radius of gyration of an object is defined as

$$r = (\mu_{20} + \mu_{02})^{1/2} \tag{13.19}$$

and

$$r \cdot B = \text{constant} \tag{13.20}$$

(where μ_{20} and μ_{02} are second order central moments and B is the axial distance of the object from the sensor) since the radius of gyration of an object would be *directly* proportional to the mean image diameter and *inversely* proportional to the distance of the object along the optical axis. Then,

$$M'_1 = (\mu_{20} + \mu_{02})^{1/2} \cdot B = r \cdot B \tag{13.21}$$

$$M'_2 = M_2/r^4 \tag{13.22}$$

$$M'_3 = M_3/r^6 \tag{13.23}$$

$$M'_4 = M_4/r^6 \tag{13.24}$$

$$M'_5 = M_5/r^{12} \tag{13.25}$$

$$M'_6 = M_6/r^8 \tag{13.26}$$

$$M'_7 = M_7/r^{12} \tag{13.27}$$

Although M'_2 through M'_7 are now independent of object distance, this normalization method requires a priori knowledge of B for the utilization of M'_1. In our deployment configuration B will be the focal length of the imaging system where the light sheet is located, and hence it will be known. For stereoscopic and holographic systems, B can be derived from the imagery.

The rotational, translational, and size invariance of the computer code generated to implement Eqs. (13.2–13.27) was tested by the analysis of 15 image fields. An "L"-shaped binary "object" was generated proportionately in four different sizes and placed in fields of four sizes, resulting in eight combinations of image-to-field size. The shapes were translated, rotated, translated and rotated, placed in disproportionately sized fields (which equates to axial displacement), and all of these.

The central moments to third order and functions M_1 through M_7 were first generated for each field without size normalization using the radius of gyration. Results show that the method is invariant for translation, rotation, and reflection but that the algorithm could not identify the same discretely sized object located in fields of differing size. After size normalization was incorporated into the algorithm, the desired size invariance was achieved. Also, function M'_7 did change sign for the mirror-image test fields.

It must be noted that this set of tests was conducted on "ideal" image data; that is, with an image field data array that was digitally initialized with discrete values (no error). The tests did show, however, that a digital representation of an object shape can be uniquely described with the software developed, regardless of the position and/or orientation of the object in the image field.

To test the utility of the method for actual marine particles, the images of marine animals and aggregates recorded in situ in a sediment trap in the
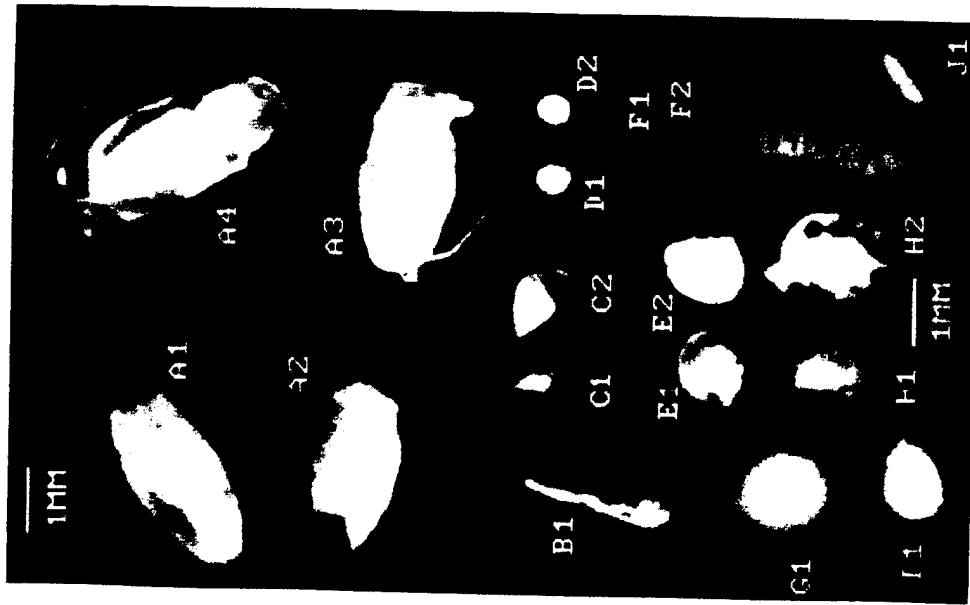
Fig. 13-3. Test images used for verification of pattern recognition strategy.

subtropical North-central Pacific were analyzed. The methodology used in recording the images is discussed in Costello et al. (1989). The pattern recognition (PR) algorithm was applied to the images of 18 marine particles shown in Fig. 13-3 (one group of four, five pairs, and four individuals). To effectively "classify" these images, the PR algorithm must generate classification parameters (feature vectors) that are similar on an intragroup and dissimilar on an intergroup basis. Twelve factors each were generated by operating on the target

silhouette (low-frequency information), target outline (high-frequency information), and the full 8-bit image of the target which includes a contribution from any interior structure. The 12 factors were as follows: the zero-order central moment (image power); the seven normalized invariant moment functions (Eqs. 13.21 through 13.27) as first formulated by Hu (1962) with the size normalization as proposed by Dudani et al. (1977); and the following four moment-generated elliptical classification factors as developed by Teague (1980).

$$\alpha = \left(\frac{2\{\mu_{20} + \mu_{02} + [(\mu_{20} - \mu_{02})^2 + 4\mu_{11}^2]\}^{1/2}}{\mu_{00}} \right)^{1/2} \tag{13.28}$$

$$\zeta = \left(\frac{2\{\mu_{20} + \mu_{02} - [(\mu_{20} - \mu_{02})^2 + 4\mu_{11}^2]\}^{1/2}}{\mu_{00}} \right)^{1/2} \tag{13.29}$$

$$\Gamma = \tfrac{1}{2}\tan^{-1}(2\mu_{11}(\mu_{20} - \mu_{02})^{-1}) \tag{13.30}$$

$$F = \mu_{00}/\pi\alpha\zeta \tag{13.31}$$

These factors characterize any image as a constant intensity ellipse with intensity F inside and zero outside, defined major axis α, minor axis ζ, and angular orientation Γ within the two-dimensional coordinate field. The method is also computationally attractive since it requires the computation of moments to only second order.

Figure 13-4 depicts three-dimensions of the 36 dimensions available in our classification space and shows how an appropriate classification (separation) of the group, pairs, and individuals is effected in a three-dimensional classification space even though some are not distinguishable in one or both of the two-dimensional classification planes. Two of the classification factors depicted, M'_1 and M'_2 (Eqs. 13.21 and 13.22) are, in fact, normalized forms of the classification factors (X and Y) originally used by Hu (1962) in his study of automatic alphabetic character recognition. The third factor, α (Eq. 3.28), is a convolved, weighted summation of the other two factors. To our knowledge this approach to the combination of shape recognition factors is unique in that it utilizes highly shape-discriminate factors (the moment invariant functions) as well as factors that emphasize general shape and optical image power (the elliptical factors). Although further work with additional in situ images is required, it appears that the method can adequately address the shape-diverse and the shape-amorphous nature of marine particles. Because of the computationally intensive nature of machine vision and pattern recognition, further work with additional in situ images is also required for the determination of the value and utility of the information content specific to each of the 36 available classification dimensions. However, the method has proven invariant to target translation, rotation, and

they are located and imaged. This requires the development of new, large-volume, in situ instrumentation to augment traditional small-particle methods. The large volume of data required to understand the temporal and spatial distributions of various particle classes demands an automated classification and analysis method.

We are developing a new instrument, MAPPER, to enumerate and image individual particles at rapid sampling rates (on the order of hundreds of liters per minute). To address the large quantity of imagery expected, a classification and analysis scheme based on the method of moment invariants has been developed and presented. Any pattern recognition/classification method is most effective when the particles under analysis exhibit a high degree of intraclass similarity and interclass diversity. However, some types of marine particles (e.g., marine snow and other aggregates) would be generally amorphous to traditional classification schemes. A variation of the method (Teague, 1980) has also been incorporated that will have utility in the study of these generally amorphous types of particles. The utility of this approach for the classification of aggregated particles lies in the retention of the ability to discriminate between the dominant aggregate shapes (chain, comet, elliptical, spherical, etc.) with the quantification of individual particle backscattering or sidescattering (depending on deployment configuration).

Since remote sensing reflectance R_{rs} is highly backscattering-dependent, and the backscattering and sidescattering coefficients are similar (Petzold, 1972), both the MAPPER and the ROV deployment configurations will enhance the interpretation of R_{rs}. This information, when combined with large-particle classification and enumeration constitutes a requisite step toward optical model closure and inversion for a significant part of the world ocean.
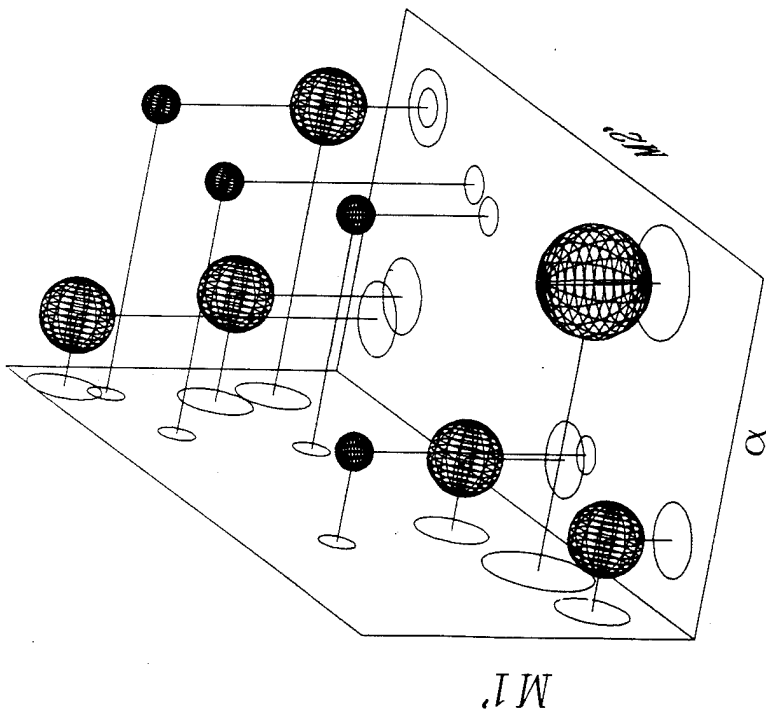

Fig. 13-4. Schematic depicting three dimensions of our 36-dimensional classification strategy. Groups or individuals not resolved in either of the classification planes shown are resolved in the intersection of the planes.

"apparent" size and has successfully classified (separated) computer-generated test patterns, alphanumeric characters, and images of marine particles acquired in situ. Further, image power can be related to $\beta(90°)$, image size can be used to determine the large-particle ends of size distributions, and size and shape can be used to estimate c values for comparison with c-meter perturbations.

Summary

One of the research areas which requires further exploration in the effort toward marine optical model *closure and inversion* is the effect of large particles on the underwater light field. The temporally and spatially variable concentration (and, hence, optical effect) of large particles demands an understanding of not only the size and number but also the optical nature of the individual particles. The macroscopic size of the particles allows their study on an individual basis once

Determination of Saharan Dust Radiance and Chlorophyll From CZCS Imagery

K. L. Carder,[1] W. W. Gregg,[1,2] D. K. Costello,[1] K. Haddad,[3] and J. M. Prospero[4]

An atmospheric correction algorithm is derived for oceanic areas of low chlorophyll a plus phaeophytin a concentrations ($\langle C \rangle \leq 0.25$ mg/m^3). The algorithm simultaneously corrects for the radiance effects of two different aerosol types observed in coastal zone color scanner (CZCS) imagery. The algorithm, called the two-component method, is applied to data from a time series of CZCS orbits during which both Saharan dust and a bluish haze were present. The method is evaluated by comparing the ocean chlorophyll concentrations after atmospheric correction to those measured in situ and to those determined by single-component methods from CZCS imagery. Reasonable agreement is found between the chlorophyll values estimated by the two-component method and in situ values, and the derived chlorophyll values for a Sargasso Sea region varied by less than 6% during a major influx of Saharan dust to the region. Aerosol and chlorophyll fields appeared confounded in imagery derived using single-component methods when multiple aerosol types were present, but no confounding was observed for imagery generated by the two-component method. The time series of aerosol radiance values due to Saharan dust was consistent with the changes in dust concentration and particle size measurements from an adjacent aerosol collection site on the Florida coast.

1. Introduction

Scattering by aerosols represents an important optical component of the atmosphere, which must be removed from Coastal Zone Color Scanner (CZCS) imagery before water-leaving radiances, and hence chlorophyll, may be determined. Furthermore, because of the temporal and spatial variability of the aerosol concentrations and their optical characteristics the proportion of the total radiance observed by the sensor which is due to aerosol scattering cannot be estimated and removed a priori as can Rayleigh scattering.

Up to 90% of the total radiance received at the CZCS sensor for most cloud-free scenes is due to the intervening atmosphere [Gordon et al., 1983a]. Aerosol scattering may be responsible for 10–40% of the radiance. Yet the success of the CZCS atmospheric correction algorithms in estimating and subsequently removing these atmospheric effects is evident from their ability to determine the water-leaving radiance within about 10% for much of the world ocean and chlorophyll concentrations to within 30–40% [Gordon et al., 1983a].

This accuracy is subject to some qualifications, however. The atmospheric correction algorithms have been most accurate during the first year (1978–1979) of CZCS operation before sensor degradation became significant and are most successful where a single aerosol type exists. Multiple aerosol types present in the same scene can confound these single-component atmospheric correction algorithms. Such a situation occurs with Saharan dust events. Major outbreaks of Saharan dust aerosols can be present as far west as Miami, Florida, especially during June, July, and August

[Prospero and Carlson, 1972; Savoie and Prospero, 1977; Carder et al., 1986]. Saharan dust differs in its spectral reflectance characteristics from the marine (sea salt) aerosols, and bluish hazes that are often present. A bimodal size distribution for marine aerosols (hydrated sea salts) has been observed, with the concentration and modal diameter for the larger fraction increasing with wind speed [Patterson et al., 1980]. While the submicron fraction may exhibit blue-rich scatter, the scatter for the dominant large-particle fraction is not expected to be spectral. Near land, where small-particle sources are important [Patterson et al., 1980], modified maritime hazes may exhibit blue-dominant scattering. In addition, small particles may be important above the marine boundary layer. Scattering by Saharan dust, which can contain rather large particles (volume distribution mode for this study was between 4 and 8 μm diameter [Carder et al., 1986]), is unlikely to exhibit spectral scattering unless spectral absorption is significant. These aerosols absorb more strongly in the blue wavelengths [Patterson, 1981], however, and are consequently reddish-brown in color [Prospero and Carlson, 1972].

In this paper we present an algorithm to distinguish two aerosol types in an image and then determine their relative concentrations by observing the radiance contribution from each type at the satellite. The algorithm builds on the clear water radiance theory [Gordon and Clark, 1981] in which the water-leaving radiance values for all CZCS channels except the blue (443 nm) can be designated a priori when chlorophyll concentrations are less than 0.25 mg/m^3. Such is often the case in the summer away from coastal areas. We demonstrate the effectiveness of the "two-component" method by observing a time series of CZCS images in late June 1980 when an outbreak of Saharan dust passed over Florida. During this period, chlorophyll pigment concentrations were measured in the western Sargasso Sea, and crustal aerosol concentrations, sizes, and chemical characteristics were determined at a coastal site near Miami, Florida.

This study has relevance to the Global Backscatter Experiment (GLOBE) and the Laser Atmospheric Wind Sounder (LAWS) activities because it presents a method that can be

[1]Department of Marine Science, University of South Florida, St. Petersburg.
[2]Now at Research and Data Systems, Greenbelt, Maryland.
[3]Marine Research Laboratory, Florida Department of Natural Resources, St. Petersburg.
[4]Rosenstiel School of Marine and Atmospheric Science, University of Miami, Miami, Florida.

applied to the existing CZCS data set to provide statistics on the spatial and temporal extent of high-backscattering dust particles. Furthermore, the methodology is applicable to future data sets from planned ocean color sensors. Synergistically, the anticipated wind speed and aerosol backscatter data from LAWS will provide information on the height and transport speed of aerosols. These data are valuable to improved interpretation of spectral aerosol radiance imagery from the passive ocean color sensors. Estimates of the flux to the ocean of aeolian aerosols containing such micronutrients as iron are needed to evaluate the potential effect on marine primary productivity [e.g., *Martin and Gordon*, 1988]. Thus Earth-observing system instruments such as the Moderate Resolution Imaging Spectrometer (MODIS), the High Resolution Imaging Spectrometer (HIRIS), and LAWS may together play an important role in providing data to improve such flux calculations.

2. BACKGROUND AND THEORY

The Nimbus 7 satellite is in a sun-synchronous orbit at a nominal altitude of 955 km with ascending node (northward crossing of the equatorial plane) near local noon. The CZCS sensor is a scanning radiometer with a ±39° cross-track scan of the six coregistered spectral channels, four in the visible wavelengths (443, 520, 550, and 670 nm), one in the far red (750 nm), and one in the infrared (10.5–12.5 μm) [*Hovis et al.*, 1980]. The sensor has a ground resolution of 825 m at nadir, and the scan mirror can be tilted up to 20° forward or backward along its ground track to reduce specularly reflected sun glint from the sea surface.

The single-component atmospheric correction algorithm is based on quasi-single-scattering theory and the clear-water radiance technique [*Gordon and Clark*, 1981; *Gordon et al.*, 1983a]. Single-scattering theory allows radiance arising from Rayleigh scattering (L_r), radiance arising from aerosol scattering (L_a), and water-leaving radiance (L_w) to be separated. The clear-water radiance technique utilizes knowledge of the water-leaving radiance of low-chlorophyll sea water at 520, 550, and 670 nm and knowledge of the radiance due to Rayleigh scattering to determine the radiance due to aerosol scattering by measuring the total radiance received at the sensor (L_t) at each of the wavelengths. The water-leaving radiance at 443 nm (the band most sensitive to chlorophyll absorption) can then be determined through spectral extrapolation to 443 nm of the aerosol radiance. Treatment of the Rayleigh and aerosol scattering in a single-scattering sense (e.g., as independent terms) results in errors in aerosol radiance values less than 10% for aerosol optical thicknesses (τ_a) ≤ 0.6 for scenes unaffected by sunglint [*Gordon et al.*, 1983a]. The difference between aerosol radiance calculations made using single-scattering versus multiple-scattering methods increases with aerosol optical thickness, observational zenith angle, and, to a lesser extent, solar zenith angle. However, for aerosol optical thicknesses (τ_a) ≤ 0.6, *Gordon and Castano* [1989] demonstrated that for a wide variety of aerosol types, this difference is linear with L_a and can be determined within 5–8% except at the edges of the CZCS scan. Thus given knowledge of the scan mirror forward tilt angle (e.g., 0° or +20°) and the cross-track scan angle, multiple-scattering estimates of aerosol radiance can be determined from single-scattering calculations of aerosol radiance.

Using the notation and arguments of *Gordon et al.* [1983a] and single-scattering theory, the total radiance $L_t(\lambda)$ received at the satellite can be divided into its components: the radiance values arising from Rayleigh scattering $L_r(\lambda)$, the contribution arising from $L_a(\lambda)$, and the water-leaving radiance $L_w(\lambda)$ diffusely transmitted to the top of the atmosphere $L_w(\lambda)t(\lambda)$ [*Gordon*, 1978; *Tanre et al.*, 1979; *Gordon et al.*, 1983a]:

$$L_t(\lambda) = L_r(\lambda) + L_a(\lambda) + L_w(\lambda)t(\lambda) \qquad (1)$$

Gordon [1978] showed, through comparisons with "exact" multiple-scattering calculations using a number of likely aerosol models, that multiple-scattering effects from the ocean to the satellite could be neglected with an error of about 3% if attenuation of the path radiance was ignored. Note that these path radiance values observed at the satellite implicitly include effects due to ozone absorption.

The contribution of $L_t(\lambda)$ due to Rayleigh scattering can be determined a priori from the sun and spacecraft zenith angles. The diffuse transmittance of the atmosphere, $t(\lambda)$, is considered to be known, since it is primarily a function of Rayleigh and ozone optical thicknesses (τ_r and τ_{0z}) and the satellite zenith angle (θ) and is only secondarily a function of aerosol attenuation, which is dominated by near-forward scattering [*Tanre et al.*, 1979; *Gordon and Clark*, 1981; *Gordon et al.*, 1983a]. This leaves $L_a(\lambda)$ and $L_w(\lambda)$ as the only unknowns in the equation.

The solution to equation (1) is effected by deriving an expression for the ratio of aerosol radiances in CZCS channels 1, 2, and 3 to channel 4, where subscripts denote the channel number and correspond to λ at 443, 520, 550, and 670 nm, respectively.

$$L_a(\lambda_i)/L_a(\lambda_4) = \varepsilon(\lambda_i, \lambda_4)[F_0'(\lambda_i)/F_0'(\lambda_4)] \qquad (2)$$

where

$$\varepsilon(\lambda_i, \lambda_4) = \frac{\omega_a(\lambda_i)\tau_a(\lambda_i)p_a(\theta, \theta_0, \lambda_i)}{\omega_a(\lambda_4)\tau_a(\lambda_4)p_a(\theta, \theta_0, \lambda_4)} \qquad (3)$$

Here, $\omega_a(\lambda_i)$ is the single-scattering albedo of the aerosol (assumed for marine aerosols to be 1.0), $\tau_a(\lambda_i)$ the aerosol optical thickness, and $p_a(\Theta, \Theta_0, \lambda_i)$ is the aerosol phase function. For nonabsorbing aerosols, $\varepsilon(\lambda_i, \lambda_4)$ is a term dominated by the aerosol optical thickness, since phase functions for most likely aerosol models at CZCS observational angles relative to the sun are only weakly dependent upon wavelength [*Gordon*, 1978; *Gordon and Clark*, 1981; *Gordon et al.*, 1983a]. The Θ and Θ_0 are the zenith angles of a pixel to the satellite and sun, respectively. $F_0'(\lambda)$ in equation (2) is the extraterrestrial solar irradiance corrected for absorption by an ozone layer of optical thickness τ_{0z}.

Now, (1) may be expressed as

$$L_t(\lambda_i) - L_r(\lambda_i) - t(\lambda_i)L_w(\lambda_i) = L_a(\lambda_i)$$

$$= S(\lambda_i, \lambda_4)[L_t(\lambda_4) - L_r(\lambda_4) - t(\lambda_4)L_w(\lambda_4)] \qquad (4)$$

where

$$S(\lambda_i, \lambda_4) = \varepsilon(\lambda_i, \lambda_4)[F_0'(\lambda_i)/F_0'(\lambda_4)] \qquad (5)$$

The clear-water radiance theory [*Gordon and Clark*, 1981] is now invoked to determine $L_a(\lambda_i)$ in (4) for each pixel in a small, clear-water region. The epsilon values derived for

spectral bands 2, 3, and 4 using (5) are spatially averaged and used to "type" the aerosol. The basis for the theory is that where chlorophyll a plus phaeophytin a concentrations $\langle C \rangle$ are less than 0.25 mg/m³, the normalized water-leaving radiance $\{L_w(\lambda_i)\}$ at 520, 550, and 670 nm can be designated a priori, within 10%, to be 0.498, 0.30, and <0.015 mW/cm²/μm/sr, respectively, for the CZCS [Gordon and Clark, 1981; Gordon et al., 1983a]. For a given wavelength, $L_w(\lambda_i)$ can be related to $\{L_w(\lambda_i)\}$ through

$$L_w(\lambda_i) = \{L_w(\lambda_i)\}t(\theta_0, \lambda_i)\mu_0 \qquad (6)$$

where $\mu_0 = \cos\theta_0$, and [Gordon and Clark, 1981]

$$t(\lambda) = \exp\{-[\tau_r(\lambda)/2 + \tau_{0z}(\lambda) + (1 - \omega_a(\lambda)F)\tau_a(\lambda)]/\mu_0\} \qquad (7)$$

F is the probability that a photon scattered by an aerosol is directed in a forward direction, and the term $(1 - \omega_a F)\tau_a$ is generally unknown. For typical aerosol models, however, $(1 - \omega_a F) < 1/6$, so for $\tau_a \leq 0.6$ the entire term can be ignored with an error in $t(\lambda)$ of less than 10% for small solar zenith angles [Gordon and Clark, 1981]. Thus $\varepsilon(520, 670)$, $\varepsilon(550, 670)$, and $\varepsilon(670, 670)$ can be determined over clear water and then applied to regions where $\langle C \rangle$ is greater than 0.25 mg/m³. It should be noted that while the aerosol type is fixed by this method, the aerosol concentration may vary.

$\varepsilon(443, 670)$ is determined by a power function [Angstrom, 1964; Gordon and Clark, 1981] with Angstrom exponent $\eta(\lambda_i)$:

$$\varepsilon(\lambda_i, \lambda_4) = (\lambda_i/\lambda_4)^{\eta(\lambda_i)} \qquad (8)$$

and $\eta(\lambda_1)$ is the spectral average of $\eta(\lambda_2)$ and $\eta(\lambda_3)$. This method is usually applied to a 5 × 5 pixel region of a clear-water portion of the scene in order to characterize the spectral nature of the scattering by the aerosol "type" associated with that region. The derived epsilon values are then assumed invariant over the entire scene [see Gordon et al., 1983a]. The "type" of aerosol is thus assumed constant for the entire scene, but the concentration can vary as observed using $L_a(670)$, since at this wavelength, $L_w(670) \approx 0$. The aerosol can also be "typed" pixel by pixel for the entire scene if no region in the scene has $\langle C \rangle \geq 0.25$ mg/m³. This approach is computationally quite expensive, however, and is rarely used.

Chlorophyll a plus phaeophytin a concentrations $\langle C \rangle$ are then determined from the water-leaving radiances by regression equations of the form [Gordon et al., 1983a]

$$\langle C \rangle = A[L_w(\lambda_i)/L_w(550)]^B \qquad (9)$$

We introduce the two-component method, which simultaneously determines the aerosol radiances of two widely different aerosols present in the same clear-water scene. The method follows the single-component model up through (5). However, instead of determining an $\varepsilon(\lambda_i, \lambda_4)$ value for a single aerosol type and applying it to the entire scene, $\varepsilon_j(\lambda_i, \lambda_4)$ values are determined for each of two aerosol types. The method works best if there are different portions of the scene where each aerosol type dominates and can be characterized independently, even though much of the scene contains mixtures of the two types. Thus the aerosol "typing" is of an operational rather than theoretical nature unless additional knowledge of the aerosol spectral characteristics is available.

The $S_j(\lambda_i, \lambda_4)$ values corresponding to the $\varepsilon_j(\lambda_i, \lambda_4)$ values are then calculated by (5) pixel by pixel and placed into a 2 × 3 matrix to determine the aerosol radiances for each component, $L_{aj}(670)$, $j = 1, 2$:

$$\begin{bmatrix} S_1(520, 670) & S_2(520, 670) \\ S_1(550, 670) & S_2(550, 670) \\ 1 & 1 \end{bmatrix} \begin{bmatrix} L_{a_1}(670) \\ L_{a_2}(670) \end{bmatrix} = \begin{bmatrix} L_a(520) \\ L_a(550) \\ L_a(670) \end{bmatrix} \qquad (10)$$

$L_{a1}(670)$ and $L_{a2}(670)$ are the radiances at 670 nm for aerosol types 1 and 2. Each row of the coefficient matrix represents a particular wavelength, while the columns represent the two aerosol types. The method applies only to low chlorophyll waters where $L_w(\lambda_i)$ can be specified for $i = 2, 3, 4$. $\varepsilon_j(\lambda_i, \lambda_4)$ values are determined by selecting regions in the scene where the aerosols are predominantly of one type and individually determinable by the clear-water method of Gordon and Clark [1981]. Thus the only unknowns in (10) are $L_{aj}(670)$ values. The resulting problem is an overdetermined system (10), which is solved by a least squares method using QR factorization [Strang, 1986]. Solution of (10) provides the contribution $L_{aj}(670)$ of each aerosol type to the aerosol radiance at 670 nm.

The radiance contribution of each aerosol type to the total aerosol radiance observed in the blue channel is estimated as

$$L_a(443) = S_1(443, 670)L_{a_1}(670) + S_2(443, 670)L_{a_2}(670) \qquad (11)$$

The chlorophyll pigment concentration $\langle C \rangle$ is determined by solving (4) for $L_w(433)$ and $L_w(550)$ and substituting in [Gordon et al., 1983a]

$$\langle C \rangle = 1.13[L_w(443)/L_w(550)]^{-1.71} \qquad (12)$$

3. METHODS

Calibrated radiance and temperature tapes (CRTT) for five sufficiently cloud free CZCS images in late June 1980 were obtained from NASA for processing and comparison with ship and coastal data collected when a major Saharan dust event was observed over southern Florida [Carder et al., 1986]. These tapes were processed using the Florida Department of Natural Resources Marine Resource Geobased Information System (Gould Concept 32/27 with Comtal display and ELAS applications software). Processing of the imagery was carried out using the revised sensor calibration values for Gain 1 and the revised F_0 values from Table IV of Gordon et al. [1983a]. The sensor calibration equation provided by Gordon et al. [1983b] was used to adjust CZCS calibration as a function of orbit number (time). Spacecraft position and orientation data were provided directly on the CRTTs.

4. RESULTS AND DISCUSSION

On June 19 and 20, 1980, a major influx of Saharan dust into the western Sargasso Sea was recorded at 25°59'N latitude, 75°59'W longitude in holographic microscopy samples of the surface waters and in sediment trap data from 30-m depth [Carder et al., 1982, 1986]. The main pulse of the dust did not begin to arrive at Miami, Florida, until approximately 3 days later. Surface winds for the region were generally weak and from the south, with a more easterly and

TABLE 1. Values for Elements $\varepsilon_j(\lambda_i, \lambda_4)$ for Bluish Aerosols and Saharan Dust for CZCS Orbits in June 1980

	λ, nm	Bluish Aerosol	Saharan Dust
Orbit 8326	443	2.067	0.989
June 17, 1980	520	1.682	1.033
	550	1.330	0.961
	670	1	1
Orbit 8381	443	1.364	0.952
June 21, 1980	520	1.245	1.013
	550	1.130	0.940
	670	1	1
Orbit 8464	443	1.482	0.987
June 27, 1980	520	1.394	1.026
	550	1.119	0.964
	670	1	1
Orbit 8478	443	1.732	0.943
June 28, 1980	520	1.470	1.002
	550	1.246	0.940
	670	1	1
Orbit 8492	443	1.655	0.968
June 29, 1980	520	1.429	1.018
	550	1.185	0.951
	670	1	1

southeasterly component for the upper level winds in the eastern extreme of the study region [Carder et al., 1986].

CZCS imagery for orbit 8326 (June 17, 1980) covering the Florida Straits and western Sargasso Sea is shown in Plate 1. Plate 1 is the color-enhanced, atmospherically uncorrected subscene of orbit 8326, showing Palm Beach, Florida, on the western edge. A strong aerosol gradient is apparent along the eastern edge of Plate 1. The area corresponds to the approximate position of the influx of Saharan dust on this date [Carder et al., 1986]. Analysis of spectral reflectances of Saharan dust captured on filter pads indicated that such aerosols backscattered strongly in the red wavelengths [Patterson, 1981; Prospero and Carlson, 1972], in contrast to the white-scattering marine aerosols and blue-scattering hazes that were likely present in portions of the scene.

Table 1 contains $\varepsilon_j(\lambda_i, \lambda_4)$ values used in the two-component aerosol model (equations 10 and 11)) for the five scenes in late June 1980. Aerosol type 1 (column 2, Table 1) has $\varepsilon_j(\lambda_i, \lambda_4)$ values greater than 1.0, typical of fine hazelike aerosols. It was derived using the single-component clear-water method [Gordon and Clark, 1981] from the imagery just to the east of the Bahamas in Plate 1 for orbit 8326 and from high $\varepsilon_j(\lambda_i, \lambda_4)$ regions for the other images. A mean of $\varepsilon_j(\lambda_i; \lambda_4)$ values from 5 × 5 pixel areas was used to minimize the effect of noise. Aerosol type 2 has epsilon values of <1.0, which would be expected for blue-absorbing aerosols such as Saharan dust. The Saharan $\varepsilon_j(\lambda_i, \lambda_4)$ values were derived from regions of low $\varepsilon_j(\lambda_i, \lambda_4)$ and relatively high $L_a(670)$ for each scene. Care was taken to avoid the eastern and western edges of the scenes because the validity of the single-scattering assumption decreases at the limbs of the CZCS scan [see Hovis et al., 1980; Gordon and Castano, 1987].

Saharan Aerosol Radiance Variations

Five sufficiently cloud free CZCS images were atmospherically corrected by the two-component method to generate a
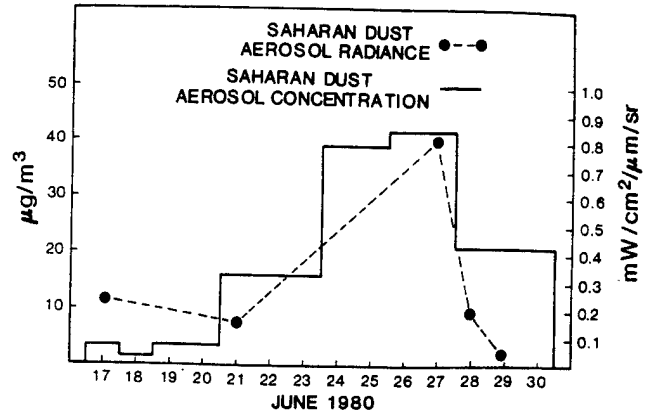

Fig. 1. Comparison of aerosol mass concentration data (2- and 3-day means) from a coastal aerosol collection tower with instantaneous aerosol radiance values for Saharan dust over adjacent waters in the Florida Straits.

sequence of Saharan dust aerosol radiance images at 670 nm ($L_a(670)$). The part of the sequence from June 27 to 29, 1980, clearly shows the movement of the Saharan dust over Florida (yellow-red patches in Plate 2). The dust was centered over the Bahamas by June 27 and just west of south Florida on June 28. By June 29 it was centered over the Yucatan Channel and the Loop Current region of the southeastern Gulf of Mexico.

A 25 × 25 pixel area was selected in the Florida Straits near the coastal, aerosol-filtration site (see small box in Plate 2a) in order to quantify the movement of the Saharan dust over Florida. The time series of dust aerosol radiances corrected for slant-path length is compared for this site with observed aerosol concentrations collected nearby at the University of Miami (Figure 1). These results suggest a covariation between Saharan dust radiance and Saharan dust concentration and demonstrate the ability of the two-component algorithm to identify and monitor blue-absorbing aerosols.

The maximum desert aerosol radiance value progressed westward with time (Plate 2), but the maxima changed little from June 27 to June 29. The desert aerosol radiance values near Miami (Figure 1) decreased markedly after June 27, however, but the aerosol concentration at the base of the air column decreased more gradually with time. This suggests that most of the residual desert aerosols in the air column on June 28 and 29 were in the lower part of the atmosphere where they were available for filtration.

The Saharan aerosol radiance values off Miami from June 17 were likely enriched by anthropogenic aerosols from the Miami area, since the surface winds were from the southwest at that time [Carder et al., 1986]. Such yellowish hazes would be spectrally more similar to Saharan dust than to the blue-rich aerosol haze (see $\varepsilon_j(\lambda_i, \lambda_4)$ values in Table 1) derived from the region northeast of the Bahamas.

The improved correspondence between surface measures of aerosol mass concentration and Saharan aerosol radiance between June 21 and 27 indicates that dust in the marine boundary layer generally covaried with the total column aerosol radiance and that the size distribution was not rapidly changing. It also suggests that between June 21 and 29, the desert aerosol radiance dominated the contributions to total radiance measured at the satellite.

Plate 1. An atmospherically uncorrected subscene of CZCS orbit 8326, June 17, 1980. The red shading indicates Saharan dust (eastern edge), blue indicates bluish haze (center), and yellow-brown indicates coastal aerosols and chlorophyll pigments (Florida Straits). Continuous lines show latitude and longitude.
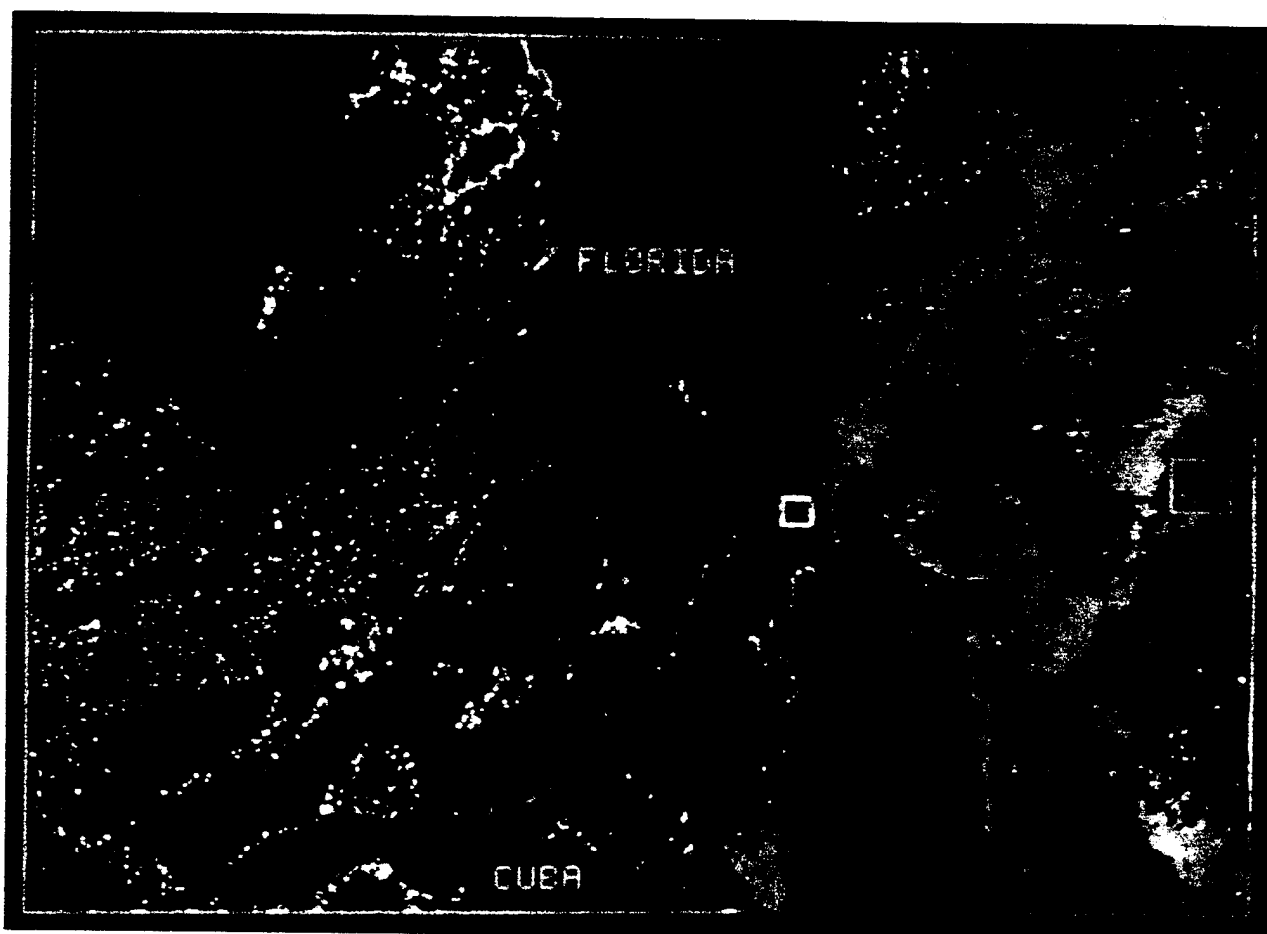

Plate 2a

Plate 2. Time series over Florida of aerosol radiance $L_a(670)$ due to Saharan dust on (a) June 27, 1980, (b) June 28, 1980, and (c) June 29, 1980. Red and yellow shading in each frame indicates the main dust pulse as inferred from the dust aerosol radiances. The color table indicates Saharan dust aerosol radiance values (mW/cm^2/μm/sr). Bright regions (clouds, land, and shoal areas) are masked in black.
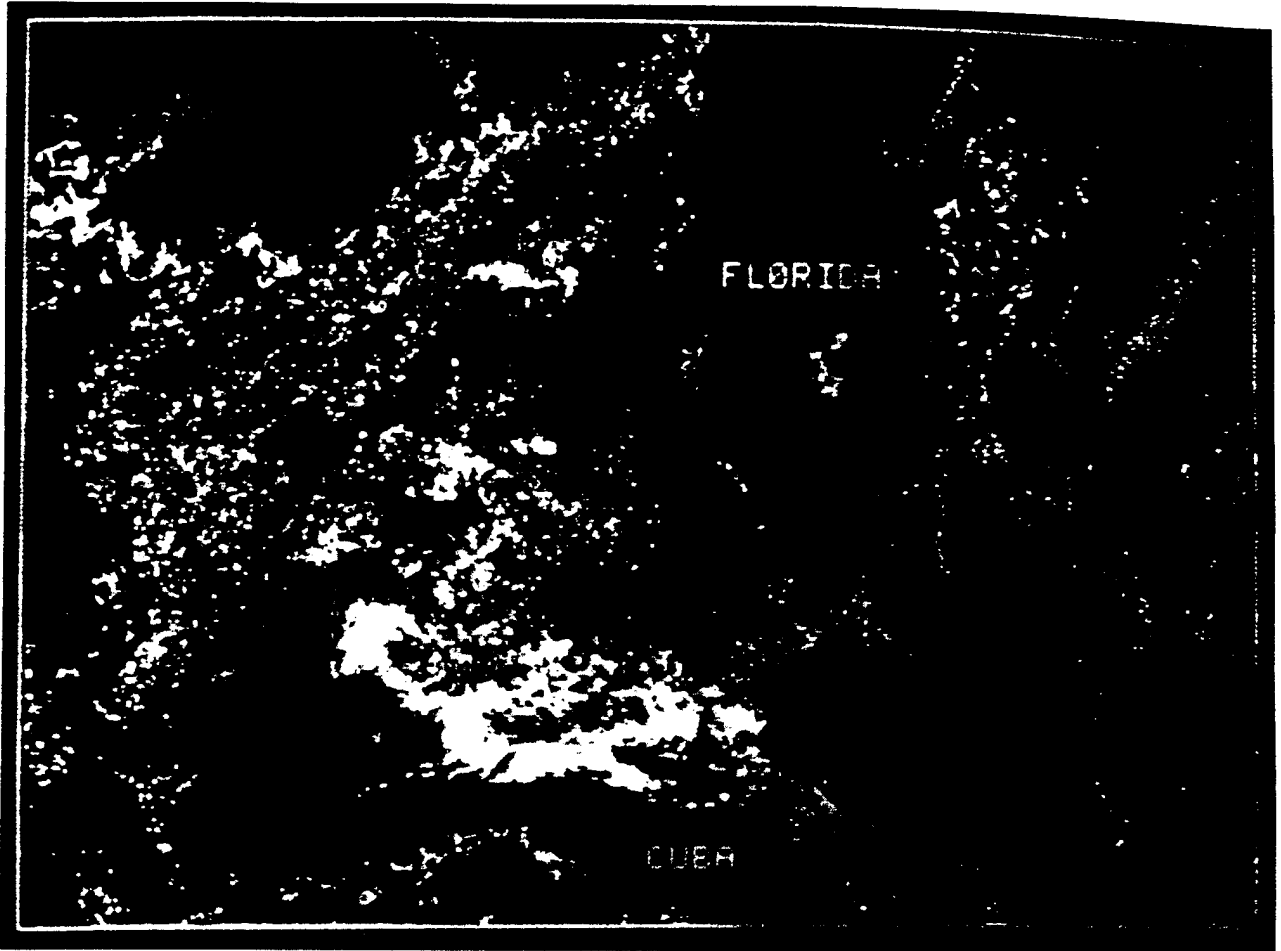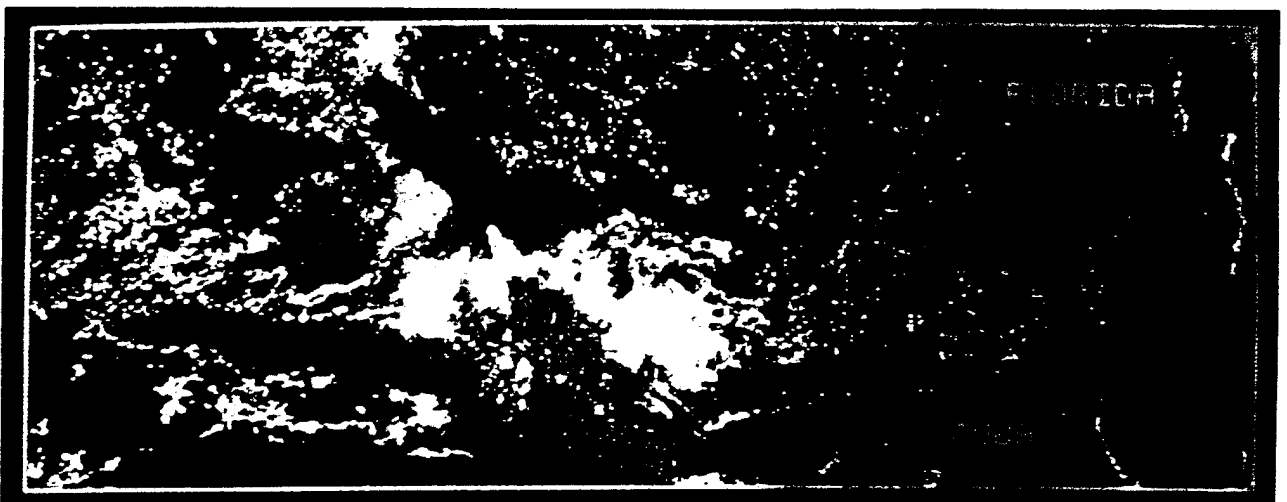
Plate 2b
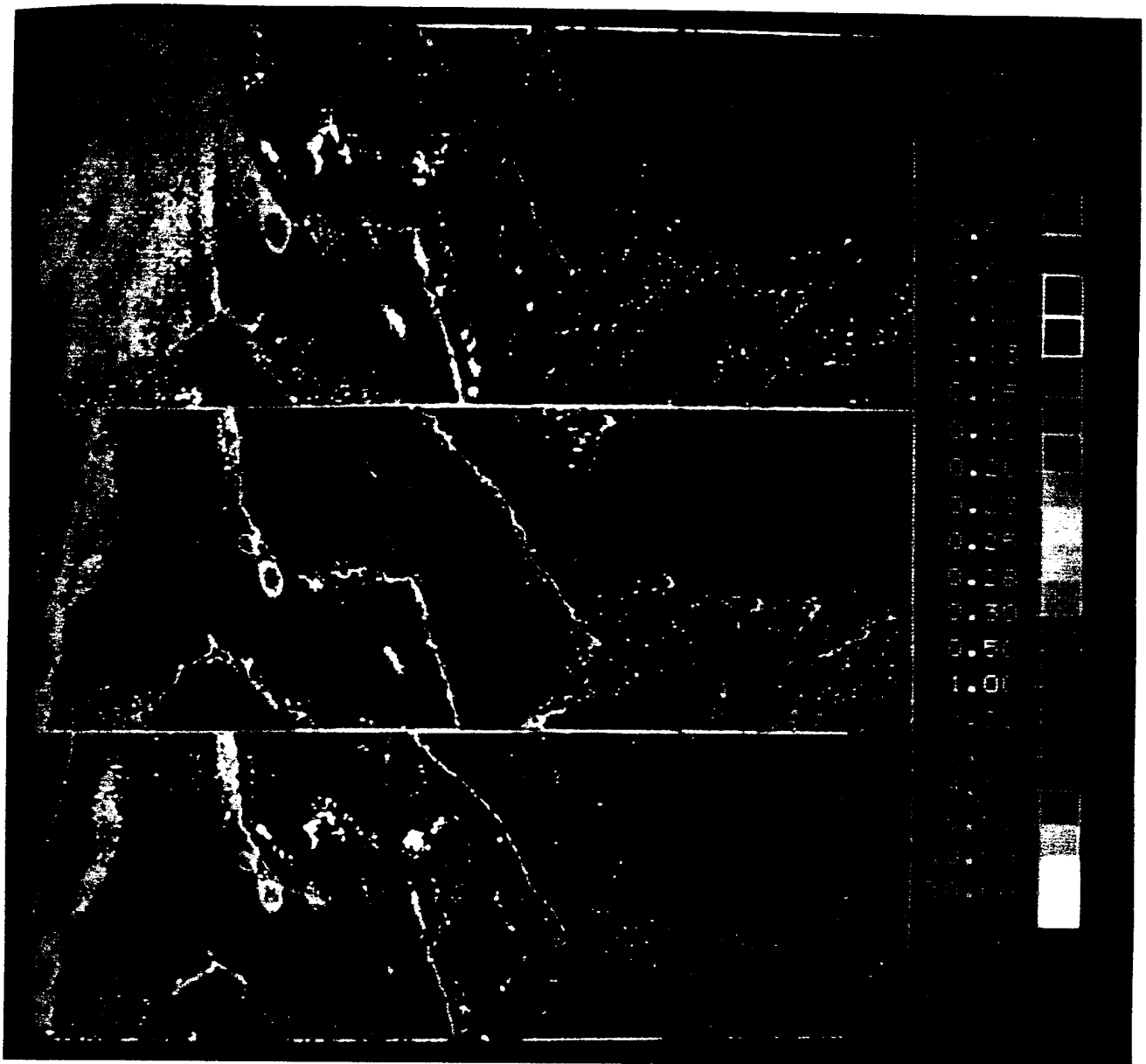

Plate 2c

Plate 2.   (continued)

Plate 3. Chlorophyll pigment concentrations (mg/m^3) after correction for atmospheric effects: (a) Single-component, bluish-haze correction, (b) two-component Saharan dust/bluish haze correction, and (c) single-component, anthropogenic aerosol correction.

Carder et al. [1986] showed that the leading edge of the dust reaching Miami on June 21–23 was large-particle-rich and heavy-mineral-rich compared to the trailing edge of June 27–30. This would indicate that the lead edge of the dust plume should have a lower ratio of dust radiance to unit mass concentration, since the light scattered is proportional to the cross-sectional area for particles which are large relative to the wavelength of light [*Van de Hulst*, 1957] and mass is proportional to the particle volume.

This expectation is confirmed by the radiance/mass ratios: 0.073–0.09 (kW km)/(g μm sr) for June 21 (depending upon whether the nondust aerosol background mass concentration was 0 or 4 μg/m^3) and 0.20 (kW km)/(g μm sr) for June 27. However, if other confounding factors such as variation in the vertical distribution of dust were of only minor importance during this time span, the factor of 2 variation in the radiance-to-mass ratio suggests that the aerosols at the leading edge were roughly twice the diameter of the aerosols at the trailing edge. Mass concentration data of *Carder et al.* [1986] show mode values of 2.5–5.0 μm in diameter for both heavy mineral and non–heavy mineral classes for June 20–23, and modes of 0.5–1.0 μm and 1.0–2.5 μm in diameter for the heavy and non–heavy mineral classes, respectively, for June 25–27. This size change is quite close to that required to explain changes in the radiance-to-mass ratios.

Care must be taken, however, in interpreting total column, single-scattering aerosol radiance values in terms of aerosol concentrations measured at the base of the column. Vertical inhomogeneities in aerosol concentration and type, changes in particle size and specific gravity distributions with time, and variations in the applicability of single-scattering theory with aerosol type, optical thickness, and viewing geometry all contribute uncertainty to any interpretation.

Gordon and Castano [1989] recently demonstrated for a

TABLE 2. Comparison of in Situ Chlorophyll a Plus Phaeophytin a, $\langle C \rangle$

Station	$\langle C \rangle$, mg/m^3			
	In Situ	One-Component Anthropogenic	One-Component Bluish Aerosol	Two-Component Method
1: 25°55'N, 76°00'W	0.045 ± 0.014	0.108 ± 0.013	0.126 ± 0.015	0.080 ± 0.009
2: 26°15'27"N, 79°20'30"W	0.09	0.139 ± 0.021	0.200 ± 0.026	0.148 ± 0.013

Values are determined from CZCS orbit 8326 using the two-component method and the single-component method for each of two different aerosol types.

wide variety of aerosol types that the single-scattering approximation of aerosol radiance (used here) varies linearly with "exact," multiple-scattering calculations of aerosol radiance. The linear relationship is primarily a function of the scan angle for a given mirror tilt (20° in our case). According to their analyses, then, the Saharan aerosol radiance values for June 21 and 27 (Figure 1) are about 5–7% lower than the true, multiple-scattering values would be, and those for June 17 and 28 are about 15–25% too low. Such adjustments to Figure 1 to better simulate true multiple-scattering aerosol radiance values would actually improve the correspondence between the time series sequences for Saharan dust aerosol radiance and concentration.

Chlorophyll Concentrations

Consistency of CZCS-derived chlorophyll determinations before, during, and after Saharan dust passage are observed as an indirect test of the two-component algorithm. After removal of the atmospheric radiance, equation (12) was applied to the water-leaving radiance imagery to derive the pigment concentration $\langle C \rangle$ for June 17, 1980 (orbit 8326) (see Plate 3), for which in situ chlorophyll values were available. Plate 3a shows pigment concentrations resulting from application of the single-component atmospheric correction method. The $\varepsilon_j(\lambda_i, \lambda_4)$ values were derived using the clear-water technique for pixels in an area northeast of the Bahamas which was dominated by a bluish haze (hereafter referred to as the bluish-aerosol method). Plate 3b shows the results of the two-component method. Plate 3c shows the results of the single-aerosol method using a clear-water pixel region in the Florida Straits area near Palm Beach, where haze from the adjacent metropolitan area appears to have been transported by weak southwesterly winds. This will be referred to as the anthropogenic aerosol method.

Comparing this imagery to the total radiance imagery of Plate 1 suggests that pigments in Plate 3a covary with the reddish aerosols in the northeastern portion of the scene and with the anthropogenic aerosols in the Florida Straits near Miami. The two-component method produced a quite uniform chlorophyll field in the Sargasso Sea as one would expect, with no evidence of covariance with the aerosols apparent in Plate 1. The anthropogenic method produces a chlorophyll field much closer to the two-component field except under the reddish aerosols at the eastern and southeastern portions of the image.

In situ chlorophyll measurements are available for the period June 17–21, 1980. Comparison of these measurements with those from 11 × 11 pixel areas from orbit 8326 illustrates the relative accuracies of the methods in determining chlorophyll a plus phaeopigments a $\langle C \rangle$ for different loca-

tions in the scene (Table 2). The locations of the in situ measurements are also identified in Table 2 and can be geolocated using Plate 1. Three of the in situ measurements were made in regions covered by clouds in orbit 8326, so a mean of these values was taken and compared to the nearest cloud-free 11 × 11 pixel area (hereafter referred to as station 1). A significant anomaly in the CZCS-derived pigments due to cloud saturation is typically manifest on the east side of clouds in CZCS data [Mueller, 1988]. To avoid these areas, we selected 11 × 11 pixel areas that were east of any visible saturation effect, at least 10 pixels on the downscan side of clouds, and maintained a border of at least one pixel to the north, south, and west sides of clouds. The other site (station 2) was in the Florida Straits.

The measured chlorophyll values are lower than CZCS-derived values using either the single- or the two-component methods (Table 2). The two-component method overestimates the chlorophyll concentration by 64–78%, while the single-component method overestimates the chlorophyll concentration by 54–140% (anthropogenic aerosol) and by 122–180% (bluish aerosol). The performance of the single-component anthropogenic method improved when the region observed was covered by an aerosol with epsilons that were similar in type to the anthropogenic epsilon values (e.g. in the Florida Straits). There were no in situ chlorophyll stations in an area covered with bluish aerosols, such as northeast of Grand Bahamas Island. As a result, tests of chlorophyll retrievals using the bluish aerosol, single-component method under ideal conditions were not possible.

The two-component method provided consistent results, and in addition, its performance was independent of location and of aerosol type(s). It provided results nearly as good as those of the single-component method specifically calibrated through epsilon selection for the study or comparison area, and its use did not manifest the severe deterioration in performance exhibited by single-component methodologies applied to regions containing aerosols with epsilon values dissimilar to those of the calibration area.

To check for scene-to-scene consistency of chlorophyll values as the Saharan dust cloud moved across the Sargasso Sea, a 51 × 51 pixel region northeast of Grand Bahamas Island (large box in Plate 2a) was monitored from June 17 to 28, 1980, using the two-component method. Table 3 shows mean chlorophyll values of 0.0875 ± 0.005 mg/m^3 (constant within 6%) for that period, even though the aerosols varied from bluish, hazelike epsilons on June 17, to reddish Saharan dustlike epsilons on June 27. During this period, Saharan aerosol radiance values ranged from 0.0716 to 1.1458 mW/cm^2/μm/sr. This clear-water region was not in the field of view of the CZCS on June 29.

TABLE 3. Time Series of Chlorophyll *a* Plus Phaeophytin *a* Concentrations Before, During, and After a Saharan Dust Event

Date (Orbit)	Saharan Dust Aerosol Radiance, mW/ cm^2/μm/sr	Pigment, mg/m^3
June 17, 1980 (8326)	0.0716 ± 0.04085	0.078 ± 0.0066
June 21, 1980 (8381)	0.9258 ± 0.17065	0.099 ± 0.0084
June 27, 1980 (8464)	1.1458 ± 0.10426	0.088 ± 0.0071
June 28, 1980 (8478)	0.3283 ± 0.25879	0.085 ± 0.0074

Concurrent aerosol radiances at 670 nm determined from the same subscene are also shown. Mean values for a 51 × 51 pixel subregion of the Sargasso Sea are listed.

The lowest chlorophyll *a* plus phaeophytin *a* values measured for the northern Sargasso Sea and Gulf Stream during a CZCS validation cruise in June 1979 were 0.05–0.09 mg/m^3 [*Gordon et al.*, 1983b], values consistent with our measured values of 0.045 and 0.09 mg/m^3. The upper end of this range is also consistent with our 4-day mean value of 0.0875 mg/m^3 which was determined by the two-component method northeast of the Bahamas, a region expected to contain waters with very low chlorophyll pigment values. Thus it appears that the CZCS-derived values of Tables 2 and 3 are biased high by about 0.04 mg/m^3. To estimate the decay in radiometric sensitivity for the CZCS blue channel, *Gordon et al.* [1983b] assumed that the lowest summer chlorophyll *a* plus phaeophytin *a* values for the Sargasso Sea region was about 0.09 mg/m^3. A pigment estimate was required for the imagery used in these analyses in order to estimate water-leaving radiance values for this pigment-sensitive band. This conservative selection is about 0.04 mg/m^3 higher than the lowest values measured both in summer 1979 and in summer 1980. This assumed value also turns out to be very close to our derived mean value (Table 3). It is possible that by using, as we did, the *Gordon et al.* [1983b] calibration values derived from their study of the sensitivity decay of CZCS blue channel, we have been limited to retrievals for $\langle C \rangle$ that are no lower than top end of the 0.05- to 0.09-mg/m^3 range expected for the Sargasso Sea during the summer. This may explain at least some of the overestimation in $\langle C \rangle$ observed using single- and two-component aerosol radiance methodologies in determining chlorophyll concentrations for the Sargasso Sea.

The two-component method appears to have spectrally separated Saharan dust radiance contributions to the total aerosol radiance detected with the CZCS from those due to a bluish haze always present in the low-wind scenes that were investigated. The spectral characteristics of these two aerosol components were quite distinct (Table 1), which must have aided in the spectral classification process. The surface winds were very light during most of this period, suggesting that large-diameter, whitish marine aerosols were likely not providing a significant scattering contribution to the aerosol radiance during the study. The epsilon values expected for such aerosols would be close to 1.0, so it is possible that during periods of high wind the aerosol radiance due to large marine aerosols could be classified by the technique as "Saharan dust." Such a misclassification would be less likely for Saharan dust found much closer to its source, however, since very "red" epsilon values of as

low as 0.3–0.4 have been observed over the Atlantic off the coast of north Africa (A. Morel, personal communication, 1989). The form of the spectral extrapolation function for such strongly absorbing aerosols would likely require a change from an Angstrom exponential form (equation (8)) to some other form. A linear form is suggested by the linear decrease with wavelength (from 430 nm to 620 nm) of the imaginary part of the index of refraction for Saharan dust captured on filter pads [see *Patterson*, 1981].

5. CONCLUSIONS

During the latter half of June 1980 a major influx of Saharan dust passed over the western Sargasso Sea and the southern part of the Florida peninsula. During much of this period of time, CZCS imagery exhibited sharply defined frontal boundary features in the atmosphere, with a bluish, hazelike character on one side and a slightly reddish, turbid appearance on the other. To smoothly remove atmospheric radiance effects in order to view the ocean without a significant residual atmospheric signature in the water-leaving radiance field, a method was required to remove aerosol radiance effects due to more than a single aerosol component or type.

A two-component method for spectrally separating Saharan dust and bluish haze contributions to the total aerosol radiance was developed and applied, resulting in dust aerosol radiances that were consistent as a function of time with the dust concentration and size changes observed at a nearby field station. Furthermore, covariance between chlorophyll and aerosol radiance fields was not evident in the imagery. As a result, chlorophyll pigment (chlorophyll *a* plus phaeophytin *a*) concentration values extracted by the two-component technique were stable (0.0875 ± 0.005 mg/m^3) over time for a region of the Sargasso Sea over which the aerosol radiance values changed from those characteristic of a bluish haze to those of a turbid, reddish dust. With this method the CZCS-derived chlorophyll values for this region were consistent with CZCS-derived and field values for the clearest waters of the northern Sargasso reported for the prior year (0.05–0.09 mg/m^3) but were some 64–78% higher than synoptically measured values.

The chlorophyll pigment values determined using a single-aerosol, CZCS method overestimated chlorophyll pigment concentrations by 54–180%, depending upon the aerosol type in the portion of the scene under comparison. For epsilon values (aerosol types) consistent with the aerosol resident in the study area the single-component method performed as well as did the two-component method. However, for regions with mixed aerosol types, or epsilons no longer consistent with the resident aerosol, the single-component method delivered values that were no longer consistent with either historical or measured numbers. While the two-component method provided relatively stable chlorophyll pigment values which were insensitive to the aerosol type resident in the region, the 50–80% enrichment or high bias apparent for both methods may be attributable to an assumption used in estimating the reduction of sensitivity for the blue channel of the CZCS with time since launch: that the chlorophyll pigments for the clearest part of the northern Sargasso Sea were 0.09 mg/m^3. This number is very close to the value derived from the two-component method. The blue channel plays no role in the derivation of aerosol spectral

characteristics or epsilon values using the clear-water radiance methodology, so the chlorophyll assumption listed above had no effect on any of the aerosol radiance values reported.

Since aerosol radiance is a characteristic of the total air column, it provides a different kind of information than is provided by single-point aerosol measurements (aircraft or ground station). Passive spectral radiometry from satellites provides broad and repeat coverage that can complement data provided by both the GLOBE and LAWS missions, especially if the source of each general spectral type of aerosol in the scene can be inferred from ancillary information. GLOBE and future LAWS data will reveal the vertical structure of backscattering by the larger particles, and CZCS, Sea-WiFS, MODIS, and HIRIS data can provide the spectral character of the total column backscattering, suggesting probable aerosol types and possible sources for them. Horizontal and vertical aerosol fluxes may ultimately be estimated from contemporaneous and sequential MODIS and LAWS imagery combined with aircraft and ground station sampling of aerosol size and composition.

REFERENCES

Angstrom, A., The parameters of atmospheric turbidity, *Tellus, 16,* 64, 1964.

Carder, K. L., R. G. Steward, and P. R. Betzer, In situ holographic measurements of the sizes and settling rates of oceanic particulates, *J. Geophys. Res., 87,* 5681–5685, 1982.

Carder, K. L., R. G. Steward, P. R. Betzer, D. L. Johnson, and J. M. Prospero, Dynamics and composition of particles from an aeolian input event to the Sargasso Sea, *J. Geophys. Res., 91,* 1055–1066, 1986.

Gordon, H. R., Removal of atmospheric effects from satellite imagery of the oceans, *Appl. Opt., 17,* 1631–1636, 1978.

Gordon, H. R., and D. J. Castano, Coastal zone color scanner atmospheric correction algorithm: multiple scattering effects. *Appl. Opt., 26,* 2111–2122, 1987.

Gordon, H. R., and D. J. Castano, Aerosol analysis with the coastal zone color scanner: A simple method for including multiple

Gordon, H. R., and D. K. Clark, Clear water radiances for atmo spheric correction of coastal zone color scanner imagery, *Appl Opt., 20,* 4175–4180, 1981.

Gordon, H. R., D. K. Clark, J. W. Brown, O. B. Brown, R. H. Evans, and W. W. Broenkow, Phytoplankton pigment concentrations in the Middle Atlantic Bight: Comparison of ship determinations and CZCS estimates, *Appl. Opt., 22,* 20–36, 1983a.

Gordon, H. R., J. W. Brown, O. B. Brown, R. H. Evans, and D. K. Clark, Nimbus 7 CZCS: Reduction of its radiometric sensitivity with time, *Appl. Opt., 22,* 3929–3931, 1983b.

Hovis, W. A., et al., Nimbus-7 coastal zone color scanner: System description and initial imagery, *Science, 210,* 60–63, 1980.

Martin, J. H., and R. M. Gordon, Northeast Pacific iron distribution in relation to phytoplankton productivity, *Deep Sea Res., 35,* 177–196, 1988.

Mueller, J. M., Nimbus-7 CZCS: Electronic overshoot due to cloud reflectance, *Appl. Opt., 27,* 438–440, 1988.

Patterson, E. M., Optical properties of crustal aerosol: Relation to chemical and physical characteristics, *J. Geophys. Res., 86,* 3236–3246, 1981.

Patterson, E. M., C. S. Kiang, A. C. Delaney, A. F. Wartburg, A. C. D. Leslie, and B. J. Huebert, Global measurements in remote continental and marine regions: Concentrations, size distributions, and optical properties, *J. Geophys. Res., 85,* 7361–7376, 1980.

Prospero, J. M., and T. N. Carlson, Vertical and areal distribution of Saharan dust over the western equatorial North Atlantic Ocean, *J. Geophys. Res., 77,* 5255–5265, 1972.

Savoie, D. L., and J. M. Prospero, Aerosol concentration statistics for the northern tropical Atlantic, *J. Geophys. Res., 82,* 5954–5964, 1977.

Strang, G., *Introduction to Applied Mathematics,* 758 pp., Wellesley-Cambridge Press, Wellesley, Mass., 1986.

Tanre, D., M. Herman, P. Y. Deschamps, and A. deLeffe, Atmospheric modeling for space measurements of ground reflectances, including bidirectional properties, *Appl. Opt., 18,* 3587–3594, 1979.

Van de Hulst, H. C., *Light Scattering by Small Particles,* 470 pp., Dover, New York, 1957.

K. L. Carder and D. K. Costello, Department of Marine Science, University of South Florida, 140 Seventh Avenue, South, Saint Petersburg, FL 33701.

W. W. Gregg, Research and Data Systems, Greenbelt, MD 20770.

K. Haddad, Marine Research Laboratory, Florida Department of Natural Resources, Saint Petersburg, FL 33701.

J. M. Prospero, Rosenstiel School of Marine and Atmospheric Science, University of Miami, Miami, FL 33149.

State of the Art Instrumentation for Measuring Ocean Aggregates

by

Kendall L. Carder, David Costello, and Robert G. Steward

Introduction

Ocean aggregates, by their very nature, are more difficult to measure accurately than nonaggregated particles in a laboratory. They can be extremely friable and are easily disintegrated. Shear forces as small as 0.2 dyn cm^{-2} can break apart loosely associated, high order estuarine aggregates (Krone, 1976). Their size and shape may also change by colliding with other particles in the water column or on surfaces of vessels used in the sampling or measurement processes. Fresh biologically aggregated fecal pellets can often be handled repeatedly without disintegration. Older, biochemically altered pellicles, on the other hand may be quite friable.

Because of the susceptibility of aggregates to modifications in size, shape, and other properties prior to or during measurement, certain in situ techniques provide inherently less intrusive measurements of aggregates than do laboratory methods. Also, because of the heterogeneity of particle size and composition in the ocean, methods that extract individual particle characteristics or properties from the measurements are inherently superior to bulk measurements. As

a result, the major portion of this review will concentrate on in situ methods for measuring individual particles, or laboratory measurements that might be adapted to in situ applications.

Physical Structure

Perhaps the most fundamental measurement of particle size is volume, which does not require a shape discriminator. Because of this, the sphere-equivalent diameter or radius of a particle is often used as a de facto particle size standard. Thus, instruments that measure volume directly (e.g. by use of particle electrical resistivity methods) provide particle volume data unbiased by shape. Unfortunately, these methods draw particles through a small oriface in a dielectric tube, often disrupting aggregates.

On the other hand, particle shape is very important for purposes of identifying or categorizing particles, calculating their drag, surface area, settling speed, optical properties and diffusion. Mathematical relationships among size categories (e.g. major and minor axes, perimeter, cross-sectional area, surface area, volume) can be provided given a general shape category for a particle. Because of the dependence of scattering and absorption coefficients on the areal cross section of particles projected normal to the incident light, for example, the shape and orientation of a particle also have significant effects upon optical measurements of a particle. Shape and orientation are also quite important to particle settling dynamics, especially for noncompact particles (Lerman, 1979).

132

Internal Structure

The internal structure of a particle is also important to its settling dynamics and its microscopic identification. For solid particles such as mineral grains and most fecal pellets, the internal mass distribution or mass density directly affects settling speed. Knowledge of particle density permits the general classification of ocean particles into heavy mineral, nonheavy mineral, fecal pellet, and other categories. It also permits the calculation of mass from a measured volume. This is important since the mass of individual ocean particles is generally too small for direct measurement.

Aggregates and lysed phytoplankton cells have a somewhat open internal structure. If seawater can effectively flow through the interstices of a particle, this occluded water can be considered in somewhat the same way as are pore waters in sediment. While it reduces the apparent mean density of the particle, if water can flow through as well as around the particle, it provides complications when making particle settling velocity calculations (see Appendix 1).

The flow or diffusion rate of sediment pore waters is often described in terms of porosity and tortuosity (see Berner, 1980). The porosity is considered the ratio of the volume of the interstices to the volume of the sediment and interstices. Tortuosity is a measure of the mean path length a water parcel must travel to move a unit distance in the vertical through the sediment. These concepts may be helpful when conceptualizing the occluded water or pore water of aggregates. The simplest pore is a tube. When falling parallel to its length, it would have a tortuosity of 1. The same tube falling at a 45° angle would have a tortuosity of 1.41. However, we can show by a simple

example that the pore water flushing rate of a settling aggregate is somewhat different than that for sediment, due in part to the pressure differential across the particle induced by the balance between inertial and drag forces.

Because the water inside a cylindrical tube falling vertically is not restricted, it might appear at first to provide little of the added buoyancy to the tube that would occur if the ends were capped off. However, there is significant drag on the inside of the tube, so much of the fluid inside is not flushed when it settles a distance equal to the tube length. As the diameter is reduced to capillary dimensions under laminar flow conditions, and as the tube is lengthened, a much larger fraction of the original fluid remains after it has settled a distance equal to its length (see Fig. 1 and Appendix 1). The drag of this retained water has provided an added "buoyancy" to the pipe, even though its tortuosity is still 1.0. Adding tortuosity will increase the drag of pore waters, reduce their flushing, and increase the "buoyancy" provided by the occluded pore waters.

Since we don't know the internal structure of aggregates, we can only make some estimates of porosity based upon other measureables and some assumptions. If we consider an aggregate of diameter d consisting of a collection of solid particles of density ρ_s and occluded water of density ρ_w, the porosity of the particle or water fraction is f_w, and the solid fraction is f_s. The mean density of the particle can then be expressed as

$$\bar{\rho} = \frac{M_s + M_w}{V_s + V_w} = \rho_s f_s + \rho_w f_w = f_s(\rho_s - \rho_w) + \rho_w,$$

where M_s and V_s are mass and volume of the solid part of the aggregate,

respectively. M_w and V_w are the mass and density of the water, respectively, and $f_s + f_w = 1$. Since the water density is known, methods for determining $\bar{\rho}$ and ρ_s are required in order to determine f_s and f_w.

The density ρ_s of the solid or nonaqueous part of an aggregate can be determined by allowing it to settle to it own density level in an isotonic density gradient. Given time the original pore waters of the aggregate will be replaced by the density gradient media due to flushing and diffusion (Carder and Steward, 1984), and the density at any depth of the gradient can be determined from its index of refraction.

If one assumes that by a combination of tortuosity and high capillarity (long, narrow pores), flow through the aggregate is small compared to flow around it, the mean density of the aggregate $\bar{\rho}$ can be determined by inverting Stokes settling equation. For a sphere of diameter, d, this becomes

$$\bar{\rho} = \frac{\rho_w + 18w_a \, \eta}{980 \; d^2}$$

where w_a is the aggregate settling speed and η is the water viscosity. A method for measuring the flushing rate or flow through the aggregate in lieu of the above assumption is discussed in Appendix 2.

This exercise has allowed us to focus on the types of measurements required to better understand the settling dynamics of particles and aggregates, but the mechanics of aggregation and disintegration should also be mentioned. Aggregates form as a result of collisions between particles. These collisions can be caused by at least four mechanisms

(see Lerman, 1979): i) Brownian motion-induced particle diffusion; ii) water shear; iii) differential settling speeds; iv) and biological filtering or scavenging. In additon, retardation of settling and particle buildup on density interfaces enhances the probability of collisions or biological filtering and scavenging.

The first mechanism is most important in causing aggregation of colloidal or small particles under low shear conditions (e.g. $du/dz <$ 0.1 sec^{-1}), while differential settling is most effective for larger particles. Water shear is the dominant mechanism for $du/dz > 0.5$ sec^{-1} (Lerman, 1979). Water shear is typically most effective above the pycnocline and in the near bottom nepheloid layer. Both regions are usually regions of significant vertical shear. The sheet and layer, stepped density structure in the pycnocline provides a region where low density particles slow or accumulate at density interfaces, greatly increasing the probability of particle collisions. Here, also, there is a likelihood that detrital filter feeders would concentrate.

The primary disintegration mechanism for aggregates is high shear stress. Krone (1976) points out the shear strength of various orders of estuarine aggregates, above which disaggregation to a lower order aggregate occurs. Storms, breaking internal waves, and high bottom stress are candidate mechanisms for causing stresses exceeding ocean aggregate shear strength.

Optical Properties of Particles

The effects of particle shape and index of refraction are secondary to the effect of particle size on light scattering in the ocean (Jerlov, 1976). This property is exploited by particle sizing

instruments that measure the particle attenuation coefficient c_p or estimate the particle scattering coefficient b_p.

In general, all of the light energy impinging directly on a large particle of geometrical cross section G is scattered or absorbed, while an equal amount of light energy passing near the particle is scattered by diffraction (e.g. recall Babinet's principle, Van de Hulst, 1957). Thus the ratio of the total energy removed by a particle from a proceeding wave to the energy physically intercepted by a particle of cross sectional area G corresponds to an attenuation cross section or efficiency factor $Q_c \doteq 2 = Q_a + Q_b$. Q_a and Q_b are the absorption and scattering cross sections, respectively.

For sizing purposes, then, the attenuation coefficient for a spherical particle i is

$$c_i = G \ Q_c$$

or

$$c_i = \frac{\pi d_i^2}{4} Q_c \doteq \frac{\pi d_i^2}{4}(2) = \frac{\pi d_i^2}{2},$$

the absorption coefficient is

$$0 \leq a_i = \frac{\pi d_i^2}{4} Q_a \leq \frac{\pi d_i^2}{4}(1),$$

and the scattering coefficient is

$$1 \leq b_i = \frac{\pi d_i^2}{4} Q_b \leq \frac{\pi d_i^2}{2}.$$

An important question, then is "what constitutes a large particle?" For spherical particles with real refractive indices near 1.0 relative to the medium, Van de Hulst (1957) has derived

relationships among Q_a, Q_b, and Q_c, particle diameter d, and the refractive index m relative to the medium. These relationships are shown in Figure 2, where rho = $2\pi\eta_w d(m-1)/\lambda$, λ is the wavelength in vacuo, and η_w is the refractive index of water. It is clear that when rho is smaller than about 3, the particle becomes an inefficient scatterer, and when rho exceeds 8 to 10, $Q_c \doteq 2$, regardless of the absorbtion coefficients (related to the imaginary part η' of the refractive index according to $\eta' = a_p\lambda/4\pi$). Increases in η' force Q_c closer to 2 for smaller rho values, and decrease Q_b values to 1.0. Again for large rho values, Q_c is much less variable than Q_b.

For phytoplankton, the absorption coefficient a_p is less than 15% of the attenuation coefficient for much of the visible light spectrum (550-640 nm) (Bricaud et al. 1983).

Since $c_p = a_p + b_p$, then $b_p \geq 0.85 c_p$. For quartz grains, $b_p \doteq c_p$. However, for large opaque particles such as certain fecal pellets, the absorption coefficient can equal the total scattering coefficient, or $b_p = 0.5 c_p$. Because of the variation in a_p in the oceans, attenuation or c meters are inherently more accurate than scattering or b meters as particle sizing devices.

In order that an optical particle sizing meter measure the signal due to a single particle rather than from an ensemble of particles, the measurement or sampling volume must be very small, or the particle concentration must be very dilute. Two methods are presently in use by automatic laboratory particle sizing and counting devices to increase the odds of measuring single particles. One method used by HIAC/ROYCO draws the media fluid through a narrow flow constriction (e.g. 100 μm x 1000 μm cross section), inducing turbulence to make the particles

138

tumble. The largest particle cross section presented to the 100 μm x 100 μm cross section of collimated light passing across this constriction is recorded as a pulse height and counted.

A second method, used by Spectrex, focuses a scanning laser beam down to a narrow waist where an illuminated particle will intercept the greatest fraction of the incident radiant flux and provide the largest scattered or attenuated signal. Pulse length discrimination is used to reject signals that are too short (particle at the beam edge) or too long (particle not at the beam waist) to have been centered in the intensity maximum at the waist of the scanning beam. This method requires no fluid flow and thus is less destructive, but the pulse discrimination process provides about a 15% uncertainty in the projected cross sectional area of the particle. The methods also differ in that the first measures the "largest" areal dimension of a particle, while the second measures a random areal dimension. The scanning beam method in present use measures near-forward scattered light rather than light attenuation, adding an additional uncertainty if the particle absorption coefficient of particles is heterogeneous. However, the attenuation principle could be incorporated together with the scanning beam methodology to avoid the absorption uncertainty.

These automatic techniques are probably both adaptable to in situ observations, but discrimination of one particle type from another except by size would not be possible. That is the reason particle imaging and sizing systems are most commonly in use for studying marine particles and aggregates in situ.

Particle Imaging Methods

The in situ methods presently in use for imaging particles and aggregates fall into two categories: photographic and holographic. Because vidicon tubes and area array sensors for television have an order of magnitude lower resolution than photography, they can be considered for only low resolution photographic applications. For this reason, they are not considered independently in this review even though they provide real time data.

The choice of methodology used to image particles is often dependent upon the size of the particles of interest. As a rule of thumb, the number of particles of diameter d in the ocean decreases as the function d^{-k}, where k is typically between 3 and 5. For living particles Sheldon et al. (1972) found a value of about 3, while for all particles, a value near 4 may be more representative (see Lerman et al. 1977).

With a paucity of particles at larger sizes, one must either measure a given volume continuously for a long time to observe a statistically representative population of large particles, increase the volume of water imaged, or use a concentration mechanism. Because the depth of field of a photographic system is inversely proportional to its magnification, high magnification systems have very little depth of field. The odds of a free-falling or floating particle of the appropriate size occurring at the focal distance may be quite small, unless they come to rest on a fixed horizontal, optical surface such as the bottom of a sediment trap. However, photographic systems can be quite useful for the in situ imaging of large particles where magnification can be much less than 1.0, providing for adequate depths of field for large sample volumes.

The photographic methods are typically used to image large particles and aggregates with fractional magnification values to increase the depth of field. A large sample volume increases the probability that a particle of interest (e.g. marine snow) will be in the sampling volume. The cost of increasing the sample volume in this way is an image that appears to be perhaps 25% longer and wider at the near edge of the volume than it does at the far edge, even with a "perfect" pinhole camera (see Fig. 3). For an actual camera with a finite aperture, the particle images will appear to be out of focus at the near and far edges of the sample volume. Reduction in the depth of the sample volume ameliorates both the magnification and the focusing problem, but reduces the number of particles imaged. Increasing the radiant flux of the source and/or the sensitivity of the film can provide a larger f-stop for the system, improving the depth of focus by reducing the camera aperture.

At least two in situ photographic particle imaging and sizing systems are presently in use for measuring aggregates and particles. One of moderate resolution (diameter > 50 μm) measures backscattering along with photographic images with 1/4 magnification (Johnson and Wangersky, 1985). The backscattering meter is used to activate a strobe only when imaging larger particles or organisms. While the sample volume of the imaging system is not discussed, it appears to be of order 10-20 ml.

A system of lower resolution (diameter > 500 μm; 1/40 magnification) but much larger sample volume (.66 m^3) has been been described by Honjo et al. (1984) for studying large amorphous

aggregates or marine snow. A particle at the near edge of the sample volume relative to the camera would appear to be about 29% larger than would the same particle at the far edge (e.g. see Fig. 3). This ± 14.5% uncertainty in size could be easily reduced by narrowing the depth of the lighted or sample volume viewed. This modification and others will be discussed in detail by Vernon Asper in a later talk.

Methods using holographic microscopy are more useful for measurement systems requiring image magnification, since the diffraction patterns from all particles in a volume are recorded rather than the images from the particles at a given focal plane. In the image reconstruction process the diffraction patterns on the film diffract light such that images of the original particles can be formed by moving an image screen along the optical axis of the system (see Fig. 4). Transmission or Gabor holography has been the method of choice in ocean applications because of the inherent stability and low power requirements of the method.

Magnification of the diffraction patterns (already much larger than the original particle) onto the holographic film can be achieved with lenses (see Thompson et al., 1967; Carder et al., 1982), but most of the magnification is performed during the holographic reconstruction process. Total system magnification factors of more than 500 can be achieved (Costello et al., in press) with a sample depth of more than 3.5 cm. Typical sample volumes range from about 1 to 4 cm^3 (Carder et al., 1982). Adequate resolution of the reconstructed image is achieved if three or more diffraction rings are captured on the hologram and if the particle moves a distance less than 1/10 its diameter during the exposure (Thompson et al., 1967).

Holography is of additional interest in studies of aggregate behavior at density interfaces because the phase contrast due to differences in refractive index across the interface and mixing induced by settling particles can be visualized. Transmission or Gabor holography is adequate to visualize mixing between fluids of relatively high contrast in refractive index (see Appendix II), but for more sensitivity, multiple beam, multiple wavelength, multiple pass or double exposure holographic interferometry methods can be employed (Vest, 1979). Such studies are important because i) density interfaces increase the probability of aggregate formation, ii) aggregates cause mixing by flushing occluded water below the interface as low density, low viscosity cylindrical streamers, iii) these streamers provide a faster, preferred pathway for subsequent aggregates, and iv) because vertically elongated aggregates are formed when subsequent aggregates overtake slower aggregates in the streamer (see Appendix II). These density interface processes involving aggregates have ramifications on aggregate collision probabilities, size, shape, settling speed, fluid mixing, and most likely feeding behavior, and should be considered for study as the technology becomes available.

Photographic and holographic methods can both be used to measure particle settling speeds by taking sequential photographs or holograms. However, the fluid must not be moving relative to the imaging system, and gravity should be the only acceleration on the particles. Carder et al. (1982) and Costello et al. (in press) have achieved platform stability and stationary fluid conditions by holographically imaging particles inside a large sediment trap suspended from the surface by a system of damped buoys in tandem (see

Fig. 5). A constant downward particle settling velocity through multiple images confirms platform stability.

For studies of eolian mineral transport from Asia to and through the central north Pacific we have developed a multiple sample sediment trap equipped with vertical and horizontal axis holographic cameras. Figure 5 shows a 0.66 m^2 collection cone, horizontal camera and laser housings, a vertical camera housing, the sampling chamber assembly and battery pack/timer. The vertical laser is inside the collection cone. The sampling chamber has six collection cups with windows which are sealed except during sampling. The cone is deployed and retrieved open. One-way valves permit filling and flushing of the cone. A programmable delay of typically six hours is used to avoid sampling of most particles entrained in the cone during deployment. Then the first cup is pulled by a lead weight and locked into place. Burn wires are used to control the cup progression by releasing an elastic locking mechanism upon a signal from the timer.

A dense (1.11 gm/ml), viscous (0.053 poise), isotonic mixture of sugar, dextran and saltwater in the cup dramatically slows the speed of fecal pellets and minerals to permit multiple holograms of the same particles before they leave the 1 cm diameter laser beam. Typical frame rates are 1/minute to 1/15 sec. for the horizontal camera, and 1/6 minutes for the vertical camera. Each camera contains 250 exposures of 35 mm high speed holographic film (Kodak 50-253).

Reconstructed holograms of typical quartz-like particles, heavy minerals, fecal pellets, and aggregates are shown in Figure 6. The Stokes settling equation for prolate spheroids was used to calculate density values of about 2.6, 5.0, 1.136, and 1.12 gm/ml for

these classes of particles (Carder et al., in press). Fecal pellets captured at greater depth had densities as high as 1.21 gm/ml.

Other Methods

For robust particles such as some fecal pellets, laboratory measurements can be made to enhance our understanding of their nature. Light microscopy of carefully collected aggregates by SCUBA divers has been used (Alldredge, 1972). Scanning electron microscopy with individual particles electron dispersive x-ray analysis might be used on similarly collected aggregates to better determine the composition of the heavier elements of the aggregate components.

It is known that large aggregates break apart when passing through the Coulter Counter (Sheldon, 1967; Hunt, 1982), and the same fate may await aggregates passing through a flow cell cytometer, an instrument used to estimate individual particle size and fluorescent properties by light absorption, scattering and fluorescence (e.g. see Olson et al., 1985; Yentsch et al., 1983). For robust fecal pellets, it may be possible to qualitatively estimate their pigment content by fluorescence, and their degree of opacity may be a useful fecal pellet classifier. Sizing can be performed by either light attenuation or near-forward scattering techniques similar to those discussed earlier, and scattering at large angles is thought to provide a measure of internal structure and/or index of refraction (R. Spinrad, personal communication). More details about flow cell cytometry are provided later in the talk by K. Stolzenbach.

A final laboratory method useful for sizing nonodisperse distributions of very small (30 Angstroms to 3 μm) particle populations

is Photon Correlation Spectroscopy (PCS). It may be useful for studying Brownian motion induced aggregation since it provides a measure of the particle diffusion coefficient A_p. Since large particles diffuse more slowly than small ones due to the frictional drag of the water viscosity, the particle diameter can be expressed by the Stokes-Einstein equation as

$$d = \frac{kT}{3\pi A_p},$$

where k is the Boltzman constant and T is the absolute temperature (Ford, 1983). The Brownian motion of each particle imparts a small Doppler shift in the wavelength of the scattered light. This Doppler shift is too small to be effectively analyzed spectroscopically. However, interference between this doppler-shifted scattered light and that of incident light as a function of time produces a beat frequency at the receiver which increases as the Doppler-induced wavelength difference increases. Recalling that these beats are a measure of group wave or envelope frequency, the beat period γ is proportional to $\lambda/\Delta\lambda$. The spectra of beat frequencies due to interference of scattered light from all particles in the sample volume are analyzed using the auto-correlation function of the scattered signal (Ford et al., 1973). The spectral distribution of the scattered intensity as a function of frequency ω is Lorentzian in shape

$$I(\omega) = \frac{(constant)}{^2 + (\omega-\omega_o)^2},$$

where ω_o is the incident frequency. It is centered around the

146

incident frequency w_o, with half-width at half-height of

$$\Gamma = A_p \, \frac{4\pi\eta}{V_o} \, \sin^2(\theta/2),$$

where A_p is the particle translational diffusion coefficient, η is the index of refraction of the medium, λ_o is incident wavelength, and θ is the scattering angle. Combination with the Stokes-Einstein expression permits determination of the effective diameter of a spherical particle.

It may be possible to use this photon correlation spectroscopy technique to observe the increase in the effective or mean diameter of a population of colloidal particles as Brownian motion induces aggregation. Instruments such as Langley Ford or the Coulter Model N4 are designed for laboratory use, and the method is vibration sensitive. Even the motility of micro-organisms affects the results, so use in a shore-based facility is probably a firm requirement for PCS applications at present. However, many colloidal particles form at the river-ocean interface, so this restriction may not be as severe as it first appears.

Summary

A number of optical methods are in use presently in laboratory instruments which may be adaptable for in situ applications. These include automatic particle sizing by light attenuation or light scattering methodologies. These methods do not provide particle shape and orientation discrimination, however.

For large particles (diameter > 50 μm) photographic techniques have been developed to measure particle size and shape, and these methods could be modified by particle measurement inside a stable sediment trap to measure particle settling speeds by taking sequential photographs of particle position. These methods sample volumes from about 10 ml to 0.6 m^3, with sizing accuracies of better than ± 15%, depending upon the magnification and sample depth.

For intermediate to small particles (nominally 5 μm to 5000 μm diameter), transmission holographic microscopy is being used to sequentially image particles in sample volumes of .5 to 4 cm^3, depending upon the application. Particle size, shape, orientation, position in three-space, and velocity in three-space are determined holographically for all particles in the sample volume. Magnification is uniform with particle distance from the camera, so size ambiguities do not result from the position of the particle in the sample. Particle size, shape and settling speed used with Stokes settling equations then provide a measure of the particle density. The flushing rate of occluded water for aggregates can be determined at density interfaces either holographically or using holographic interferometry.

A number of laboratory methods are not expected to be successfully adapted to in situ application. Flow cell cytometry equipped with

particle sizing by attenuation or scattering methodologies and fluorescence provides single particle or cell characteristics for classification and sorting. Shipboard sea trials have been successful. Photon correlation spectroscopy is not expected to be useful at sea because of effects of ship vibration on the motion of colloidal and small particle populations. For shore based facilities, experiments on the growth in size of colloidal and small aggregates due to Brownian motion induced collisions may be directly observable use photon correlation spectroscopy.

Acknowledgements

References Cited

Alldredge, A.L., 1972. Abandoned larvacean houses: a unique food source in the pelagic environment. Science 177: 885-887.

Berner, R.A., 1980. Early Diagenesis: a Theoretical Approach. Princeton Univ. Press, Princeton, N.J., 241 p.

Bricaud, A., A. Morel and L. Prieur, 1983. Optical efficiency factors of some phytoplankters. Limnol. Oceanogr. 28(5): 816-832.

Carder, K.L. and R.G. Steward, 1984. Evaluation of Stokes settling equation for variable density aggregates. Final Report, ONR Contract N00014-83-K-0082, University of south Florida, St. Petersburg, 14 p.

Carder, K.L., R.G. Steward, and P.R. Betzer, 1982. In situ holographic measurements of the sizes and settling rates of oceanic particulates. J. Geophys. Res. 87(C8): 5681-5685.

Carder, K.L., D. Costello, R. Young and P. Betzer, in press. Dynamics and composition of holographically recorded particles from ADIOS I. EOS, Fall AGU Meeting, December 1986.

Costello, D., R. Young, K. Carder and P. Betzer, in press. Multiple-sample sediment traps with in situ holographic imaging of particles. EOS, Fall AGU Meeting, December 1986.

Ford, N.C., Jr., 1983. Theory and practice of correlation spectroscopy. In B. Dahneke (ed.): Measurement of Suspended Particles by Quasi-Elastic Light Scattering, Wiley, New York.

Ford, N.C., Jr., R. Gabler and F.E. Karasz, 1973. Self-beat spectroscopy and molecular weight. Advances in Chemistry Series 125: 25-54.

Happel, J. and H. Brenner, 1973. Low Reynolds Number Hydrodynamics, 2nd rev. ed., Noordhoff, Leyden.

Honjo, S., K.W. Doherty, Y.C. Agrawal and V.L Asper, 1984. Direct optical assessment of large amorphous aggregates (marine snow) in the deep ocean. Deep-Sea Research 32(1): 67-76.

Hunt, J.R., 1982. Particle dynamics in seawater: implications for predicting the fate of discharged particles. Environmental Science and Technology 16: 303-309.

Jerlov, N.G., 1976. Marine Optics, Elsevier, New York, 231 p.

Johnson, B.D. and P.J. Wangersky, 1985. A recording backward scattering meter and camera system for examination of the distribution and morphology of macroaggregates. Deep-Sea Research 32(9): 1143-1150.

Krone, R.B., 1976. Engineering interest in the benthic boundary layer. In I. McCave (ed): The Benthic Boundary Layer, Plenum, New York, 143-156.

Lamb, H., 1945. Hydrodynamics, 6th ed. Dover, New York.

Lerman, A., 1979. Geochemical processes water and sediment environments, Wiley, New York, 481 p.

Lerman, A., K.L. Carder and P.R. Betzer, 1977. Elimination of fine suspensoids in the oceanic water column. Earth Planet. Sci. Lett. 37: 61-70.

Olson, R.J., D. Vaulot and S.W. Chisholm, 1985. Marine phytoplankton distributions using shipboard flow cytometry. Deep-Sea Res. 32(10): 1273-1280.

Schlichting, H., 1955. Boundary Layer Theory. Pergamon, New York, 535 p.

Sheldon, R.W., A. Prakash and W.H. Sutcliffe, Jr., 1972. The size distribution of particles in the ocean. Limnol. Oceanogr. 17: 327-340.

Thompson, B.J., J.H. Ward and W.R. Zinkey, 1967. Applications of
hologram techniques for particle size analysis. Applied Optics
6(3): 519-526.

Van de Hulst, H.C., 1957. Light scattering by small particles,
pp. 172-199, Wiley, New York.

Vest, C.M., 1979. Holographic Interferometry. Wiley, New York,
465 pp.

Yentsch, C.M., and others, 1983. Flow cytometry and cell sorting: A
powerful technique for analysis and sorting of aquatic particles.
Limnol. Oceanogr. 28: 1275-1280.

Figure Legends

Figure 1. Family of approximate settling velocity curves as a function
of radius R for open (solid) and capped (open) circular
tubes of varying length L, falling parallel to the long
axis. The wall thickness dr is 0.1 times the radius, and
the wall density is 2.65 gm/ml. Sea water density is 1.02
gm/ml and viscosity is 0.01 poise. Note that for long open
tubes the settling speed approximates those of capped tubes
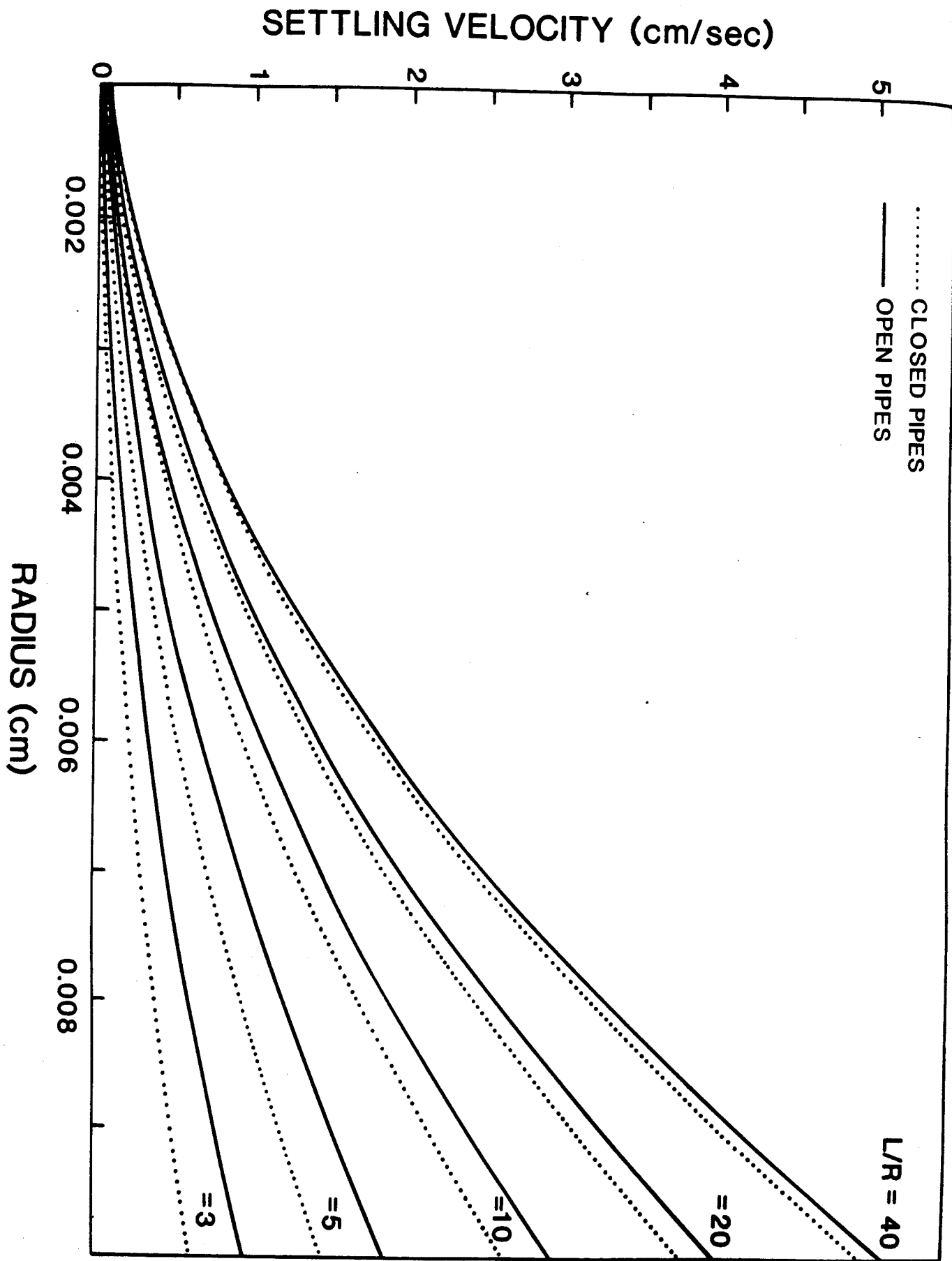(see Appendix 1 for details)

Figure 2. Families of curves for the cross sections for attenuation,
total scattering and absorption as a function of rho for
different values of the imaginary or absorbing part η' of
the index of refraction. The parameter rho is the optical
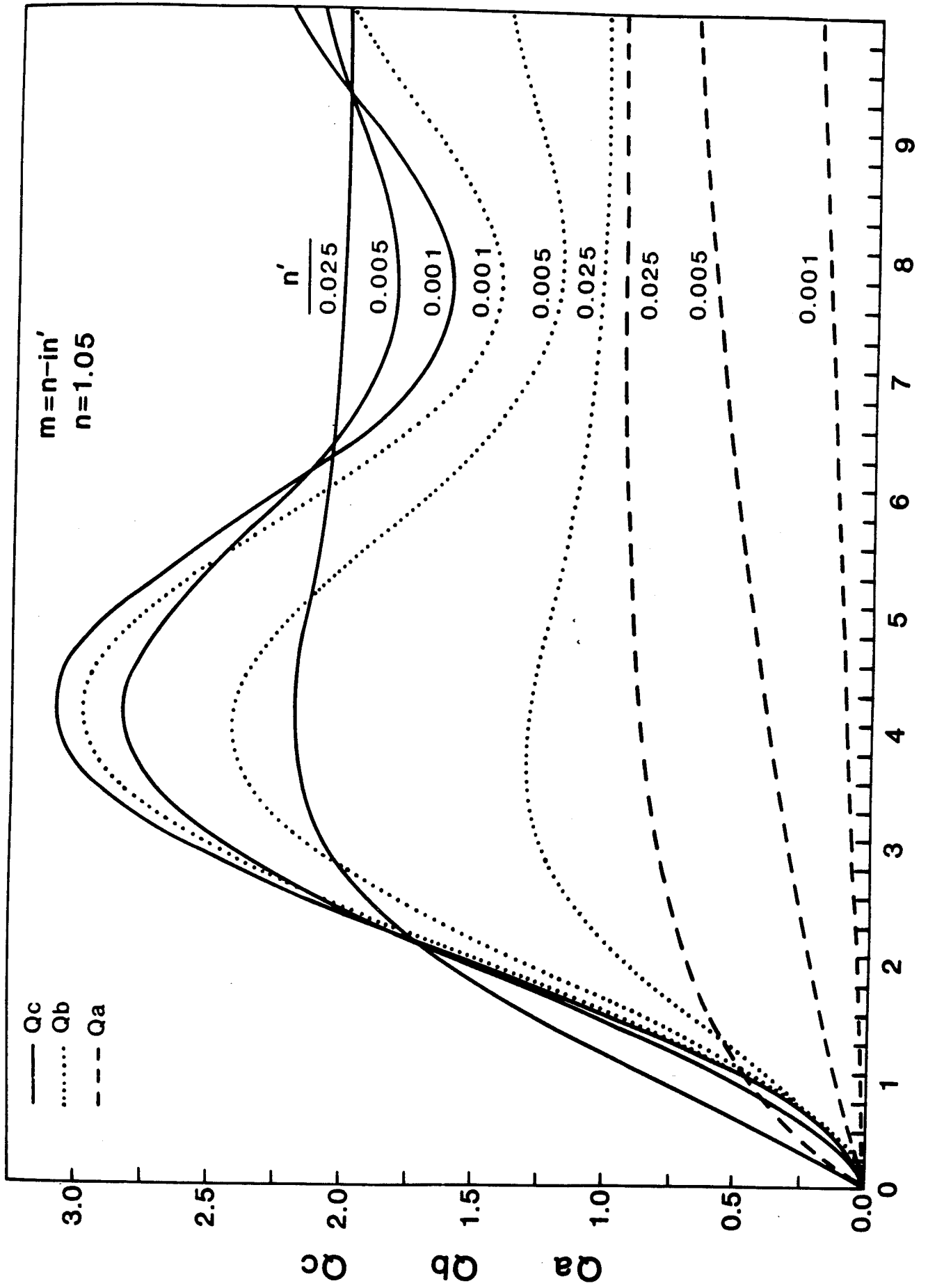size of a particle and is defined in the text.

Figure 3. A schematic representation showing the ambiguity in particle
size for a pinhole camera with a large depth of field. L_1
is the image on the film of either object L_1 or L_2, at the
front and rear edges of the sample volume. L_2 is about 30%
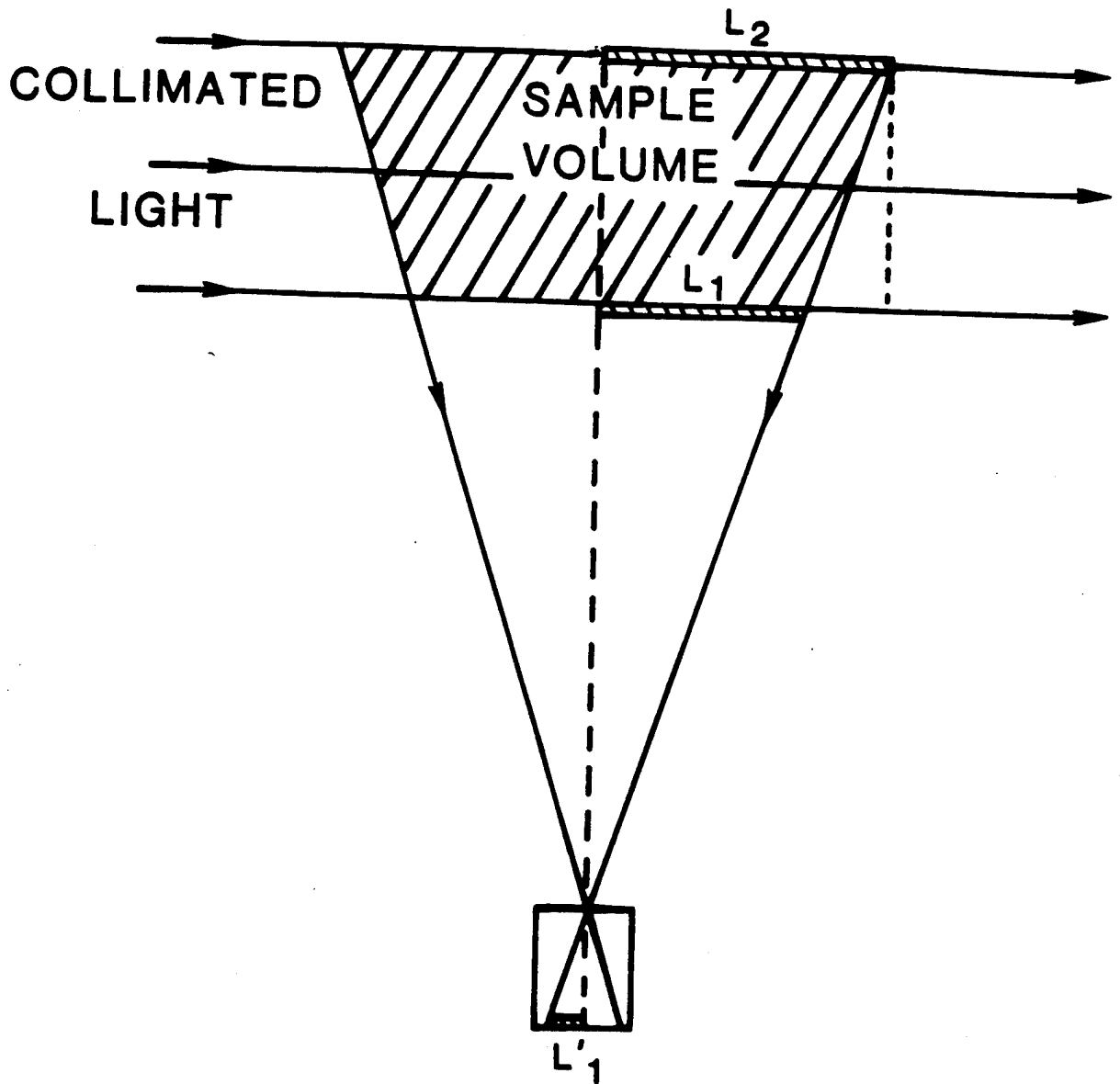longer than is L_1.

Figure 4. A schematic of Gabor or transmission holography. Planar
wavefronts of a collimated laser beam are diffracted by a
particle P. Diffracted light (spherical wavefronts)
constructively interfere with planar wavefronts at the film
plane producing high density or dark circular diffaction
rings. Destructive interference occurs between the dark
rings, providing low density or light rings. Placing the
developed hologram back in the film plane and passing a
collimated laser beam through it in the opposite direction
causes light scattering off the diffraction rings themselves
such that constructive interference occurs at P, creating
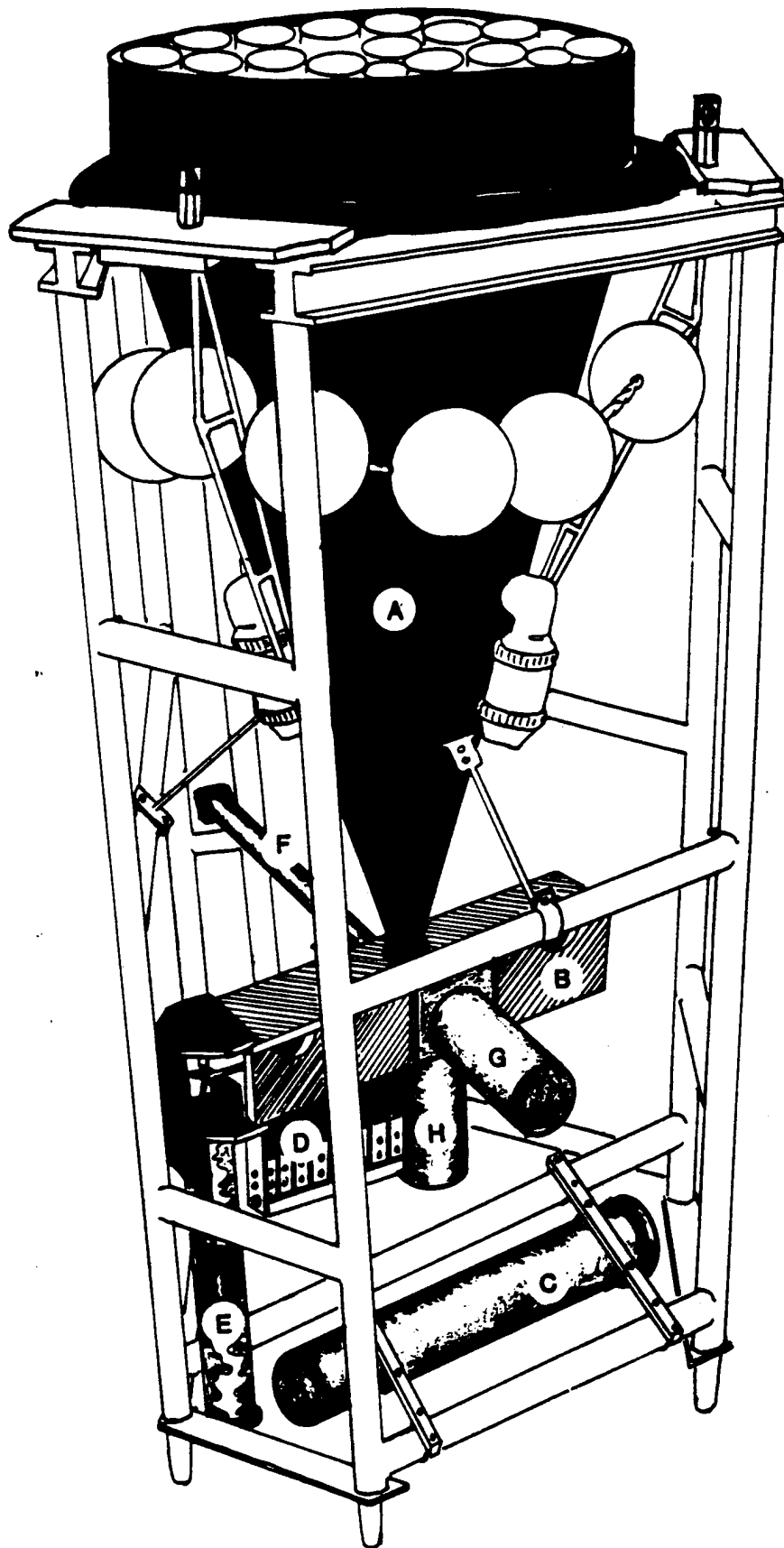the image of the original particle at the position P.

Figure 5. Drawing of a sediment trap equipped with horizontal and
vertical axis holographic camera systems for viewing
particles orthogonally. At the apex of the inverted conical
concentrator (A) is the six-cup viewing and sampling
assembly (B). The timer/battery pack (horizontal
cylinder at bottom) controls the timing sequence of cups
(C), laser on/off cycles, and camera firing. Motive force
for advancing cup assembly through sequentially fired
registration pins (D) is provided by a lead weight in the
long plexiglass sleeve (E) vertically attached to the trap
frame. The horizontal laser housing (F), horizontal camera
housing (G), and verticle camera housing (H) are shown.

Figure 6. Photographs of reconstructed of in situ particles captured
in the north central Pacific gyre during March/April, 1986.

SETTLING VELOCITY (cm/sec)

RADIUS (cm)

CLOSED PIPES
OPEN PIPES

L/R = 40

=20

=10

=5

=3

COLLIMATED

LIGHT

SAMPLE
VOLUME

L_2

L_1
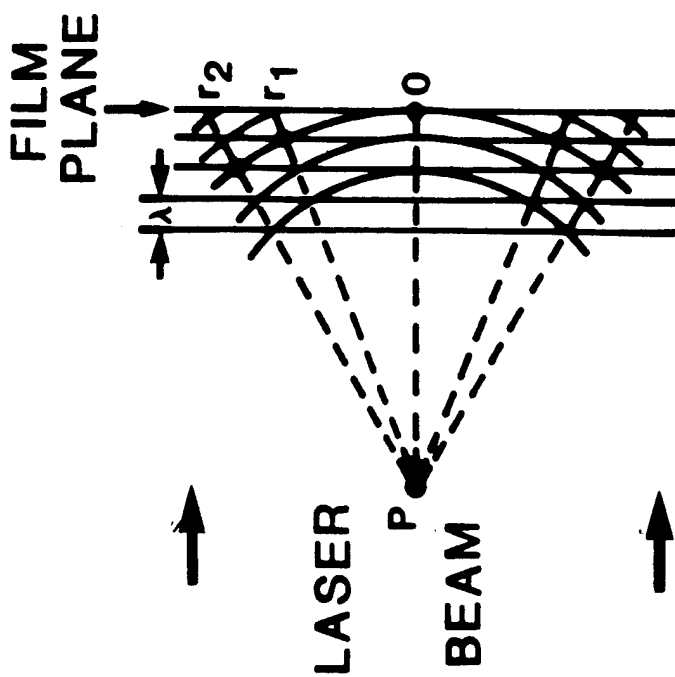
L'_1

ROTATED VIEW OF FILM OR HOLOGRAM

FILM PLANE

LASER BEAM
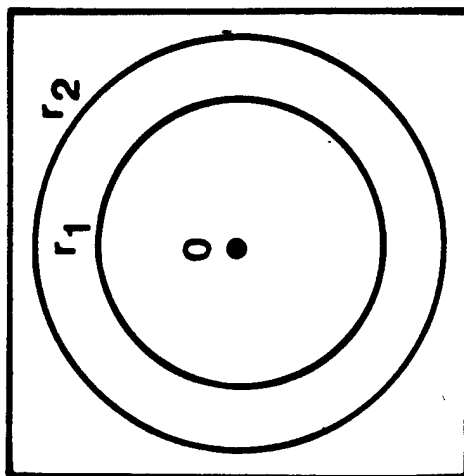
Figure 6. Holographic reconstructions of particles imaged in situ
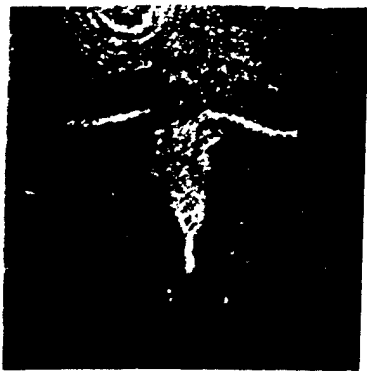
a) Copepod:(37X)
   850 um X 550um

b) Fecal pellet: (513X)
   48.7um X 22.2um
   1.136g/cc
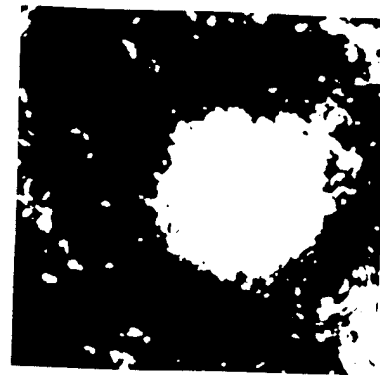
c) Fecal pellet: (258X)
   90um dia., 1.137 g/cc
   1.137 g/cc

d) Aggregate: (513X)
   62.8um X 41.9um
   1.12 g/cc

e) Aggregate: (513X)
   54.2um X 52.4um
   1.12 g/cc

f) Aggregate: (513X)
   35.7um X 36.1um
   1.12g/cc
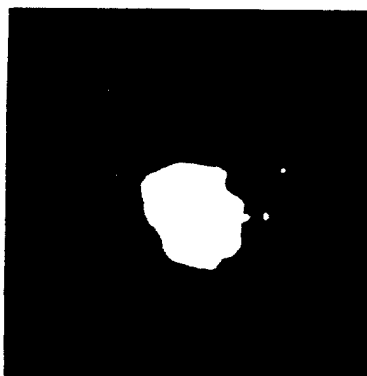
g) Quartz: (513X)
   31.6um X 21.1um
   2.61g/cc

h) Heavy Minerals: (513X)
   21.4um X 15.3um
   5.1g/cc

APPENDIX I

The flushing rate of aggregates is important to consider in terms of its effect on the buoyancy of particles. For many flocculated mineral materials, the flushing rates are of the order of minutes to tens of minutes and appear to be controlled by the rate of diffusion (Lerman, 1979; p. 312). In cases of aggregates stopping on density interfaces, the flushing time is of the order $t = L^2/D$, where L is the particle length and D is the molecular diffusion coefficient for salt or te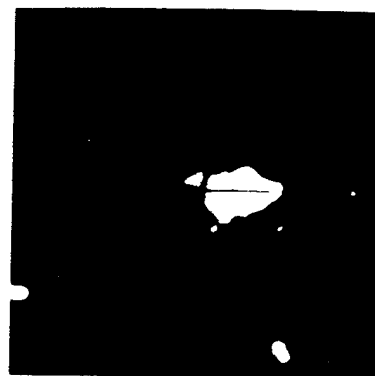mperature. Except at density interfaces, the time it takes such aggregates to settle a distance L is typically short compared to the diffusional flushing rate, and flushing has little effect on the Stokes settling rate calculations.

For aggregates with larger structural components and pores, the effect of flushing rate on Stokes settling calculations and particle buoyancy may need to be considered. As a simple illustration, suppose a pore is modelled as a long, hollow tube of radius R and length L. If it settles parallel to L, a first order estimate of its drag is that for a long cylinder (Happel and Brenner, 1975):

$$F_D = \frac{2 \pi \eta U_s L}{\ln (L/R) - .72} \qquad \text{(A1}$$

where η is the fluid viscosity and U_s is the settling speed. The pressure differential dp required at low Reynolds numbers to force water through the tube at mean internal velocity U_i is (Schlicting, 1955)

$$dp = - \frac{4\eta L U_i}{R^2} . \qquad \text{(A2}$$

162

In order to estimate the pressure differential between the bottom and top of the tube created by a settling velocity U_s, consider the drag force F_{DD} on a disk settling face down (Lamb, 1945; Happel and Brenner, 1973) in the limit of no thickness:

$$F_{DD} = 5.1 \ \pi \ \eta \ U_s R. \tag{A3}$$

This equation approximates the part of the drag on a cylinder that results from the flat end surfaces.

Combining equations A2 and A3

$$dp \ (\pi R^2) = F_{DD}$$

$$\frac{4 \ \eta \ L \ U_i}{R^2} \ (\pi R^2) = 5.1 \ \pi \eta \ U_s \ R$$

or

$$\frac{U_i}{U_s} = \frac{5.1 \ R}{4 \ L} = 1.275 \ R/L. \tag{A4}$$

Thus, for $L/R = 10$, the pore velocity U_i is about 13% of the settling speed. This result is for a vertically oriented tubular pore of uniform cross section and no tortuosity.

To consider the settling speed of a circular, thin-walled tube, the buoyancy force on the tube must be calculated, including that of the internal pore water carried with it. The volume of pore water carried with the tube in settling a distance equal to its length L is

$$V_{pore} = \pi R^2 L \ f_{pore}, \tag{A5}$$

163

where $f_{pore} = \dfrac{U_s - U_i}{U_s}$ (A6

is the fraction of the pore retaining unflushed water.

The volume of the tube is

$$V_c = \pi L[(R + dr)^2 - R^2] \doteq 2 \pi L\, R dr \quad \text{(A7}$$

for $dr << R$. The average density of the tube and entrained pore water is

$$\bar{\rho} = \frac{V_{pore}\rho_w + V_c\rho_c}{V_{pore} + V_c}. \quad \text{(A8}$$

Combining eqs. A4, A5, A6, and A7,

$$\bar{\rho} = \frac{(1 - 1.275\ R/L)\ \rho_w + 2dr/R\ \rho c}{(1 - 1.275\ R/L) + 2\ dr/R}.$$

Setting the buoyant force equal to the drag force for the open tube,

$$\pi(R + dr)^2 Lg(\bar{\rho} - \rho w) = \frac{2\pi\eta\ U_s L}{\ln (L/R) - .72},$$

and solving for the settling velocity provides

$$U_s = \frac{g}{2\eta}(R + dr)^2(\ln (L/R) - .72)(\bar{\rho} - \rho_w). \quad \text{(A9}$$

This equation provides the family of curves shown in Fig. 1 for an open tube with $dr/R = 0.1$, $\rho_c = 2.65$, and variable values of R/L. The settling curves for capped tubes are also shown, and the fraction of pore water retained can be calculated from the curve differences.

DYNAMICS AND COMPOSITION OF PARTICLES FROM AN AEOLIAN INPUT EVENT TO THE SARGASSO SEA

Kendall L. Carder, Robert G. Steward, and Peter R. Betzer

Department of Marine Science, University of South Florida, St. Petersburg

David L. Johnson

Baker Laboratory, State University of New York, Syracuse

Joseph M. Prospero

Rosentiel School of Marine and Atmospheric Science, University of Miami, Florida

Abstract. A major outbreak of Saharan dust (>40 μg aerosols/m³ air) passed over the western Sargasso Sea in late June 1980. The flux of aeolian particles across the air-sea interface was calculated based upon free-floating sediment trap data (30-m depth). During the early-to-middle portions of this event, we observed in the trap samples, large numbers of "giant" (>20- μm diameter) aeolian particles that were not observed in aerosol samples collected at Miami, Florida, 426 km to the west. To better intercompare data collected at the two sites, a simple aeolian particle settling model was developed. Scanning electron microscopy with automated image analysis and X ray energy spectroscopy of individual particles from the two sites provided size and compositional data as primary inputs to the model. The compositional differences between aerosols from the two sites, although not great, may have been due in part to the localized nature of particle sources and storm centers. The time history of the aerosol concentration over the western Sargasso during the month of June as simulated by the model was compared with the time history of aerosols arriving at Miami. These results suggest that a significant portion of the deposition flux is comprised of giant particles. Particles in this size range are not efficiently collected by conventional sampling techniques, and hence reported estimates of depositional fluxes could be significantly biased too low.

Introduction

On June 19, 1980, at a site about 111 km east of the Bahamas (26.0°N, 76.0°W), a free-floating sediment trap set at 30-m depth captured a suite of aeolian mineral particles larger than has been previously reported in the literature for the Sargasso Sea region. Some 93% of the mass flux of mineral particles were >16- μm diameter. On one holographic frame (3.3 mL volume), 28 particles ranging in size from 15- to 40- μm diameter were imaged and had specific gravities representative of minerals. These particles were individual, unaggregated grains as confirmed by a holographic micro-velocimeter [Carder et al., 1982] and by scanning electron microscopy with automated

image analysis and X ray energy spectroscopy (SAX). A large fraction (45%) of the mineral mass flux was contributed by heavy minerals. The "giant" aeolian particles represented the lead edge of an aeolian input event. Subsequent daily traps collected smaller particles. The short residence times of large particles (<36 hours) and the low summer primary productivity of the Sargasso Sea suggest that biological filtration and particle scavenging [see Lerman et al., 1977; Deuser et al., 1981] were negligible removal mechanisms for these aeolian inputs.

The two most likely sources for this aeolian material were fallout from the Mount St. Helens explosive eruptions of 1980 and dust from North Africa. However, there are difficulties reconciling our data with these sources. It seems improbable that the large particles we collected could have derived from the Mount St. Helens eruption. The collection on June 19-20, 1980, was made well after the three volcanic eruptions of Mount St. Helens. Also, the sample contained a significantly higher mass fraction of heavy mineral (Ti, Fe) particles than has been reported in literature dealing with aerosols from Mount St. Helens or those collected at this great distance (>6000 km) from the other probable source, the Sahara Desert. Also, fly-ash or other likely man-made particles were not observed in the samples using scanning electron microscope/energy dispersive X ray (SEM/EDXA) analyses (morphology and composition).

To help corroborate the source for the aeolian material, we analyzed filter samples of airborne particles collected at Miami, Florida. These samples were compared with samples collected simultaneously in the water column in the Sargasso Sea 426 km to the east. These comparisons included individual particle size, shape, mineralogy, metal content, density, settling speed, and mass flux. Based upon their calculated residence times in the water, the particles from the sediment trap were used to reconstruct the aerosol mass concentrations over the Sargasso Sea for a 3.5-week period. The model aerosol concentrations were compared with those filtered on the appropriate day at Miami. This provided a calibration of parameters for a particle flux model and, in effect, a 30-m sedimentation column experiment.

Measurement Techniques

A cruise on the NOAA vessel R/V Researcher to the western Sargasso Sea from June 17 to

25, 1980, coincided with the early portion of a large input event of aeolian particles to the region. Independently, a routine sampling program for aerosols was being performed at Miami. Subsequent to the cruise, a cooperative study of aerosol and oceanic particles was arranged. Aerosol filter samples were selected for a time period encompassing that of the cruise. These samples were then analyzed in an analogous manner to samples collected in a sediment trap at 30-m depth [see Carder et al., 1982] at the Sargasso Sea location 426 km to the east. Also, for direct comparison with sediment trap data, aerosol data were converted from a mass flux to mass concentration.

Aerosol Sampling

Samples were collected by drawing air through 20x25 cm Whatman 41 filters at volume flow rates of about 1.2 m³ STP-min. For the nominal 1-day sampling periods, the sampled air volumes were normally about 1500 m³ STP. Flow rates were determined at the beginning and at the end of the sampling periods by measuring the pressure drop within calibrated orifice-plate outlet tubes; the calibrations are traceable to National Bureau of Standards (NBS) standards [Savoie, 1978; Savoie and Prospero, 1977, 1980]. Exact sampling periods were obtained from elapsed time meters. To minimize contamination from local soil and pollutant sources, the pump was controlled by a wind direction sensor and was activated only during periods of onshore winds. Under nomiral flow conditions, the filter head inlet has a computed particle size cutoff at 90-μm diameter for spheres of density 2.65 and 63 μm for density 5.2. However, we would expect that the actual performance of the inlet is considerably less than ideal and that the large particle sampling efficiency decreases rather rapidly for sizes >20-μm diameter.

Particle Trap Sampling

The sediment trap equipped with a holographic particle velocimeter (HPV) used in the free-drifting mode during our collections in the western Atlantic Ocean was constructed of 46-cm-diameter polyvinyl chloride (PVC) pipe, 120 cm in length. Two hinged doors, 28 cm above the trap bottom, were open during deployment and sealed shut at the end of the collection period by rubber tubing attached to the underside of each door. Closure was initiated with an electronic timer. A 2-mW HeNe laser was mounted inside the trap and aimed across a 4.5-cm-square settling chamber which was 50 cm in height. The laser was turned on, and the holographic camera triggered remotely with a digital timer. A more complete description of the in situ system can be found by Carder et al. [1982].

Prior to their first deployment, the traps were acid washed (4 m HCl) and then kept completely covered between use. Sodium azide was used to inhibit biological activity. The sediment trap with the HPV was deployed on four occasions (June 18, 19-20, 21, and 22-23), the first two collections being made at 30 m and the latter two at 100-m depth.

After retrieval, the collected material was vacuum filtered in a clean bench using Sterifil[R] containers. Tared, acid cleaned, Nuclepore[R] polycarbonate membranes (47-mm diameter, 0.45-μm pore size) were used for all filtrations. After a rinse with 250 mL of triple deionized water, the membranes were placed in individual freezer vials and vacuum desiccated over silica gel.

To determine the total mass flux (mg/m²/d), each membrane was given an additional deionized water rinse in a shore-based laboratory [Eggimann, 1975], redesiccated for 48 hours, and then weighed in a clean room to the nearest microgram on a Perkin-Elmer AD-2 automicrobalance. Subsequently, each membrane was subjected to a three-stage dissolution process. The initial step, designed to mobilize carbonates and referred to as the weak acid leach, consisted of a 2-hour treatment with 25% (vol/vol) redistilled acetic acid [Chester and Hughes, 1967; Eggimann, 1975]. The second step which utilized a 3-hour interaction with 2.0 M Na_2CO_3 removed biologically precipitated (amorphous) silica [Eggimann et al., 1980]. Finally, the remaining refractory components were solubilized by a series of high-temperature leaches with sequential additions of hydrochloric, nitric, and hydrofluoric acids [Eggimann and Betzer, 1976].

Chemical analyses for aluminum, calcium, iron, magnesium, and manganese were performed on the weak acid-soluble fraction by atomic absorption spectroscopy (AAS). Silicon was determined for the weak base soluble and refractory fraction on a Technicon Auto Analyzer II [Eggimann and Betzer, 1976]. Aluminum, iron, magnesium, and manganese determinations in the refractory portion were made by AAS [Eggimann and Betzer, 1976].

Additionally, for individual particle analysis by scanning electron microscope/energy dispersive X ray [Hanna et al., 1980], materials from the trap and atmospheric samples were filtered through 25 mm, 0.4-μm pore size Nuclepore[R] membranes, rinsed with 50 mL deionized water, placed in polycarbonate petri dishes, dried over silica gel, and sent to the State University of New York at Syracuse for processing.

Scanning Electron Microscopy

Radial sections of the Nuclepore membranes for SAX characterization of individual particles were cut with stainless steel surgical scissors. Using plastic forceps, these were placed on 1-cm graphite SEM stubs that had been freshly painted with colloidal graphite in isopropanol. These operations were carried out in a class-100 clean bench. The specimens were then coated with a 20- to 30-nm-thick layer of carbon in a high-vacuum evaporator. All samples were maintained in clean specimen boxes and kept in a desiccator before and after SAX analyses.

The SAX examinations were performed using an Etec Autoscan coupled to a Kevex 5100C X ray spectrometer and multichannel analyzer. Both pieces of equipment were interfaced with a LeMont Scientific B 10-E Image Analysis system. Depending upon the mass loading of the filter

and the preanalysis visual inspection of the sample, SEM magnifications of X200 to X800 were employed. All samples were analyzed using a 30-kV accelerating voltage, 25-mm working distance, 0° stage tilt, a 60° X ray takeoff angle, and a 3-s X ray acquire time (40% dead time).

Details of the process by which SAX creates "object vectors" for individual particles can be found by Johnson [1983]. The particle types were classified by a linear sorting algorithm developed over a 2-year period of analysis of suspended marine particles and sediment trap materials. The classification scheme is available upon request. The individual particle object vector descriptions have been maintained on computer disk.

Determination of the mineral composition of individual aerosol particles is difficult due to the small sample size. To aid in their identification, aerosol as well as sediment trap particles were subjected to SAX analyses. One central assumption of the technique is that the particle volume (and thus mass) is determined by assuming the particles to be prolate ellipsoids of revolution about the long axis. This assumption will also have a direct bearing upon the calculated settling velocities of the particles. An analysis of the likely heavy mineral (e.g., hematite, magnatite, pyrite) crystalline structures suggests that most such particles are relatively compact, with shapes reasonably represented by prolate ellipsoids. Long (>3:1 length-to-width) columnar or fibrous crystals (e.g., rutile, asbestos) are an exception, and they can be better represented by long cylinders. A second assumption is that an appropriate density can be assigned to each particle based upon the best geochemical intuition of particle type as judged by X ray elemental composition. The accuracy of both of these assumptions will be examined later by testing a calculation based upon residence times for particles captured at 30-m depth in a particle trap.

The formulas used in calculating the particle characteristics from the SEM size and shape information are as follows [after Lerman, 1979]:

	Prolate Ellipsoid	Circular Cylinder
Volume	$4/3 \, a^3 p$	$2 \, a^3 p$
Settling Velocity ($\parallel$ c)	$\dfrac{5p}{4+p} Ba^2$	$9/4[\ln(2p) - 0.72]Ba^2$

where a is the width/2, c is the length/2, b is the thickness/2 (unmeasured but assumed equal to a), and $p = c/a$. Also, $B = 2(\rho_1 - \rho_2)980/9$, where ρ_1 and ρ_2 are the densities of the particle and medium and η is the viscosity of the medium.

For a particle of length 2c and length-to-width ratio p the circular cylindrical volume representation of a particle would result in a volume (mass) that would be 1.5 times the volume calculated using a prolate ellipsoid representation. For particles settling parallel to the long or c axis, however, the two representations provide the same settling speed for $p = 3.2$. For longer particles, the

cylindrical representation (due largely to increased mass) provides faster speeds. For shorter particles, the ellipsoidal shape provides faster speeds (due largely to the reduced drag on an ellipsoid).

Since the cylindrical model of the residence times for the longer particles collected ($p > 3.2$) in the sediment trap provided more realistic back calculations of the time history of aerosol concentrations in the atmosphere over the Sargasso Sea (see later section), the cylindrical particle representation was used for particles with length-to-width ratios > 3.2 (< 30% of the samples).

Once the particle volumes have been estimated, particle mass distributions can be determined by plotting

$$AM_j = A \sum_{i=1}^{n} V_{ij} \, \rho_i \qquad (1)$$

as a function of particle diameter (spherical-equivalent). Here M_j is the total mass of particles in the jth diameter class, and V_{ij} is the volume of the ith particle with density ρ_i in the jth diameter class. A is a calibration factor relating the mass on the filter pad to the mass of particles viewed in each SEM field.

Another way of categorizing the particles is to determine the mass M_k of all particles in the kth mineral class, and summing all M_k values to determine the total mass of particles in the sample field of the SEM:

$$MA = A \sum_{k=1}^{m} M_k = A \sum_{k=1}^{m} \sum_{i=1}^{n} \rho_k \, V_{ik} \qquad (2)$$

Setting mass MA equal to the measured particle mass per cubic meter of air filtered for the aerosol filters allows determination of the distribution of mass as a function of particle diameter and mineral class for the average mass concentration of aerosol particles for each of the days when filter samples are available (June 18-27, 1980). A similar technique equating the total iron, silica, and calcium mass measured chemically for the trap samples with the total mass of iron, silica, and calcium determined for the minerals in the SAX field of view permits calibration of the mass for each SAX sample. These elements made up the bulk (>75%) of the metals of the mineral portions of each sample. The organically dominated particles produced low energy or no X rays and could thus be ignored, since they were not likely to have been of aeolian origin. Similarly, for comparison with the aerosol samples, calcium-rich particles were not included in order to avoid local biogenous input effects. Weak-base-soluble amorphous silica determinations [Eggimann et al., 1980] provided a measure of biogenic silica, which proved to be negligible for these samples.

Results

The aerosol data for June 18-27, 1980, can be displayed in a variety of ways. We chose to categorize them on the basis of particle size

TABLE 1.   Variation of the Heavy Mineral (HM) and Nonheavy Mineral
(NHM) Mass Concentration Values With Size
(Sphere-Equivalent Diameter) and Time for Aerosol Samples
Filtered at Miami, Florida, During June 1980

Diameter μm	June 18-20	June 20-23	June 23-25	June 25-27
HM Mass Concentration, μg/m³				
0.5-1.0	0.0307	0.1734	0.5115	4.1726
1.0-2.5	0.5334	1.1746	2.8919	3.3424
2.5-5.0	0.9580	1.9835	5.9922	1.8231
5.0-10.0	0.4388	0.7742	2.7030	0.2311
10.0-15.0	0.2591	0.0000	2.6833	0.0000
15.0-20.0	0.0000	0.0000	0.0000	0.0000
Total	2.22	4.1057	14.7819	9.5692
NHM Mass Concentration, μg/m³				
0.5-1.0	0.0168	0.3185	0.3777	6.7404
1.0-2.5	0.1964	3.0966	6.3070	15.7233
2.5-5.0	0.2921	5.1763	10.8277	8.8331
5.0-10.0	0.2129	3.0761	7.0624	1.8702
10.0-15.0	0.0000	0.0000	0.0000	0.0770
15.0-20.0	0.2931	0.0000	0.0000	0.0000
Total	1.0113	11.6675	24.5748	33.2440

Fig. 1a.   Heavy mineral aerosol mass concentration versus diameter
curves for Miami and In Western Sargasso in late June 1980.

Fig. 1.   Aerosol mass concentration versus diameter curves for Miami
and the western Sargasso during a Saharan dust "storm" in late June
1980.   The Sargasso data were converted from data on the aeolian
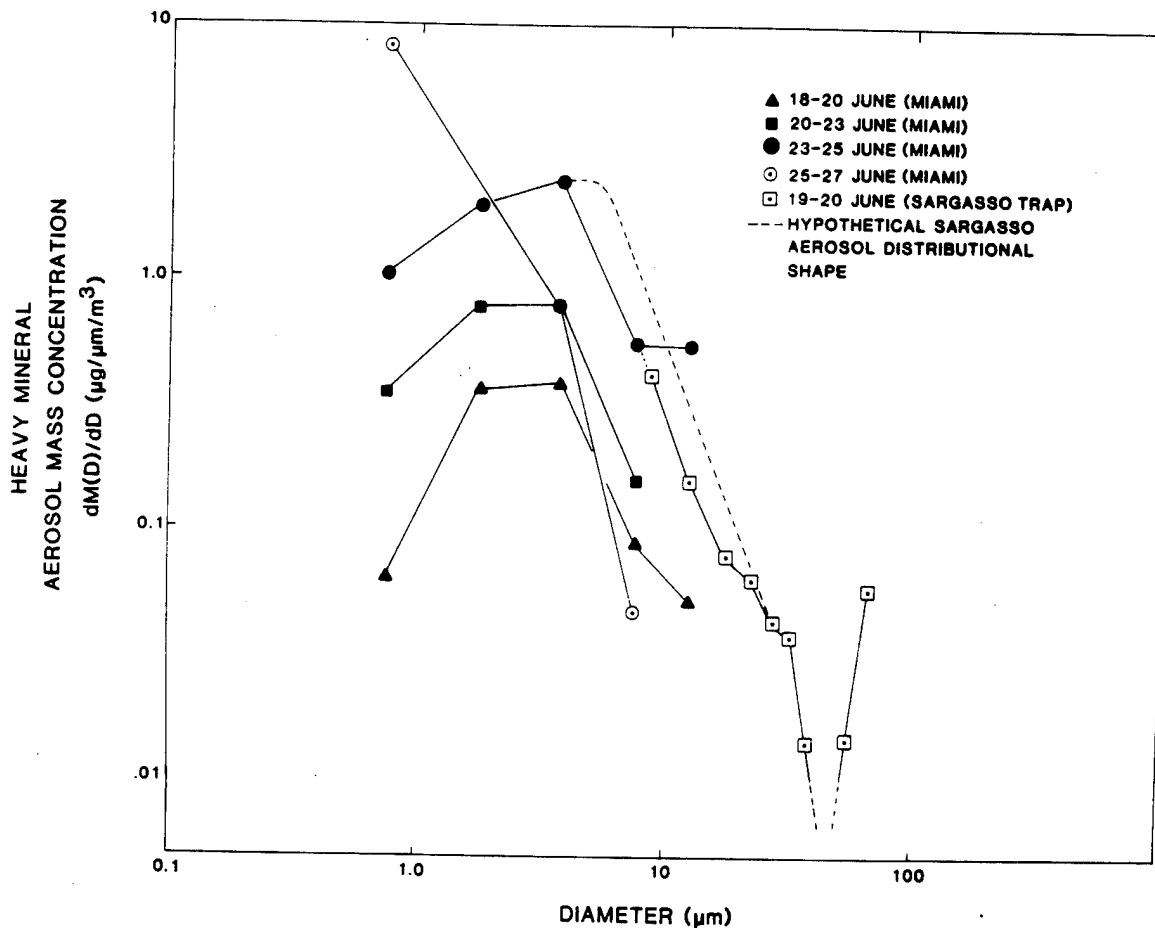particle flux into a sediment trap at 30-m depth.   (a) Heavy mineral
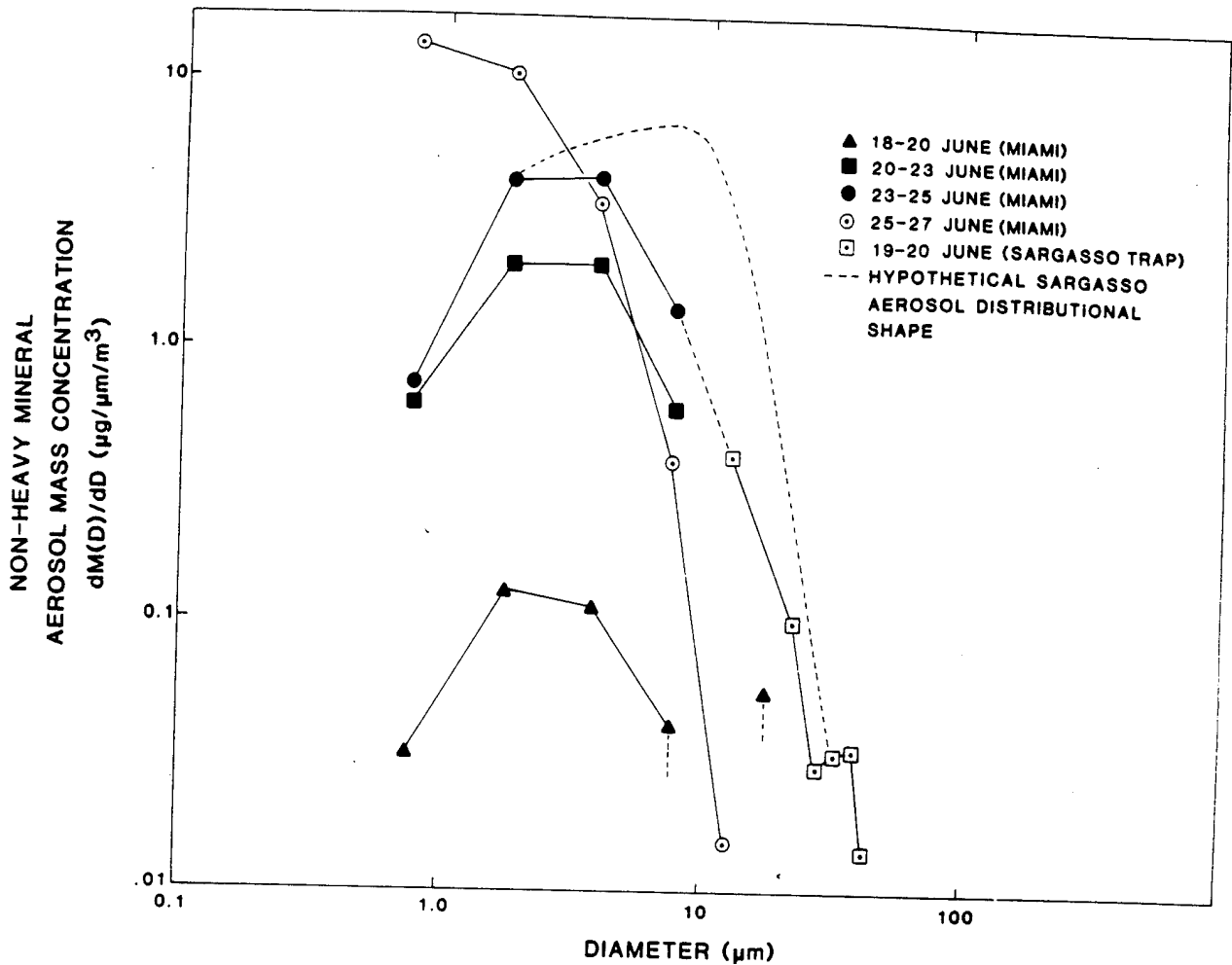and (b) nonheavy mineral data are shown.

Fig. 1b. Nonheavy mineral aerosol mass concentration versus diameter for Miami and In Western Sargasso in late June 1980.

and density, since these are the major determinants of particle settling velocity. Thus heavy mineral (HM) and "nonheavy mineral" (NHM) categories will be used throughout the paper as general density categories. The heavy mineral designation encompasses titanium-rich, iron-rich, iron-only, and hematite-bearing mineral categories with all other minerals falling into the nonheavy mineral class. These categories are based on the specific SAX sorting algorithm, which uses relative X ray intensities. They are not intended as a bulk chemical analysis. Specifically excluded from consideration are particles of biological origin. The specific gravity values assigned to the heavy minerals are as follows: Ti-rich (e.g., rutile: 4.2), Fe-rich (e.g., hematite-bearing, goethite: 4.2), and Fe-only (magnetite, pyrite, hematite: 5.2). The specific gravity values assigned to NHM minerals were centered about the value 2.65.

Table 1 displays the variation of heavy mineral and nonheavy mineral aerosol mass concentrations with size and time for Miami samples. At the leading edge of the aeolian input event (June 18-20), 68% of the mass concentration consisted of heavy minerals. At the trailing edge of the event (June 25-27), only 22% of the particle mass consisted of

heavy minerals. At the same time, the particle size distributions were fairly constant with time during the event (see Figure 1) until after June 25, when a significant increase in small particles and decrease in large particles occurred. Trap-derived aerosol mass concentration distributions with size were computed for the Sargasso Sea by dividing the mass flux value for each aeolian particle captured in a trap by its calculated settling speed in air. Figure 1 will be discussed in more detail below.

Table 2 depicts the variation of heavy mineral and nonheavy mineral vertical mass flux values (mass concentration times particle settling velocity) with size and time, calculated for Miami aerosol samples. Notice that while the mass concentration of particles filtered during June 25-27 was greater than during June 23-25, the vertical mass flux of particles during June 23-25 was almost 4.5 times the flux occurring during June 25-27. The reason for this result is the change in particle size and composition between the two samples, as is evident in the percent mass flux data plotted as a function of particle size in Figure 2. These curves have been normalized and plotted on log-log paper for ease of intercomparison.

TABLE 2. Variation of the Heavy Mineral (HM) and Nonheavy Mineral (NHM)
Vertical Mass Flux Values Calculated as a Function of Size
(Sphere-Equivalent Diameter) and Time for Aerosol Samples
Filtered at Miami, Florida

Diameter, μm	June 18-20	June 20-23	June 23-25	June 25-27
HM Mass Flux, mg/m^2/d				
0.5-1.0	0.0002	0.0012	0.0034	0.0278
1.0-2.5	0.0193	0.0424	0.1044	0.1207
2.5-5.0	0.1597	0.3308	0.9992	0.3040
5.0-10.0	0.2915	0.5144	1.7959	0.1535
10.0-15.0	0.4590	0.0000	4.7527	0.0000
15.0-20.0	0.0000	0.0000	0.0000	0.0000
Total	0.9297	0.8888	7.656	0.6060
NHM Mass Flux, mg/m^2/d				
0.5-1.0	0.0001	0.0012	0.0014	0.0258
1.0-2.5	0.0041	0.0645	0.1313	0.3274
2.5-5.0	0.0280	0.4964	1.0384	0.8471
5.0-10.0	0.0815	1.1774	2.7032	0.7158
10.0-15.0	0.0000	0.0000	0.0000	0.0785
15.0-20.0	0.6102	0.0000	0.0000	0.0000
Total	0.7239	1.7395	3.874	1.995

Superimposed on Figure 2 is the relative
flux of particles collected in the Sargasso Sea
sediment trap as a function of sphere-equiva-
lent diameter. The other curves are for
Saharan dust samples filtered during a major
dust outbreak in late fall 1973, some 2000 and
5000 km west of the Sahara [modified from
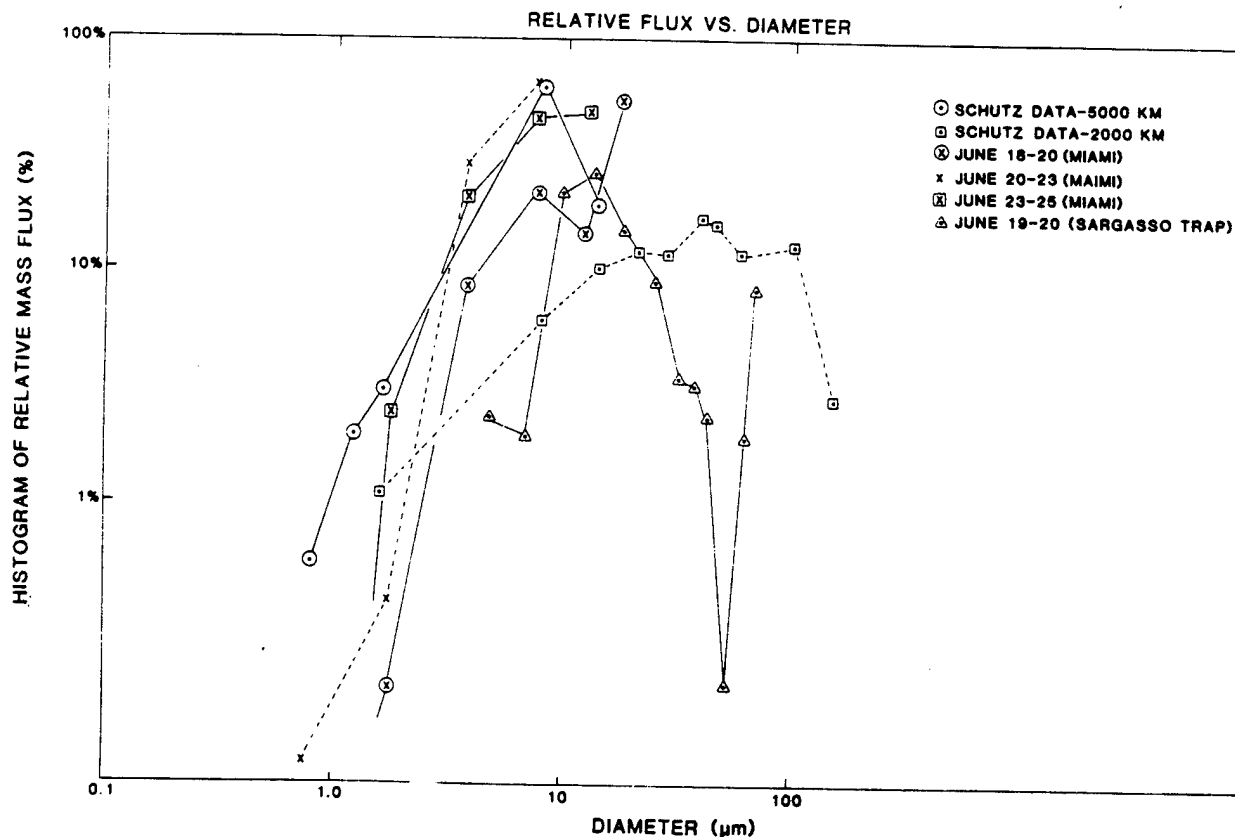Schutz, 1979]. Notice that the shape of the

Fig. 2. Distribution of relative mass flux as a function of diameter
for Miami aerosols, for aeolian particles in a Sargasso Sea sediment
trap, and for historical winter aerosol data sampled at about 11°N
latitude in the Atlantic.

TABLE 3. Variation (%) of the Heavy Mineral and Nonheavy Mineral Vertical Mass Flux as a Function of Particle Size and Mineral Class for a Sediment Trap Sample Collected at 30-m Depth in the Sargasso Sea on June 20, 1980

	Diameter, μm					
	<1.00	<2.00	<4.00	<8.00	<16.0	>16.0
Heavy Minerals						
Fe rich	0.00	0.00	0.00	0.08	1.01	12.63
Fe only	0.00	0.00	0.03	0.15	1.27	22.84
Ti rich	0.00	0.00	0.00	0.02	0.38	7.18
Total	0.00	0.00	0.03	0.25	2.67	42.65
Nonheavy Minerals						
Si rich	1.00	0.00	0.00	0.03	0.14	1.99
Si only	0.00	0.00	0.00	0.02	0.49	30.96
Misc. macro	0.00	0.00	0.00	0.10	0.85	5.27
Other NHM	0.00	0.00	0.00	0.11	1.03	13.38
Total	0.00	0.00	0.00	.26	2.52	51.60

5000 km Schutz curve is similar to the shapes of the Miami aerosol flux data of June 20-23 and 23-25. Neither the Schutz 5000 km nor the Miami curves displays data for particles larger than 20- μm diameter, while the Sargasso particle trap curve presents data out to 65 μm. This suggests that either the aerosol complement over the Sargasso site was significantly different from that over Miami, or that the aerosol filtration technique seriously discriminates against the large, fast-settling particles.

The mass flux data from the sediment trap located at 30-m depth in the Sargasso Sea are presented in Table 3 as the mass fraction of the sample present in a particular size and mineral class. This is an example of the SAX readouts for the aerosol samples as well. More than 93% of the mass flux in this sample was contributed by particles >16- μm diameter. Also, a significant fraction (>42%) of the mineral mass flux to the trap was due to heavy minerals (Ti-rich, Fe-only, and Fe-rich).

Daily dust concentrations for the month of June measured at Miami are presented in Figure 3. Also included for comparison are dust concentrations measured at Barbados, West Indies, during the same period. The tropical and subtropical aerosol concentrations were continually high throughout June, with the Miami concentrations only reaching those levels near the end of June.

Discussion

There are a number of conceivable sources for the nonbiogenic particles we measured in the water column: fallout from the Mount St. Helens eruption and soil material transported by winds from the North American or African continents.

The major volcanic explosions of Mount St. Helens on May 18 and 25 and June 13, 1980, have been extensively documented in the scientific literature [eg. Pollack, 1981; Danielsen, 1981; Gandrud and Lazrus, 1981;

Vossler et al., 1981; Chuan and Woods, 1981; Farlow et al., 1981; Ogren et al., 1981; Patterson, 1981; and references therein). The plume from the largest eruption (May 18) had circled the globe as many as 2 times by the time our samples were collected on June 19, 1980, at 26°N, 90°W in the western North Atlantic. While most of the ash particles from Mount St. Helens were found to have left the stratospheric plume within several days of the first major eruption [Gandrud and Lazrus, 1981], we could not initially rule out the possibility that Mount St. Helens (MSH) dust may have made some contribution to the samples that we collected in the Sargasso Sea on June 19-20.

The compositions of Saharan dust and volcanic debris are quite similar, and a distinction between these materials cannot be easily made on the basis of measured elemental concentrations. Saharan dust has a complement of major metal concentrations relative to Fe or Al that fall within a factor of 2 of those found in crustal rocks [Rahn et al., 1979; Glaccum, 1978]. A reworking of the MSH plume data of Vossler et al. [1981] suggests that most of the major mineral elements also fall within a factor of 2 (relative to Fe) of crustal elemental composition.

The size distributions of MSH stratospheric aerosols collected in late May to early June from the first two major eruptions contained particles generally smaller in diameter than 3 μm, with modes from 0.3 to 0.6 μm; those collected a day after the third major eruption contained particles generally smaller than 6.0- μm diameter [Farlow et al., 1981]. An aged stratospheric plume sample collected on June 17 contained only aerosols smaller than 4.0- μm diameter [Chuan and Woods, 1981]. The older stratospheric aerosols consisted largely of acid droplets or acid-ash globules. Therefore it is unlikely that MSH contributed to the large particles collected by the sediment trap.

The size distribution for Saharan dust particles from 1.3- to 10- μm diameter varies
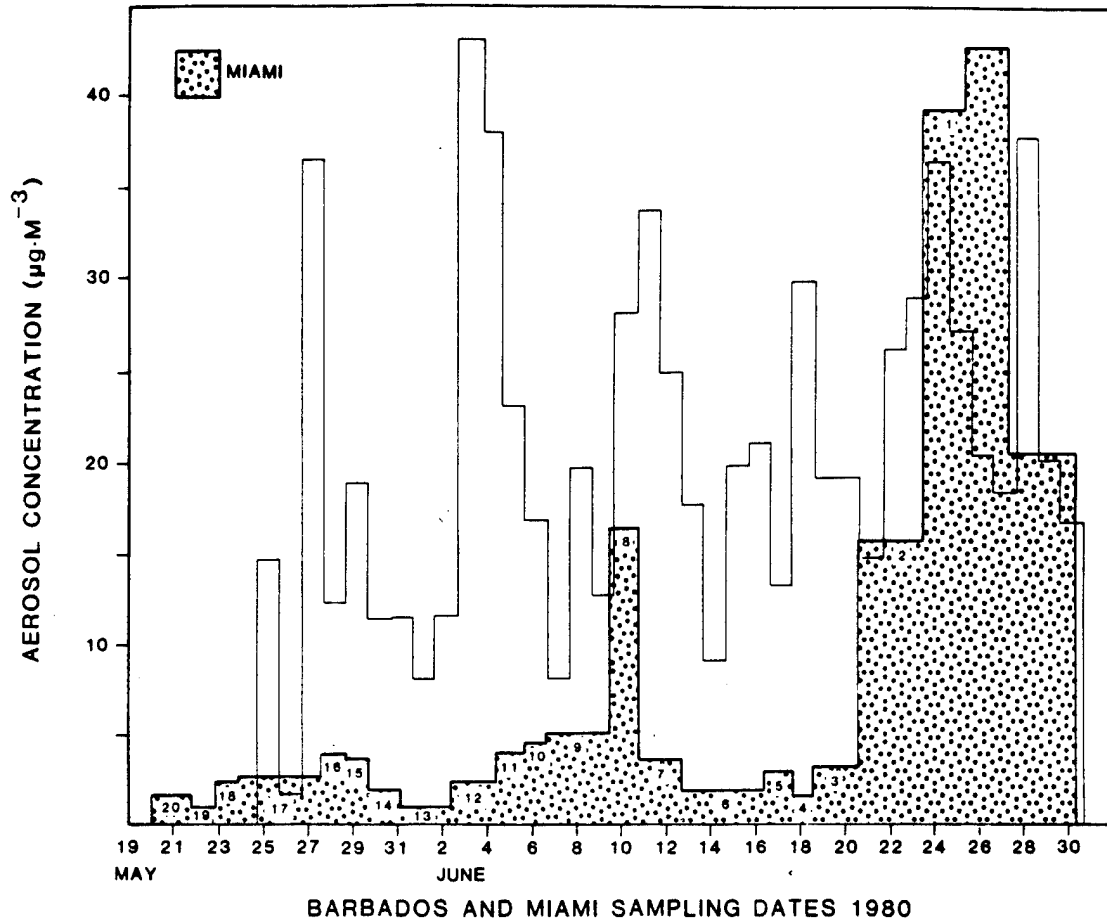
Fig. 3. Time history of aerosol mass concentration measured by filtration during late May-June 1980 at Miami, Florida, and Barbados, West Indies (13°10'N, 59°30'W). The numbered horizontal line segments represent collection or integration periods for each sample.

on average very little from soil aerosols measured elsewhere [Patterson and Gillette, 1977]. Saharan dust transport measurements and model calculations over the North Atlantic Ocean have been summarized by Schutz [1979]. While the mode diameter of mineral aerosol particles collected in Miami during the summer of 1974 has been reported by Savoie [1978] to be 2-3 μm, a small mass of particles >10 μm was found. No significant difference in size distribution was seen by Savoie between 1974 Miami and Barbados data. However, Saharan aerosols of large size (>15- μm diameter as far as 5000 km from the source) have been measured in June at Barbados [Prospero et al., 1970] and in the late fall on the 1973 Meteor cruise [Schutz, 1979]. In fact, the "anomalous" mineral size distribution curve of Prospero et al. [1970] for Barbados closely resembles our hypothetical distribution (Figure 1b) in shape, with a mode at about 7.5- μ m diameter, with 25% of the mass of the sample above 10- μ m diameter and 4% in the fraction above 20 μ m. This sample (26.2 μg/m³ air) also represented one of the largest aerosol concentrations measured during a 2-day sampling period in Barbados up to that date.

Most of the mass flux (>93% by weight)

measured in the upper Sargasso Sea and reported by Carder et al. [1982] was contributed by particles > 16- μm diameter, and a significant fraction consisted of heavy minerals. These initial Sargasso Sea data do not appear to conform to either the size or the mineral compositions of the reported MSH aerosols. In size, at least, the Sargasso particles collected could have been of Saharan origin, especially when one considers that flux measurements bias size distributions toward the larger sizes and bias composition toward the denser components.

There are a number of lines of evidence that lead us to believe that the mineral particles that we see falling through the water column are composed primarily of soil carried by winds from North Africa. Studies carried out at Barbados for the past 20 years have shown that large quantities of soil dust are routinely transported across the Atlantic each year, the maximum transport occurring in June and July [Prospero and Nees, 1977, 1985]. The dust transport occurs in a series of pulses that are often associated with disturbances that emerge from the coast of Africa at a rate of 1-2 a week during the summer [Carlson and Prospero, 1972; Prospero and Carlson, 1972]. In past

experiments, the progress of dust outbreaks across the Atlantic could be followed in data obtained from a network of stations as a series of large day-to-day variations in dust concentration [Savoie and Prospero, 1977; Prospero et al., 1979]. These studies show that Miami (and, presumably, the Bahamas to the east) is often impacted by African dust in the summer months, although not as frequently as stations in the lower latitudes, where the easterly trade wind flow is deep and persistent throughout the summer. Although the Miami area usually lies within the easterlies at this time of year, it is subject to meteorological patterns that can disrupt this flow.

During June 1980, the synoptic tropical weather pattern was relatively normal. The Azores high was consistently strong, and the easterly flow was persistent. No major atmospheric disturbances occurred during this period. Normally at this time of year, an east-west ridge of high pressure is positioned across north Florida, a feature that is usually conducive to steady southeasterly surface winds in Miami and the Bahamas. On June 18 the ridge moved over south-central Florida. On the June 19, the day of greatest relevance to this work, it was positioned over south Florida, resulting in weak southerly surface winds. Similar winds were experienced in the cruise area. Over Florida, the upper level winds (850 and 700 mbar) during June 18 and 19 were relatively weak, 5-15 knots, and southwesterly to westerly. No conventional upper level winds are available for the cruise area, but cloud motion vectors computed at the National Hurricane Center (NOAA, Miami) showed weak easterly to southeasterly winds. These general conditions persisted through the remainder of the month.

An examination of GOES satellite imagery for June [M. Matson, personal communication, 1984] shows no evidence of any major material input from North America until after the completion of the experiment. On June 22 and 23, a large hazy polluted area of high pressure emerged from the east coast. The hazy area traveled east and then south as the moving high approached the Bermuda high. By June 27, the cruise had been completed, and the area of haze extended from the mid-latitudes down to 30°N at 45°-55°W, a region 20° to 25° east of our study area. However, an immense area of haze caused by Saharan dust lay to the south of the pollution haze in the June 27 imagery. In any event, one would not expect large North America derived particles to be present in such an air parcel, especially after such a long trajectory around the Bermuda high.

In summary, the meteorological pattern for the latter half of June shows that south Florida and the cruise area were in a transitional zone on the northern edge of the easterlies. Despite the evidence of southerly to westerly surface winds over Florida, there is no evidence of any local strong meteorological features that could mobilize significant amounts of large diameter soil material. Also, the synoptic situation in the higher latitudes shows no evidence of strong winds or storms that could generate a major

dust episode, nor does it favor transport from the continental United States to the study area.

Our primary reason for assuming a North African source is that the Barbados data show that there were large amounts of Saharan dust present in the lower latitudes during this period (Figure 3), when the easterly flow was quite strong throughout the Caribbean. Hence Saharan dust could be carried into the research area even on westerly winds. We point out that the major dust peak observed in Miami at the end of June was clearly Saharan, and yet the surface level winds were southerly to southwesterly for the entire period.

Direct comparison of the sediment trap data with that collected at Miami was hampered by the phase difference in synoptic data collected at the two sites. Comparing the size distribution curves for the aerosols in Figures 1a and 1b indicates the June 23-25 Miami data provide the closest agreement in size and concentration with the Sargasso data. This suggests that aerosols of these characteristics arrived at Miami at least 72 hours after similar particles entered the Sargasso Sea. A second distorting influence at first glance is the fact that the small (circa 3- μm diameter) aeolian particles collected by the trap at 30-m depth must have passed through the air/sea interface weeks before the "giant" particles did so. Thus each particle collected at 30-m depth was a small fraction of the aerosol cloud passing overhead at 0814 hours on June 20 (trap closure) less the residence time of the particle in the water column. The aerosol filter data at Miami were collected over 2- to 4-day periods and are shown as numbered bins in Figure 3. Those trap particles with residence times falling in the appropriate time bin (e.g., trap closure time minus particle residence time plus phase lag equals time of a given aerosol collection bin) can then be compared with particles of like size and composition collected on the aerosol filter in Miami at that time. Also, due to long residence times, the fine particle fraction is more subject to diffusion, aggregation, and biological filtration influences [Lerman et al., 1977; Deuser et al., 1981], which cause residence time "smearing."

Aerosol filters for SAX analysis were only available for the period June 18-27, 1980. However, aerosol mass concentration data were available for the entire month. By matching peaks/valleys in the aerosol mass concentration data (Figure 3) with those present in the data (Table 4) for each individual mineral type (e.g., titanium-rich or iron-only) of mass concentration versus residence time, an average time lag of 72 hours for the Miami data was estimated. The surface winds during sampling at the Sargasso site were very weak during the entire sampling period, suggesting that upper level winds were responsible for the dust transport. Since mid-to-upper level winds at the two sites differed somewhat in direction, it is likely that a different pulse of Saharan aerosols was sampled at Miami than at the Sargasso site. However, the similarity in particle characteristics at the two sites

Table 4. Variation of Sargasso Sea Aerosol Mass Concentrations ($\mu g/m^3$) With Time When Based Upon Three-Model Aerosol Size Distributions for Heavy and Nonheavy Minerals

Bin	NHM June 23-25	NHM June 25-27	NHM Hypothetical	HM June 23-25	HM June 25-27	HM Hypothetical	Total June 23-25	Total June 25-27	Total Hypothetical	Total M	Total/M June 23-25	Total/M June 25-27	Total/M Hypothetical
1										39.34			
2	16.99		20.41	10.82		5.73	27.81		26.14	15.77	1.76		1.66
3	7.45	153.06	2.88	3.48	7.06	1.80	10.93	160.12	4.68	3.23	3.38	49.57	1.45
4	5.55	58.69	2.34	0.637	8.60	0.28	6.19	67.29	2.62	1.56	3.97	43.13	1.68
5	6.73	38.71	3.57	1.58	3.91	0.70	8.31	42.62	4.27	2.99	2.78	14.25	1.45
6	3.21	12.78	2.24	0.71	1.66	0.44	3.92	14.44	2.68	1.94	2.02	7.44	1.38
7	1.60	5.23	1.48	0.47	1.06	0.40	2.07	6.29	1.88	3.68	0.56	1.71	0.51
8	3.31	11.93	3.93	1.30	2.34	1.37	4.61	14.27	5.25	16.76	0.28	0.85	0.31
9	1.56	4.38	1.86	0.61	1.02	0.63	2.17	5.40	2.49	5.18	0.42	1.04	0.48
10	1.42	3.93	1.92	0.44	0.54	0.45	1.85	4.47	2.37	4.78	0.38	0.94	0.50
11	0.45	1.06	0.64	0.52	0.65	0.52	0.97	1.71	1.16	4.14	0.23	0.41	0.28
12	1.14	2.45	1.75	0.25	0.27	0.26	1.39	2.72	2.01	2.40	0.58	1.13	0.84
13	0.86	1.71	1.45	0.00	0.00	0.00	0.86	1.71	1.45	0.52	1.66	3.29	2.79
14	1.25	2.43	2.17	0.00	0.00	0.00	1.25	2.43	2.17	2.01	0.62	1.21	1.08

The residence time bins correspond to Miami (M) filtering periods with June 23-25 as bin 1, June 20-23 as bin 2, etc. (see Figure 3).

suggests that the samples of aeolian particles collected at the two sites were from the same general aerosol population.

Sargasso Site Aerosol Concentrations

To estimate the total mass concentration of aerosols present over the Sargasso during the time period represented by any residence time bin, an appropriate aerosol mass versus size distribution curve must be selected. Then the ratio of the area under the entire distributional curve to that under the portion of the curve representative of a particular residence time bin provides the multiplier needed to calculate the total Sargasso Sea aerosol mass concentration using the sediment trap data.

Three different model aerosol size distribution functions were selected for each of the nonheavy and heavy mineral categories. They are among the distributions shown in Figure 1: (1) the small-particle dominant curve from June 25-27, (2) the midsized-particle dominant curve from June 23-25 plus Sargasso Sea trap-derived aerosol data, and (3) the large-particle dominant hypothetical distributions shown linking the June 23-25 data together with the large-particle end of the Sargasso Sea sediment trap-derived aerosol distribution. All of the model aerosol distributions represented were bounded by actual data, and they provide a range from large-particle dominant to small-particle dominant distributions.

The results using these various model functions are summarized in Table 4 along with the appropriate time bin from Figure 3. Bin 2 corresponds to the June 20-23 sample period, and bin 8 corresponds to the June 9-10 period. The Sargasso aerosol mass concentrations resulting from each of the heavy and nonheavy mineral model size distribution functions and their totals (NHM + HM) are listed as well as the total Sargasso model concentrations ratioed to the measured Miami values.

The significant relative maxima values in bins 1-2 and bin 8 are present for all model functions. The June 9-10 maxima in the Miami data are also reflected in the Sargasso data corresponding to that period, especially for the heavy mineral data (columns 5, 6, and 7 in Table 4). These peaks indicate a reasonable degree of spatial coherence between the sites. To indicate which of the model functions provides Sargasso aerosol concentration estimates that most closely simulate Miami data, ratios of Sargasso to Miami aerosol concentrations for the model functions are shown in Table 4 (columns 12-14). A perfect match (identical concentrations) would yield a ratio of 1.0.

No single distribution curve can provide concentrations that effectively simulate Miami concentrations for the entire month of June. During the early storm period (bins 1 to 5), the size distribution at the Sargasso Sea Station must have been large-particle dominant (e.g., hypothetical or June 25-27 types of distributions). Otherwise, the aerosol concentration would have been unrealistically high (note columns 8, 9, and 10 in Table 4). These distributions are very representative in

shape of the "anomalous" Barbados distribution with giant particles reported by Prospero et al. [1970] for a similar aerosol storm event. The earlier periods are best simulated using the fine-particle dominant aerosol distribution of June 25-27, which is also similar to prestorm and poststorm Barbados data of Prospero et al. [1970]. Data for early June simulations are noisy due to a paucity of particles in any given bin, and are considered much less reliable. This could be due to biological scavenging and filtration [Lerman et al., 1977; Deuser et al., 1981], the effects of which would be more apparent for small particles with long residence times.

In an earlier paper [Schutz, 1979], it was speculated that since Saharan particles of diameter larger than 20 μm found 2000 km from the source could not be explained by the numerical simulations performed at that time, the giant particles detected must have been agglomerates of smaller particles. However, the giant aeolian particles measured with the SEM in this study as well as those measured holographically in situ [Carder et al., 1982] were definitely not agglomerates, but were individual particles. Also, the method used by Prospero et al. [1970] in obtaining their size distributions (settling velocity in distilled water) suggests that the particles were not agglomerates or aggregates. Compositionally, however, their Barbados data contained very little in the way of heavy minerals, only an occasional grain of zircon. ESSA 5 satellite images of the African dust storm have depicted eight separate storm centers or clouds, demonstrating the potentially local nature of particle sources and their suites of mineral types for a given aerosol storm event, accounting conceptually at least for differences in mineral composition with storm location.

Jaenicke and Schutz [1978], during an aerosol study at Cape Verde Islands, noted that the largest insoluble aerosol fraction (>40- μm diameter) arrived one day ahead of the next smaller fraction. From this sequence of events, they concluded that the main transport of mineral dust occurs in the layers above the trade wind inversion, as had been suggested earlier by Prospero and Carlson [1972] and Carlson and Prospero [1972]. These particles were then sedimented into the boundary layer air with the fastest settling particles arriving first. Our observations seem to corroborate this concept for the western North Atlantic: the surface winds were light to calm throughout our study period, yet a heavy haze blanketed the area. Evidence from later sediment trap deployments in the Sargasso Sea indicates that the giant particles discussed in this report were less dominant. At Miami we also noted the arrival of the larger particles (>5- μm diameter) as many as 5 days ahead of the smaller particles (Figure 1).

It seems clear that present aerosol transport models are not adequately addressing the transport of giant particles from the Sahara to the Sargasso Sea. These giant particles significantly increase aeolian sedimentation fluxes during such aerosol storm events. Whether the giant Saharan dust particles

reported by Prospero et al. [1970] for Barbados and in this report for the Sargasso are representative of the lead edge of aerosol storm events, or whether they are truly unusual and statistically insignificant occurrences, cannot be determined until additional unbiased size data are available. However, it is quite clear that these large particles, when present, deliver a large fraction of the aeolian mass flux to the ocean.

References

Carder, K. L., R. G. Steward, and P. R. Betzer, In-situ holographic measurements of the sizes and settling rates of oceanic particulates, J. Geophys. Res., 87(C8), 5681-5685, 1982.

Carlson, T. N., and J. M. Prospero, The large-scale movement of Saharan air outbreaks over the northern equatorial Atlantic, J. Appl. Meteorol., 11(2), 283-297, 1972.

Chester, R., and M. J. Hughes, A chemical technique for the separation of ferro-manganese minerals, carbonate minerals, and absorbed trace elements from pelagic sediments, Chem. Geol., 2, 249-262, 1967.

Chuan, R., and D. Woods, Characterization of aerosols from eruptions of Mt. St. Helens, Science, 211(20), 830-832, 1981.

Danielsen, E., Trajectories of Mount St. Helens eruption plume, Science, 211(20), 819-821, 1981.

Deuser, W. G., E. H. Ross, and R. F. Anderson, Seasonality in the supply of sediment to the deep Sargasso Sea and implications for the rapid transfer of matter to the deep ocean, Deep Sea Res., 28A(5), 495-505, 1981.

Eggimann, D. W., The West African Shelf-- Chemical evidence of particle transport to the eastern Atlantic basin, M.S. thesis, 170 pp., Univ. of South Fla., Tampa, 1975.

Eggimann, D. W., and P. R. Betzer, A new method for the decomposition and analysis of refractory oceanic suspended materials, Anal. Chem., 48, 886-890, 1976.

Eggimann, D. W., F. T. Manheim, and P. R. Betzer, Dissolution and analysis of amorphous silica in marine sediments, J. Sediment. Petrol., 50, 215-225, 1980.

Farlow, N., V. Oberbeck, K. Snetsinger, G. Ferry, G. Polkowski, and D. Hayes, Size distributions and mineralogy of ash

Holographic microvelocimeter for use in studying ocean particle dynamics

Kendall L. Carder

Department of Marine Science
University of South Florida
St. Petersburg, Florida 33701

Abstract

Laboratory measurements were made of the sizes, shapes, and settling speeds of microscopic ocean-type particles by recording sequential transmission holograms of clay aggregates and glass shot in a settling chamber. Density values for particles that were approximate spheroids were determined using a modified Stokes settling equation. The successful application to this problem of inexpensive, off-the-shelf components and low power, HeNe lasers improves the feasibility of remote, *in situ* measurements of ocean particle settling dynamics.

Introduction

Studies of the dynamics of particles in the oceans have been seriously hampered by lack of a means of measuring the settling speed and density of suspended particles on an individual basis. These two variables can be related through the various forms of the Stokes settling equation.[1]

$$w = \frac{2g\,(\varrho_p - \varrho)\,a^2}{9\,\eta} \qquad (1)$$

where a is a characteristic dimension dependent upon particle shape (for a sphere a is the radius), ϱ_p is the density of the particle, ϱ is the density of water, η is viscosity, and g is acceleration due to gravity. However, even if we limit our study to the mineral particles found in the oceans, the density of a suite of such particles can vary from about 2.7 gm/ml for unaggregated quartz particles to less than 1.06 gm/ml for aggregated clay particles.[2] The low values occur because water is occluded in the clumping of clay particles. The upshot of this argument is that the range of settling speeds resulting from such a spread in values for density for a given size particle varies by a factor of about 50. Obviously, models of particle behavior in the oceans based upon such uncertain information cannot even be considered.

Photomicrographic studies of settling particles have been made[3] with great difficulty due to field limitations, but holography circumvents that problem. Sequential holographic recordings permit quantification of particle size, shape and settling speeds. Application of Eq. 1 results in an estimate of the particle density ϱ_p.

Collection and storage of ocean particle samples for laboratory analysis can result in sampling artifacts (e.g., aggregate formation or disintegration, cell lysing). Accurate measurements of settling rates of individual ocean particles must ultimately be performed *in situ* in a turbulence-damping, stationary settling chamber. Such a system will require a compact, low power, holographic photomicrography package, preferably using inexpensive off-the-

shelf components. Results using components applicable to such a system are presented in this paper.

Background

Holographic photomicrography has found wide application in aerosol[4] studies, and holographic cine cameras[5,6] have been developed for studying plankton behavior in ocean waters. Since the stability requirement for recording moving particles is that the particle not move more than about one-tenth its mean diameter during the exposure,[4] ruby, argon or xenon pulsed lasers have been employed to illuminate such relatively fast moving particles.

For fine oceanic particles, the settling speeds are generally in the range of 10^{-1} to 10^{-5} cm/sec. Consequently, the exposure times can be considerably longer. Also, since fine particles fall at a rate that increases as the square of the mean diameter of the particle, the exposure time T can be related to the mean particle diameter d by

$$d/10 = Kd^2T. \qquad (2)$$

Thus, $T = (10Kd)^{-1}$ for particles falling through a stationary fluid. For spherical particles $K \doteq (54)\,(\varrho_p{-}\varrho)$ sec^{-1}cm^{-1}. K is about 90 sec^{-1}cm^{-1} for quartz to about 1.3 sec^{-1}cm^{-1} for phytoplankton and aggregates. T then for fine quartz particles can range from about 11 seconds (10^{-4} cm diameter) to .11 seconds (10^{-2} cm diameter). Obviously, lower density particles can tolerate even longer exposure times. However, if the medium is moving, then the net particle speed must be considered.

With these relaxed exposure time criteria, one can consider using a continuous, low power HeNe laser for the coherent light source and a lensless 35 mm camera as the recorder. By taking sequential shots separated in time by ΔT, the change in position of particles in the fluid is measured in 3-space, and the true velocities of all of the particles in the sample volume are recorded simultaneously. Thus, settling or swimming velocities can be recorded for microscopic particles in a stationary medium.

The Experiment

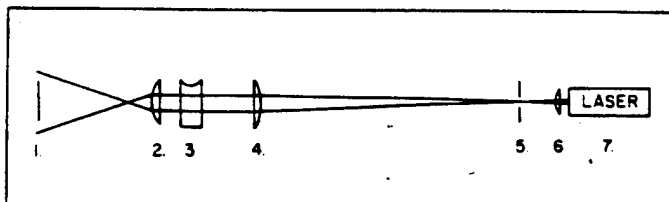The optical design for studying the densities and dynamics of par-

Figure 1. Schematic of the holographic recording components: 1) film plane of the 35 mm camera body; 2) 28 mm focal length lens; 3) 76.2 mm diameter x 1.2 m long settling cuvette with optical ports; beam scattering volume (76.2 mm long x 12 mm diameter) was 25 cm below the air/water interface; 4) 336 mm focal length lens; 5) 300 μm pinhole; 6) 25 mm lens; 7) 1 mW HeNe laser.

ticles in ocean water is similar to that of the Thompson camera[4] except that a 1 mW continuous HeNe laser (Hughes Model 3180H) was used as the coherent light source, and a Nikon Model F2A 35 mm camera body with motor drive was used as a sequential image recorder (see Figure 1). For reconstruction, the cuvette was replaced by a hologram which was moved along the optical axis until a particle of interest came into focus.

The cuvette was nearly filled with filtered water containing 3.5% NaCl. It was then allowed to sit until only Brownian motion remained. Particle-laden water of lower density was carefully superimposed over it so that the particles were required to settle through a slight density interface. This minimized mixing as a significant advective transport mechanism. For fast settling particles (e.g., glass spheres 10–50 μm) images were recorded every 0.3 sec. For slower settling particles (e.g., clay aggregates) images were recorded every 5 seconds. Latex spheres (10.1 and 18.04 μm diameter) were used as standard sizing particles (see Figure 2).
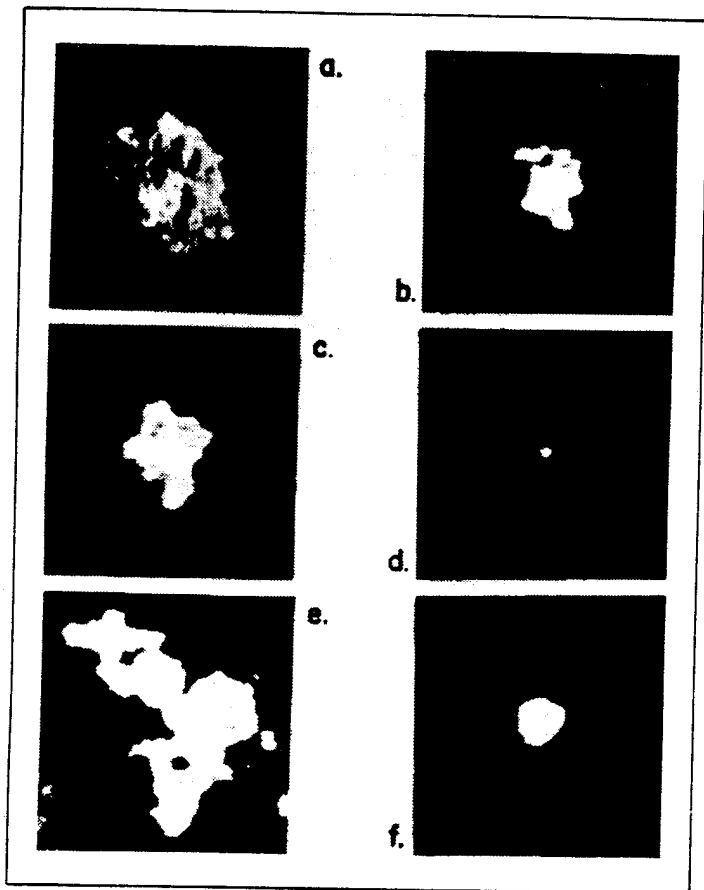
Figure 2. Holographic reconstructions of various particles: (a) aggregate #1 in Table 1; (b) aggregate #2 in Table 1; (c) aggregate #3 in Table 1; (d) 10.2 μm diameter standard latex sphere; (e) large, irregular aggregate, 209 μm in length; and (f) glass shot #7 in Table 1. Settling direction is toward the bottom of the page.

Aggregates were created by mixing Magdalena River water (Columbia, S.A.) with filtered Sargasso Sea water. The suspension was stirred gently for several hours and allowed to settle. Later, the aggregate fluff was resuspended by gentle stirring, resulting in aggregate diameters in the 50 to 200 μm size class. These particles were holographically recorded settling through the cuvette, and reconstructions of several of them are shown in Figure 2.

Many of the aggregates recorded were approximately prolate spheroids in shape, although a few were quite irregular. In prolate spheroids, the polar semi-axis c is longer than the equatorial radius a. Such aggregates were observed to fall with the polar axis parallel to the direction of settling, so the equation for their set-

tling speed is[1]

$$w = \frac{2g(\varrho_p - \varrho)(1-E)a^2}{9\eta(1-0.2E)}$$ (3)

where $E = 1 - c/a$ is a measure of distortion of the sphere. Equation 3 was then used to determine the density of aggregates of nearly spheroidal shape (see Table 1).

Table 1. Settling characteristics of clay aggregates (approximate prolate spheroids) and glass shot (approximate spheres); ϱ was 1.025 for salt water.

No.	Type	a (μm)	c (μm)	E	w (cm/sec)	ϱ_p (gm/ml)
1	aggregate	41	65	-.40	.070	1.14
2	aggregate	26	37	-.42	.034	1.20
3	aggregate	41	48	-.18	.008	1.04
4	glass shot	25	25	0	.21	2.60
5	glass shot	24	24	0	.22	2.69
6	glass shot	18	18	0	.13	2.89
7	glass shot	21	24	-.14	.20	2.88

The range of densities (1.04 to 1.20 gm/ml) determined for the aggregated particles falls within the range listed by various other authors[2,7] for oceanic particles. However, the range of $\varrho_p - \varrho$ is so wide that the accuracy of the method cannot be seriously tested using clay aggregates.

Glass shot of spherical shape (PF-11 Cataphote Corporation, Jackson, Miss.) were used as a better indication of the accuracy of the method. The manufacturer lists the range of particle densities ϱ_p to be 2.42 to 2.99 gm/ml. While all of the densities determined for the glass shot fell within this range, it would be desirable to use calibration particles in the future which have a narrower density range. At that time a more exhaustive study of the errors involved in the method will be made. This preliminary study has convinced the author that off-the-shelf components similar to those used in this experiment can provide holographic data of sufficient resolution for particle settling studies both in the laboratory and in situ.

Observations and Conclusions

1. Each settling aggregate could be easily followed from one hologram frame to the next due to its distinctive shape.
2. None of the particles was observed to be tumbling.
3. Less symmetrical particles were observed to settle on a slight bias.
4. Densities calculated for the particles were within the ranges expected.

References

1. Lerman, A., D. Lal and M. F. Dacey. Stokes' settling and chemical reactivity of suspended particles in natural waters: In Gibbs. R. (ed.), Suspended Solids in Water. Plenum. N. Y., pp. 17–47. 1974.
2. Krone. R. B., Engineering interest in the benthic boundary layer: In McCave, I. N. (ed.), The Benthic Boundary Layer. Plenum, N. Y., pp. 143–156. 1976.
3. Krone. R. B., A study of rheological properties of estuarial sediments. Hydraulic Engineering Laboratory and Sanitation Engineering Research Laboratory, Univ. California. Berkeley. 1963.
4. Thompson, B. J., J. H. Ward and W. R. Zinky. Application of hologram techniques for particle size analysis, Appl. Opt.. Vol. 6. pp. 519–526. 1967.
5. Heflinger, L. O., G. L. Stewart and C. R. Booth. Holographic motion pictures of microscopic plankton, Appl. Opt., Vol. 17, pp. 951–954. 1978.
6. Stewart, G. L., J. R. Beers and C. Knox. "Application of Holographic Techniques to the Study of Marine Plankton in the Field and Laboratory—II.," Proc. Soc. Photo-Opt. Instrum. Eng., Vol. 41. San Diego, pp. 183–194. 1973.
7. Pierce, J. W., Suspended sediment transport at the shelf break and over the outer margin: In Stanley, D. J. and D. J. P. Swift (eds.), Marine Sediment Transport and Environmental Management. Wiley. N. Y., pp. 437–458. 1976.

Aggregation of diatom bloom in a mesocosm: Bulk and individual particle optical measurements

DAVID K. COSTELLO,* KENDALL L. CARDER*
and WEILIN HOU*

Abstract—Optical measurements were acquired during a controlled. diatom-dominated. phytoplankton bloom and aggregation event engineered in a 1200 liter laboratory mesocosm. Observations included beam attenuation (c) at 660 nm and particle absorption spectra for phytoplankton and detritus. Despite intense bloom conditions in the mesocosm (chlorophyll a concentrations exceeding 165 mg/l and c exceeding 9 m^{-1}). most optical parameters covaried linearly with biochemical parameters. There were significant positive correlations for dry mass versus the particle attenuation coefficient (c_p) at 660 nm. particulate organic carbon versus the computed particle scattering coefficient (b_p) at 660 nm. and chlorophyll a versus the measured particulate absorption coefficient (a_p) at 660 nm. and chlorophyll a versus the measured absorption coefficient for phytoplankton (a_ϕ) at 673 nm.

Multiple-component model simulations of optical and biochemical measurements accurately predicted particulate organic carbon (POC). particulate organic nitrogen (PON). and chlorophyll a concentrations using c_p and a_p measurements. Similar equations for c_p and a_p estimates using the biochemical measurements are also presented. New commercially available instruments to measure $c(\lambda)$ and $a(\lambda)$ should make remote PON. POC. and Chl a estimates practical upon measurements of site-specific relationships similar to those presented here.

INTRODUCTION

The optical properties of water are affected by dissolved and suspended material, and, in shallow areas, by the bottom albedo. The properties of water are well known (Smith and Baker, 1981; Morel and Prieur, 1977), the absorption and fluorescent effects of dissolved material are reasonably well understood (Bricaud *et al.*, 1981; Carder *et al.*, 1989, 1991; Hawes *et al.*, 1992; Hayase and Tsubota, 1985), and investigations of the effects of the bottom albedo are now underway (Carder *et al.*, 1993; Costello and Carder, 1994; Lee *et al.*, 1994). Due to the sheer enormity of the task and the cost of in-situ sampling, however, a comprehensive understanding of the coupling of the optical properties to the biophysical state of the suspended material is still elusive.

Time series measurements of in-situ optical properties have been made with moored and floating arrays during the past decade to understand the dynamics of the marine biosphere (Dickey 1991; Marra *et al.*, 1992; Smith *et al.*, 1991). While changes in the optical properties have been observed, time series of correlative bio-chemical data often have been missed as ships have not been available to continuously monitor the system. A

---

*University of South Florida. Marine Science Department. 140 7th Avenue South. St. Petersburg, FL 33701, U.S.A.

mesocosm, on the other hand, creates a captive environment for a mixed phytoplankton population that allows the co-acquisition of optical and bio-chemical data. Carefully designed mesocosm studies, furthermore, allow the study of phenomena not otherwise easily available, including growth, bloom, and aggregation of a phytoplankton community.

The term 'marine snow' was first used to describe large, rapidly sinking marine aggregates by Suzuki and Kato (1953) more than four decades ago. Since that time, marine particle aggregation has been found to be ubiquitous (Alldredge and Silver, 1988; Alldredge and McGillivary, 1991; Asper *et al.*, 1992; Honjo *et al.*, 1984; Riebesell, 1992; Wells and Shanks, 1987). It has been hypothesized that marine snow has a significant role in carbon export from the euphotic zone and sequestration at depth (Fowler and Knauer, 1986; Hill and Nowell, 1990; Hill, 1992; Jackson, 1992; Jackson and Lochman, 1992; Stolzenbach, 1993). Little is known, however, regarding the optical properties of aggregated particles. This is due both to the fragile nature of the aggregates, which makes sample collection problematic, and to the difficulties in relating measurements of inherent optical properties (IOPs; Preisendorfer, 1961) of the water to particle optical properties (e.g. Betzer *et al.*, 1974; Biscaye and Eittreim, 1974; Carder *et al.*, 1974; Siegel *et al.*, 1989). IOP measurements often utilize sample volumes too small to consistently include the statistically 'rare' large particles; however, even when the large-particle concentration is relatively low, it can produce significant effects on the underwater light-field (Carder and Costello, 1994). Large particle effects would be manifest in applications (e.g. remote sensing of ocean color and LIDAR) which utilize larger sample volumes.

In-situ quantification of large-particle optical effects, however, remains problematic not only because of the large sample volumes required to accurately quantify the concentration of marine snow particles, but also because concentrations of large particles are temporally and spatially variable.

The Significant Interactions Governing Marine Aggregation (SIGMA) mesocosm experiment (Alldredge *et al.*, 1995) provided the opportunity to acquire optical measurements of a phytoplankton community during growth, bloom, and aggregation stages in a controlled and captive environment. Numerous ancillary measurements allowed an analysis of the correlation of optical measurements to other biochemical parameters.

METHODS

The experiment was conducted in a temperature-controlled (12.5–13°C) environmental chamber utilizing a 1400 liter-capacity, fiberglass tank filled with 1150 liters of seawater from the Santa Barbara Channel, California, which had been filtered through a subsand filter. Fifty liters of unfiltered seawater were added as an inoculum for the tank on 6 March 1993 (sample Day 0). Artificial light was provided by halogen bulbs set at a 14 h light: 10 h dark cycle. The tank was slowly stirred (2.6 rpm) by a plexiglass propeller near the bottom which produced an average calculated sheer rate of 1.3 s^{-1}. Water samples were drawn from a spigot located 30 cm from the tank bottom. The spigot projected 10 cm into the tank.

Bulk measurements

Beam attenuation was measured using a 25 cm pathlength Seatech transmissometer. This instrument utilizes a 660 nm collimated source and has an in-water half-angle of

acceptance for forward scattered light of 1.8° (Bartz *et al.*, 1978). The measured beam attenuation value, c_m (m^{-1}), was computed according to

$$c_m = -\frac{1}{r} \ln (T) = (-4) \ln \left(\frac{V_c}{5}\right) \tag{1}$$

where V_c is a calibrated voltage, the factor -4 is the negative reciprocal of the transmissometer pathlength, r, ln is a Napierian logarithm, and the factor 5 is the voltage level for 100% transmission.

A beam attenuation coefficient corrected for the forward-scattered light-acceptance angle, c (m^{-1}), was computed using a 2nd-order polynomial fit to the correction for this instrument (Bartz *et al.*, 1978).

$$c = 0.0003(c_m)^2 + 1.375(c_m) - 0.1459 \tag{2}$$

This correction is essentially linear and assumes a particle size distribution with a hyperbolic slope value of -2.9 and an index of refraction relative to water, m, of 1.05.

The filter pad absorption measurements follow the method of Mitchell and Kiefer (1988) using the pathlength amplification factor coefficients of Bricaud and Stramski (1990). Filter pad transmission for particle-laden sample pads and blank pads were measured with a Spectron Engineering, Inc. 256-channel spectral radiometer (resolution 2.6 nm, half-bandwidth 7 nm) to yield particle absorption coefficients (a_p) from 400 to 750 nm. Absorption spectra for detrital material, a_d, were also obtained after pigment extraction with hot methanol (Kishino *et al.*, 1985; Roesler *et al.*, 1989). The absorption spectra for phytoplankton, $a_\phi = a_p - a_d$, were calculated on a channel-by-channel basis.

The particulate absorption coefficient at 660 nm, a_p, can be utilized in conjunction with the beam attenuation coefficient at 660 nm, c, to estimate the particulate scattering coefficient at 660 nm, b_p: $b_p = c - a_p - a_w$. At 660 nm, absorption by water, a_w, is 0.4 m^{-1} (Smith and Baker, 1981) and scattering by water and absorption by dissolved material are negligible (Jerlov, 1976).

Individual particle reflectivity

Video images of individual aggregates were collected 30–35 cm below the surface using the large-field camera (LFC) and structured lightsheet modules from the Marine Aggregated Particle Profiling and Enumerating Rover (MAPPER). The MAPPER system uses four diode lasers (675 nm for the mesocosm configuration), each set at the corner of a square, and line-generator optics to create a thin ($\approx$1 mm) sheet of illumination. Three, longpass-filtered, video cameras with different magnifications have coincident image planes in the light sheet (see Costello *et al.* (1991, 1992) and Costello and Carder (1994) for details).

The MAPPER LFC used a Sony HyperHAD CCD camera (XC-75) with optics producing a pixel resolution of 285 μm at 640H × 480V digitization. The video imagery was recorded in S-VHS format (measured at 410 HTVL resolution) and processed by our Image Control and Examination (ICE) system, an automated, frame-by-frame, video data reduction system (Costello *et al.*, 1992; Hou *et al.*, 1994). The ultimate resolution of the LFC data was about 450 μm. In order to minimize potential measurement errors

(especially in the horizontal dimension; see Costello *et al.* (1994)) all targets with fewer than 10 grouped pixels, 1 mm equivalent spherical diameter, were ignored in the LFC data.

The closeness of the indices of refraction of marine-aggregate material and water (Honjo *et al.*, 1984) results in low target reflectivity, a property important for image formation. Because images are formed by reflected illumination, which is attenuated along the total optical path (source to target and target to sensor), material that can be successfully imaged at one attenuation level may not be successfully imaged at a higher attenuation level. Particle discrimination depends on an image radiance threshold below which signals are considered to be background noise. Unless this threshold value is changed to compensate for attenuation changes, low-reflectivity particles that can be successfully imaged/counted at low c values may not be successfully imaged/counted at higher c values. The c values for these image data sets range from 2.54 to 8.40 m^{-1}.

For material of a constant reflectivity R, the pixel gray-scale value (GS) is a function of c

$$GS = tR(I_o\, e^{-(d_1 c)})\, e^{-(d_2 c)} = tRI_o\, e^{-c(d_1 + d_2)} \qquad (3)$$

where t is the transfer function of the imaging system, assumed constant, I_o is the illumination power, also assumed constant for the laser diode sources (see Costello *et al.* (1991), d_1 (m) is the average distance from laser projectors to the target, and d_2 (m) is the distance from the target to the sensor. For the MAPPER LFC, $d_1 + d_2$ equals 0.34 m, and a target saturating the sensor at GS = 255 at $c = 2.54\, m^{-1}$, for example, would only produce a GS value of 35 at $c = 8.4\, m^{-1}$. Conversely, material producing a GS value of 1, the sensitivity threshold of the system at $c = 8.4\, m^{-1}$, would produce a GS value of 8 at $c = 2.54$ m^{-1}. Material imaged at gray-scale values 1–7 at $c = 2.54$ would not be visualized and counted at $c = 8.4$. This is equivalent to an image processing threshold which varies with c. Uncorrected reflectivity (or size) determinations will be biased toward brighter (often larger) measurements for sample sets with lower c values. In order to ensure that material at or above the same reflectivity level was being measured, an image processing gray-scale threshold (GST, Fig. 1) was calculated, for each image set, according to

$$GST_i = 1\, e^{(0.34(8.4 - c_i))} \qquad (4)$$

where the factors 1 and 8.4 are, respectively, the minimum gray-scale possible and the c value for the highest attenuation found, on Day 12. The measured c value for Days 8 to 14 is c_i. Note that if a camera system with a low signal-to-noise ratio were used, the minimum gray-scale value would not be 1, but would need to exceed the noise level.

Average particle reflectivity data were calculated by normalizing to the reflectivity calculated for the sample set with the lowest c value (Day 8, $c = 2.54\, m^{-1}$) according to

$$R_i(\text{norm}) = \frac{R_i}{R_1} = \frac{GS_i}{GS_1}\, e^{(0.34(x - 2.54))} \qquad (5)$$

where the factor 2.54 is the c value for the sample set with the lowest attenuation (Day 8) and c_i is the c value for Days 8 to 14.

RESULTS

Bulk measurements

Values of c were typically larger below the afternoon thermocline, induced by lighting, of the mesocosm (Alldredge *et al.*, 1995) than either above the thermocline or in the
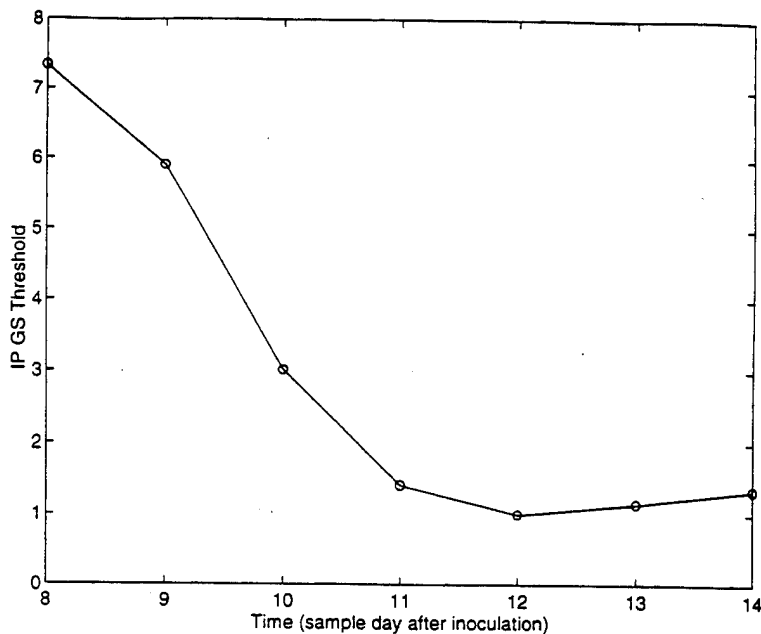
Fig. 1.   Image processing gray-scale threshold utilized for sample Days 8 to 14 calculated from equation (1).

homogenous water column which resulted shortly after lights were turned off. The c values increased dramatically to a maximum on the afternoon of Day 11 and then lessened gradually (Fig. 2). The variance of the signal (patchiness due to large particles) increased significantly on the afternoon of sample Day 10 and was sustained through Day 14.

The absorption spectra of the particles, a_p, were smoothed with a 7-element Hanning filter. The spectral values increased from Days 7 to 11 and decreased on Days 12 and 13 [Fig. 3(a)]. There is a change in slope between wavelength of 450 and 550 nm on Day 13 versus Day 10. The maximum values recorded in the two major chlorophyll a absorption bands were 3.92 m^{-1} at 435 nm and 2.15 m^{-1} at 673 nm, both on Day 11.

The phytoplankton absorption spectra [Fig. 3(b)] are very similar to the total absorption data [Fig. 3(a)], differing primarily at wavelengths below 440 nm where detrital absorption is highest. Detrital absorption was generally 15%, or less, of particle absorption. The highest value, 0.64 m^{-1}, was recorded at 403 nm on Day 12. The maximum a_ϕ values recorded for the two major chlorophyll a absorption bands were 3.46 m^{-1} at 440 nm and 2.06 m^{-1} at 673 nm, again, both on Day 11.

Data from Alldredge et al. (1995) were used to calculate the chlorophyll a specific-absorption coefficients (m^2/mg chl a), a_ϕ^* (Fig. 4). Because the chlorophyll a concentration value for Day 12.5 appears anomalously slow, the a_ϕ^* value derived for that sample is shown but not connected in the plot.

Individual particle reflectivity

Relative to earlier measurements, particle reflectivity increased by over a factor of three on Day 11 (Fig. 5). It should be noted that the particles imaged were >1 mm diameter and,
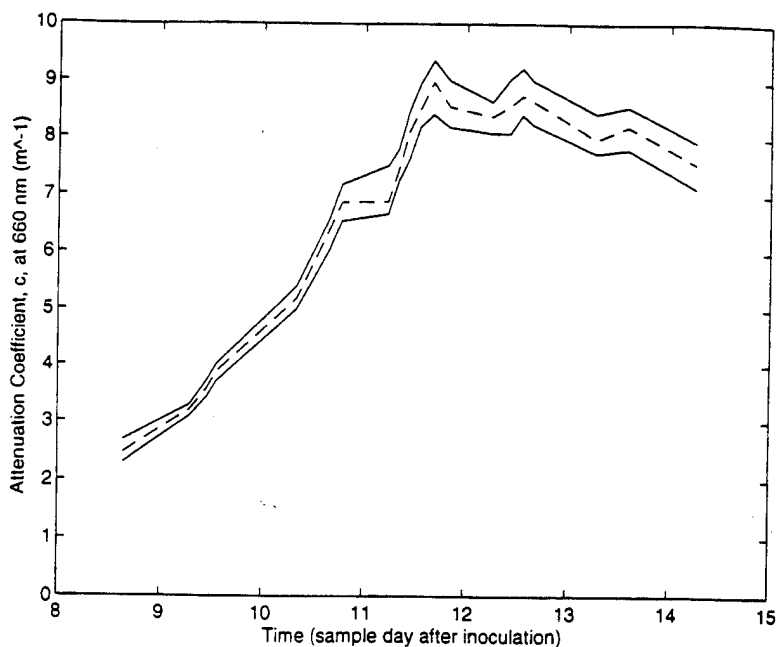
Fig. 2.   Minimum, mean, and maximum attenuation coefficients for sample Days 8–14.

therefore, were not individual phytoplankton but rather aggregates of particles. The components of these aggregates were below the spatial resolution of the imaging system.

In marine aggregate formation, transparent exopolymer particles (TEP) often provide an attachment surface for smaller particles (Alldredge *et al.*, 1993; Passow *et al.*, 1994). The increase in reflectivity on Day 11 may represent an increase in the total cross-sectional area of the phytoplankton associated with TEP. To investigate this hypothesis, we transformed the phytoplankton particle abundance (number/ml) size distribution data for Days 9 to 13 presented in Alldredge *et al.* (1994) into phytoplankton area abundance (μm^2/ml) size distributions. The curves were then integrated and the results multiplied by the percentage of phytoplankton associated with TEP for sample Days 9 to 13 (Alldredge *et al.*, 1994). The normalized curve of phytoplankton area associated with TEP exhibits a shape similar to the particle reflectivity curve (Fig. 5). These results support the hypotheses that aggregate reflectivity during this experiment was a function of the total area of the small particles attached to a TEP matrix.

Correlation of optical and biochemical measurements

In order to explore the utility of optical techniques during bloom and aggregation conditions, correlations were calculated between our optical measurements and the biochemical data from Alldredge *et al.* (1995). The Alldredge data utilized were the concentrations of the two dominant diatoms in the mesocosm, *Chaetoceros* and *Thalassiosira* (cells/ml), the carbon:nitrogen ratio (C:N), chlorophyll *a* concentration (mg/m^3), Particulate Organic carbon and nitrogen (POC and PON, mg/l), dry mass (mg/l), and the TEP area (mm^2/ml). The highest r^2 correlations found were for a_p with chlorophyll *a*
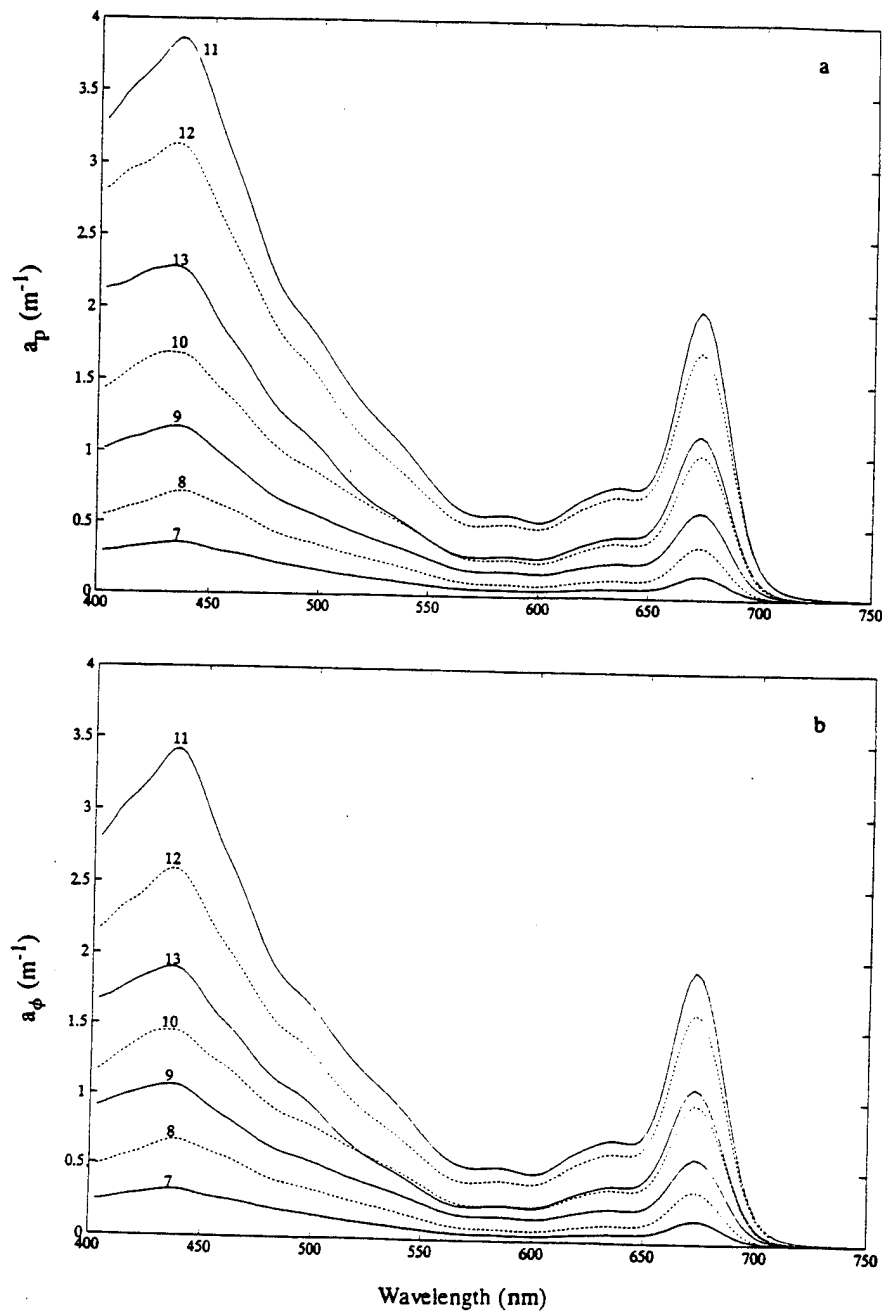
Fig. 3. (a) The absorption coefficient for particulates (a_p) as a function of wavelength for sample Days 7–13. (b) The absorption coefficient for phytoplankton (a_φ) as a function of wavelength for sample Days 7–13. The phytoplankton absorption coefficient was calculated by subtracting the absorption coefficient for detritus (a_d) from the absorption coefficient for particulates (a_p) on a channel-by-channel basis.
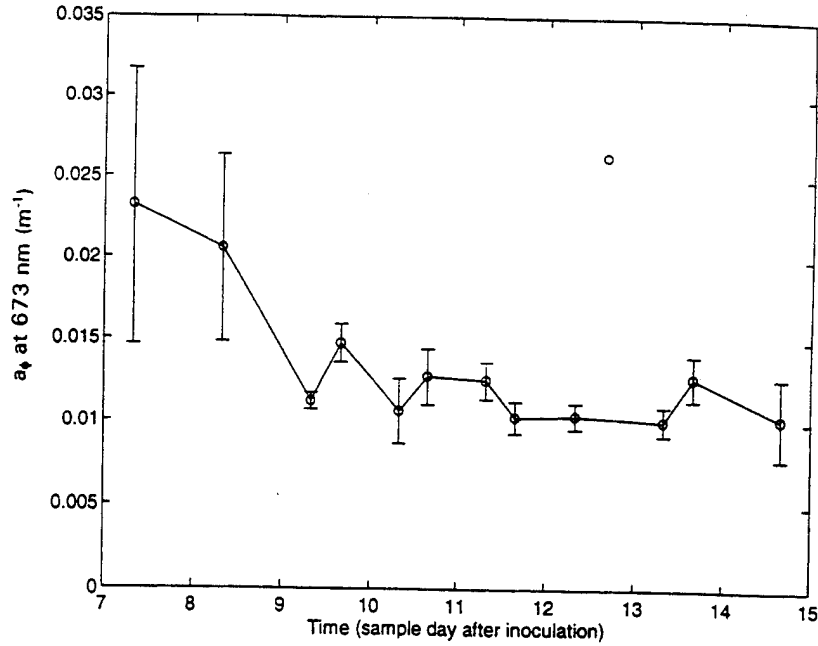
Fig. 4.   Chlorophyll *a*-specific absorption coefficient ($a_\phi^* = a_\phi/$[chl *a* concentration]) at 673 nm.
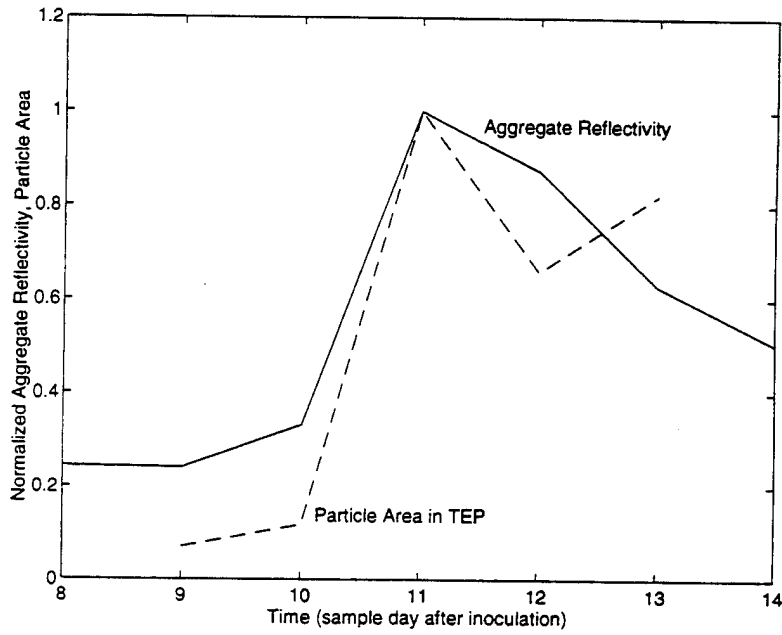
Fig. 5.   Average normalized aggregate reflectivity for sample Days 8–14 and phytoplankton area associated with TEP. For presentation purposes, both curves have been normalized by their maximum values.
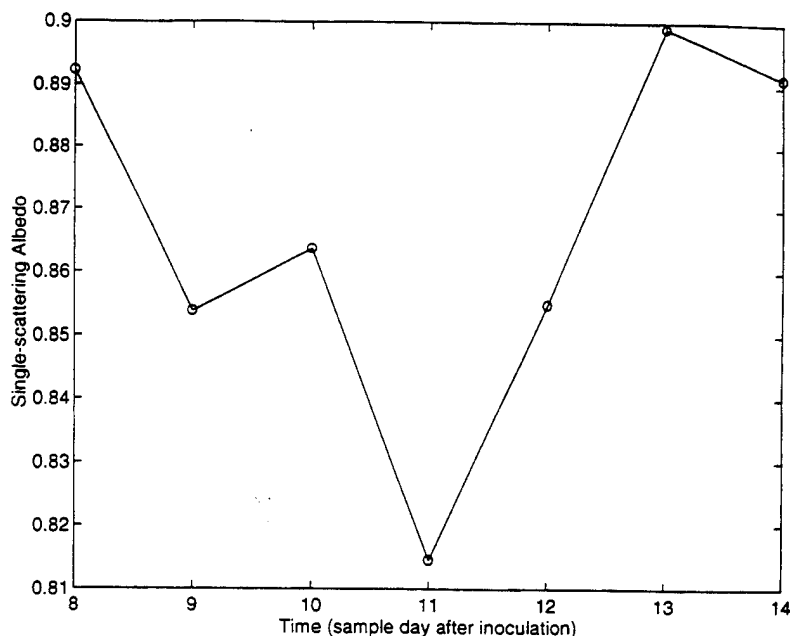
Fig. 7. The single-scattering albedo (SSA) for sample Days 8–14. The SSA is the ratio of scattering to attenuation and was calculated by SSA $= b_p/c_p = (c_p - a_p)/c_p$.

The correlations between the two optical measurements, a_p and c_p, was low ($r^2 = 0.73$). The single-scattering albedo (SSA) of the particles is approximately given by $b_p/c_p \approx (c_p - a_p)/c_p$ (Gordon *et al.*, 1983) and should act conservatively. That is, it should only change when the material or the packaging of the material changes (Kirk, 1994). The SSA decreased by about 10% from Day 8 to Day 11 (Fig. 7). This can be explained as a larger increase in absorption than in attenuation by the phytoplankton population. The SSA then increased by about 10% from Day 11 to Day 14, implying a change in the particle characteristics resulting in increased scattering (supported by the increase in large-particle reflectivity, Fig. 6) and/or decreased absorption (supported by the a_p data, Fig. 3) after Day 11. It is notable, however, that the abrupt change was centered at Day 11 and, again, coincided with nutrient depletion and an abrupt change in the C:N ratio (Alldredge *et al.*, 1995). This change in SSA is equivalent to a change in the c_p and a_p correlation.

Generally, c_p and a_p covary linearly until Day 11 when the $c_p:a_p$ ratio becomes non-linear with an overall r^2 value of 0.73 [Fig. 8(a)]. Regardless of the cause of the change in the $c_p:a_p$ relationship on Day 11, it also coincided with the change in the C:N ratio. Noting this, we normalized the daily a_p values with the daily C:N ratio values and scaled it with the factor 16/106, the Redfield Ratio values for the N:C ratio. The resulting curve, called the C:N normalized curve [Fig. 8(b)], exhibits much greater linearity ($r^2 = 0.96$), with a range similar to the original data.

The improvement in correlation between c_p and a_p after normalization by the C:N ratio [Fig. 8(b)] encouraged us to investigate multivariate relationships among the measured variables. Six multiple-regression computations were performed utilizing the c_p and a_p coefficients and POC, PON and chl *a* concentrations from the mornings of Days 8 to 14. The regressions performed were of the form

Table 1. *Squared correlation coefficients for optical* (660 nm) *and biochemical measurements, morning samples.* 95% *and* 99% *confidence levels for* r^2 *are* 0.57 *and* 0.76, *respectively* (*Sokal and Rohlf,* 1981)

	Chaetocerous (cells/ml)	Thallassiosira (cells/ml)	C:N Ratio	Chlorophyll a (mg/m^{-3})	POC (mg/l)	PON (mg/l)	Dry Mass (mg/l)	TEP Area (mm ^{2}/ml)
ap	0.09	0.95	0.14	0.97	0.52	0.90	0.77	0.40
bp	0.58	0.74	0.69	0.74	0.97	0.82	0.94	0.40
cp	0.49	0.80	0.61	0.82	0.94	0.88	0.97	0.42
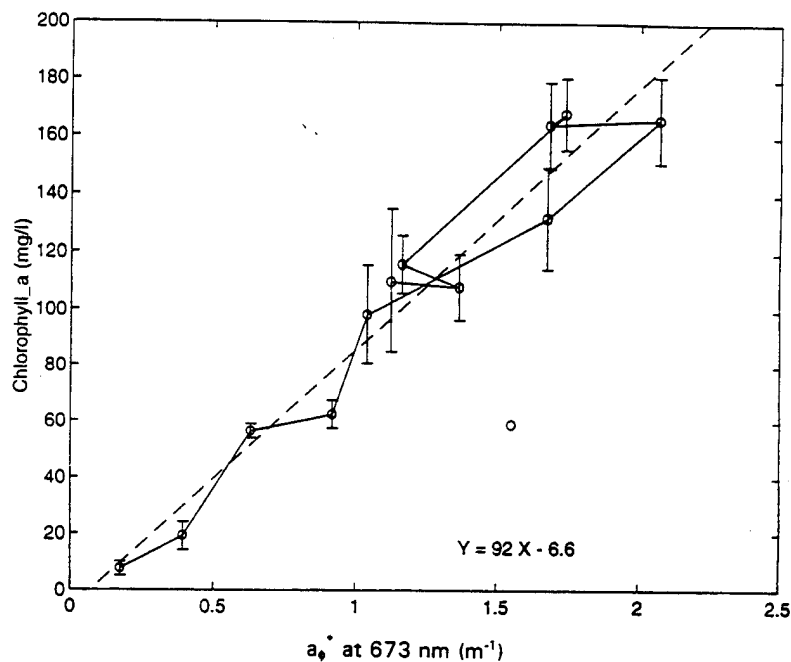
Fig. 6. The phytoplankton absorption coefficient at 673 nm versus measured chlorophyll a concentration for sample Days 8–14. The squared correlation coefficient, r^2, for all data points is 0.77 ($n = 13$). The chl a measurement for sample Day 12.5 appears anomalously low and is shown but not connected in the plot. Without data point 12.5, $r^2 = 0.94$ ($n = 12$). The regression line for the 12-point correlation is also plotted.

concentration (0.97), b_p with POC (0.97), and c_p with dry mass (0.97) (Table 1). Low correlations ($r^2 < 0.42$) were found between TEP and the optical parameters. This latter is not surprising since TEP is optically transparent by definition.

The phytoplankton absorption coefficient at 673 nm, a_p 673, should correlate well with the chl a concentration since 673 nm is essentially a chl a-specific, absorption wavelength (Bidigare *et al.*, 1990). Considering all data points, the r^2 value for a correlation of chlorophyll a and a_ϕ 673 was 0.77 (Fig. 6). Without the data for Day 12.5 (as discussed above and plotted in Fig. 5), the r^2 value was 0.94.
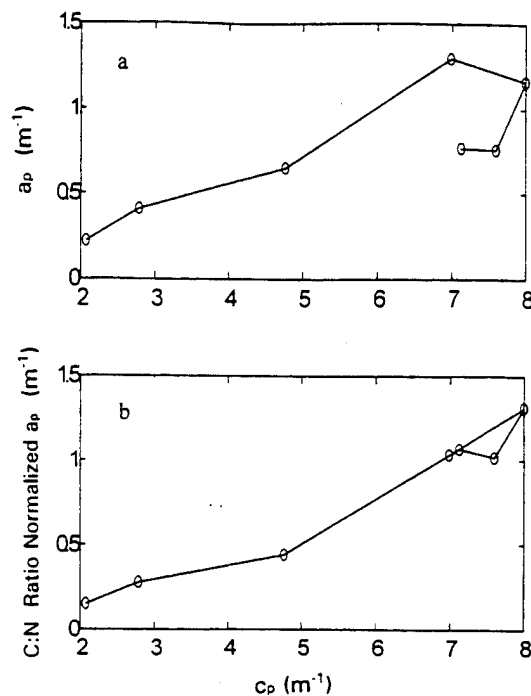
Fig. 8. (a) The particulate absorption coefficient (a_p) at 660 nm versus the attenuation coefficient for particulates (c_p) at the same wavelength. The time series begins on Day 8 in the lower left of the plot. Note the departure from linearity on Day 11 ($r^2 = 0.73$, $n = 7$). (b) The same data as in Fig. 9(a) with the a_p time series normalized by the C:N ratio time series and scaled by the factor 16/106, the Redfield N:C ratio ($r^2 = 0.96$, $n = 7$).

$$Y = A + B_{Y1}X_1 + B_{Y2}X_2 \qquad (6)$$

where Y is the quantity being estimated (either chl a, POC, PON, a_p, or c_p), X_1 and X_2 are either the optical measurements, c_p and a_p, or the biochemical measurements, POC and PON. The B_{Yi} terms are the partial regression coefficients, and A is the Y-axis intercept.

The regression equations are shown in standard format (normalized by the standard deviations of the independent and dependent variables) in Table 2. The standard partial

Table 2. Multiple regression equations (standard form) for optical (660 nm) and biochemical measurements, morning samples

POC = $1.31(c_p) - 0.40(a_p)$
PON = $0.48(c_p) + 0.54(a_p)$
Chl a = $0.24(c_p) + 0.78(a_p)$
c_p = 0.62(POC) + 0.42(PON)
a_p = -0.27(POC) + 1.17(PON)
Chl a = -0.13(POC) + 1.08(PON)

Table 3.   Multiple regression predictor equations for optical (660 nm) and biochemical measurements, morning samples, with coefficients of multiple determination (r^2). 95% and 99% confidence levels for r^2 are 0.78 and 0.90, respectively (Sokal and Rohlf, 1981)

$$POC = -0.88 + 0.95(c_p) - 1.83(a_p) \qquad r^2 = 0.98$$

$$PON = 0.05 + 0.04(c_p) + 0.26(a_p) \qquad r^2 = 0.96$$

$$chl\ a = -8.80 + 5.29(c_p) + 111(a_p) \qquad r^2 = 0.98$$

$$c_p = 0.54 + 0.85(POC) - 5.51(PON) \qquad r^2 = 0.99$$

$$a_p = -0.16 - 0.06(POC) + 2.44(PON) \qquad r^2 = 0.92$$

$$chl\ a = -25.6 - 4.00(POC) - 319(PON) \qquad r^2 = 0.95$$

regression coefficients describe how many standard deviation units the dependent variable will change in response to a change of one standard deviation unit of an independent variable. This format has utility for comparisons with other measurements taken within similar independent variable value ranges. These data indicate that c_p is a good indicator of POC while a_p is a better indicator of PON and chl a, and that a_p and POC are negatively correlated. They also show that a change in POC would affect c_p more than a similar change in PON and that PON is a strong indicator of both a_p and chl a.

The predictor equations and their associated coefficients of multiple determination, R^2, values are shown in Table 3. The R^2 values are equivalent to r^2 values in one-dimensional linear regression, they describe the percentage of the variation of the dependent variable which can be ascribed to the combined changes of the independent variables. Noting that a limited number of observations ($n = 7$) were utilized in the regressions, these high R^2 values (0.92–0.99, with the 95% and 99% significance levels for R^2 being 0.78 and 0.90, respectively) indicate that the biochemical and optical measurements are closely coupled. To illustrate this, Figs 9(a) and 9(b) show the chl a, and the POC and PON concentrations estimated using the equations in Table 3 along with the measured concentrations. The figures are visual evidence that optical and biochemical parameters in the mesocosm were, indeed, closely coupled, albeit not necessarily in a straightforward manner.

DISCUSSION

The data presented here show convincing evidence that the optical properties measured within the mesocosm were closely coupled with the biophysical state of the organisms in that nearly every parameter measured or computed changed dramatically when nutrients were depleted (Day 11). Specifically, attenuation peaked and its variance increased, absorption peaked, average large-particle reflectivity more than tripled, the single scattering albedo exhibited a minimum, and the c_p and a_p relationship became non-linear. In spite of these sometimes abrupt changes, the r^2 correlations between many biochemical and optical measurements remained quite high, with several >0.90.

There are limits to this study. A natural zooplankton/phytoplankton-predator/prey relationship was absent. There was no vertical particle flux. The particle assemblage was limited by the absence of terrigenous, resuspended, and eolian mineral particles, and by the domination of diatoms. The presence of mineral particles, for example, would increase
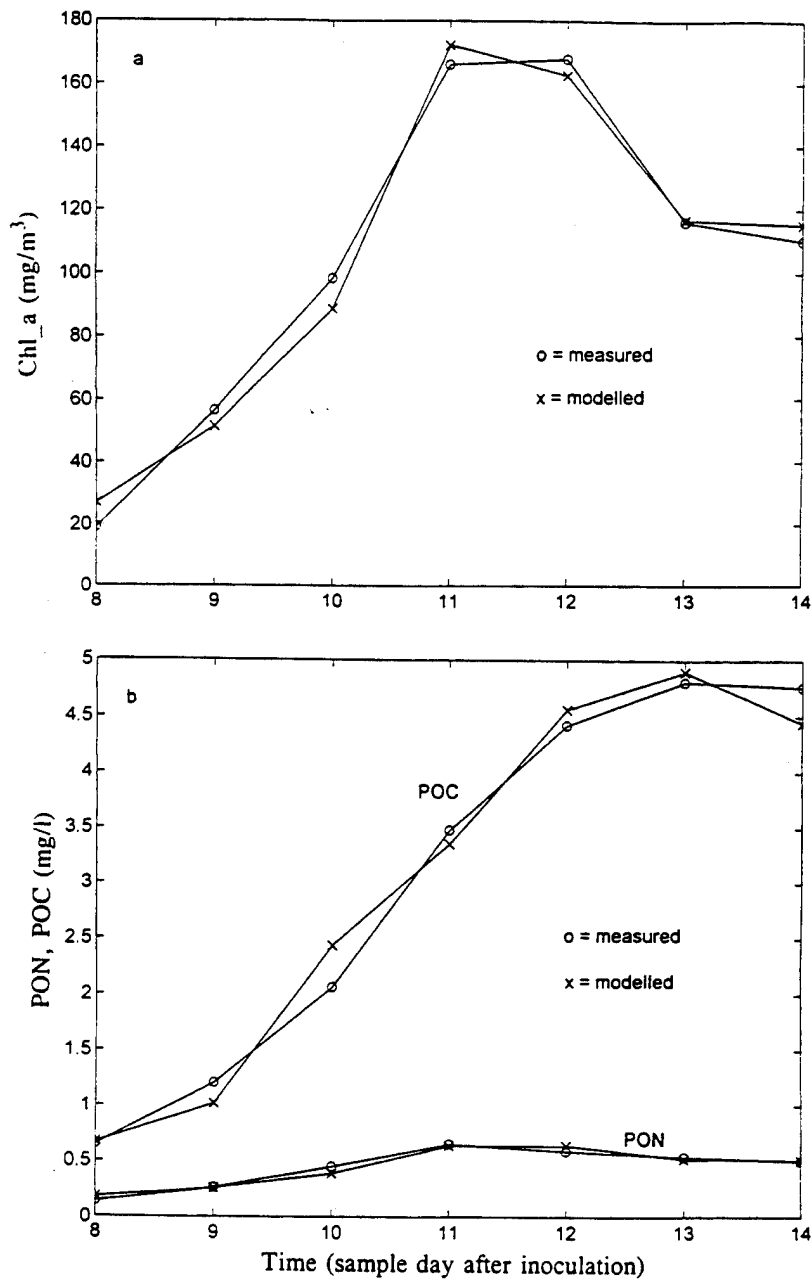
Fig. 9. (a) Measured and modelled chlorophyll a concentration for samples Days 8–14. The coefficient of multiple determination. $r^2 = 0.99$. $n = 7$. (b) Measured and modelled POC (upper curves) and PON (lower curves) concentrations. The coefficients of multiple determination, $r^2 = 0.98$ for POC and 0.97 for PON. $n = 7$ (see text for discussion).

b_p with no affect on a_p, POC, PON or chl a. The result would be an injection of noise in the correlations utilizing b_p or c_p data. A higher/lower light environment for the same species mix may have reduced/increased the pigment per cell, increasing/decreasing the chlorophyll-specific absorption and scattering coefficients (Stramski and Morel, 1990).

A change in species composition and light environment can markedly affect the chlorophyll-specific absorption and scattering coefficients (Bricaud *et al.*, 1983; Morel and Bricaud, 1981, 1986; Stramski and Morel, 1990). This may be largely due to size and intracellular pigment concentration for absorption, and due to the relative concentration of various non-aqueous components on the scattering.

Calcareous species tend to have higher specific scattering coefficients than dinoflagellates or diatoms because calcite has a high refractive index ($n \approx 1.60$). Diatom opal has a refractive index ($n \approx 1.42$) lower than cellulose ($n \approx 1.55$), starch ($n \approx 1.53$), sugar ($n \approx 1.55$), fat ($n \approx 1.47$), or pigments ($n \approx 1.45$–1.54). The mean refractive index range, however, is quite narrow for typical dry weight concentrations of materials found in various species ($n \approx 1.520$–1.562), with diatoms at the low end and coccolithophorids at the high end. The effective index of refraction for phytoplankton depends most on the aqueous fraction of the cell (Aas, 1981) and there is likely to be as large a variation in cellular refractive index with physiological condition for a given species as there is on average between species.

A cellular increase in pigments or in energy storage products such as starch and fat would increase the refractive index of a cell by replacing water ($n \approx 1.34$) with high refractive index materials ($1.45 \leq n \leq 1.54$). Laboratory findings with diatoms have shown, for example, that silicon starvation can lower the silicon content per cell by a factor of two to three and can also encourage fat formation (Paasche, 1980), thus lowering the ratio of a relatively low index material to higher index materials and affecting b_p but not a_p. When phytoplankton resting cysts are formed in response to environmental stress, chlorophyll may be reduced, water content may be reduced, and storage products may be increased (Taylor, 1980). This would tend to decrease a_p while increasing b_p, changing the c_p and a_p relationship by more than a change in a_p or b_p alone.

Many of the above-proposed complications did occur in this mesocosm experiment. Although dominated by the diatoms, *Thalassiosira* and *Chaetoceros*, the ratio of the two species changed dramatically as did average cell size and the physiological state of the organisms (Alldredge *et al.*, 1995). In short, the mesocosm experiment permitted synoptic optical and biochemical measurements of the life-cycle of a phytoplankton community under high-nutrient, bloom, and post-bloom conditions. The high correlations between the optical and biochemical measurements, through conditions ranging from common to extreme, bode well for the use of in-situ and, perhaps, remotely sensed optical techniques toward a greater understanding of biochemical processes. Site-specific and time-dependent calibrations of equations relating optical and chemical assessments of phytoplankton will be required, however, unless the natural cycle of a specific environment is predictable enough for historical relationships to be used.

SUMMARY

In this study, optical measurements of a captive phytoplankton community were made during growth, bloom and aggregation stages. Considering the ranges of the parameter values measured, the data presented here are applicable to both large-sample-volume,

Carder K. L., S. K. Hawes, K. A. Baker, R. C. Smith, R. G. Steward and B. G. Mitchell (1991) Reflectance model for quantifying chlorophyll *a* in the presence of productivity degradation products. *Journal of Geophysical Research*, **96**, 20,599–20,611.

Carder K. L., P. Reinersman, R. F. Chen, F. Muller-Karger, C. O. Davis and M. Hamilton (1993) AVIRIS calibration and applications in coastal oceanic environments: tracer of soluble and particulate constituents of the Tampa Bay Coastal Plume. *Remote Sensing of the Environment* (Special Issue on Imaging Spectrometry), pp. 487–500.

Carder K. L. and D. K. Costello (1994) Optical effects of large particles. In: *Ocean optics*, R. W. Spinrad, K. L. Carder and M. J. Perry, editors, Oxford University Press, New York, NY, pp. 243–257.

Costello D. K., K. L. Carder, P. R. Betzer and R. W. Young (1989) In-situ holographic imaging of settling particles: Applications for individual particle dynamics and oceanic flux measurements. *Deep-Sea Research*, **36**, 1595–1605.

Costello D. K., K. L. Carder and R. G. Steward (1991) Development of the marine aggregated particle profiling and enumerating rover (MAPPER). In: *Underwater imaging, photography, and visibility*, Richard W. Spinrad, editor, *Proc. SPIE* 1537, Bergen, Norway, pp. 161–172.

Costello D. K., K. L. Carder and W. Hou (1992) Structured visible diode laser illumination for quantitative underwater imaging. In: *Ocean optics XI*, Gary D. Gilbert, editor, *Proc. SPIE* 1750, Bergen, Norway, pp. 95–103.

Costello D. K. and K. L. Carder (1994) New instrumentation and platforms for subsurface optical measurements. In: *Ocean optics XII*, Jules S. Jaffe, editor, *Proc. SPIE* 2258, Bergen, Norway.

Costello D. K., W. Hou and K. L. Carder (1994) Some effects of the sensitivity threshold and spatial resolution of a particle imaging system on the shape of the measured particle size distribution. In: *Ocean optics XII*, Jules S. Jaffe, editor, *Proc. SPIE* 2258, Bergen, Norway.

Dickey T. D. (1991) The emergence of concurrent high-resolution physical and bio-optical measurements in the upper ocean and their applications. *Review of Geophysics*, **29**, 383–413.

Fowler S. W. and G. A. Knauer (1986) Role of large particles in the transport of elements and organic compounds through the oceanic water column. *Progress in Oceanography*, **16**, 147–194.

Gordon H. R., D. K. Clark, J. W. Brown, O. B. Brown, R. H. Evans and W. W. Broenkow (1983) Phytoplankton pigment concentration in the Middle Atlantic Bight: Comparison of ship determinations and CZCS estimates. *Applied optics*, **22**, 20–36.

Hawes S. K., K. L. Carder and G. R. Harvey (1992) Quantum fluorescence efficiencies of fulvic and humic acids: Effects on ocean color and fluorometric determination. In: *Ocean optics XI*, Gary D. Gilbert, editor, *Proc. SPIE* 1750, Bergen, Norway.

Hayase K. and H. Tsubota (1985) Sedimentary humic and fulvic acid as fluorescent organic materials. *Geochimica et Cosmochimica Acta*, **49**, 159–163.

Hill P. S. and A. R. M. Nowell (1990) The potential role of large, fast-sinking particles in clearing nepheloid layers. *Philosophical Transactions of the Royal Society of London*, **331**, 103–107.

Hill P. S. (1992) Reconciling aggregation theory with observed vertical fluxes following phytoplankton blooms. *Journal of Geophysical Research*, **97**, 2295–2308.

Honjo S., K. W. Doherty, Y. C. Agrawal and V. Asper (1984) Direct optical assessment of large amorphous aggregates (marine snow) in the deep ocean. *Deep-Sea Research*, **31**, 67–76.

How W., D. K. Costello, K. L. Carder and R. G. Steward (1994) High-resolution marine particle data from MAPPER, a new, in-situ optical ocean instrument. *EOS* American Geophysical Union/ASLO (75), **3**, 21.

Jackson G. A. (1992) Effect of coagulation on nutrient and light limitation of an algal bloom. *Limnology and Oceanography*, **37**, 77–89.

Jackson G. A. and S. E. Lochmann (1992) Effect of coagulation on nutrient and light limitation of an algal bloom. *Limnology and Oceanography*, **37**, 77–89.

Jerlov N. G. (1976) *Marine optics*. Elsevier Oceanography Series No. 14, Elsevier Scientific Publishing Company, Amsterdam, Oxford, New York, 231 pp.

Kirk J. T. O. (1994) *Light and photosynthesis in aquatic ecosystems*. Second Edition, Cambridge University Press, Cambridge, 509 pp.

Kishino M., M. Takahashi, N. Okami and S. Ichimura (1985) Estimation of the spectral absorption coefficients of phytoplankton in the sea. *Bulletin of Marine Science*, **37**, 634–642.

Lee Z. P., K. L. Carder, S. K. Hawes, R. G. Steward, T. G. Peacock and C. O. Davis (1994) A model for interpretation of hyperspectral remote sensing reflectance. *Applied optics*, **33**, 5721–5732.

Marra J., T. Dickey, W. S. Chamberlin, C. Ho, T. Granata, D. A. Kiefer, C. Langdon, R. Smith, K. Baker, R.

remotely-sensed, optical measurements and to in-situ optical measurements using instruments with inherently smaller sample volumes. Even though a mesocosm study involves inherent limitation, these results show that optical and biochemical parameters were closely coupled even at extreme values. The import of this finding is that the degree of correlation was sufficiently high to allow a reasonable anticipation of finding useful correlations between optical and biochemical parameters in natural waters with various phytoplankton assemblages. The equation coefficients for field exercises must be specifically calibrated for each site and time, perhaps during deployment and retrieval activities for moored or floating instrumentation arrays that include absorption and attenuation meters for monitoring the biochemical changes in phytoplankton populations.

REFERENCES

Aas E. (1981) The Refractive Index of Phytoplankton. Institute Report Series, No. 46, Institute for Geofysikk, Universitetet I, Oslo, Norway, 61 pp.

Alldredge A. L. and M. W. Silver (1988) Characteristics, dynamics, and significance of marine snow. *Progress in Oceanography*, **20**, 41–58.

Alldredge A. L., T. C. Granata, C. C. Gotschalk and T. D. Dickey (1990) The physical strength of marine snow and its implications for particle disaggregation in the ocean. *Limnology and Oceanography*, **35**, 1415–1428.

Alldredge A. L. and P. McGillivary (1991) The attachment probabilities of marine snow and their implications for particle coagulation in the ocean. *Deep-Sea Research*, **38**, 431–443.

Alldredge A. L., U. Passow and B. E. Logan (1993) The abundance and significance of a class of large, transparent organic particles in the ocean. *Deep-Sea Research*, **36**, 159–171.

Alldredge A. L., C. C. Gotschalk, U. Passow and U. Riebesell (1994) Sigma tank experiment: Aggregate abundance and background data. In: Sigma Data Report 1. Santa Barbara Tank Experiment. Report to the Office of Naval Research, Section II.

Alldredge A. L., C. C. Gotschalk, U. Passow and U. Riebesell (1995) Mass aggregation of diatom blooms: Insights from a mesocosm study. *Deep-Sea Research II*, **42**, 9–27.

Asper V. L., S. Honjo and T. H. Orsi (1992) Distribution and transport of marine snow aggregates in the Panama Basin. *Deep-Sea Research*, **39**, 939–952.

Bartz, R., J. R. V. Zaneveld and H. Pak (1978) A transmissometer for profiling and moored observations in water. In: *Ocean Optics V. Proc. SPIE* 160, Bergen, Norway, pp. 102–108.

Betzer, P. R., K. L. Carder and D. W. Eggimann (1974) Light-scattering and suspended particulate matter on a transect of the Atlantic Ocean at 11°N. In: *Suspended solids in water*, R. Gibbs, editor, Plenum, New York, pp. 295–314.

Biscaye P. E. and S. L. Eittreim (1974) Variations in benthic boundary layer phenomena: Nepheloid layer in the North American basin. In: *Suspended solids in water*, R. Gibbs, editor, Plenum, New York, pp. 227–260.

Bidigare R. R., M. E. Ondrusek, J. H. Morrow and D. A. Kiefer (1990) In-vivo absorption properties of algal pigments. *Ocean Optics X*, Richard W. Spinrad, editor, *Proc. SPIE*, 1302, Bergen, Norway, pp. 290–302.

Bricaud A., A. Morel and L. Prieur (1983) Optical efficiency factors for some phytoplankters. *Limnology and Oceanography*, **28**, 816–832.

Bricaud A., A. Morel and L. Prieur (1981) Absorption by dissolved organic matter of the sea (yellow substance) in the UV and visible domain. *Limnology and Oceanography*, **26**, 43–53.

Bricaud A. and D. Stramski (1990) Spectral absorption coefficients of living phytoplankton and nonalgal biogenous matter: A comparison between the Peru upwelling area and the Sargasso Sea. *Limnology and Oceanography*, **35**, 562–582.

Carder K. L., P. R. Betzer and D. W. Eggimann (1974) Physical, chemical, and optical measures of suspended particle concentrations: their intercomparison and applications to the west African shelf. In: *Suspended solids in water*, R. Gibbs, editor, Plenum, New York, pp. 173–193.

Carder K. L., R. G. Steward, G. Harvey and P. Ortner (1989) Marine humic and fulvic acids: Their effects on remote sensing of ocean chlorophyll. *Limnology and Oceanography*, **34**, 68–81.

Bidigare and M. Hamilton (1992) Estimation of seasonal primary production from moored optical sensors in the Sargasso Sea. *Journal of Geophysical Research*, **97**, 7399–7412.

Mitchell B. G. and D. A. Kiefer (1988) Chlorophyll *a*-specific absorption and fluorescence excitation spectra for light-limited phytoplankton. *Deep-Sea Research*, **35**, 635–663.

Morel A. and A. Bricaud (1981) Theoretical results concerning light absorption in a discrete medium, and application to specific absorption of phytoplankton. *Deep-Sea Research*, **28**, 1375–1393.

Morel A. and A. Bricaud (1986) Inherent optical properties of algal cells including picoplankton: theoretical experimental results. In: *Phytosynthetic picoplankton*, T. Platt and W. K. W. Li, editors, Canadian Bulletin of Fisheries and Aquatic Sciences, Ottawa, **214**, 521–559.

Morel A. and L. Prieur (1977) Analysis of variations in ocean color. *Limnology and Oceanography*, **22**, 709–722.

Paasche E. (1980) Silicon. In: *The physiological ecology of phytoplankton*, I. Morris, editor, University of California Press, Berkeley, California, 623 pp.

Passow U., A. L. Alldredge and B. E. Logan (1994) The role of particulate carbohydrate exudates in the flocculation of diatom blooms. *Deep-Sea Research*, **41**, 335–357.

Preisendorfer R. W. (1961) Application of radiative transfer theory to light measurements in the sea. (Symposium on Radiant Energy in the Sea). UGGI Monograph No. 10, 11–30.

Riebesell U. (1992) The formation of large marine snow and its sustained residence in surface waters. *Limnology and Oceanography*, **37**, 63–76.

Roesler C. S., M. J. Perry and K. L. Carder (1989) Modeling in-situ phytoplankton absorption from total absorption spectra in productive inland marine waters. *Limnology and Oceanography*, **34**, 1510–1523.

Siegel D. A., T. D. Dickey, L. Washburn, M. K. Hamilton and B. G. Mitchell (1989) Optical determination of particulate abundance and production variations in the oligotrophic ocean. *Deep-Sea Research*, **36**, 211–222.

Smith R. C. and K. S. Baker (1981) Optical properties of the clearest natural waters (200–800 nm). *Applied optics*, **20**, 177–184.

Smith R. C., K. J. Waters and K. S. Baker (1991) Optical variability and pigment biomass in the Sargasso Sea as determined using deep sea optical mooring data. *Journal of Geophysical Research*, **96**, 8665–8686.

Sokal R. R. and F. J. Rohlf (1981) *Biometry*, Second Edition, W. H. Freeman and Company, New York, 859 pp.

Stolzenbach K. D. (1993) Scavenging of small particles by fast-sinking porous aggregates. *Deep-Sea Research*, **40**, 359–369.

Stramski D. and A. Morel (1990) Optical properties of photosynthetic picoplankton grown in different physiological states as affected by growth irradiance. *Deep-Sea Research*, **37**, 245–266.

Suzuki N. and K. Kato (1953) Studies on suspended materials. Marine snow in the sea. Part 1. Source of marine snow. *Bulletin of the Faculty of Fisheries, Hokkaido University*, **4**, 132–135.

Taylor F. J. R. (1980) Basic biological features of phytoplankton cells. In: *The physiological ecology of phytoplankton*, I. Morris, editor, University of California Press, Berkeley, U.S.A., 623 pp.

Wells J. T. and A. L. Shanks (1987) Observations and geological significance of marine snow in a shallow-water, partially enclosed marine embayment. *Journal of Geophysical Research*, **92**, 13,185–13,190.

Reprinted from

Visual Communications and Image Processing '95

SPIE

P

PROCEEDINGS
SERIES

Volume 2501

Multi-spectral Imagery, Hyper-spectral Radiometry, and Unmanned Underwater Vehicles: Tools for the Assessment of Natural Resources in Coastal Waters.

David K. Costello, Kendall L. Carder,
Robert F. Chen, Thomas G. Peacock, and N. Sandy Nettles

all at:

University of South Florida
Marine Science Department
140 Seventh Avenue South
St. Petersburg, FL USA 33701
INTERNET: dkc@monty.marine.usf.edu

INTRODUCTION

In many coastal oceans of the world, the flora and fauna are under stress. In some areas, seagrasses, coral reefs, fish stocks, and marine mammals are disappearing at a rate great enough to capture the attention of, and in some cases, provoke action by local, national, and international governing bodies. The governmental concern and consequent action is most generally rooted in the economic consequences of the collapse of coastal ecosystems. In the United States, for example, some experts believe that the rapid decline of coral reef communities within coastal waters is irreversible. If correct, the economic impact on the local fisheries and tourism industries would be significant. Most scientists and government policy makers agree that remedial action is in order. The ability to make effective management decisions is hampered, however, by the convolution of the potential causes of the decline and by the lack of historical or even contemporary data quantifying the standing stock of the natural resource of concern. Without resource assessment, neither policy decisions intended to respond to ecological crises nor those intended to provide long-term management of coastal resources can be prudently made.

This contribution presents a methodology designed to assess the standing stock of immobile coastal resources (eg. seagrasses and corals) at high spatial resolution utilizing a suite of optical instrumentation operating from unmanned underwater vehicles (UUVs) which exploits the multi-spectral albedo and fluorescence signatures of the flora and fauna.

INSTRUMENTATION

The instrumentation suite, the Bottom Classification/Albedo Package (BCAP), is an ensemble of optical sensors designed to acquire multi-spectral video imagery and hyper-spectral radiometric data using passive or active illumination. Figure 1 depicts BCAP deployed with the OV-II UUV (discussed below).

BCAP can utilize several different rare-earth-doped metal-halide light sources for broad-band or narrow-band bottom illumination and/or fluorescence exitation. Hyperspectral (512 channels, ca. 2.5 nm resolution) upwelling and downwelling spectrometers, two diode lasers with excitation wavelengths of

650 and 675 nm, a 6-wavelength, image-intensified (GEN-III-Blue), CCD bottom-imaging camera (Xybion, Inc. IMC-301), and a nine-channel light attenuation and absorption meter (WET Labs, Inc. ac-9) are the primary components.

The IMC-301 imager has a dynamic range of ten orders of magnitude and is capable of imaging albedo and/or fluorescence variations of the bottom. It is used for bottom classification and object identification purposes. The instrument employs a six-filter wheel (Table 1) which spins at 300 rpm in order to synchronize each channel with the NTSC video rate of 30 frames/sec. This allows the acquistion of a complete cycle of spectral imagery every 0.2 sec (6 frames). The instrument can also be remotely locked on any of the six channels. The minimum exposure gate is 15 nanoseconds.

TABLE 1. Specifications for optical filters utilized in the IMC-301 bottom camera.

Channel	Wavelength Center (nm)	Bandwidth FWHM (nm)	Comment
1	460	20	chlorophyll a and c absorption maxima
2	520	20	Co-pigment absorption maxima, coral fluorescence
3	575	30	Phycoerythrin fluorescence maxima, coral fluorescence
4	620	20	Pigment absorption minimum, water absorption "hingepoint"
5	685	30	Chlorophyll a fluorescence maxima
6	730	40	Fluorescence band

The hyperspectral (512 channels, ca. 2.5 nm resolution) upwelling and downwelling spectrometers (Remote Ocean Systems, Inc., ROS512) record the downwelling irradiance (E_d) and the upwelling radiance (L_u). A calibrated spectrum for the instrument is shown in Figure 2. Intercalibration is provided by ratio with a known spectral reflectance material (Spectralon, Labsphere, Inc.).

The dual lasers function, together with the imaging cameras, as an optical altimeter for light propagation modelling and to quantify the chlorophyll-a content of the bottom sediment. The choice of wavelengths, 650 and 675 nm, respectively, are a local minimum and maximum of the chlorophyll_a absorption spectrum (Figure 3). This choice of wavelengths also minimizes "cross-talk" with the absorption spectrum of chlorophyll-c, a pigment often present with chlorophyll-a.

UNMANNED UNDERWATER VEHICLES

ROV Design and Configuration

The ROV available for this work is the result of a joint design project by the authors in conjunction with Hydrobotics Engineering Canada, Inc. The system is dubbed "ROSEBUD" (Remotely Operated System

for Bio-optical Underwater Deployment) and is a one-of-a-kind vehicle specifically designed to accomodate the entire suite of instrumentation described above. The control electronics and power delivery systems were designed to support this instrumentation using umbilical lengths of 75, 105, 205, and 385 m. All these umbilical lengths are available using load-bearing connectors because the circuitry incorporated compensates for voltage drops in any of the first three individual umbilicals or in a combination of all of the lengths (producing a 385 m umbilical capability). This is most significant regarding the metal-halide arc lamps, the ballasts for which specify 277 VAC within ±10%. This multi-component unmbilical is unique in ROV systems and will allow deployments tailored to the operational depth/range requirements and minimizing the deck space and personnel requirements for umbilical tending.

The range of current conditions for which ROV operations are feasible is largely a function of the hydrodynamic drag of the vehicle/umbilical and the thruster power available. Since a center-payload vehicle has an inherent drag increase versus a single-hull, minimal payload vehicle, ROSEBUD was equipped with a small-diameter (ca. 2 cm) neutrally buoyant umbilical and 4 horizontal thrusters generating 120 lb of horizontal thrust. This thrust is differentially distributable to two (port/starboard) thruster pairs. To enhance payload capability ROSEBUD was equipped with two vertical thrusters generating 60 pounds of thrust, which is differentially distributable in order to add a dimension of active vehicle trim.

Other features include a 180° pan-and-tilt camera mounted on a 350° tilt platform (all remotely controllable) which provide a full 4π viewing capability for the navigation camera. Twin coaxial cables in the umbilical and a remotely-actuated, high-speed video switcher in the vehicle provides for monitoring any two of three vehicle cameras. The high-speed switcher could also allow the topside recording of time-multiplexed, stereo video. A vehicle microcontroller (Pisces Design, Inc.) controls some vehicle functions and frees umbilical twisted-wire pairs by multiplexing control signals and serial data with one of the video signals. Another microcontroller also overlays compass heading, depth, altitude, and system control parameters on the Control Console Monitor, provides data recording redundancy and video recording synchronization, and encodes time and system parameters in the vertical blanking period of each video frame. ROV position relative to the mother-ship is acoustically determined to ± 1 m (Trackpoint LXT, ORE).

Autonomous Underwater Vehicle Ocean Voyager II (OVII AUV)

The Ocean Voyager II (OV-II, Figure 1) is an autonomous, untethered, underwater vehicle developed for University of South Florida, Marine Science Department by the Department of Ocean Engineering, Florida Atlantic University. In contrast, for example, to the Massachusetts Institute of Technology ODESSEY AUV which is designed for deep-water, long-range missions, and the Wood's Hole Oceanographic Institution ABE AUV which is optimized for deep-water, short-range, long duration deployments, the OV-II is a small vehicle optimized for coastal applications including long-range, bottom-following missions. The OVII is 2.4 m in length, has a maximum diameter of 0.6 m, a depth rating of 600 m, a maximum speed of 5 knots, and a range of 100 km (@ 3 knots) with inexpensive lead-acid batteries. In sea trials at FAU and at USF, the prototype vehicle successfully performed missions following 3-dimensional waypoints on a completely autonomous basis. The payload bay of this prototype vehicle is currently being modified for integration of the BCAP system.

The abilty to accomodate BCAP and ancilllary instrumentation on an autonomous platform is due, in large part, to the utilization of an Intelligent Distributed Control System (IDCS, Smith, 1994). In essence, the IDCS consists of a main controller which is responsible for high level scheduling and for monitoring numerous (up to 32K) microcontrolled subsystems called "nodes". Each node consists of sensor(s), actuator(s) and a microcontoller. The node microcontroller (the "Neuron Chip", Motorola) is actually three, integrated microcontrollers with built-in communications firmware. These follow LONwork protocols where nodes are addressed as network variables and multi-tasking and event-driven scheduling are supported. The IDCS allows all network data to be addressed by any node, for node actuators to respond to information from other nodes independent of the main controller, and for essentially an unlimited number of sensor system configurations/permutations to be deployed without reprogramming the main controller.

The advantages of the AUV platform are primarily that the vehicle is weather independent, can repeatedly cover large areas without requiring ship support, and that operations are not limited by the presence of an umbilical. This lack of an umbilical is initially, however, a disadvantage because the bottom data can not be monitored by humans in real time and the mission adjusted if deemed necessary. The ROV will be utilized, therefore, early in the mission-planning learning curve.

MISSION SCENARIOS

An equation describing the effect of daylight passive albedo on upwelling radiance provides an example for one of the five envisioned deployment missions:

$$L_i = \frac{\alpha_i}{\pi} E_{di} \, e^{-h(\frac{a_i}{\mu_d} + \frac{c_i}{\cos \theta'})} + PR \qquad (1)$$

where the subscript i denotes a channel number, L_i is the radiance recorded by the camera, α is the spectral albedo, E_d is the downwelling irradiance at vehicle depth, a_i and c_i, respectively, are the absorption and attenuation coefficients for each channel measured by the ac-9 instrument, μ_d is the average cosine of the downwelling light field, θ' is the viewing angle off nadir, and h is the height of the vehicle above bottom. Here, the spectral bottom albedo, α_i, is assumed lambertian. For non-lambertian bottoms, the factor π would be replaced by the bidirectional reflectance function (BDRF). PR is a factor introduced to include power to the sensor from various sources of path radiance. Since this is largely a function of scattering into and out of the viewing path by contributions from adjacent areas and by downwelling light, estimation of this term is most important for high-contrast bottoms.

In this deployment scenario, E_{di} is measured by the downwelling spectral irradiometer and calculated according to:

$$E_{di} = \int\limits_{\lambda_{li}}^{\lambda_{ui}} E_d(\lambda)d\lambda \qquad\qquad (2)$$

where λ_{li} and λ_{ui} are the lower and upper wavelengths where the filter transmittance $T_f > 0.1\%$. For missions involving fluorescence and/or operations at night, the general form of equations 1 and 2 is retained, but the specific parameters differ substantially. In all scenarios, the goal of benthic assessment is to determine one variable, α_i, for spectral albedo missions or the fluorescence efficiency, F_e, for spectral fluorescence missions. These parameters generate the primary feature vectors which allow image classification. To realize these goals, the optical properties of the water column, especially those of the layer between the vehicle and the bottom, must also be carefully assessed.

PRELIMINARY FEASIBILITY ANALYSIS

Preliminary laboratory and field work shows that the distinct multi-spectral albedo signatures of bottom sediments, seagrasses, algae, and macroalgae will allow discrimination of bottom types (Figure 4). Similarly, fluorescence signatures of various coral species (*Agaricia, Montastria, and Diploria*) and coralline algae (Figure 5) stimulated by UV-A irradiance may allow identification of individual species. Additionally, the amplitude of the fluorescence has been shown to be indicative of the state of health of the organisms (Hardy et al. 1992). In all scenarios, imagery from the IMC-301 are available to confirm the spectral classifications.

TARGET DATA PRODUCTS

Both the ROSEBUD ROV and the OV-II have successfully undergone sea trials simulating bottom-following missions. BCAP deployment with ROSEBUD is scheduled for March 1995. BCAP deployments with OV-II are scheduled to begin in April 1995. Both vehicles can be acoustically tracked (Trackpoint LXT, ORE, Inc.) relative to the support ship and relative to a transponder fixed to the sea bottom. This provides for area mapping, and subsequent reassessments, with fixed geographical references.

These albedo maps, when combined with knowledge of the downwelling light field, E_d, vehicle altitude, and the water depth and optical characteristics, will allow calibration/interpretation of larger-scale spectral imagery (Figure 6) acquired from air platforms (Carder et al. 1993a; 1993b; 1993c; Costello et al. 1995).

SUMMARY

The purpose of this work is to allow classification and quantification of seagrasses, macrophytes, corals, and bottom sediments by the automated extraction of their spectral albedo and fluorescence, and feature shape analysis. The importance of this approach is threefold: 1) the spectral albedo and fluorescence signatures not only make classification/quantification possible but may permit remote

assessment of the health of the organisms (e.g. bleached versus healthy corals); 2) the instrumentation and vehicle platforms involved provide not only for relatively rapid assessment at high resolution of standing stocks but also for the periodic reassessment of mapped areas to quantify changes in standing stock to help in governmental policy making; and 3) if the bathymetry of an area of interest is available and a reasonable estimate of the water column constituents can be made, the classification algorithms developed with this approach may allow frequent monitoring of resources for similar environments by airborne and spaceborne platforms.

REFERENCES

Bidigare, R. R., M. E. Ondrusek, J. H. Morrow, and D. A. Kiefer. 1990. In vivo absorption properties of algal pigments. In: Ocean Optics X, Richard W. Spinrad, Editor, Proc. SPIE. 1302. 290-302.

Carder, K.L., P. Reinersmann, R.F. Chen, F. Muller-Karger, C.O. Davis and M. Hamilton (1993a) AVIRIS calibration and application in coastal oceanic environments. Remote Sens. Environ. 44:205-216.

Carder, K.L., R.G. Steward, R.F. Chen, S. Hawes, Z. Lee and C.O. Davis (1993b) AVIRIS calibration and application in coastal oceanic environments: tracers of soluble and particulate constituents of the Tampa Bay Coastal Plume. Photogram. Engr. & Remote Sensing. Special Issue on Imaging Spectrometry. 487-500.

Carder, K.L., Z.P. Lee and R.F. Chen (1993c) Unmixing of Spectral Components Affecting AVIRIS Imagery of Tampa Bay. In: Imaging Spectrometry of the Terrestrial Environment, SPIE Vol. 1937, 77-90.

Costello, D.K., I.I. Kaminer, K.L. Carder and R.M. Howard (1995) The use of unmanned vehicle systems for coastal ocean surveys: Scenarios for joint underwater and air vehicle missions. Proceedings: Workshop on Undersea Robotics and Intelligent Control, Instituto Superior Tecnico (I.S.T.), Lisboa, Portugal.

Hardy, J.T., F.E. Hoge, J.K. Yungel and R.E. Dodge (1992) Remote detedtion of coral 'bleaching'using pulsed-laser fluorescence spectroscopy. Mar. Ecol. Prog. Ser. 88:247-255.

Smith, S.M. (1994) Implications of low cost distributed control systems in UUV design. Proceedings: AUVS '94 - Intelligent Vehicle Systems and Technology, Detroit, MI.
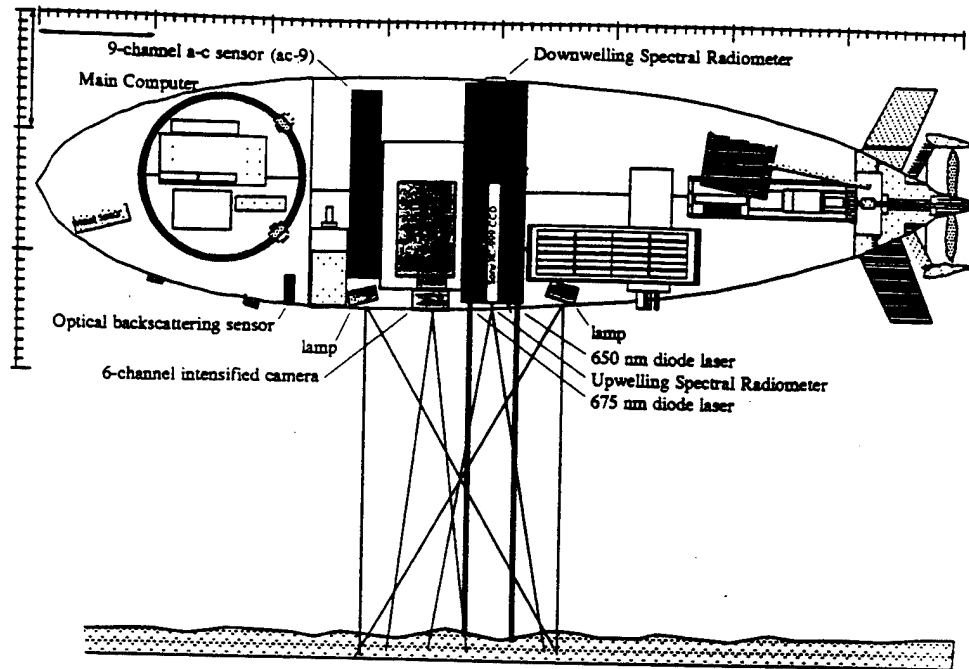
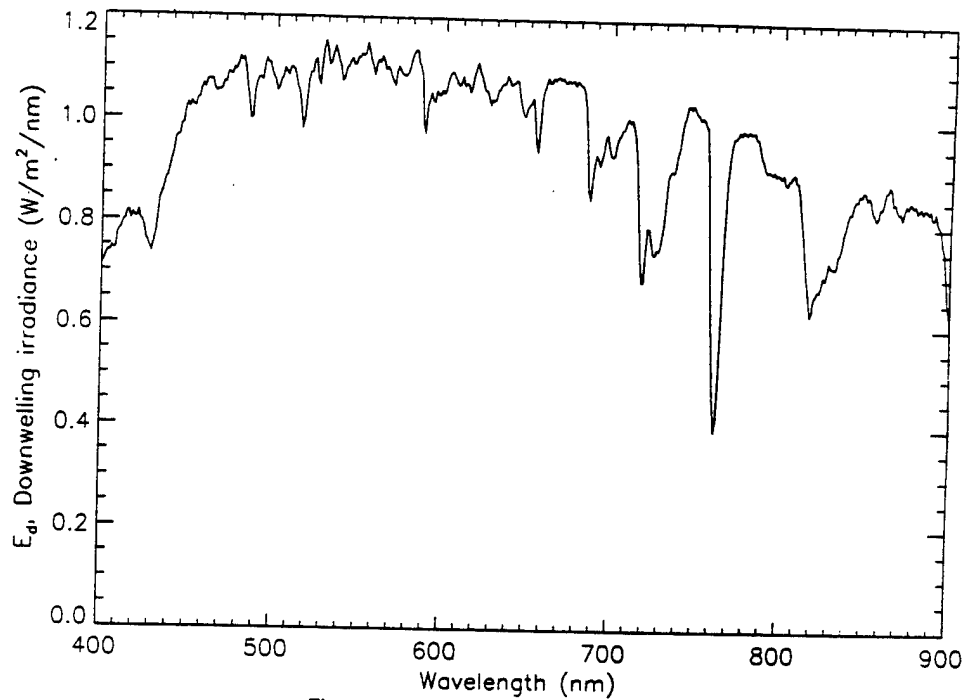Figure 1 Ocean Voyager II UUV with Bottom Classification/Albedo Package

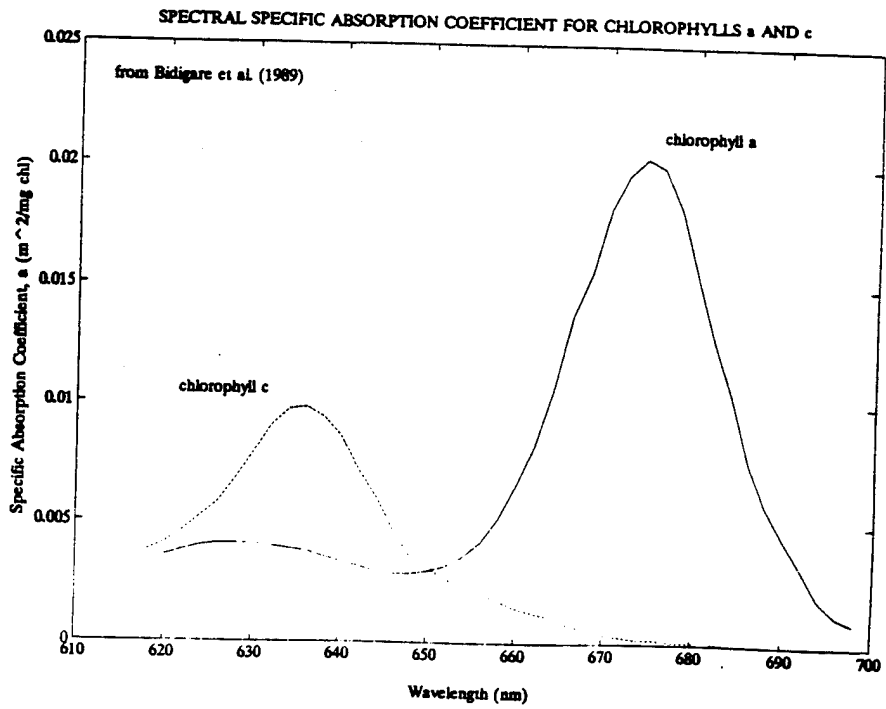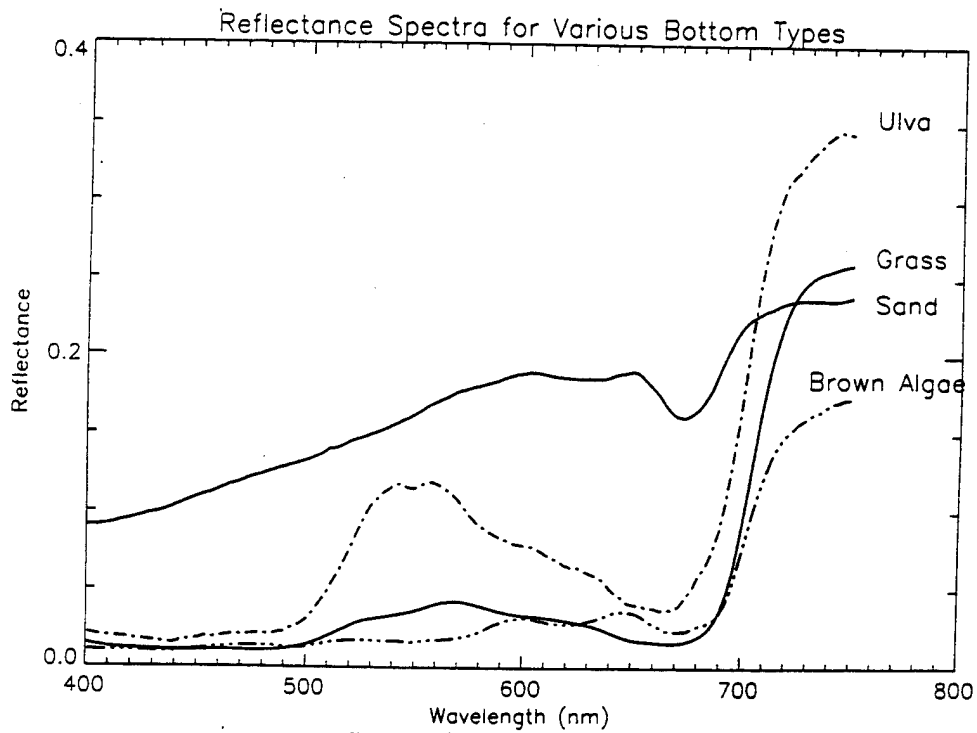Figure 2 $E_d = L_g * \pi / \rho_g$, $\rho_g = 0.1$

SPECTRAL SPECIFIC ABSORPTION COEFFICIENT FOR CHLOROPHYLLS a AND c

from Bidigare et al. (1989)

chlorophyll a

chlorophyll c

Specific Absorption Coefficient, a (m^2/mg chl)

Wavelength (nm)

FIGURE 3

Reflectance Spectra for Various Bottom Types

Ulva

Grass

Sand

Brown Algae

Reflectance

Wavelength (nm)

Figure 4 (Broadband Illumination)
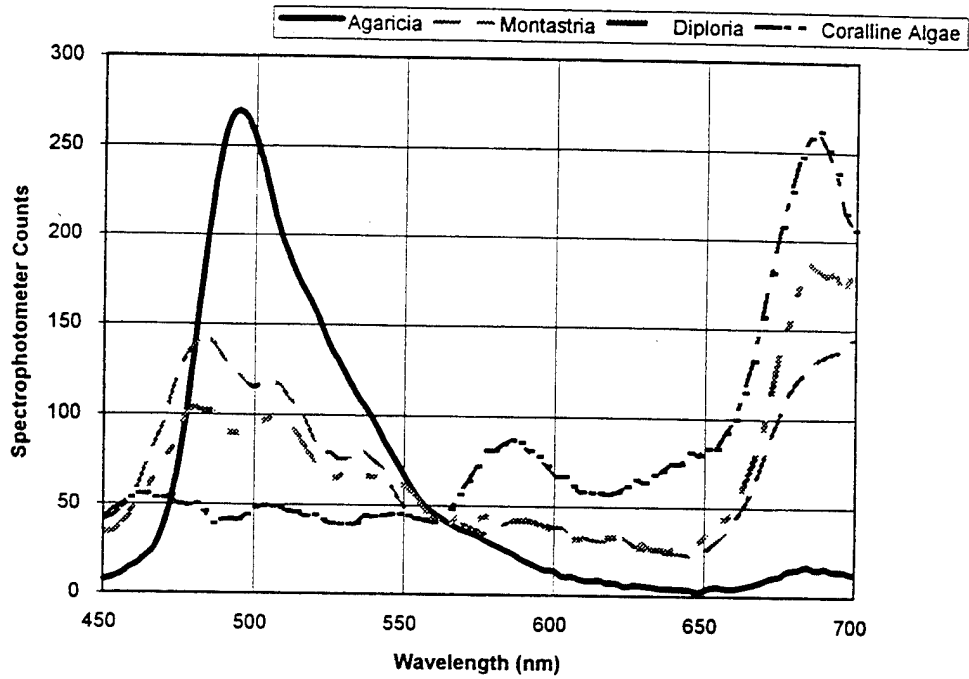
Figure 5. Fluorescence Spectra - Various Corals and Coralline Algae
UV - A Stimulation, Gallium - Doped Metal Hallide Arc
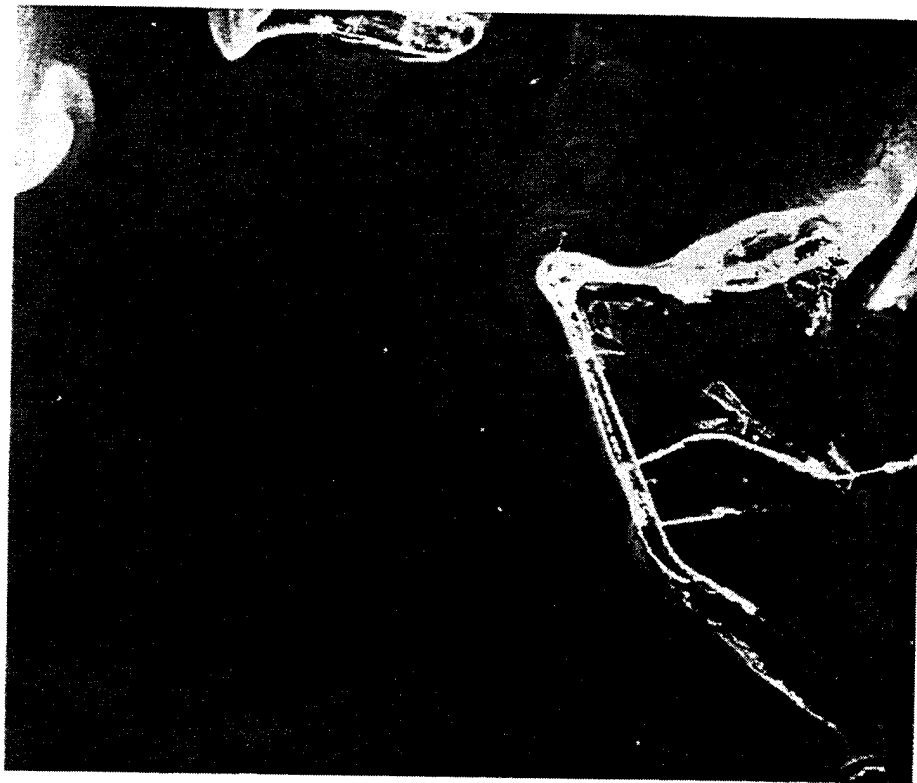
Figure 6. Atmospherically corrected image from AVIRIS of the mouth of Tampa Bay.

The Use of Unmanned Vehicle Systems for Coastal Ocean Surveys: Scenarios for Joint Underwater and Air Vehicle Missions

David K. Costello, Isaac I. Kaminer, Kendall L. Carder and Richard M. Howard

PREPRINT

from

INTERNATIONAL PROGRAM DEVELOPMENT IN UNDERSEA ROBOTICS & INTELLIGENT CONTROL

THE USE OF UNMANNED VEHICLE SYSTEMS FOR COASTAL OCEAN SURVEYS: SCENARIOS FOR JOINT UNDERWATER AND AIR VEHICLE MISSIONS *

David K. Costello [‡]   Isaac I. Kaminer [†]   Kendall L. Carder [‡]   Richard M. Howard [†]

1 INTRODUCTION

Recent aircraft sensors and technology (e.g. Airborne Visable and Infra-Red Imaging Spectrometer, Airborne Oceanography Lidar , HYDICE) have stimulated interest in high spatial and spectral resolution studies of the coastal zone (e.g. Carder et al., 1993a; 1993b; 1993c; Hamilton et al., 1993; Lee et al., 1994). Optical surveys of coastal waters have numerous and diverse applications. Civilian applications include pollution monitoring, mapping water depth and bottom type, and quantifying sediment transport (load and direction) and natural resources (e.g. fisheries, seagrasses, corals, sponges, marine mammals). Military institutions have interest in most of the above applications as well as in locating lost objects, mine counter-measures (MCM), and underwater optical communication.

In all of these applications both in situ (in water) and remote (airborne, spaceborne) measurements are required at least for initial surface mapping and/or algorithm development and validation. Also required is optimization of platform sensors (spectral and S/N ratio) to measure the different spectral signatures of the optical constituents and the integration of the different spatial scales inherent to the different platform measurements in a geo-referenced database as well as sensor optimization. The convolved, optical signal from numerous, changing, optically-active constituents is complex and demands spectral and spatial data of high resolution in order to correctly interpret the contributions to much larger scale phenomena.

This contribution submits that many coastal ocean mapping/search missions can be most efficiently performed by joint missions involving unmanned underwater vehicles (UUVs) and unmanned air vehicles (UAVs).

We will first present a background section which describes the nature of the underwater light field in coastal areas. We then define the relevant radiometric quantities which must be measured or modelled, specify the sensor packages required, and propose three phases of evolution for a joint UUV/UAV mission. Finally, issues regarding the control and co-ordination of multiple unmanned vehicles are addressed.

2 BACKGROUND

In many coastal areas, the critical step in optical methodologies involves partitioning the photons received by air- or space-borne optical sensors into those scattered by the atmosphere, the air-sea interface, particles in the water, and those reflected from the bottom. Successful partioning, however, requires the measurement or modelling of all of the constituents that can absorb or redirect the photon flux.

Water molecules, for example, affect light profoundly and in a manner that has been relatively well researched and documented (Morel and Prieur, 1977; Smith and Baker, 1981). In natural waters, plant pigments (e.g. chlorophylls, carotenoids, etc.) can also play a significant role in water color. The efficiency of the different absorption and fluorescence bands for these pigments has been recently an area of intense research and is becoming increasingly better understood (Kishino et al., 1984; Mitchell and Kiefer, 1988; Sathyendranath et al., 1987).

In many coastal areas but rarely found in significant concentrations over coral reefs, for example, is Colored Dissolved Organic Matter (CDOM or "gelbstoff"), a biogenic degradation product of terrestrial or marine origin which can covary with other chemical parameters. The complexity of mapping even one optically-active constistuent is shown in Carder et al. (1989), who found that terrestrial and marine CDOM had differing spectral signatures. Using this information, CDOM images from AVIRIS were mapped into salinity images (Carder et al., 1993b). Other factors that can affect the underwater light field in coastal areas include suspended sediments and aggregates (see Carder and Costello, 1994; Costello et al., 1994, 1995a), and the spectral reflectivity of the bottom,

that is, the bottom albedo (Costello and Carder, 1994a; 1994b; Costello et al., 1995b).

For an optically thick, homogenous ocean (e.g., well-mixed, deep water), the following equation (Morel and Prieur, 1977; Carder and Steward, 1985) describing remote sensing reflectance, R_{rs}, can be applied:

$$R_{rs}(\lambda) = L_w(\lambda)/E_d(\lambda) = \{f\, b_b(\lambda)/[a(\lambda)+b_b(\lambda)]\}(t/n)^2/Q(\lambda),$$
(1)

where the parameters which are functions of the wavelength λ are noted. Here L_w is the water-leaving radiance, E_d is the downwelling irradiance, b_b and a are the backscattering and absorption coefficients of water and its suspended particles, and $Q(\lambda) = E_u(\lambda)/L_u(\lambda)$ (the ratio of the upwelling irradiance to the upwelling radiance) is only weakly dependent upon λ (Gordon and Morel, 1983). The squared term provides for the radiance divergence and sea-air transmittance, t, of radiance leaving the water. For measurements of upwelling light made from beneath the sea surface, this term becomes 1.0, and $Lw(\lambda)$ becomes $L_u(\lambda)$. The index of refraction of seawater, n, is about 1.334. This equation contains no provision for transpectral phenomena such as water-Raman scattering (considered negligible for near-shore environments) or fluorescence due to CDOM and chlorophyll a (not necessarily negligible for certain wavelengths). Provision for these can be made by adding an additional term (e.g. see Gordon, 1979; Carder and Steward, 1985; Stavn, 1990; Marshall and Smith, 1990; and especially Lee et al. 1994). The ratio f/Q can be approximated for most remote sensing geometries a 0.009360 ± 01 (Gordon, 1989; Morel and Gentilli, 1993).

For an optically shallow environment (e.g. depths shallower than about 2.0 optical thicknesses), bottom reflectance needs to be considered. Equation 1 (e.g. see Lee et al., 1994) can be expanded as follows:

$$R_{rs}(\lambda)_s = R_{rs}(\lambda)_d(1 - exp\{-[k_d(\lambda) + k_u(\lambda)]D\})(2)$$
$$+(t/n)^2(\alpha/\pi)exp\{-[k_d(\lambda) + k_u(\lambda)]D\}(3)$$

where the subscripts s and d depict shallow- and deep-water conditions, α is the bottom albedo, the bottom reflectance is considered to be Lambertian [e.g., $E_u(\lambda)/\pi Lu(\lambda)$ at the bottom], and D is the water-column depth. The term $(1 - exp\{-[k_d(\lambda) + k_u(\lambda)]D\})$ only becomes important when the depth D is smaller than about 0.5 optical depths. The diffuse attenuation coefficients k_d and k_u are for downwelling and upwelling light, respectively, and are largely a function of $a(\lambda) + b_b(\lambda)$ divided by the average slant-path enhancement of the rays relative to the vertical (see Kirk, 1983; Lee et al., 1994). For

non-Lambertian bottom types, the value π is replaced by the bi-directional reflectance distribution function BRDF.

3 UNDERWATER AND AIR MEASUREMENT REQUIREMENTS

Eqs. 1 and 3 can be inverted for $\alpha(\lambda)$ mapping missions if depth or the effects of in-water constituents are known, measured, or adequately estimated, for remote bathymetry missions if $\alpha(\lambda)$ or the effects of in-water constituents are known, measured, or adequately estimated, and for in-water constituent missions if $\alpha(\lambda)$ or depth is known, measured, or adequately estimated. An object search mission is, in fact, an $\alpha(\lambda)$ mission where features incompatible with their spectral surroundings are identified. Ship- or air-vehicle- derived ocean imagery data can be used to extrapolate from near-bottom data acquired by underwater vehicle transects across or along the coastal transition zone or across reef tracts. Alternatively, in situ data can be used to validate algorithms used with remotely sensed data.

Eqs. 1 and 3 can be calibrated by comparing in situ remote-sensing reflection ($R_{rs}(\lambda)$) values obtained by an air vehicle above the surface (where $L_w(\lambda)$ and $E_d(\lambda)$ can be measured directly) to in situ measurements of $R_{rs}(\lambda)$ obtained near the bottom which will provide data regarding $\alpha(\lambda)$ and the effect of in-water constituents. In the case of Remotely-controlled Underwater Vehicle (RUV) measurements, even investigations very near the bottom are feasible, yielding more accurate, model-inversion estimates of $\alpha(\lambda)$ than can presently be obtained using Autonomous Underwater Vehicle (AUV) data from typically more than 3 m above the bottom.

Comparison of $L_u(\lambda, z)$ measured by the underwater vehicle and $L_w(\lambda)$ measured by the air vehicle allows investigation of the air/sea transmittance term, $(t/n)^2$ and Fresnel-reflectance of skylight. Hydro-carbon slicks at the surface, for example, change the Fresnel reflectance factor, absorb UV wavelengths, and fluoresce in visible and IR wavelengths, often in ways that can "fingerprint" the materials.

$R_{rs}(\lambda)$ can be measured near the surface from an AUV measuring the downwelling irradiance $E_d(\lambda, z)$ and upwelling radiance $L_u(\lambda, z)$, where z indicates sensor depth. By gently porpoising the AUV, these values can be obtained for different depths, and diffuse attenuation coefficients are obtained through

$$E_d(\lambda, z + \Delta z) = Ed(\lambda, z)exp[-kd(\lambda, z) \times \Delta z], \quad (4)$$

and a similar expression for $k_u(\lambda, z)$ can be obtained involving L_u instead of E_d.

The instrumentation required to obtain the necessary measurements discussed above is detailed in Section 5 and can be grouped into imaging and non-imaging sensors. The GEN-III multi- channel-plate intensified camera listed allows the utilization of bottom fluoresensce information for classification purposes. The hyperspectral spectrometers listed were developed by the Optical Oceanography group at the University of South Florida and have a 1.5 nm half- bandwidth over the range of 350-900 nm. Commercial instruments have been developed (WET Labs, Inc.) to provide direct measurements of beam attenuation, c, and absorption, a, at 9 wavelengths and they also yield the total scattering coefficient b since $b = c - a$. Backscattering, b_b, sensors are also available for several wavelengths and multi-channel volume scattering $\beta(\theta)$ instruments are under development.

4 MISSION CONSIDERATIONS

In all survey scenarios, a geo-referenced data base is required in order to assess environmental changes. As an example, Shipping- channel bathymetry after major storms could be ascertained with an underwater vehicle performing a fairly dense grid survey that maps integrated vehicle altitude and depth (corrected for tidal variation) into a geo-referenced data base. If, however, bottom albedo data were also integrated into the data base, subsequent aerial surveys then could be performed utilizing an air vehicle (much larger field-of-view (FOV)) with an underwater vehicle to obtain the required in-water measurements to invert equation 3. Since in-water constituents are generally much more conservative in the horizontal dimension than in the vertical, the underwater vehicle could perform a sparse grid and still satisfy data collection requirements to accomodate the air vehicle FOV. The measured bathymetry in the sparse grid would also calibrate the calculated, high-spatial-resolution bathymetry and to verify the assumption of a relatively stable bottom albedo. Such rapid surveys could alert authorities of navigational hazards and of the need for accurate updates of regional bathymetry maps.

Similar economy could be realized in a high-resolution survey of natural resources such as seagrass beds or coral reef sanctuaries. An UAV flying at 100 m altitude over a 25 m water column with off-the-shelf sensors and optics could easily resolve a 30 cm feature under calm conditions within a flight swath of 120 m (400 pixels/swath width). The optical filter effects of water, however would limit the spectral information available for feature identification. An AUV at 10 m altitude and an 8 m flight swath could, then, resolve a 2 cm object and also have spectral information available to allow feature identification.

A dense-grid AUV mission would allow classification of a coral reef community, for example, referenced to the wide-FOV, UAV database. In a subsequent AUV/UAV mission, the AUV could be directed to investigate only those features which do not match the previously acquired and calibrated UAV database. An identical scenario would be appropriate for MCM missions.

The critical requirement for performing autonomous vehicle surveys in coastal waters is precision, geo- referenced vehicle control, with the ability to accurately repeat a ground track. The evolution of vehicle systems toward meeting this requirement is addressed in the following sections.

5 MULTI-SENSOR SYSTEM DEVELOPMENT

The challenges inherent in the fusion of the large-volume, multi-sensor data stream for optical coastal mapping/search missions dictate that tethered vehicles be utilized in the developmental phase. This not only allows for human supervision, but also allows data fusion and vehicle control computations to be performed aboard the support vessel.

Vehicle configuration evolution is envisioned in three phases. The configurations and sensor requirements are described below.

- PHASE I - Remotely-controlled Underwater Vehicle (RUV) with Remotely-controlled Air Vehicle (RAV, towed aerostat/blimp) with geo-referenced map construction/correlation computations and data fusion performed on mothership.

  - RUV
    * Vehicle - Shipboard DGPS and ship heading
      · Acoustic range and bearing relative to ship
      · RUV heading, depth, and pitch and roll
      · 3-D RUV position control.
    * Sensors - Spectral irradiometer ($Ed(\lambda, z)$,cosine collector)
      · Spectral radiometer ($Lu(\lambda, z)$, Gershun tube)
      · 9-channel absorption/attenuation sensor (WETLabs, ac-9)
      · 6-channel intensified bottom camera (Xybion, IMC-301)

- Optical backscattering sensor (Seatech, LSS, or equivalent)
- Fluorometer (for *chl_a* determination)
- Color CCD camera (for RGB-to-HSI image conversion for 256-color mapping)

- RAV
  * Vehicle
    - DGPS, heading, altitude, and pitch and roll
    - 3-D RAV position control.
  * Sensors
    - Spectral irradiometer ($E_d(\lambda, z)$, cosine collector)
    - Spectral radiometer ($L_w(\lambda, z)$, Gershun tube)
    - Color CCD camera (for RGB-to-HSI image conversion for 256-color mapping)

- PHASE II - AUV with Unmanned Air Vehicle (UAV - Vertical Take- off and Landing, VTOL) with geo-referenced map construction/comparison computations and data fusion performed on mothership.

  - AUV - all of Phase I plus Intelligent Distributed Control System (IDCS, Smith, 1994) and telemetry to mothership.

  - UAV - all of Phase I plus Integrated Navigation, Guidance and Control System (IGNCS) and telemetry to mothership.

- PHASE III - AUV with UAV-VTOL without mothership support (geo- referenced map construction/comparison computations and data fusion performed on AUV and/or UAV.

  - AUV - all of Phase I plus Intelligent Distributed Control System (IDCS) and telemetry to UAV.

  - UAV - all of Phase I plus Integrated Navigation, Guidance and Control System and telemetry to AUV. Possible line-of-sight or satellite-link telemetry to land-based support facility.

- PHASE IV - As a continuation of Phase III we propose to develop a virtual world capability wherein the 3D animation of the UAV's and AUV's executing their missions will be available real-time to viewers in remote locations.

5.1 PHASE I: RAV SYSTEM DEVELOPMENT

As discussed earlier the first stage of the joint underwater/air remote sensor development system will consist of integrating an RUV with an RAV. The complete RAV system will include the RAV, the motion/payload sensor package onboard the RAV and the ship based RAV mission control system. In particular, the actual RAV will be an aerostat (aerodynamically-shaped balloon, or non-rigid airship) towed by a mother ship approximately 45 feet long with a diameter of 15 feet providing a volume of 4000 cubic feet for an expected payload of 50 to 100 lbs. Full-up weight of the RAV will be about 250 lbs; the exact payload capacity will depend upon the power system chosen for the ducted-fan propulsion units to be used for thrust actuation. Two ducted fans, one on each side of 24- to 30-inch diameter, will be used to provide up to 40 lbs of thrust to maneuver and propel the RAV against ± 15 knot winds at a speed of 5 to 10 knots. These fan units will require a power input of about 5 horsepower each. A single ducted fan located along the centerline at the aft end of the RAV in the vertical stabilizer will act to provide a pitching or yawing moment for directed flight. Each of the three ducted-fan units will be vectoring to move the RAV along the desired flight path. (The two units would be sufficient, being able to apply asymmetric power for turning, but the use of a third unit in the tail will provide for increased efficiency in maneuvering.)

The RAV will be equipped with a number of onboard sensors. These will fall into two categories: motion and payload sensors. The motion sensors will be used by the control system to control vehicle's attitude and position with respect to the ship. The motion sensor suite will consist of a GPS receiver and the Inertial Measurement Unit (IMU) and will provide the following information: aerostat's GPS position, attitude rates and attitude angles such as pitch, roll and magnetic heading. The payload sensors will consist of the sensing devices capable of obtaining optical coastal mapping/search missions data. The complete control of the RAV will be provided by the ship based mission control computer system (MCCS). This system will include all the necessary I/O to interface with the ducted fans and sensor hardware on the RAV. Furthermore, the MCSS will be equipped with a GPS receiver to provide the differential GPS capability for obtaining the precise RAV position. All the vehicle managment functions will be performed by the MCCS. These functions will include the basic motion control of

the vehicle, the higher level mission management control and the interface with the users aboard the ship.

The mission management level will accept the commands from the RAV users as well as the information about the air and sea conditions. This information will be used to generate the position/veloctiy and attitude commands used by the basic control level to control the RAV.

The basic motion control algorithm will use the motion sensor data and the the RAV position and orientation commands from the mission management level to drive the RAV actuators to achieve the desired aerostat position and orientation with respect to the ship. All the sensor data and the actuator commands will be transported over the RAV tow tether line.

Finally, the graphical user interface included with the MCCS will provide the mission control panel and will consist of a number of dials, knobs and various other graphical devices displayed on the computer screen. These devices will present the data obtained by the RAV motion and payload sensors as well as providing the user with the ability to enter commands for RAV control.

On a typical mission the RAV will be launched from the mother ship and will be positioned by the MCCS outside of the ship's wake at the desired position and orientaiton with respect to the ship. The experience gained in the development of a complete RAV system will provide a critical stepping stone towards the achievement of an autonomous flight by a VTOL UAV discussed in the next section.

5.2 PHASE II: UAV SYSTEM DEVELOP-MENT

In this section we will present issues involved in the development of the UAV system for the missions outlined in Section 5. Again as in the previous section the key components of the complete UAV system will include the UAV itself, the Mission Control Computer System, the motoion and paylod sensors aboard the UAV and the telemetry link between the mother ship and the UAV.

The mission scenario calls for a VTOL UAV to be launched from the mother ship and track a preprogrammed geo-referenced path at a certain altitude above the water. While in loiter the UAV will provide MCCS with continuos data stream which will include the information about the vehicle's position, velocity, attitude as well as the optical and video data necessary for the mission of coastal water surveying. The data will be displayed by MCCS to the users and will also be stored in the memory. Thus the mission scenario calls for the development of a sophisticated user interface and data col-

lection system as a part of MCCS, mission management functions within MCCS capable of generating the desired geo-referenced trajectories for UAV and for UAV capable of tracking these trajectories autonomously while collecting the mission data and maintaining the telemetry link with MCCS. For this phase the UAV/AUV mission coordination will be done by the users aboard the ship.

A significant amount of work has been done at NPS towards the autonomous flight of an UAV. In particular, extensive work has been done on the development of a high-fidelity 6 DOF nonlinear model of the UAV (Kuechenmeister, 1993). This was followed by the development of the hardware-in-the-loop simulation of the UAV with the rapid prototyping capability (Moats, 1994). Several control algorithms have already been tested using this simulation. The development of a detailed DGPS and IMU error models has been accomplished. These were used to develop a navigation system consisting of the appropriate DGPS and IMU data processing algorithms and of a Kalman filter for integrating DGPS with IMU (Marquis, 1993). The filter provides a real-time estimate of vehicle's geo-referenced position. Most importantly a great deal of analytical and simulation work has been done to develop integrated guidance and control algorithms for precise tracking of the geo-referenced trajectories (Kaminer et al., 1993,1994a,1994b). These algorithms rely on the availability of the estimated vehicle geo-referenced position data from the navigation system. A brief discussion of the VTOL UAV and of the development of the integrated control guidance algorithms now follows.

5.3 VTOL UAV ARCHYTAS

A detailed description of ARCHYTAS static and dynamics characteristics can be found in (Kuechenmeister, 1993; Moats, 1994, Stoney, 1993). Archytas, a Greek contemporary of Plato, was credited with successfully flying a mechanical bird; the name is appropriate for the VTOL UAV developed at NPS. The ARCHYTAS vehicle possesses no flying surfaces and relies solely on powered lift for flight provided by a rotating ducted propeller. Control of the aircraft is obtained through the use of four moveable control vanes positioned in the propeller wake of the ducted fan (Weir, 1988). The main features of the ARCHYTAS are a vertical–take–off–and–landing (VTOL) capability, lightweight construction, safe handling operation, compact size and minimal support equipment required.

An important aspect of the ARCHYTAS design is the improvement in static performance provided by the efficiency of the ducted–fan construction. The addition of the shroud around the three–bladed propeller results in in-

Table 1: PHYSICAL CHARACTERISTICS OF ARCHYTAS

Inlet Diameter, A	29.25 in
Propeller Radius, R	12 in
Exit Radius	23.375 in
Inlet Area Ratio	1.219
Exit Area Ratio	1.115
Exterior Contour	Tapered Rear
Propeller Location, % chord	25 %
Number of Blades	3
Engine Speed, Max.	8000 rpm
Engine Speed, Nom.	6500 rpm
Tip Speed, Max.	838 fps
Tip Speed, Nom.	680 fps
Power Loading, $\frac{BHP(\rho_0/\rho)}{R^2/4}$	$7.25\ HP/ft^2$
Maximum Thrust	120 lbs
Mass Moment of Inertia, I_x	$1.8241\ slug - ft^2$
Mass Moment of Inertia, I_y	$1.7997\ slug - ft^2$
Mass Moment of Inertia, I_z	$1.6147\ slug - ft^2$
Prop Mass Moment of Inertia, I_{rx}	$0.0311\ slug - ft^2$
Prop Mass Moment of Inertia, I_{ry}	$0.0067\ slug - ft^2$
Prop Mass Moment of Inertia, I_{rz}	$0.0067\ slug - ft^2$

creased mass flow through the fan, and thus more stat thrust when compared to a conventional propeller co figuration (Kress, 1992). The ARCHYTAS is shown Figure 1 and its characteristics are tabulated in Table

The moveable control vanes are used in combination exert the desired control forces and torques on ARCH TAS. Roll control is achieved by deflecting the four van simultaneously, while pitch and yaw control are obtaine by deflecting two pairs of vanes, each pair acting in tl required direction. Thus, for control purposes, the van act as if the vehicle were equipped with *ailerons* for r control, *elevator* for pitch control and *rudder* for yaw co trol. Powered lift is controlled by adjusting the rpm's _ the propeller.

The full-scale nonlinear equations of motion for ARCHYTAS have been derived in (Kuechenmeister, 1993). However, a brief discussion is included for completeness of presentation. Let $\{I\}$ denote an inertial coordinate system (in this case a geo-referenced frame well-suited for coastal surveying misisons) and let $\{B\}$ represents the right hand rule coordinate system attached to the vehicle's center of gravity. Furthermore, let

- P denote the position vector from the origin of $\{I\}$ to the center of gravity of the air vehicle

Forebody with radio receiver control computer, stability sensors, fiber optic transducers, magnetometer and power converters

Fiber Optic Canister

Dual hi-res CCD video cameras on pan-tilt mount

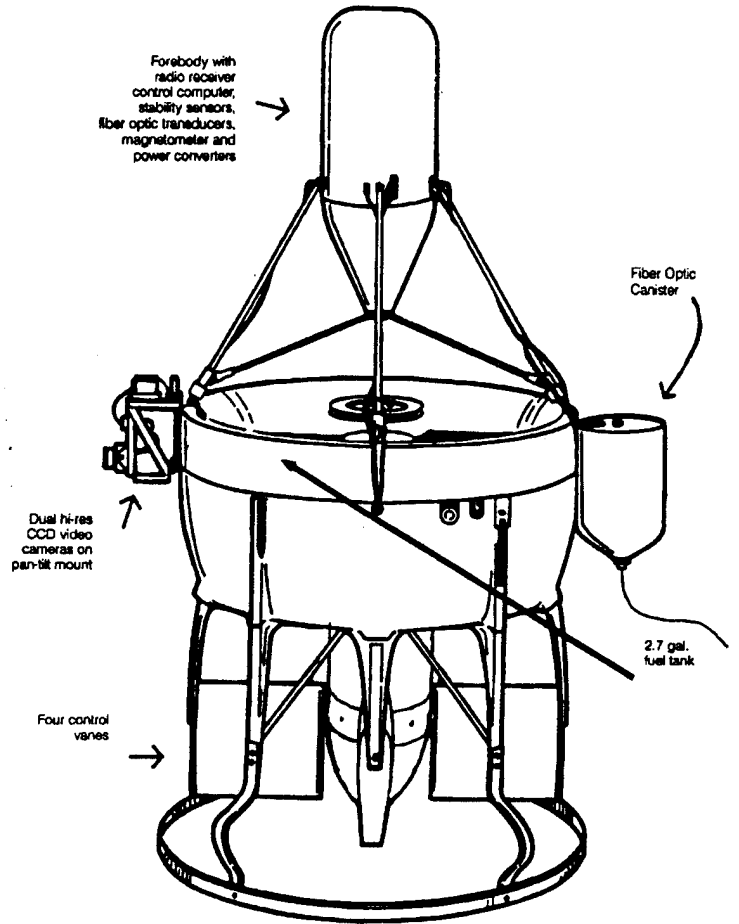Four control vanes

2.7 gal. fuel tank

Figure 1: ARCHYTAS.

- $V = [u\; v; w]'$ denote the velocity measured at the center of gravity of the air vehicle, with respect to $\{I\}$, resolved in $\{B\}$.

- $\Omega = [p\; q\; r]'$ represent the angular velocity of the $\{B\}$ coordinate system with respect to $\{I\}$, resolved in $\{B\}$.

- $\Lambda = [\phi\; \theta\; \psi]'$ denote the vector of Euler angles which describe the orientation of $\{B\}$ with respect to $\{I\}$

- $\mathcal{R}(\Lambda)$ represent the rotaiton matrix from $\{B\}$ to $\{I\}$

- $\mathcal{Q}(\Lambda)$ denote the matrix satisfying the relationship $\frac{d}{dt}\Lambda = \mathcal{Q}(\Lambda)\,\Omega$

- G = the gravity vector expressed in $\{I\}$.

Using above notation the vehicle dynamics can be expressed in the state space form as follows:

$$\mathcal{G} = \begin{cases} \frac{d}{dt}V &= \mathcal{F}_V(V,\Omega,\Lambda,U), \\ \frac{d}{dt}\Omega &= \mathcal{F}_\Omega(V,\Omega,\Lambda,U), \\ \frac{d}{dt}P &= \mathcal{R}(\Lambda)V, \\ \frac{d}{dt}\Lambda &= \mathcal{Q}(\Lambda)\,\Omega, \end{cases} \tag{5}$$

where $\mathcal{F}_V$ and $\mathcal{F}_\Omega$ are continuously differentiable functions, $(V,\Omega,P,\Lambda)'$ is the state space vector and U is the vector of control inputs: ailerons, rudder, elevator and engine rpm. To condense the notation, we define

$$X_{dyn} := \begin{bmatrix} V \\ \Omega \end{bmatrix}, \qquad X_{kin} := \begin{bmatrix} P \\ \Lambda \end{bmatrix},$$

$$\mathcal{L}(.) := \begin{bmatrix} \mathcal{R}(.) & 0 \\ 0 & \mathcal{Q}(.) \end{bmatrix},$$

where $X_{dyn} \in R^6$, $X_{kin} \in R^6$ and $\mathcal{L} \in R^{6x6}$.

The term $\mathcal{Q}(\Lambda)$ in equation (5) was derived for a 2-3-1 sequence of Euler rotations, and is therefore not defined for $\psi = \pm\pi/2$. The choice of this sequence has to do with the fact that in hover (a typical trim condition for ARCHYTAS) the x-direction of the body-fixed coordinate system $\{B\}$ is aligned with the thrust vector, which corresponds to a negative z-direction in $\{I\}$. Therefore, at this trim value the pitch angle θ is $\pi/2$, i.e the $\{I\}$ frame is rotated by $\pi/2$ about inertial y-direction to align itself with $\{B\}$. Furthermore, this trim condition was used for controller design since for the range of velocities V and Ω considered the dynamics of the vehicle do not change. The trim condition is therefore characterized by $V_0 = \Omega_0 = 0$, $\Lambda_0 = [0\; \pi/2\; 0]'$ and

$$U_0 = [rpm\; elevator\; rudder\; ailerons]'_0 = [6387.2\; 0\; 0\; 0.187]',$$

where the nonzero setting of ailerons is needed to counteract the torque imparted by the rotation of the propeller

and the propeller setting of 6387.2 rpm generates sufficient powered lift to compensate for gravity. Now, the linearized model of ARCHYTAS in hover ($V_0 = \Omega_0 = 0$) admits the following state-space representation:

$$\mathcal{G}_l := \begin{cases} \delta\dot{X}_{dyn} &= \mathcal{A}_1\delta X_{dyn} + \mathcal{A}_2\delta X_{kin} + \mathcal{B}\delta U \\ \delta\dot{X}_{kin} &= \delta X_{dyn}, \end{cases} \tag{6}$$

where the matrices $\mathcal{A}_1, \mathcal{A}_2, \mathcal{B}$ were obtained by linearizing equations (5) about the trim condition and $\delta X_{dyn}, X_{kin}, \delta U$ represent small perturbations of the these variables around their trim values.

5.4 INTEGRATED GUIDANCE AND CONTROL ALGORITHM DEVELOPMENT

Following the steps outlined in (Kaminer et al., 1994b) a linear controller $\mathcal{C}_l$ was designed for the linear plant (6) using Linear Quadratic Regulator synthesis. The controller used powered lift, elevator and rudder inputs to track ramp commands in the position vector P and ailerons to track ramp commands in the roll angle ϕ. Therefore, the controller included a total of four integrators on roll and position errors. Since the plant had integrators from each control input to each commanded output no additional integrators were required. Considerations such as command and control bandwidth, closed loop damping and performance robustness were included in the design process. For brevity of discussion the design steps are omitted here. Finally, the linear controller $\mathcal{C}_l$ had the following state-space representation:

$$\mathcal{C}_l = \begin{cases} \delta\dot{X}_c &= \begin{bmatrix} \delta P - \delta P_c \\ \delta\phi - \delta\phi_c \end{bmatrix} \\ \delta U &= \mathcal{C}_c\delta X_c + \mathcal{D}_{c1}\delta X_{dyn} + \mathcal{D}_{c2}\delta X_{kin} \end{cases}$$

where $\delta\phi_c$ and δP_c correspond to small perturbations about the nominal values of the commanded ϕ and P. Next, the controller $\mathcal{C}_l$ was gain-scheduled to account for change in the vane effectiveness as a function of rpm. Since the powered lift T generated by the propeller is given by (see Kuechenmeister, 1993):

$$T = 0.0297\; rpm - 104.7, \tag{7}$$

the gain-scheduling variable α (see Kaminer et al., 1994a) was selected as:

$$\alpha = \frac{0.0297\; rpm_0 - 104.7}{0.0297\; rpm - 104.7}, \tag{8}$$

where $rpm_0 = 6387.2$ is the value of rpm at hover. This led to the family of linear gain-scheduled controllers $\mathcal{C}_l(\alpha)$

defined by

$$\mathcal{C}_l(\alpha) = \begin{cases} \delta \dot{X}_c = \begin{bmatrix} \delta P - \delta P_C \\ \delta \phi - \delta \phi_c \end{bmatrix} \\ \delta U = \begin{bmatrix} 1 & 0 \\ 0 & \alpha I_{3 \times 3} \end{bmatrix} (\mathcal{C}_{c1} \delta X_{c1} + \mathcal{C}_{c2} \delta X_{c2} \\ \quad\quad + \mathcal{D}_{c1} \delta X_{dyn} + \mathcal{D}_{c2} \delta X_{kin}) \end{cases}$$

(9)

The family of controllers $\mathcal{C}_l(\alpha)$ was implemented on the nonlinear plant using the methodology outlined in (Kaminer et al., 1994b):

$$\mathcal{C}(\alpha, \Lambda) := \begin{cases} P_E = \mathcal{R}(\Lambda)^{-1}(P - P_C) \\ \Lambda_E = \mathcal{Q}(\Lambda)^{-1}(\Lambda - \Lambda_C) \\ \dot{X}_c = \begin{bmatrix} 1 & 0 \\ 0 & \alpha I_{3 \times 3} \end{bmatrix} (\mathcal{C}_c \begin{bmatrix} P - P_C \\ \phi - \phi_c \end{bmatrix} \\ \quad + \mathcal{D}_{c1} \dot{X}_{dyn} + \mathcal{D}_{c2}[\dot{P}_E{}' \quad \dot{\Lambda}_E{}']') \\ U = X_c, \end{cases}$$

(10)

where $\mathcal{C}_c$, $\mathcal{D}_{c1}$, $\mathcal{D}_{c2}$ have been specified in (9).

The implementation equations (10) can now be further simplified by taking into account the sensor suite available on ARCHYTAS. As mentioned earlier the ARCHYTAS position P is povided by the onboard GPS receiver. The receiver information is complemented with the onboard accelerometers which measure $\dot{V}$. Therefore, rather than differentiating V the acceletometer signal, which is quite noise-free, can be used directly.

5.5 SIMULATION RESULTS

The ARCHYTAS equations (5) and controller (10) were implemented using the nonlinear simulation package *SYS-TEM_BUILD*. The control system was tested on a number of trajectories, such as straight line flight, including climb and descent, circles in the $x - y$ plane and, particularly, helixes.

In this section we will present the results of a simulation where the control system was required to track a helix. Initially, the vehicle was trimmed in hover. Then the following sequence of commands was generated:

1. at $t = 0$ *sec* vehicle was commanded to track a straight line in inertial x-direction. This was done by generating a ramp command in x;

2. at $t = 8$ *sec* a helix command in P and ϕ was given (see Figure 2). The ϕ command was necessary since along the helix the vehicle maintained nonzero angular rate.

3. Throughout the manuever the pitch command θ_c was set to $\pi/2$ to provide proper vehicle orientation required by trim condition.

This command sequence resulted in ARCHYTAS tracking a straight line followed by a helix. Figure 2 shows the 3D plot of the helix command and the position of the vehicle.

5.6 TELEMETRY REQUIREMENTS

The critical element of the UAV system is a full duplex telemetry link, which must provide reliable communications betweem the MCCS and the UAV. This is particularly true since all the lower control level algorithms will be done by MCCS. Currently, NPS has developed a reliable uplink from MCCS to the UAV using Futaba telemetry setup for RC aircraft. With this setup all the control actuator signals are generated by MCCS. The MCCS drives a Futaba transmitter using an analog interface, developed at NPS. The encoded signal is then transmitted to the UAV on the Futaba datalink. The Futaba receiver aboard the UAV converts this signal to PWM commands which drive the UAV control actuators. This setup was successfully tested in the hardware-in-the-loop simulation. Unfortunatley, the Futaba link used for this test has low power and may have to be replaced by a more powerful link for the field tests.

The downlink will have to include motion sensor and payload data. Currently the NPS is testing a radio modem from REPCO capable of transmitting a 9600 baud in broadcast mode. This link will be used to transmit the motion sensor data from the Inertial Measurement Unit (IMU) aboard the ARCHYTAS to MCCS. With the available bandwidth the complete IMU message is transmitted 25 times a second (25 Hz). This data rate is sufficient for the real-time feedback control of the vehicle. However, for the surveying missions the payload data must be included in the downlink transmission from ARCHYTAS. This requirement suggests two possible scenarios for the downlink architecture:

1. The motion sensor data, which includes GPS and IMU data is transmitted on a dedicated link. Similarly, the payload data is transmitted on another dedicated link. The carrier frequencies must in this case be well seperated to avoid interference problems. This has the advantage of having a dedicated link for the motion data. The disadvantage is that the total number of links to and from ARCHYTAS is now equal to three.

2. The motions sensor and the payload data share the downlink. This reduces the total number of links by one and the power requirements for the onboard telemetry equipment. However, the probability of corrupting the motion sensor data increases.

The bandwidth, power and architecture requirements on the downlink will be worked out in collaboration with the USF team during PHASE I of the project. Recall, PHASE I will serve as a stepping stone towards the autonomous VTOL flight in PHASE II and will be critical in ironing out the details of telemetry link requirements.

6 PHASE III: AUTONOMOUS UAV/AUV OPERATION

The last phase of the complete remote sensor data collection and fusion system calls for the development of independent UAV/AUV mission without the support from the mother ship. The complete system will consist of one or multiple UAV's and AUV's operating in a prescribed region with a mission control computer system located onshore. The MCCS will monitor the mission progress and communicate the commands or changes in the mission scenarios via a telemetry link to UAV. The communication with AUV will be accomplished using a repeater on UAV and buoy equipped with an antenna and towed by the AUV(s). At this phase both vehicles will be launched from a possible beach location and will proceed to execute a prescribed mission scenario. The AUV's will be equipped with Intelligent Distributed Control Systems while UAV's will have the Integrated Guidance, Navigation and Control Systems onboard. These systems will allow the vehicles to react to unpredicted random events in a reasonable fashion. Most of the essential components required for such a mission will have been developed in the previous phases. The key remaining problem will be the development of the reliable telemetry link between the MCCS and the AUV. As suggested earlier, one way this can be done is via a repeater aboard the UAV. The details of the solution to this problem will emerge following the completion of PHASE II.

7 PHASE IV: VIRTUAL WORLD LABORATORY

As a continuation of Phase III we propose to develop a virtual world capability wherein the 3D animation of the UAV's and AUV's executing their missions will be available real-time to viewers in remote locations. In a typical Phase III mission the autonomous vehicles (UAV and AUV) will perform their missions while communicating real-time with the MCCS. This communication link includes the payload data as well as the data obtained from the motion sensors aboard the UAV and AUV. Furthermore, in the Virtual World setup the motion sensor data processed by the MCCS will be placed on the Ethernet bus connecting the MCCS with the graphics workstation.

Figure 2: 3D plot of the helix command and of ARCHY-TAS position

The virtual prototyping software residing on the workstation will use the motion data from UAV and AUV to drive the virtual simulation display of both vehicles. This display will also include instrumentaion panels displaying the data in a format familiar to submarine and aircraft pilots.

The Virtual World lab will provide scientists and engineers in a remote location with the ability to observe the motion of the autonomous vehicles real-time as the mission progresses. This will allow them to be active participants in the mission planning and execution using a low volume/low bandwidth link. (As opposed to using a TV camera which will require another dedicated high bandwidth link as well as some means of filming the mission progress by a third party.) Furthermore, the graphics terminal can be displayed in an Aquarium where the visitors will be able to observe the mission progress real-time.

Most of the essential components required for the virtual world lab have already been developed at the NPS. The virtual prototyping software Designer's Workbench by Corepheus has been acquired by NPS and used to create the virtual simulations of the ARCHYTAS flight discussed in section 5.4 (see Lagier, 1994; Selnick, 1994). In (Lagier, 1994) the basic capability for virtual simulation and data display of ARCHYTAS flight using Designer's Workbench was developed. This capability also included the procedure for importing the ARCHYTAS flight simulation data into the Designer's Workbench virtual environment. This was done by generating the flight simulation data and storing into a a data file of appropriate format. The data file was then imported into Designer's Workbench and used to drive the virtual simulation. and the flight data displays. The work in (Lagier, 1994) was extended in (Selnick, 1994) where the procedure for generating animation links was streamlined and a more sophisticated instrumentation panel for displaying the ARCHYTAS flight data was created.

The work in (see Lagier, 1994; Selnick, 1994) did not include real-time interface between the simulation software such as the one to be used by MCCS and Designer's Workbench. In fact all the virtual simulation was done using imported data files. Developing such a real-time interface between MCCS and Designer's Workbench is critical to creating a true virtual world laboratory. Fortunately, such a capability is available on the latest version of the software system used by MCCS. In fact, it provides users with the option of sending the data processed by the MCCS via the Ethernet bus to multiple computer destinations. One such destination can include the workstation hosting the Designer's Workbench software. (Designer's Workbench already provides users with the capability for importing Ethernet data real-time to drive the virtual simualtion). Currently, the efforts are under way at NPS to develop the real-time interface between the MCCS software and Designer's Workbench.

8 SUMMARY

Coastal oceans are dynamic and productive environments which attract much of the world's population and provide the terminus for world shipping routes. As such they are vulnerable to changes brought on by physical processes and anthropogenic inputs. Because of their valuable natural resources, tourism, shipping and other forms of commerce, coastal areas are of great economical significance. Protection of natural water resources, coastlines, facilities, and shipping requires the acquisition of a database which is unprecedented. The acquisition of this database dictates the use of state-of-the-art sensors and platforms.

We have attempted to provide a background for the understanding of the variables involved in coastal remote sensing and to describe the sensors and measurements required in order to deconvolve these variables. Joint AUV/UAV missions may offer the most appropriate and economical vehicle platforms for accomplishing many tasks. Finally, we have presented an outline for the evolution of the integrated, multiple-vehicle/sensor system required to accomplish precision, geo- referenced coastal surveys.

9 BIBLIOGRAPHY

Carder, K. L. and D. K. Costello (1994) Optical effects of large particles. In: Ocean Optics, Spinrad, Carder, Perry (eds.), Oxford University Press, London.

Carder, K.L., P. Reinersman, R.F. Chen, F. Muller-Karger, C.O. Davis and M. Hamilton (1993a) AVIRIS calibration and application in coastal oceanic environments. Remote Sens. Environ. 44:205-216.

Carder, K.L., R.G. Steward, R.F. Chen, S. Hawes, Z. Lee and C.O. Davis (1993b) AVIRIS calibration and application in coastal oceanic environments: tracers of soluble and particulate constituents of the Tampa Bay Coastal Plume. Photogram. Engr. & Remote Sensing. Special Issue on Imaging Spectrometry. 487-500.

Carder, K.L., Z.P. Lee and R.F. Chen (1993c) Unmixing of Spectral Components Affecting AVIRIS Imagery of Tampa Bay. In: Imaging Spectrometry of the Terrestrial Environment, SPIE Vol. 1937, 77-90.

Carder, K. L., R. G. Steward, G. R. Harvey, and P. B. Ortner (1989) Marine humic and fulvic acids: Their effects on remote sensing of ocean chlorophyll. Limnol. Oceanogr. 34:68-81.

Carder, K.L. and R.G. Steward (1985) A remote-sensing reflectance model of a red tide dinoflagellate off west Florida. Limnol. Oceanogr. 30:286-298.

Costello, D.K, K.L. Carder and W. Hou (1995a) Aggregation of a diatom bloom in a mesocosm: bulk and individual-particle optical measurements. DeepSea Research. In press.

Costello, D.K., K.L. Carder, T.G. Peacock, and N.S. Nettles (1995b), accepted to Visual Communications and Image Processing '95. Taipei, Taiwan. Multi-spectral Imagery, Hyper-spectral Radiometry, and Unmanned Underwater Vehicles: Tools for the Assessment of Natural Resources in Coastal Waters.

Costello, D.K., K.L. Carder. (1994a) New instrumentation and Platforms for Subsurface Optical Measurements. Ocean Optics XII, J.S. Jaffey, ed. Bergen, Norway.

Costello, D.K. and K.L. Carder. (1994b) Using unmanned vehicle systems for ground-thruthing oceanographic satellite data. AUVS '94 - Intelligent Vehicle Systems and Technology, Proc. Asso. for Unmanned Vehicle Systems, Detroit, MI.

Costello, D.K., K.L. Carder, R.G. Steward and A. Alldredge. (1994). The Distribution and Optical Properties of Large Marine Particles: Data From a Culture Tank and Field Experiments. EOS AGU (75) 3, 35.

Gordon, H. R. (1989) Dependence of the diffuse reflectance of natural waters on the sun angle. Limnol. Oceanogr. 34, 1484-1489.

Gordon, H.R. and A. Morel (1983) Remote Assessment of Ocean Color for Interpretation of Satellite Visible Imagery: A Review. Springer-Verlag, New York.

Gordon, H.R. (1979) Diffuse reflectance of the ocean: The theory of its augmentation by chlorophyll a fluorescence at 685 nm. Appl. Opt. 18(8):1161-1166.

Hamilton, M., C. O. Davis, S. H. Pilorz, W. J. Rhea and K. L. Carder (1993) Examination of chlorophyll distribution in Lake Tahoe, using Airborne Visible and Infra-Red Imaging Spectrometer (AVIRIS). . Remote Sens. Environ. 44:217-230.

Kaminer I., A.M. Pascoal, P.P. Khargonekar, and C. Silvestre (1993), A Velocity Algorithm for the Implementation of Gain-Scheduled Controllers with Applications to Rigid Body Motion Control. Proc. 1993 Conference on Decision and Control, San Antonio, TX, pp. 1043 - 1048.

Kaminer I., A.M. Pascoal, P.P. Khargonekar, and E. Coleman, (1994a) A Velocity Algorithm for the Implementation of Nonlinear Gain-Scheduled Controllers. Accepted for publication in *Automatica*.

Kaminer I., A.M. Pascoal, C. Silvestre, and P.P. Khargonekar (1994b) On the Implementation of Gain Scheduled Trajectory Tracking Controllers for Autonomous Vehicles. Preprint.

Kuechenmeister D. R. (1993) A Non-Linear Simulation of an Autonomous Unmanned Air Vehicle. Master's Thesis, Naval Postgraduate School, Monterey, CA.

Kress G. A. (1992) Preliminary Development of a VTOL Unmanned Air Vehicle for the Close Range Missions. Master's Thesis, Naval Postgraduate School, Monterey, CA.

Kirk, J.T.O. (1983) Light and Photosynthesis in Aquatic Ecosystems, Cambridge University Press, Cambridge.

Kishino, M., C. R. Booth and N. Okami (1984) Underwater radiant energy absorbed by phytoplankton, detritus, dissolved organic matter, and pure water. Limnol. Oceanogr. 29(2), 340-349.

Lagier M. (1994) An Application of Virtual Prototyping to the Flight Test and Evaluation of Unmanned Air Vehicle. Master's Thesis, Naval Postgraduate School, Monterey, CA.

Lee, Z. P., K.L. Carder, S.K. Hawes, R.G. Steward, T.G. Peacock, and C.O. Davis (1994) Model for interpretation of hyperspectral remote sensing reflectance, Appl. Opt. 33, 5721-5732.

C.W. Marquis III (1993) Integration of Differential GPS and Inertial Navigation Using Complementary Kalman Filter. Master's Thesis, Naval Postgraduate School, Monterey, CA.

Marshall, B.R. and R.C. Smith (1990) Raman scattering and in-water ocean optical properties. Appl. Opt. 29:71-84.

Mitchell, B.G. and D.A. Kiefer (1988) Chlorophyll a specific absorption and fluorescence excitation spectra for light-limited phytoplankton. Deep-Sea Research 35(5), 639- 663.

M.L. Moats (1994) Automation of Hardware-in-the-Loop Testing of Control Systems for Unmanned Air Vehicles. Master's Thesis, Naval Postgraduate School, Monterey, CA.

Morel, A. and B. Gentilli (1993) Diffuse reflectance of oceanic waters (2): Bi- directional aspects. Appl. Opt. 32, 6864-6879.

Morel, A. and Prieur, L. (1977) Analysis of variations in ocean color. Limnol. Oceanogr. 22:709-722.

Sathyendranath, S., L. Lazzara and L. Prieur (1987) Variations in the spectral values of specific absorption of phytoplankton. Limnol. Oceanogr. 32(2), 403-415.

Selnick A.P. (1994) Virtual Prototyping as an Aid to Control Systems Design. Master's Thesis, Naval Postgraduate School, Monterey, CA.

Smith, R.C. and K. S. Baker (1981) Optical properties of the clearest natural waters. Appl. Opt. 20, 177-184.

Stavn, R.H. (1990) Raman scattering effects at the shorter visible wavelengths in clear ocean waters. In: Ocean Optics X, Proc. SPIE 1302, 94-100.

Stoney R. B. (1993) Design, Fabrication, and Test of a Vertical Attitude Take-off and Landing Unmanned Air Vehicle. Master's Thesis, Naval Postgraduate School, Monterey, CA.

Weir, R. J. (1988) Aerodynamic Design Considerations for Free-Flying Ducted Propeller. Proc. of the 1988 Flight Mechanics Conference, AIAA, Washington D.C., pp 720-731.

Bulk and Individual-particle Optical Measurements.
April 14-22, 1994, East Sound, San Juan Islands, WA

David K. Costello, Weilin Hou, and Kendall L. Carder

University of South Florida, Marine Science Department
140 7th Avenue South, St. Petersburg, FL 33701-5016
Voice 813-553-3953, Lab 813-893-9503, FAX 813-893-9189, Email dkc@monty.marine.usf.edu

Introduction

This report presents data collected as part of the SIGMA program during April 14-22, 1994, in East Sound, San Juan Islands, WA. The data collected involves individual particle characteristics and distribution as well as the optical measurements, the beam attenuation coefficient (m^{-1}) and particulate, detrital, and pigment absorption coefficients (m^{-1}).

Since presentation of the entire database at full resolution is impractical except in electronic format, only a synopsis can be presented here. The entire database, however, is accessible electronically via the world-wide web (www). Please contact the authors for access instructions. We also ask that this data (both that presented here and via www) be treated as "Preliminary" and the authors consulted before citation or other formal utilization.

Methods

Bulk measurements

Beam attenuation was measured using a 25 cm pathlength Seatech transmissometer. This instrument utilizes a 660 nm collimated source and has an in-water half-angle of acceptance for forward scattered light of 1.8° (BARTZ et al., 1978). A beam attenuation coefficient corrected for the forward-scattered light-acceptance angle, c (m^{-1}), was computed as in COSTELLO et al. 1995.

The filter pad absorption measurements follow the method of MITCHELL and KIEFER (1988) using the pathlength amplification factor coefficients of BRICAUD and STRAMSKI (1990). Filter pad transmission for particle-laden sample pads and blank pads were measured with a Spectron Engineering, Inc. 256-channel spectral radiometer (resolution 2.6 nm, half-bandwidth 7 nm) to yield particle absorption coefficients (a_p) from 400 to 750 nm. Absorption spectra for detrital material, a_d, were also obtained after pigment extraction with hot methanol (ROESLER et al., 1989; KISHINO et al., 1985). The absorption spectra for phytoplankton, $a_\phi = a_p - a_d$, were calculated on a channel-by-channel basis.

The particulate absorption coefficient at 660 nm, a_p, can be utilized in conjunction with the beam attenuation coefficient at 660 nm, c, to estimate the particulate scattering coefficient at 660 nm, b_p: $b_p = c - a_p - a_w$. At 660 nm, absorption by water, a_w, is 0.4 m^{-1}

(SMITH and BAKER, 1981) and scattering by water and absorption by dissolved material are negligible (JERLOV, 1976).

Individual Particle Characteristics and Distributions

Images of individual particles were secured using the Marine Aggregated Particle Profiling and Enumerating Rover (MAPPER, Figure 1). A brief description of the system and the data reduction methodology follows. The reader is referred to COSTELLO et al. 1991, 1992, 1994a, and 1994b for details and algorithms.

The MAPPER system uses three, long-pass-filtered video systems of differing magnification, but with co-incident image planes, to image particles as they pass through a thin sheet of 685 nm light produced with four Toshiba TOLD-9149 diode lasers. The three video records are recorded (S-VHS) on-board MAPPER as the system free-falls through the water column. The descent rate was adjusted to about 15 cm/s for the East Sound deployments yielding a vertical-profile resolution of 5 mm at the NTSC video rate of 30 frames/s. An adaptive, target-detection gray-scale threshold (GST) was utilized to enhance particle detection in near-surface waters during daylight deployments when some ambient illumination above the 675 nm filter-pass threshold could be present. We also employed closing tolerances for the three systems (the distance in image-space which is searched by the algorithm in the attempt to "connect" pixels above GST) which were functions of each system's magnification and signal-to-noise ratio. Generally the search radius ranged from 350-750 μm.

Pixel resolutions (at 640Hx480V digitization) for the three systems were 17.5 μm, 92 μm, and 285 μm. For all three systems, targets which constituted less than eight grouped pixels need to be discarded in order to satisfy the Nyquist sampling frequency of the $\approx$400 line horizontal resolution of the S-VHS recording media (e.g. $\approx$25 μm for the highest resolution system). This theoretically yields a practical resolution of $\approx$50 μm for the highest resolution system. However, considerations involving electronic "overshoot" in digital processing of analog images combined with the physical complexity of images of natural particles dictate that targets constituting less than 10 grouped pixels be disgarded (see COSTELLO et al. 1994b). The realistic resolution, then, for the MAPPER imaging systems for the East Sound deployments was 62 μm equivalent spherical diameter (ESD) or about a factor of 2.5 less than pixel resolution.

The particle size data from all three systems were processed on a frame-by-frame basis utilizing a computer-controlled S-VHS VTR (JVC BR-S605UB), an infinite-window Time Base Corrector (NOVA 900S Super TBC, also under computer control), and a combination Frame-grabber/array-processor (Data Translation DT-2867). Data from the three systems were combined to yield particle size distributions (PSD, #/cm^3) and normalized by bin width (cm, using progressive volume-doubling bins, ie. $2^{1/3}$ diameter bins) to yield particle size spectra (PSS, #/cm^4). Again a PSS is available for every 5 mm vertical slice of the water column, the data presented here are integrated into 1 m vertical increments.

Individual particle characteristic calculations included particle reflectivity, 3-D (x,y,z) position, ESD size, equivalent sperical projection (ESP) size, fill-factor (F, the reciprocal of the image 2-D "porosity"), and the semimajor axis (a), semiminor axis

(ζ), and angular orientation (Γ) of the ellipse enclosing the geometric spread of the particle image. The last five quantities are computed using algorithms rooted in the theory of Moment Invariant Functions and, as such, are useful in automated pattern recognition (HU, 1962, TEAGUE, 1980) and have been shown to have utility in describing marine particulates (COSTELLO et al. 1994b). The ESP size descriptor would emphasis the geometric spread of a medusa, for example, even if much of the organism was below the image processing GST and not visualized. An automated ESD calculation, on the other hand, would shrink the visualized area into the smallest possible circle significantly distorting the description of the size of the medusa.

Finally, the MAPPER large-field-camera system, the system with the lowest magnification, includes two mirrors as well as the light sheet in its field-of-view. This produces hyper-stereo images of particles from which 3-dimensional particle shape and volume can be computed (COSTELLO et al. 1991). An additional utilization of the hyper-stereo module is to deploy MAPPER with only one of the four lasers energized thereby recording light scattered by an individual particle in three discreet directions. Depending on the particle's position within the image, the scattering angles vary from about 20 to 170 degrees.

Results

MAPPER was deployed 25 times consisting of a total of 14 4-laser deployments and 11 1-laser deployments (Table 1). Each deployment consisted of multiple downcasts. Transmissometry data was collected on each downcast. The maximum deployment depth was 26.25 m, the depth of the water column, that is, on one occasion we let MAPPER touch bottom. One downcast from each deployment was processed. The digital imagery constitutes 24.5 Gigabytes.

The time of collection and depths for filter pad absorption samples are shown in Table 2. In all, 34 samples were processed.

Bulk measurements

Beam attenuation coefficient profiles (Figure 2) show that most of the changes in water clarity took place in the upper 10 m. Exceptions to this are the profiles from 1200 hrs 4/19 and 2000 hrs 4/21 which showed increased attenuation down to 20 m. In all profiles, attenuation increased near the bottom.

Figure 3 shows the average beam attenuation coefficient above and below 10m from April 14th through April 21st. Attenuation in the surface layer increased dramatically on the 19th and then varied considerably from sample to sample. This apparent oscillation could be attributed to tidal influences which were not apparent in the less frequent sampling prior to this date. The oscillation was generally confined to the upper layer and exhibited maxima both at midnight and at noon. This again suggests that the change in particulate attenuation at the station was due to physical (tidal) processes rather than biological processes.

Figure 4a through 4I shows the particulate absorption (a_p) spectra for April 14 through 21st. The depths from which samples were taken are indicated. The highest attenuation coefficient measured (nearly 0.2 m^{-1}) was in the chlorophyl_a absorption

band near 440 nm for the surface sample of 4/19/95, morning. The water column was most homogenous during the beginning of the experiment (4/14 and 4/15). Again, the spectral resolution (2.6 nm) of the absorption data precludes complete presentation except in electronic form. The numbers which generated Figure 4 (as well as a_4 and a_d data) are available via www.

Particulate absorption at 660 nm, ap660 (Figure 5), has utility since the transmissometer also functions at the 660 nm wavelength. As discussed above, the particulate attenuation coefficient, cp660, can be calculated from the transmissometer data and utilized along with ap660 to investigate multi-variate relationships between these two optical parameters and biochemical measurements (COSTELLO et al. 1995). This anaysis is currently underway and not presented here.

Individual Particle Characteristics and Distributions

Since SIGMA is most interested in large particle formation, large particle abundance as a function of depth is shown in Figure 6a through 6n. This presentation also allows ready comparison with the data presented by Alldredge and Gotschalk elsewhere in this report. The data was binned into 1-meter increments. For all plots, the rightmost line is for particles between 0.56 and 1.12 mm dia., the central line represents particles between 1.12 and 3.57 mm dia. and the leftmost plot (barely visable in most cases) is for particles exceeding 3.57 mm dia.

Figures 7a through 7n shows the PSS (#/cm^4) for all MAPPER 4-laser deployments (14). The minimum particle size included was 62 μm and data was integrated in 1-m depth bins. These plots are presented so that the reader can get a sense of the particle size distribution through the course of the experiment. The numbers used to generate these plots are available via the www.

Two other parameters are presented as averages above and below 10m. The Fill factor (Figure 8), the reciprocal of image 2-dimensional porosity, varied considerably through time and between the two layers. There also appears to be a positive correlation between the Fill factor and individual particle, averaged reflectance. While a positive correlation between these two parameters is rather intuitive, it may also be useful in automatically classifying particles when utilized on an individual particle basis. That investigation is currently underway.

References

BARTZ, R., J. R. V. ZANEVELD and H. PAK (1978) A transmissometer for profiling and moored observations in water. In: *Ocean Optics V.* Proc. SPIE 160, pp. 102-108.

BRICAUD, A. and D. STRAMSKI (1990) Spectral absorption coefficients of living phytoplankton and nonalgal biogenous matter: A comparison between the Peru upwelling area and the Sargasso Sea. *Limnography and Oceanography*, 35, 562-582.

COSTELLO, D. K., K. L. CARDER and W. HOU (1995) Aggregation of a diatom bloom in a mesocosm: Bulk and individual particle optical measurements. *Deep-Sea Research II*, (42) 1. pp. 29-45.

COSTELLO, D. K. and K. L. CARDER (1994a) New instrumentation and platforms for subsurface optical measurements. In: *Ocean Optics XII*, Jules S. Jaffe, Editor, Proc. SPIE 2258, Bergen, Norway.

COSTELLO, D. K., W. HOU and K. L. CARDER (1994b) Some effects of the sensitivity threshold and spatial resolution of a particle imaging system on the shape of the measured particle size distribution. In: *Ocean Optics XII*, Jules S. Jaffe, Editor, Proc. SPIE 2258, Bergen, Norway.

COSTELLO, D. K., K. L. CARDER and W. HOU (1992) Structured visible diode laser illumination for quantitative underwater imaging. In: *Ocean Optics XI*. Gary D. Gilbert, Editor, Proc. SPIE 1750, pp. 95-103.

COSTELLO, D. K., K. L. CARDER and R.G. STEWARD (1991) Development of the Marine Aggregated Particle Profiling and Enumerating Rover (MAPPER). In: *Underwater Imaging, Photography, and Visibility*, Richard W. Spinrad, Editor, Proc. SPIE 1537, pp. 161-172.

HU, M. (1962) Visual Pattern recognition by moment invariants. *IRE Tranactions on Information Theory*, IT-8, 179.

JERLOV, N. G. (1976) *Marine Optics*. Elsevier Oceanography Series No. 14, Elsevier Scientific Publishing Company, Amsterdam-Oxford-New York, 231 pp.

KISHINO, M., M. TAKAHASHI, N. OKAMI and S. ICHIMURA (1985) Estimation of the spectral absorption coefficients of phytoplankton in the sea. *Bulletin of Marine Science*, 37, 634-642.

MITCHELL, B. G. and D. A. KIEFER (1988) Chlorophyll *a*-specific absorption and fluorescence excitation spectra for light-limited phytoplankton. *Deep-Sea Research*, 35, 635-663.

ROESLER, C. S., M. J. PERRY and K. L. CARDER (1989) Modeling in situ phytoplankton absorption from total absorption spectra in productive inland marine waters. *Limnology and Oceanography*, 34, 1510-1523.

SMITH, R. C. and K. S. BAKER (1981) Optical properties of the clearest natural waters (200-800 nm). *Applied Optics*, 20, 177-184.

TEAGUE, M. R. (1980) Image analysis via the general theory of moments. *Journal of the Optical Society of America* 70 (8).

Table 1. MAPPER deployments. All deployments are with 4-lasers except those designated as B, D, F, or H which are 1-laser deployments. The deployment downcast processed is listed under DC#.

Date	Depth	TC time	DC#	DC duration
4/14	19.3500	14:11:36	2	110 s
4/15	22.2600	09:10:52	1	116
4/16	21.1000	09:21:56	1	114
4/17	20.9300	09:30:42	1	100
4/18A	22.7800	09:16:18	2	106
4/18B	23.0600	10:49:15	1	114
4/19A	19.8800	12:38:08	1	103
4/19B	21.7300	12:56:38	2	106
4/19C	24.3900	20:04:47	1	104
4/19D	23.5900	20:18:57	1	99
4/20A	24.3900	00:01:07	1	116
4/20B	23.5900	00:21:23	2	146
4/20C	23.5300	06:31:40	1	104
4/20D	23.8600	06:46:39	1	121
4/20E	21.2000	12:32:04	1	125
4/20F	23.8600	12:52:25	2	119
4/20G	25.1800	20:02:21	1	106
4/20H	25.0000	20:19:37	1	127
4/21A	23.3200	23:58:18	1	122
4/21B	24.9100	00:13:58	1	106
4/21C	24.1200	06:00:03	2	117
4/21D	26.2400	06:04:42	2	145
4/21E	25.4400	12:36:16	1	135
4/21F	25.1800	12:58:05	2	130

TOTAL = 2,661 seconds processed = 24.5 Gigabytes

Table 2. Filter Pad Absorption Samples

Date	Depth(m)	Date	Depth(m)	Date	Depth(m)
4/14/94 morning	0 5 12 2	4/17/94 morning	0 5 8 21	4/19/94 evening	4 12 21
4/15/94 morning	0 5 16 21	4/18/94 morning	0 5 8 16 21	4/20/94 morning	6 12 21
4/16/94 morning	0 5 12 16 21	4/19/94 morning	0 8 21	4/21/94 morning	6 12 21

Figure 1

Beam Attenuation, East Sound

Figure 2

Beam Attenuation, East Sound

Figure 3

4/14/94 morning

a

5m
0m
12m

4/15/94 morning

b

0m
5m
16m
21m

Particulate Absorption Coefficient (m^-1)

wavelength (nm)

Figure 4

Figure 4

Figure 4

Figure 4

Figure 4

Particulate Absorption at 660 nm, East Sound
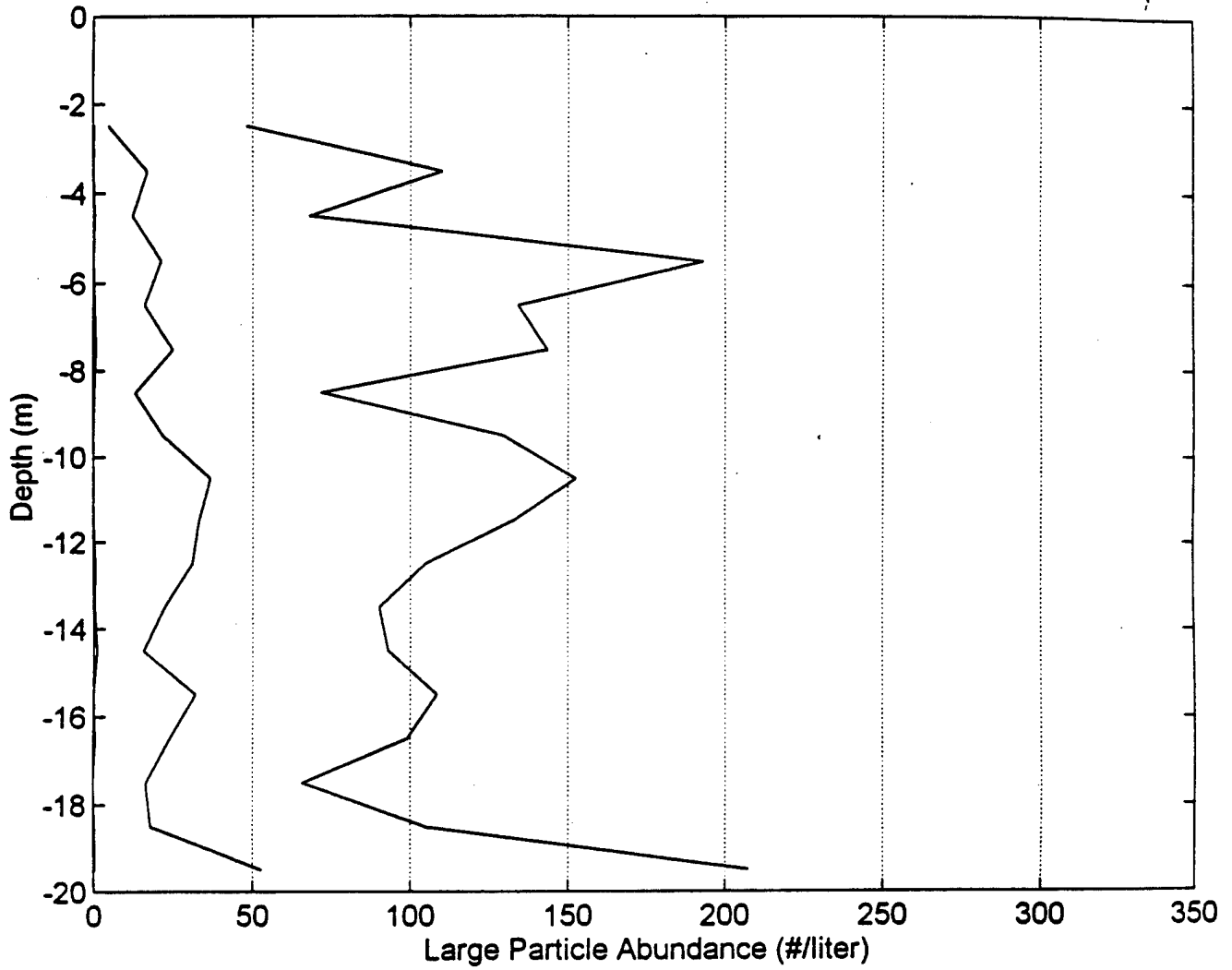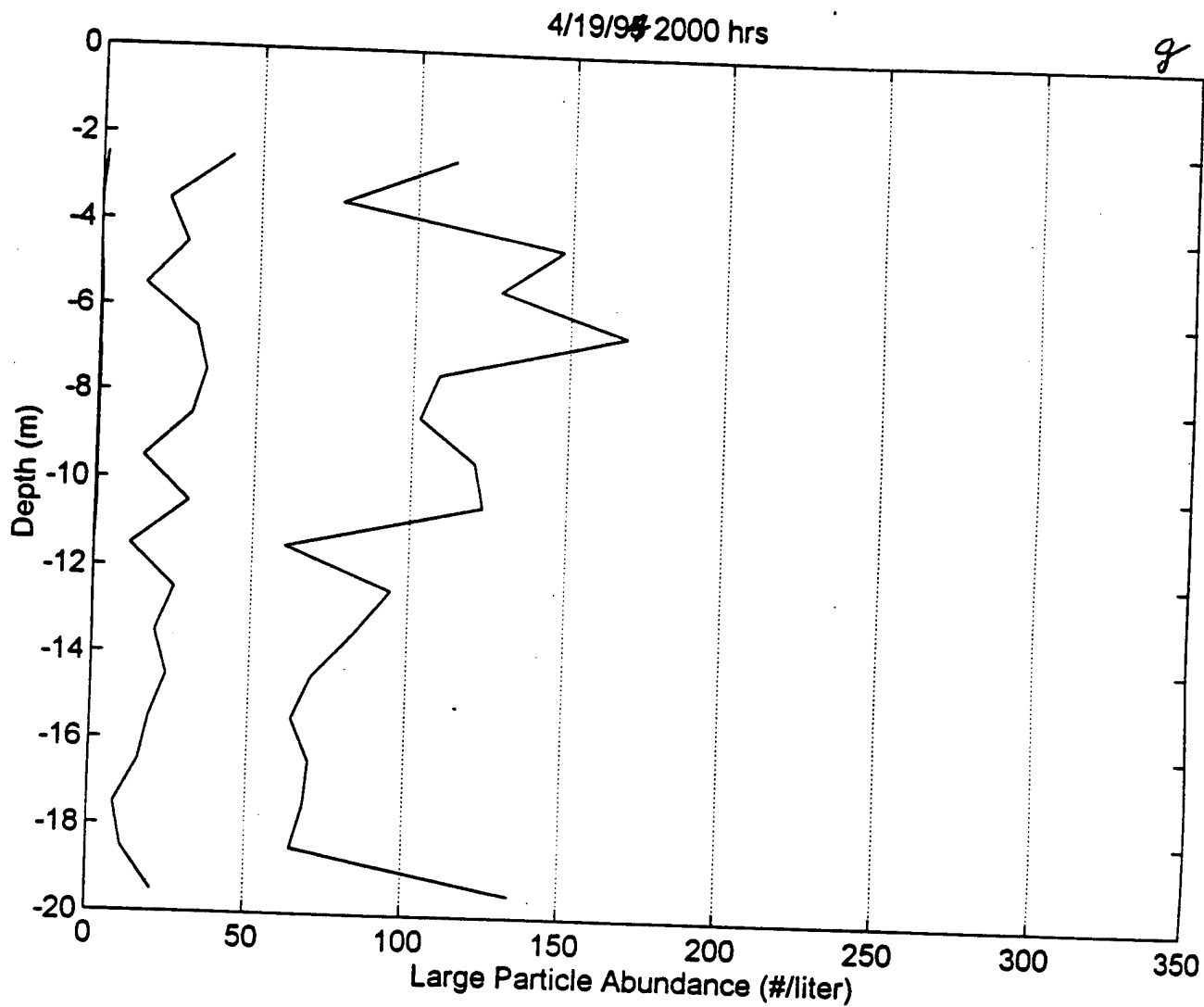
Figure 5

4/14/95 1410 hrs

a

Figure 6

4/15/94 0910 hrs

b

Figure 6
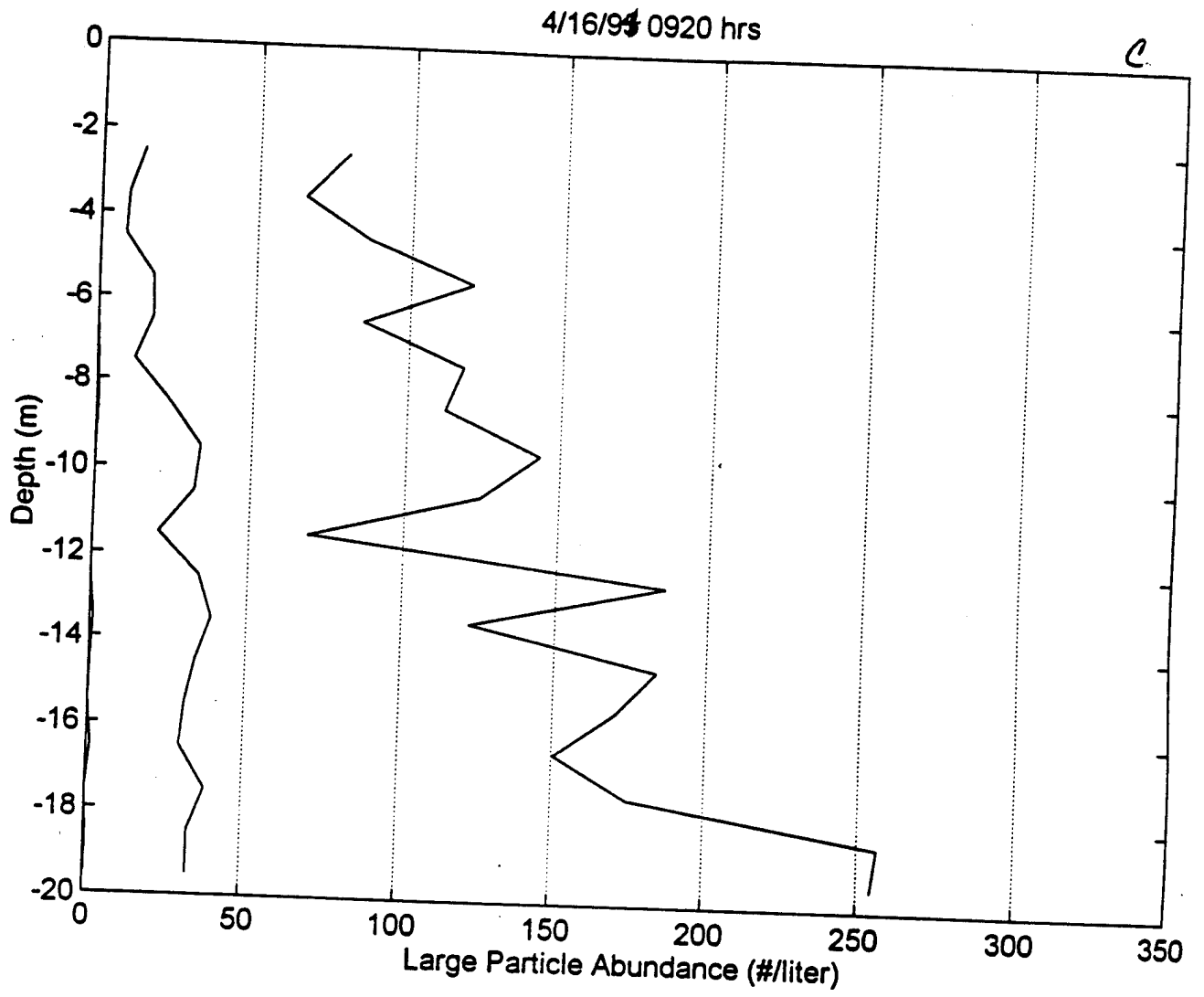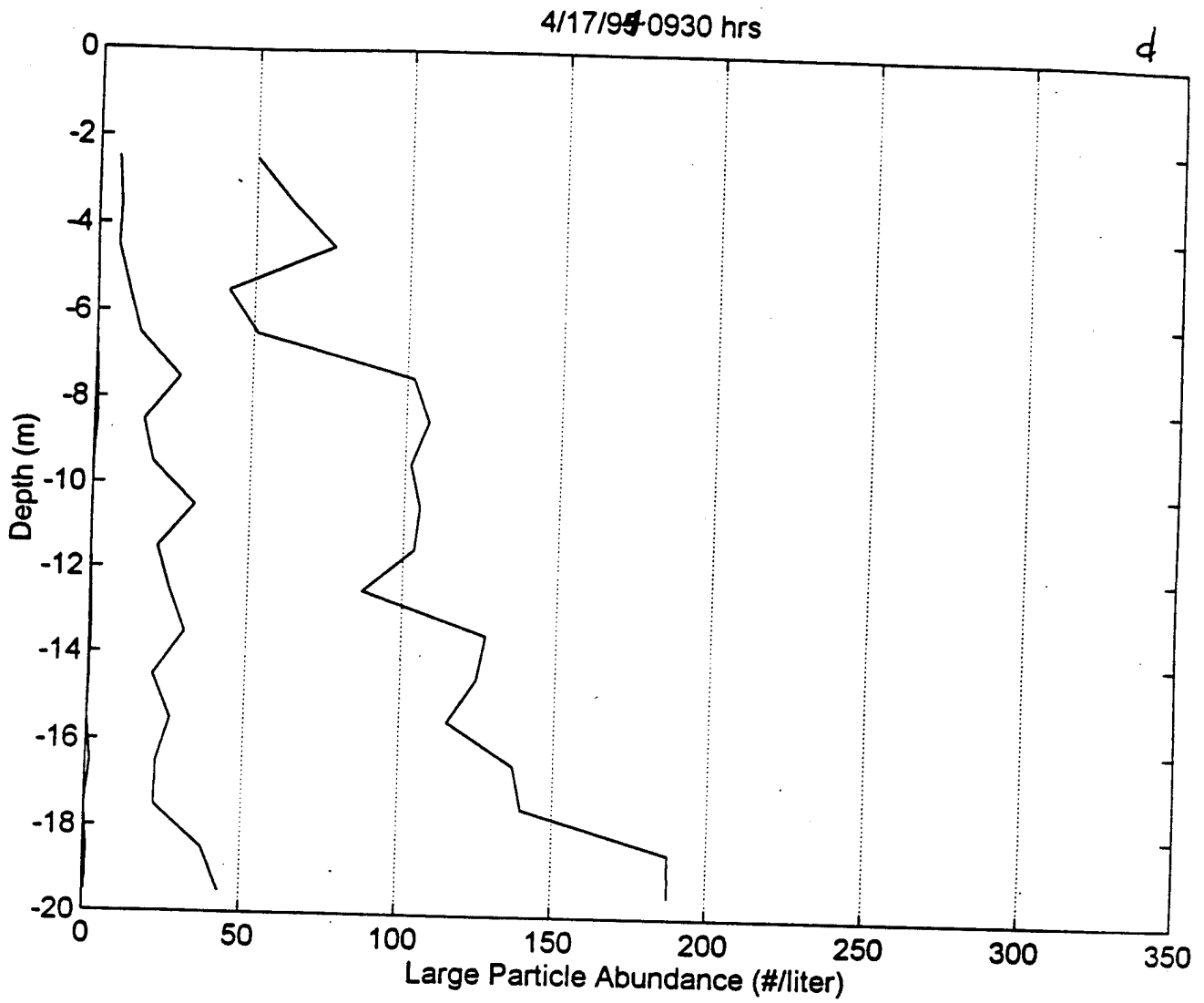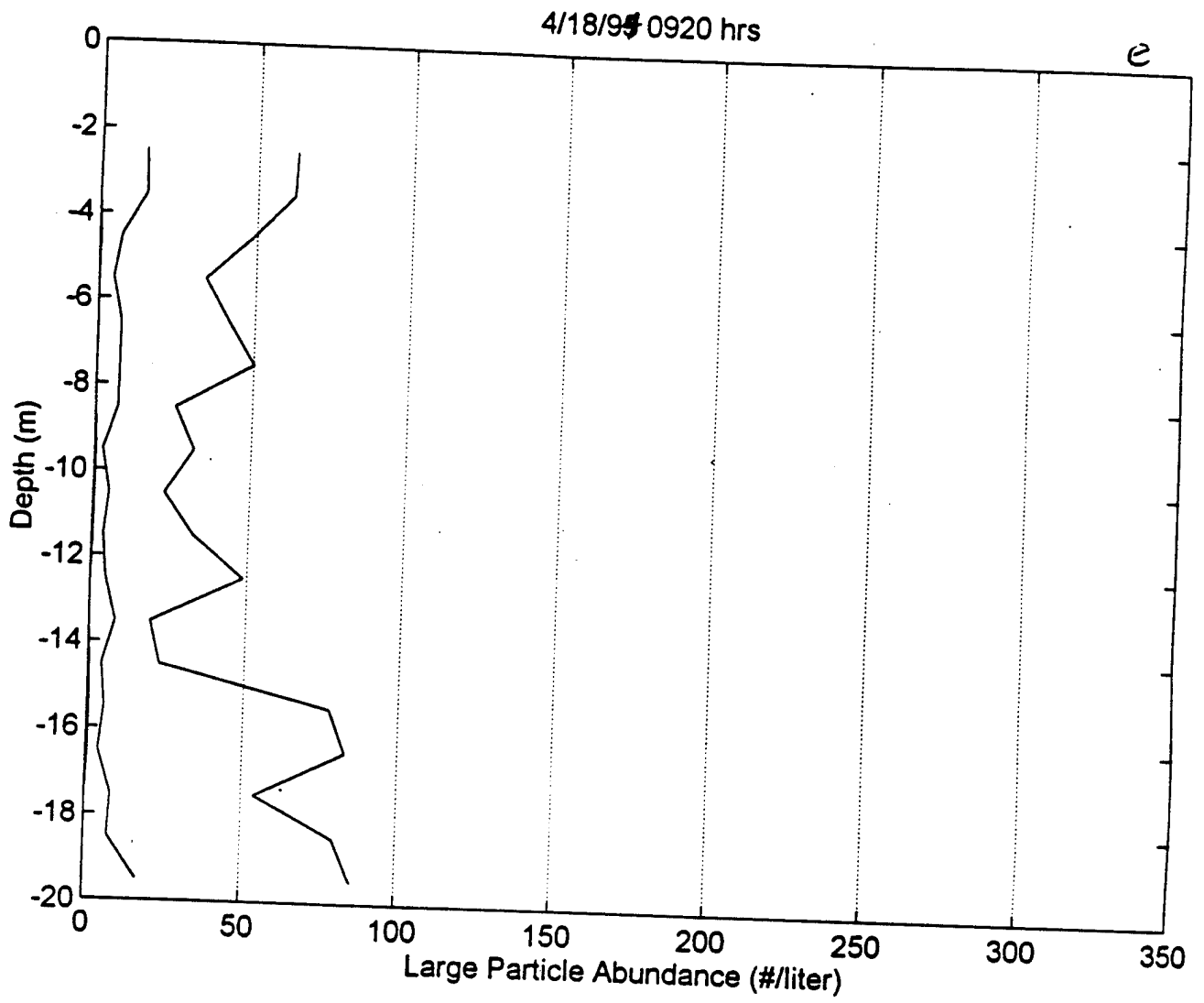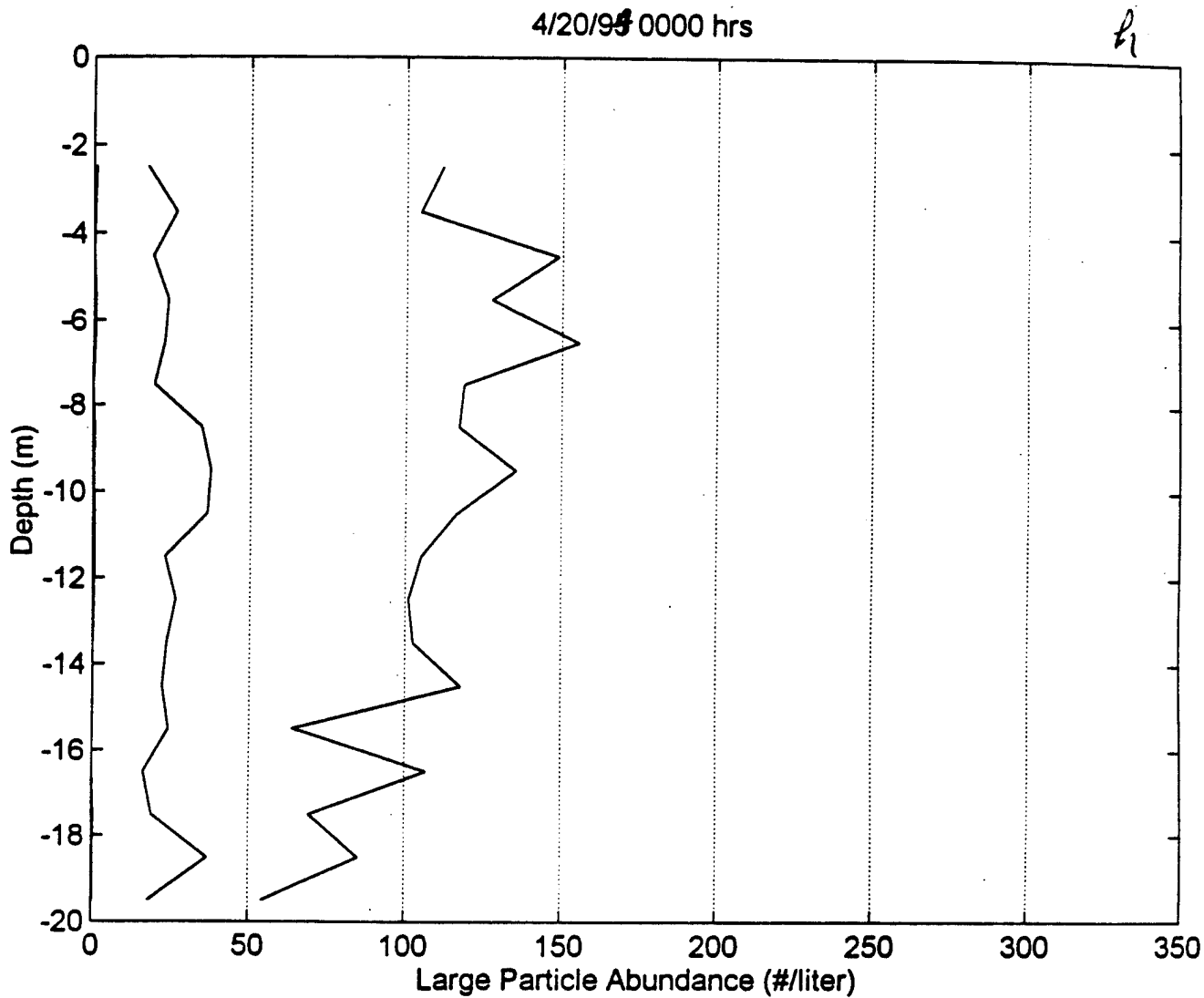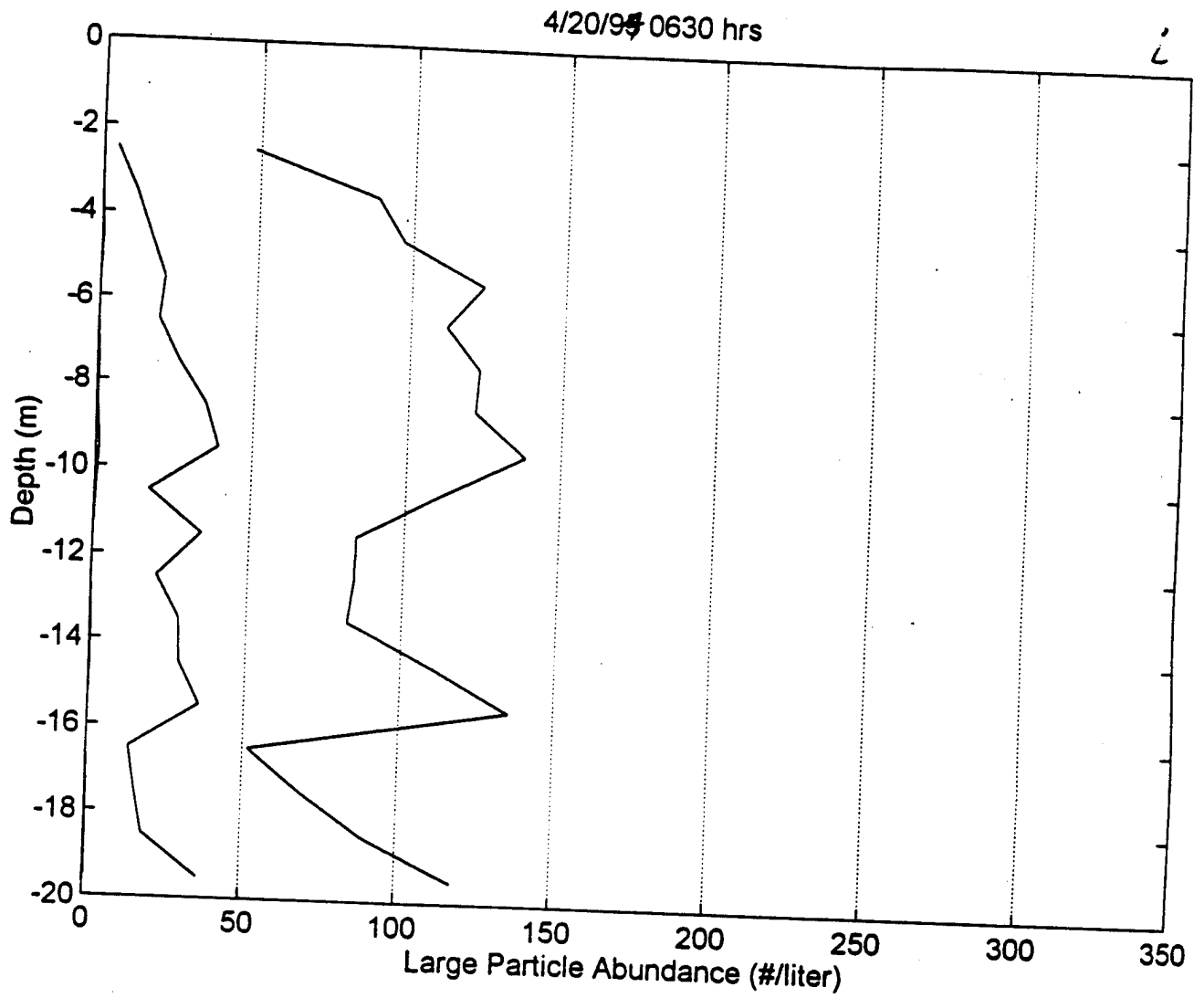
4/16/94 0920 hrs

C

Figure 6

4/17/95 0930 hrs

Large Particle Abundance (#/liter)

Depth (m)

d

Figure 6

4/18/95 0920 hrs

Figure 6

4/19/94 1240 hrs

Figure 6

4/19/95 2000 hrs

Figure 6

4/20/95 0000 hrs

Figure 6

4/20/95 0630 hrs

Figure 6

4/20/94 1230 hrs

Large Particle Abundance (#/liter)

Depth (m)

Figure 6

4/20/94 2000 hrs

Figure 6

4/21/9? 0000 hrs

L.

Figure 6

4/21/94 0600 hrs

Figure 6

4/21/94 1230 hrs

n

Figure 6

4/14/95 1400h, East Sound

Log10 Particle Concentration (#/cm^4)

Log10 Particle Size (mm)

Depth (m)

a

Figure 7

4/15/95 0910h, East Sound

b

Log10 Particle Concentration (#/cm^4)

Depth (m)

Log10 Particle Size (mm)
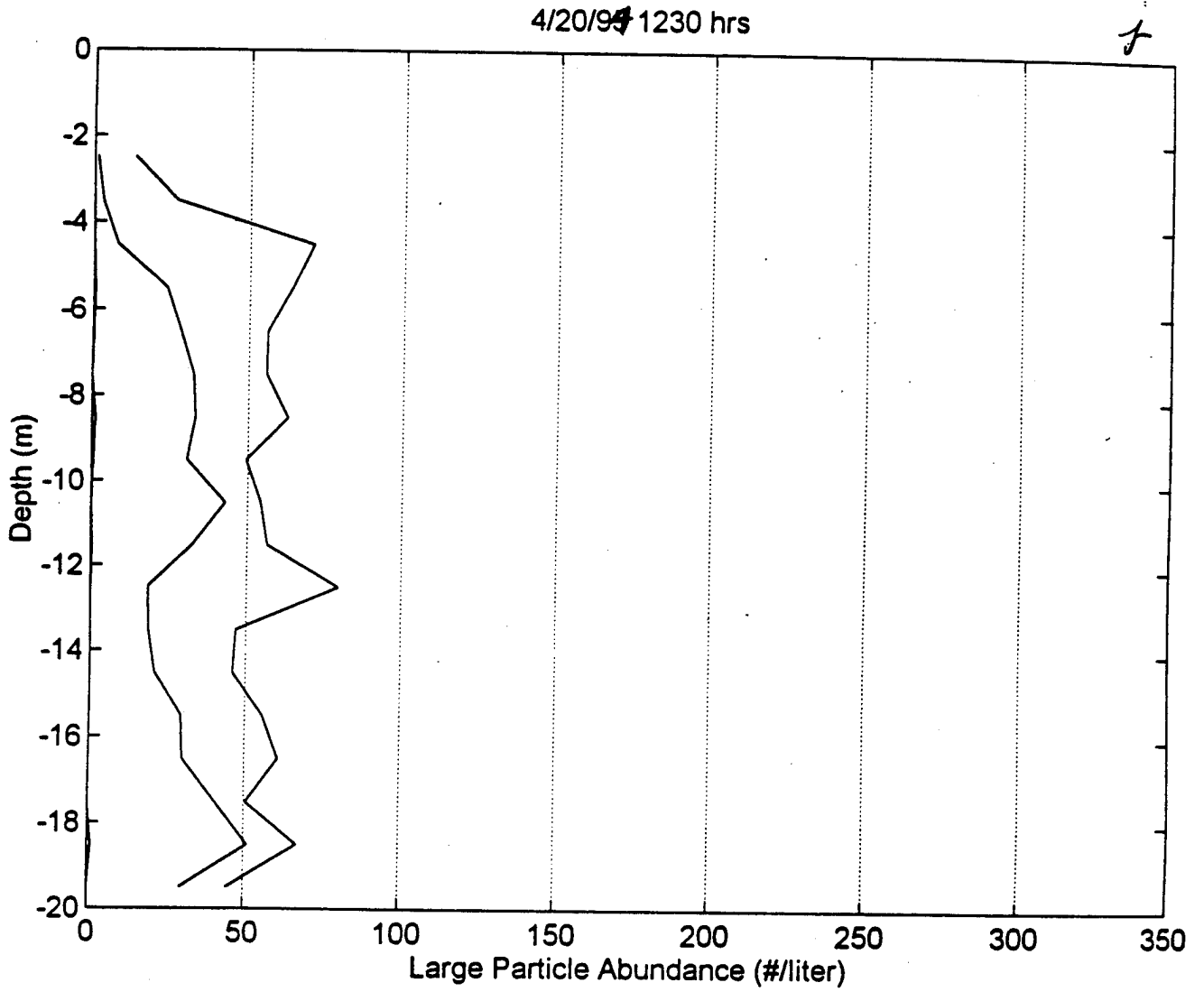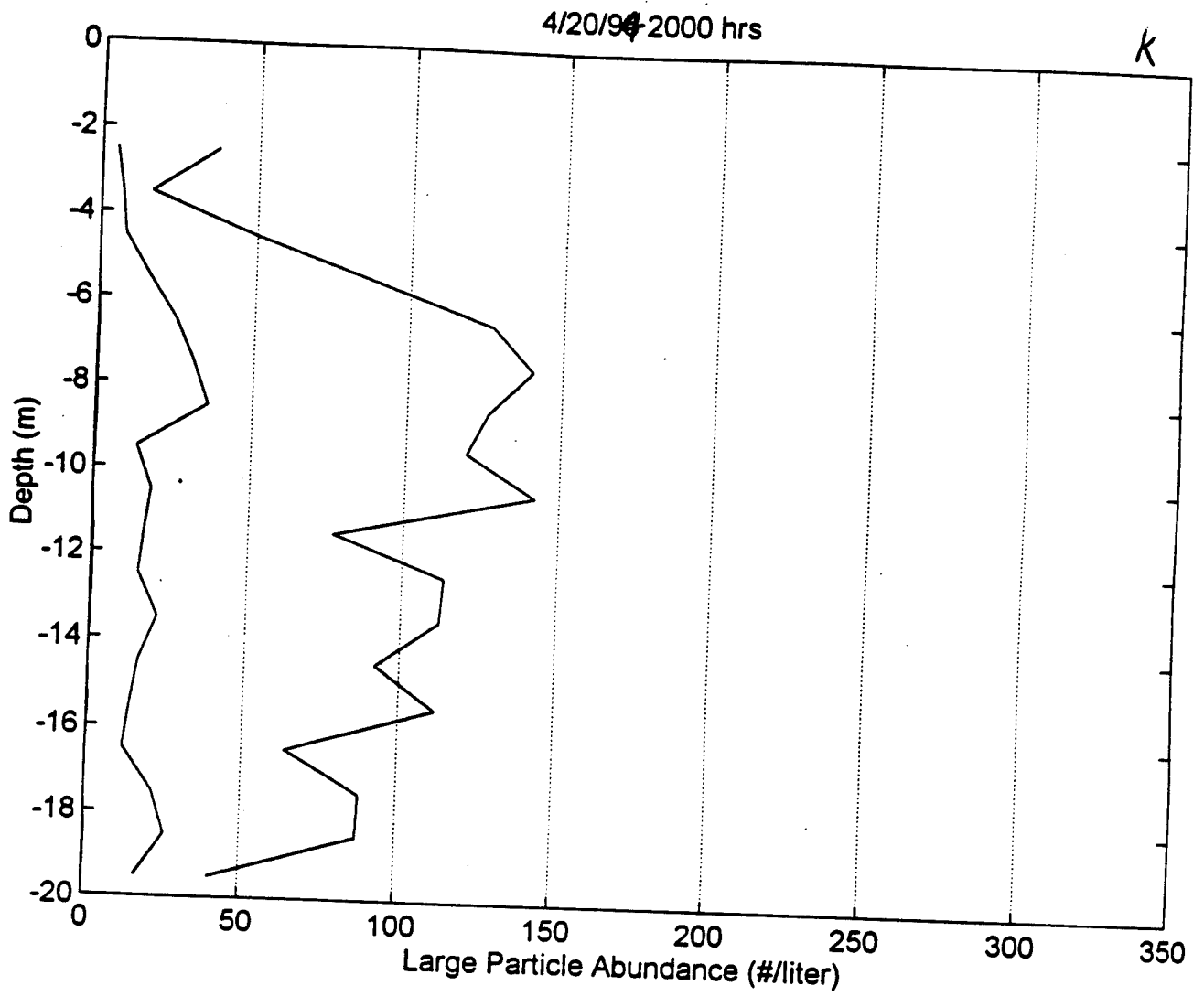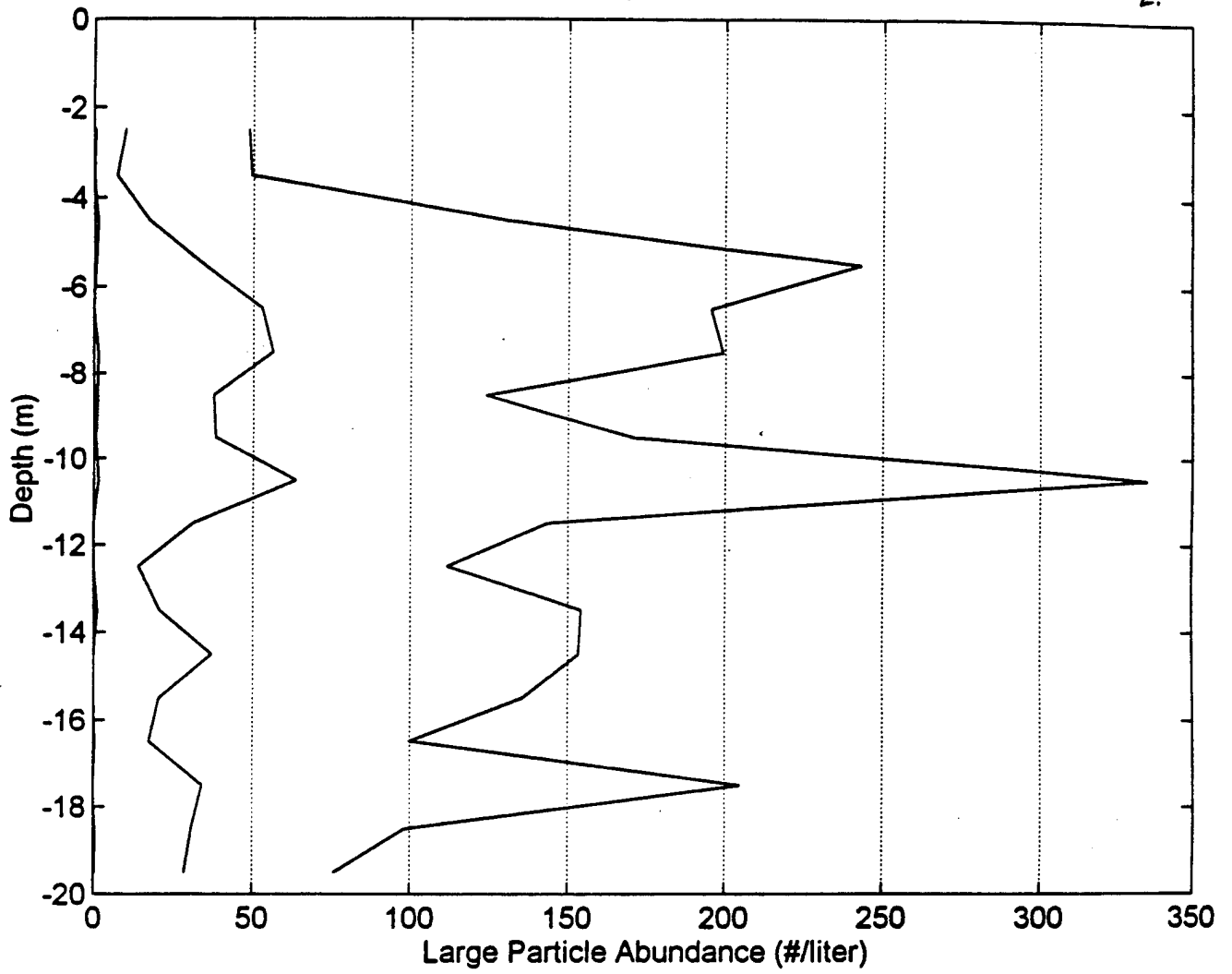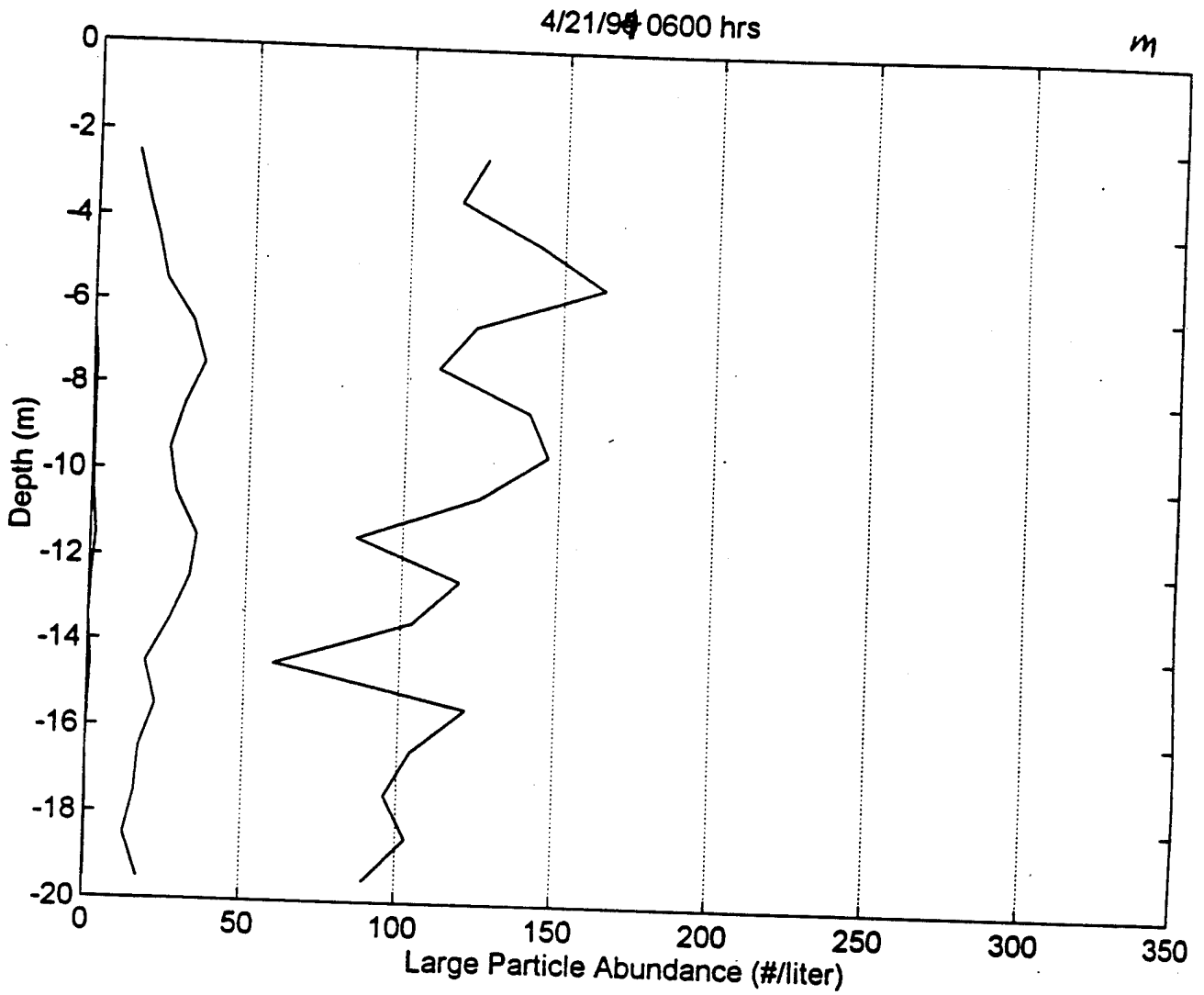
Figure 7

4/16/94 0920h, East Sound

c

Log10 Particle Concentration (#/cm^4)

Log10 Particle Size (mm)

Depth (m)

Figure 7

4/17/95 0930h, East Sound

d

Figure 7

4/18/95 0920h, East Sound

e

Log10 Particle Concentration (#/cm^4)

Log10 Particle Size (mm)

Depth (m)
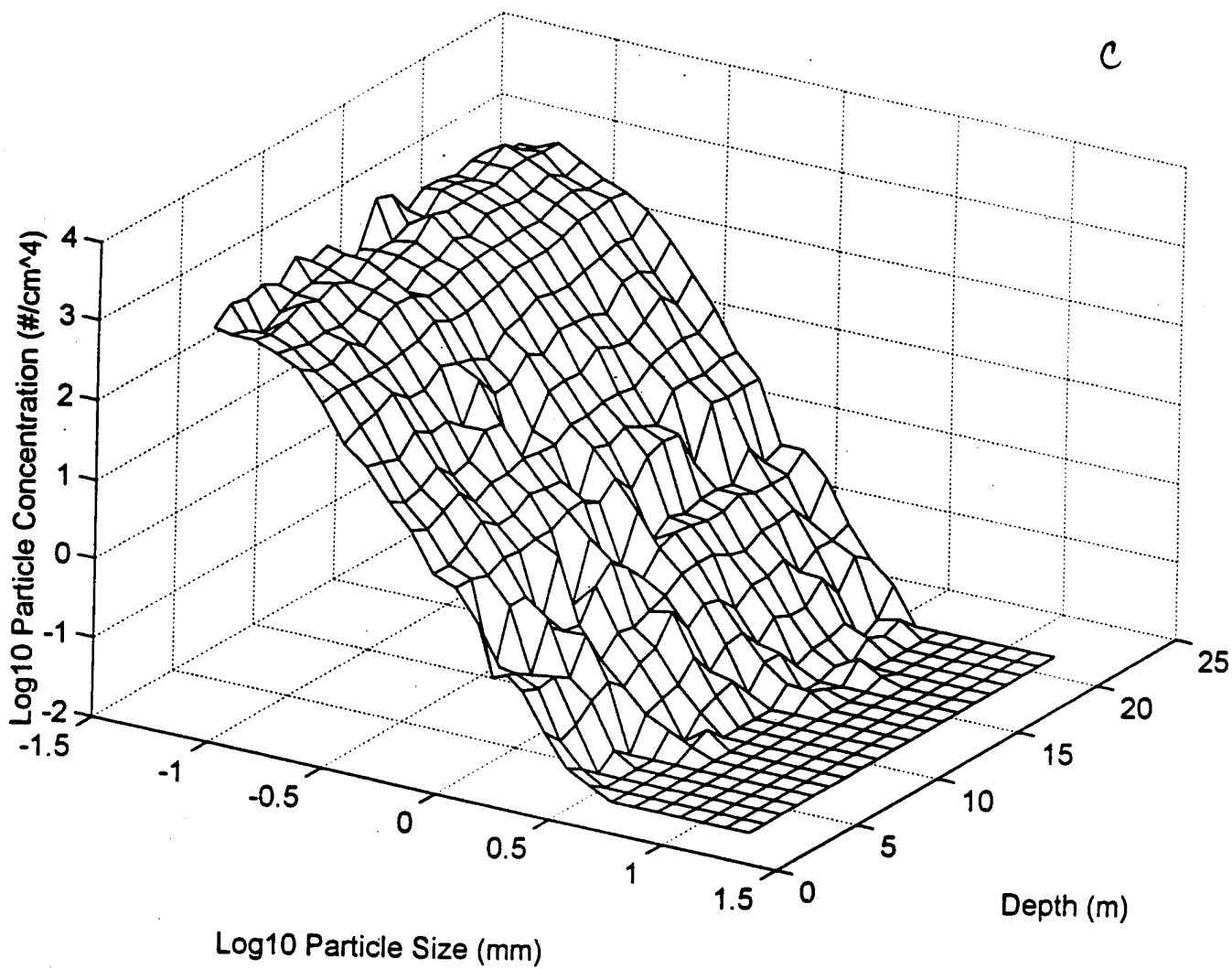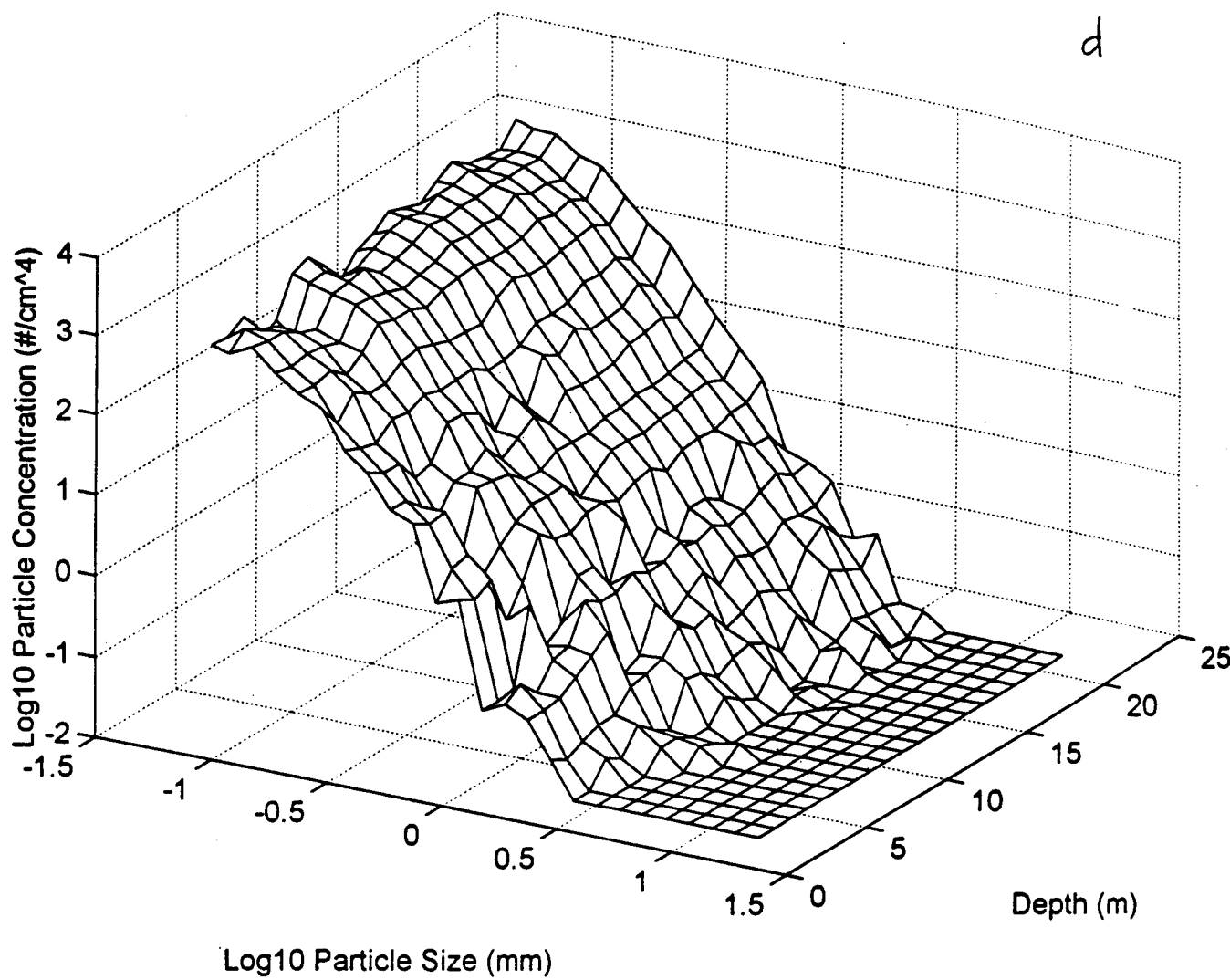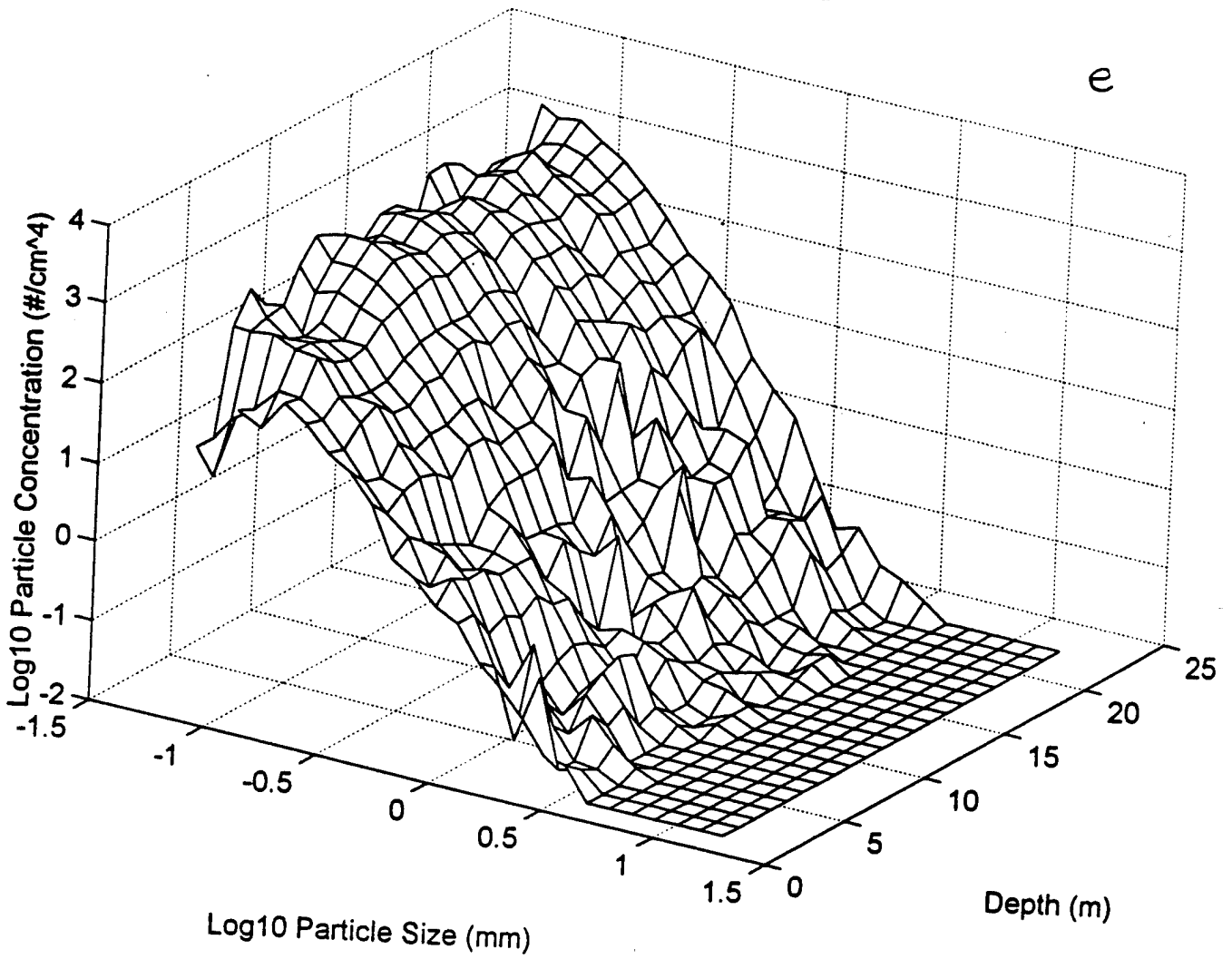
Figure 7

4/19/94 1200h, East Sound

Figure 7

4/19/95 2000h, East Sound

g

Figure 7

4/20/95 0000h, East Sound

h
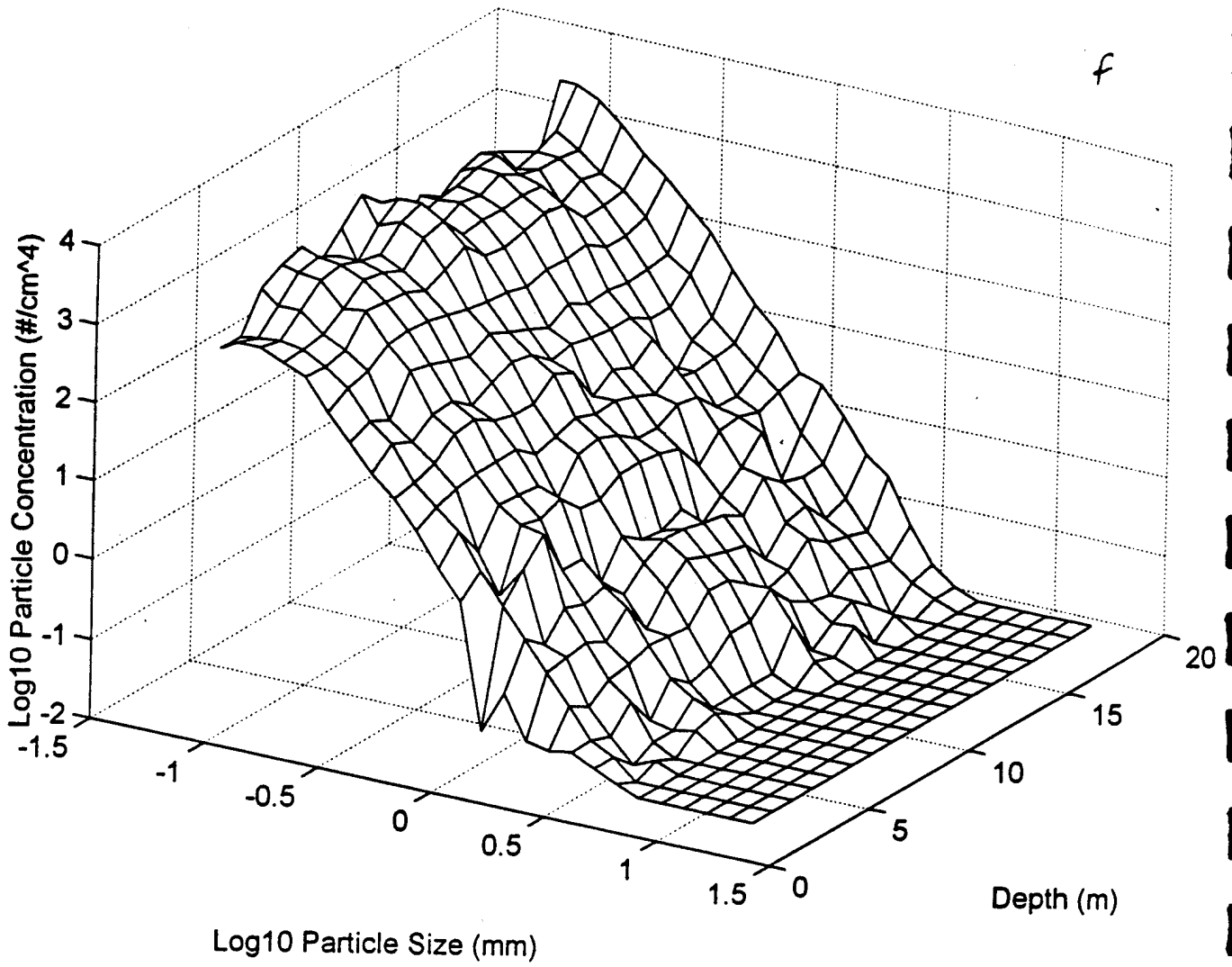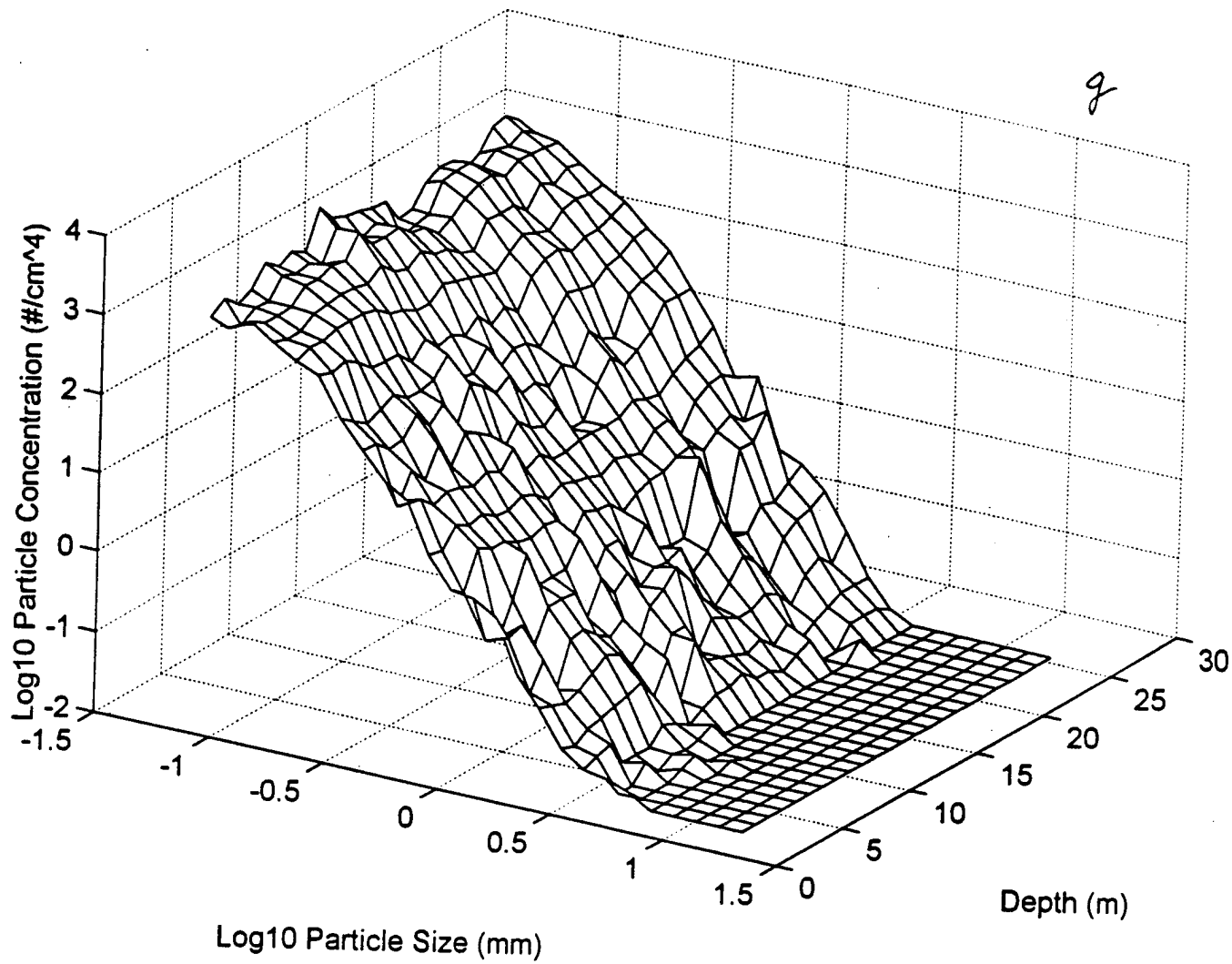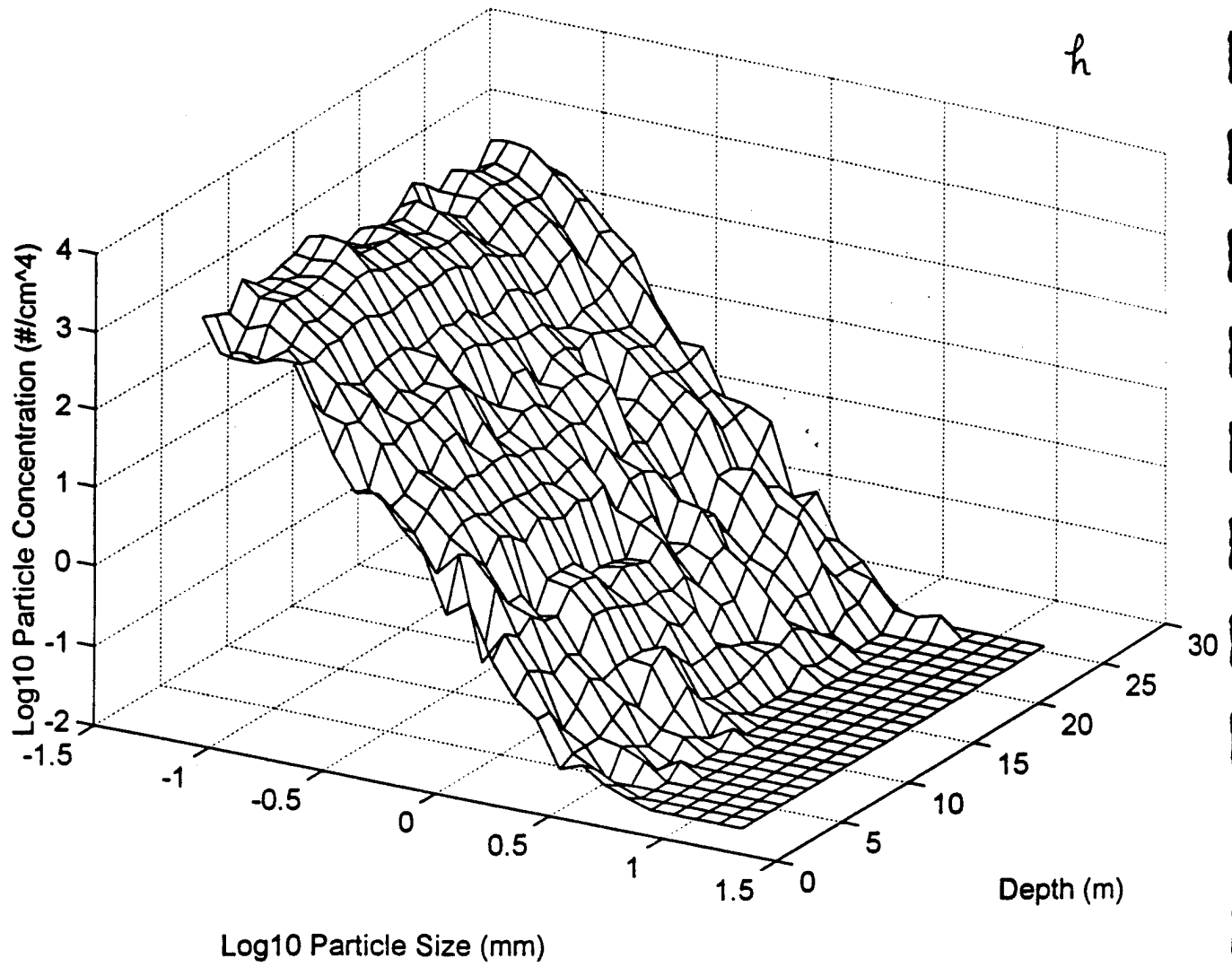
Figure 7

4/20/94 0630h, East Sound
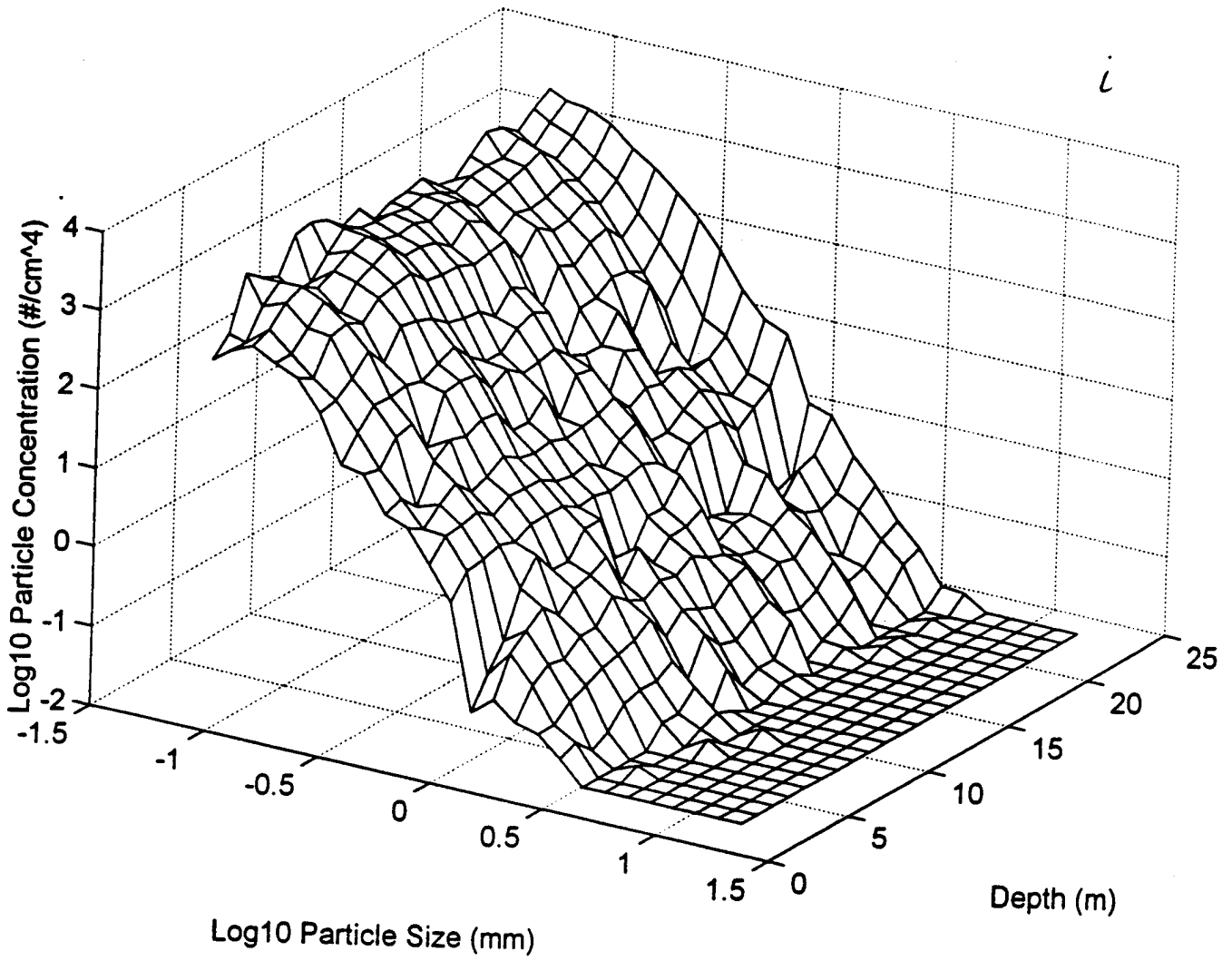
Figure 7

4/20/94 1230h, East Sound
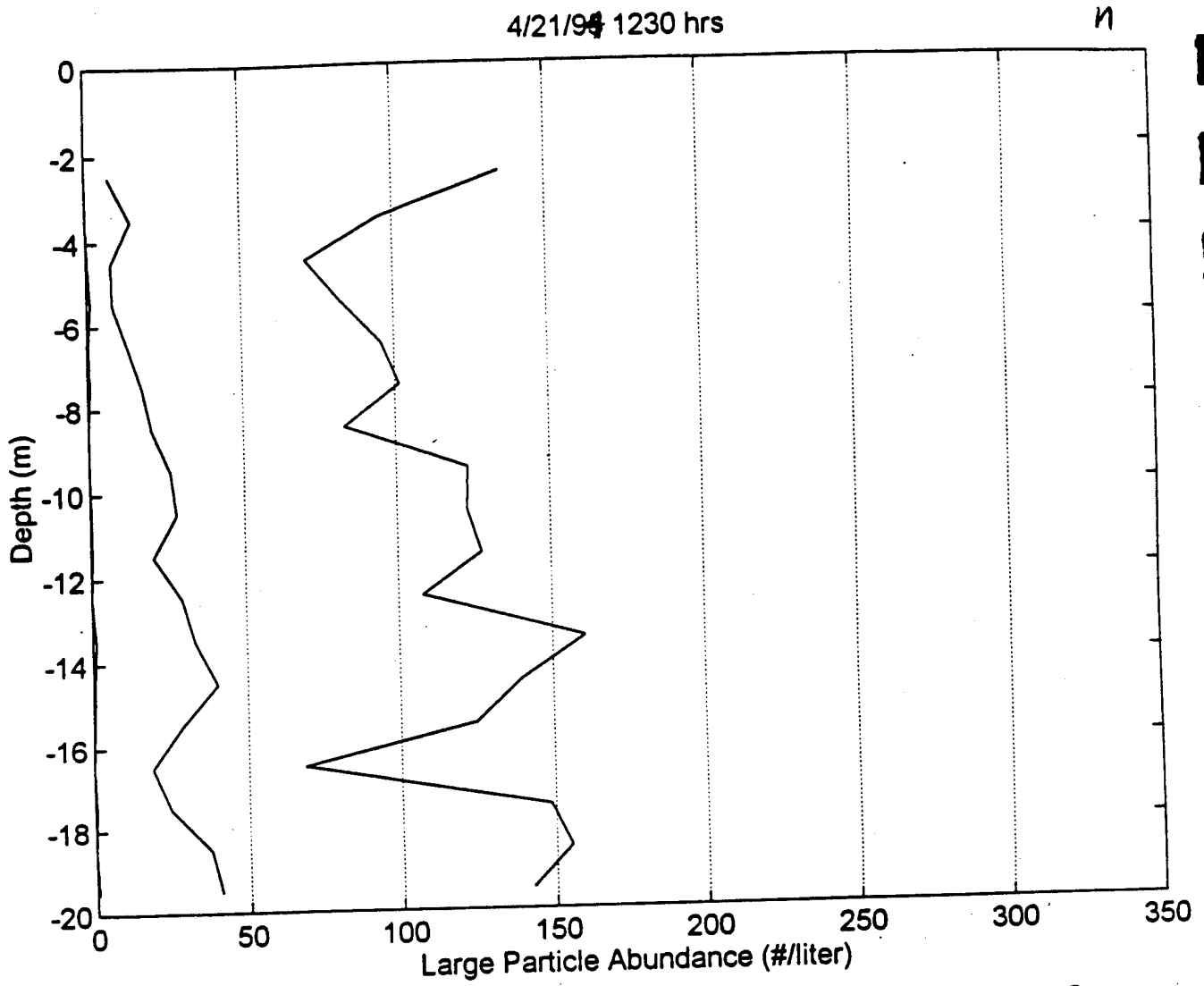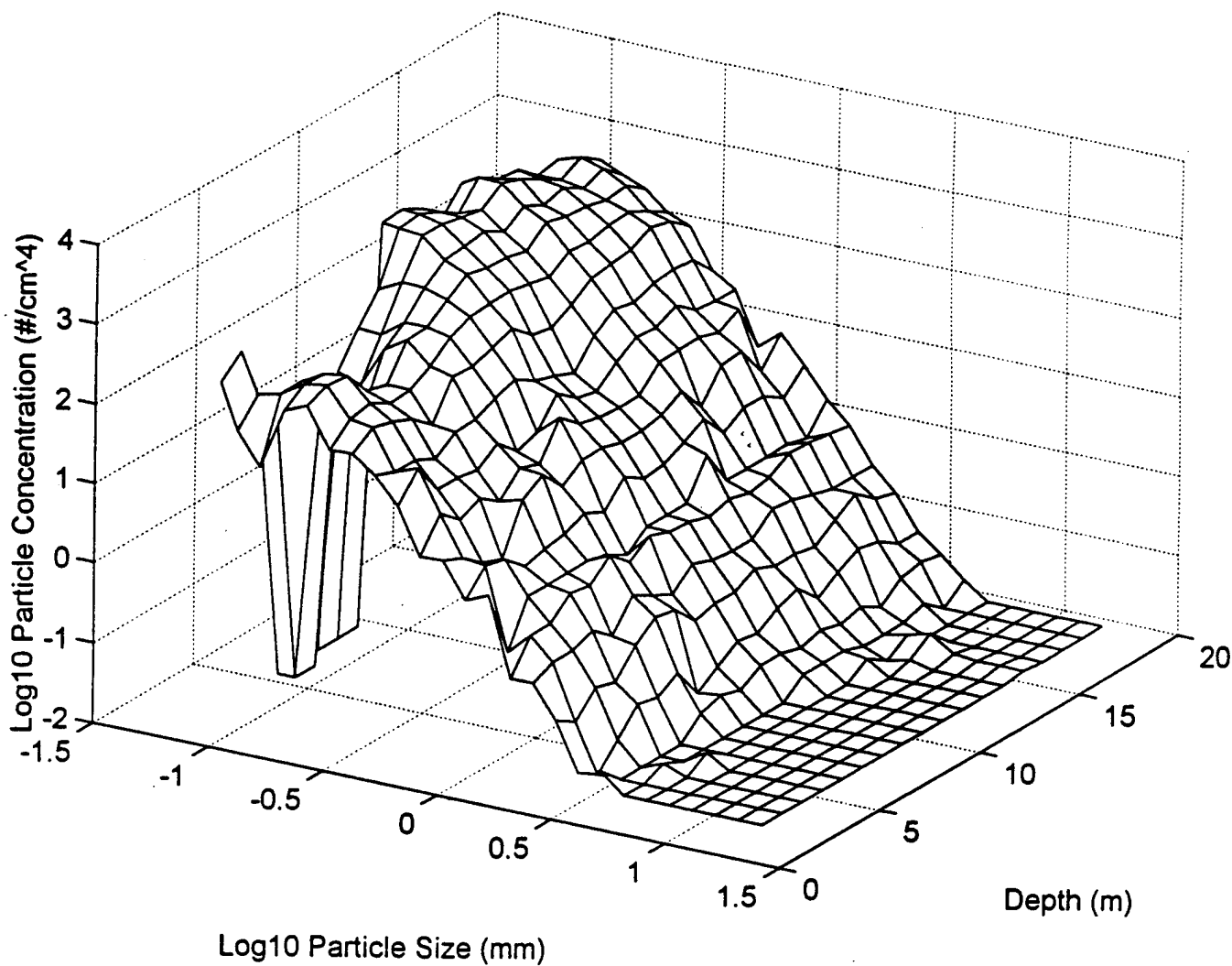
j

Figure 7

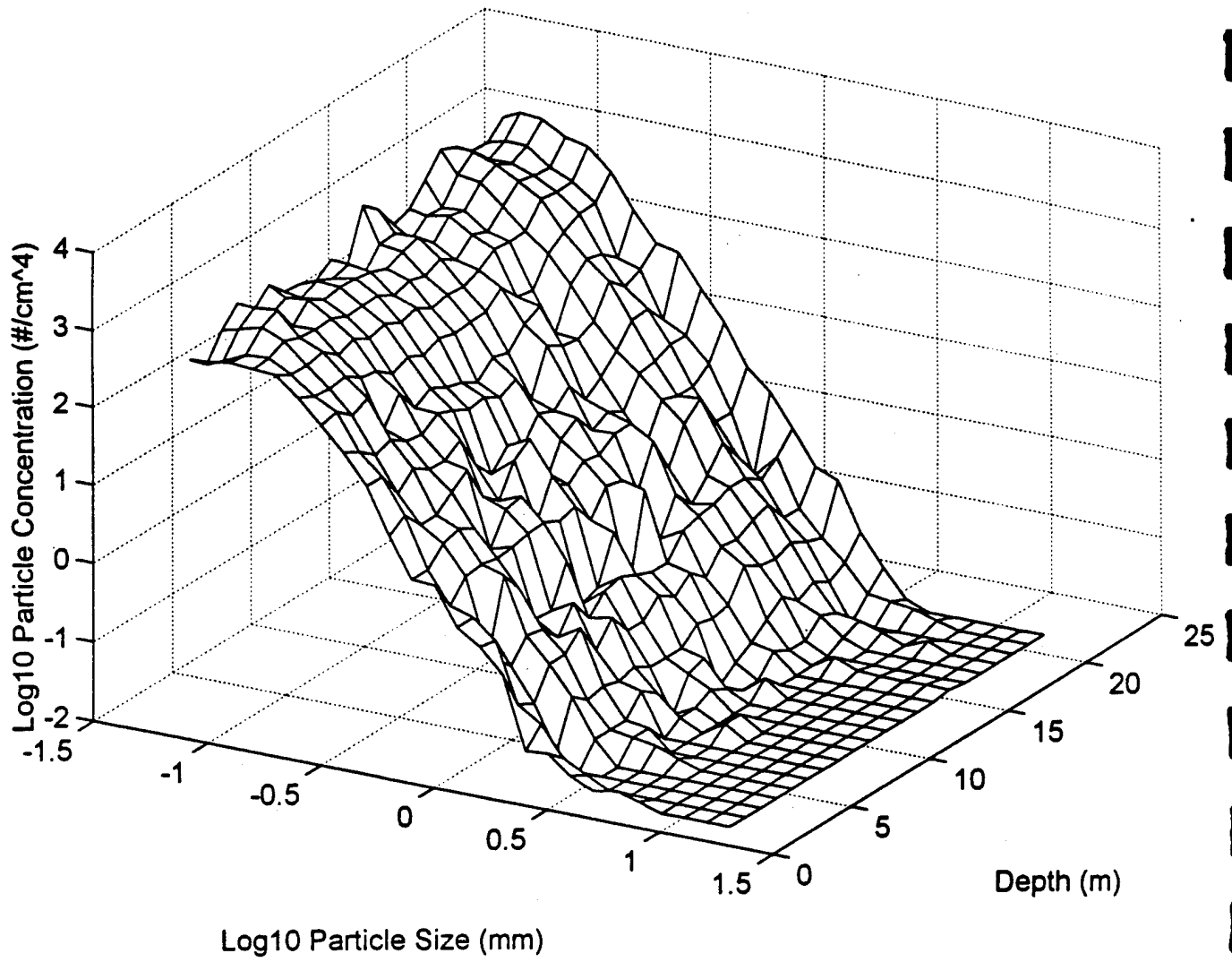VIII-40
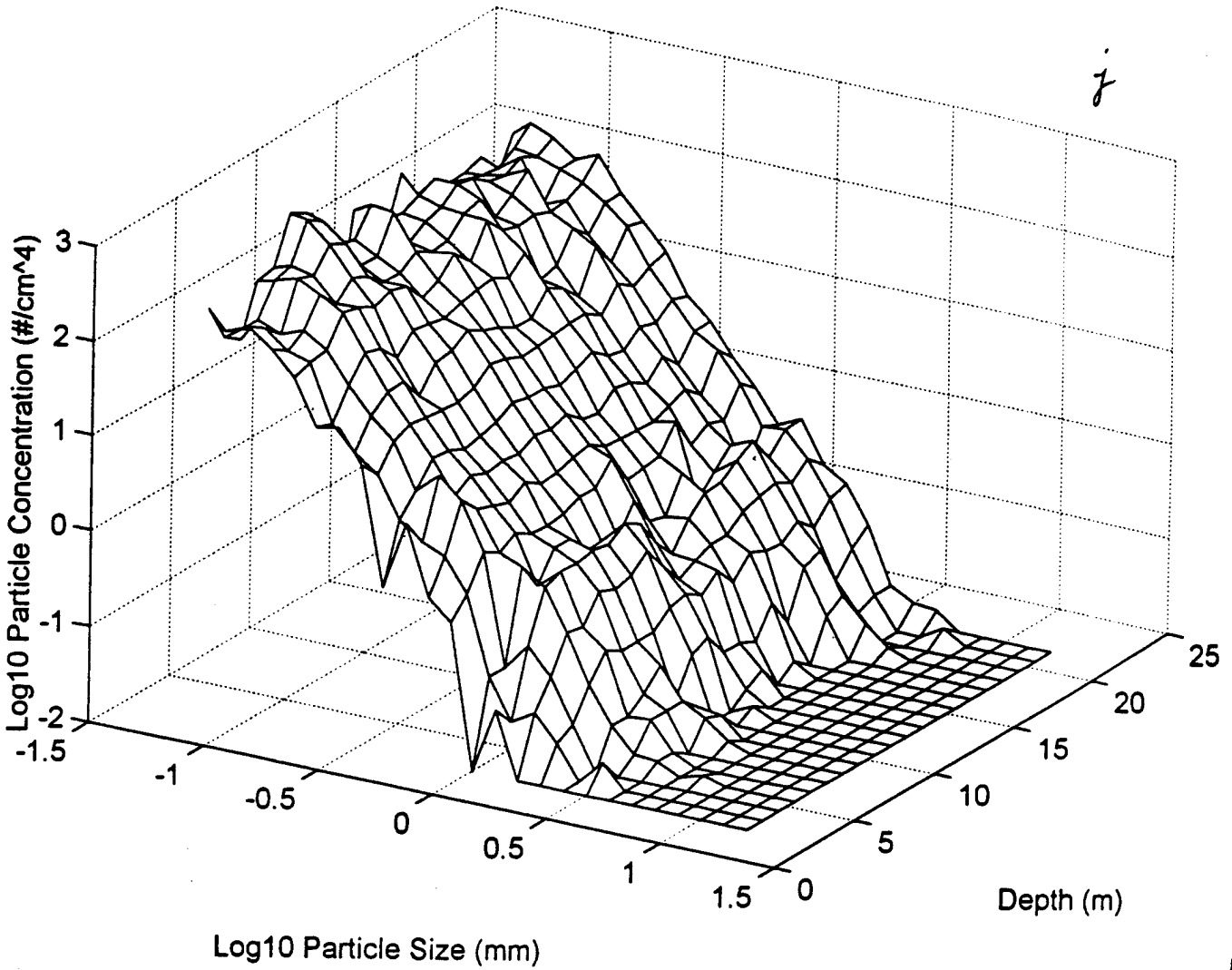
4/20/94 2000h, East Sound

Figure 7

4/21/95 0000h, East Sound

L
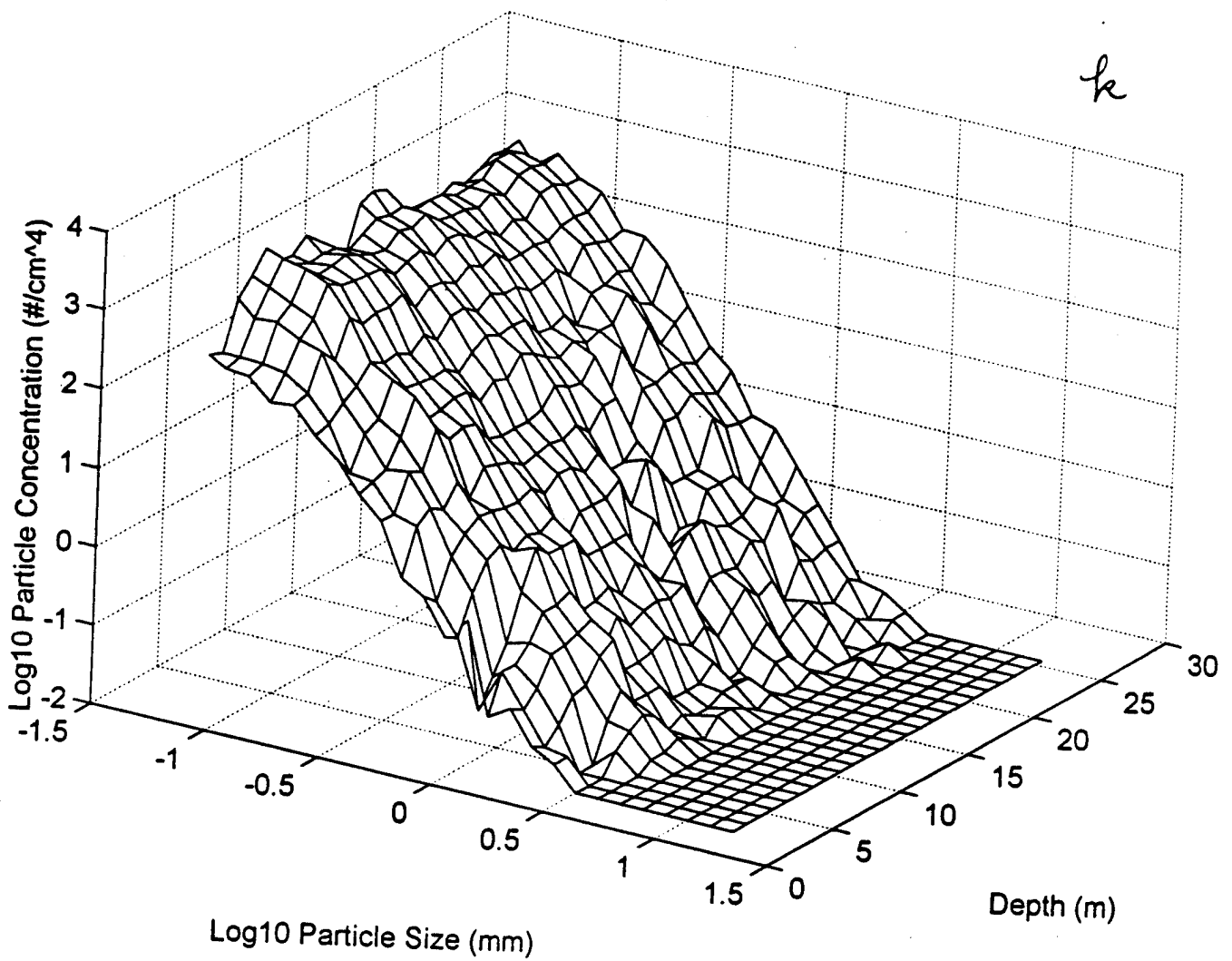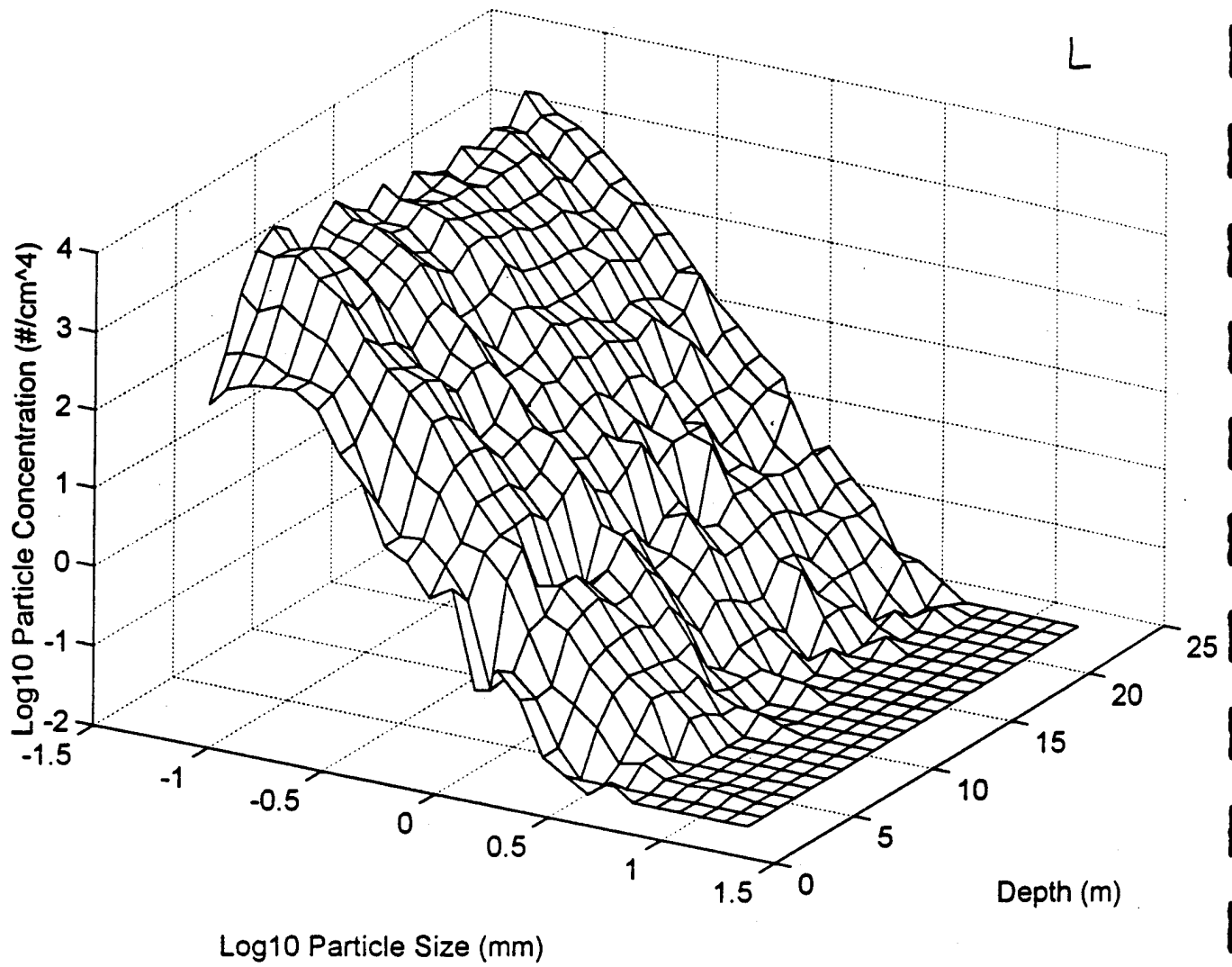
Figure 7

4/21/95 0600h, East Sound

Figure 7
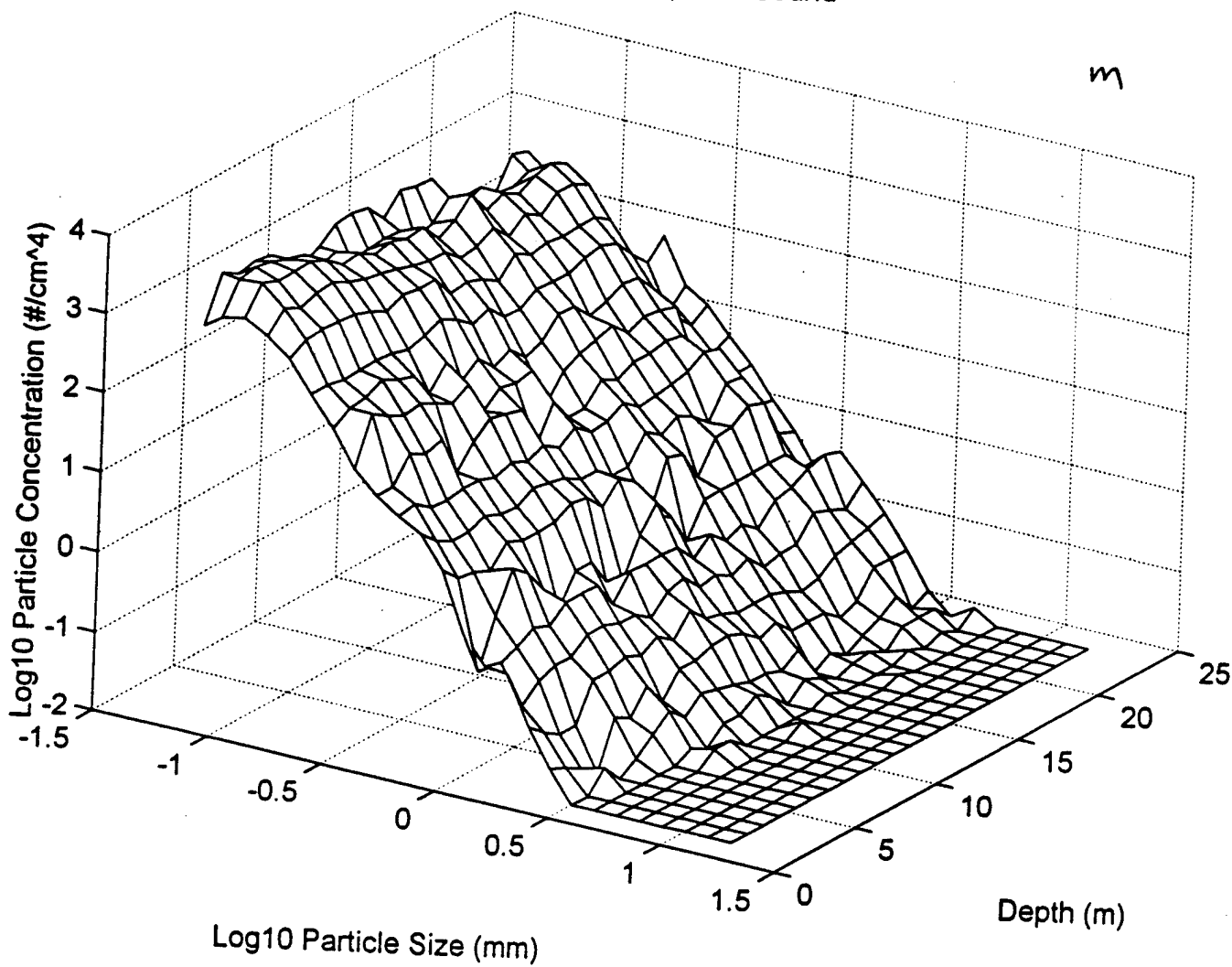
4/21/94 1230h, East Sound
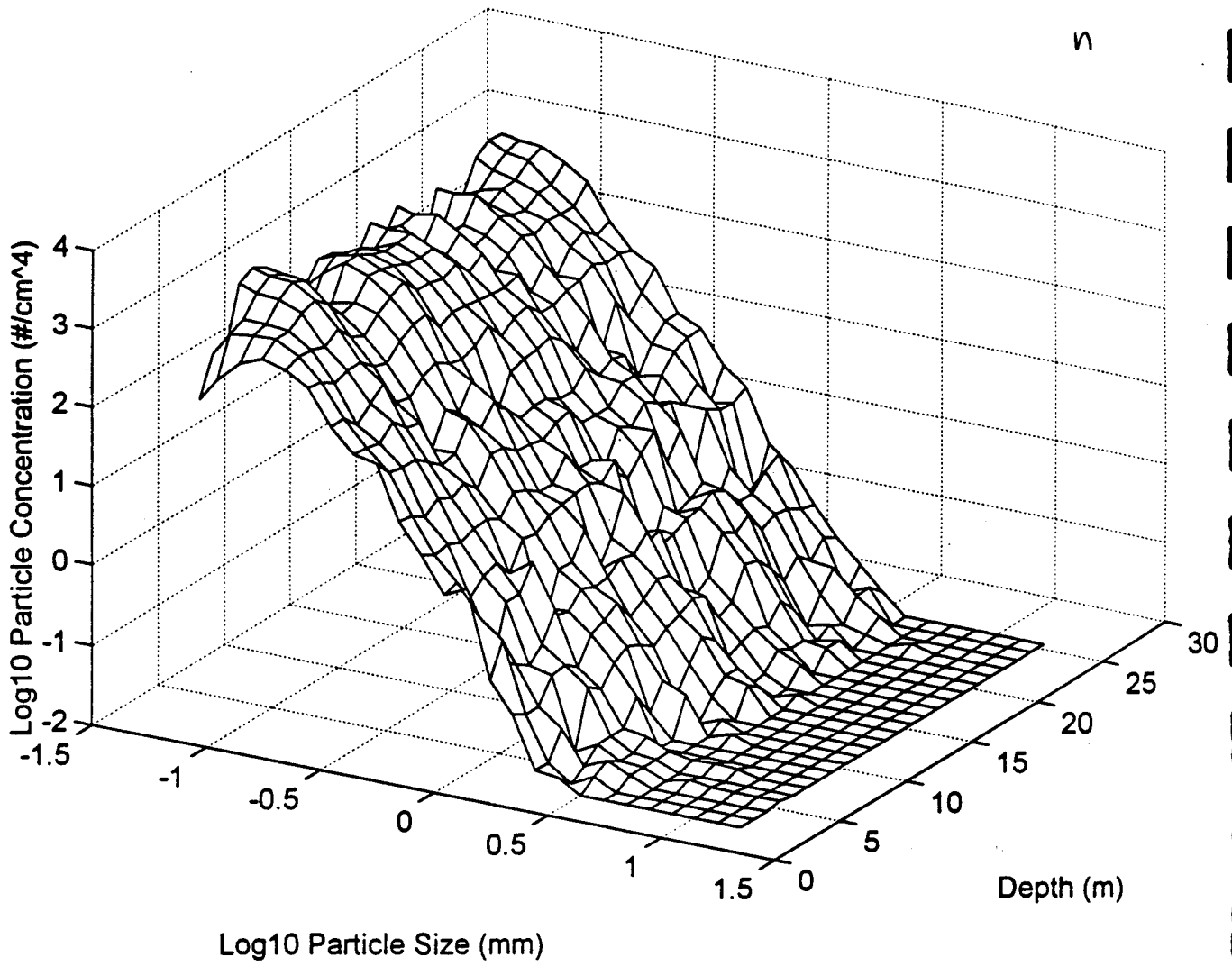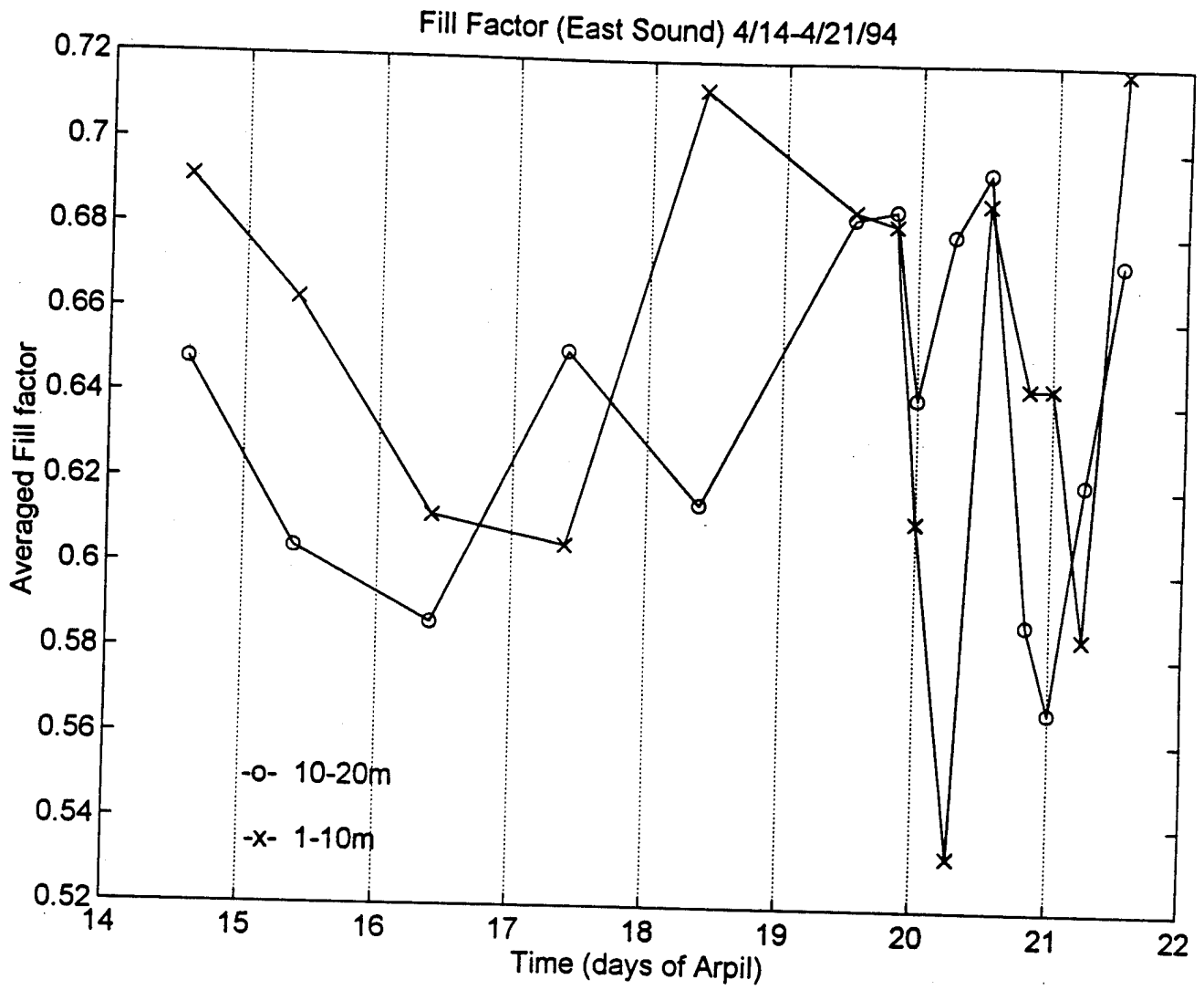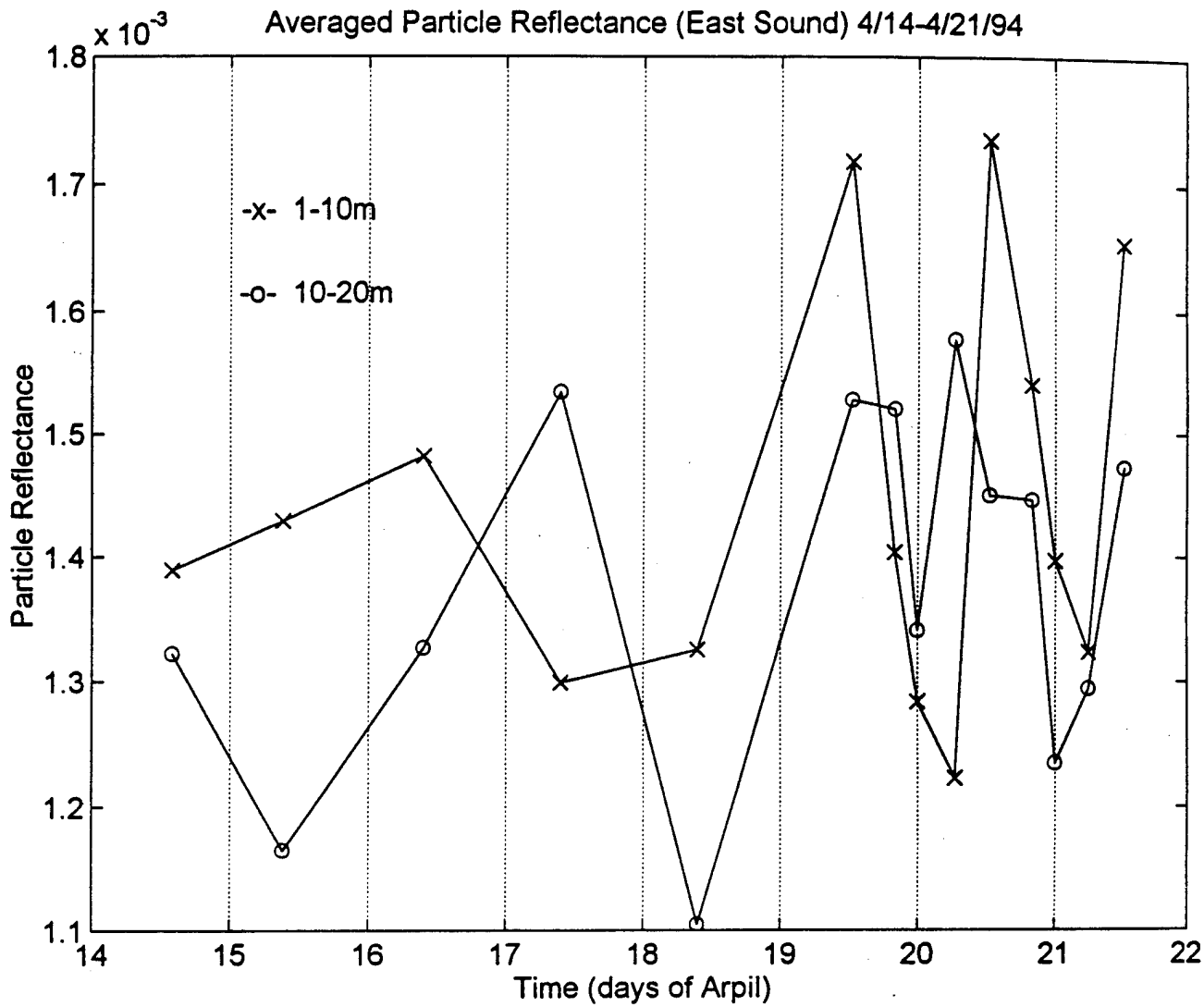
Log10 Particle Concentration (#/cm^4)

Depth (m)

Log10 Particle Size (mm)

Figure 7

Fill Factor (East Sound) 4/14-4/21/94

Averaged Fill factor vs. Time (days of Arpil)

-o- 10-20m

-x- 1-10m

Figure 8

Figure 9

Reprinted from

Ocean Optics XII

13–15 June 1994
Bergen, Norway

SPIF
P
PROCEEDINGS
SERIES

Volume 2258

New Instrumentation and Platforms for Subsurface Optical Measurements

David K. Costello* and Kendall L. Carder*

*Department of Marine Science, University of South Florida, 140 7th Avenue South
St. Petersburg, FL 33701-5016, U.S.A.

ABSTRACT

The underwater light field is affected by the geometry of the incident radiance, the sea-surface state, the inherent optical properties of the water-column constituents, the distribution of these constituents, and, in shallow areas, the bottom albedo. New instrumentation and platforms designed to assist in the quantification of the above are herein described. The new instrumentation includes the Marine Aggregated Particle Profiling and Enumerating Rover (MAPPER), the next-generation MAPPER II system, and the Bottom Classification and Albedo Package (BCAP). The new platforms include a custom-manufactured Remotely Operated Vehicle (ROV) designed to deploy the MAPPER II module, the BCAP module, and a vertical-profiling instrument suite, and an Autonomous Underwater Vehicle (AUV) designed for optical measurements in coastal waters. These include the deployment of the BCAP module on long-range, bottom-mapping missions.

1.0 INTRODUCTION

In the new millenia, our planet will be encircled with a host of orbiting machines. These satellites will enable a truly global, instantaneous information network serving communications, commerce, entertainment, security, and both theoretical and applied scientific research. While some of these research platforms will be looking outward, in search of information from the rest of our solar system and beyond, most will be looking inward with a solitary purpose, to monitor the planet from which they were launched. These space-based, inward-looking machines will be built and launched not out of curiosity but out of the necessity to acquire global data in order to address global questions arising from an ecosystem under stress. Many of these global questions involve, either directly or subtly, the coastal oceans, the areas where most of our populations live and where manifestations of man's affects on the oceans are most likely to appear. Among many others, these global questions include agriculture, mariculture and fisheries production, deforestation, desertification, ozone depletion, air and water quality, international security, global warming, and complex chemical and heat exchanges among the air, land, and sea. As with any instrument system, however, this space-based, remote sensing network will require calibration, algorithm validation, and the interpretation of the remotely sensed data.

This contribution focuses on new instrumentation and platforms designed for underwater optical measurements for the calibration of algorithms and the validation of satellite data regarding a significant part of our planet's surface, the coastal ocean. The instrumentation discussed includes the Marine Aggregated Particle Profiling and Enumerating Rover (MAPPER) and the next-generation MAPPER II system, both of which use structured, diode laser illumination for particle imaging, and the Bottom Classification and Albedo Package (BCAP), a suite of instrumentation which includes hyperspectral radiometers, a multi-channel intensified bottom imager, and commercial instrumentation. The platforms discussed are two Unmanned Underwater Vehicle systems (UUVs), a Remotely Operated Vehicle (ROV) custom-manufactured for the deployment of optical instrumentation and a state-of-the-art Autonomous Underwater Vehicle (AUV).

2.0 INSTRUMENTATION

2.1 BOTTOM CLASSIFICATION AND ALBEDO PACKAGE (BCAP)

Bottom-reflected radiance is quite apparent at depths to 30 m in hyperspectral, water-leaving radiance (AVIRIS data) off Florida when bottom albedos exceed 0.3 even when pigment levels exceed 0.4 mg/m^3. This perturbation can be exploited to estimate bottom depth and to locate bottom features with contrasting albedos if measurements of the submarine light field and the water-column and bottom constituents that affect it can be obtained for calibration and validation purposes. This not only includes measuring the traditional water-column constituents and their absorption, scattering, and fluorescence properties, but also the reflectance and fluorescence properties of the bottom plants and sediments. This information will facilitate the development of models and algorithms for the remote determination of nearshore bottom sediment types, flora concentration/characteristics, water column constituents (dissolved and particulate), and bottom features (eg. foreign objects) incompatible with the natural spectral/spatial setting.

The Bottom Classification/Albedo Package (BCAP) is an ensemble of optical sensors under development at USF. BCAP principle components are hyperspectral (512 channel) upwelling radiance/reflectance and downwelling irradiance meters, a dual-laser range finder/chlorophyll probe, and a 6-wavelength, image-intensified, CCD bottom camera for bottom classification and object identification purposes. The prototype radiometer has a nominal resolution of 3 nm from 350-900 nm^2. The two diode lasers (Melles Griot Electro-Optics) can function as near-bottom range finders providing the high-resolution altitude determination necessary for light propagation modelling. They will also be utilized in an attempt to quantify the chlorophyll_a content of the bottom sediment, exploiting the differential absorption of the pigment at the two different laser wavelengths. One laser emits at 675 nm, a major peak of the chl_a absorption spectra, while the other laser emits at 650 nm, a local minima of the chl_a absorption spectra (see Figure 1). The 650 nm wavelength choice also minimizes potential crosstalk with the absorption spectra of chl_c, a pigment often present with chl_a.

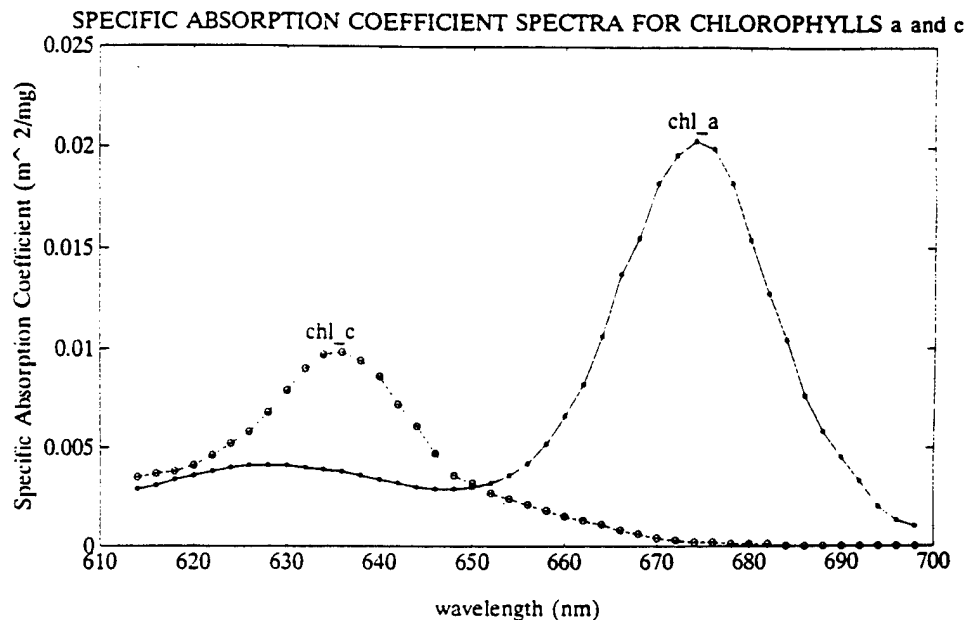SPECIFIC ABSORPTION COEFFICIENT SPECTRA FOR CHLOROPHYLLS a and c

Figure 1. Specific absorption spectra for chlorophylls *a* and *c* (from Bidigare, et. al. 1990, see text for discussion).

The 6-channel (see Table 1 for filter specifications), Xybion IMC-301 imager utilizes a recently developed, Generation-III, micro-channel plate image intensifier with an extended blue photocathode (GEN-III-Blue) which has a dynamic range of over ten orders of magnitude. Tests in our laboratory showed that a less sensitive, GEN-II-RED was capable of imaging fluorescence from macrophytes, seagrasses, and benthic diatoms, and would, therefore, be capable of imaging albedo and/or fluorescence variations of the bottom. The increase in instrument response afforded by a GEN-III-Blue vs. a GEN-II-RED at an important chl_a fluorescence band (685 nm), for example, is a factor of three. The calibration consistency of the IMC-301 GEN-III-Blue imager is, however, currently unknown. To provide unambiguous data, the calibrated 512-channel spectral reflecto-meter/radiometer will obtain spectra from a known (as a function of altitude) segment of the IMC-301 image, thus providing calibration constants for the imager. Another 512-channel spectral radiometer, equipped with a cosine collector, will obtain the spectra of the downwelling light field illuminating the bottom. Calibrated reflectance panels (Spectralon) will be used to calibrate bottom reflectance (albedo) measurements.

Center wavelength	FWHM bandwidth	Comments
460	20	Chl_c absorption maxima
520	20	Co-pigment absorption maxima, coral fluorescence
575	30	Phycoerythrin fluoresence maxima coral fluorescence
620	20	Pigment absorption minima
685	30	Chl_a fluorescence maxima
730	40	Fluorescence band

Table 1. Filter specifications for the Xybion IMC-301 Instrument.

For active bottom-mapping missions utilizing spectral albedo and stimulated fluorescence, a high-pressure, rare-earth-doped light source (Deep-Sea Power and Light) provides a relatively smooth illumination spectra for spectral albedo measurements and sufficient blue intensity to investigate stimulated fluorescence. A short-pass filtered, metal hallide arc lamp will be utilized for multi-channel fluorescence investigation during night deployments. In both scenarios, calibration is provided by the downward-looking spectroradiometer and calibrated reflectance panels.

Ancillary, commercially available instrumentation will measure the water inherent optical properties (IOP's) and physical properties and dissolved and particulate matter concentrations. These sensors include a nine-channel absorption/attenuation meter (ac-9, WET Labs), a multi-channel volume scattering meter (WET Labs, available FY 1995), an optical backscattering meter (OBS, Seatech), and a CTD (Falmouth).

2.2 MAPPER AND MAPPER II

Another potentially significant factor affecting the underwater light field in coastal waters is the changing suite of particulates. This includes sediment introduced by riverine or coastal erosional processes, dust flux, as well as biological production and the accompanying detritus. In oceanic Case I waters, the water-leaving radiance is primarily backscatter from water molecules and the small (<10 μm equivalent spherical diameter, ESD) particles present[3]. In coastal waters, however, much larger particles can be present and can have a significant effect on the light field[4,5]. Costello et al.[6] calculated that attenuation in Monterey Bay (July 1993) by particles larger than 70 μm diameter exceeded the attenuation by the numerically dominant, smaller-particle fraction. Their calculations were based on data from a 25 cm pathlength, SeaTech transmissometer and the conversion of the imaged geometrical cross-sections of the particles to effective optical cross-sections using an attenuation efficiency factor[7], $Q_c = 2$, for optically large particles. It should be noted, however, that the transmissometer sample volume was much less than the imagery volume and, therefore, biased data toward the smaller particle fraction[4].

The particle imagery was obtained using the Marine Aggregated Particle Profiling and Enumerating Rover (MAPPER), an instrument system developed during the ONR Accellerated Research Initiative Significant Interactions Governing Marine Aggregation (SIGMA). The MAPPER system (see Figure 2) and the type of data acquired are described elsewhere[8,9,10,11]. Succinctly, MAPPER is a free-fall, vertical profiling system which utilizes structured, visible diode laser illumination to produce a thin sheet of light at the image planes of three, synchronized CCD video cameras of differing magnifications. This unique, synchronous imagery from the three independent cameras allowed an investigation (see Costello et al.[12], this volume) of imaging artifacts which would not be noticed nor quantifiable in a system with a single camera.

MAPPER realizes 50 μm resolution in the horizontal dimensions and sub-centimeter vertical resolution. The density of the MAPPER database is illustrated in Figure 3 which shows the 3-dimensional spatial distribution of large particles (ESD > 215 μm) in a randomly-chosen water volume from Monterey Bay of dimensions 29 mm x 58 mm x 100 mm (0.67 l). These data allow not only the 3-dimensional reconstruction of the particle distribution but also the classification of particles by shape and by reflectivity (eg. zooplankton vs. phytoplankton aggregates). This type of data is available for the entire database. For most purposes, however, the data are most often displayed in bins as a function of depth. Figure 4 shows particle size distribution data from the Monterey Bay deployments presented in one-meter depth bins.

Although the MAPPER system dependably (119 data tapes secured out of 120 attempted) captures unprecedented high-resolution imagery, the size of the present system (0.66 m^3, 100 kg) precludes incorporation into other platforms capable of other deployment modes. Hence, a second-generation MAPPER II is under development. MAPPER II will be configured as a small (0.016 m^3, and 10 kg), modular package capable of incorporation into the platforms discussed below.
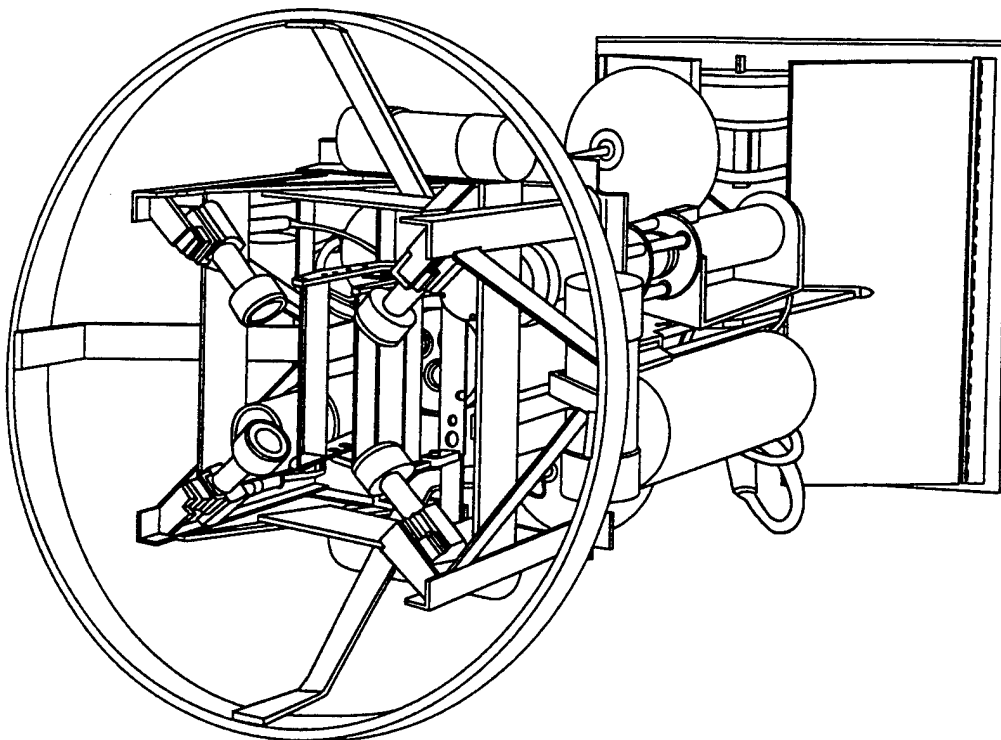
Figure 2. MAPPER. The normal vector out of this page describes the fall direction of MAPPER. The laser sheet is at the leading edge of the sensor. See Costello et al.[8,9] for more details.
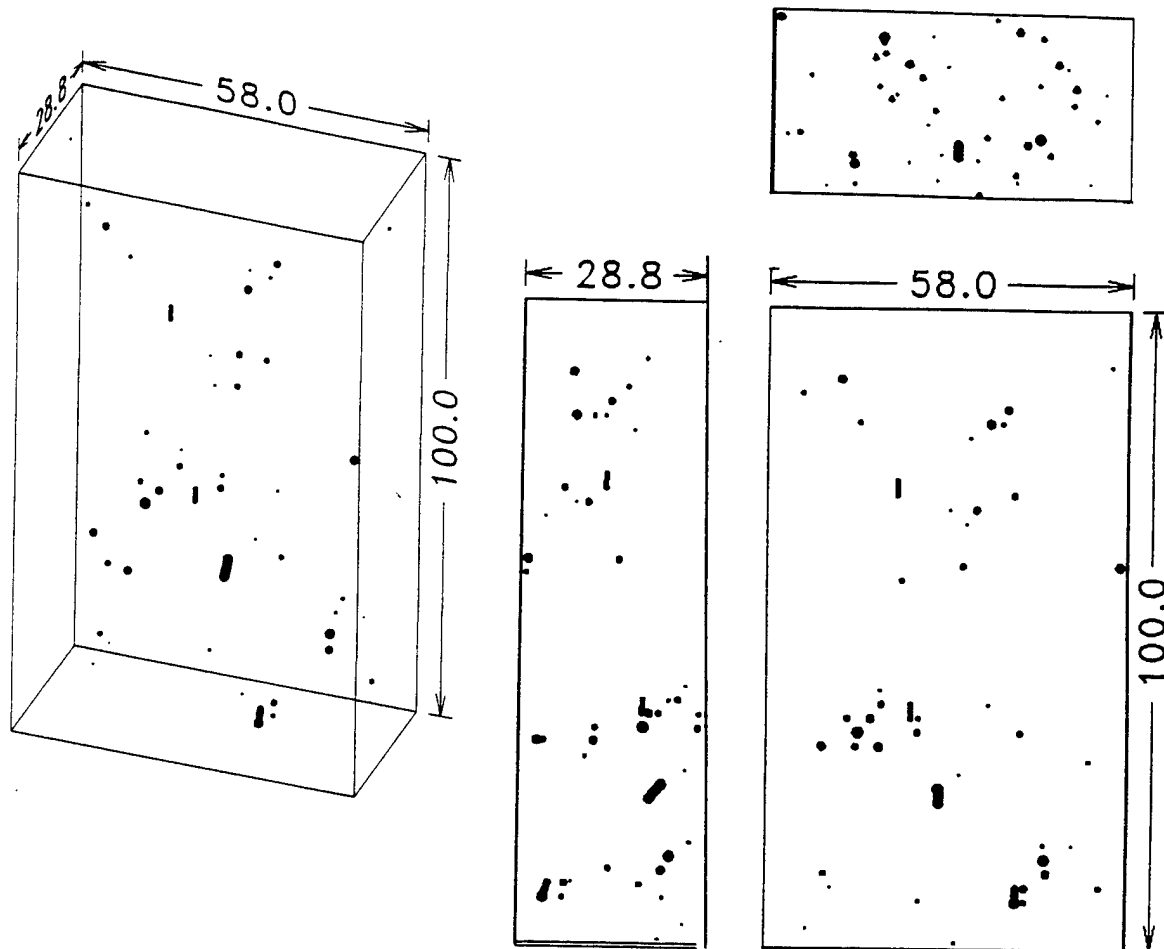
Figure 3. 3-dimensional reconstruction of particles (diameter > 210 μm) in a water volume at 10 m depth in Monterey Bay. Particle patchiness is evident by examination of the three orthogonal views on the left.
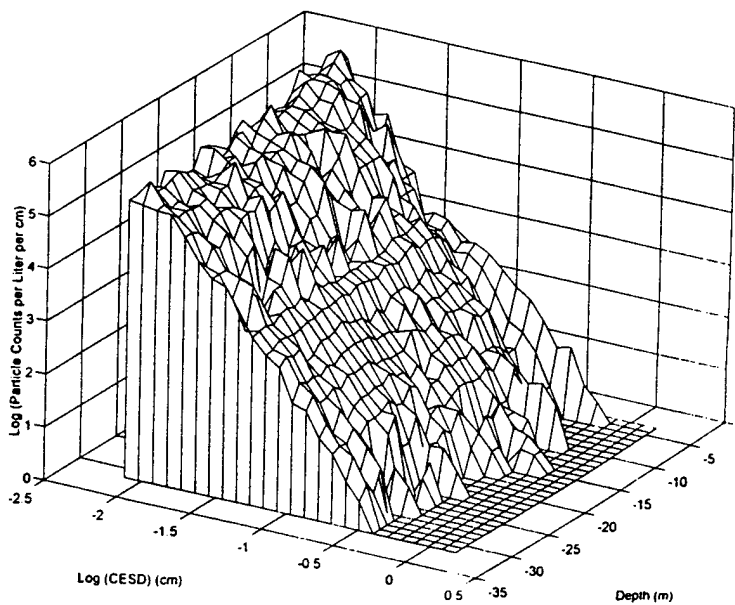
Figure 4. Particle size distribution spectra from Monterey Bay in one-meter depth bins (MAPPER data).

3.0 PLATFORMS

3.1 Remotely Operated System Equipped for Bio-optical Underwater Deployment (ROSEBUD)

The land-analog to the ROSEBUD ROV is a pickup truck with variable load configurations. A concept drawing for the system is shown in Figure 5. The ROV has a low optical-profile to minimize instrument shadows. Four horizontal thrusters developing up to 120 lbs. of thrust will help alleviate common ROV control problems associated with umbilical drag, surface and sub-surface currents, and mothership drift. The primary ROSEBUD design objective is to enable incorporation of a diverse set of instrumentation on a "plug-and-play" basis. An open, central cargo bay lined with instrument mount racks, for example, will accommodate approximately 0.25 m^3 of instrumentation.

The fiscal philosophy behind the design is the minimization of the costs of sophisticated ROV technology which is not applicable to ROSEBUD's envisioned missions. The result of this approach will be a robust vehicle at a fraction of the cost of the acquisition (and modification) of many more sophisticated systems. The sophistication of ROSEBUD will lie in more flexible payload configurations and deployment parameters and in an artificial-intelligence approach to data acquisition and integration. The digital and analog data from the instruments, for example, will be integrated in a VXWorks LON network using Motorola neural network hardware and protocol (see AUV section below) where data from any of the instruments are available to any other instrument node as required without interruption of the high-level system controller. In this operating system, the instrumentation plugged into the system is automatically recognized and the power and data stream requirements are automatically accomodated. Other planned enhancements include a four-channel, fiber-optic video mutiplexer, an articulated instrument rack, moveable vertical thrusters (to accomodate hydrodynamically different instrument configurations), and a passively articulated instrument tray to accomodate instrumentation requiring constant orientation relative to the water flow.

ROSEBUD will be used for concept- and sensor-development activities prior to sensor transitions to an AUV. It will also be used for very-near-bottom (< 2 m) studies.
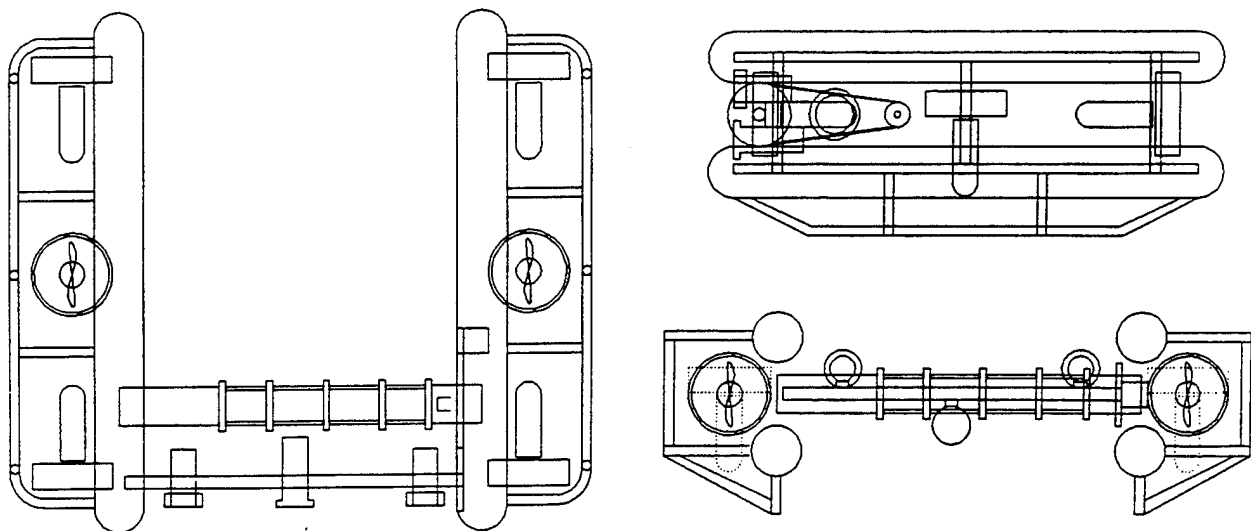
Figure 5. Concept drawing for the ROSEBUD ROV. Three orthogonal views are shown, see text for discussion.

3.2 Autonomous Underwater Vehicle Ocean Voyager II (OVII AUV)

The Ocean Voyager II (OVII) is an autonomous, untethered, underwater vehicle under development for USF/DMS by the Department of Ocean Engineering, Florida Atlantic University. In contrast to MIT's ODESSEY vehicle which is designed for deep-water, long-range missions, and WHOI's ABE vehicle which is optimized for deep-water, short-range, long duration deployments, the OVII (Figure 6) is a small vehicle optimized for coastal applications including longe-range, bottom-following missions. The OVII is 2.4 m in length, has a maximum diameter of 0.6 m, a depth rating of 600 m, a maximum speed of 5 knots, and a theortical range of 480 km (@ 3 knots). In sea trials at FAU and at USF, the prototype vehicle successfully performed missions following 3-dimensional waypoints on a completely autonomous basis. The payload bay of this prototype vehicle is currently being modified for integration of the BCAP system and, to our knowledge, will be the first Autonomous Underwater Vehicle dedicated to optical oceanography. The next-generation OVII has a three-piece modular design in order to accommodate several sensor suites under developed at USF Department of Marine Science. All modular-vehicle configurations share the aft propulsion section, most configurations share the forward control section, and multiple, interchangable, central sections are under development. For some deployment configurations (using the MAPPER II module, for example) modified forward sections will be utilized.
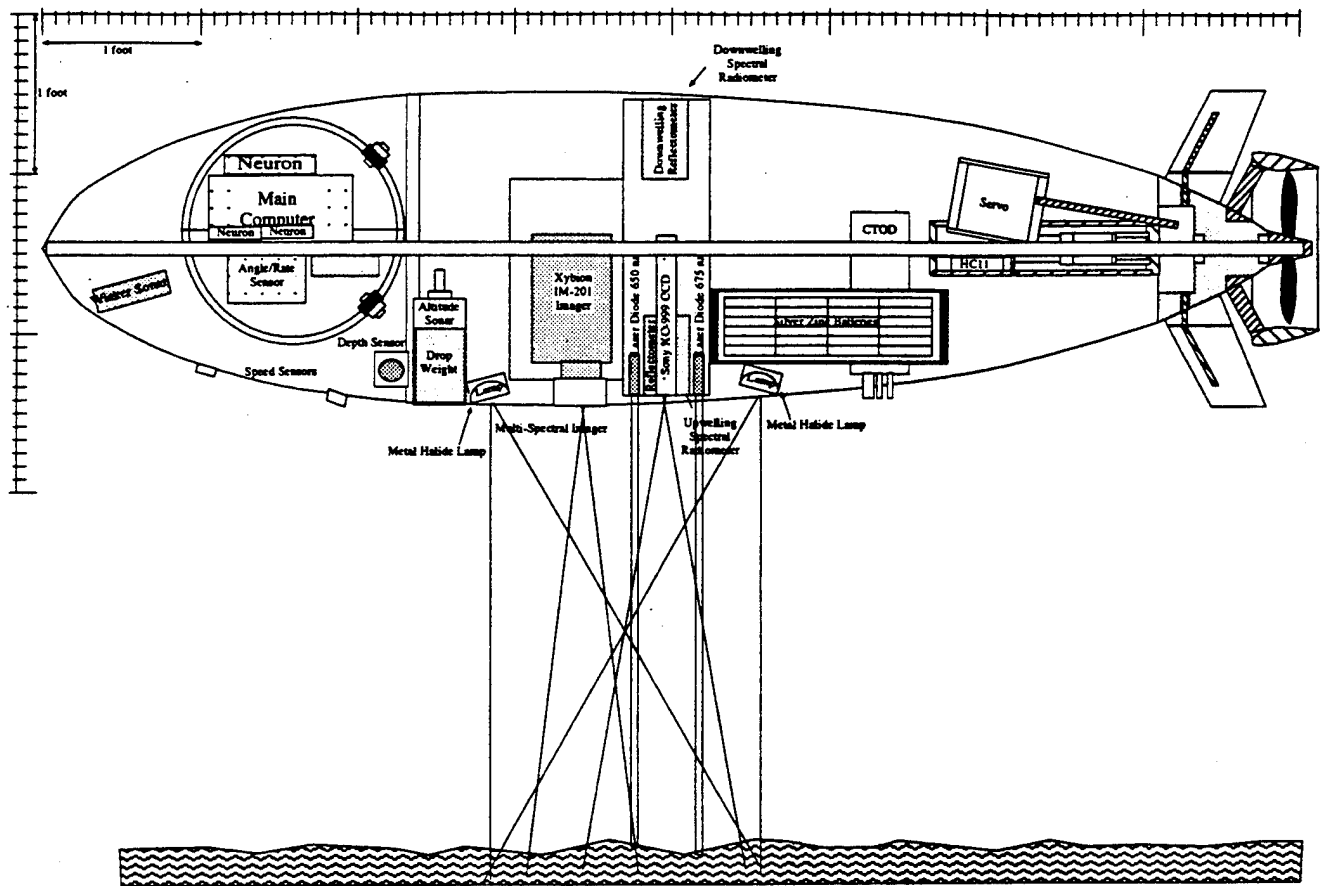
Figure 6. Depiction of the Ocean Voyager II AUV equipped with the BCAP module, see text for discussion (Figure courtesy of Sam Smith, Ocean Engineering, Florida Atlantic University).

The modularity of the OVII is unique among non-defense UUVs and arose out of the diversity of the planned instrument packages. In large part, the modularity is possible because of the utilization of an Intelligent Distribution Control System (IDCS)[13]. In essence, the IDCS consists of a main controller which is responsible for high level scheduling and for monitoring numerous (up to 32K) microcontrolled subsystems called "nodes". Each node consists of sensor(s), actuator(s) and a microcontoller. The node microcontroller (the "Neuron Chip", Motorola) is actually three, integrated microcontrollers with built-in communications firmware. These follow LONwork protocols where nodes are addressed as network variables and multi-tasking and event-driven scheduling are supported. The IDCS allows all network data to be addressed by any node, for node actuators to respond to information from other nodes independent of the main controller, and for essentially an unlimited number of sensor system configurations/permutations to be deployed without reprogramming the main controller.

4.0 MISSION SCENARIO

Coastal areas are complicated environments where most of our population lives. The difficulties described above are magnified near-shore because of complex and often rapidly changing physical processes. Tidal processes, inertial currents, upwelling, buoyant plumes, and internal waves are but a few mechanisms that change rapidly and require synoptic sampling. Satellites provide synoptic data, but calibration/validation of each image requires rapid, multiple-vessel coverage of the optical features (e.g. fronts, plumes, etc.) of interest. The more we learn about coastal areas, the more significant they become in terms of our understanding of global processes.

4.1 Coastal Ocean Color, the Primary Mission

The complexity of coastal waters demands that a wide variety of data be acquired in order to interpret satellite ocean color data. Water molecules, for example, affect light profoundly but in a manner that has been relatively well researched and documented[14,15]. In natural waters, plant pigments (eg. chlorophylls, carotenoids, etc.) can also play a significant role in water color. The efficiency of the different absorption and fluorescence bands for these pigments has been recently an area of intense research and is becoming increasingly understood[16,17,18]. In many coastal areas, one significant agent affecting light is Colored Dissolved Organic Matter (CDOM or "gelbstoff"), a biogenic degradation product of terrestrial or marine primary production. Carder et al.[19] found that terrestrial and marine CDOM had differing spectral signatures. For a given river plume, however, CDOM images can be mapped into salinity images from AVIRIS[20].

Other factors that can affect the underwater light field and, hence, remotely sensed water color in coastal areas are suspended sediments (associated with riverine input or resuspended from the bottom by currents), the magnitude and shape of the particle size distribution (phytoplankton blooms and/or aggregation can have significant effects on water clarity[4,6]) and bottom albedo. For an optically thick, homogenous ocean (e.g., well-mixed, deep water), the following equation[14,21] describing remote sensing reflectance, R_{rs}, can be applied:

$$R_{rs}(\lambda) = L_w(\lambda)/E_d(\lambda) = \{0.33b_b(\lambda)/[a(\lambda)+b_b(\lambda)]\}(t/n)^2/Q, \tag{1}$$

where the parameters which are functions of the wavelength λ are noted. Here L_w is the water-leaving radiance measured from space, E_d is the downwelling irradiance, b_b and a are the backscattering and absorption coefficients of water and its suspended particles, and $Q = E_u(\lambda)/L_u(\lambda)$ (the ratio of the upwelling irradiance to the upwelling radiance), is only weakly dependent upon λ (Gordon and Morel[22]). The squared term provides for the radiance divergence and sea-air transmittance, t, of radiance leaving the water. The index of refraction of seawater, n, is about 1.334. This equation contains no provision for transpectral phenomena such as water-Raman scattering (considered negligible for near-shore environments) or fluorescence due to CDOM and chlorophyll a (not necessarily negligible for certain wavelengths). Provision for these can be made by adding an additional term[21,23,24,25].

For an optically shallow environment (e.g. depths shallower than about 2.0 optical thicknesses), bottom reflectance needs to be considered. Equation 1 can be expanded as follows:

$$R_{rs}(\lambda)_s = R_{rs}(\lambda)_d(1-\exp\{-[k_d(\lambda)+k_u(\lambda)]D\}) + (t/n)^2(\alpha/\pi)\exp\{-[k_d(\lambda)+k_u(\lambda)]D\}, \tag{2}$$

where the subscripts s and d depict shallow- and deep-water conditions, α is the bottom albedo, the bottom reflectance is considered to be Lambertian [e.g. $E_u(\lambda) \approx \pi L_u(\lambda)$ at the bottom], and D is the water-column depth. The term $(1-\exp\{-[k_d(\lambda)+k_u(\lambda)]D\})$ only becomes important when the depth D is smaller than about 0.5 optical depth. The diffuse attenuation coefficients k_d and k_u are for downwelling and upwelling light, respectively, and are largely a function of $a(\lambda) + b_b(\lambda)$ multiplied by the average slant-path enhancement of the rays relative to the vertical[1,26].

Satellite- or aircraft-derived ocean color data can be used to extrapolate from the data acquired on ship or AUV transects across or along the coastal transition zone of the ocean. Alternatively, *in situ* data can be used to validate algorithms used with remotely sensed data.

Once the atmospheric effects have been removed from remotely sensed data, Eqs. 1 and 2 can be validated by comparing remote-sensing reflection ($R_{rs}(\lambda)$) values to *in situ* measures of $R_{rs}(\lambda)$ and the combined terms found on the right sides of the equations. Of these, the bottom albedo, $\alpha(\lambda)$, is the most stable, with short-term temporal variability expected to be relatively low. This argues that α could be mapped before or after a major field validation effort. This mapping, however, would be prohibitively time consuming from a surface vessel using instrumentation hung over the side. A properly instrumented tow-body could provide the required areal coverage but altitude control and obstacle avoidance near the bottom would be problematic, especially in rough weather. Bottom mapping, however, is an ideal mission for an AUV.

The primary remaining validation variables that require measurement are $R_{rs}(\lambda)$, $a(\lambda)$, and $b_b(\lambda)$ from Eq. 1 and $k_d(\lambda)$ and $k_u(\lambda)$ from Eq. 2. The water depth D can also be determined, often after the fact, using depth charts and tidal models. This information is, however, readily available in an AUV deployment.

$R_{rs}(\lambda)$ can be measured near the surface from an AUV measuring the downwelling irradiance $E_d(\lambda,z)$ and upwelling radiance $L_u(\lambda,z)$, where z indicates sensor depth. By programming vehicle depth changes (Fig. 7), these values can be obtained for different depths, and diffuse attenuation coefficients are obtained through

$$E_d(\lambda,z+\Delta z)=E_d(\lambda,z)\exp[-k_d(\lambda,z)*\Delta z], \tag{3}$$

and a similar expression for $k_u(\lambda,z)$ involving L_u instead of E_d. Instruments have been developed to provide direct measurements of beam attenuation, c, and absorption, a, at 9 wavelengths and also yield the total scattering coefficient b since b = c - a. Backscattering sensors are also available for several wavelengths and multi-channel volume scattering $\beta(\theta)$ instruments are under development.

All of these instruments can be incorporated into the sensor suite of a UUV (that is, an ROV or an AUV) that also includes temperature, salinity, beam attenuation, pressure (depth), height above bottom, water and bottom velocity relative to the AUV, and six-color bottom imagery for albedo/fluorescence.

4.11 AUV Deployment Scenario

Ocean color measurements require a solar zenith angle which allows adequate light penetration into the water column. For the purpose of illustration, we will use a six-hour sampling window, from 1000 to 1600 hours. An ideal mission scenario would utilize multiple OVII vehicles to maximize areal coverage during the

sample window. Even a single OVII, however provides coverage not available with a surface vessel. For water depth of 30 m, for example, it is desirable to obtain bottom albedo as well as optical vertical profiles and the AUV would cruise at 25-28 m depth obtaining down-welling irradiance and upwelling radiance spectra. The upwelling radiance would include any contribution from the bottom. If optical profiles were desired at one-kilometer intervals, for example, the AUV could, every kilometer, rise to 20 m, level off, cruise for 10 seconds acquiring data, perform the same tasks at 15, 10, and 5 m, and then dive back to 25 m (see Figure 7). Assuming an OVII cruise speed of 4 knots, a vertical ascent rate of 0.5 m/sec and descent rate of 1.0 m/sec, 10-second cruises at intermediate depths, and vertical profiling stations at one kilometer intervals, the OVII could complete 43 sample stations (that is, acquire 43 vertical profiles underway), and map 90% of the bottom along the transect.
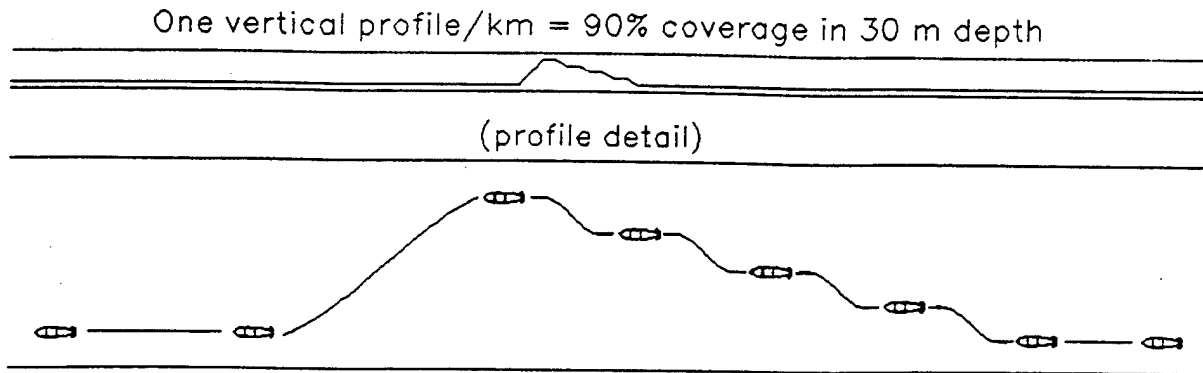
Figure 7. Vertical profiling scenario for an AUV which minimizes measurement perturbations which can be induced by vehicle pitch-angle. The neural node containing the 3-axis tilt sensor communicates with the optical instrumentation node and measurements are taken during level flight.
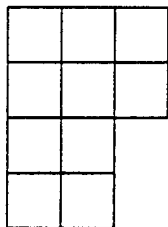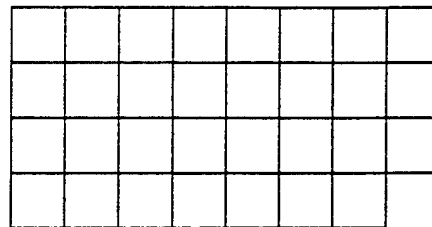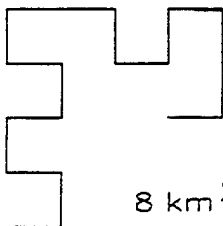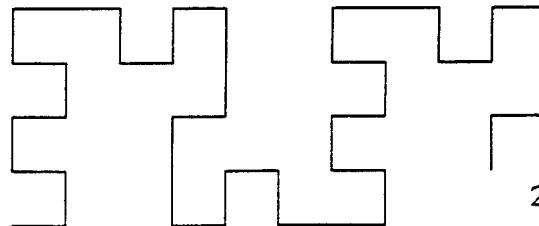
Figure 8. Areal coverage provided by a surface vessel and by an AUV both performing vertical optical profiles within a 6-hour sample window. See text for discussion.

For contrast, a surface vessel with an experienced crew able to perform a vertical optical profile in only 15 minutes, and allowing an additional 5 minutes to steam to the next station, could only complete 18 stations and would have albedo measurements of a very small percentage of the bottom. Figure 8 shows the areal coverage provided in this scenario by a surface vessel and an AUV for a grid with a station spacing of 1 km and for a mapping mission with the transect stations bracketing a 1 km swath. In the grid mission, the AUV is 210% more efficient in obtaining vertical profiles than the surface vessel and is 150% more efficient in the transect mission. Addtionally, the bottom albedo data is easily obtained with an AUV but is essentially not available from a surface vessel.

5.0 SUMMARY

The technology enabling the use of air- and space-borne optical sensors to study coastal waters is rapidly advancing in response to our growing awareness of the importance of these areas to global concerns. The calibration, algorithm validation, and interpretation of the remotely sensed data, however, requires the collateral development of instrumentation and platforms capable of providing ground-truth in the complicated coastal environment.

The instrumentation described herein provides high-resolution particle size distributions, hyperspectral measurements of the underwater light field, and spectral bottom albedo. These when combined with other commercially available instruments, will allow us to approach optical model closure in coastal waters, and calibrate/validate alforithms for remote-sensing platforms.

Finally, we feel the UUV platforms described herein are requisite components in this endeavor. The ROV allows precise vertical positioning of optical instrumentation away from ship shadow. It also allows for sensor package integration and testing prior to its incorporation into an AUV, the weather-independent, cost-effective, underwater platform of the future.

ACKNOWLEDGEMENTS

REFERENCES CITED

1. Lee, Z. P., K.L. Carder, S.K. Hawes, R.G. Steward, T.G. Peacock, and C.O. Davis (1994) A model for interpretation of hyperspectral remote sensing reflectance, Appl. Opt. (in press).

2. Steward, R. G., K. L. Carder, and T. G. Peacock (1994) High resolution, in water optical spectrometry using the Submersible Upwelling and Downwelling Spectrometer (SUDS). EOS AGU/ASLO (75) 3, 102.

3. Stramski, D. and D. A. Kiefer (1991) Light scattering by microorganisms in the open ocean. Prog. Oceanog. 28,343-383.

4. Carder, K. L. and D. K. Costello (1994) Optical effects of Large Particles. In: Ocean Optics. Spinrad, Carder, and Perry, editors, Oxford University Press, New York, N.Y.

5. Baker, E.T. and J.W. Lavelle (1984) The effect of particle size on the light attenuation coefficient of natural suspensions. J. Geophys. Res. 89, 8197-8203.

6. Costello, D.K., K.L. Carder, R.G. Steward and A. Alldredge (1994) The Distribution and Optical Properties of Large Marine Particles: Data From a Culture Tank and Field Experiments. EOS AGU/ASLO (75), 3, 35.

7. Van de Hulst, H. C. (1957) Light Scattering by Small Particles. John Wiley, New York.

8. Costello, D.K., K.L. Carder and R.G. Steward. (1991) Development of the Marine Aggregated Particle Profiling and Enumerating Rover (MAPPER). Underwater Imaging, Photography, and Visibility, Richard W. Spinrad, Editor, Proc. SPIE 1537, 161-172.

9. Costello, D.K, K.L. Carder and W. Hou (1992) Structured visible diode laser illumination for quantitative underwater imaging. Ocean Optics XI. Gary D. Gilbert, Editor, Proc. SPIE 1750, 95-103.

10. Costello, D.K., K.L. Carder, W. Hou and R.G. Steward (1994) 3-dimensional particle size spectra, transmissometry and temperature profiles, and filter pad absorption data. In: Monterey Bay Field Experiment Data Report to the Office of Naval Research under the Accelerated Research Initiative, Significant Interactions Governing Marine Aggregation (SIGMA). 24 pp.

11. Hou, W., D.K. Costello, K.L. Carder and R.G. Steward (1994) High-resolution Marine Particle data from MAPPER, a new, in situ optical ocean instrument. EOS AGU/ASLO (75), 3, 21.

12. Costello, D.K., W. Hou and K.L.Carder (1994) Some effects of the sensitivity threshold and spatial resolution of a particle imaging system on the shape of the measured particle size distribution. Ocean Optics XII, Bergen, Norway.

13. Smith, S.M. (1994) Implications of low cost distributed control systems in UUV design. AUVS '94 - Intelligent Vehicle Systems and Technology, Detroit, MI.

14. Morel, A. and Prieur, L. (1977) Analysis of variations in ocean color Limnol. Oceanogr. 22:709-722.

15. Smith, R.C. and K. S. Baker (1981) Optical properties of the clearest natuaral waters (200-800 nm). Appl. Opt. (20), 2, 117-184.

16. Kishino, M., C. R. Booth and N. Okami (1984) Underwater radiant energy absorbed by phytoplankton, detritus, dissolved organic matter, and pure water. Limnol. Oceanogr. 29(2), 340-349.

17. Mitchell, B.G. and D.A. Kiefer (1988) Chlorophyll a specific absorption and fluorescence excitation spectra for light-limited phytoplankton. Deep-Sea Res. 35(5), 639-663.

18. Sathyendranath, S., L. Lazzara and L. Prieur (1987) Variations in the spectral values of specific absorption of phytoplankton. Limnol. Oceanogr. 32(2), 403-415.

19. Carder, K. L., R. G. Steward, G. Harvey, and P. Ortner (1989) Marine humic and fulvic acids: Their effects on remote sensing of ocean chlorophyll. Limnol. Oceanogr. 34(1): 68-81.

20. Carder, K.L., R.G. Steward, R.F. Chen, S. Hawes, Z. Lee and C.O. Davis (1993) AVIRIS calibration and application in coastal oceanic environments: tracers of soluble and particulate constituents of the Tampa Bay Coastal Plume. Photogram. Engr. & Remote Sensing. Special Issue on Imaging Spectrometry. 487-500.

21. Carder, K.L. and R.G. Steward (1985) A remote-sensing reflectance model of a red tide dinoflagellate off west Florida. Limnol. Oceanogr. 30:286-298.

22. Gordon, H.R. and A. Morel (1983) Remote Assessment of Ocean Color for Interpretation of Satellite Visible Imagery: A Review. Springer-Verlag, New York.

23. Gordon, H.R. (1979) Diffuse reflectance of the ocean: The theory of its augmentation by chlorophyll a fluorescence at 685 nm. Appl. Opt. 18(8):1161-1166.

24. Stavn, R.H. (1990) Raman scattering effects at the shorter visible wavelengths in clear ocean waters. In: Ocean Optics X, Proc. SPIE 1302, 94-100.

25. Marshall, B.R. and R.C. Smith (1990) Raman scattering and in-water ocean optical properties. Appl. Opt. 29:71-84.

26. Kirk, J.T.O. (1983) Light and Photosynthesis in Aquatic Ecosystems, Cambridge University Press, Cambridge.

Using Unmanned Vehicle Systems for Ground-Truthing Oceanographic Satellite Data

David K. Costello and Kendall L. Carder

University of South Florida
Department of Marine Science
140 Seventh Avenue South
St. Petersburg, FL 33701
dkc@monty.marine.usf.edu

Using Unmanned Vehicle Systems for Ground-Truthing Oceanographic Satellite Data

David K. Costello and Kendall L. Carder

University of South Florida
Department of Marine Science
140 Seventh Avenue South
St. Petersburg, FL 33701
dkc@monty.marine.usf.edu

ABSTRACT

Some of the clearest weather for satellite remote sensing occurs immediately after the passage of cold fronts, with strong northerly winds interrupting traditional ship sampling activities. Major wind events, however, provide energetics to drive the vertical mixing and circulation processes that are most important in providing nutrients to the plants near the sea surface. If these events are missed or not sampled due to the cost and/or scheduling complexity of providing enough large vessels, very important mechanisms affecting spectral water visibility will be poorly sampled and our ability to interpret data acquired from spacecraft will be compromised. Unmanned Underwater Vehicles, alternatively, are not weather dependent and offer relatively inexpensive and flexible (short lead times for scheduling) systems for validating satellite data and providing ancillary measurements unattainable from space. Additionally, a UUV is vastly superior to surface vessels as a platform for securing the types and density of data required for ground-truthing ocean color satellite data.

A scenario is presented for coastal applications of the Ocean Voyager II UUV for validating satellite data for chlorophyll_a and colored dissolved organic matter concentrations, water temperature, spectral transparency, and the spectral bottom albedo.

1. INTRODUCTION

In the new millenia, our planet will be encircled with a host of orbiting machines. The task of most of these satellites will be to enable a truly global, instantaneous information network. The business of this network will be communications, commerce, entertainment, security, and both theoretical and applied scientific research. Some of these research platforms will be looking outward, in search of information from the rest of our solar system and beyond. The rest will be looking inward with a solitary purpose, to monitor the planet from which they were launched. These space-based, inward-looking machines will be built and launched not out of curiosity but out of the necessity to acquire global data in order to address global questions. These global questions include agriculture, mariculture and fisheries production, deforestation, desertification, ozone depletion, air and water quality, international security, global warming, chemical and heat exchanges among the air, land, and sea, and other observations to record an ecosystem under stress. As with any instrument system, however, these space-based, remote sensing systems require calibration, algorithm validation, and the interpretation of the remotely sensed data.

This contribution focuses on the use of complementary machines for the new millenia, Unmanned Underwater Vehicle systems (UUVs) and specifically Autonomous Underwater Vehicles (AUVs) to calibrate algorithms and validate satellite data regarding a significant part of our planet's surface, the coastal ocean. Our emphasis for this purpose is remote sensing and interpretation of ocean color.

2. Ocean Color in Coastal Waters

From the perspective of the earth, the sun is a point-source, blackbody radiator with a color temperature of 6000 degrees Kelvin. With minor adjustments for solar Fraunhoffer absorption lines, the quantity and spectral quality of the solar power output intercepted by our planet is well known. As this solar radiation encounters our planet, the atmosphere changes the directionality and spectral quality of the radiation through scattering and differential absorption. When this radiation encounters the ocean, some is specularly reflected and the rest, after refraction, enters the water column. As a photon travels down within the water column, it can be forward-scattered, scattered back toward the surface, or absorbed. A small fraction of the energy scattered by water molecules is transformed by inelastic scattering into lower frequency radiation (water Raman). When a photon is absorbed by a phytoplankter, the energy can be harvested by the plant pigments in the phytoplankton growth process, or emitted at a different frequency. This emission can be as heat or, if the frequency is in the visible waveband, this process is termed fluorescence or trans-spectral scattering. Those photons which are emitted or scattered back toward the surface may eventually be collected by a satellite sensor. Interpretation of this collected spectral energy, however, is not straightforward. Even in a best-case scenario, a cloud-free day in deep, low-absorption (Case I) waters, for example, over 90% of the light collected by a ocean color sensor will be from atmospheric scattering (Gordon et al., 1983). In coastal areas, difficulty in data interpretation can be compounded by the existence of a convolved suite of dissolved and particulate material of both terrestrial and marine origin. Additionally, the water-leaving radiance can contain photons which have been reflected off the bottom. Here the brightness and color of the bottom, the spectral bottom albedo, would contribute to the remotely sensed signal. This effect has been quantified in NASA's Airborne Visible/Infrared Imaging Spectrometer (AVIRIS) imagery of the Eastern Gulf of Mexico where depths were as deep as 30 m and chlorophyl concentration more than 0.4 mg/m^3 (Carder et al., 1993a,b,c). Finally, terrestrial (especially anthropogenic) input into the atmosphere can make data interpretation even more complex (see Carder et al., 1991).

3. Difficulties with Traditional Ground-Truth Operations

It has been recognized for some time by the ocean color community that parameterization of the complex system of radiative transfer inherent in remote sensing required validation data from the scene, that is, ground truth. Primarily due to the physical difficulty and the expense of data acquisition at sea, however, a very small percentage of the ocean has been sampled synoptically with a satellite observation and most of the sampling data have been collected in fair weather. In some areas, attempts at synoptic field and remote sampling are often foiled by cloud cover and ships scheduled weeks or months or years in advance can seldom accelerate or delay a

schedule.

In most of the world ocean, some of the clearest weather for satellite observations of earth occur immediately after frontal passages. Using the coastal eastern Gulf of Mexico for example, it is local sea lore that when the wind changes from the prevailing easterly to a southerly direction, it will continue to rotate clockwise, and a frontal weather system, a "Northerner", will pass through the area. After passage of the front, humidity is low, the sky cloud-free, and visibility high, ideal for satellite remote sensing. Unfortunately for the sea-going oceanographer seeking validation data, however, a frontal passage is ususally difficult to predict reliably and is accompanied by higher winds and seas. The clear skys after the frontal passage also may be short-lived.

To take maximum advantage of these clear skys over coastal waters using traditional sampling techniques, multiple ships must be able to be staged with relatively short notice. The ships must be large enough (read "expensive") to allow research activities in less than ideal weather conditions. There should be multiple ships to provide reasonable temporal and spatial coherence with the spacecraft data acquired from the rapidly changing, high-energy, coastal environment. Even if multiple ships were operating in an area of interest, however, they could rarely be orchestrated for a joint mission on short notice. The cost of vessel operations requires that they be scheduled heavily and far in advance.

4. Data Requirements for Coastal Ocean Color Interpretation

Coastal areas are complicated environments where most of our population lives. The difficulties described above are magnified near-shore because of complex and often rapidly changing physical processes. Tidal processes, inertial currents, upwelling, buoyant plumes, and internal waves are but a few mechanisms that change rapidly and require synoptic sampling. The more we learn about coastal areas, the more significant they become in our understanding of global processes for they are the exchange sites for land-sea fluxes and are likely to be where manifestations of changes brought on by humans are first detected in the ocean. Their complexity, however, demands that a wide variety of data be acquired in order to interpret the satellite data.

Water molecules, for example, affect light profoundly but in a manner that has been relatively well researched and documented (Morel and Prieur, 1977; Smith and Baker, 1981). In natural waters, plant pigments (eg. chlorophylls, carotenoids, etc.) can also play a significant role in water color. The efficiency of the different absorption and fluorescence bands for these pigments has been recently an area of intense research and is becoming increasingly understood (Kishino et al., 1984; Mitchell and Kiefer, 1988; Sathyendranath et al., 1987). In many coastal areas, one significant agent affecting light is Colored Dissolved Organic Matter (CDOM or "gelbstoff"), a biogenic degradation product of terrestrial or marine origin. Carder et al. (1989) found that terrestrial and marine CDOM had differing spectral signatures and for a given river plume, CDOM images could be mapped into salinity images from AVIRIS (Carder, et al., 1993b). Other factors that can affect the underwater light field and, hence, remotely sensed water color in coastal areas are suspended sediments (associated with riverine input or resuspended from the bottom by currents), the magnitude and shape of the particle size distribution (phytoplankton blooms and/or aggregation can have significant affects on water clarity,

see Carder and Costello, 1994, Costello et al., 1994a), and bottom albedo. For an optically thick, homogenous ocean (e.g., well-mixed, deep water), the following equation (Morel and Prieur, 1977; Carder and Steward, 1985) describing remote sensing reflectance, R_{rs}, can be applied:

$$R_{rs}(\lambda) = L_w(\lambda)/E_d(\lambda)$$
$$= \{0.33 b_b(\lambda)/[a(\lambda) + b_b(\lambda)]\}(t/n)^2/Q, \quad (1)$$

where the parameters which are functions of the wavelength λ are noted. Here L_w is the water-leaving radiance measured from space, E_d is the downwelling irradiance, b_b and a are the backscattering and absorption coefficients of water and its suspended particles, and $Q = E_u(\lambda)/L_u(\lambda)$ (the ratio of the upwelling irradiance to the upwelling radiance) and is only weakly dependent upon λ (Gordon and Morel, 1983). The squared term provides for the radiance divergence and sea-air transmittance, t, of radiance leaving the water. The index of refraction of seawater, n, is about 1.334. This equation contains no provision for transpectral phenomena such as water-Raman scattering (considered negligible for near-shore environments) or fluorescence due to CDOM and chlorophyll a (not necessarily negligible for certain wavelengths). Provision for these can be made by adding an additional term (e.g. see Gordon, 1979; Carder and Steward, 1985; Stavn, 1990; Marshall and Smith, 1990).

For an optically shallow environment (e.g. depths shallower than about 2.0 optical thicknesses), bottom reflectance needs to be considered. Equation 1 can be expanded as follows:

$$R_{rs}(\lambda)_s = R_{rs}(\lambda)_d(1 - \exp\{-[k_d(\lambda) + k_u(\lambda)]D\})$$
$$+ (t/n)^2(\alpha/\pi)\exp\{-[k_d(\lambda) + k_u(\lambda)]D\}, \quad (2)$$

where the subscripts s and d depict shallow- and deep-water conditions, α is the bottom albedo, the bottom reflectance is considered to be Lambertian [e.g., $E_u(\lambda)/\pi L_u(\lambda)$ at the bottom], and D is the water-column depth. The term $(1 - \exp\{-[k_d(\lambda) + k_u(\lambda)]D\})$ only becomes important when the depth D is smaller than about 0.5 optical depth. The diffuse attenuation coefficients k_d and k_u are for downwelling and upwelling light, respectively, and are largely a function of $a(\lambda) + b_b(\lambda)$ multiplied by the average slant-path enhancement of the rays (see Kirk, 1983; Lee et al., 1994) relative to the vertical.

5. AUV's for Coastal Optical Oceanography

Satellite- or aircraft-derived ocean color data can be used to extrapolate from the data acquired on ship or AUV transects across or along the coastal transition zone of the ocean. Alternatively, *in situ* data can be used to validate algorithms used with remotely sensed data.

Once the atmospheric effects have been removed from remotely sensed data, Eqs. 1 and 2 can be validated by comparing remote-sensing reflection ($R_{rs}(\lambda)$) values to *in situ* measures of $R_{rs}(\lambda)$ and the combined terms found on the right sides of the equations. Of these, the bottom albedo, $\alpha(\lambda)$, is the most stable, with short-term temporal variability expected to be relatively low. This argues that α could be mapped before or after a major field validation effort. This mapping, however, would be prohibitively time consuming from a surface vessel using instrumentation hung over the side. A properly instrumented tow-body could provide the required areal coverage but altitude control and obstacle avoidance near the bottom would be problematic. Bottom mapping, however, is an ideal mission for an AUV.

The primary remaining validation variables that require measurement are

$R_{rs}(\lambda)$, $a(\lambda)$, and $b_b(\lambda)$ from Eq. 1 and $k_d(\lambda)$ and $k_u(\lambda)$ from Eq. 2. The water depth D can also be determined, often after the fact, using depth charts and tidal models. This information is, however, readily available in an AUV deployment.

$R_{rs}(\lambda)$ can be measured near the surface from an AUV measuring the downwelling irradiance $E_d(\lambda,z)$ and upwelling radiance $L_u(\lambda,z)$, where z indicates sensor depth. By gently porpoising the AUV, these values can be obtained for different depths, and diffuse attenuation coefficients are obtained through

$$E_d(\lambda,z+\Delta z)=E_d(\lambda,z)exp[-k_d(\lambda,z)*\Delta z, \quad (3)$$

and a similar expression for $k_u(\lambda,z)$ involving L_u instead of E_d. Instruments have been developed to provide direct measurements of beam attenuation, c, and absorption, a, at 9 wavelengths and also yield the total scattering coefficient b since b = c - a. Backscattering sensors are also available for several wavelengths and multi-channel volume scattering $\beta(\theta)$ instruments are under development.

All of these instruments can be incorporated into the sensor suite of an AUV that also includes temperature, salinity, beam attenuation, pressure (depth), height above bottom, water and bottom velocity relative to the AUV, and six-color bottom imagery for albedo (see Costello et al., 1994b).

6. AUV Configuration

Figure 1 depicts the Ocean Voyager II equipped with the Bottom Classification/Albedo Package (BCAP), an ensemble of optical sensors to be built at USF. BCAP principle components are hyperspectral (512 channel) upwelling radiance/reflectance and downwelling irradiance meters, a dual-laser range finder/chlorophyll probe, and a 6-wavelength, image-intensified, CCD bottom camera for bottom classification and object identification purposes. A high-pressure, rare-earth-doped light source (Deep-Sea Power and Light) provides a relatively smooth illumination spectra for active, spectral albedo and bottom mapping measurements and sufficient blue intensity to investigate stimulated fluorescence, potentially significant data for bottom classification. The bottom reflectance and downwelling irradiance meters are under development at USF. The prototype has a nominal resolution of 3 nm from 350-900 nm. The two diode lasers (Melles Griot Electro-Optics) can function as range finders providing the high-resolution altitude determination necessary for light propagation modelling. They are also utilized in an attempt to quantify the chlorophyll_a content of the bottom sediment exploiting the differential absorption of the pigment at the two different laser wavelengths. One laser emits at 675 nm, a major peak of the chl_a absorption spectra, while the other laser emits at 650 nm, a local minima of the chl_a absorption spectra (see figure 2). The 650 nm wavelength choice also minimizes potential crosstalk with the absorption spectra of chl_c, a pigment often present with chl_a.

The 6-channel, IMC-301 imager (Xybion) utilizes a recently developed, Generation-III, Micro-Channel Plate Image Intensifier with an extended blue photocathode (GEN-III-Blue) which has a dynamic range of over ten orders of magnitude. Tests in our laboratory showed that a less sensitive, GEN-II-RED was capable of imaging fluorescence from macrophyte, seagrasses, and benthic diatoms and would, therefore, be capable of imaging albedo and/or fluorescence variations of the bottom. The increase in instrument

SPECIFIC ABSORPTION COEFFICIENT SPECTRA FOR CHLOROPHYLLS a and c
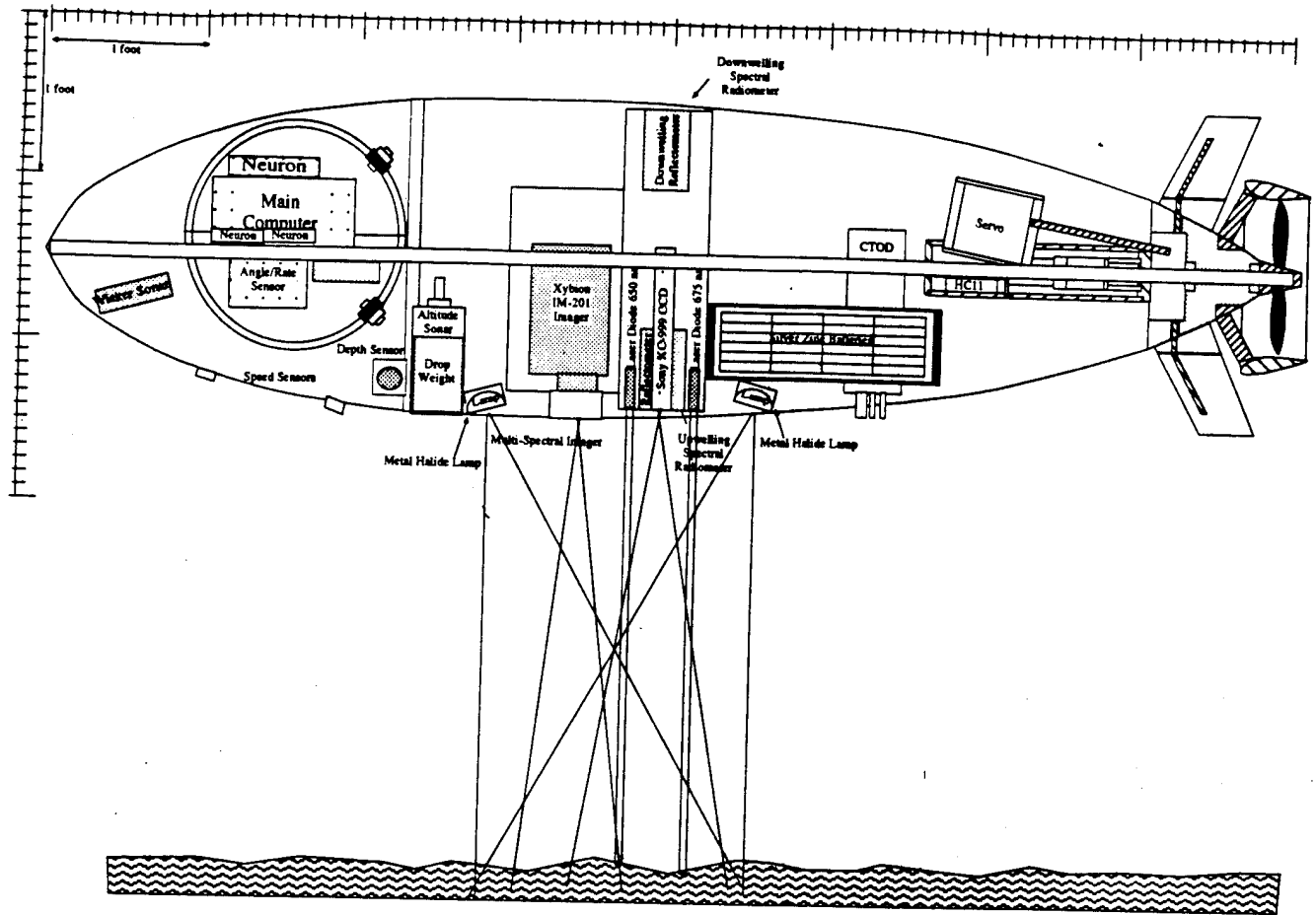
Figure 1. Depiction of an AUV (Ocean Voyager II) equipped for coastal optical oceanography, see text for discussion (Figure courtesy of S. Smith, Ocean Engineering, Florida Atlantic Univ.).
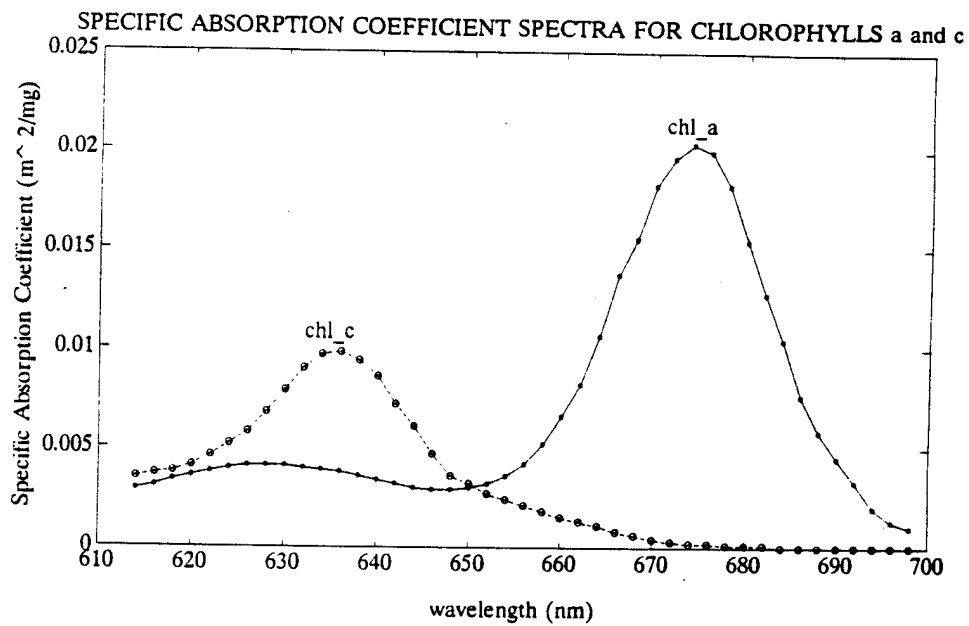
Figure 2. Specific absorption coefficients for chlorophylls *a* and *c* (see text for discussion).

response afforded by a GEN-III-Blue vs. a GEN-II-RED at an important chl_a fluorescence band (685 nm), for example, is a factor of three. The calibration consistency of the IMC-301 GEN-III-Blue imager is, however, currently unknown. To provide unambiguous data, the calibrated 512-channel spectral reflecto-meter/radiometer will obtain spectra from a known (as a function of altitude) segment of the IMC-301 image, thus providing calibration constants for the imager. Another 512-channel spectral radiometer, equipped with a cosine collector, will obtain the spectra of the downwelling light field.

Ancillary instrumentation (not shown in Fig 1) will focus on the water inherent optical properties (IOP's) and physical properties and dissolved and particulate matter concentrations. These sensors include a nine-channel absorption/attenuation meter (ac-9, WET Labs), a multi-channel volume scattering meter (WET Labs, available FY 1995), a backscattering (OBS) meter (Seatech), a 660 nm transmissometer (Seatech), and a CTD (Falmouth).

7. Deployment Scenario

Ocean color measurements require a solar zenith angle which allows adequate light penetration into the water column. For the purpose of illustration, we will use a six-hour sampling window, from 1000 to 1600 hours. An ideal mission scenario would utilize multiple OVII vehicles to maximize areal coverage during the sample window. Even a single OVII, however provides coverage not available with a surface vessel. Assuming an OVII cruise speed of 4 knots, a vertical ascent/descent rate of 0.5 m/sec, water depth of 25 m, and vertical vehicle oscillations (vertical profiling stations) at one kilometer intervals, the OVII could complete 43 sample stations, 86 vertical profiles (performed while underway), and

map nearly 90% of the bottom along the transect.

For contrast, a suface vessel with an experienced crew able to perform a vertical optical profile in only 15 minutes, and allowing an additional 5 minutes to steam to the next station, could only complete 18 stations and would have albedo measurements of a very small percentage of the bottom.

In summary, the ideal mission scenario would utilize multiple AUVs and a network (multiple pairs) of bottom-moored acoustical beacons to enable coordinated, precise AUV navigation. Other than AUV deployment/retrieval operations, the primary role of the surface vessel in this scenario would be to recover pairs of navigation beacons and to make ancillary (e.g., wet chemistry) measurements. The density of data that would be acquired in this type of coastal operation would enable the validation of satellite data in this complex marine environment.

References

Bidigare, R.R., M.E. Ondrusek, J.H. Morrow and D.A. Kiefer (1990) In-vivo absorption properties of algal pigments. In: *Ocean Optics X*, R. W. Spinrad (ed.) SPIE Vol. 1302, 290-302.

Carder, K. L. and D. K. Costello (1994) Optical effects of large particles. In: *Ocean Optics*, Spinrad, Carder, Perry (eds.), Oxford University Press, London.

Carder, K.L., P. Reinersman, R.F. Chen, F. Muller-Karger, C.O. Davis and M. Hamilton (1993a) AVIRIS calibration and application in coastal oceanic environments. *Remote Sens. Environ.* 44:205-216.

Carder, K.L., R.G. Steward, R.F. Chen, S. Hawes, Z. Lee and C.O. Davis (1993b) AVIRIS calibration and application in coastal oceanic environments: tracers of soluble and particulate constituents of the Tampa Bay Coastal Plume. *Photogram. Engr. & Remote Sensing*. Special Issue on Imaging Spectrometry. 487-500.

Carder, K.L., Z.P. Lee and R.F. Chen (1993c) Unmixing of Spectral Components Affecting AVIRIS Imagery of Tampa Bay. In: *Imaging Spectrometry of the Terrestrial Environment*, SPIE Vol. 1937, 77-90.

Carder, K. L., W. W. Gregg, D. K. Costello, K. Haddad, and J. M. Prospero (1991) Determination of Saharan dust radiance and chlorophyll from CZCS imagery. *J. Geophys. Res.* 96 (D3): 5369-5378.

Carder, K.L. and R.G. Steward (1985) A remote-sensing reflectance model of a red tide dinoflagellate off west Florida. *Limnol. Oceanogr.* 30:286-298.

Costello, D.K., K.L. Carder, R.G. Steward and A. Alldredge. (1994a). The Distribution and Optical Properties of Large Marine Particles: Data From a Culture Tank and Field Experiments. *EOS* AGU (75) 3, 35.

Costello, D.K., K.L. Carder, and R.G. Steward. (1994b) New instrumentation and Platforms for Subsurface Optical Measurements. *Ocean Optics XII*, Bergen, Norway.

Gordon, H.R., D.K. Clark, J.W. Brown, O.B. Brown, R.H. Evans, and W.W. Broenkow (1983) Phytoplankton pigment concentration in the Middle Atlantic Bight: Comparison of ship determinations and CZCS estimates. *Appl. Opt.* 22: 20-36.

Gordon, H.R. and A. Morel (1983) *Remote Assessment of Ocean Color for Interpretation of Satellite Visible Imagery: A Review*. Springer-Verlag, New York.

Gordon, H.R. (1979) Diffuse reflectance of the ocean: The theory of its augmentation by chlorophyll *a* fluorescence at 685 nm. *Appl. Opt.* 18(8):1161-1166.

Kirk, J.T.O. (1983) *Light and Photosynthesis in Aquatic Ecosystems*, Cambridge University Press, Cambridge.

Kishino, M., C. R. Booth and N. Okami (1984) Underwater radiant energy absorbed by phytoplankton, detritus, dissolved organic matter, and pure water. *Limnol. Oceanogr.* 29(2), 340-349.

Lee, Z. P., K.L. Carder, S.K. Hawes, R.G. Steward, T.G. Peacock, and C.O. Davis (1994) A model for interpretation of hyperspectral remote sensing reflectance, *Appl. Opt.* (in press).

Marshall, B.R. and R.C. Smith (1990) Raman scattering and in-water ocean optical properties. *Appl. Opt.* 29:71-84.

Mitchell, B.G. and D.A. Kiefer (1988) Chlorophyll *a* specific absorption and fluorescence excitation spectra for light-limited phytoplankton. *Deep-Sea Research* 35(5), 639-663.

Morel, A. and Prieur, L. (1977) Analysis of variations in ocean color *Limnol. Oceanogr.* 22:709-722.

Sathyendranath, S., L. Lazzara and L. Prieur (1987) Variations in the spectral values of specific absorption of phytoplankton. *Limnol. Oceanogr.* 32(2), 403-415.

Stavn, R.H. (1990) Raman scattering effects at the shorter visible wavelengths in clear ocean waters. In: *Ocean Optics X*, Proc. SPIE 1302, 94-100.

PROCEEDINGS REPRINT

Reprinted from

Ocean Optics XII

13–15 June 1994
Bergen, Norway

P

Volume 2258

Some Effects of the Sensitivity Threshold and Spatial Resolution of a Particle Imaging System on the Shape of the Measured Particle Size Distribution

D. K. Costello,* W. Hou,* and K. L. Carder*

*Department of Marine Science, University of South Florida, 140 7th Avenue South, St. Petersburg, FL 33701, U.S.A.

ABSTRACT

Numerous scientific research efforts require knowledge of the particle volume concentration. For many studies, this information is required as a function of particle size. These particle volume spectra are often inferred from optically measured particle areal size distributions after the areal size distributions have been transformed into equivalent spherical diameter (ESD) distributions. Resolution and sensitivity differences between imaging systems will result in different shapes for the measured particle size distribution. Artifacts will be introduced at the small-particle end of the distribution by the finite spatial resolution of an imaging system while, on the large particle end, artifacts due to under-sampling (a direct corollary of finite spatial resolution) become probable. Additionally, the sensitivity threshold of the imaging system is not only fundamental to the determination of the particle edge but also determines the optical density (reflectivity) level below which material will not be imaged. All this affects the measured size of a particle. Finally, if non-spherical and/or porous particles are present, the measured size distributions, when particle sizes are presented in equivalent spherical diameter (ESD), are no longer necessarily representative of the original 1-dimensional geometric projections of the particles, an important consideration for some applications.

This contribution utilizes laboratory data and unique, synchronous, ocean field data collected by three coincident imaging systems to evaluate these effects in the study of large marine particles. Also, for applications which require a measure of the geometric spread of a particle (e.g. perimeter/area ratio)and/or applications involving partially translucent particles, an algorithm rooted in the theory of moment invariants is presented which avoids the distortions to the particle size distributions when the size of non-spherical and/or porous particles are presented as ESD.

1. INTRODUCTION

Electronic imaging is one of society's most rapidly advancing technologies. The evolution is being driven by the desire to provide greater quantities of higher-quality information at an increasingly faster rate. The fields of entertainment, banking, medicine, communications, among many others are benefitting and expanding. This expansion tends to drive down the cost of the necessary equipment, which allows more researchers to enter the arena with new applications, again accelerating the expansion.

An important subset of electronic imaging is digital image processing (DIP). DIP is in widespread industrial use in applications including communications, process and quality control, employee identification, signature verification, etc. One of these applications, in both the industrial and the scientific arena, is object counting and sizing, the measurement of the particle size distribution in an environment. Although the imaging environment and the nature of the particles can vary widely (e.g. tablets, droplets, bubbles, cells, bacteria, aggregates, dust), processing an image in the digital domain is strictly governed by rules inherent to the process.

This contribution focuses on a specific application, the use of DIP technology to describe the *in situ* size distribution of marine particles. Laboratory and theoretical work are presented which show how the percieved size distributions can vary depending on the resolution and sensitivity of the system. Additionally, problems which arise when the size of non-spherical and/or porous particles are presented as equivalent spherical diameter (ESD) are dicussed and illustrated. It should be noted here that the "porosity" of a particle can be an artifact of the finite sensitivity of the imaging system employed; that is, the "holes" may be filled with a material which can not be visualized by a particular imaging sytem but would be vizualized by a system of higher sensitivity. An alternate approach to describing the functional "size" of a non-spherical and/or porous particle is presented and compared to the ESD representation. We propose that this approach has utility in applications such as particle settling which require a measurement which is representative of the geometric spread (e.g. 1/compactness) or extent of the particle and also more accurately describes the size (and, by inference, mass) of aggregated particles. These can often be formed upon a matrix of transparent exopolymers (TEP)[1,2]. Finally, field imagery acquired by three coincident, synchronous CCD video systems is presented which shows the effects of variable resolution on size distributions acquired *in situ* as well as on the images of individual particles.

2. IMAGE RESOLUTION

A great potential pitfall inherent in digital image processing, spurious resolution, is illustrated in the following hypothetical example. A researcher involved in a land-use study acquires high-resolution, photographic imagery from an aircraft at an altitude which yields a horizontal field-of-view (FOV) of 1.28 km. At the laboratory, an image analysis workstation automatically transfers the photographic images to VHS video tape. The video images are then digitized at 1,280H x 960V pixel resolution. The image analysis workstation software package, then, yields voluminous data with one-square-meter accuracy. The actual resolution, however, is a function of the lowest resolution component in the data acquisition/processing system and the VHS video tape recorder has only a horizontal resolution, for example, of about 240 lines. Pixel resolution in this example over-estimates actual resolution by at least a factor of 6, and, if the Nyquist sampling frequency theorem is considered, by at least a factor of 12. When errors attributable to spurious vertical resolution are also considered, the actual areal resolution could be overestimated by two orders of magnitude.

2.1 The Video Signal

In order to understand digital image processing the conversion of the analog video signal to digital data needs to be considered. Image frame grabbers perform this conversion in real-time, utilizing flash analog-to-digital converters (ADCs). "Real-time" for NTSC video is 30 frames per second (25 for the PAL standard), and the conversion most often follows the convention shown in Figure 1 (the PAL standard differs slightly). The 1 volt (V) video signal is divided into 140 IRE units with a baseline (0 IRE units) corresponding to 0.286 V. In the A/D conversion, some additional voltage (usually 0.054 V) above the baseline is used as a reference black level. The voltage range above this level (0.66 V) is converted by an 8-bit flash ADC to 255 gray scales (GS). Numerous tests in our laboratory with several different frame grabbers confirm that the conversion is, in fact, linear. There are several variables involved in the reproduction of the A/D conversion convention shown in Figure 1., however, and, as variables, they can be changed.

Equation 1 describes the volts to gray scale conversion utilized to process images with a Data Translation Inc. Integrated Image Processor and Precision Frame Grabber (DT-2867).

$$V = (2048 - ZO) * 3.272 * 10^{-4} + 2.311^{-4} * (ADR * GS) / (GN * 255) \tag{1}$$

PIXEL GRAY SCALE vs. VIDEO SIGNAL LEVEL
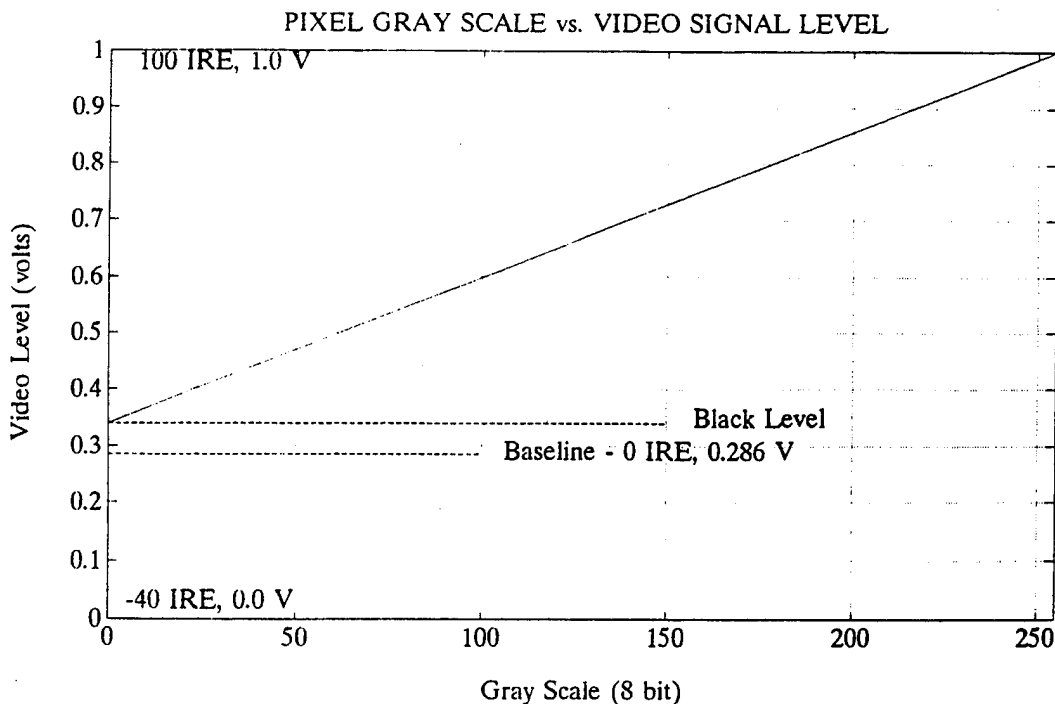
Figure 1. The relationship of pixel gray scale to video signal level (see text for discussion).

Note that, generally, in the conversion from video-signal voltage level (V) to digitized gray scale (GS), the zero offset (ZO), the gain level (GN), and the A/D reference (ADR) can all be changed in the frame grabber control software and/or through hardware adjustments. It is relevant here that changing the V to GS conversion variables will confound any algorithm which utilizes GS thresholds for particle edge detection. Also, at higher voltage levels, it takes relatively longer for video circuitry to return to black level (electronic overshoot). This results in brighter targets measuring longer in the horizontal dimension than similarly sized targets of lower gray scale (illustrated below). The amount of this elongation is a function of the programmed black level. A consequence of the above is also that even identical imaging systems will produce differring measurements of a particle suite when different ADC variables are utilized.

2.2 Laboratory Measurements

To investigate the effects of video format resolution and system radiometric sensitivity on the shape of a measured size distribution, a diffusly backlit, 1951 USAF test target negative was imaged using an interline-transfer CCD camera (Sony XC-75). The camera specifications include a S/N ratio of 56 dB and horizontal resolution of 570 TV lines (HTVL). The images were recorded at each of two aperture settings (f/8 and f/16) in both VHS (240 HTVL) and S-VHS (400 HTVL) formats and were also grabbed directly at full resolution by the DT-2867. The light source was current- and voltage-regulated to $\pm$ 1.0%.

Target groups (-2, 1 to 6), (-1, 1 to 6), and (0, 1 to 6) were utilized. The 1951 USAF test pattern displays three vertical and three horizontal bars in each sub-group and decrease in linear dimension and spacing from sub-group to sub-group by a factor of $2^{-1/6}$ ($2^{-1/3}$ in area). The line spacing of the smallest target sub-group processed, (-1,6), is 280 μm and, with the imaging configuration and digitization (640H x 480V pixels) utilized, was slightly less than 2 pixels (one pixel representing a 150 x 150 μm square).

The images acquired were processed with our Image Control and Examination (ICE) system. ICE was developed in our laboratory and provides for unattended, frame-by-frame, image digitization, processing, and

target detection. The target detection algorithm is written in the C language and allows for adaptive, target-intensity and variable thresholds and closing tolerence (search area for the connection of pixels above threshold, the utility of an adaptive closing tolerence is under evaluation). It also adjusts for bright-pixel recovery delays (pixel overshoot) in the horizontal dimension due to electronic circuitry.

For the purposes of this exercise, comparing the DIP response at different intensity values for different resolution with off-the-shelf systems, we did not utilize available ICE hardware: an infinite-window time-base corrector (Nova 900S Super TBC), a Umatic-SP 3/4" industrial video tape recorder (Sony), or a programmable-resolution frame grabber (Epix Video MUX). Tests with this more sophisticated but often unavailable hardware will be considered in a future report. The ADC convention follows that shown in Figure 1 and the ICE system variables were severely constrained. That is, the target detection closing tolerance and the horizontal overshoot-compensation values were set to zero. The result at GS threshold 1, for example, is that any video voltage above 0.34 V is interpreted as target area. Processing the images at GS threshold levels 0 through 30 in 5-GS-unit increments, then, acts as a surrogate for imaging sensitivity and allows the quantification of measurement artifacts due to both system sensitivity and resolution.

Figure 2 shows the computed particle size distributions for, respectively, the SVHS and VHS formats at f/8 and at f/16. Results from the directly grabbed images did not differ substantially from the SVHS results.

Since each sub-group contains 6 targets (3 each, horizontal and vertical), a perfectly measured size distribution would be a horizontal line at a value of 6 (shown by the dotted line in each plot) for all bins except the last two "overflow" bins which would be zero in a perfect measurement. The overflow bins were used because targets which are not resolved will be lumped together and placed in a larger size group, perhaps even larger than the largest real target. A comparison of Figures 2a and 2b (the SVHS and VHS formats at F/8) shows that the higher-resolution SVHS format did, in fact, resolve more targets than the VHS format and that resolution for both formats apparently improved as the processing threshold was increased. A comparison of Figures 2c and 2d (the two formats at f/16) is not as straightforward with both formats performing better than at f/8.

Another way to analyze these results is to sum the targets detected, since there are 108 individual targets in the 16 subgroups utilized, and adjacent targets which are not resolved would be lumped together into a single, larger target. Figure 3 shows total targets detected for Figures 2a through 2d at the different GS threshold levels. The highest number of detected targets was 103 with SVHS at f/16 and a GS threshold of 15. The best performance for both formats was at f/16 and GS thresholds of 20 or less. At higher GS threshold levels, both formats "lost" targets at f/16. Conversely, at f/8, SVHS again outperformed VHS, but both formats performed better at increasing GS thresholds.

Since an increasing GS threshold effectively reduces the blur surrounding even a perfectly focused target due to edge diffraction or imperfect alignment of a target image with a pixel edge (in the horizontal and the vertical) and the blur to the right of a target (in the horizontal) caused by electronic overshoot, linear measurements were taken in order to estimate the relative errors due to the above phenomena. The vertical measurement errors for all cases were minimal except for the smallest targets at f/8 where the imperfect alignment of a target image on the pixel matrix could introduce a porportionately significant error. The errors in the horizontal dimension were, however, much more substantial and are shown in Figure 4 for f/8 and Figure 5 for f/16. Also shown are the computed errors after corrections for the horizontal electronic overshoot for both "high" and the "low" signal cases. For the high-signal case (f/8), the target GS values were about 200 counts (corresponding to 0.86 V) and it was assumed that the overshoot was simply a function of system resolution. Therefore, three pixels of the original horizontal measurements for VHS (640 pixels/240 HTVL = 3 when rounded up) and two pixels of the original horizontal measurements for SVHS (640 pixels/400 HTVL = 2 when rounded up) were attributed to overshoot. The errors for both formats after this correction were reduced to within about 5% across the size spectrum for the high-signal case. For the low signal case (f/16) shown in Figure

USAF 1951 Target Measured @ F16 on SVHS

threshold = 30
threshold = 25
threshold = 20
threshold = 15
threshold = 10
threshold = 5

c

USAF 1951 Target Measured @ F16 on VHS

threshold = 30
threshold = 25
threshold = 20
threshold = 15
threshold = 10
threshold = 5

d

Target Size (pixels)

USAF 1951 Target Measured @ F8 on SVHS

threshold = 30
threshold = 25
threshold = 20
threshold = 15
threshold = 10
threshold = 5

a

Target Counts

USAF 1951 Target Measured @ F8 on VHS

threshold = 30
threshold = 25
threshold = 20
threshold = 15
threshold = 10
threshold = 5

b

Target Counts

Target Size (pixels)

Figure 2. See text for discussion.

5, the target GS values were about 50 counts (corresponding to 0.47 V) and it was assumed that the overshoot was minimal, not a function of resolution, and that both formats would return to black level in one horizontal pixel. The measurement errors after this correction were also confined to about 5%.
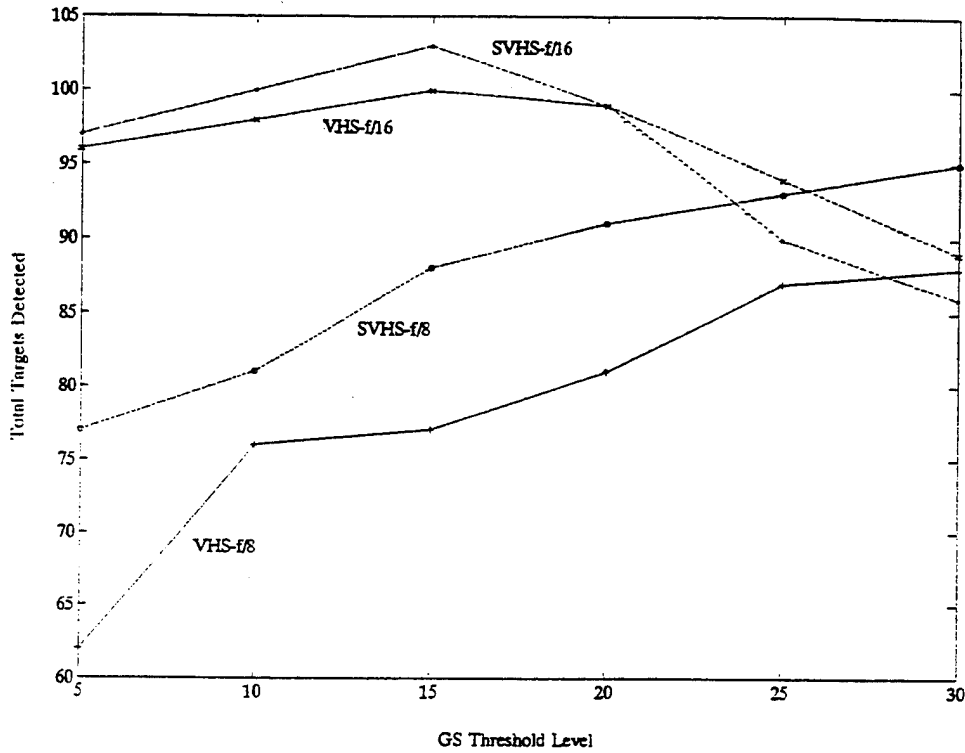
Figure 3. Total targets detected using the SVHS and the VHS format at f/8 and f/16 (see text for discussion).
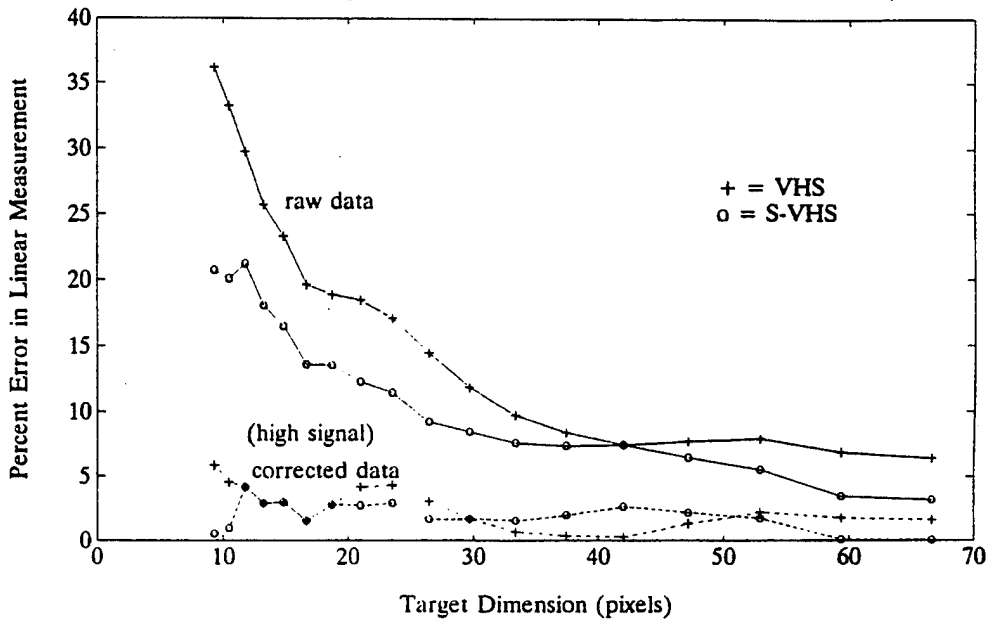
Figure 4. Horizontal measurement error after overshoot correction at f/8 (see text for discussion).

The goal of this work is to develop an algorithmic correction for electronic overshoot which adapts to target brightness and resolution. The motivation is from field imagery where the brightness of the images of a copepod and a diatom aggregate, for example, can easily differ by an order of magnitude (see Section 4.1).
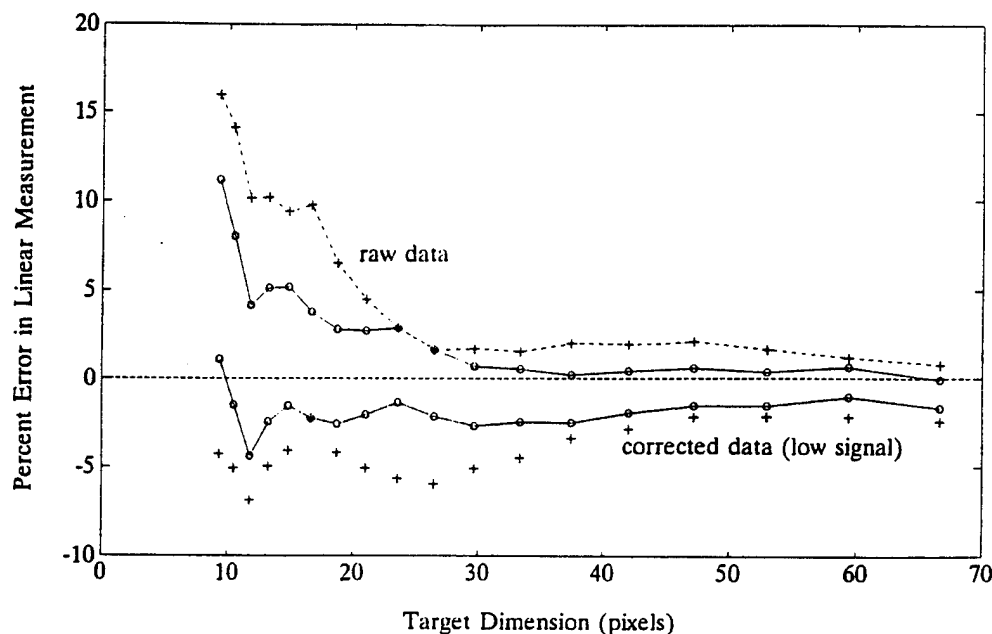
Figure 5. Horizontal measurement error after overshoot correction at f/16 (see text for discussion).

3. THE PARTICLE SIZE DISTRIBUTION

For certain modelling or classification studies, particle counts need to be separated into size bins. A particle size distribution spectrum is obtained by dividing the counts in a bin by the width of the bin. These spectra are often described by the hyperbolic (Junge-type) power law distribution:

$$\frac{dN}{dD} = kD^{-B} \tag{2}$$

where dN is particle counts of size D, dD is a diameter interval (i.e. D_2-D_1), k is a concentration constant which normalizes the distribution, and B is the negative slope of the distribution in log-log coordinate space. The utility of this form is that, since it describes a spectrum with known normalization, intercomparison can be made between measurements with different sample volumes and (with the assumption of a continuous distribution) with measurements spanning different ranges of the size spectrum.

Equation 2 can be used to calculate the number of particles within a size range of interest, particle area, volume, or mass (when an average density is assumed). The integration for particle volume is shown below.

$$dV = \frac{\pi}{6}D^3 dN = \frac{\pi}{6}kD^{3-B}dD \tag{3}$$

$$V = \int_{D_1}^{D_2} \frac{\pi}{6}kD^{3-B}dD \tag{4}$$

$$V=\frac{\pi k}{6(4-B)}(D_2^{4-B}-D_1^{4-B}),B\neq4 \tag{5}$$

$$=\frac{\pi k}{6}\ln(\frac{D_2}{D_1}),B=4 \tag{6}$$

When the measured particles are solid spheres and the imaging system accurately records their sizes, equations 3 through 6 are exact. If, however, the particles are not spherical and/or have "holes", the equations are approximations. For aggregated particles built on a matrix of TEP, for example, utilizing a size distribution (Eq. 1) where the diameter is ESD, would lead to significant errors in a volume determination (Eq. 5 or 6).

3.1 Effects of the Conversion to Equivalent Spherical Diameter

Because physical forces often arrange small, individual particles in spherical form (e.g. water droplets), the equivalent spherical diameter is widely used as a particle size descriptor. By definition, ESD is an exact dimensional descriptor for spherical particles. It also provides for exact conversion back to measured particle cross-sectional area with the caveat that the area measurement retrieved is only the area represented in the original measurement; that is, only the measurable area above some image intensity threshold and not necessarily the cross-sectional area of the particle as imaged by another system. Particles that are, indeed, spherical but have areas within their image which fall below sensitivity threshold of an imaging system, (e.g. bubbles, cells, spherical aggregates formed around a semi-translucent matrix, etc.) will be misrepresented by an ESD description. For example, consider a young versus an older Larvacean house. The Larvacean is a barely-macroscopic marine animal which creates translucent filtering structures or nets which gradually accumulate marine material. When the amount of accumulated material reduces filtering efficiency, the houses are discarded by the animal. In the conversion of measured optical area to ESD, a new Larvacean house would be quantified much differently than a remnant house, even if both had the same geometrical cross-section, since more of the house would be visualized because of the accumulated debris.
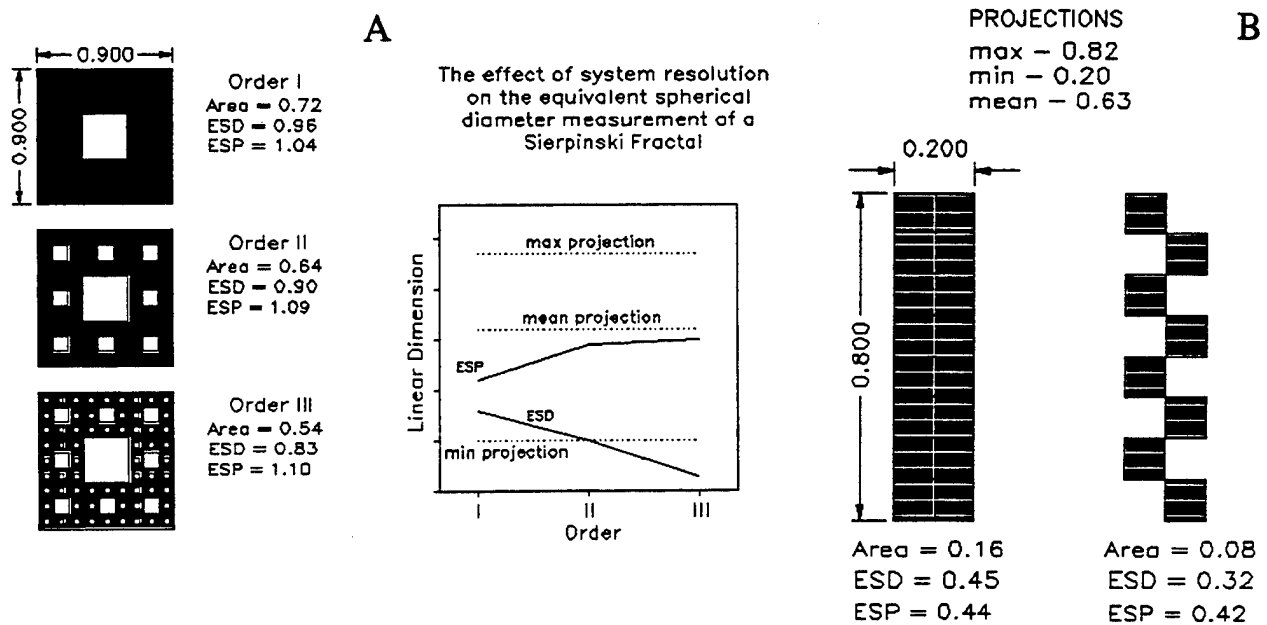
Figure 6. ESD of a fractal object and of a particle with a complicated edge (see text for discussion).

To illustrate, consider Figure 6a which depicts different measurement strategies applied to a 2-dimensional fractal object, the "Sierpinski Carpet". The fractal scheme of the object is apparent upon inspection. Fractal Orders I, II, and III are illustrated and are analogous to the same object viewed by three imaging systems of normalized magnification of 1X, 3X and 9X.

The graph in the lower right of the figure shows how the ESD measurement would change as a function of system resolution (or object distance, depending on the scenario). Also plotted are horizontal lines for the maximum (in this case, the diagonal), the minimum (in this case, dx or dy in pixel space), the mean (defined as the average of all projections obtained by rotating the object through 360 degrees in 1 degree increments) geometric projections of the object, and the "equivalent spherical projection" (ESP), which is discussed below. Even in the Order I object, the ESD is significantly less than the mean or maximum geometrical projection and, at order III, is significantly less than even the minimum geometric projection. Again, for applications where the geometric projection is important or where there is a question whether apparent holes or particle edge features are real or merely below imaging resolution or sensitivity threshold, the ESD representation is deficient. For these types of applications, an alternative to the ESD representation is required.

3.2 Equivalent Spherical Projection (ESP), An Alternative to ESD

To summarize the above, the ESD representation of particle size is deficient when: 1) the application requires a measure of the geometric projections of particles for dynamical considerations (i.e. differential settling and impact probabilities); 2) for some mass flux considerations (i.e. when particles with organic components which are not imaged at the image system maximum sensitivity level),and; 3) in efforts which require the inter-calibration of imaging systems of different resolution. What is required in these circumstances is a methodology which emphasizes the geometrical spread of the intensity image of a particle instead of the collapsed sum of the image intensity. One method to accomplish this follows.

The method of moment invariants can be used to describe the distribution of radiance from a particle within an x - y field (i.e. a digitized particle image). The method was first proposed by Hu[3] and utilized in alphabetic character recognition. The method was expanded by Teague[4] and by Dudani et al.[5], applying it to automatic identification of aircraft. The expanded method was tested on computer-generated objects and proposed for application for automatic identification of individual and aggregated marine particles by Costello et al[6]. Carder and Costello[7] tested the expanded method on images of marine particles acquired by an *in situ* holographic imaging system[8]. They reported that the method successfully identified (separated in classification-space) the images of several different types of particles.

The technique is generated as follows. The two-dimensional (i + j)th order moments of a reflectance density distribution function $\rho(x,y)$, the image, are defined in terms of Riemann integrals (proper, bounded) as[23]

$$m_{ij} = \int_{-\infty}^{\infty} \int_{-\infty}^{\infty} x^i y^j \rho(x,y) dx dy \qquad i,j = 1,2,3 \ldots \qquad (7)$$

For the purposes of this section, a description of particle size, $\rho(x,y)$ is treated as a binary distribution (equal to 1 if the processing threshold is exceeded and otherwise equal to 0) and only moments to second order are required . The higher-order moments are utilized in pattern recognition strategies[3,4,5,6,7] and are not constrained to binary computations. The low-order ordinary moments are especially useful to the extent that m_{10}/m_{00}, m_{01}/m_{00} locate the (x, y) coordinate position for the centroid of the image intensity distribution which, in this application of the technique, is the centroid of the binary particle.

For this approach to be useful for automated image analysis, however, the sample-space vectors generated must be invariant with object position and/or orientation within the image field. Translational invariance can be achieved by the determination of object centroid (from the first and zero order ordinary moments) and recalculation of the ordinary moments relative to image centroid of the object. This first step toward both translational and rotational invariance, however, can be achieved (and computational time minimized) by transforming the ordinary moments (m_{ij}) into central moments (μ_{ij}), moments relative to the centroid of the object image. Using the notation of Hu[3]:

$$\mu_{00} = m_{00} = \mu \tag{8}$$

$$\mu_{10} = \mu_{01} = 0 \tag{9}$$

$$\mu_{20} = m_{20} - \mu\bar{x}^2 \tag{10}$$

$$\mu_{11} = m_{11} - \mu\bar{x}\bar{y} \tag{11}$$

$$\mu_{02} = m_{02} - \mu\bar{y}^2 \tag{12}$$

where $\bar{x} = m_{10}/m_{00}, \quad \bar{y} = m_{01}/m_{00}$.

Note that the first-order central moments μ_{10}, μ_{01} are equal to zero under this tranformation. This follows intuitively since the first order "spread" of an object relative to any axis of a coordinate system drawn through its centroid would center about the origin.

These central moments can then be utilized to produce moment functions which possess the desired invariance with rotation and translation. Seven such functions were first formulated in the pioneering work by Hu[3]. Two of these functions are relevant here and are presented following the form of Dudani et al.[5]:

$$M_1 = (\mu_{20} + \mu_{02}) \tag{13}$$

$$M_2 = (\mu_{20} - \mu_{02})^2 + 4\mu_{11}^2 \tag{14}$$

which correspond to the classification factors, X and Y, utilized by Hu[3]. Four additional, moment-generated, elliptical classification (measurement) factors, originally developed by Teague[4], are relevant here.

$$\alpha = ((\mu_{20} + \mu_{02} + ((\mu_{20} - \mu_{02})^2 + 4\mu_{11}^2)^{1/2})2/\mu_{00})^{1/2} \tag{15}$$

$$\zeta = ((\mu_{20} + \mu_{02} - ((\mu_{20} - \mu_{02})^2 + 4\mu_{11}^2)^{1/2})2/\mu_{00})^{1/2} \tag{16}$$

$$\Gamma = (1/2)\tan^{-1}(2\mu_{11}(\mu_{20} - \mu_{02})^{-1}) \tag{17}$$

$$F = \mu_{00}/\pi\alpha\zeta \tag{18}$$

These factors characterize any image as a constant intensity ellipse with intensity F inside and zero outside, defined by the semimajor axis α, semiminor axis ζ, and angular orientation Γ within the 2-dimensional coordinate field. The method is also computationally attractive since it requires the computation of moments to only second order. Additionally, since α, ζ, and F can be expressed in terms of μ_{00} (an invariant quantity) and the Moment Invariant Functions, M_1 and M_2 (Eq. 13 and 14), the results are invariant to object rotation and/or translation. The factor Γ, on the other hand, contains object orientation information and, hence, is not an invariant function. (Note that equations 15 and 16 presented here differ from equations for α and ζ shown in Carder and Costello[7],

their's containing a typographical error.)

In order to provide insight into the mathematics employed, consider Equations 15 and 16 as applied to the image of an ideal sphere. In this case, $\mu_{11} = 0$, $\mu_{20} = \mu_{02}$ and the equations are equivalent, consisting of a linear dimension normalized by a factor of two in the numerator and by the square root of the image power in the denominator. The square root of the image power, however, also is embedded in the numerator, a result of the inclusion of image power as a factor in the original moment-generating function (Eq. 7). The linear dimension, then, is directly equivalent to the radius of the sphere and exactly equal to ESD/2. Therefore, $2\alpha = 2\zeta = ESP = ESD$. For non-spherical particles, the area of the elipse, $\pi\alpha\zeta$, can be transformed to the ESP dimension by $ESP = 2(\alpha\zeta)^{1/2}$.

For the Sierpinski Carpet shown in Figure 6a, for example, the increased interior porosity between Orders I and III changed the calculated ESD by 15% while the ESP changed only 4%. Figure 6b demonstrates the consequences of using ESD for two particles similar in maximum and minimum dimensions but with one having an intricate edge. (This could also demonstrate the same particle, with the edge intricacy resolved in one system but not in another.) Here, the ESPs for the two objects differ by 5% while the ESDs differ by 40%.

3.3 Relationship Between the ESD and the ESP Representation of Length

The relationship between the ESD and the ESP representation of object length is not readily apparent. A simple observation which sheds light on the relationship is that, for a common, naturally occurring particle shape, an ideal sphere, the ESD and ESP are equivalent. For particles with holes or otherwise not conforming to this ideal shape, the ESD describes the diameter of the collapsed area of an object while the ESP describes the diameter of the geometric spread of the object. A higher level of understanding of the relationship can be realized through the observation that μ_{00} is the measured area of a binary object (the sum of all pixels above threshold, regardless of position). Then following the definition of ESD, $ESD = [(4/\pi)\mu_{00}]^{1/2}$, and from the previous section $ESP = [(4/\pi)\pi\alpha\zeta]^{1/2} = 2(\alpha\zeta)^{1/2}$. This is the diameter of the spherical equivalent of the moment-generated ellipse (or sphere, in the case of X-Y symmetry). The relationship between ESD and ESP is perhaps most readily illustrated by their ratio, ESD/ESP which can be expressed as $[(4/\pi)\mu_{00}]^{1/2}/[2(\alpha\zeta)^{1/2}]$ and reduced to $(\mu_{00})^{1/2}/(\pi\alpha\zeta)^{1/2}$. Now recalling Eq. 18, $F = (\mu_{00})/(\pi\alpha\zeta)$, which describes the measured object area over the computed area of the geometric spread of the object, and is directly related to the object "porosity". When porosity is defined as the percentage of the area of the geometric spread of the object which is not filled by the object, $F = (1 - \text{porosity})$ and, hence, could be termed the "fill-factor". Therefore, the ratio, $ESD/ESP = (F)^{1/2}$, the square root of the object fill-factor, a potentially valuable analytical measurement. Additionally, through the functions involved in the ESP computation, information regarding object shape and orientation are also available and, when higher-order moments are considered, automated image pattern recognition is possible.

4.0 Field Measurements

In situ particle imagery was obtained in 40 deployments of the Marine Aggregated Particle Profiling and Enumerating Rover (MAPPER), an instrument system developed during the ONR Accellerated Research Initiative Significant Interactions Governing Marine Aggregation (SIGMA). The MAPPER system and the type of data acquired are described by Costello et al.[9] (this volume) and elsewhere[6,10,11]. Succinctly, MAPPER is a free-fall, vertical profiling system which utilizes structured, visible diode laser illumination to produce a thin sheet of light at the image planes of three, synchronized CCD video cameras of differing magnifications. This unique, synchronous imagery from the three independent cameras allows the investigation of imaging artifacts which would not be noticed nor quantifiable in a system with a single camera.

4.1 Individual particles

Figure 7 shows the ESD and ESP measurements of a circa 15 mm diameter organism ("jellyfish") imaged by the MAPPER "medium field" (MF) camera. Much of the organism is transparent at the sensitivity level of this imaging system, that is, the sensor did not collect enough photons from those areas to raise the output voltage above 0.34 volts. With higher system sensitivity or higher illumination, and/or by manipulating the variables in Equation 1, the transparent areas would be visualized and the ESD measurement would change considerably more substantially than the ESP measurement as is illustrated in the graph at the lower right.

Figure 8 is a mosaic of the three images of a single particle simultaneously acquired by all three MAPPER cameras. It shows the effects of size-measurement artifacts introduced by the spatial resolution (here a function of magnification) of an imaging system combined with electronic overshoot. The images were digitized at 640 x 480 pixels from the three time-coded S-VHS video tapes which are recorded *in situ* during a MAPPER deployment. During this series of deployments (April 1994, East Sound, San Juan Islands, WA), the pixel resolution for the three MAPPER imaging systems were 285 μm, 85 μm, and 17.5 μm, respectively, for the large-field (LF), medium-field (MF), and small-field (SF) cameras. The three images at the bottom of the figure are normalized to the SF magnification.

Figure 9 plots the measurements of the particle from the three systems at GS threshold values 3 through 24. The ESD measurements at the three different manifications differ considerably while the ESP measurements generally agree. Processing at higher GS thresholds, on the other hand, did not affect any of the measurements substantially with the exception of the SF ESP measurement which fell appreciably at GS = 9, apparently when one or both of the organism's antenna becoming "disconnected" at that GS threshold level.

4.2 Size Distributions

Figure 10 shows size distribution spectra (expressed as ESD) for the entire water column for a MAPPER deployment during the East Sound experiment. The data were generated by analysis of the images of 60,130 individual particles. Curves for each of the three systems are plotted as is the interpolated curve for all three systems (solid line). Since the three systems do not have the same field-of-view (FOV), small-scale particle patchiness could affect inter-curve agreement, but we feel that much of the disagreement is due to differences in resolution. This hypothesis is supported by Figure 11 which presents the data for the 60,130 particles using the ESP expression of particle length. Here, the three fields agree more closely in magnitude and in slope.

Finally, Figure 12 shows the interpolated curves from Figures 10 and 11. The curve obtained using the ESP calculation for diameter shows a smoother, more linear slope (B = 3.57 vs 3.49) than that obtained using the ESD because of the better agreement between the different fields. This is consistent with assumption of continuity which is intrinsic to the Junge-type description of the size distribution (Eq. 2).

5.0 Summary

This work originated from analysis of the data generated by MAPPER, a unique, *in situ* instrument which utilizes three synchronized, co-incident imaging systems. Analysis of some of the size distribution spectra from multiple systems showed distinct "bumps" which were indicative of a discrete population. The population, however, was sized differently by the different systems. In the MAPPER system, however, the target range is fixed by the structure-light sheet, the FOV is known, and conventional target sizing is not ambiguous. This work is part of the effort to understand sizing discrepancies between systems.

This contribution demonstrates the following:
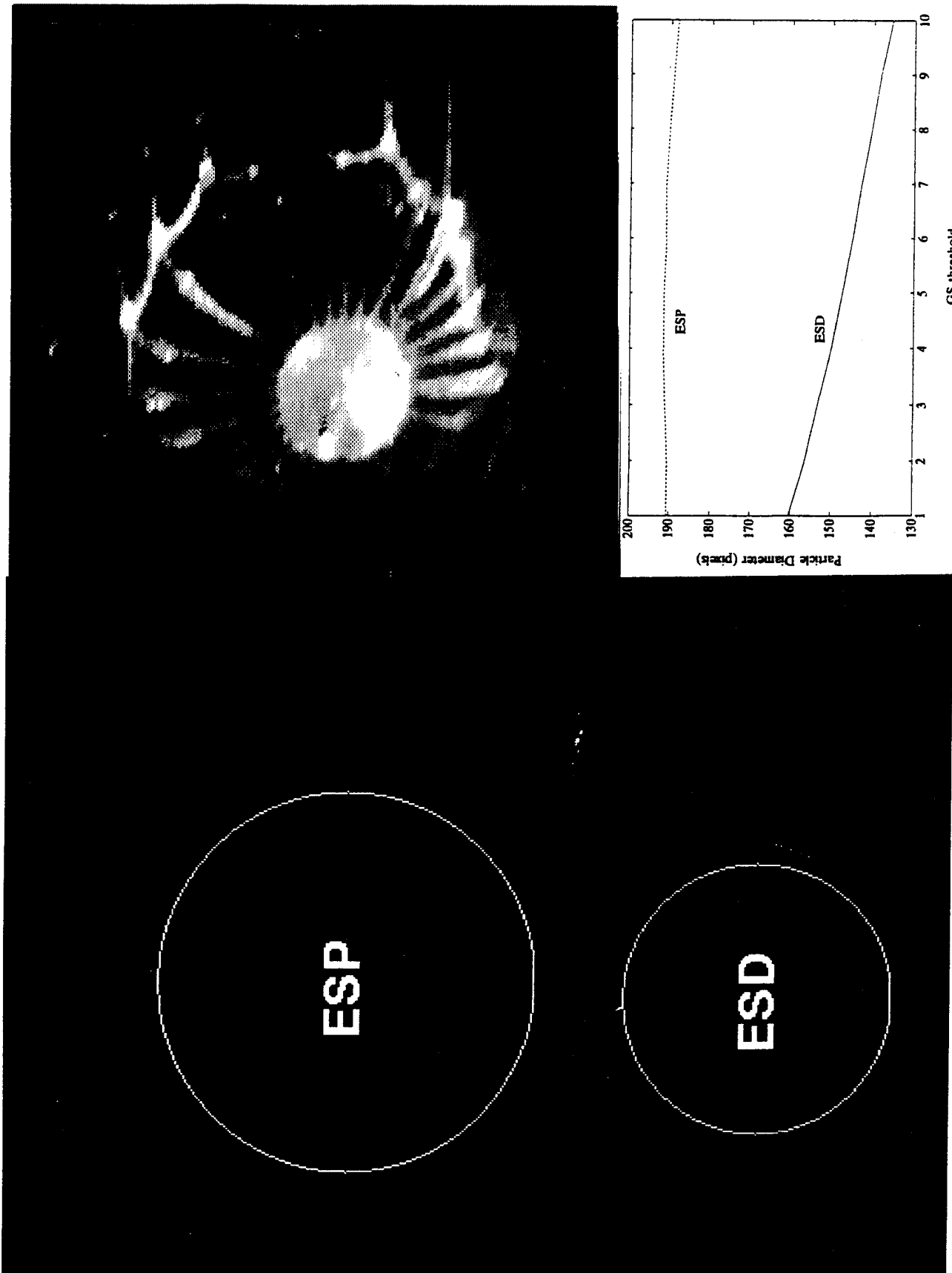
Figure 7. The ESP and ESD representations of the size of a marine organism (see text for discussion).

Figure 8. Three simultaneous images of a copepod at three different magnifications, (see text for discussion).

Figure 10. ESD particle size distribution.

Figure 12. ESD and ESP interpolated size distributions.

Figure 9. Particle diameter espressed as ESD and ESP.

Figure 11. ESP particle size distribution.

1) System response to bright targets is a function of target contrast, sensor sensitivity, threshold setting, and image resolution. Its effect on particle size can be interpreted and corrected.

2) Image resolution affects derived particle size spectra. Errors depend on particle contrast, threshold setting, resolution, and particle compactness. A modified size descriptor ESP, which is $ESD/(F)^{1/2}$, has a much lower sensitivity than ESD to variations in resolution. This allows more accurate intercalibration of imaging systems of differing resolution and radiometric sensitivity.

3) For high-resolution systems, ESD/ESP provides a measure of the compactness of the particles and the method utilized to generate the ESP also provides particle shape and orientation information, prerequisites for automated pattern recognition.

In summary, through the use of Digital Image Processing, researchers are now able to rapidly identify, enumerate, size, and classify targets within an image. An automated DIP system, moreover, allows for unattended processing of a virtually unlimited number of images. Great care needs to be taken, however, to insure that the artifacts introduced by the finite spatial resolution and radiometric sensitivity of the system are understood and accounted for in the data produced. We hope this work makes a contribution toward a greater understanding of the strengths and limitations of DIP technology in *in situ* applications where the optical properties of potential targets are often not well known and, by definition, not controlled.

Acknowledgements

References

1. Alldredge, A.L., U. Passow, and B.E. Logan (1993) The abundance and significance of a class of large, transparent organic particles in the ocean, Deep-Sea Res. 40: 1131-1140.

2. Passow, U., A.L. Alldredge and B.E. Logan, In press. The role of particulate carbohydrate exudates in the flocculation of diatom blooms, Deep-Sea Res.

3. Hu, M. (1962) Visual Pattern Recognition by Moment Invariants. IRE Trans. Inf. Theory, IT-8, 179.

4. Teague, M.R. (1980) Image analysis via the the general theory of moments. J. Opt. Soc. Am., v. 70, n. 8.

5. Dudani, S.A., K.A. Breeding, and R.B. McGee. (1977) Aircraft identification by moment invariants. IEEE Trans. Comput. C-26, 39-45.

6. Costello, D.K., K.L. Carder and R.G. Steward. (1991) Development of the Marine Aggregated Particle Profiling and Enumerating Rover (MAPPER). Underwater Imaging, Photography, and Visibility, Richard W. Spinrad, Editor, Proc. SPIE 1537, 161-172.

7. Carder, K. L. and D. K. Costello (1994) Optical effects of Large Particles. Ocean Optics. R.W. Spinrad, K.L. Carder, and M.J. Perry, and R.W. Spinrad, editors, Oxford University Press, New York, N.Y.

8. Costello, D.K., K.L. Carder, P.R. Betzer, and R.W. Young. 1989. In-situ holographic imaging of settling particles: Applications for Individual Particle Dynamics and Oceanic Flux Measurements. Deep-Sea Research, 36, 10, 1989.

9. Costello, D.K., W. Hou and K.L.Carder (1994) Some effects of the sensitivity threshold and spatial resolution of a particle imaging system on the shape of the measured particle size distribution. Ocean Optics XII, Bergen, Norway.

10. Costello, D.K, K.L. Carder and W. Hou (1992) Structured visible diode laser illumination for quantitative underwater imaging. Ocean Optics XI. Gary D. Gilbert, Editor, Proc. SPIE 1750, 95-103.

11. Hou, W., D.K. Costello, K.L. Carder and R.G. Steward (1994) High-resolution Marine Particle data from MAPPER, a new, in situ optical ocean instrument. EOS AGU/ASLO (75), 3, 21.

UNIVERSITY OF SOUTH FLORIDA
Marine Science Department
140 Seventh Avenue South
St. Petersburg, FL 33701
INTERNET: dkc@monty.marine.usf.edu
bstew@monty.marine.usf.edu
OMNET: k.carder
Voice: 813-893-9503
FAX: 813-893-9189
December 14, 1993

DATA REPORT
(9 text pages and 29 figures)
SIGMA TANK EXPERIMENT

David K. Costello, Kendall L. Carder and Robert G. Steward

This report is presented in three sections, **FILTER PAD ABSORPTION, TRANSMISSOMETRY,** and **IMAGERY.** Table 1 shows when our different samples were collected and a collection of figures which will let you get a qualitative feel for the data. The numbers which generated all this are in ASCII format (14 files, 126 Kbytes). The ASCII text file, CARDER.TXT, is appended to this document. It explains the data file contents, measurement procedures, and units.

1. FILTER PAD ABSORPTION

Figure 1 - shows a surface representing detrital spectral absorption (m^{-1}) for the period day 9 through day 14.5. All these spectral plots show the amplitude of the absorption coefficient in the z-axis (up), time (sample day) in the y-axis (to the right) and spectral channel (256 channels, nominal bandwidth 2.5 nm) on the x-axis (to the left). The curve was normalized at the chlorophyll-a absorption peak at 673 nm to remove the effects of pigment that was not fully extracted by the hot methanol extraction. The maximum detrital absorption coefficient $a_d = 0.64\ m^{-1}$ was measured on day 12.

Figure 2 - shows the surface for pigment spectral absorption (m^{-1}). The blue peak (438 nm) and the red peak (673 nm) are denoted.

Figure 3 - has the same axis as Fig. 2 and is Fig. 2 data normalized at 673 nm. Since the 673 absorption peak is "chlorophyll-a specific", this normalization removes the chlorophyll-a contribution and changes are due to other substances or package effects.

Figure 4 - shows **specific absorption** (m^2/(mg chl a)) and, therefore, is related to the "efficiency" of the absorbing substance. The peaked sample is a result of the relatively "low" chlorophyll numbers (59 mg/m^3) for day 12.5.

CARDER LAB - SIGMA TANK EXPERIMENT DATA REPORT

Figure 5 - ditto Figure 4 using a chlorophyll-a number for day 12.5 equal to 134 mg/m^3. This number was interpolated from Alice's data and our 673 nm absorption data and allows one to see some features that are swamped in figure 4. Most of the structure along the time axis (to the right) is from the regular increase in absorption (across the spectrum, but more so in the blue end) between morning and afternoon samples. The only exception to this can be seen in day 11 when it actually decreased.

Figure 6 - shows detrital/total absorption which increased during the day and decreased during the night until day 11 when the pattern reversed.

Figure 7 - shows the chl_a specific absorption coefficient (m^2/mg). Note that this measure of light harvesting ability was low at night and rose during days 9, 10, 12, and 13 but dropped during day 11. The apparently dramatic rise on day 12, however, argues that the chl_a measurement on day 12.5 is inaccurate.

Figure 8 - shows the measured absorption coefficient at 673 nm vs. measured chlorophyll (Alldredge data including day 12.5 measurements). The r^2 is 0.79.

Figure 9 - same as Figure 8 with the day 12.5 chl_a measurement excluded. The r^2 is 0.94.

Figure 10 - shows the spectra for the "average" morning and afternoon.

Figure 11 - shows the curves for the daily morning samples. Note the steady increases from day 7 to day 10, the leap up to day 11 values, then the decline on days 12 and 13. More interesting, I think, is the change in the pigment composition which can be seen by comparing day 10 with day 13 between 475 and 550 nm. This kind of change is typical of increasing accessory pigments.

Figure 12 - shows sample data before and after filtering with a 7 element Hanning window. The smoothing is required to utilize derivative analysis.

Figure 13 - shows weight specific absorption coefficient spectra (m^2/mg) for different pigments. These are the kind of spectra used in the derivative analysis which follows. These data are from Bidigare et al. 1990.

Figure 14 - uses the 2nd order spectral derivative to enhance curvature of the spectra and, since positive bumps in the spectra mean something is absorbing in that band, can be used for pigment identification. Since this is a second derivative, the negative peaks in the plot correspond to positive peaks (negative curvature) in the data. The four plots are averages from a). the first "half" of the experiment (day 7 to day 11), b). the second half (day 11 to day 14.5), c). all mornings, and d). all afternoons. The major chlorophyll-a peaks at 438 and 673 are obvious as is a minor chlorophyll-a peak ca. 620. Evidence of Chlorophyll-c absorption shows up around 630, 590, and 460. There is no indication of any chlorophyll-b. The two peaks at 413 and 420

CARDER LAB - SIGMA TANK EXPERIMENT DATA REPORT

represent a major spectral feature and are hard to figure. Signal/noise is lowest in the blue, but this isn't noise. The two sets of curves track right down to 400 nm. It could be that photoprotective carotenoid activity throughout the day/(experiment) shifted the afternoon/(last half) absorption peak toward the red whereas the minor chlorophyll-c peak around 410-415 nm was enhanced by absorption from another substance in the same band in the morning/(first half) samples. Bacteria, flagellates, phaeophytin a, and ciliates all have been found to have an absorption band between 410-415 nm.

2. TRANSMISSOMETRY

Figure 15 - shows samples of the transmissometer trace for days 8 through 13. The water started to clear a bit on days 12 and 13 either from aggregates dropping out or scavenging the smaller particles.

Figure 16 - shows the minimum, mean, and maximum attenuation coefficient for all samples (at depth).

Figure 17 - shows the mean data curve from Figure 12 and another curve showing only the daily samples nearest to 1530 hours. This shows the effect the thermocline development had on the deep layer. Material settled out of the warmer upper layer during the day raising the concentration in the deeper layer.

Figure 18 - shows the water clarity associated with thermocline development and dissipation for day 11. The x-axis is time but also indicates depth increasing to the right, the instrument was slowly profiled. At 0530 hours the tank was well mixed. At 1600 hours a strong thermocline had developed between 10 and 20 cm and there was also some structure to 30 cm (note that c increases on average). By 2000 hours the tank was again well mixed.

Figure 19 - shows particulate attenuation at 660 nm (c_p660), particulate absorption at 660 nm (a_p660), derived particle scattering at 660 nm (b_p660), and the single-scattering albedo, omega (b_p/c_p), which can be thought of as an indicator of particle "packaging" since it involves both scattering and absorption and, when particles aggregate, for example, scattering is affected much more readily than absorption.

Figure 20 shows attenuation (corrected for the instrument's forward-scatter acceptance angle) vs. Alice's particulate nitrogen data. The correlation is .9998 for the first four days (8-11) and .995 for all data.

CARDER LAB - SIGMA TANK EXPERIMENT DATA REPORT

3. IMAGERY

The MAPPER design utilizes instrument translation to define the sample volume. Since translation was not possible in the tank, we attempted to use the volume imaged per frame (field-of-view x sheet thickness) to determine the sample volume. The optical effects of the increasing particle concentration changed the sheet thickness and, therefore, the sample volume. The primary effects, forward-scatter, absorption, and the changing S/N in 90° scatter (reflectivity) are convolved and result in a sheet thickness (sample volume) which is a function not only of the bulk optical properties of the medium but also of the individual particle reflectivity. It is always the case, for any imaging system, that the sample volume is a function of target reflectivity. At some level of low reflectivity (high transparency) the target return is below the sensor threshold. Usually, with structured-light systems, bulk forward-scatter and absorption do not introduce significant uncertainty into sample volume calculations. In the tank, however, these effects became increasingly significant as attenuation rose from high (≈ 2.5 m^{-1}) to extreme (≈ 9 m^{-1}) values. In these circumstances, measuring sheet thickness with a calibrated reflector, for example, yields the sample volume for that reflectance, which is not necessarily the sample volume for the particles.

Figure 21 illustrates this hypothetically. The three curves depict intensity distributions across a structured-light sheet at different attenuation coefficients. Here the original gaussian distribution has been redistributed by very-near-forward scatter and dampened by absorption. The horizontal lines are sensor response thresholds for differing target reflectances. Projecting the intersections of the lines with the curves onto the abscissa defines the differing sheet thickness for differing target reflectivity at differing attenuation values. The sheet thickness for a 10% reflector in this scenario, for example, varies from 1.2, 2.4, and 3.9 mm for c values 0.5, 2.5, and 5.0 m^{-1} respectively. A 1.0% reflector would be detected in about the same thickness at c = 0.5 and 5.0, but in a larger thickness at c = 2.5, and a 0.1% (or less) reflector won't be imaged at all at c much larger than 2.5.

The only measured tank optical variable available to help deconvolve some of this was attenuation. So, we took our first sheet-thickness measurements in all fields (the lowest c values) and modelled the shape of the intensity distribution that would have resulted at the subsequently measured c values. On day 10.5, the gain was increased on the medium-field camera and the electronic shutter disabled on the small-field camera. So the modelling for these fields used day 7 measured thickness for days 7-10 and day 10.5 measured thickness for days 10.5-14. Since the very-near-forward scattering function was unknown, we used the assumption that all attenuation was due to absorption and scattering out of the sheet. This is, admittedly, an imperfect assumption since it ignores the redistribution of intensity by very-near-forward scattering which, again, is unknown.

Figure 22 provides an overview of the results. It shows the range of the changes (about 2-3 orders of magnitude maximum) for the cumulative size distributions for particles greater than 100 μm. The data from the medium and large fields agree fairly well. The shape and slope of the small-field curves look reasonable but are a factor of 2 or so below the other curves. This

could be a result of the S/N ratio for this field, that is, the small-field curves may be too low. On the other hand, bulk, very-near-forward scatter could have effectively increased the sheet thickness for the two, lower magnification fields more than attenuation decreased it. That is, the medium and large field curves may be too high.

Figure 23 is a 3-D plot of the non-accumulated spectra (from $\approx 100 \ \mu m$ to ≈ 8 mm ESD). To mesh the small-field data with the other data the first five bins were multiplied by a factor of two. It is presented to show the "shape" of the database. The increase in the large size is notable but so is the lack of dramatic increase in the smaller size classes.

Figure 24 shows the change in the slope of the accumulated size distribution spectra (#/l/mm) determined from the large-field camera data from day 7 and day 14. The exponent in the curve-fit changes from -8.6 for day 7 to -4.9 for day 14.

In discussion, it is difficult to determine error bars for these numbers. Without the ability to translate the instrument, the sample volume determination is problematic, especially for the smaller size bins. To get a feeling for how good or bad these results might be, we converted to particle volumes assuming that, especially in a tank, total particle volume will be a conservative function of primary production.

Figure 25, then, shows total particle volume vs. time for our smallest size bins ($85 <$ dia $<$ $170 \ \mu m$). Also plotted is Alice's primary productivity data. The volume curve seems out-of-phase with the production curve but does resemble the first "hump" of Alice's data if, indeed, there are actually two "humps" in that data.

Figure 26 shows the same for Marine Snow (dia. $> 500 \ \mu m$), note the ordinate change of scale. Considering this data, it looks like there could, indeed, be two real humps in the primary productivity data.

Figure 27 is the same plot for big aggregates (dia. > 2 mm). Again, note the change in ordinate scale. The absence of the first hump seems logical (particles need time to get this big) but this absence, combined with the presence of the secondary hump, might argue for two production cycles. The first cycle associated with small particles and the second cycle associated with production involving the very large aggregates.

Finally, our size spectras come from three independent systems operating at different resolution levels. This difference in resolution can distort particle size distributions when transformed to ESD distributions, especially when dealing with porous particles (particles with intricate edges or holes). These distortions are, again, a function of the resolution of each system and therefore, would not be detected in data from a single system. To deal with this, our data have been corrected for particle porosity on an individual-particle basis. This doesn't change total particle numbers but it does affect the slope of the distribution. Change is not major unless the targets have intricate edges and/or contain holes. Many target algorithms trace edges and compute the enclosed area without excluding holes. Since we are very interested in

how the particles interact with light, all our algorithms exclude any holes.

Figure 28 shows how the porosity correction affects the slopes of data from this experiment. Differences in comparisons with spectra generated with algorithms which do not exclude holes would be more radical. Note that the first bin of every field is discarded in the correction since, generally, it only contributes particles to larger bins while gaining none.

Figure 29 illustrates the effect of expressing a particle areal measurement in ESD units, with and without hole exclusion. Any "real" size distribution will be distorted. (Of course, "real" size can differ according to what information is desired, the problem is how to compare measurements made at different resolutions.) The "Real" size for this exercise is defined as the "average" particle diameter whether or not there are holes. Essentially, an ESD conversion (with holes included or excluded) shrinks all the particles and moves the measured curve to the left. When excluding holes, more holes can be resolved in larger particles and the larger particles are shrunk more. The result is fewer bins and an increased negative slope. If these are variably "holey" particles (invariably the case) and holes are not excluded, the measured curve lies to the right of the "real" curve. Again, the larger sizes have more resolvable holes and, this time, hole inclusion results in more bins and a less negative slope. The ESD conversion then moves the resulting curve to the left, compresses the bins, and increases the negative slope. This slope increase, however, is less severe than in the first case because the ESD distortion is only driven by the intricacy of the particle edge, not by the edge plus the interior.

CARDER LAB - SIGMA TANK EXPERIMENT DATA REPORT

Contents of the file CARDER.TXT

SIGMA TANK EXPERIMENT
K. CARDER DATA

Description of data files:

Total number = 14 (125,932 bytes)

File	Size (bytes)	Description
ABS_TIME.DAT	1x13 (210)	Day and time for filter pad absorption samples (eg. 8.25 = 0800 hours, day 8)
LAMDA.DAT	1x122 (2,196)	Wavelength vector (452-753 nm) for all absorption matrices.
TOTAL.ABS	122x13 (25,620)	Total filter pad absorption coefficient, 13 samples, units - reciprocal meter. Method follows Mitchell and Kiefer 1988 (DSR 35(5) 635-663) using the pathlength amplification factor coefficients of Bricaud and Stramski 1090 (L&O 35(3) 562-582).
DETRITAL.ABS	122x13 (25,620)	Filter pad absorption (m^-1) after pigment extraction with hot methanol (a modification of the method of Kishino, et al. 1985 (Bull. Mar. Sci. 37(2) 634-642)
PIGMENT.ABS	122x13 (25,620)	The result of subtracting the detrital absorption matrix from the total absorbtion matrix (m^-1).
C_TIME.DAT	1x20 (360)	Day and time for the twenty transmissometer profiles.
C_METER.DAT	124x20 (39,928)	Matrix of transmissometer profiles, units m^-1. Each profile has 124 data points which are average readings at 0.5 second intervals, therefore, each record represents 62 seconds. The first part of each record (ca 50 data points) shows the clearer, upper layer (if present).

CARDER LAB - SIGMA TANK EXPERIMENT DATA REPORT

MAP_TIME.DAT 1x10 (162)   Day and time for the 10 MAPPER image module deployments. Each deployment generated data from a small-field, a medium-field, and a large-field camera, that is, three overlapping data matrices (SMALL.DAT, MEDIUM.DAT, & LARGE.DAT).

S_DIABIN.DAT 1x14 (252)   Equivalent Spherical Diameter Size bins (14 centers, in units mm) used for plotting SMALL.DAT, an array of 8 size distribution spectra.

M_DIABIN.DAT 1x14 (252)   Equivalent Spherical Diameter Size bins (14 centers, in units mm) used for plotting MEDIUM.DAT, an array of 8 size distribution spectra.

L_DIABIN.DAT 1x14 (252)   Equivalent Spherical Diameter Size bins (14 centers, in units mm) used for plotting LARGE.DAT, an array of 8 size distribution spectra.

SMALL.DAT   14x8 (1820)   Eight Accumulated Particle Number Spectra (units - #/l/mm). One for each sample day 7 through and including 14 (morning samples) which consist of 14 size bins listed in S_DIABIN.DAT. Each individual particle was binned according to the equivalent spherical diameter after a correction for particle porosity relative to an ideal sphere.

MEDIUM.DAT   14x8 (1820)   Eight Accumulated Particle Number Spectra (units - #/l/mm). One for each sample day 7 through and including 14 (morning samples) which consist of 14 size bins listed in M_DIABIN.DAT. Each individual particle was binned according to the equivalent spherical diameter after a correction for particle porosity relative to an ideal sphere.

CARDER LAB - SIGMA TANK EXPERIMENT DATA REPORT

LARGE.DAT   14x8 (1820)   Eight Accumulated Particle Number Spectra (units - #/l/mm). One for each sample day 7 through and including 14 (morning samples) which consist of 14 size bins listed in S_DIABIN.DAT. Each individual particle was binned according to the equivalent spherical diameter after a correction for particle porosity relative to an ideal sphere.

SIGMA TANK EXPERIMENT - CARDER SAMPLES (dkc 5/31/93)

SAMPLE DAY	C-METER (upper and lower levels) (sample #)	ABSORPTION (total, detritus, & pigments) (sample #)	IMAGERY (all three magnifications) (sample #)
7.25		1	1
7.50			
7.75			
8.00			
8.25		2	2
8.50			
8.75	1		
9.00			
9.25	2	3	
9.50	3,4	4	3
9.75			
10.00			
10.25	5	5	
10.50		6	4
10.75	6,7		5
11.00			
11.25	8,9	7	6
11.50	10,11	8	7
11.75	12,13		
12.00			
12.25	14	9	8
12.50	15,16	10	9
12.75	17		
13.00			
13.25	18	11	10
13.50	19	12	
13.75			
14.00			
14.25	20	13	

Table 1
SIGMA TANK DATA REPORT
CARDER LAB

Table 2   Total absorption coefficient. Day is given in fractions to indicate time of day. Wavelength is in nm.

total abs.cost

wavelength	date	7.33	8.33	9.33	9.67	10.33	10.67	11.33	11.67	12.33	12.67	13.33	13.67	14.67
403		2.89E-01	5.28E-01	9.94E-01	1.33E+00	1.40E+00	2.48E+00	3.22E+00	2.91E+00	2.75E+00	2.86E+00	2.11E+00	2.29E+00	2.17E+00
405		2.91E-01	5.49E-01	9.93E-01	1.30E+00	1.43E+00	2.66E+00	3.28E+00	2.88E+00	2.83E+00	2.87E+00	2.15E+00	2.51E+00	2.07E+00
408		2.96E-01	5.54E-01	1.07E+00	1.35E+00	1.48E+00	2.59E+00	3.37E+00	3.01E+00	2.90E+00	2.72E+00	2.10E+00	2.47E+00	2.13E+00
411		3.06E-01	5.95E-01	1.08E+00	1.36E+00	1.56E+00	2.72E+00	3.57E+00	2.89E+00	2.93E+00	2.93E+00	2.18E+00	2.40E+00	2.26E+00
413		3.20E-01	6.03E-01	1.07E+00	1.39E+00	1.56E+00	2.69E+00	3.50E+00	3.00E+00	3.00E+00	2.93E+00	2.16E+00	2.47E+00	2.22E+00
416		3.21E-01	6.14E-01	1.10E+00	1.41E+00	1.56E+00	2.83E+00	3.51E+00	2.99E+00	2.97E+00	3.11E+00	2.20E+00	2.48E+00	2.26E+00
419		3.35E-01	6.09E-01	1.10E+00	1.44E+00	1.63E+00	2.82E+00	3.57E+00	3.11E+00	2.95E+00	3.06E+00	2.22E+00	2.57E+00	2.26E+00
421		3.25E-01	6.23E-01	1.10E+00	1.45E+00	1.65E+00	2.83E+00	3.68E+00	3.12E+00	2.98E+00	3.03E+00	2.25E+00	2.59E+00	2.31E+00
424		3.43E-01	6.55E-01	1.14E+00	1.47E+00	1.65E+00	2.84E+00	3.64E+00	3.13E+00	3.06E+00	3.10E+00	2.28E+00	2.59E+00	2.34E+00
427		3.43E-01	6.68E-01	1.15E+00	1.47E+00	1.68E+00	2.90E+00	3.69E+00	3.11E+00	3.08E+00	3.17E+00	2.26E+00	2.55E+00	2.28E+00
430		3.52E-01	6.89E-01	1.16E+00	1.55E+00	1.71E+00	2.95E+00	3.80E+00	3.20E+00	3.12E+00	3.19E+00	2.25E+00	2.61E+00	2.31E+00
432		3.58E-01	7.06E-01	1.18E+00	1.53E+00	1.70E+00	2.98E+00	3.85E+00	3.22E+00	3.15E+00	3.23E+00	2.30E+00	2.64E+00	2.33E+00
435		3.67E-01	7.20E-01	1.16E+00	1.53E+00	1.63E+00	2.98E+00	3.92E+00	3.30E+00	3.15E+00	3.21E+00	2.30E+00	2.62E+00	2.35E+00
438		3.59E-01	7.34E-01	1.19E+00	1.56E+00	1.71E+00	2.97E+00	3.89E+00	3.19E+00	3.12E+00	3.20E+00	2.28E+00	2.57E+00	2.27E+00
440		3.59E-01	7.27E-01	1.17E+00	1.52E+00	1.68E+00	2.93E+00	3.88E+00	3.13E+00	3.12E+00	3.15E+00	2.25E+00	2.54E+00	2.29E+00
443		3.53E-01	6.99E-01	1.14E+00	1.50E+00	1.64E+00	2.86E+00	3.67E+00	3.08E+00	3.00E+00	3.06E+00	2.17E+00	2.51E+00	2.21E+00
446		3.33E-01	6.81E-01	1.09E+00	1.44E+00	1.56E+00	2.79E+00	3.65E+00	2.89E+00	2.89E+00	3.03E+00	2.15E+00	2.43E+00	2.17E+00
449		3.20E-01	6.69E-01	1.06E+00	1.41E+00	1.53E+00	2.65E+00	3.51E+00	2.76E+00	2.84E+00	2.89E+00	2.05E+00	2.34E+00	2.08E+00
451		3.12E-01	6.40E-01	1.02E+00	1.37E+00	1.49E+00	2.57E+00	3.33E+00	2.63E+00	2.71E+00	2.82E+00	1.92E+00	2.30E+00	2.03E+00
454		3.03E-01	6.29E-01	9.94E-01	1.33E+00	1.43E+00	2.51E+00	3.25E+00	2.52E+00	2.62E+00	2.67E+00	1.88E+00	2.23E+00	1.94E+00
457		2.95E-01	6.11E-01	9.54E-01	1.28E+00	1.40E+00	2.42E+00	3.13E+00	2.41E+00	2.56E+00	2.61E+00	1.81E+00	2.19E+00	1.92E+00
459		2.89E-01	5.99E-01	9.20E-01	1.26E+00	1.40E+00	2.34E+00	3.02E+00	2.33E+00	2.46E+00	2.55E+00	1.77E+00	2.10E+00	1.86E+00
462		2.86E-01	5.83E-01	8.94E-01	1.22E+00	1.33E+00	2.25E+00	2.93E+00	2.26E+00	2.39E+00	2.46E+00	1.73E+00	2.01E+00	1.81E+00
465		2.78E-01	5.63E-01	8.64E-01	1.19E+00	1.29E+00	2.21E+00	2.84E+00	2.10E+00	2.31E+00	2.36E+00	1.66E+00	1.94E+00	1.75E+00
468		2.73E-01	5.43E-01	8.27E-01	1.14E+00	1.23E+00	2.12E+00	2.69E+00	2.01E+00	2.25E+00	2.27E+00	1.61E+00	1.90E+00	1.67E+00
470		2.59E-01	5.16E-01	7.91E-01	1.12E+00	1.20E+00	2.01E+00	2.61E+00	1.93E+00	2.13E+00	2.15E+00	1.54E+00	1.83E+00	1.61E+00
473		2.48E-01	4.87E-01	7.54E-01	1.06E+00	1.14E+00	1.94E+00	2.45E+00	1.82E+00	2.05E+00	2.03E+00	1.44E+00	1.78E+00	1.54E+00
476		2.33E-01	4.67E-01	7.15E-01	1.02E+00	1.08E+00	1.85E+00	2.29E+00	1.76E+00	1.96E+00	1.94E+00	1.38E+00	1.69E+00	1.46E+00
479		2.28E-01	4.42E-01	6.90E-01	9.78E-01	1.05E+00	1.78E+00	2.22E+00	1.67E+00	1.87E+00	1.87E+00	1.34E+00	1.62E+00	1.40E+00
481		2.20E-01	4.22E-01	6.67E-01	9.41E-01	1.01E+00	1.69E+00	2.11E+00	1.62E+00	1.81E+00	1.79E+00	1.28E+00	1.56E+00	1.37E+00
484		2.12E-01	4.17E-01	6.45E-01	9.13E-01	9.79E-01	1.65E+00	2.05E+00	1.53E+00	1.74E+00	1.73E+00	1.24E+00	1.54E+00	1.33E+00
487		2.05E-01	4.01E-01	6.30E-01	8.98E-01	9.55E-01	1.60E+00	2.02E+00	1.48E+00	1.72E+00	1.68E+00	1.20E+00	1.50E+00	1.31E+00
490		1.99E-01	3.93E-01	6.12E-01	8.79E-01	9.24E-01	1.57E+00	1.95E+00	1.47E+00	1.67E+00	1.65E+00	1.18E+00	1.47E+00	1.26E+00
493		1.92E-01	3.84E-01	5.94E-01	8.66E-01	9.15E-01	1.54E+00	1.93E+00	1.41E+00	1.65E+00	1.59E+00	1.15E+00	1.42E+00	1.22E+00
495		1.88E-01	3.73E-01	5.86E-01	8.42E-01	8.92E-01	1.51E+00	1.87E+00	1.37E+00	1.60E+00	1.56E+00	1.10E+00	1.38E+00	1.18E+00
498		1.78E-01	3.62E-01	5.66E-01	8.23E-01	8.75E-01	1.46E+00	1.82E+00	1.32E+00	1.56E+00	1.50E+00	1.06E+00	1.34E+00	1.14E+00

total abs.cost

Table 2 Total absorption coefficient. Day is given in fractions to indicate time of day. Wavelength is in nm.

wavelength	date	7.33	8.33	9.33	9.67	10.33	10.67	11.33	11.67	12.33	12.67	13.33	13.67	14.67
501		1.72E-01	3.51E-01	5.45E-01	8.02E-01	8.44E-01	1.40E+00	1.76E+00	1.27E+00	1.48E+00	1.45E+00	1.03E+00	1.28E+00	1.09E+00
504		1.63E-01	3.39E-01	5.30E-01	7.72E-01	8.15E-01	1.35E+00	1.68E+00	1.21E+00	1.43E+00	1.40E+00	9.86E-01	1.23E+00	1.05E+00
507		1.56E-01	3.24E-01	5.08E-01	7.45E-01	7.81E-01	1.31E+00	1.61E+00	1.16E+00	1.36E+00	1.31E+00	9.15E-01	1.16E+00	9.84E-01
509		1.50E-01	3.12E-01	4.90E-01	7.22E-01	7.64E-01	1.24E+00	1.56E+00	1.10E+00	1.30E+00	1.25E+00	8.63E-01	1.10E+00	9.16E-01
512		1.44E-01	3.00E-01	4.72E-01	6.99E-01	7.35E-01	1.21E+00	1.50E+00	1.06E+00	1.24E+00	1.19E+00	8.16E-01	1.06E+00	8.74E-01
515		1.37E-01	2.90E-01	4.51E-01	6.69E-01	7.01E-01	1.16E+00	1.43E+00	1.01E+00	1.19E+00	1.14E+00	7.76E-01	1.00E+00	8.30E-01
518		1.32E-01	2.76E-01	4.40E-01	6.45E-01	6.81E-01	1.11E+00	1.37E+00	9.58E-01	1.13E+00	1.09E+00	7.36E-01	9.50E-01	7.86E-01
521		1.26E-01	2.66E-01	4.23E-01	6.29E-01	6.54E-01	1.07E+00	1.33E+00	9.34E-01	1.08E+00	1.03E+00	6.94E-01	9.04E-01	7.45E-01
523		1.22E-01	2.57E-01	4.05E-01	6.02E-01	6.31E-01	1.03E+00	1.27E+00	8.85E-01	1.05E+00	9.94E-01	6.57E-01	8.66E-01	7.09E-01
526		1.17E-01	2.47E-01	3.88E-01	5.84E-01	6.00E-01	9.91E-01	1.23E+00	8.57E-01	1.02E+00	9.56E-01	6.30E-01	8.35E-01	6.78E-01
529		1.10E-01	2.37E-01	3.75E-01	5.71E-01	5.83E-01	9.64E-01	1.18E+00	8.13E-01	9.70E-01	9.11E-01	5.97E-01	7.96E-01	6.43E-01
532		1.05E-01	2.26E-01	3.64E-01	5.51E-01	5.60E-01	9.33E-01	1.15E+00	7.80E-01	9.39E-01	8.81E-01	5.78E-01	7.72E-01	6.23E-01
535		1.03E-01	2.17E-01	3.49E-01	5.30E-01	5.36E-01	8.94E-01	1.11E+00	7.44E-01	9.13E-01	8.53E-01	5.59E-01	7.43E-01	5.94E-01
538		9.80E-02	2.08E-01	3.37E-01	5.10E-01	5.14E-01	8.63E-01	1.06E+00	7.21E-01	8.66E-01	8.09E-01	5.27E-01	7.03E-01	5.70E-01
540		9.19E-02	1.96E-01	3.20E-01	4.91E-01	4.94E-01	8.23E-01	1.01E+00	6.81E-01	8.33E-01	7.66E-01	5.02E-01	6.82E-01	5.35E-01
543		8.74E-02	1.84E-01	3.03E-01	4.67E-01	4.71E-01	7.83E-01	9.57E-01	6.49E-01	7.87E-01	7.26E-01	4.73E-01	6.40E-01	5.14E-01
546		8.18E-02	1.73E-01	2.91E-01	4.42E-01	4.43E-01	7.50E-01	8.99E-01	6.16E-01	7.47E-01	6.78E-01	4.40E-01	6.04E-01	4.91E-01
549		7.71E-02	1.60E-01	2.69E-01	4.16E-01	4.12E-01	7.03E-01	8.44E-01	5.83E-01	7.10E-01	6.30E-01	4.12E-01	5.69E-01	4.57E-01
552		7.19E-02	1.48E-01	2.53E-01	3.89E-01	3.82E-01	6.65E-01	7.82E-01	5.41E-01	6.69E-01	5.97E-01	3.79E-01	5.36E-01	4.29E-01
555		6.73E-02	1.35E-01	2.35E-01	3.66E-01	3.55E-01	6.22E-01	7.33E-01	5.01E-01	6.22E-01	5.49E-01	3.54E-01	5.12E-01	4.05E-01
558		6.20E-02	1.23E-01	2.19E-01	3.39E-01	3.25E-01	5.85E-01	6.87E-01	4.64E-01	5.87E-01	5.05E-01	3.24E-01	4.85E-01	3.78E-01
561		5.89E-02	1.14E-01	2.04E-01	3.20E-01	3.02E-01	5.50E-01	6.45E-01	4.33E-01	5.49E-01	4.79E-01	3.09E-01	4.56E-01	3.56E-01
563		5.57E-02	1.05E-01	1.92E-01	3.03E-01	2.85E-01	5.23E-01	6.11E-01	4.07E-01	5.21E-01	4.59E-01	2.84E-01	4.38E-01	3.51E-01
566		5.33E-02	9.95E-02	1.84E-01	2.89E-01	2.67E-01	5.04E-01	5.90E-01	3.85E-01	5.09E-01	4.47E-01	2.83E-01	4.29E-01	3.45E-01
569		5.07E-02	9.39E-02	1.77E-01	2.80E-01	2.59E-01	4.92E-01	5.67E-01	3.77E-01	4.94E-01	4.30E-01	2.76E-01	4.20E-01	3.32E-01
572		5.02E-02	9.05E-02	1.74E-01	2.77E-01	2.54E-01	4.91E-01	5.67E-01	3.73E-01	4.95E-01	4.15E-01	2.73E-01	4.19E-01	3.33E-01
575		4.93E-02	9.11E-02	1.75E-01	2.78E-01	2.56E-01	4.92E-01	5.64E-01	3.80E-01	4.98E-01	4.20E-01	2.73E-01	4.22E-01	3.31E-01
578		4.93E-02	9.02E-02	1.77E-01	2.78E-01	2.56E-01	5.00E-01	5.65E-01	3.87E-01	5.05E-01	4.22E-01	2.82E-01	4.22E-01	3.38E-01
581		4.93E-02	9.10E-02	1.80E-01	2.81E-01	2.61E-01	5.04E-01	5.78E-01	3.93E-01	5.09E-01	4.33E-01	2.83E-01	4.26E-01	3.48E-01
584		4.89E-02	9.01E-02	1.80E-01	2.83E-01	2.62E-01	5.13E-01	5.88E-01	4.06E-01	5.13E-01	4.31E-01	2.89E-01	4.32E-01	3.50E-01
587		4.85E-02	9.00E-02	1.81E-01	2.83E-01	2.69E-01	5.14E-01	5.81E-01	4.11E-01	5.20E-01	4.35E-01	2.92E-01	4.32E-01	3.51E-01
589		4.81E-02	8.83E-02	1.79E-01	2.79E-01	2.68E-01	5.08E-01	5.75E-01	4.10E-01	5.16E-01	4.25E-01	2.84E-01	4.25E-01	3.50E-01
592		4.68E-02	8.41E-02	1.72E-01	2.72E-01	2.55E-01	5.00E-01	5.57E-01	4.01E-01	5.01E-01	4.10E-01	2.82E-01	4.20E-01	3.39E-01
595		4.49E-02	8.08E-02	1.68E-01	2.63E-01	2.45E-01	4.86E-01	5.36E-01	3.90E-01	4.87E-01	3.95E-01	2.73E-01	4.07E-01	3.37E-01
598		4.40E-02	7.74E-02	1.63E-01	2.54E-01	2.36E-01	4.68E-01	5.19E-01	3.79E-01	4.76E-01	3.87E-01	2.67E-01	4.00E-01	3.30E-01
601		4.34E-02	7.58E-02	1.59E-01	2.52E-01	2.31E-01	4.65E-01	5.15E-01	3.75E-01	4.72E-01	3.85E-01	2.63E-01	4.02E-01	3.21E-01

total abs.cost

Table 2 Total absorption coefficient. Day is given in fractions to indicate time of day. Wavelength is in nm.

wavelength	date 7.33	8.33	9.33	9.67	10.33	10.67	11.33	11.67	12.33	12.67	13.33	13.67	14.67
604	4.42E-02	7.73E-02	1.61E-01	2.56E-01	2.37E-01	4.73E-01	5.21E-01	3.91E-01	4.80E-01	3.89E-01	2.73E-01	4.06E-01	3.29E-01
607	4.54E-02	8.15E-02	1.70E-01	2.69E-01	2.54E-01	4.93E-01	5.44E-01	4.01E-01	5.02E-01	4.08E-01	2.86E-01	4.23E-01	3.42E-01
610	4.76E-02	8.81E-02	1.81E-01	2.84E-01	2.71E-01	5.21E-01	5.81E-01	4.30E-01	5.33E-01	4.37E-01	3.08E-01	4.45E-01	3.60E-01
613	4.98E-02	9.38E-02	1.93E-01	3.01E-01	2.87E-01	5.51E-01	6.20E-01	4.59E-01	5.67E-01	4.60E-01	3.29E-01	4.64E-01	3.79E-01
616	5.22E-02	1.02E-01	2.02E-01	3.18E-01	3.10E-01	5.80E-01	6.55E-01	4.94E-01	5.95E-01	4.86E-01	3.46E-01	4.84E-01	3.95E-01
619	5.53E-02	1.07E-01	2.10E-01	3.32E-01	3.28E-01	6.03E-01	6.86E-01	5.14E-01	6.22E-01	5.05E-01	3.66E-01	5.06E-01	4.11E-01
622	5.64E-02	1.11E-01	2.19E-01	3.43E-01	3.43E-01	6.24E-01	7.03E-01	5.37E-01	6.41E-01	5.14E-01	3.80E-01	5.18E-01	4.19E-01
625	5.74E-02	1.14E-01	2.24E-01	3.50E-01	3.51E-01	6.40E-01	7.24E-01	5.58E-01	6.59E-01	5.35E-01	3.89E-01	5.34E-01	4.30E-01
628	5.90E-02	1.19E-01	2.33E-01	3.59E-01	3.61E-01	6.59E-01	7.44E-01	5.81E-01	6.76E-01	5.49E-01	4.07E-01	5.42E-01	4.38E-01
631	6.18E-02	1.23E-01	2.42E-01	3.71E-01	3.77E-01	6.83E-01	7.68E-01	6.04E-01	6.95E-01	5.69E-01	4.22E-01	5.59E-01	4.50E-01
634	6.34E-02	1.27E-01	2.49E-01	3.80E-01	3.93E-01	7.00E-01	7.90E-01	6.31E-01	7.12E-01	5.84E-01	4.37E-01	5.66E-01	4.65E-01
637	6.48E-02	1.28E-01	2.51E-01	3.81E-01	3.95E-01	7.02E-01	7.96E-01	6.41E-01	7.22E-01	5.87E-01	4.41E-01	5.70E-01	4.65E-01
640	6.46E-02	1.26E-01	2.47E-01	3.75E-01	3.91E-01	6.95E-01	7.84E-01	6.34E-01	7.15E-01	5.80E-01	4.35E-01	5.67E-01	4.63E-01
643	6.41E-02	1.21E-01	2.41E-01	3.65E-01	3.78E-01	6.78E-01	7.62E-01	6.23E-01	6.95E-01	5.63E-01	4.24E-01	5.55E-01	4.54E-01
646	6.30E-02	1.18E-01	2.36E-01	3.57E-01	3.69E-01	6.67E-01	7.43E-01	6.17E-01	6.84E-01	5.52E-01	4.21E-01	5.50E-01	4.51E-01
649	6.42E-02	1.19E-01	2.38E-01	3.61E-01	3.68E-01	6.73E-01	7.49E-01	6.31E-01	6.93E-01	5.61E-01	4.32E-01	5.63E-01	4.62E-01
652	6.67E-02	1.26E-01	2.54E-01	3.82E-01	3.92E-01	7.12E-01	7.95E-01	6.75E-01	7.39E-01	5.99E-01	4.64E-01	5.97E-01	4.96E-01
655	7.41E-02	1.46E-01	2.85E-01	4.29E-01	4.46E-01	7.94E-01	9.03E-01	7.63E-01	8.30E-01	6.81E-01	5.30E-01	6.69E-01	5.56E-01
658	8.65E-02	1.76E-01	3.39E-01	5.02E-01	5.34E-01	9.25E-01	1.07E+00	9.06E-01	9.72E-01	8.09E-01	6.29E-01	7.83E-01	6.52E-01
661	1.05E-01	2.23E-01	4.08E-01	6.00E-01	6.50E-01	1.10E+00	1.30E+00	1.10E+00	1.16E+00	9.93E-01	7.66E-01	9.29E-01	7.75E-01
664	1.27E-01	2.78E-01	4.90E-01	7.17E-01	7.93E-01	1.31E+00	1.58E+00	1.32E+00	1.39E+00	1.20E+00	9.25E-01	1.10E+00	9.18E-01
667	1.52E-01	3.38E-01	5.69E-01	8.33E-01	9.28E-01	1.52E+00	1.85E+00	1.54E+00	1.60E+00	1.42E+00	1.07E+00	1.26E+00	1.05E+00
670	1.71E-01	3.85E-01	6.29E-01	9.23E-01	1.03E+00	1.68E+00	2.07E+00	1.70E+00	1.77E+00	1.58E+00	1.18E+00	1.38E+00	1.15E+00
673	1.79E-01	4.01E-01	6.53E-01	9.59E-01	1.07E+00	1.75E+00	2.15E+00	1.77E+00	1.84E+00	1.63E+00	1.22E+00	1.43E+00	1.19E+00
676	1.74E-01	3.85E-01	6.34E-01	9.34E-01	1.05E+00	1.71E+00	2.08E+00	1.71E+00	1.79E+00	1.57E+00	1.18E+00	1.38E+00	1.14E+00
679	1.58E-01	3.46E-01	5.84E-01	8.63E-01	9.71E-01	1.58E+00	1.89E+00	1.57E+00	1.64E+00	1.42E+00	1.08E+00	1.26E+00	1.03E+00
682	1.33E-01	2.90E-01	5.09E-01	7.51E-01	8.43E-01	1.38E+00	1.62E+00	1.35E+00	1.43E+00	1.21E+00	9.17E-01	1.09E+00	8.82E-01
685	1.05E-01	2.23E-01	4.12E-01	6.16E-01	6.84E-01	1.14E+00	1.31E+00	1.09E+00	1.17E+00	9.61E-01	7.34E-01	8.84E-01	7.08E-01
688	7.56E-02	1.56E-01	3.07E-01	4.70E-01	5.10E-01	8.72E-01	9.67E-01	8.13E-01	8.89E-01	7.13E-01	5.45E-01	6.70E-01	5.29E-01
691	5.07E-02	1.01E-01	2.10E-01	3.34E-01	3.48E-01	6.25E-01	6.62E-01	5.63E-01	6.29E-01	4.87E-01	3.72E-01	4.80E-01	3.77E-01
694	3.37E-02	6.18E-02	1.37E-01	2.23E-01	2.18E-01	4.25E-01	4.35E-01	3.67E-01	4.25E-01	3.22E-01	2.41E-01	3.33E-01	2.59E-01
697	2.22E-02	3.67E-02	8.83E-02	1.47E-01	1.34E-01	2.83E-01	2.83E-01	2.36E-01	2.83E-01	2.13E-01	1.53E-01	2.27E-01	1.77E-01
700	1.52E-02	2.23E-02	5.58E-02	9.69E-02	8.01E-02	1.88E-01	1.85E-01	1.49E-01	1.89E-01	1.40E-01	9.55E-02	1.57E-01	1.23E-01
703	1.08E-02	1.40E-02	3.64E-02	6.40E-02	4.58E-02	1.27E-01	1.23E-01	9.40E-02	1.27E-01	9.42E-02	6.16E-02	1.12E-01	8.81E-02
706	8.04E-03	9.42E-03	2.50E-02	4.37E-02	2.72E-02	8.76E-02	8.45E-02	6.06E-02	8.88E-02	6.75E-02	3.97E-02	8.15E-02	6.71E-02
709	6.35E-03	6.36E-03	1.83E-02	3.03E-02	1.88E-02	6.25E-02	6.14E-02	4.33E-02	6.31E-02	4.83E-02	2.70E-02	6.02E-02	4.86E-02

Table 2

Total absorption coefficient. Day is given in fractions to indicate time of day. Wavelength is in nm.

total abs.cost

wavelength date	7.33	8.33	9.33	9.67	10.33	10.67	11.33	11.67	12.33	12.67	13.33	13.67	14.67
712	5.27E-03	5.09E-03	1.36E-02	2.25E-02	1.20E-02	4.61E-02	4.95E-02	2.88E-02	4.56E-02	3.64E-02	1.90E-02	4.88E-02	3.95E-02
715	4.60E-03	3.50E-03	1.13E-02	1.68E-02	7.17E-03	3.58E-02	3.69E-02	1.75E-02	3.92E-02	2.95E-02	1.37E-02	3.96E-02	3.24E-02
718	4.02E-03	3.01E-03	7.99E-03	1.34E-02	4.64E-03	2.77E-02	2.89E-02	1.29E-02	3.08E-02	2.29E-02	8.71E-03	3.41E-02	2.67E-02
721	3.17E-03	2.47E-03	6.32E-03	1.16E-02	1.92E-03	2.37E-02	2.10E-02	7.28E-03	2.37E-02	1.52E-02	6.62E-03	2.66E-02	2.19E-02
725	2.71E-03	1.91E-03	4.95E-03	9.13E-03	1.51E-03	2.00E-02	1.87E-02	7.34E-03	1.99E-02	1.30E-02	3.58E-03	2.16E-02	1.98E-02
728	2.39E-03	1.21E-03	4.22E-03	6.87E-03	2.68E-04	1.72E-02	1.72E-02	4.86E-03	1.53E-02	1.41E-02	3.23E-03	1.62E-02	1.68E-02
731	1.82E-03	4.29E-04	3.66E-03	5.15E-03	1.84E-05	1.22E-02	1.20E-02	1.68E-03	9.89E-03	8.49E-03	1.21E-02	1.41E-02	1.32E-02
734	1.59E-03	6.83E-04	3.02E-03	4.37E-03	0.00E+00	1.05E-02	1.01E-02	0.00E+00	8.32E-03	6.73E-03	8.10E-05	1.22E-02	9.58E-03
737	1.48E-03	6.44E-04	2.24E-03	3.53E-03	0.00E+00	8.84E-03	1.05E-02	0.00E+00	8.62E-03	6.21E-03	0.00E+00	1.01E-02	9.29E-03
740	1.28E-03	3.39E-04	1.31E-03	2.84E-03	0.00E+00	7.74E-03	1.07E-02	0.00E+00	6.75E-03	5.56E-03	0.00E+00	9.68E-03	6.55E-03
743	9.32E-04	3.18E-04	1.02E-03	2.89E-03	0.00E+00	6.44E-03	9.04E-03	0.00E+00	5.15E-03	3.86E-03	0.00E+00	7.66E-03	5.49E-03
746	4.57E-04	1.98E-04	7.49E-04	2.41E-03	0.00E+00	4.70E-03	6.07E-03	0.00E+00	3.94E-03	1.98E-03	0.00E+00	5.45E-03	4.76E-03
749	6.58E-04	0.00E+00	5.31E-04	2.37E-03	0.00E+00	4.59E-03	3.35E-03	6.77E-05	3.56E-03	1.66E-03	0.00E+00	4.80E-03	3.82E-03
753	8.02E-04	0.00E+00	3.18E-04	1.48E-03	0.00E+00	3.47E-03	4.22E-03	0.00E+00	3.75E-03	1.87E-03	0.00E+00	3.62E-03	3.72E-03

detrital abs.cost

Table 3   Detrital absorption coefficient. Day is given in fractions to indicate time of day. Wavelength is in nm.

wavelength date	7.33	8.33	9.33	9.67	10.33	10.67	11.33	11.67	12.33	12.67	13.33	13.67	14.67
403	5.11E-02	5.96E-02	9.48E-02	2.61E-01	2.77E-01	4.83E-01	4.81E-01	5.23E-01	6.47E-01	5.19E-01	4.67E-01	4.86E-01	5.05E-01
405	4.36E-02	5.90E-02	1.08E-01	2.58E-01	2.65E-01	4.92E-01	5.02E-01	5.37E-01	6.45E-01	5.32E-01	4.51E-01	4.96E-01	4.78E-01
408	4.46E-02	5.59E-02	1.09E-01	2.53E-01	2.57E-01	4.83E-01	4.79E-01	5.18E-01	6.34E-01	5.40E-01	4.42E-01	4.94E-01	4.71E-01
411	5.09E-02	5.65E-02	1.12E-01	2.47E-01	2.50E-01	4.72E-01	4.75E-01	5.15E-01	6.34E-01	5.50E-01	4.25E-01	4.89E-01	4.72E-01
413	5.83E-02	5.54E-02	1.04E-01	2.47E-01	2.57E-01	4.69E-01	4.65E-01	5.04E-01	6.22E-01	5.54E-01	4.08E-01	4.86E-01	4.63E-01
416	6.13E-02	5.25E-02	9.75E-02	2.45E-01	2.66E-01	4.72E-01	4.80E-01	5.15E-01	6.18E-01	5.22E-01	4.11E-01	4.79E-01	4.57E-01
419	5.83E-02	5.01E-02	9.27E-02	2.46E-01	2.67E-01	4.83E-01	4.82E-01	5.08E-01	5.87E-01	4.90E-01	4.21E-01	4.50E-01	4.58E-01
421	5.09E-02	4.99E-02	9.74E-02	2.45E-01	2.54E-01	4.69E-01	4.77E-01	5.05E-01	5.90E-01	4.83E-01	4.26E-01	4.19E-01	4.49E-01
424	4.37E-02	5.12E-02	1.02E-01	2.43E-01	2.46E-01	4.61E-01	4.67E-01	4.96E-01	5.82E-01	4.91E-01	4.17E-01	4.14E-01	4.41E-01
427	3.70E-02	5.15E-02	1.09E-01	2.42E-01	2.36E-01	4.47E-01	4.66E-01	4.95E-01	5.81E-01	4.98E-01	3.99E-01	4.15E-01	4.30E-01
430	3.29E-02	4.82E-02	1.10E-01	2.30E-01	2.39E-01	4.48E-01	4.67E-01	4.89E-01	5.56E-01	4.89E-01	3.90E-01	4.12E-01	4.25E-01
432	3.39E-02	4.68E-02	1.11E-01	2.20E-01	2.33E-01	4.25E-01	4.59E-01	4.81E-01	5.49E-01	4.77E-01	3.78E-01	4.03E-01	4.18E-01
435	4.12E-02	4.41E-02	1.10E-01	2.12E-01	2.29E-01	4.20E-01	4.55E-01	4.76E-01	5.39E-01	4.69E-01	3.72E-01	4.08E-01	4.02E-01
438	4.95E-02	4.33E-02	1.07E-01	2.07E-01	2.25E-01	4.05E-01	4.42E-01	4.64E-01	5.32E-01	4.54E-01	3.61E-01	3.93E-01	3.85E-01
440	5.30E-02	4.14E-02	1.00E-01	2.02E-01	2.18E-01	4.01E-01	4.17E-01	4.41E-01	5.15E-01	4.47E-01	3.47E-01	3.78E-01	3.71E-01
443	4.98E-02	4.10E-02	9.59E-02	1.92E-01	2.10E-01	3.86E-01	4.03E-01	4.25E-01	4.89E-01	4.34E-01	3.37E-01	3.55E-01	3.60E-01
446	4.18E-02	4.09E-02	9.38E-02	1.87E-01	2.06E-01	3.79E-01	3.85E-01	4.08E-01	4.77E-01	4.20E-01	3.15E-01	3.44E-01	3.51E-01
449	3.28E-02	3.95E-02	9.25E-02	1.79E-01	1.99E-01	3.69E-01	3.88E-01	4.08E-01	4.68E-01	3.98E-01	3.08E-01	3.36E-01	3.38E-01
451	2.69E-02	3.79E-02	8.99E-02	1.74E-01	1.97E-01	3.65E-01	3.73E-01	3.95E-01	4.63E-01	3.74E-01	2.89E-01	3.30E-01	3.30E-01
454	2.51E-02	3.66E-02	8.68E-02	1.69E-01	1.83E-01	3.53E-01	3.70E-01	3.90E-01	4.50E-01	3.55E-01	2.80E-01	3.16E-01	3.12E-01
457	2.85E-02	3.57E-02	8.31E-02	1.65E-01	1.72E-01	3.39E-01	3.59E-01	3.77E-01	4.29E-01	3.43E-01	2.62E-01	3.02E-01	2.97E-01
459	3.19E-02	3.41E-02	7.66E-02	1.60E-01	1.59E-01	3.23E-01	3.39E-01	3.56E-01	4.08E-01	3.29E-01	2.50E-01	2.82E-01	2.80E-01
462	3.54E-02	3.24E-02	6.97E-02	1.54E-01	1.50E-01	3.09E-01	3.18E-01	3.36E-01	3.89E-01	3.16E-01	2.42E-01	2.68E-01	2.73E-01
465	3.70E-02	3.14E-02	6.20E-02	1.46E-01	1.43E-01	2.98E-01	2.96E-01	3.14E-01	3.70E-01	3.02E-01	2.31E-01	2.47E-01	2.61E-01
468	3.74E-02	3.04E-02	5.66E-02	1.40E-01	1.36E-01	2.80E-01	2.80E-01	2.98E-01	3.53E-01	2.88E-01	2.22E-01	2.30E-01	2.56E-01
470	3.40E-02	2.89E-02	5.11E-02	1.33E-01	1.28E-01	2.67E-01	2.67E-01	2.84E-01	3.34E-01	2.72E-01	2.04E-01	2.17E-01	2.39E-01
473	2.72E-02	2.73E-02	4.87E-02	1.24E-01	1.19E-01	2.53E-01	2.54E-01	2.70E-01	3.20E-01	2.54E-01	1.96E-01	2.10E-01	2.29E-01
476	1.97E-02	2.58E-02	4.48E-02	1.18E-01	1.12E-01	2.43E-01	2.43E-01	2.59E-01	3.07E-01	2.43E-01	1.79E-01	2.02E-01	2.15E-01
479	1.48E-02	2.51E-02	4.45E-02	1.14E-01	1.05E-01	2.31E-01	2.30E-01	2.46E-01	2.94E-01	2.30E-01	1.72E-01	1.92E-01	2.04E-01
481	1.49E-02	2.41E-02	4.26E-02	1.10E-01	1.01E-01	2.24E-01	2.23E-01	2.38E-01	2.82E-01	2.19E-01	1.63E-01	1.80E-01	1.96E-01
484	1.74E-02	2.40E-02	4.15E-02	1.05E-01	9.61E-02	2.14E-01	2.13E-01	2.27E-01	2.71E-01	2.16E-01	1.54E-01	1.74E-01	1.85E-01
487	2.15E-02	2.34E-02	3.75E-02	9.91E-02	9.23E-02	2.03E-01	2.04E-01	2.18E-01	2.60E-01	2.09E-01	1.45E-01	1.72E-01	1.78E-01
490	2.38E-02	2.28E-02	3.25E-02	9.47E-02	8.56E-02	1.93E-01	1.95E-01	2.08E-01	2.49E-01	2.05E-01	1.32E-01	1.65E-01	1.71E-01
493	2.45E-02	2.13E-02	2.90E-02	9.06E-02	7.96E-02	1.87E-01	1.86E-01	2.00E-01	2.39E-01	1.91E-01	1.24E-01	1.55E-01	1.66E-01
495	2.13E-02	2.03E-02	2.59E-02	8.66E-02	7.27E-02	1.83E-01	1.77E-01	1.90E-01	2.30E-01	1.84E-01	1.16E-01	1.39E-01	1.62E-01
498	1.62E-02	1.89E-02	2.48E-02	8.29E-02	6.79E-02	1.74E-01	1.64E-01	1.78E-01	2.19E-01	1.75E-01	1.13E-01	1.29E-01	1.52E-01
501	1.20E-02	1.84E-02	2.29E-02	7.94E-02	6.37E-02	1.66E-01	1.53E-01	1.67E-01	2.10E-01	1.69E-01	1.10E-01	1.21E-01	1.43E-01

detrital abs.cost

Table 3 Detrital absorption coefficient. Day is given in fractions to indicate time of day. Wavelength is in nm.

wavelength date	7.33	8.33	9.33	9.67	10.33	10.67	11.33	11.67	12.33	12.67	13.33	13.67	14.67
504	1.10E-02	1.76E-02	2.07E-02	7.67E-02	5.86E-02	1.57E-01	1.43E-01	1.57E-01	2.02E-01	1.61E-01	1.04E-01	1.13E-01	1.37E-01
507	1.19E-02	1.73E-02	1.94E-02	7.39E-02	5.34E-02	1.48E-01	1.37E-01	1.51E-01	1.93E-01	1.49E-01	9.68E-02	1.05E-01	1.32E-01
509	1.14E-02	1.66E-02	1.83E-02	7.10E-02	4.92E-02	1.41E-01	1.33E-01	1.46E-01	1.85E-01	1.38E-01	9.35E-02	9.75E-02	1.27E-01
512	9.05E-03	1.61E-02	1.85E-02	6.75E-02	4.89E-02	1.32E-01	1.30E-01	1.41E-01	1.75E-01	1.28E-01	8.90E-02	8.90E-02	1.20E-01
515	7.13E-03	1.54E-02	1.81E-02	6.38E-02	4.69E-02	1.26E-01	1.25E-01	1.35E-01	1.66E-01	1.21E-01	8.41E-02	8.38E-02	1.15E-01
518	8.07E-03	1.52E-02	1.81E-02	6.09E-02	4.42E-02	1.21E-01	1.18E-01	1.29E-01	1.60E-01	1.12E-01	7.82E-02	7.80E-02	1.10E-01
521	1.08E-02	1.47E-02	1.59E-02	5.91E-02	3.94E-02	1.17E-01	1.13E-01	1.24E-01	1.57E-01	1.06E-01	7.60E-02	7.57E-02	1.06E-01
523	1.41E-02	1.43E-02	1.39E-02	5.77E-02	3.55E-02	1.15E-01	1.06E-01	1.17E-01	1.51E-01	1.04E-01	7.09E-02	7.16E-02	1.04E-01
526	1.58E-02	1.33E-02	1.22E-02	5.66E-02	3.38E-02	1.11E-01	1.02E-01	1.13E-01	1.46E-01	1.02E-01	6.92E-02	6.72E-02	1.01E-01
529	1.59E-02	1.28E-02	1.15E-02	5.49E-02	3.04E-02	1.10E-01	9.88E-02	1.09E-01	1.40E-01	9.77E-02	6.45E-02	6.36E-02	9.80E-02
532	1.40E-02	1.26E-02	1.14E-02	5.27E-02	2.82E-02	1.05E-01	9.63E-02	1.06E-01	1.37E-01	9.18E-02	6.48E-02	5.93E-02	9.26E-02
535	1.05E-02	1.25E-02	1.11E-02	5.03E-02	2.56E-02	1.00E-01	9.27E-02	1.02E-01	1.31E-01	8.79E-02	6.04E-02	5.60E-02	8.89E-02
538	6.12E-03	1.21E-02	1.12E-02	4.88E-02	2.52E-02	9.59E-02	8.81E-02	9.78E-02	1.27E-01	8.40E-02	5.83E-02	5.33E-02	8.58E-02
540	2.31E-03	1.17E-02	1.11E-02	4.78E-02	2.50E-02	9.30E-02	8.56E-02	9.48E-02	1.22E-01	8.12E-02	5.49E-02	5.14E-02	8.35E-02
543	4.95E-04	1.11E-02	1.10E-02	4.78E-02	2.45E-02	8.99E-02	8.37E-02	9.24E-02	1.19E-01	7.53E-02	5.30E-02	4.91E-02	8.14E-02
546	3.10E-04	1.05E-02	1.06E-02	4.66E-02	2.33E-02	8.64E-02	8.30E-02	9.10E-02	1.15E-01	6.96E-02	5.16E-02	4.65E-02	7.89E-02
549	2.93E-03	1.01E-02	1.04E-02	4.54E-02	2.12E-02	8.29E-02	8.02E-02	8.82E-02	1.12E-01	6.35E-02	4.91E-02	4.47E-02	7.81E-02
552	6.92E-03	9.76E-03	1.02E-02	4.37E-02	1.93E-02	8.12E-02	7.70E-02	8.51E-02	1.09E-01	6.01E-02	4.84E-02	4.31E-02	7.74E-02
555	1.05E-02	9.80E-03	1.01E-02	4.33E-02	1.83E-02	7.91E-02	7.53E-02	8.31E-02	1.07E-01	5.72E-02	4.70E-02	4.10E-02	7.55E-02
558	1.11E-02	9.66E-03	9.28E-03	4.28E-02	1.76E-02	7.84E-02	7.27E-02	8.06E-02	1.04E-01	5.78E-02	4.68E-02	3.89E-02	7.27E-02
561	1.00E-02	9.41E-03	9.32E-03	4.23E-02	1.71E-02	7.74E-02	7.04E-02	7.83E-02	1.02E-01	5.70E-02	4.53E-02	3.73E-02	7.03E-02
563	9.01E-03	8.92E-03	9.11E-03	4.14E-02	1.65E-02	7.72E-02	6.75E-02	7.56E-02	9.98E-02	5.78E-02	4.43E-02	3.66E-02	6.89E-02
566	8.48E-03	8.51E-03	9.36E-03	4.06E-02	1.57E-02	7.63E-02	6.64E-02	7.40E-02	9.67E-02	5.74E-02	4.47E-02	3.67E-02	6.67E-02
569	7.56E-03	8.44E-03	8.87E-03	4.00E-02	1.52E-02	7.53E-02	6.51E-02	7.27E-02	9.57E-02	5.73E-02	4.41E-02	3.65E-02	6.46E-02
572	5.93E-03	8.48E-03	9.10E-03	3.98E-02	1.56E-02	7.46E-02.	6.38E-02	7.17E-02	9.53E-02	5.77E-02	4.45E-02	3.61E-02	6.38E-02
575	3.87E-03	8.42E-03	9.39E-03	4.03E-02	1.63E-02	7.44E-02	6.39E-02	7.19E-02	9.59E-02	5.82E-02	4.44E-02	3.47E-02	6.45E-02
578	2.22E-03	8.51E-03	1.01E-02	4.00E-02	1.73E-02	7.45E-02	6.48E-02	7.27E-02	9.63E-02	5.68E-02	4.45E-02	3.40E-02	6.40E-02
581	1.02E-03	8.40E-03	1.04E-02	3.90E-02	1.72E-02	7.34E-02	6.59E-02	7.36E-02	9.66E-02	5.44E-02	4.38E-02	3.41E-02	6.24E-02
584	4.70E-04	8.41E-03	1.08E-02	3.83E-02	1.75E-02	7.27E-02	6.62E-02	7.36E-02	9.59E-02	5.17E-02	4.28E-02	3.51E-02	6.04E-02
587	3.41E-04	8.20E-03	1.12E-02	3.79E-02	1.73E-02	7.15E-02	6.54E-02	7.26E-02	9.45E-02	5.15E-02	4.17E-02	3.49E-02	5.89E-02
589	7.25E-04	8.18E-03	1.13E-02	3.82E-02	1.70E-02	7.06E-02	6.41E-02	7.14E-02	9.34E-02	5.03E-02	4.00E-02	3.43E-02	5.86E-02
592	1.04E-03	7.84E-03	1.13E-02	3.77E-02	1.65E-02	6.83E-02	6.35E-02	7.07E-02	9.23E-02	4.96E-02	3.90E-02	3.38E-02	5.83E-02
595	1.40E-03	7.59E-03	1.15E-02	3.73E-02	1.59E-02	6.64E-02	6.33E-02	7.05E-02	9.20E-02	4.87E-02	3.78E-02	3.37E-02	5.72E-02
598	2.64E-03	7.24E-03	1.18E-02	3.69E-02	1.55E-02	6.48E-02	6.23E-02	6.95E-02	9.10E-02	4.80E-02	3.77E-02	3.24E-02	5.65E-02
601	5.72E-03	7.05E-03	1.19E-02	3.66E-02	1.52E-02	6.39E-02	6.10E-02	6.82E-02	8.98E-02	4.70E-02	3.74E-02	3.14E-02	5.59E-02
604	9.20E-03	6.72E-03	1.13E-02	3.63E-02	1.51E-02	6.45E-02	5.96E-02	6.67E-02	8.82E-02	4.66E-02	3.77E-02	3.16E-02	5.53E-02
607	1.07E-02	6.51E-03	1.12E-02	3.57E-02	1.49E-02	6.45E-02	5.94E-02	6.59E-02	8.56E-02	4.87E-02	3.81E-02	3.23E-02	5.41E-02

Table 3

Detrital absorption coefficient. Day is given in fractions to indicate time of day. Wavelength is in nm.

wavelength / date	7.33	8.33	9.33	9.67	10.33	10.67	11.33	11.67	12.33	12.67	13.33	13.67	14.67
610	9.50E-03	6.43E-03	1.14E-02	3.58E-02	1.48E-02	6.55E-02	5.97E-02	6.60E-02	8.51E-02	4.89E-02	3.89E-02	3.23E-02	5.30E-02
613	7.26E-03	6.36E-03	1.17E-02	3.57E-02	1.55E-02	6.45E-02	5.96E-02	6.59E-02	8.48E-02	4.98E-02	3.84E-02	3.22E-02	5.22E-02
616	5.44E-03	6.46E-03	1.20E-02	3.60E-02	1.61E-02	6.55E-02	5.91E-02	6.57E-02	8.54E-02	4.86E-02	3.85E-02	3.21E-02	5.19E-02
619	3.77E-03	6.44E-03	1.24E-02	3.61E-02	1.66E-02	6.53E-02	5.89E-02	6.55E-02	8.52E-02	4.87E-02	3.76E-02	3.27E-02	5.16E-02
622	2.03E-03	6.57E-03	1.30E-02	3.63E-02	1.63E-02	6.61E-02	5.92E-02	6.57E-02	8.53E-02	4.81E-02	3.82E-02	3.23E-02	5.21E-02
625	6.99E-04	6.54E-03	1.37E-02	3.67E-02	1.66E-02	6.56E-02	6.03E-02	6.67E-02	8.59E-02	4.85E-02	3.85E-02	3.24E-02	5.16E-02
628	6.67E-05	6.37E-03	1.42E-02	3.68E-02	1.65E-02	6.54E-02	6.20E-02	6.81E-02	8.61E-02	4.86E-02	3.87E-02	3.23E-02	5.15E-02
631	0.00E+00	6.14E-03	1.50E-02	3.69E-02	1.75E-02	6.57E-02	6.25E-02	6.86E-02	8.70E-02	4.81E-02	3.96E-02	3.33E-02	5.13E-02
634	0.00E+00	6.16E-03	1.51E-02	3.69E-02	1.82E-02	6.67E-02	6.29E-02	6.91E-02	8.75E-02	4.71E-02	3.97E-02	3.43E-02	5.13E-02
637	2.31E-04	6.13E-03	1.56E-02	3.72E-02	1.95E-02	6.76E-02	6.27E-02	6.90E-02	8.79E-02	4.67E-02	4.06E-02	3.48E-02	5.00E-02
640	8.32E-04	6.10E-03	1.61E-02	3.72E-02	2.00E-02	6.72E-02	6.36E-02	6.96E-02	8.77E-02	4.69E-02	4.13E-02	3.50E-02	4.91E-02
643	1.95E-03	5.85E-03	1.68E-02	3.68E-02	2.08E-02	6.64E-02	6.39E-02	6.98E-02	8.76E-02	4.70E-02	4.09E-02	3.58E-02	4.92E-02
646	3.40E-03	5.80E-03	1.71E-02	3.68E-02	2.10E-02	6.61E-02	6.38E-02	6.97E-02	8.75E-02	4.80E-02	4.06E-02	3.76E-02	4.95E-02
649	4.82E-03	5.82E-03	1.77E-02	3.73E-02	2.20E-02	6.66E-02	6.44E-02	7.04E-02	8.84E-02	5.08E-02	4.06E-02	4.02E-02	5.09E-02
652	6.04E-03	5.95E-03	1.92E-02	3.83E-02	2.36E-02	6.78E-02	6.64E-02	7.27E-02	9.13E-02	5.59E-02	4.33E-02	4.33E-02	5.35E-02
655	6.81E-03	6.22E-03	2.15E-02	3.90E-02	2.64E-02	7.05E-02	7.12E-02	7.73E-02	9.57E-02	6.29E-02	4.76E-02	4.83E-02	5.69E-02
658	6.76E-03	6.47E-03	2.39E-02	4.01E-02	2.98E-02	7.42E-02	7.64E-02	8.26E-02	1.01E-01	7.04E-02	5.30E-02	5.55E-02	5.97E-02
661	6.26E-03	6.69E-03	2.58E-02	4.11E-02	3.29E-02	7.77E-02	8.21E-02	8.83E-02	1.07E-01	7.77E-02	5.83E-02	6.26E-02	6.18E-02
664	5.75E-03	6.71E-03	2.66E-02	4.26E-02	3.56E-02	7.98E-02	8.69E-02	9.29E-02	1.11E-01	8.30E-02	6.14E-02	6.77E-02	6.47E-02
667	5.64E-03	6.72E-03	2.64E-02	4.29E-02	3.69E-02	8.05E-02	9.00E-02	9.57E-02	1.13E-01	8.48E-02	6.32E-02	6.94E-02	6.61E-02
670	4.77E-03	6.57E-03	2.47E-02	4.26E-02	3.70E-02	7.87E-02	8.97E-02	9.51E-02	1.11E-01	8.24E-02	6.21E-02	6.78E-02	6.53E-02
673	2.98E-03	6.31E-03	2.26E-02	4.09E-02	3.44E-02	7.45E-02	8.54E-02	9.07E-02	1.07E-01	7.70E-02	5.87E-02	6.26E-02	6.23E-02
676	1.11E-03	5.87E-03	1.95E-02	3.86E-02	3.07E-02	6.87E-02	7.84E-02	8.36E-02	9.90E-02	6.93E-02	5.25E-02	5.53E-02	5.71E-02
679	1.44E-04	5.48E-03	1.69E-02	3.60E-02	2.58E-02	6.23E-02	6.90E-02	7.44E-02	9.06E-02	5.94E-02	4.53E-02	4.64E-02	5.15E-02
682	0.00E+00	5.06E-03	1.44E-02	3.33E-02	2.16E-02	5.48E-02	5.87E-02	6.42E-02	8.08E-02	4.88E-02	3.83E-02	3.66E-02	4.50E-02
685	0.00E+00	4.73E-03	1.28E-02	3.03E-02	1.74E-02	4.78E-02	4.81E-02	5.40E-02	7.16E-02	3.89E-02	3.10E-02	2.78E-02	3.97E-02
688	0.00E+00	4.41E-03	1.13E-02	2.76E-02	1.34E-02	4.13E-02	4.04E-02	4.59E-02	6.25E-02	3.15E-02	2.52E-02	2.06E-02	3.45E-02
691	0.00E+00	4.21E-03	1.01E-02	2.48E-02	9.91E-03	3.64E-02	3.36E-02	3.88E-02	5.45E-02	2.49E-02	2.01E-02	1.56E-02	2.98E-02
694	1.78E-05	3.90E-03	9.04E-03	2.30E-02	7.37E-03	3.20E-02	2.88E-02	3.36E-02	4.77E-02	1.99E-02	1.68E-02	1.10E-02	2.57E-02
697	8.84E-05	3.73E-03	7.93E-03	2.12E-02	5.65E-03	2.86E-02	2.39E-02	2.85E-02	4.23E-02	1.57E-02	1.31E-02	7.63E-03	2.27E-02
700	9.81E-05	3.45E-03	6.88E-03	1.99E-02	4.29E-03	2.59E-02	2.05E-02	2.49E-02	3.81E-02	1.34E-02	1.05E-02	4.82E-03	2.06E-02
703	2.92E-04	3.35E-03	6.26E-03	1.86E-02	3.08E-03	2.37E-02	1.72E-02	2.16E-02	3.47E-02	1.13E-02	8.24E-03	2.62E-03	1.88E-02
706	1.08E-03	3.21E-03	5.96E-03	1.73E-02	2.20E-03	2.16E-02	1.47E-02	1.90E-02	3.19E-02	9.85E-03	7.13E-03	1.26E-03	1.73E-02
709	1.93E-03	3.25E-03	5.79E-03	1.68E-02	2.07E-03	1.99E-02	1.28E-02	1.70E-02	2.97E-02	8.64E-03	5.31E-03	5.00E-04	1.59E-02
712	2.28E-03	3.17E-03	5.50E-03	1.64E-02	1.61E-03	1.77E-02	1.10E-02	1.51E-02	2.73E-02	7.50E-03	4.17E-03	2.63E-04	1.45E-02
715	1.74E-03	3.05E-03	5.19E-03	1.61E-02	9.94E-04	1.69E-02	9.58E-03	1.35E-02	2.52E-02	6.88E-03	3.44E-03	2.63E-05	1.28E-02
718	1.19E-03	2.92E-03	4.89E-03	1.53E-02	4.06E-04	1.63E-02	8.17E-03	1.21E-02	2.40E-02	5.26E-03	3.45E-03	0.00E+00	1.18E-02

detrital abs.cost

Table 3

Detrital absorption coefficient. Day is given in fractions to indicate time of day. Wavelength is in nm.

wavelength date	7.33	8.33	9.33	9.67	10.33	10.67	11.33	11.67	12.33	12.67	13.33	13.67	14.67
721	1.05E-03	2.91E-03	4.82E-03	1.47E-02	4.95E-04	1.61E-02	7.90E-03	1.17E-02	2.31E-02	4.31E-03	2.84E-03	0.00E+00	1.08E-02
725	1.02E-03	2.87E-03	4.63E-03	1.41E-02	7.84E-04	1.51E-02	7.31E-03	1.10E-02	2.22E-02	3.50E-03	1.96E-03	0.00E+00	1.02E-02
728	8.97E-04	2.73E-03	4.43E-03	1.38E-02	1.07E-03	1.46E-02	7.27E-03	1.06E-02	2.08E-02	3.72E-03	9.60E-04	0.00E+00	9.15E-03
731	5.00E-04	2.52E-03	4.16E-03	1.34E-02	8.76E-04	1.40E-02	6.55E-03	9.76E-03	1.94E-02	3.88E-03	2.96E-04	0.00E+00	8.22E-03
734	2.80E-04	2.45E-03	4.23E-03	1.33E-02	8.88E-04	1.35E-02	6.22E-03	9.20E-03	1.81E-02	3.63E-03	7.12E-05	0.00E+00	7.22E-03
737	9.11E-05	2.49E-03	4.53E-03	1.31E-02	7.13E-04	1.27E-02	5.00E-03	8.01E-03	1.70E-02	3.14E-03	5.32E-09	0.00E+00	6.78E-03
740	6.54E-05	2.67E-03	4.75E-03	1.30E-02	7.04E-04	1.28E-02	3.86E-03	7.08E-03	1.67E-02	2.51E-03	1.73E-05	0.00E+00	6.90E-03
743	0.00E+00	2.61E-03	4.70E-03	1.31E-02	3.81E-04	1.22E-02	2.98E-03	6.44E-03	1.68E-02	2.47E-03	1.73E-05	0.00E+00	6.70E-03
746	0.00E+00	2.60E-03	4.47E-03	1.30E-02	1.13E-04	1.12E-02	2.89E-03	6.38E-03	1.69E-02	3.05E-03	1.73E-05	0.00E+00	6.31E-03
749	0.00E+00	2.36E-03	4.41E-03	1.29E-02	3.72E-05	9.83E-03	2.84E-03	6.28E-03	1.66E-02	3.73E-03	0.00E+00	0.00E+00	6.10E-03
753	0.00E+00	2.23E-03	4.61E-03	1.22E-02	1.84E-04	9.60E-03	2.75E-03	6.12E-03	1.62E-02	3.76E-03	0.00E+00	0.00E+00	5.70E-03

Table 4

Pigment absorption coefficient. Day is given in fractions to indicate time of day. Wavelength is in nm.

wavelength	Date: 7.33	8.33	9.33	9.67	10.33	10.67	11.33	11.67	12.33	12.67	13.33	13.67	14.67
403	2.37E-01	4.68E-01	8.99E-01	1.07E+00	1.12E+00	1.99E+00	2.74E+00	2.39E+00	2.10E+00	2.35E+00	1.64E+00	1.80E+00	1.67E+00
405	2.47E-01	4.90E-01	8.85E-01	1.05E+00	1.16E+00	2.16E+00	2.78E+00	2.34E+00	2.18E+00	2.33E+00	1.70E+00	2.01E+00	1.60E+00
408	2.51E-01	4.99E-01	9.64E-01	1.10E+00	1.22E+00	2.11E+00	2.89E+00	2.50E+00	2.27E+00	2.19E+00	1.65E+00	1.98E+00	1.66E+00
411	2.56E-01	5.38E-01	9.71E-01	1.11E+00	1.31E+00	2.25E+00	3.10E+00	2.37E+00	2.30E+00	2.38E+00	1.76E+00	1.91E+00	1.79E+00
413	2.61E-01	5.48E-01	9.66E-01	1.14E+00	1.30E+00	2.22E+00	3.03E+00	2.50E+00	2.38E+00	2.38E+00	1.75E+00	1.98E+00	1.76E+00
416	2.60E-01	5.62E-01	1.00E+00	1.17E+00	1.29E+00	2.36E+00	3.03E+00	2.48E+00	2.35E+00	2.59E+00	1.78E+00	2.00E+00	1.80E+00
419	2.77E-01	5.59E-01	1.01E+00	1.19E+00	1.36E+00	2.34E+00	3.09E+00	2.60E+00	2.36E+00	2.57E+00	1.80E+00	2.12E+00	1.81E+00
421	2.75E-01	5.73E-01	1.01E+00	1.21E+00	1.39E+00	2.36E+00	3.20E+00	2.62E+00	2.39E+00	2.55E+00	1.82E+00	2.17E+00	1.86E+00
424	3.00E-01	6.04E-01	1.04E+00	1.23E+00	1.40E+00	2.38E+00	3.17E+00	2.63E+00	2.48E+00	2.61E+00	1.86E+00	2.17E+00	1.90E+00
427	3.06E-01	6.16E-01	1.04E+00	1.23E+00	1.44E+00	2.46E+00	3.23E+00	2.61E+00	2.49E+00	2.67E+00	1.86E+00	2.13E+00	1.85E+00
430	3.20E-01	6.41E-01	1.05E+00	1.32E+00	1.47E+00	2.51E+00	3.33E+00	2.71E+00	2.56E+00	2.70E+00	1.86E+00	2.19E+00	1.88E+00
432	3.24E-01	6.59E-01	1.07E+00	1.31E+00	1.47E+00	2.55E+00	3.39E+00	2.74E+00	2.60E+00	2.75E+00	1.92E+00	2.23E+00	1.91E+00
435	3.26E-01	6.76E-01	1.05E+00	1.32E+00	1.40E+00	2.56E+00	3.46E+00	2.82E+00	2.61E+00	2.74E+00	1.92E+00	2.22E+00	1.95E+00
438	3.09E-01	6.91E-01	1.08E+00	1.36E+00	1.49E+00	2.56E+00	3.45E+00	2.73E+00	2.59E+00	2.75E+00	1.92E+00	2.17E+00	1.89E+00
440	3.06E-01	6.85E-01	1.07E+00	1.32E+00	1.46E+00	2.53E+00	3.46E+00	2.69E+00	2.61E+00	2.70E+00	1.90E+00	2.16E+00	1.92E+00
443	3.04E-01	6.58E-01	1.04E+00	1.31E+00	1.43E+00	2.47E+00	3.27E+00	2.66E+00	2.51E+00	2.63E+00	1.83E+00	2.16E+00	1.85E+00
446	2.91E-01	6.40E-01	1.00E+00	1.25E+00	1.36E+00	2.41E+00	3.27E+00	2.49E+00	2.41E+00	2.61E+00	1.83E+00	2.09E+00	1.82E+00
449	2.88E-01	6.30E-01	9.64E-01	1.23E+00	1.33E+00	2.28E+00	3.12E+00	2.36E+00	2.37E+00	2.49E+00	1.74E+00	2.01E+00	1.74E+00
451	2.85E-01	6.02E-01	9.32E-01	1.19E+00	1.29E+00	2.21E+00	2.96E+00	2.23E+00	2.24E+00	2.44E+00	1.63E+00	1.97E+00	1.70E+00
454	2.77E-01	5.93E-01	9.07E-01	1.16E+00	1.24E+00	2.15E+00	2.88E+00	2.13E+00	2.17E+00	2.32E+00	1.60E+00	1.92E+00	1.63E+00
457	2.66E-01	5.76E-01	8.71E-01	1.11E+00	1.23E+00	2.08E+00	2.77E+00	2.03E+00	2.13E+00	2.27E+00	1.55E+00	1.88E+00	1.62E+00
459	2.57E-01	5.65E-01	8.43E-01	1.10E+00	1.24E+00	2.02E+00	2.68E+00	1.97E+00	2.06E+00	2.22E+00	1.52E+00	1.82E+00	1.58E+00
462	2.51E-01	5.51E-01	8.24E-01	1.06E+00	1.19E+00	1.95E+00	2.61E+00	1.92E+00	2.01E+00	2.14E+00	1.49E+00	1.74E+00	1.54E+00
465	2.41E-01	5.32E-01	8.02E-01	1.04E+00	1.14E+00	1.91E+00	2.55E+00	1.79E+00	1.94E+00	2.06E+00	1.43E+00	1.69E+00	1.49E+00
468	2.36E-01	5.12E-01	7.71E-01	1.00E+00	1.10E+00	1.84E+00	2.41E+00	1.71E+00	1.89E+00	1.98E+00	1.39E+00	1.67E+00	1.41E+00
470	2.25E-01	4.87E-01	7.40E-01	9.83E-01	1.07E+00	1.74E+00	2.34E+00	1.65E+00	1.79E+00	1.88E+00	1.33E+00	1.61E+00	1.37E+00
473	2.21E-01	4.60E-01	7.05E-01	9.35E-01	1.02E+00	1.68E+00	2.19E+00	1.55E+00	1.73E+00	1.78E+00	1.25E+00	1.57E+00	1.31E+00
476	2.13E-01	4.41E-01	6.70E-01	8.98E-01	9.71E-01	1.61E+00	2.05E+00	1.51E+00	1.65E+00	1.70E+00	1.20E+00	1.48E+00	1.25E+00
479	2.14E-01	4.17E-01	6.45E-01	8.64E-01	9.44E-01	1.55E+00	1.99E+00	1.42E+00	1.58E+00	1.64E+00	1.16E+00	1.43E+00	1.19E+00
481	2.05E-01	3.98E-01	6.24E-01	8.31E-01	9.13E-01	1.47E+00	1.89E+00	1.39E+00	1.53E+00	1.58E+00	1.11E+00	1.38E+00	1.17E+00
484	1.95E-01	3.93E-01	6.04E-01	8.09E-01	8.83E-01	1.44E+00	1.83E+00	1.31E+00	1.47E+00	1.51E+00	1.08E+00	1.37E+00	1.14E+00
487	1.84E-01	3.78E-01	5.93E-01	7.99E-01	8.63E-01	1.40E+00	1.81E+00	1.26E+00	1.46E+00	1.47E+00	1.05E+00	1.33E+00	1.13E+00
490	1.75E-01	3.70E-01	5.79E-01	7.85E-01	8.38E-01	1.38E+00	1.75E+00	1.26E+00	1.42E+00	1.44E+00	1.05E+00	1.31E+00	1.09E+00
493	1.67E-01	3.63E-01	5.65E-01	7.75E-01	8.36E-01	1.35E+00	1.74E+00	1.21E+00	1.41E+00	1.40E+00	1.03E+00	1.26E+00	1.06E+00
495	1.67E-01	3.53E-01	5.60E-01	7.55E-01	8.19E-01	1.33E+00	1.69E+00	1.18E+00	1.37E+00	1.38E+00	9.82E-01	1.24E+00	1.02E+00
498	1.61E-01	3.43E-01	5.41E-01	7.40E-01	8.07E-01	1.28E+00	1.65E+00	1.14E+00	1.34E+00	1.33E+00	9.51E-01	1.22E+00	9.91E-01
501	1.60E-01	3.33E-01	5.22E-01	7.22E-01	7.80E-01	1.24E+00	1.60E+00	1.11E+00	1.27E+00	1.28E+00	9.17E-01	1.16E+00	9.47E-01

pigment abs.cost

Table 4

Pigment absorption coefficient. Day is given in fractions to indicate time of day. Wavelength is in nm.

wavelength	Date: 7.33	8.33	9.33	9.67	10.33	10.67	11.33	11.67	12.33	12.67	13.33	13.67	14.67
504	1.52E-01	3.21E-01	5.09E-01	6.96E-01	7.56E-01	1.20E+00	1.54E+00	1.05E+00	1.22E+00	1.24E+00	8.81E-01	1.12E+00	9.12E-01
507	1.44E-01	3.07E-01	4.89E-01	6.72E-01	7.27E-01	1.16E+00	1.48E+00	1.00E+00	1.17E+00	1.17E+00	8.18E-01	1.06E+00	8.52E-01
509	1.39E-01	2.95E-01	4.71E-01	6.51E-01	7.15E-01	1.10E+00	1.43E+00	9.59E-01	1.11E+00	1.11E+00	7.69E-01	1.00E+00	7.88E-01
512	1.35E-01	2.84E-01	4.53E-01	6.32E-01	6.86E-01	1.08E+00	1.37E+00	9.19E-01	1.06E+00	1.06E+00	7.27E-01	9.68E-01	7.54E-01
515	1.30E-01	2.74E-01	4.32E-01	6.05E-01	6.54E-01	1.03E+00	1.31E+00	8.72E-01	1.02E+00	1.02E+00	6.92E-01	9.18E-01	7.16E-01
518	1.24E-01	2.61E-01	4.22E-01	5.84E-01	6.37E-01	9.89E-01	1.25E+00	8.29E-01	9.72E-01	9.77E-01	6.58E-01	8.72E-01	6.76E-01
521	1.15E-01	2.51E-01	4.07E-01	5.70E-01	6.15E-01	9.55E-01	1.21E+00	8.11E-01	9.28E-01	9.28E-01	6.18E-01	8.28E-01	6.39E-01
523	1.08E-01	2.42E-01	3.91E-01	5.44E-01	5.95E-01	9.17E-01	1.17E+00	7.68E-01	8.95E-01	8.90E-01	5.86E-01	7.94E-01	6.05E-01
526	1.01E-01	2.34E-01	3.76E-01	5.28E-01	5.66E-01	8.80E-01	1.13E+00	7.44E-01	8.71E-01	8.54E-01	5.61E-01	7.68E-01	5.77E-01
529	9.44E-02	2.24E-01	3.64E-01	5.16E-01	5.53E-01	8.54E-01	1.09E+00	7.03E-01	8.30E-01	8.13E-01	5.32E-01	7.32E-01	5.45E-01
532	9.14E-02	2.14E-01	3.53E-01	4.98E-01	5.31E-01	8.28E-01	1.05E+00	6.73E-01	8.02E-01	7.89E-01	5.14E-01	7.13E-01	5.30E-01
535	9.29E-02	2.04E-01	3.38E-01	4.80E-01	5.11E-01	7.93E-01	1.02E+00	6.41E-01	7.82E-01	7.65E-01	4.99E-01	6.87E-01	5.05E-01
538	9.19E-02	1.95E-01	3.26E-01	4.61E-01	4.89E-01	7.67E-01	9.71E-01	6.24E-01	7.39E-01	7.25E-01	4.69E-01	6.50E-01	4.85E-01
540	8.96E-02	1.84E-01	3.09E-01	4.43E-01	4.69E-01	7.30E-01	9.23E-01	5.87E-01	7.10E-01	6.85E-01	4.47E-01	6.30E-01	4.51E-01
543	8.69E-02	1.73E-01	2.92E-01	4.19E-01	4.46E-01	6.93E-01	8.73E-01	5.56E-01	6.68E-01	6.50E-01	4.20E-01	5.91E-01	4.32E-01
546	8.15E-02	1.63E-01	2.80E-01	3.95E-01	4.20E-01	6.64E-01	8.16E-01	5.25E-01	6.32E-01	6.09E-01	3.89E-01	5.58E-01	4.12E-01
549	7.42E-02	1.49E-01	2.58E-01	3.71E-01	3.91E-01	6.20E-01	7.64E-01	4.94E-01	5.97E-01	5.67E-01	3.63E-01	5.24E-01	3.79E-01
552	6.50E-02	1.38E-01	2.43E-01	3.45E-01	3.63E-01	5.84E-01	7.05E-01	4.55E-01	5.60E-01	5.37E-01	3.30E-01	4.93E-01	3.52E-01
555	5.68E-02	1.25E-01	2.25E-01	3.23E-01	3.36E-01	5.42E-01	6.58E-01	4.18E-01	5.15E-01	4.92E-01	3.07E-01	4.71E-01	3.29E-01
558	5.09E-02	1.14E-01	2.10E-01	2.96E-01	3.08E-01	5.06E-01	6.14E-01	3.83E-01	4.83E-01	4.47E-01	2.77E-01	4.46E-01	3.05E-01
561	4.89E-02	1.04E-01	1.95E-01	2.77E-01	2.85E-01	4.72E-01	5.74E-01	3.55E-01	4.47E-01	4.22E-01	2.64E-01	4.18E-01	2.86E-01
563	4.67E-02	9.60E-02	1.83E-01	2.61E-01	2.68E-01	4.46E-01	5.43E-01	3.31E-01	4.21E-01	4.02E-01	2.39E-01	4.02E-01	2.82E-01
566	4.49E-02	9.10E-02	1.74E-01	2.49E-01	2.52E-01	4.27E-01	5.24E-01	3.11E-01	4.12E-01	3.90E-01	2.39E-01	3.92E-01	2.78E-01
569	4.32E-02	8.55E-02	1.68E-01	2.40E-01	2.43E-01	4.17E-01	5.02E-01	3.04E-01	3.98E-01	3.73E-01	2.32E-01	3.83E-01	2.68E-01
572	4.42E-02	8.20E-02	1.65E-01	2.38E-01	2.38E-01	4.16E-01	5.03E-01	3.02E-01	3.99E-01	3.57E-01	2.29E-01	3.83E-01	2.69E-01
575	4.54E-02	8.26E-02	1.65E-01	2.37E-01	2.40E-01	4.18E-01	5.00E-01	3.08E-01	4.02E-01	3.61E-01	2.29E-01	3.87E-01	2.66E-01
578	4.71E-02	8.17E-02	1.67E-01	2.38E-01	2.39E-01	4.25E-01	5.00E-01	3.14E-01	4.08E-01	3.65E-01	2.37E-01	3.88E-01	2.74E-01
581	4.83E-02	8.26E-02	1.70E-01	2.42E-01	2.43E-01	4.30E-01	5.12E-01	3.19E-01	4.13E-01	3.79E-01	2.39E-01	3.92E-01	2.85E-01
584	4.84E-02	8.17E-02	1.69E-01	2.44E-01	2.45E-01	4.40E-01	5.21E-01	3.32E-01	4.17E-01	3.79E-01	2.46E-01	3.97E-01	2.89E-01
587	4.81E-02	8.18E-02	1.69E-01	2.45E-01	2.52E-01	4.43E-01	5.16E-01	3.38E-01	4.25E-01	3.84E-01	2.51E-01	3.98E-01	2.92E-01
589	4.73E-02	8.01E-02	1.67E-01	2.41E-01	2.51E-01	4.37E-01	5.11E-01	3.38E-01	4.22E-01	3.75E-01	2.44E-01	3.91E-01	2.92E-01
592	4.58E-02	7.62E-02	1.61E-01	2.34E-01	2.39E-01	4.31E-01	4.94E-01	3.30E-01	4.09E-01	3.60E-01	2.43E-01	3.87E-01	2.81E-01
595	4.35E-02	7.32E-02	1.56E-01	2.26E-01	2.30E-01	4.20E-01	4.73E-01	3.19E-01	3.95E-01	3.47E-01	2.35E-01	3.73E-01	2.79E-01
598	4.14E-02	7.02E-02	1.51E-01	2.17E-01	2.20E-01	4.04E-01	4.57E-01	3.09E-01	3.85E-01	3.39E-01	2.29E-01	3.68E-01	2.73E-01
601	3.77E-02	6.88E-02	1.47E-01	2.15E-01	2.15E-01	4.01E-01	4.54E-01	3.07E-01	3.83E-01	3.38E-01	2.25E-01	3.70E-01	2.65E-01
604	3.50E-02	7.06E-02	1.50E-01	2.20E-01	2.22E-01	4.09E-01	4.62E-01	3.25E-01	3.92E-01	3.43E-01	2.35E-01	3.75E-01	2.74E-01
607	3.47E-02	7.50E-02	1.59E-01	2.33E-01	2.39E-01	4.28E-01	4.85E-01	3.35E-01	4.16E-01	3.59E-01	2.48E-01	3.90E-01	2.88E-01

Table 4

pigment abs.cost

Pigment absorption coefficient. Day is given in fractions to indicate time of day. Wavelength is in nm.

wavelength	Date: 7.33	8.33	9.33	9.67	10.33	10.67	11.33	11.67	12.33	12.67	13.33	13.67	14.67
610	3.81E-02	8.17E-02	1.69E-01	2.48E-01	2.56E-01	4.56E-01	5.21E-01	3.64E-01	4.47E-01	3.88E-01	2.69E-01	4.13E-01	3.07E-01
613	4.25E-02	8.74E-02	1.81E-01	2.65E-01	2.72E-01	4.86E-01	5.60E-01	3.93E-01	4.82E-01	4.10E-01	2.91E-01	4.32E-01	3.27E-01
616	4.68E-02	9.57E-02	1.90E-01	2.82E-01	2.94E-01	5.15E-01	5.96E-01	4.29E-01	5.10E-01	4.37E-01	3.08E-01	4.52E-01	3.43E-01
619	5.15E-02	1.01E-01	1.98E-01	2.96E-01	3.11E-01	5.38E-01	6.27E-01	4.48E-01	5.37E-01	4.56E-01	3.29E-01	4.73E-01	3.59E-01
622	5.43E-02	1.04E-01	2.06E-01	3.06E-01	3.26E-01	5.57E-01	6.43E-01	4.71E-01	5.55E-01	4.66E-01	3.42E-01	4.86E-01	3.67E-01
625	5.67E-02	1.08E-01	2.11E-01	3.13E-01	3.35E-01	5.74E-01	6.64E-01	4.91E-01	5.73E-01	4.86E-01	3.51E-01	5.02E-01	3.78E-01
628	5.89E-02	1.12E-01	2.19E-01	3.22E-01	3.44E-01	5.94E-01	6.82E-01	5.13E-01	5.90E-01	5.01E-01	3.68E-01	5.10E-01	3.86E-01
631	6.18E-02	1.16E-01	2.27E-01	3.35E-01	3.60E-01	6.17E-01	7.06E-01	5.35E-01	6.08E-01	5.21E-01	3.82E-01	5.26E-01	3.99E-01
634	6.34E-02	1.21E-01	2.34E-01	3.43E-01	3.74E-01	6.33E-01	7.27E-01	5.62E-01	6.25E-01	5.36E-01	3.97E-01	5.31E-01	4.14E-01
637	6.46E-02	1.22E-01	2.35E-01	3.44E-01	3.75E-01	6.34E-01	7.33E-01	5.72E-01	6.34E-01	5.40E-01	4.00E-01	5.35E-01	4.15E-01
640	6.38E-02	1.20E-01	2.31E-01	3.38E-01	3.71E-01	6.28E-01	7.20E-01	5.65E-01	6.27E-01	5.33E-01	3.94E-01	5.32E-01	4.14E-01
643	6.21E-02	1.15E-01	2.24E-01	3.28E-01	3.57E-01	6.12E-01	6.98E-01	5.53E-01	6.08E-01	5.16E-01	3.83E-01	5.19E-01	4.05E-01
646	5.96E-02	1.12E-01	2.18E-01	3.20E-01	3.48E-01	6.01E-01	6.79E-01	5.47E-01	5.97E-01	5.04E-01	3.81E-01	5.12E-01	4.02E-01
649	5.94E-02	1.13E-01	2.21E-01	3.23E-01	3.46E-01	6.07E-01	6.84E-01	5.61E-01	6.04E-01	5.11E-01	3.92E-01	5.22E-01	4.12E-01
652	6.06E-02	1.20E-01	2.35E-01	3.44E-01	3.68E-01	6.44E-01	7.29E-01	6.03E-01	6.47E-01	5.43E-01	4.21E-01	5.54E-01	4.43E-01
655	6.73E-02	1.40E-01	2.64E-01	3.90E-01	4.19E-01	7.24E-01	8.32E-01	6.86E-01	7.34E-01	6.19E-01	4.82E-01	6.20E-01	4.99E-01
658	7.97E-02	1.70E-01	3.15E-01	4.62E-01	5.04E-01	8.51E-01	9.93E-01	8.23E-01	8.71E-01	7.39E-01	5.76E-01	7.28E-01	5.92E-01
661	9.87E-02	2.16E-01	3.82E-01	5.59E-01	6.17E-01	1.02E+00	1.21E+00	1.01E+00	1.05E+00	9.15E-01	7.08E-01	8.66E-01	7.13E-01
664	1.22E-01	2.71E-01	4.63E-01	6.74E-01	7.57E-01	1.23E+00	1.49E+00	1.23E+00	1.28E+00	1.12E+00	8.64E-01	1.03E+00	8.54E-01
667	1.46E-01	3.31E-01	5.42E-01	7.90E-01	8.92E-01	1.44E+00	1.76E+00	1.44E+00	1.49E+00	1.33E+00	1.01E+00	1.19E+00	9.86E-01
670	1.66E-01	3.79E-01	6.05E-01	8.80E-01	9.94E-01	1.61E+00	1.98E+00	1.61E+00	1.66E+00	1.49E+00	1.12E+00	1.31E+00	1.09E+00
673	1.76E-01	3.95E-01	6.30E-01	9.18E-01	1.04E+00	1.67E+00	2.07E+00	1.68E+00	1.73E+00	1.55E+00	1.16E+00	1.37E+00	1.12E+00
676	1.73E-01	3.79E-01	6.14E-01	8.95E-01	1.02E+00	1.64E+00	2.01E+00	1.63E+00	1.69E+00	1.50E+00	1.13E+00	1.33E+00	1.08E+00
679	1.58E-01	3.40E-01	5.67E-01	8.27E-01	9.45E-01	1.52E+00	1.82E+00	1.50E+00	1.55E+00	1.36E+00	1.03E+00	1.22E+00	9.81E-01
682	1.33E-01	2.85E-01	4.95E-01	7.18E-01	8.21E-01	1.33E+00	1.57E+00	1.29E+00	1.35E+00	1.16E+00	8.79E-01	1.05E+00	8.37E-01
685	1.05E-01	2.18E-01	3.99E-01	5.86E-01	6.66E-01	1.09E+00	1.26E+00	1.04E+00	1.10E+00	9.22E-01	7.03E-01	8.56E-01	6.68E-01
688	7.56E-02	1.52E-01	2.96E-01	4.43E-01	4.97E-01	8.31E-01	9.27E-01	7.67E-01	8.26E-01	6.81E-01	5.19E-01	6.49E-01	4.94E-01
691	5.07E-02	9.71E-02	2.00E-01	3.09E-01	3.38E-01	5.89E-01	6.28E-01	5.24E-01	5.75E-01	4.62E-01	3.52E-01	4.64E-01	3.47E-01
694	3.37E-02	5.79E-02	1.28E-01	2.00E-01	2.11E-01	3.93E-01	4.06E-01	3.33E-01	3.77E-01	3.02E-01	2.24E-01	3.22E-01	2.34E-01
697	2.21E-02	3.30E-02	8.03E-02	1.26E-01	1.28E-01	2.55E-01	2.59E-01	2.08E-01	2.41E-01	1.97E-01	1.40E-01	2.20E-01	1.54E-01
700	1.52E-02	1.88E-02	4.89E-02	7.70E-02	7.58E-02	1.62E-01	1.64E-01	1.25E-01	1.51E-01	1.27E-01	8.50E-02	1.52E-01	1.02E-01
703	1.05E-02	1.07E-02	3.01E-02	4.54E-02	4.27E-02	1.03E-01	1.06E-01	7.24E-02	9.28E-02	8.29E-02	5.34E-02	1.09E-01	6.93E-02
706	6.96E-03	6.21E-03	1.90E-02	2.63E-02	2.50E-02	6.59E-02	6.97E-02	4.16E-02	5.69E-02	5.77E-02	3.26E-02	8.02E-02	4.99E-02
709	4.42E-03	3.11E-03	1.25E-02	1.35E-02	1.67E-02	4.26E-02	4.86E-02	2.63E-02	3.34E-02	3.96E-02	2.16E-02	5.97E-02	3.27E-02
712	2.99E-03	1.92E-03	8.09E-03	6.03E-03	1.04E-02	2.83E-02	3.85E-02	1.37E-02	1.83E-02	2.89E-02	1.48E-02	4.86E-02	2.50E-02
715	2.86E-03	4.49E-04	6.10E-03	6.59E-04	6.17E-03	1.89E-02	2.73E-02	4.00E-03	1.40E-02	2.27E-02	1.03E-02	3.96E-02	1.95E-02
718	2.84E-03	8.70E-05	3.10E-03	-1.96E-03	4.23E-03	1.14E-02	2.07E-02	8.30E-04	6.89E-03	1.77E-02	5.26E-03	3.41E-02	1.49E-02

pigment abs.cost

Table 4

Pigment absorption coefficient. Day is given in fractions to indicate time of day. Wavelength is in nm.

wavelength	Date: 7.33	8.33	9.33	9.67	10.33	10.67	11.33	11.67	12.33	12.67	13.33	13.67	14.67
721	2.12E-03	-4.38E-04	1.51E-03	-3.03E-03	1.42E-03	7.53E-03	1.31E-02	-4.43E-03	5.19E-04	1.09E-02	3.78E-03	2.66E-02	1.11E-02
725	1.70E-03	-9.64E-04	3.13E-04	-5.00E-03	7.26E-04	4.89E-03	1.14E-02	-3.69E-03	-2.34E-03	9.48E-03	1.62E-03	2.16E-02	9.65E-03
728	1.50E-03	-1.51E-03	-2.10E-04	-6.93E-03	-7.99E-04	2.67E-03	9.95E-03	-5.78E-03	-5.51E-03	1.03E-02	2.27E-03	1.62E-02	7.64E-03
731	1.32E-03	-2.09E-03	-5.00E-04	-8.25E-03	-8.58E-04	-1.78E-03	5.48E-03	-8.08E-03	-9.50E-03	4.61E-03	9.18E-04	1.41E-02	5.00E-03
734	1.31E-03	-1.77E-03	-1.22E-03	-8.91E-03	-8.88E-04	-3.06E-03	3.92E-03	-9.20E-03	-9.81E-03	3.10E-03	9.76E-06	1.22E-02	2.35E-03
737	1.39E-03	-1.84E-03	-2.29E-03	-9.54E-03	-7.13E-04	-3.90E-03	5.45E-03	-8.01E-03	-8.40E-03	3.07E-03	-5.32E-09	1.01E-02	2.51E-03
740	1.21E-03	-2.33E-03	-3.43E-03	-1.02E-02	-7.04E-04	-5.03E-03	6.83E-03	-7.08E-03	-9.96E-03	3.05E-03	-1.73E-05	9.68E-03	-3.53E-04
743	9.32E-04	-2.29E-03	-3.68E-03	-1.02E-02	-3.81E-04	-5.72E-03	6.06E-03	-6.44E-03	-1.17E-02	1.39E-03	-1.73E-05	7.66E-03	-1.21E-03
746	4.57E-04	-2.40E-03	-3.72E-03	-1.06E-02	-1.13E-04	-6.53E-03	3.17E-03	-6.38E-03	-1.29E-02	-1.07E-03	-1.73E-05	5.45E-03	-1.54E-03
749	6.58E-04	-2.36E-03	-3.88E-03	-1.05E-02	-3.72E-05	-5.24E-03	5.14E-04	-6.21E-03	-1.30E-02	-2.06E-03	0.00E+00	4.80E-03	-2.28E-03
753	8.02E-04	-2.23E-03	-4.29E-03	-1.08E-02	-1.84E-04	-6.13E-03	1.47E-03	-6.12E-03	-1.25E-02	-1.89E-03	0.00E+00	3.62E-03	-1.98E-03

DETRITAL SPECTRAL ABSORPTION FROM DAY 9 (NORMALIZED @ 673 nm)

-8-

wavelength (nm)

400

673

750

SAMPLE DAY

9   9.5   10   10.5   11   11.5   12   12.5   13   13.5   14.5
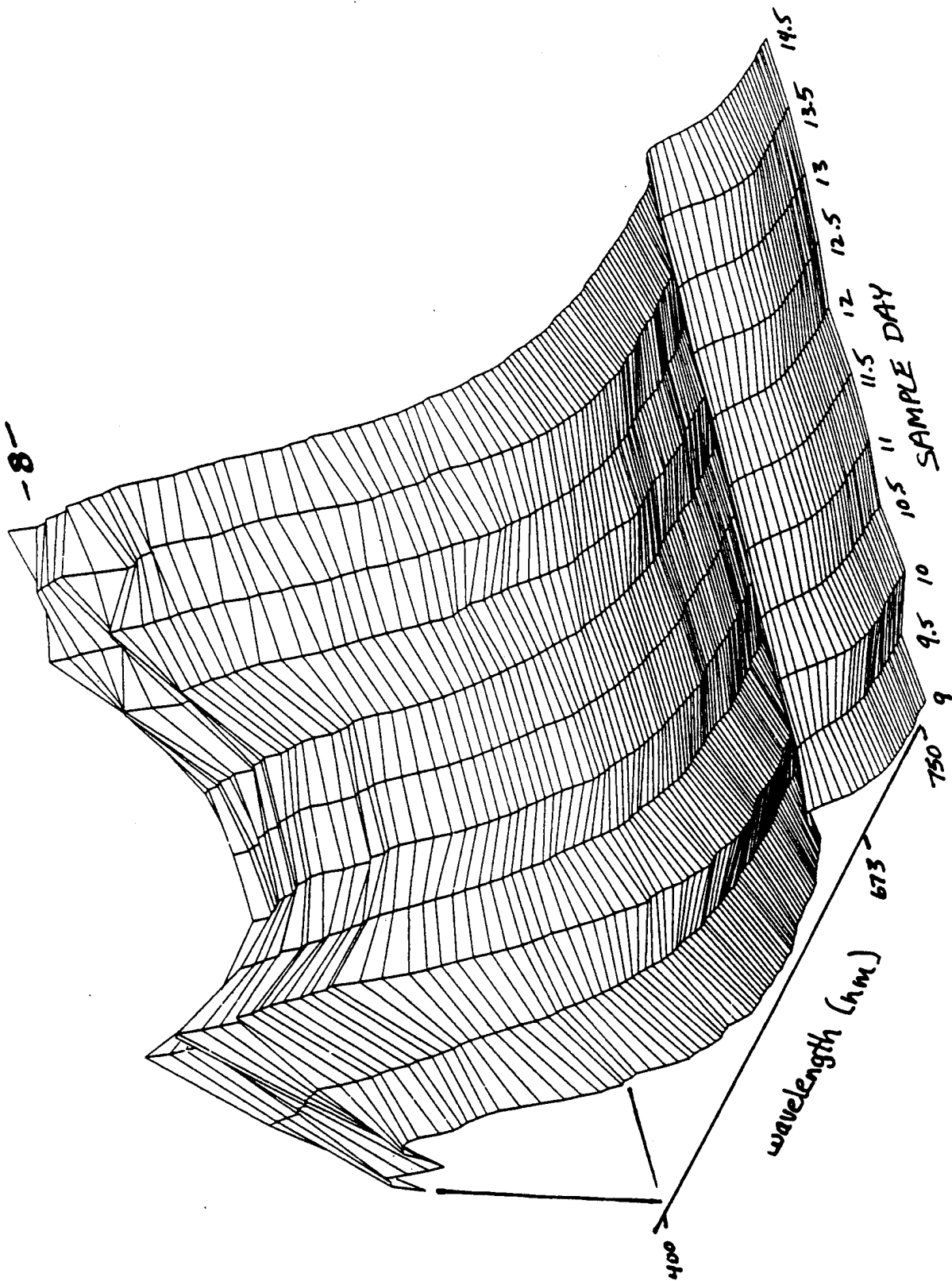
Figure 1
SIGMA TANK DATA REPORT
CARDER LAB

SIGMA TANK - SPECTRAL ABSORPTION, PIGMENTS (USF/MSL 5/20/93 dkc)
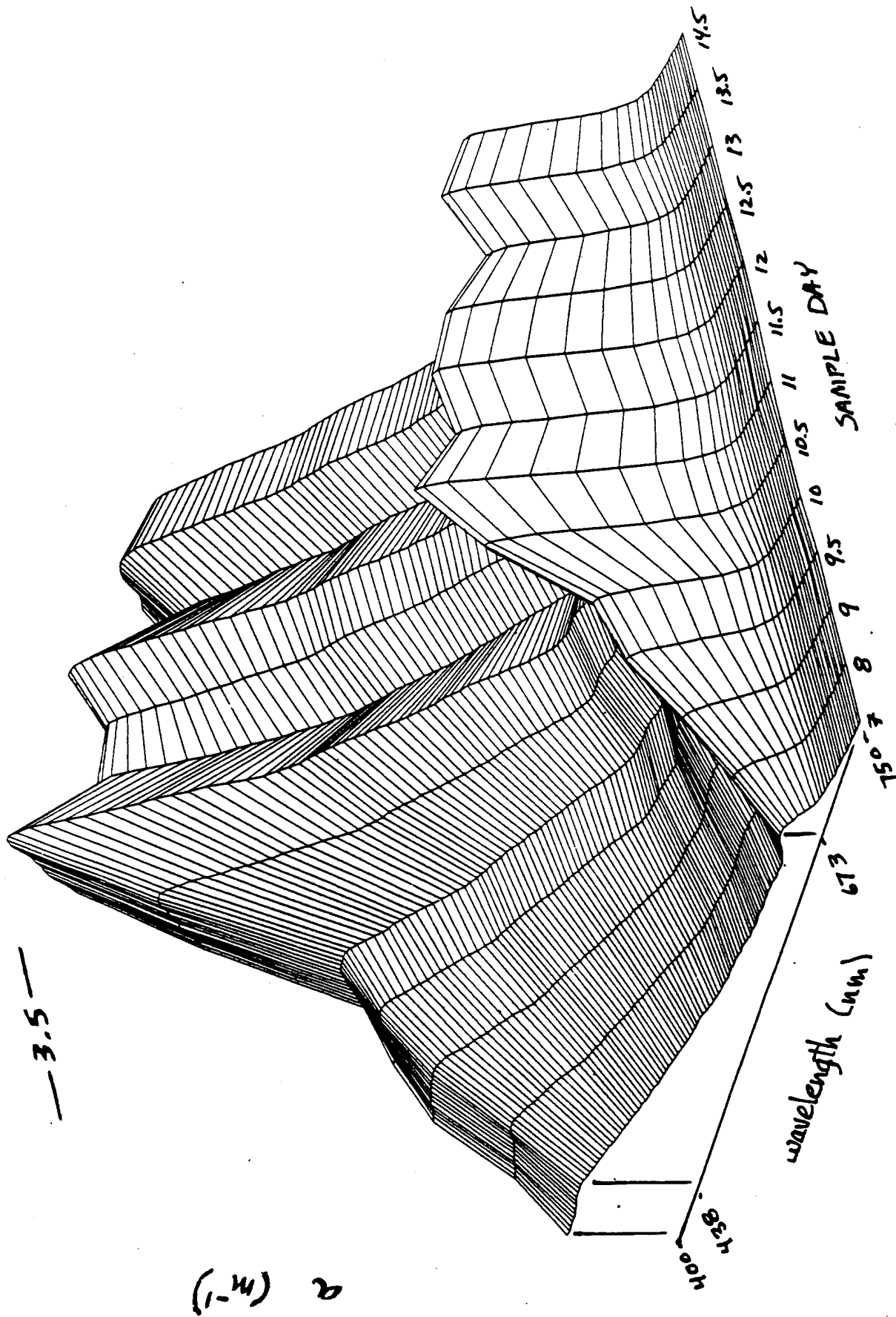
Figure 2
SIGMA TANK DATA REPORT
CARDER LAB

V-24

PIGMENT ABSORPTION NORMALIZED @ 673 nm
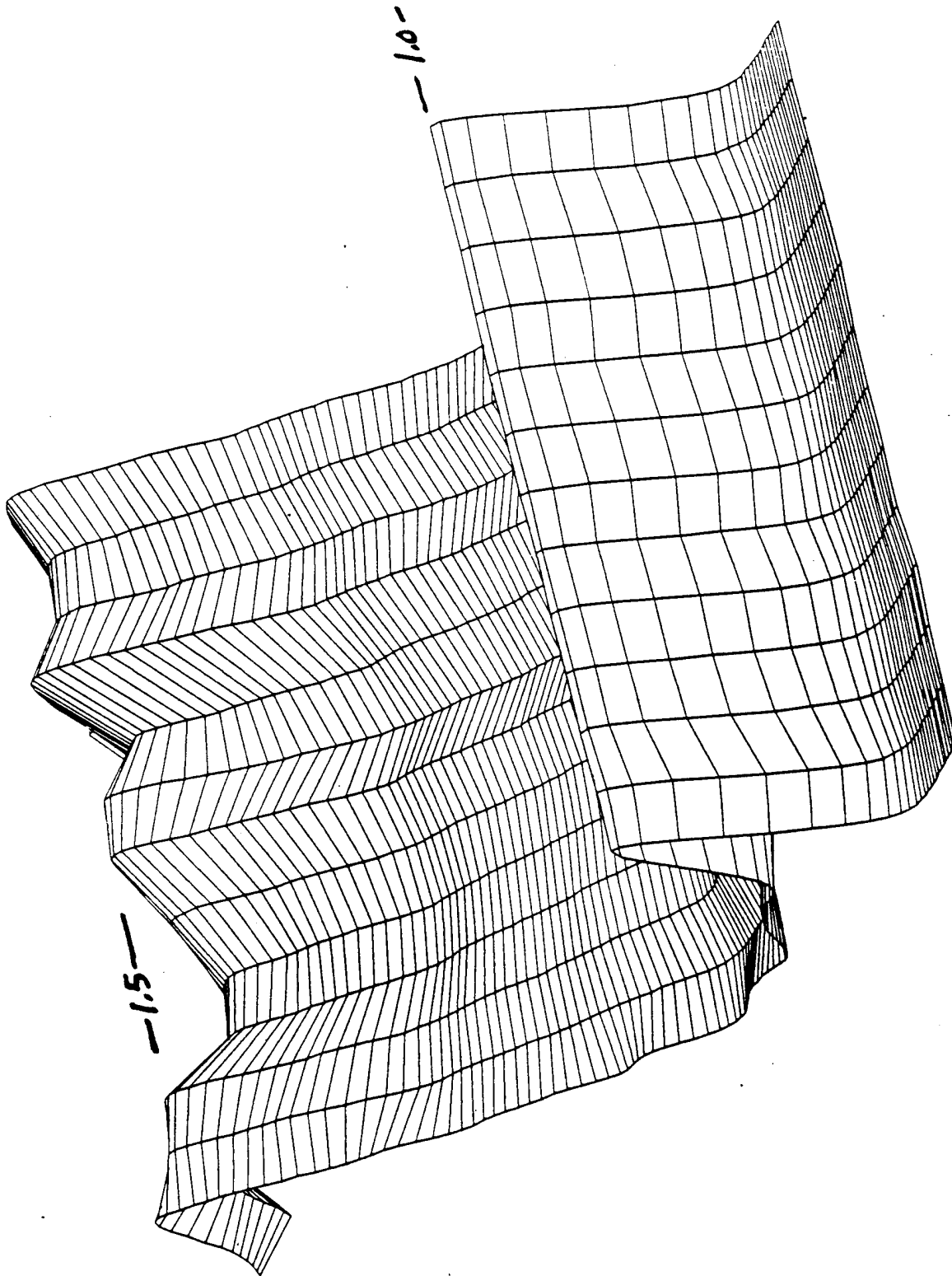
Figure 3
SIGMA TANK DATA REPORT
CARDER LAB

SIGMA TANK - SPECIFIC ABSORPTION
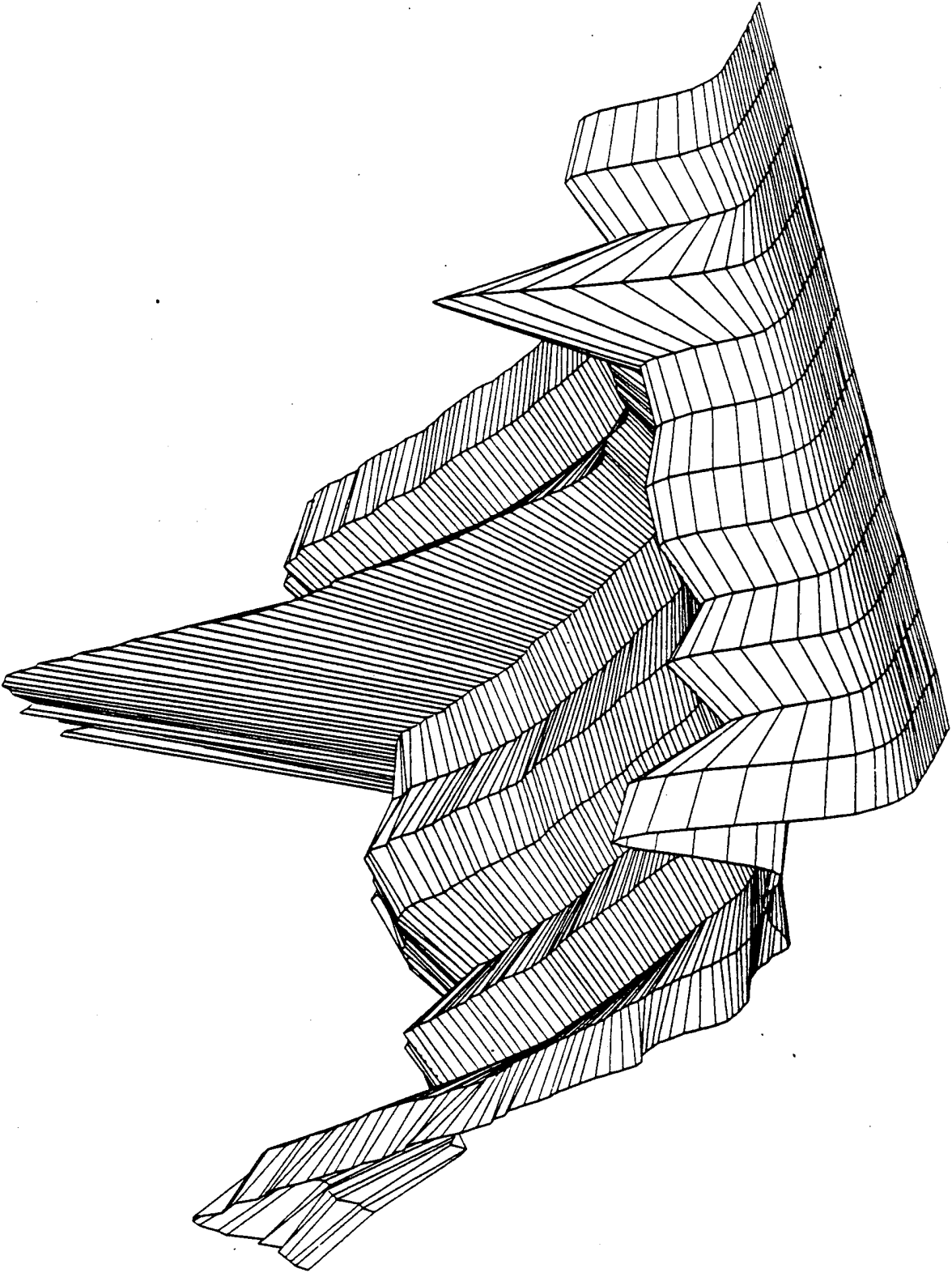
Figure 4
SIGMA TANK DATA REPORT
CARDER LAB

(using 12.5 cl

Figure Vt

SIGMA TANK - SPECIFIC ABSORPTION (data point 12.5 modified)
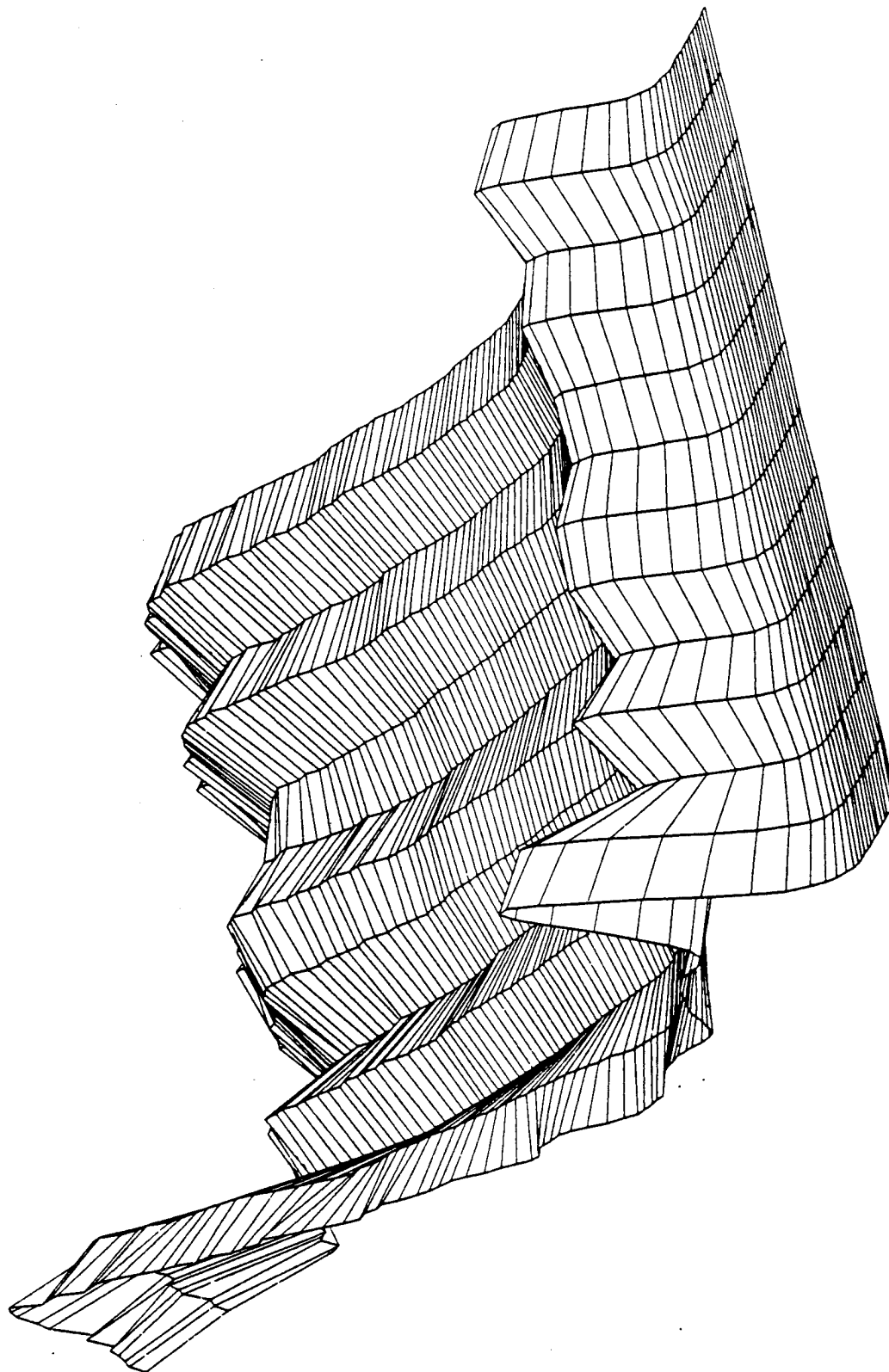
Figure 5
SIGMA TANK DATA REPORT
CARDER LAB

Percent of Total Absorption by Detritus
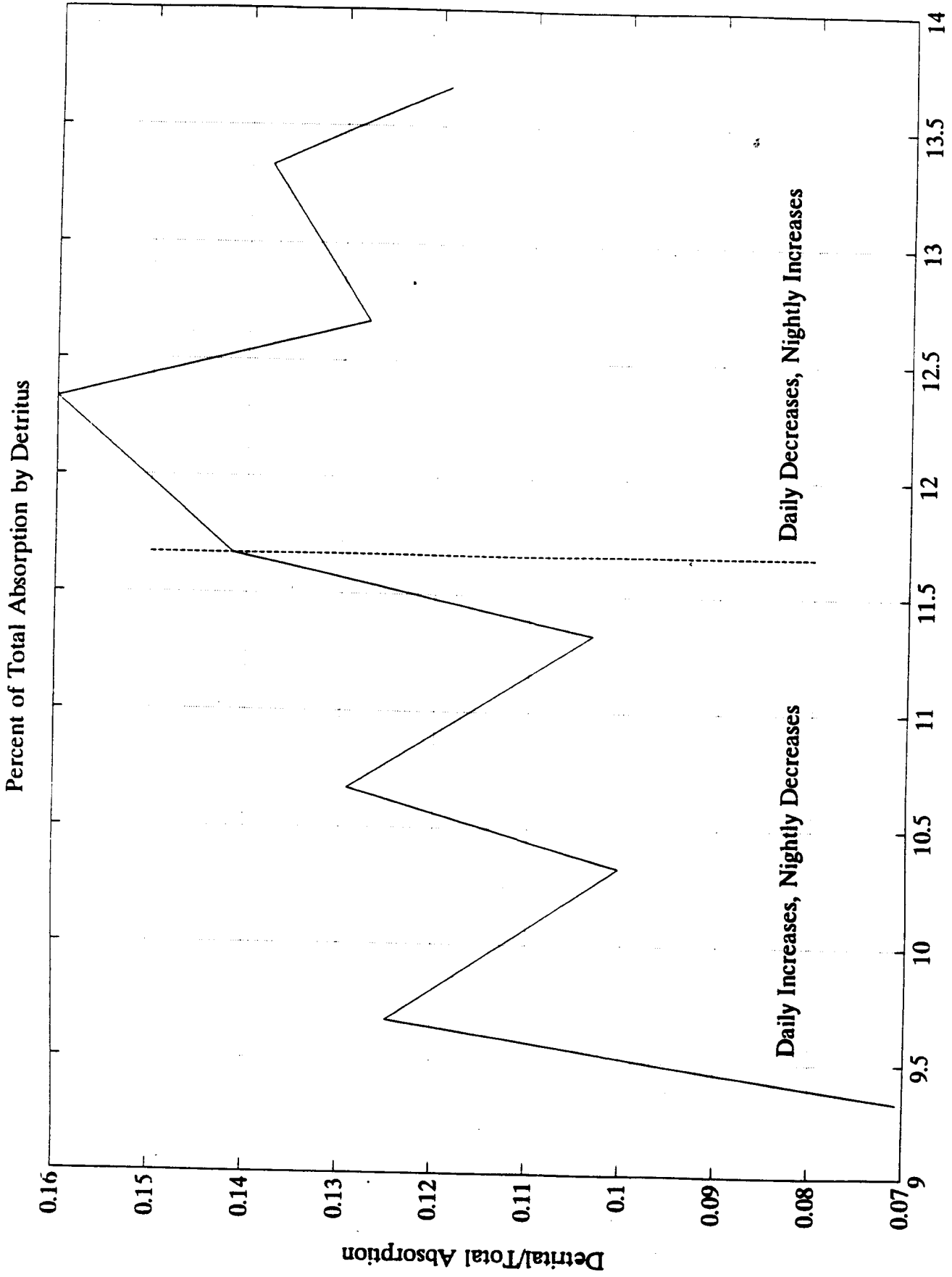
Figure 6
SIGMA TANK DATA REPORT

Daily Increases, Nightly Decreases

Daily Decreases, Nightly Increases

Sample Day after Innoculation

Detrital/Total Absorption

Chl_a Specific Absorption Coefficient (673 nm)
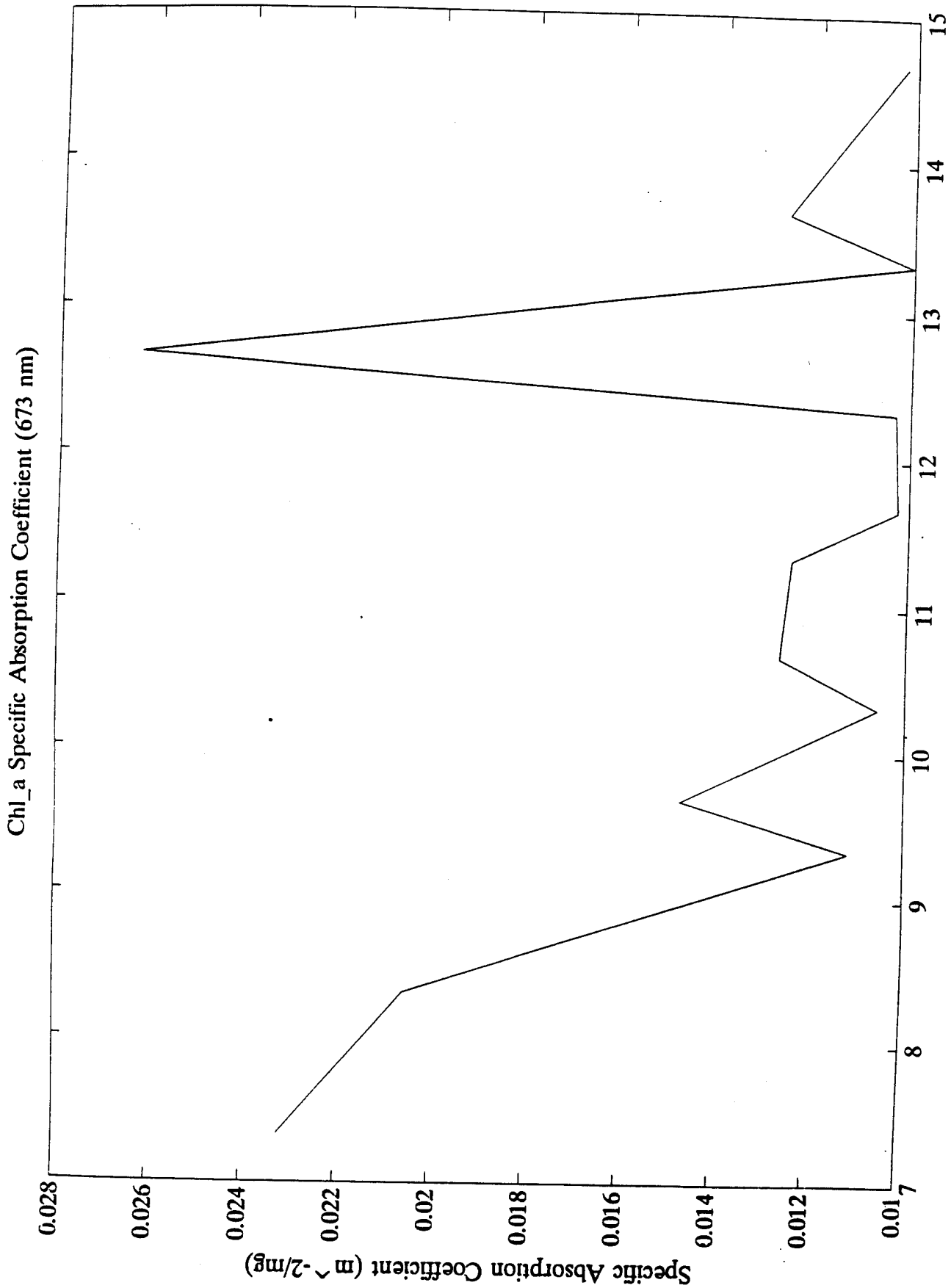
Sample Day after Innoculation

Figure 7
SIGMA TANK DATA REPORT

Specific Absorption Coefficient (m^-2/mg)

MEASURED Chl_a vs ABSORPTION @ 673 nm

$Y = .0093 X + .2893$

$r^2 = 0.79$, $n = 13$

(All data points)

Chl_a (mg/m^ 3)

Absorption Coefficient @ 673 nm (m ^ -1)
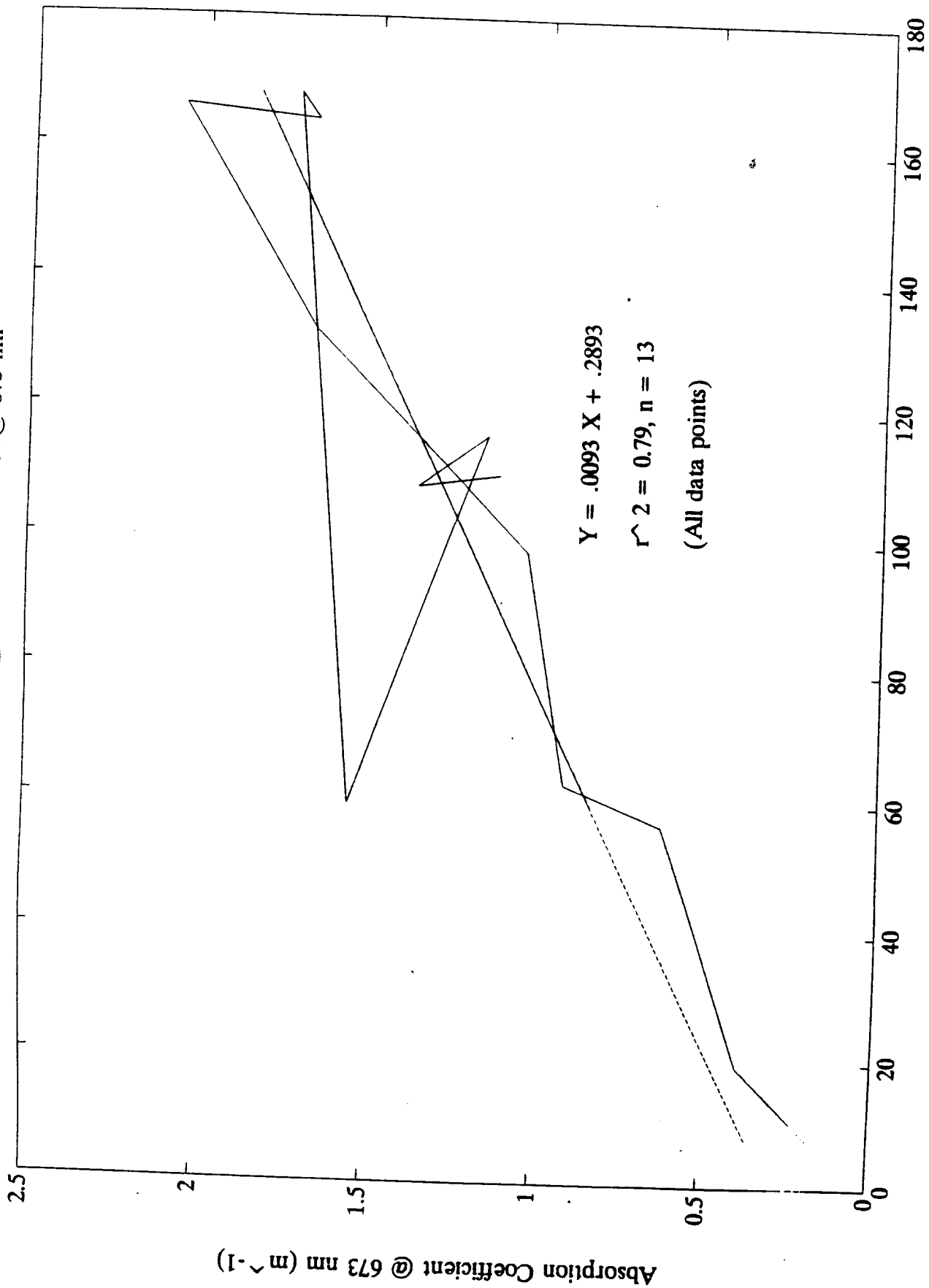
Figure 8
SIGMA TANK DATA REPORT
CARDER LAB

MEASURED Chl_a vs ABSORPTION @ 673 nm

$Y = .0102 \ X + .1388$

$r^2 = 0.94$, $n = 12$

(Chl_a data point 12.5 excluded)

Chl_a (mg/m^3)

Absorption Coefficient @ 673 nm (m^-1)
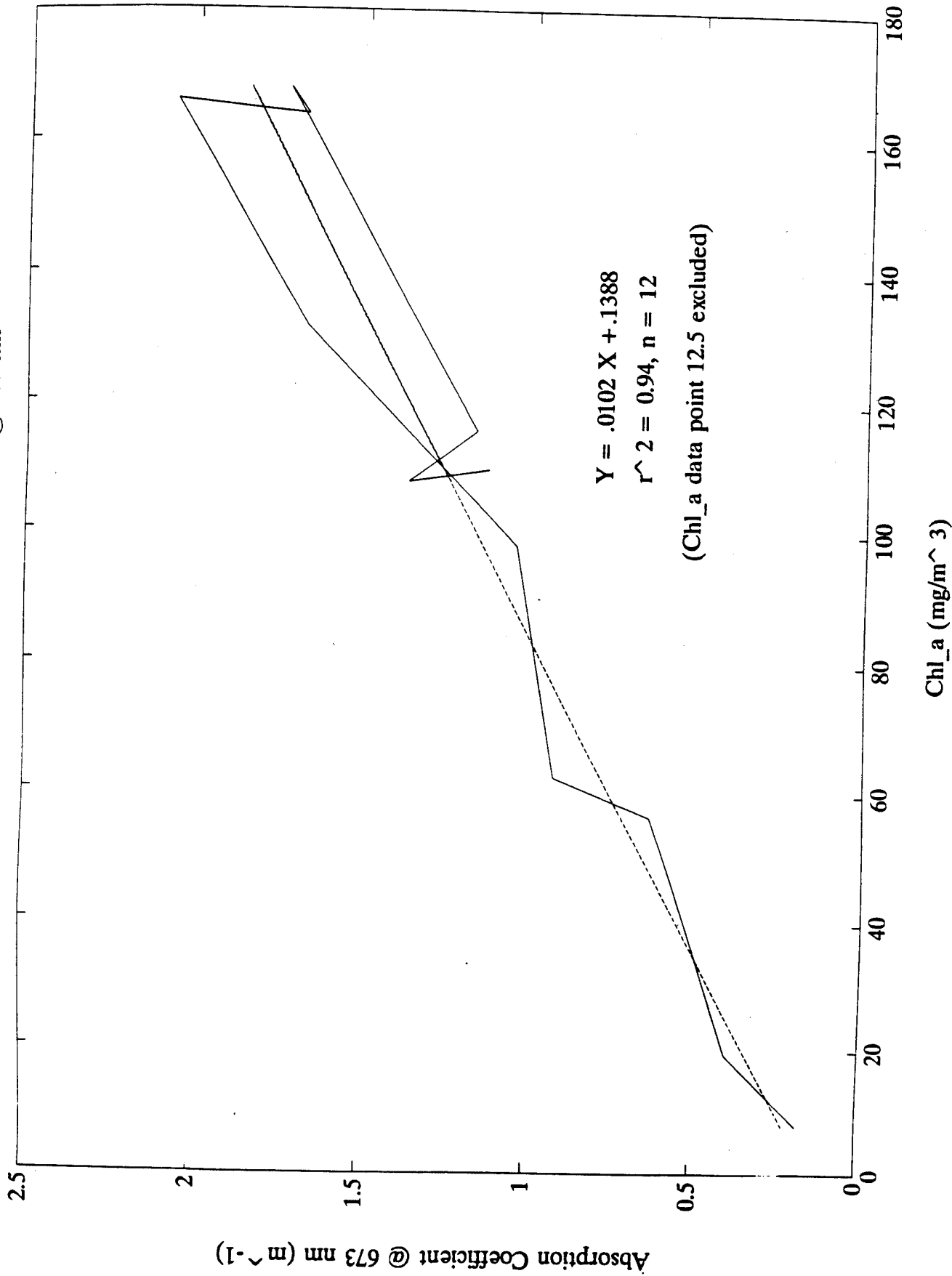
Figure 9
SIGMA TANK DATA REPORT
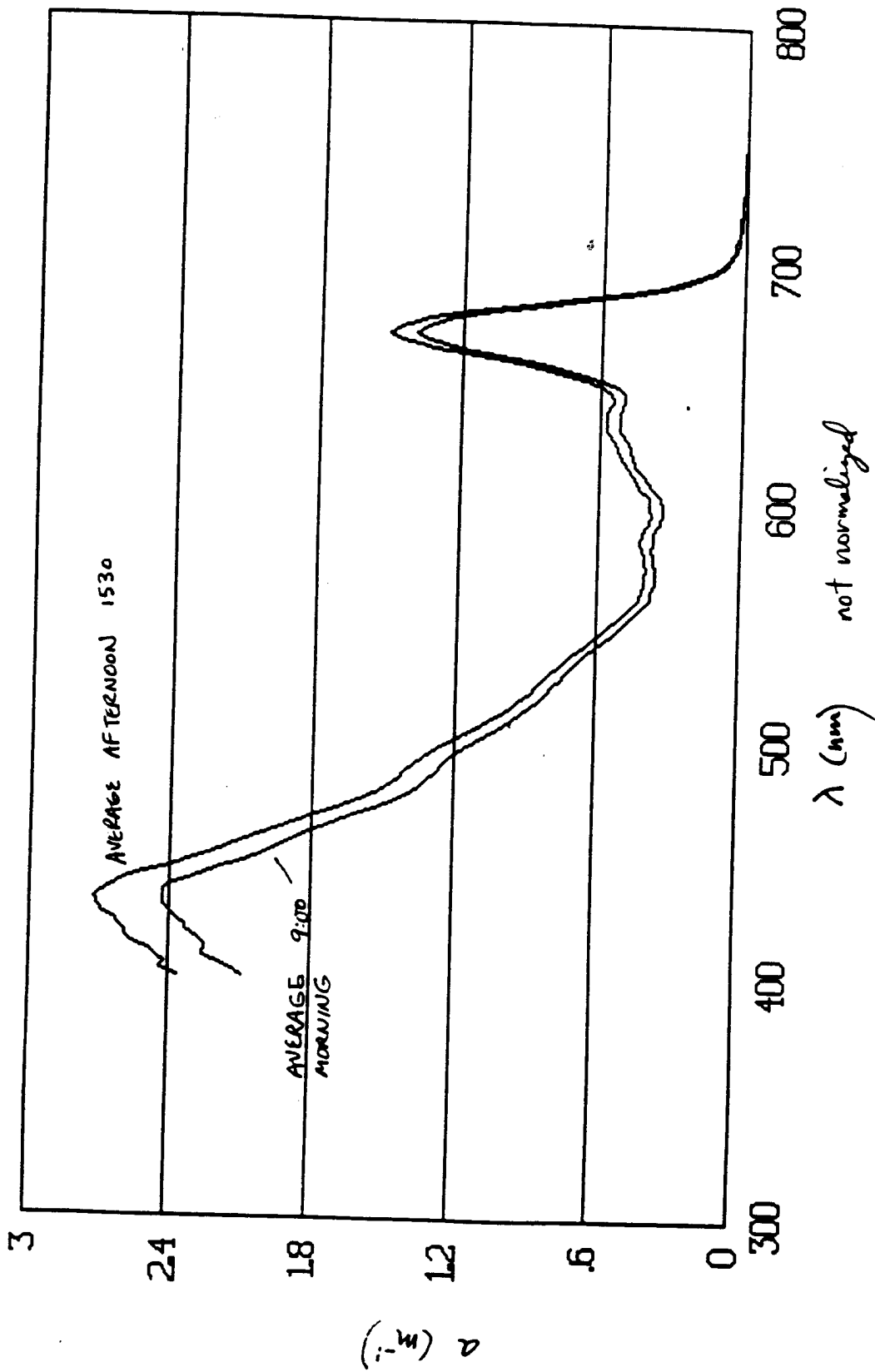
Figure 10
SIGMA TANK DATA REPORT

PIGMENT ABSORPTION CURVES FOR SIGMA TANK EXPERIMENT

- Morning measurements only
- No. indicates sample day
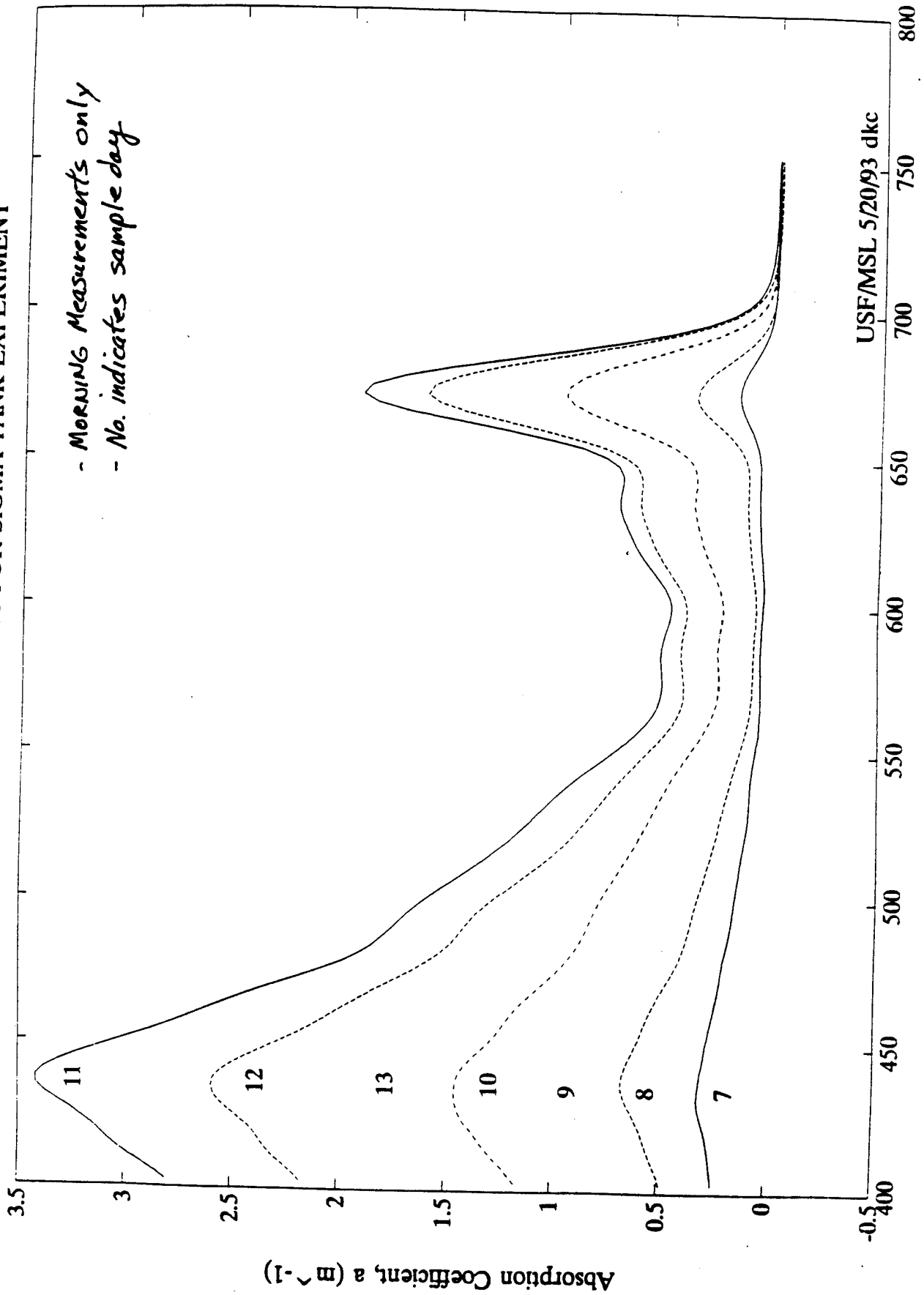
Wavelength (nm)

Figure 11
SIGMA TANK DATA REPORT

USF/MSL 5/20/93 dkc

SAMPLES OF DATA FILTERED WITH A 7 ELEMENT HANNING WINDOW

3/19 am

3/16 pm

specific absorption coefficient, ap* (m^2)/(mg chl a)

wavelength (nm)

Figure 12
SIGMA TANK DATA REPORT

V-36
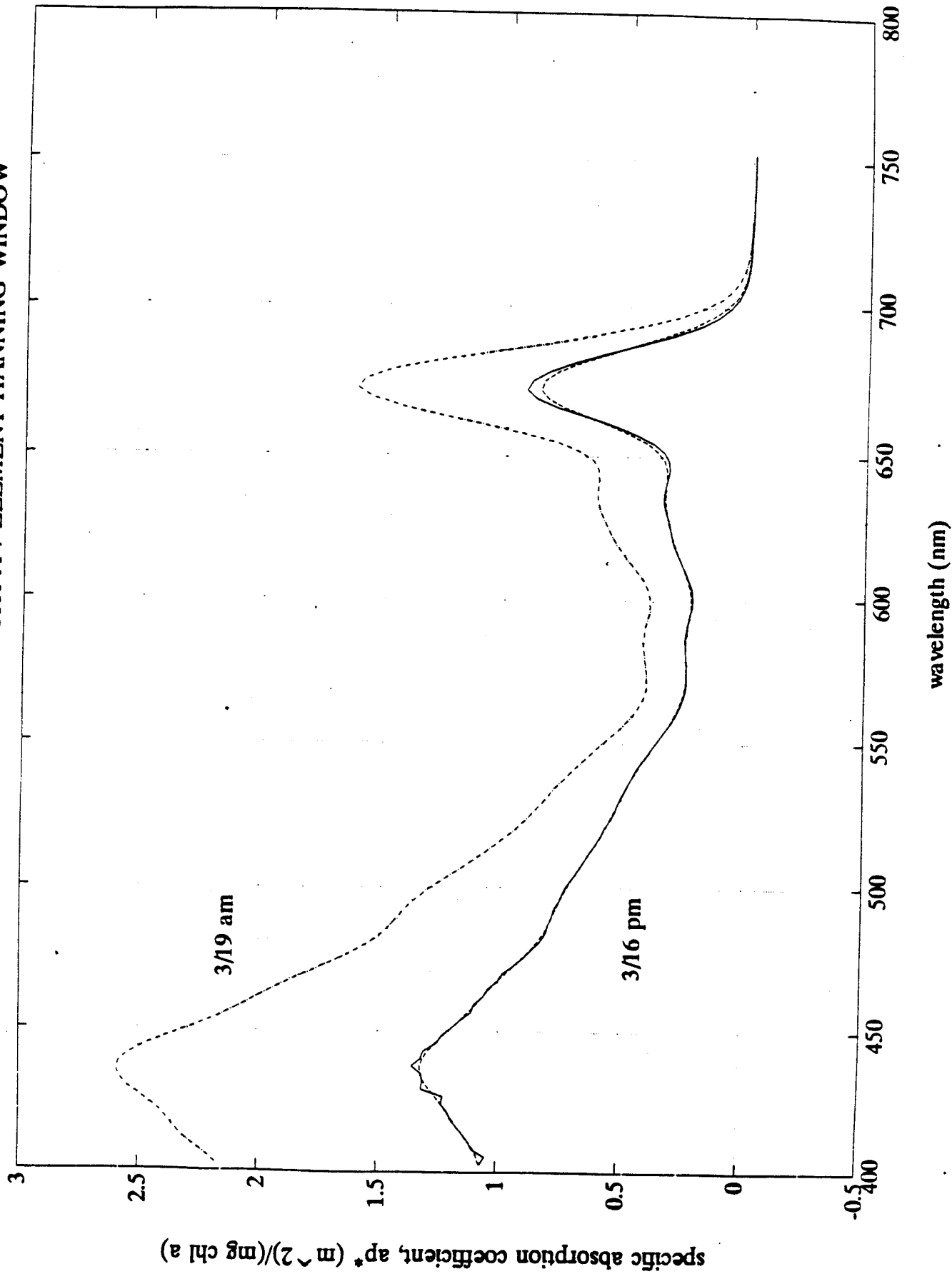
SPECIFIC ABSORPTION COEFFICIENTS FOR VARIOUS PIGMENTS (Bidigare, 90)
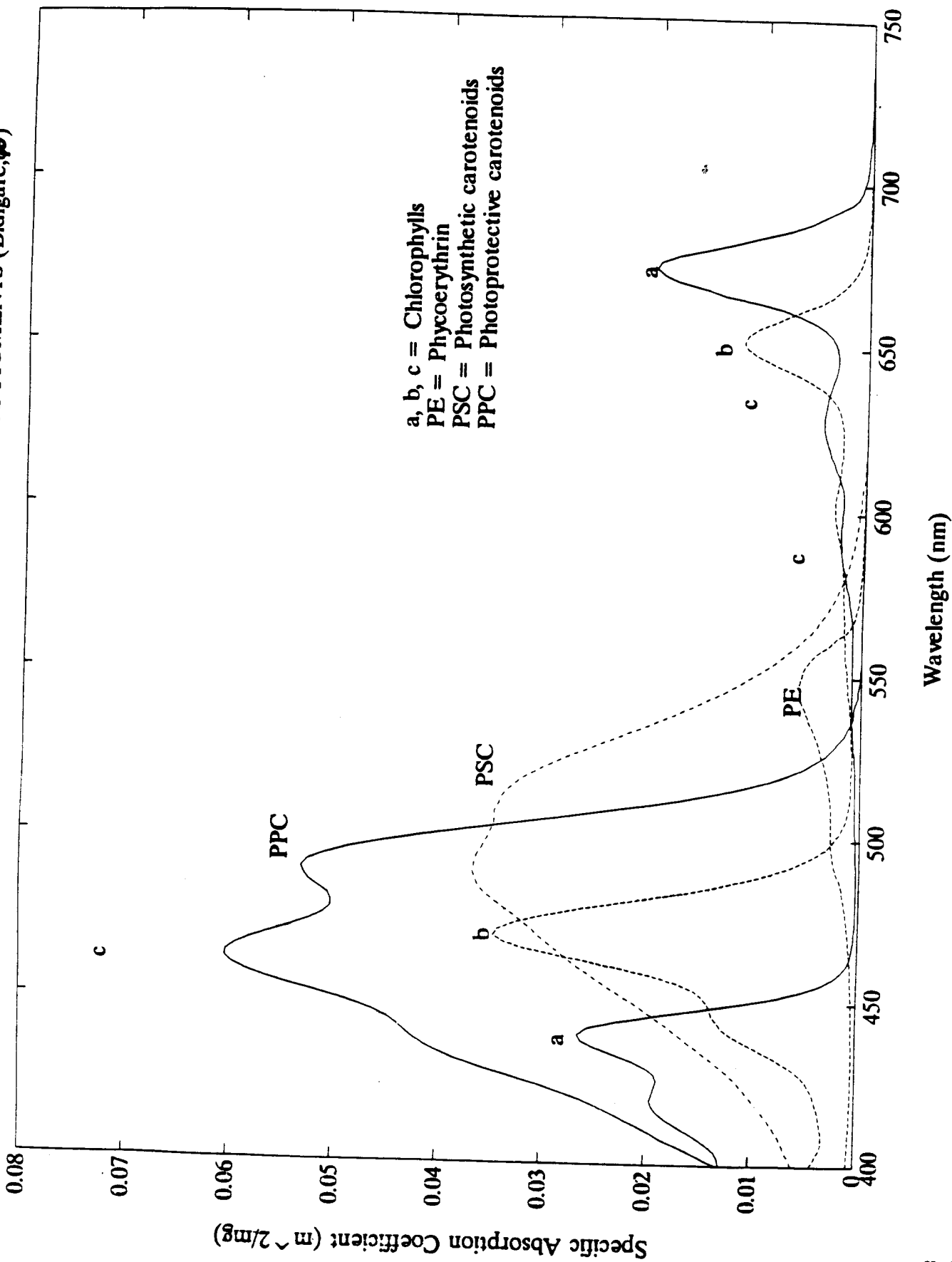
a, b, c = Chlorophylls
PE = Phycoerythrin
PSC = Photosynthetic carotenoids
PPC = Photoprotective carotenoids

Wavelength (nm)

Specific Absorption Coefficient (m^2/mg)

Figure 13
SIGMA TANK DATA REPORT
CARDER LAB

AVERAGED DERIVATIVE SPECTRA FOR AMs, PMs, 1st HALF, and 2nd HALF
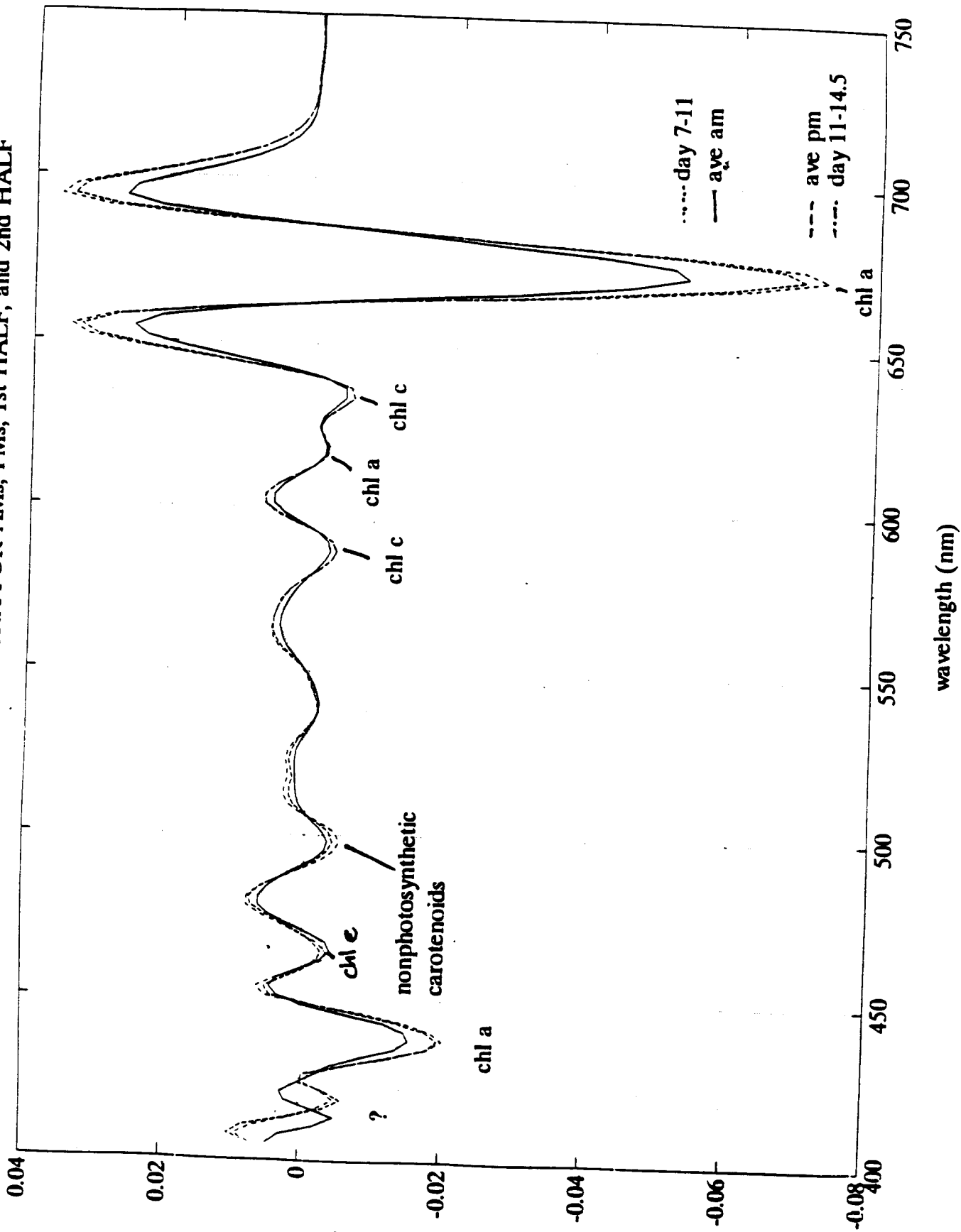
Figure 14
SIGMA TANK DATA REPORT

DAILY ATTENUATION (Samples nearest 1530 hours)

Attenuation Coefficient, c (m^-1)

Time (sec)

day 11
day 12
day 13
day 10
day 9
day 8
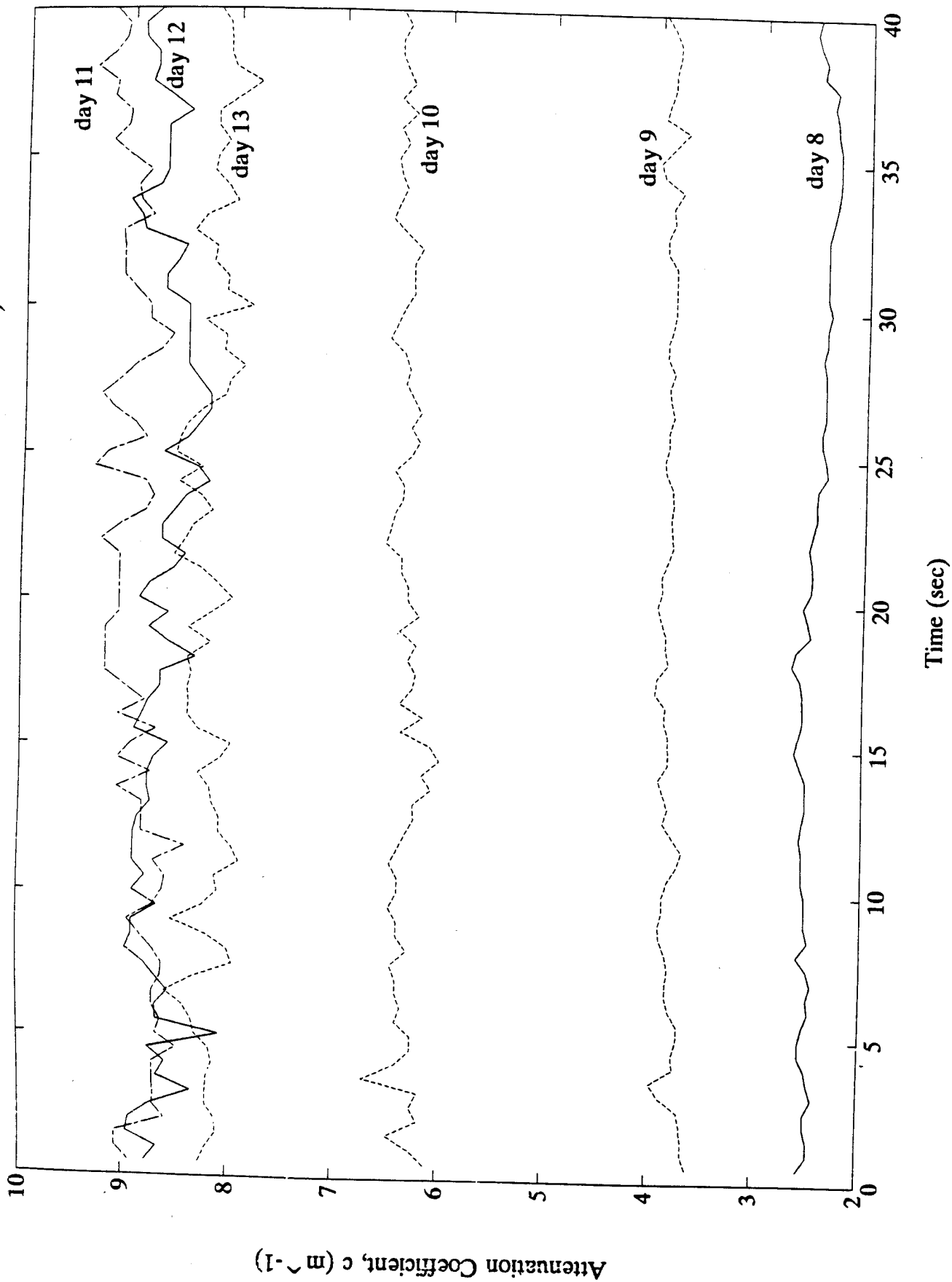
Figure 15
SIGMA TANK DATA REPORT
CARDER LAR

MAXIMUM, MEAN, AND MINIMUM ATTENUATION COEFFICIENTS

Attenuation Coefficient c (m^-1)

Time (sample day)

Figure 16
SIGMA TANK DATA REPORT
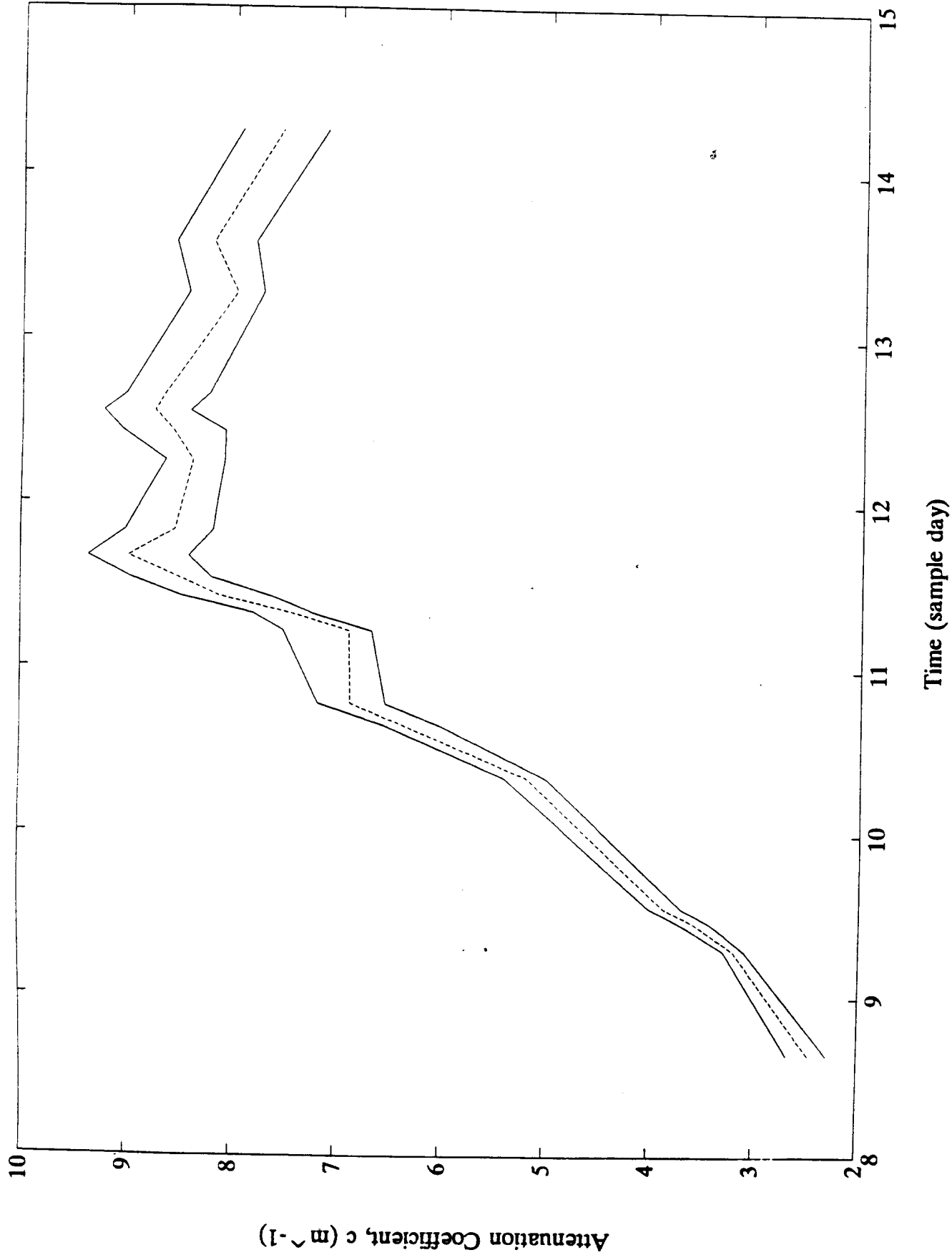
SIGMA TANK EXPERIMENT ATTENUATION COEFFICIENT

- - all samples

--- samples near 1530 hours only

Time (sample day)

Attenuation Coefficient, c (m^-1)
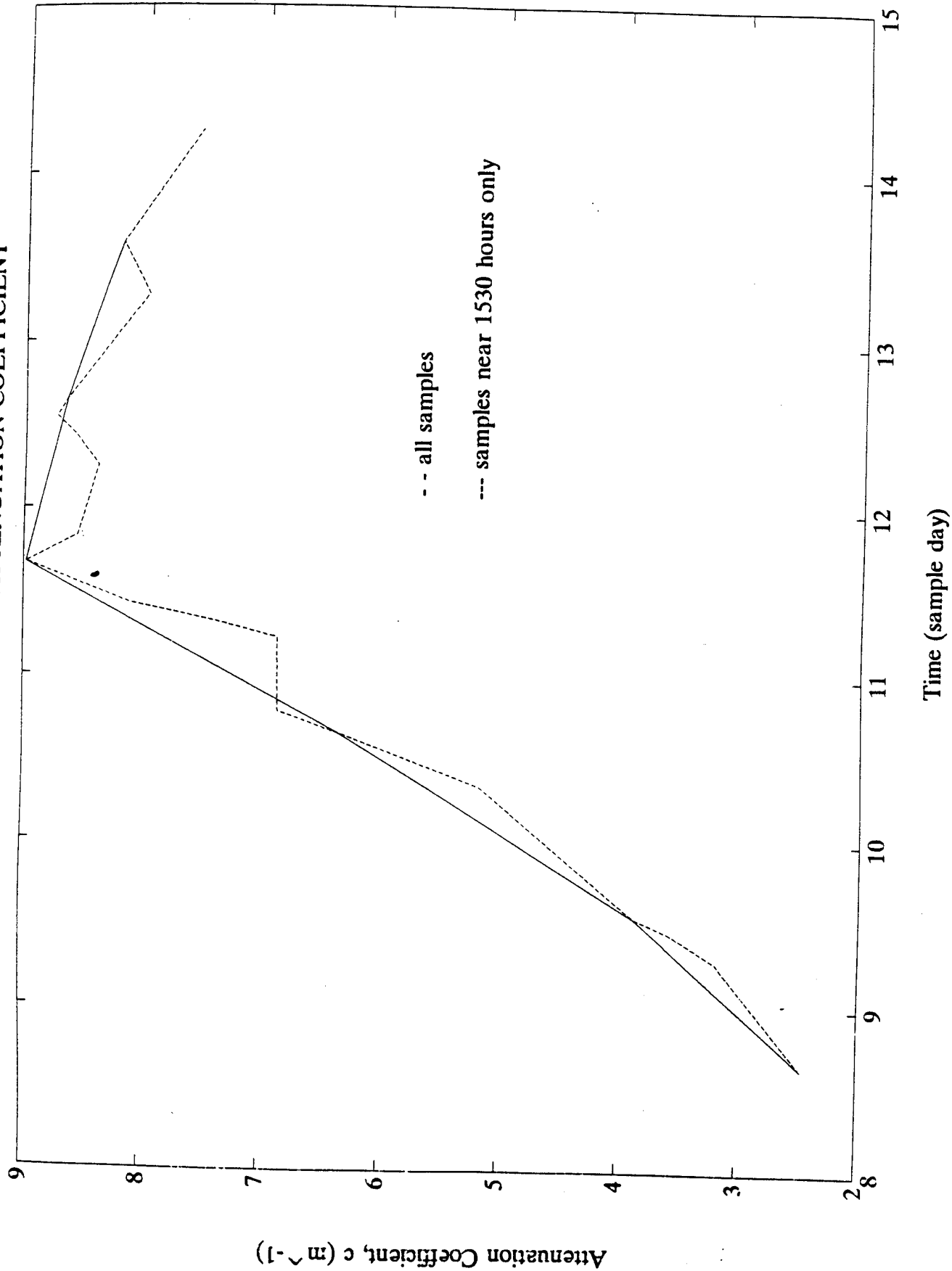
Figure 17
SIGMA TANK DATA REPORT

V-39

THERMOCLINE DEVELOPMENT - Day 11, 0530 - 2000 hours

Attenuation Coefficient c (m^-1)
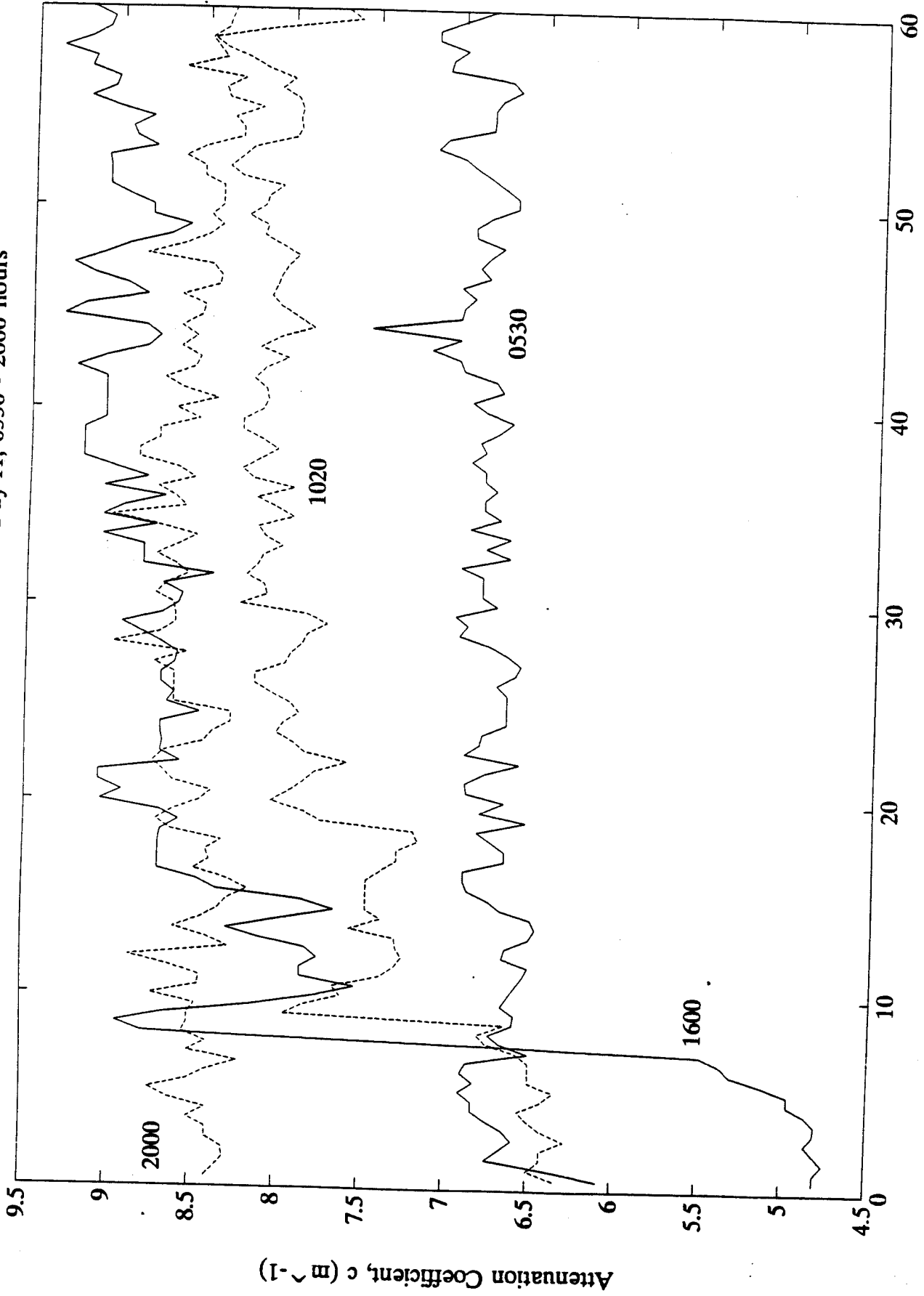
Time (sec)

Figure 18
SIGMA TANK DATA REPORT

V-40

SIGMA TANK - OPTICAL PARAMETERS

a, b, c coefficients (m^-1)

c(lp)

b(lp)

omega x 5

a(lp)
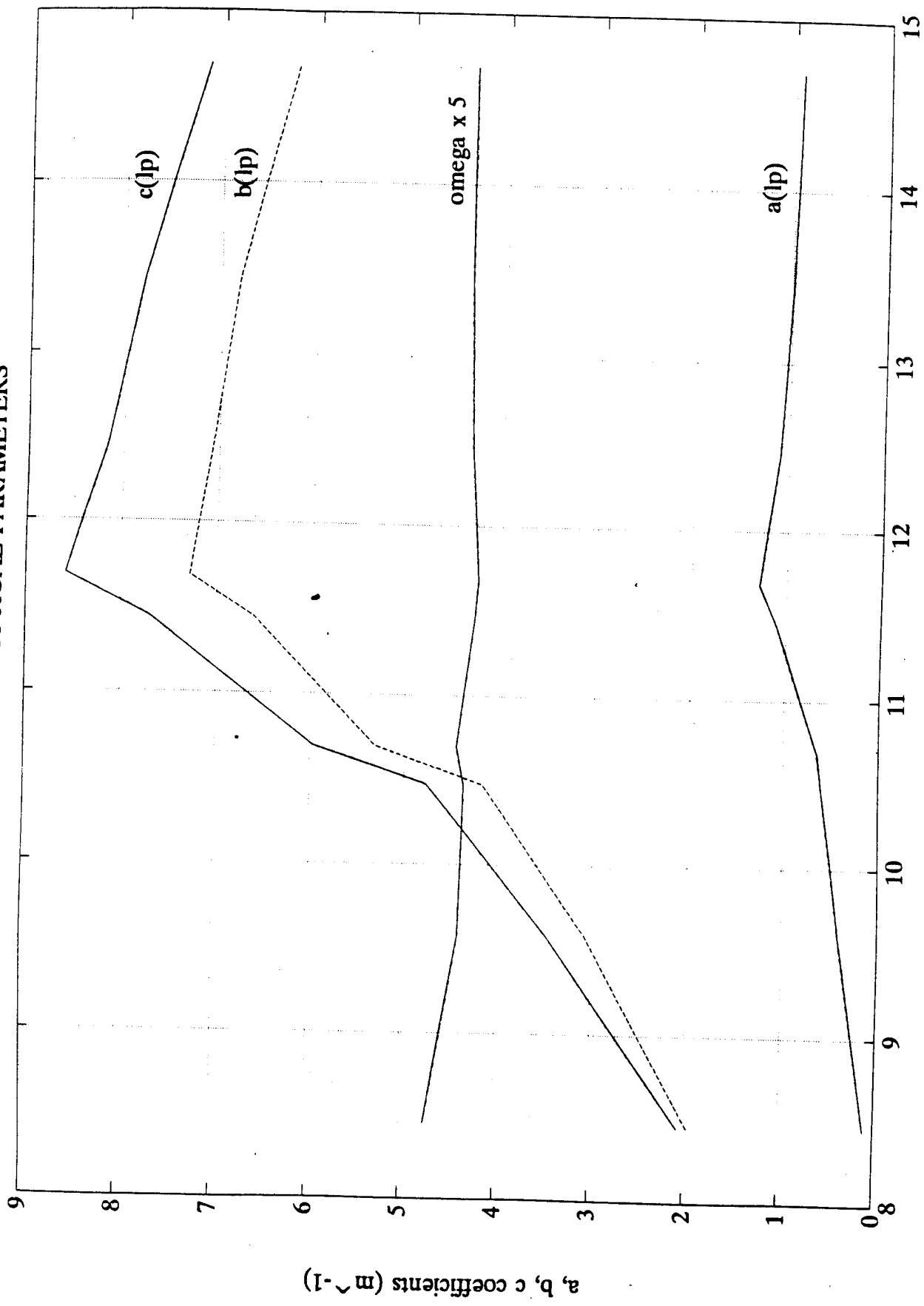
Sample Day after Innoculation

Figure 19
SIGMA TANK DATA REPORT
CARDER LAB

ATTENUATION vs. PARTICULATE NITROGEN

$$c = 12.55(N) + .64$$

Particulate Nitrogen Concentration (mg/l)

Attenuation Coefficient, c (m $^\wedge$ -1)
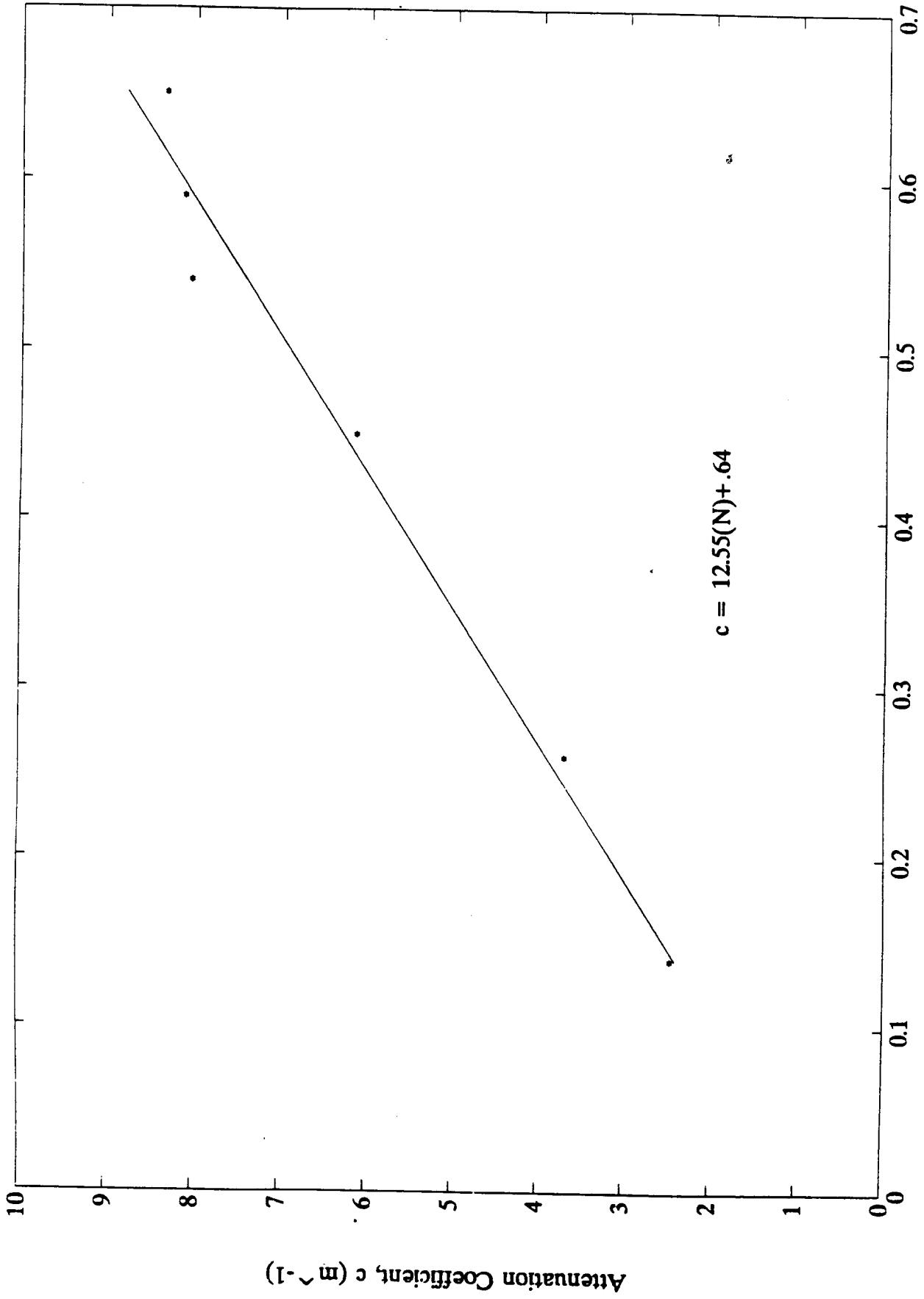
Figure 20
SIGMA TANK DATA REPORT

THEORETICAL SCATTER AND ABSORPTION EFFECT ON IMAGE VOLUME
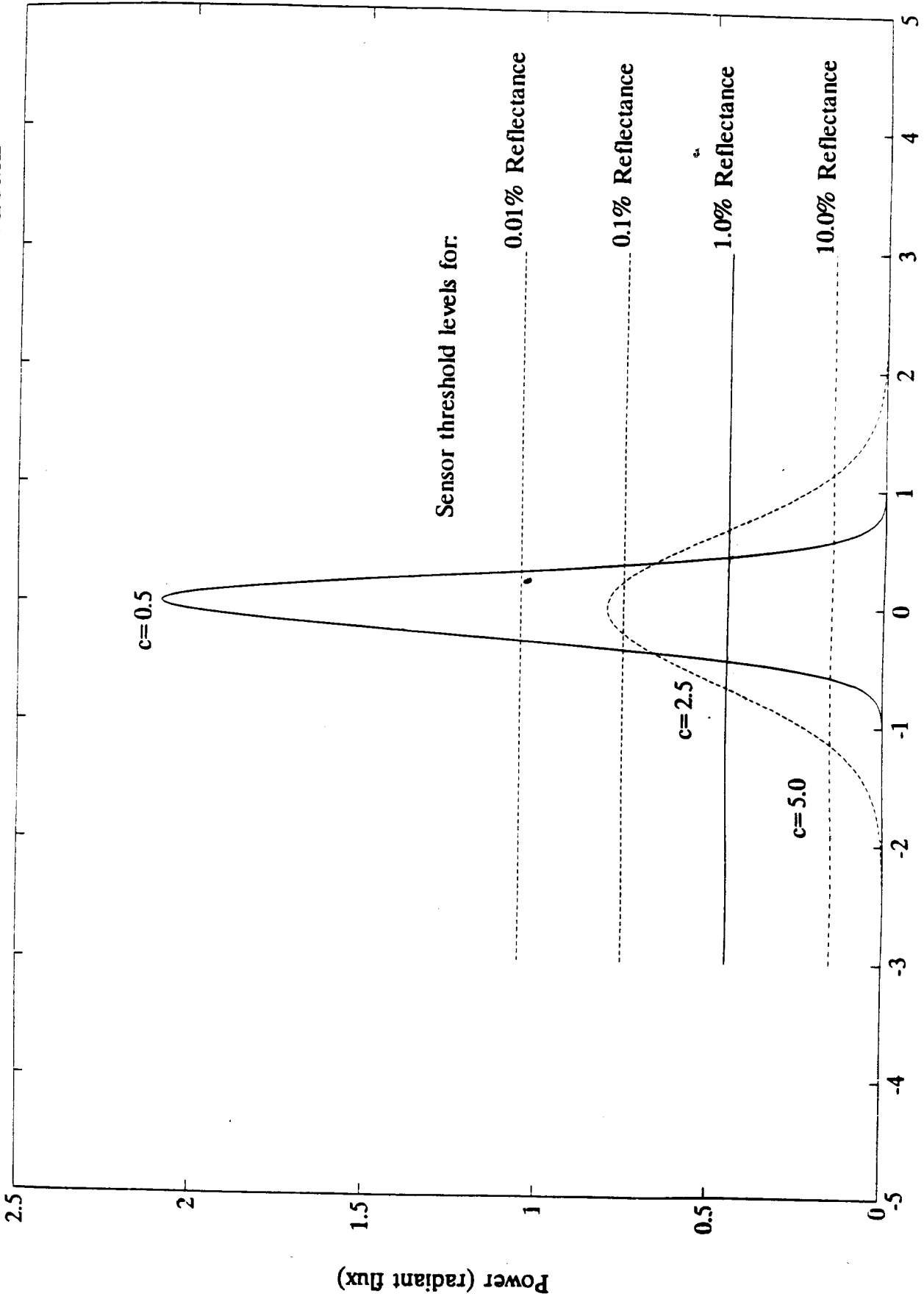
Figure 21
SIGMA TANK DATA REPORT

SIGMA TANK - MAPPER DATA - ALL SETS
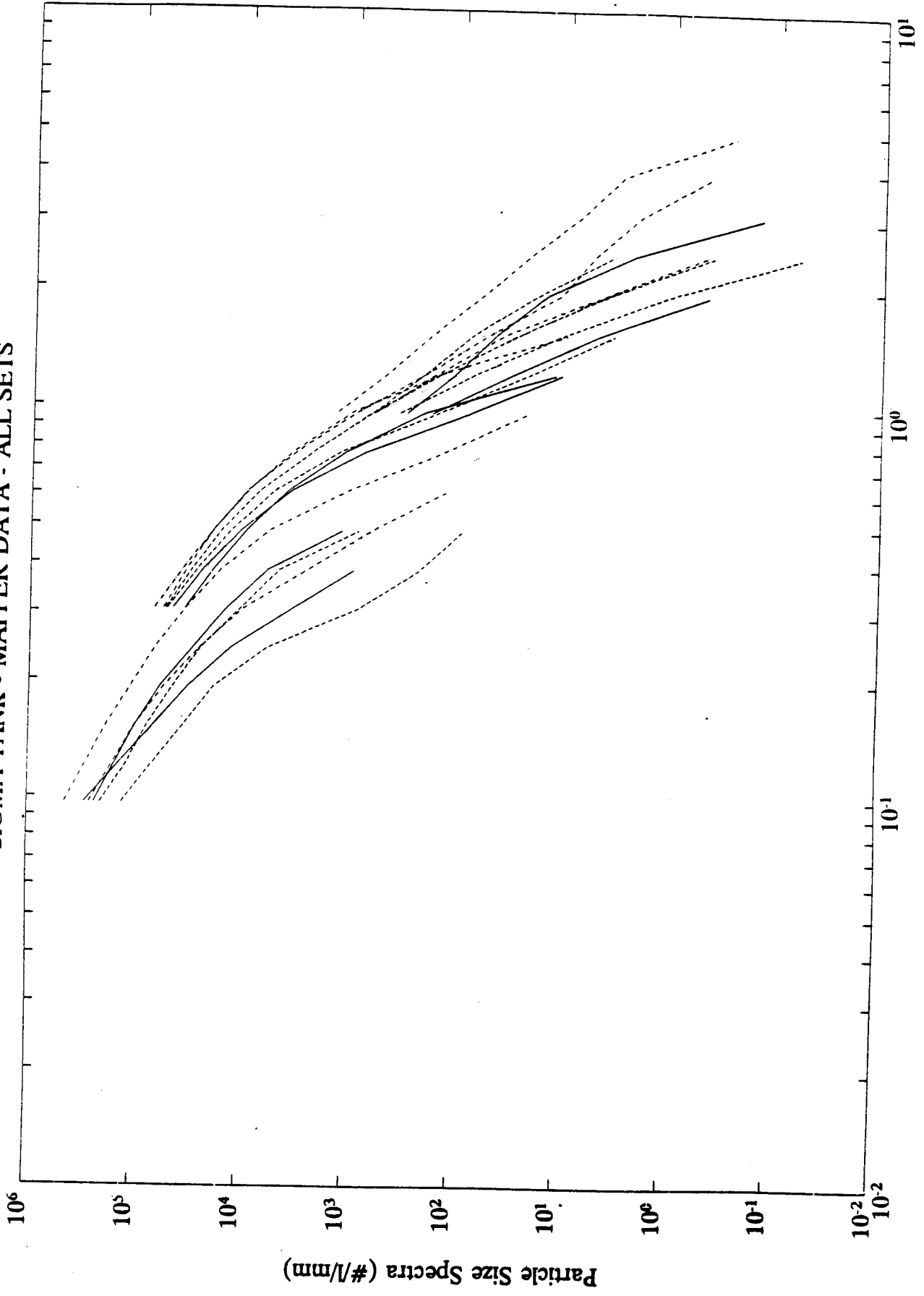
Particle Diameter (mm, corrected for porosity)

Figure 22
SIGMA TANK DATA REPORT

Particle Size Spectra (#/l/mm)

Non-accumulated Size Spectra from all three MAPPER Fields

Particle number (log) /L /mm

Particle Size (mm) (log)

Time (days)
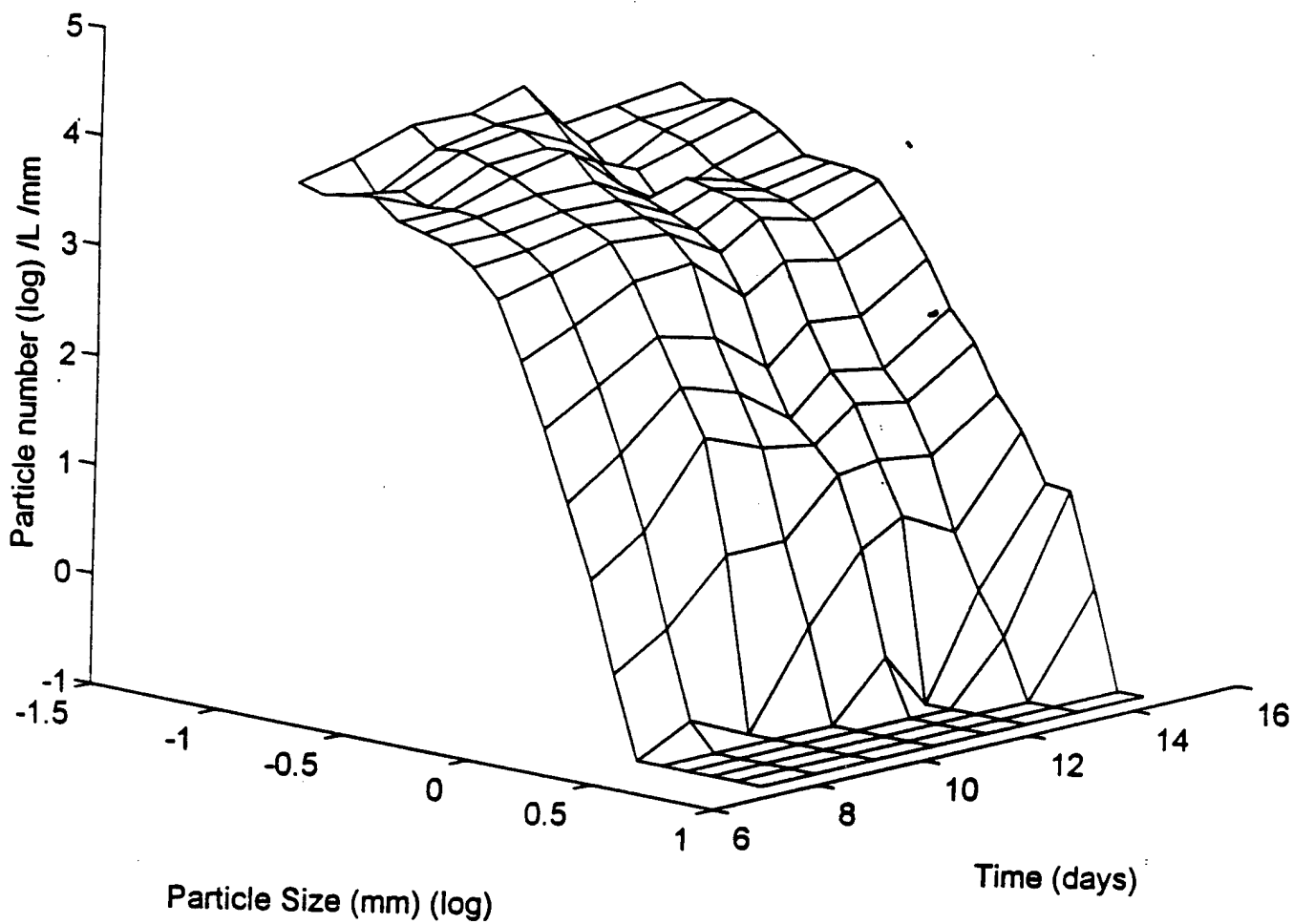
Figure 23
SIGMA TANK DATA REPORT
CARDER LAB

SIGMA TANK - LARGE PARTICLE SPECTRA SLOPE CHANGE

Day 14
N = 1474*D^ (-4.93)

Day 7
N = 161*D^ (-8.60)

MAPPER DATA
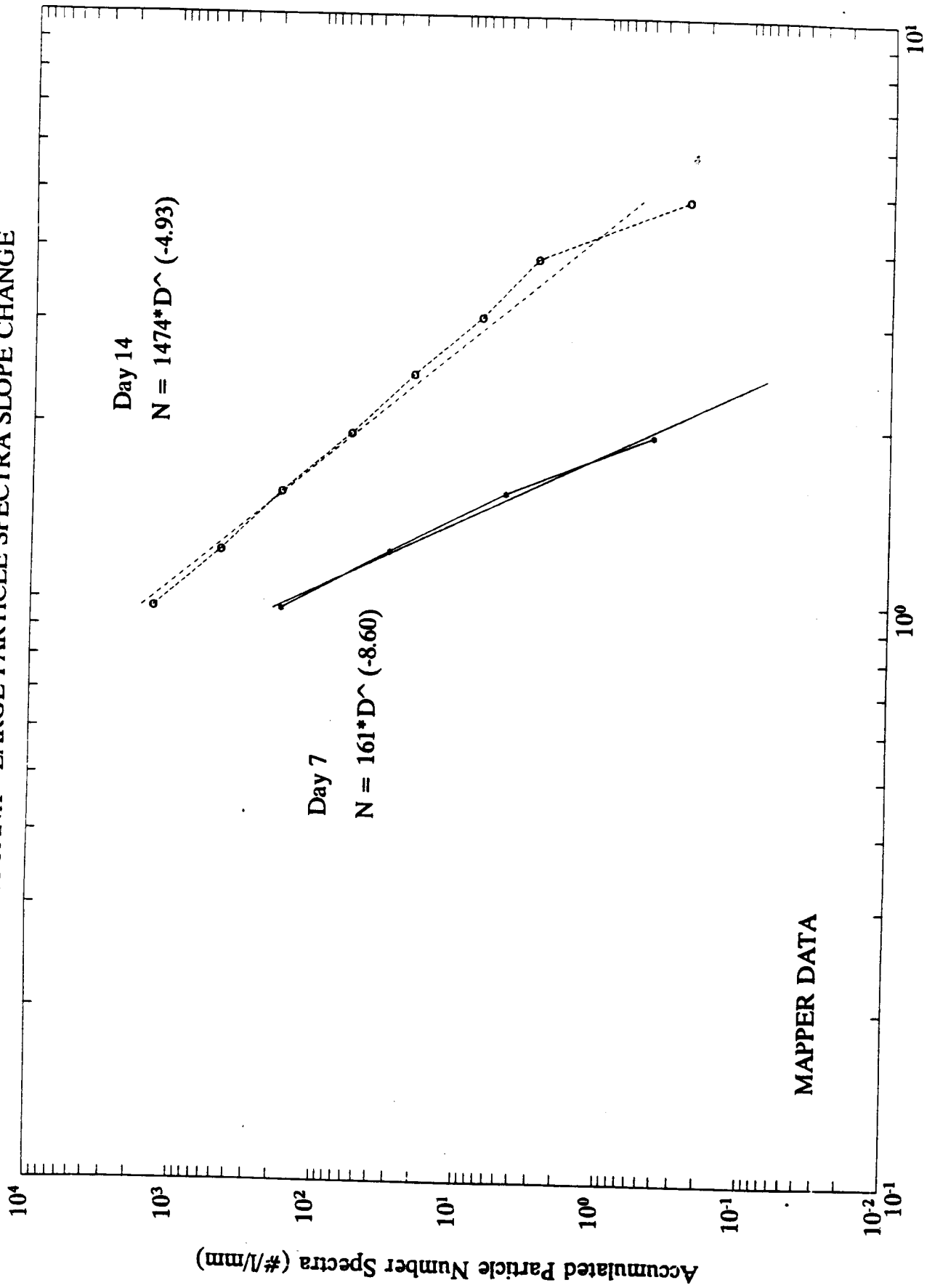
Particle Diameter (mm)

Figure 24
SIGMA TANK DATA REPORT

Accumulated Particle Number Spectra (#/l/mm)

VOLUME VS. TIME - (Particle dia. > 85 and < 170 microns)
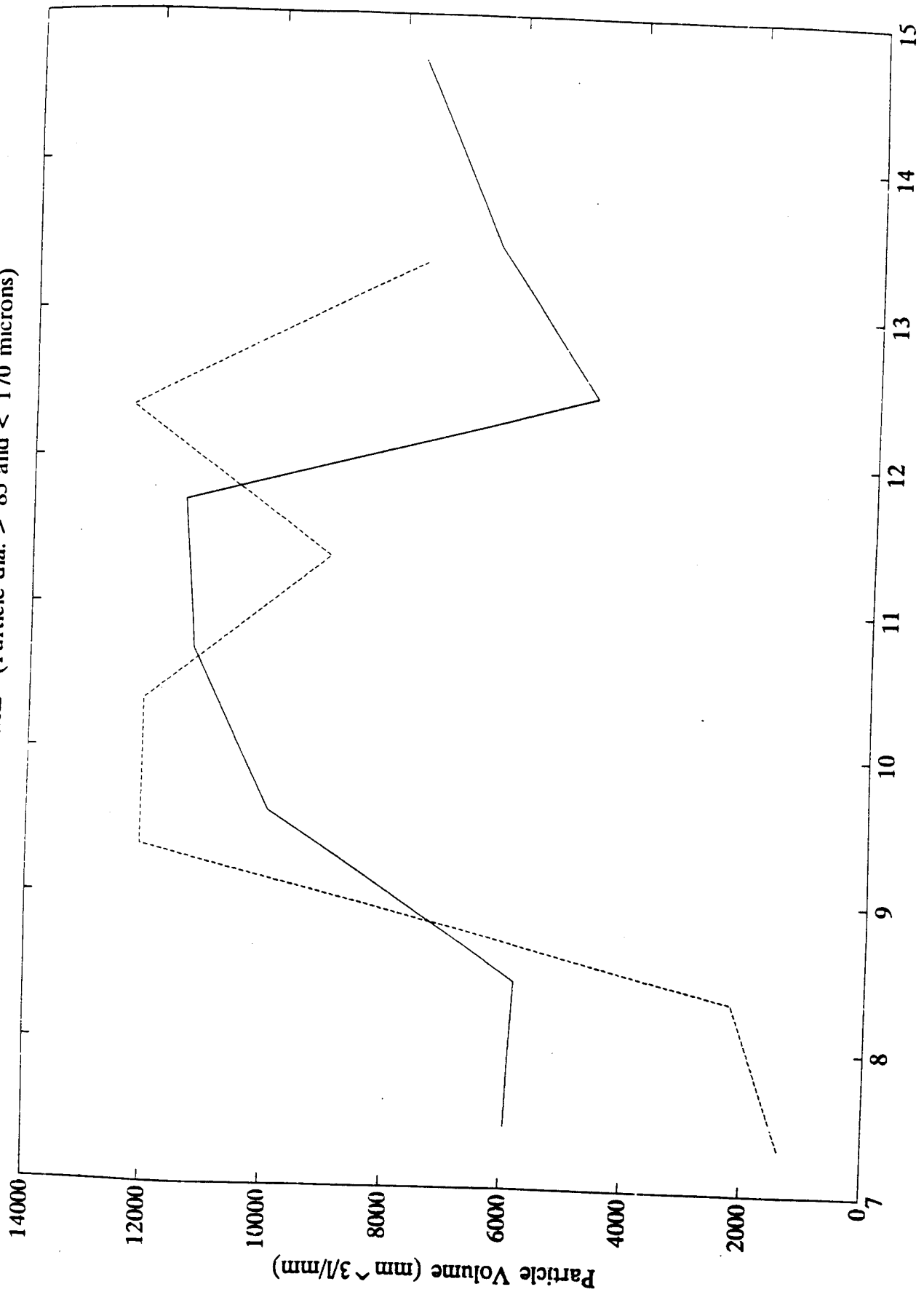
Time (sample day after innoculation)
Figure 25
SIGMA TANK DATA REPORT

V–47

TOTAL MARINE SNOW VOLUME VS. TIME - (Particle dia. > 500 micron)

o = MAPPER data
* = Primary Productivity x 2 (from A.A. data)

MAPPER data

Primary Productivity x 60 (from A.A. data)

Time (sample day after innoculation)

Particle Volume (mm ^{3}/l/mm)
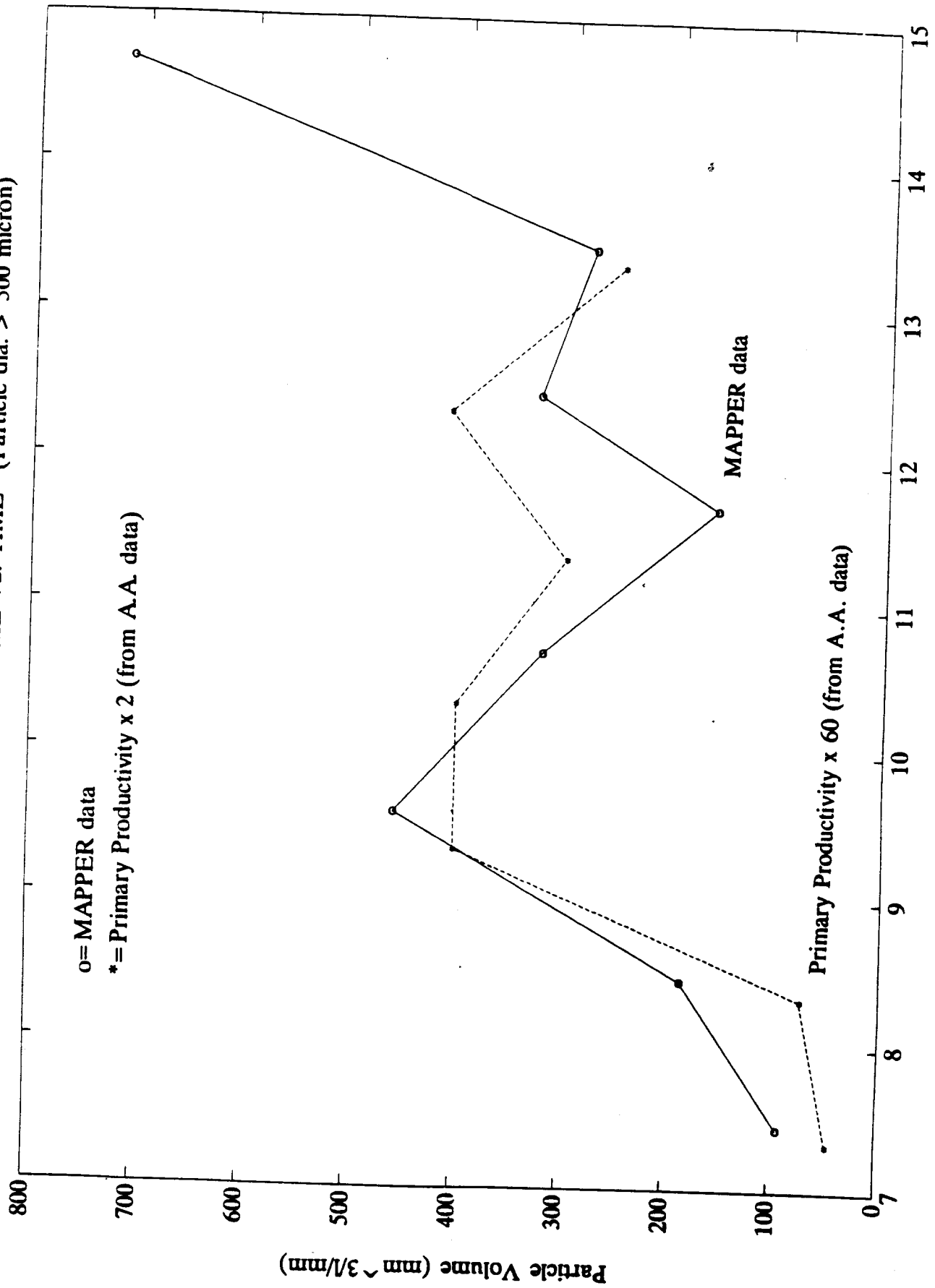
Figure 26
SIGMA TANK DATA REPORT

VOLUME VS. TIME - (Particle dia. > 2 mm)

o = MAPPER data

* = Primary Productivity x .03 (from A.A. data)

Particle Volume (mm ^{3}/l/mm)

Time (sample day after innoculation)
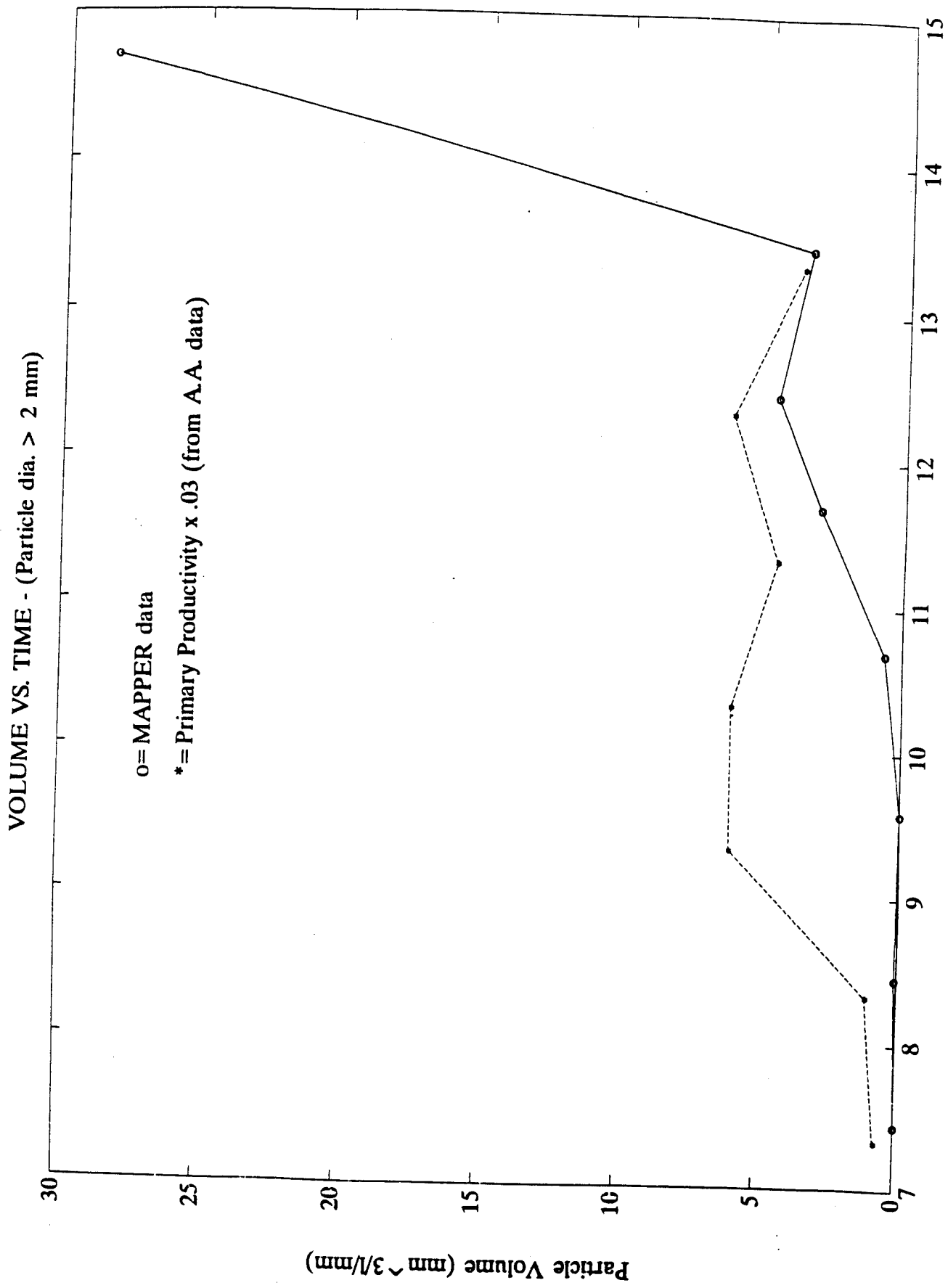
Figure 27
SIGMA TANK DATA REPORT
CARDER LAB

EFFECT OF POROSITY CORRECTION ALGORITHM, DAY 14 DATA

* = porosity corrected data

— = raw data (holes excluded)
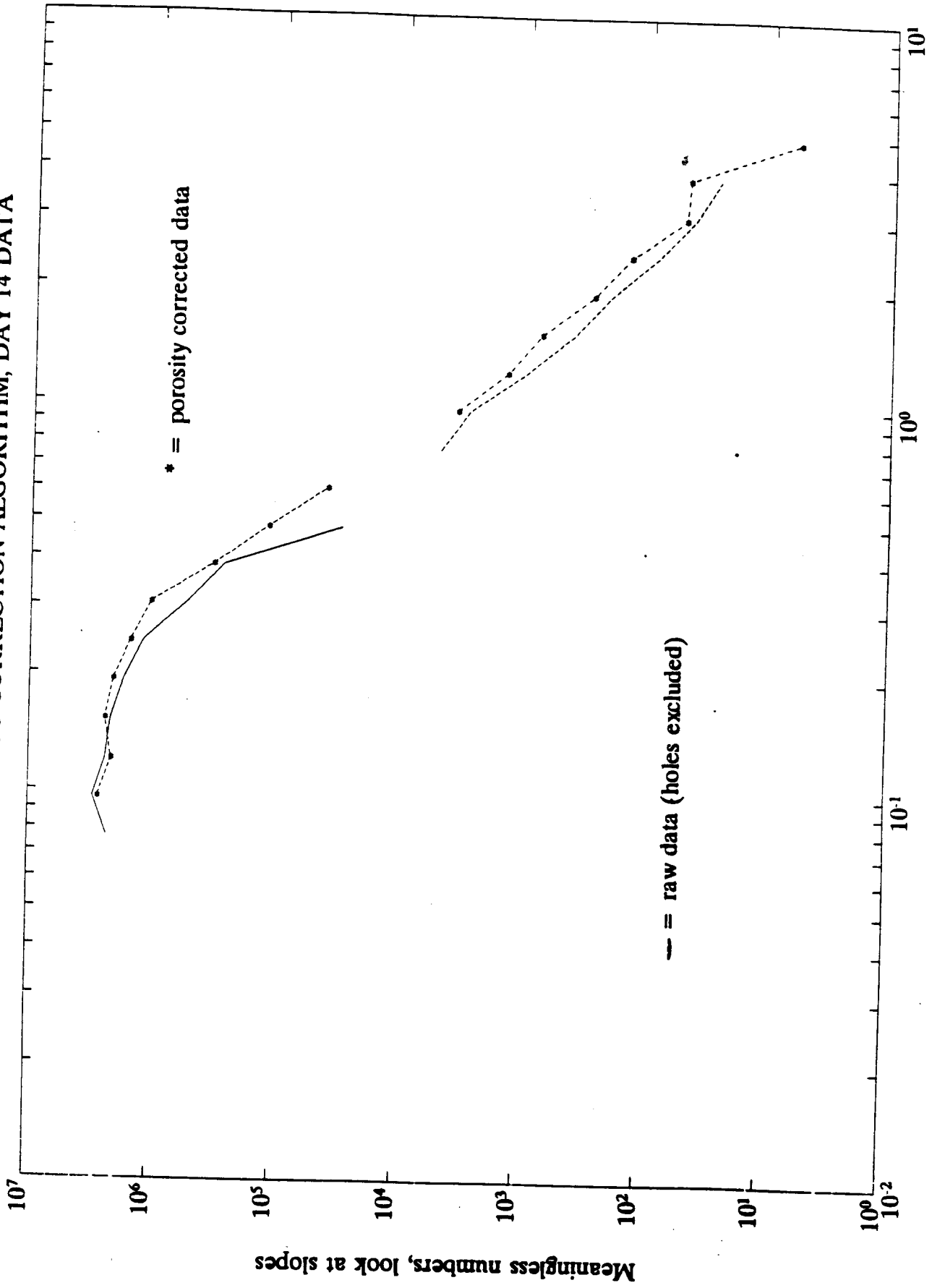
Meaningless numbers, look at slopes

Figure 28

ESD SIZE CONVERSIONS, HOLEY AND UNHOLEY

* = "Real" spectra

o = ESD conversion, "holes" excluded

x = ESD conversion, "holes" included
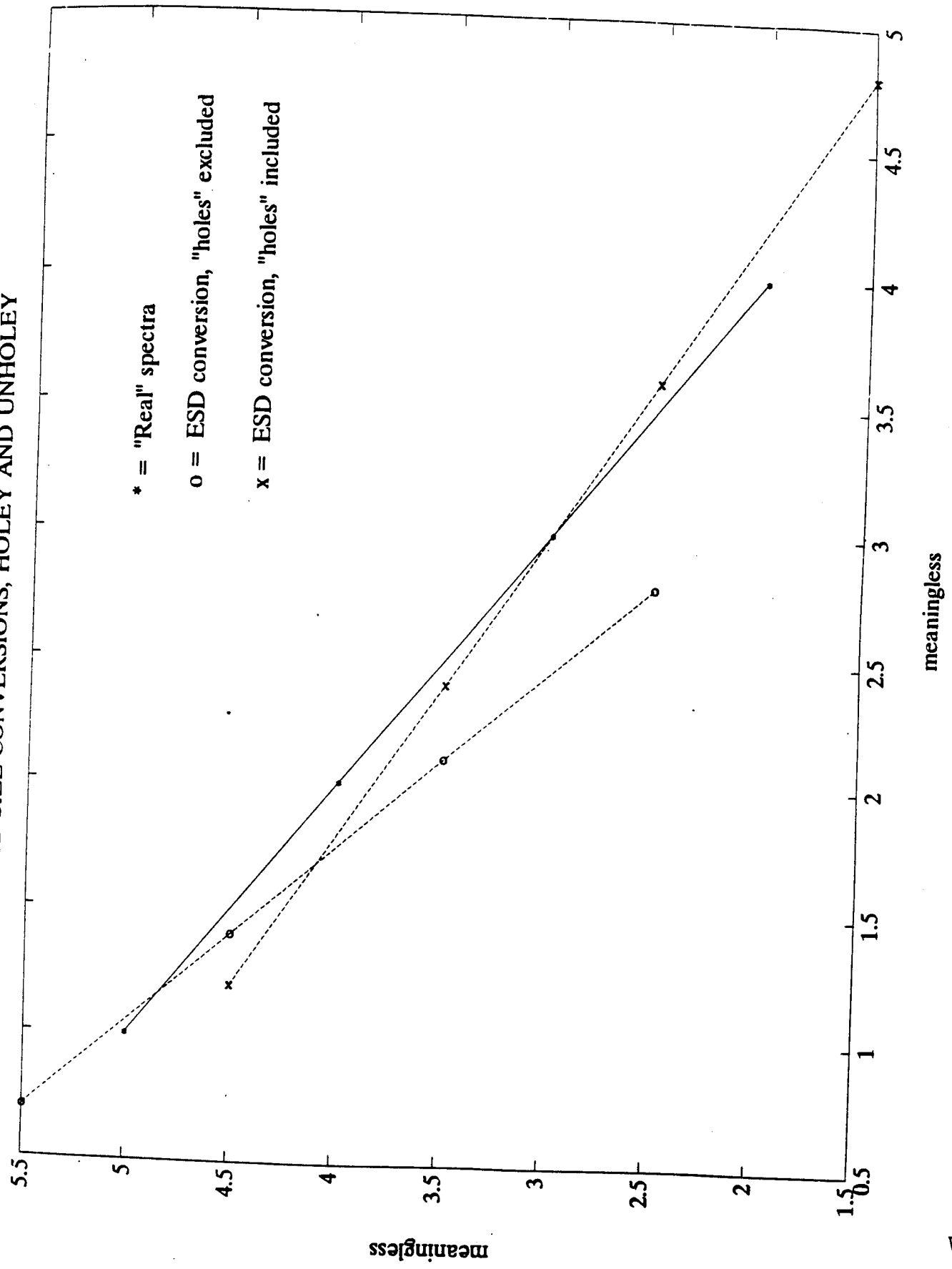
meaningless

Figure 29
SIGMA TANK DATA REPORT

(Concentration)
REDUCE ALL #'s BY FACTOR OF 10!

UNIVERSITY OF SOUTH FLORIDA
Marine Science Department
140 Seventh Avenue South
St. Petersburg, FL 33701
INTERNET: dkc@monty.marine.usf.edu
kcarder@monty.marine.usf.edu
hou@monty.marine.usf.edu
bstew@monty.marine.usf.edu
OMNET: k.carder
Voice: 813-893-9503
FAX: 813-893-9189
March 30, 1994

SIGMA DATA REPORT
(4 text pages, 3 tables, and 17 figures)
MONTEREY BAY FIELD EXPERIMENT

David K. Costello, Kendall L. Carder, Weilin Hou and Robert G. Steward

This report is presented in four sections, **NATURE OF THE DATABASE, PARTICLE SIZE DISTRIBUTIONS, TRANSMISSOMETRY,** and **FILTER PAD ABSORPTION.** Table 1 shows the water bottle samples (day/depth) that were processed for absorption measurements (69 spectra total) and displays the MAPPER deployments (day, number of downcasts, Max. depth, and vertical resolution). As you can see on Table 1, MAPPER's vertical resolution was sub-centimeter. For 38 downcasts with the MAPPER sytem, this translates into a massive database, around 1/2 Terabyte. The size of the database from the imagery (and the filter pad absorption as well) dictates electronic transfer. A synopsis of the data is presented, however, which includes mean values at the water sample bottle depths and also for distinctive layers as identified by transmissometer profiles for the particle size distributions (Table 2) and for beam attenuation (Table 3).

Anyone who would like the data, in whole or in part, can contact us to arrange Internet FTP access to the server on which the data is stored. A description of the data follows.

1. NATURE OF THE DATABASE

Table 1 gives the temporal and spatial distribution for the database. To summarize, we have 69 absorption spectra, 38 temperature profiles, 32 beam attenuation profiles, and three substantial sets of imagery (3 cameras at differing magnification) for each of the 38 downcasts. The highest resolution achieved was 50 μm horizontal, 1 mm vertical.

Figures 1 and 2 are shown to give the reader a sense of the resolution of the database by displaying the spatial distribution of the particles as reconstructed in a Computer-Aided Design environment. Figure one is included to emphasize that the data is from a 3-dimensional volume. Figure 2 shows three orthogonal views of the particles in the volume. These data are from the

medium field camera (pixel resolution $\approx$ 90 microns) at a vertical resolution of 2 mm for a 10 cm x 58 mm x 28.8 mm volume chosen at random from the imagery. The smallest particle shown, then, is 215 μm ESD and the sample volume is 1/6 liter. There were 50 particles in this volume at or above 215 μm ESD. This type of visualization is available for the entire database and should have utility for micro-patchiness, zooplankton distribution, etc.

2. PARTICLE SIZE DISTRIBUTIONS

Table 2 displays the parameters k and B of the differential particle size distribution, $dN/dD = kD^{-B}$ (units #/cm^3/cm) corresponding to the water bottle sample days/depths. The concentration parameter k is normalized at 1 cm diameter and is an explicit indicator of large particle concentration. At constant B values, an increasing k value equates to increasing particle numbers. Since B is a negative slope value, increasing B values equate to relatively fewer larger particles, etc.

Since the distributions were highly variable temporally and spatially, the data presented are from a two-meter bin centered at the reference depth. Also presented are the same data for distinct layers (as indicated by c-meter profiles), to avoid bias caused by internal wave activity; that is, a water sample from 8 meters at 1200 hours could actually correspond to a water sample at 16 meters at 1210 hours.

Figure 3 plots the same distribution parameters (k and B) for one-meter depth bins for the deepest MAPPER downcast (7/30/93 AM). Note the general trend of more large particles with increasing depth and the high concentration of large particles at 35.5 meters.

Figure 4 shows the same data converted by individual size class to volume concentration (ppm) and grouped into two size classes, 0.1-0.5 mm and > 0.5 mm ESD. Note that the 35.5 m spike is due to the larger size class, which also has a large concentration at 6.5 m.

Figure 5 breaks the same data into size classes; that is, it shows volume concentration (ppm) vs. particle size vs. depth. Here it can be seen that the particle volume spike at 35.5 m was due to particles between about 0.5 and 1.5 mm ESD while the spike at 6.5 m was due to very large particles (> 2.0 mm ESD).

3. TRANSMISSOMETRY

Table 3 shows average beam attenuation values for the shallow station in three depth bins, 0-5, 5-10, and 10-15 m. Time is hours from noon 7/23/93. On the average, the water cleared with depth.

Figure 6 is a graph of Table 3 data. Generally, attenuation increased from the morning to the afternoon. Attenuation in the surface layer increased from the 23rd to the 26th, then cleared on the 28th and again on the 31st.

Figure 7 shows beam attenuation profiles for the 23rd through the 28th for the shallow station. Again, the clearest trend is the increasing attenuation in the upper layer from the 23rd to the

26th.

Figure 8 shows beam attenuation for two deeper stations, 7/29 am and 7/30 am. The spikes in the profile are real (not noise), since the transmissometer data microcontroller averaged 10 transmissometer readings. Below 20 m, the mean beam attenuation at the two stations is similar. Above that depth, the mean beam attenuation is higher on the 30th. For intercomparison purposes, we feel only mean values can be used. The sharp layer at 14.5 m on this downcast on the 30th, for example, was displaced several meters on subsequent downcasts. Fitting a cubic polynomial to the depth of this layer vs. time suggests an internal wave of 8 m height and a period on the order of 20 minutes.

Figure 9 again displays beam attenuation from the 30th and also shows the concentration constant parameter k for the same downcast. It also shows that attenuation in the thin layer discussed above was not caused by large particles. In fact, only our smallest size bin (70 μm ESD) showed any correlation with this layer. The attenuation spike at 35.5 m, however, was caused by very large particles as evidenced by a very large k value at that depth.

4. FILTER PAD ABSORPTION

Figure 10 shows total spectral absorption for the 3 water samples (2, 7, and 15 m depth) from the shallow station, 7/24/93. Total absorption is similar at 7 and 15 m and much higher at 2 m.

Figure 11 shows detrital absorption for the same samples after hot methanol pigment extraction. Detrital absorption is highest at 2 m, lowest at 7 meters, and intermediate at 15 m.

Figure 12 shows absorption due to extractable pigments (total-detrital). This indicates that pigments decreased with depth. The shape of the curves (especially between 560 to 610 nm) also indicates a different suite of pigments in the 2 m sample vs. the 7 and 15 m samples.

Figure 13 shows total spectral absorption for the 3 water samples (5, 15, and 20 m depth) from a deeper station, 7/31/93. The 5 m curve obviously differs from the other two curves which are similar to each other except at the blue end of the spectrum.

Figure 14 (same station) shows that detritus increased substantially with depth.

Figure 15 (same station) shows that pigment absorption differed substantially at 5 m vs. 15 and 20 m. It also shows that pigment absorption between 15 and 20 meters is very similar (even in the blue) with slightly less absorption at the deeper depth.

Figure 16 displays the pigment absorption spectra for the shallow station from 7/24 through 7/26. Absorption at this station increased steadily from the 24th through the 26th and dropped on the 28th. With this presentation it is not readily clear if the pigment suite changed.

Figure 17 is the same data normalized at the chl_a specific absorption peak (673 nm). If the same suite of pigments was present each day (even at different concentrations), the curves would

be indistinguishable. Variance at 650 nm, for example, is strongly indicative of changing chl_b concentration. Variance below 550 nm, on the other hand, could be due to a number of different agents.

In summary, our results from the SIGMA Monterey Bay Field Experiment are complex. The complex nature of the database is a consequence of high-resolution sampling in an environment with multi-layer vertical structure and active vertical mixing. Our contention is that this database, in combination with data from the other SIGMA investigators, is unique and, therefore, provides a unique opportunity to transform the complexity of the SIGMA database into an enhanced comprehension of the biological and physical processes which were operative in Monterey Bay in July 1993.

CARDER GROUP - JULY 1993 MONTEREY BAY DATA REPORT

DESCRIPTION OF DATA ACQUIRED

Filter Pad Absorption Spectra (units, m^-1)
Wavelengths from 400 to 750 nm, nominal 2.5 nm resolution
Total number of spectra = 69, 23 each of the following:
Total, Detrital, and derived Pigment Absorption (Total - Detrital)

DAY	Depths (m)
7/24	2, 7, and 15
7/25	1, 3, 5, 7, and 12
7/26	3 and 10
7/28	3, 7, 12, 15, 20, and 23
7/30	2, 5, 15, and 40
7/31	5, 15, and 20

MAPPER Deployments and Available Data
(Note: * Horizontal Resolution for the particle imagery is 50 μm.
VERTICAL RESOLUTION is the "thickness" of each image in mm.)

DAY (am/pm)	# of DOWNCASTS	T (°C) PROFILES	c (m^-1) PROFILES	MAX DEPTH	VERTICAL* RESOLUTION
7/23 pm	5	5	1	16	5 (mm)
7/24 am	2	2	2	14	2
7/24 pm	4	4	4	12	2
7/25 am	3	3	3	13	3
7/26 am	3	3	3	16	2
7/26 pm	2	2	2	11	4
7/28 am	4	4	4	13	2
7/28 pm	3	3	3	10	1
7/29 am	3	3	3	32	1
7/30 am	3	3	3	42	4
7/30 pm	2	2	0	20	3
7/31 am	4	4	4	20	3
TOTALS	38	38	32	na	na
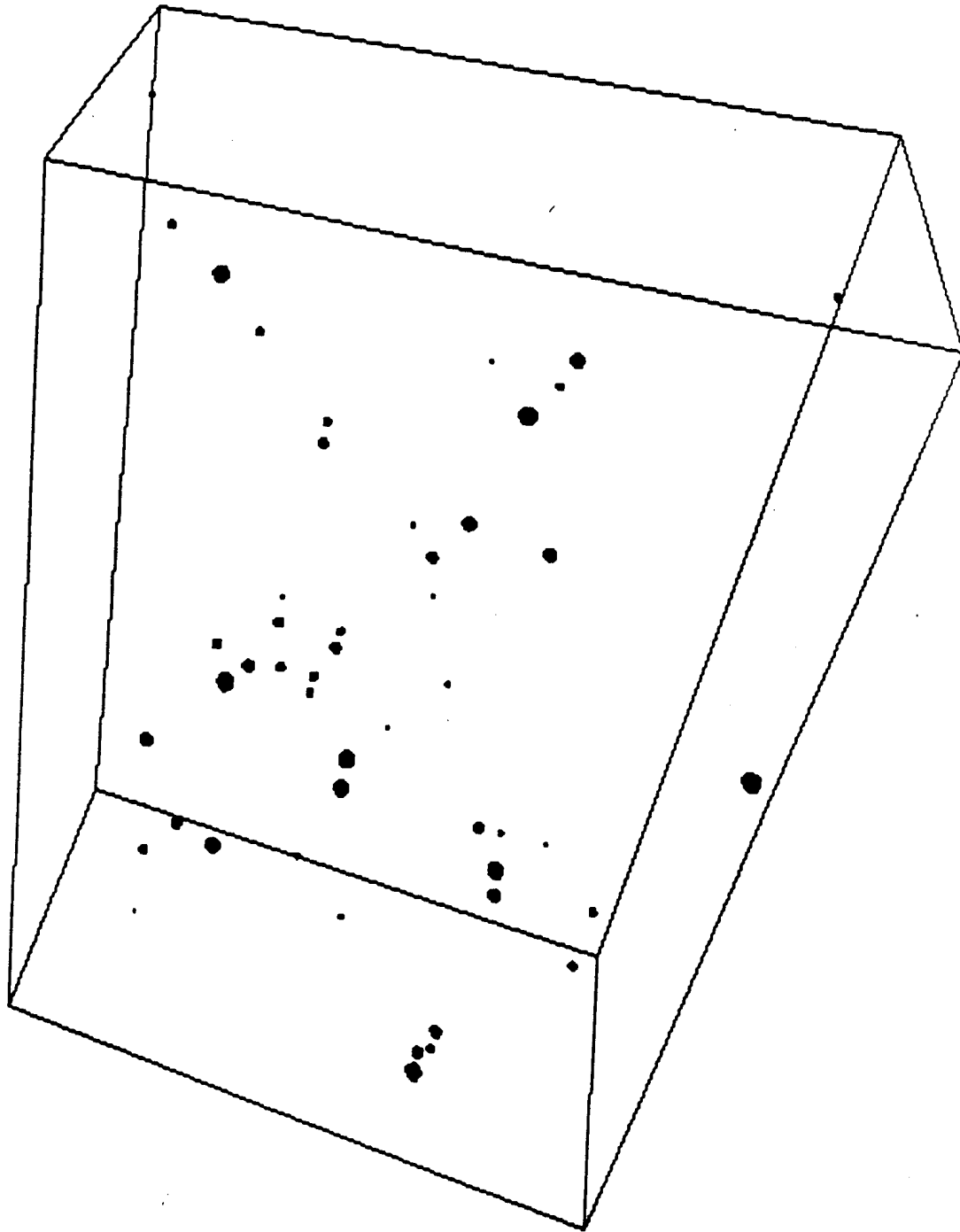
Carder Group Data Report
SIGMA Monterey Bay Field Experiment
Table 1

Carder Group Data Report
SIGMA Monterey Bay Field Experiment

3-Dimensional Distribution of Large Marine Particles (ESD > 215 μm) in a 0.167 liter volume in Monterey Bay from z=10.0 m to z=10.1 m at 11:10 am, July 29,1993.

(Dimensions are mm)
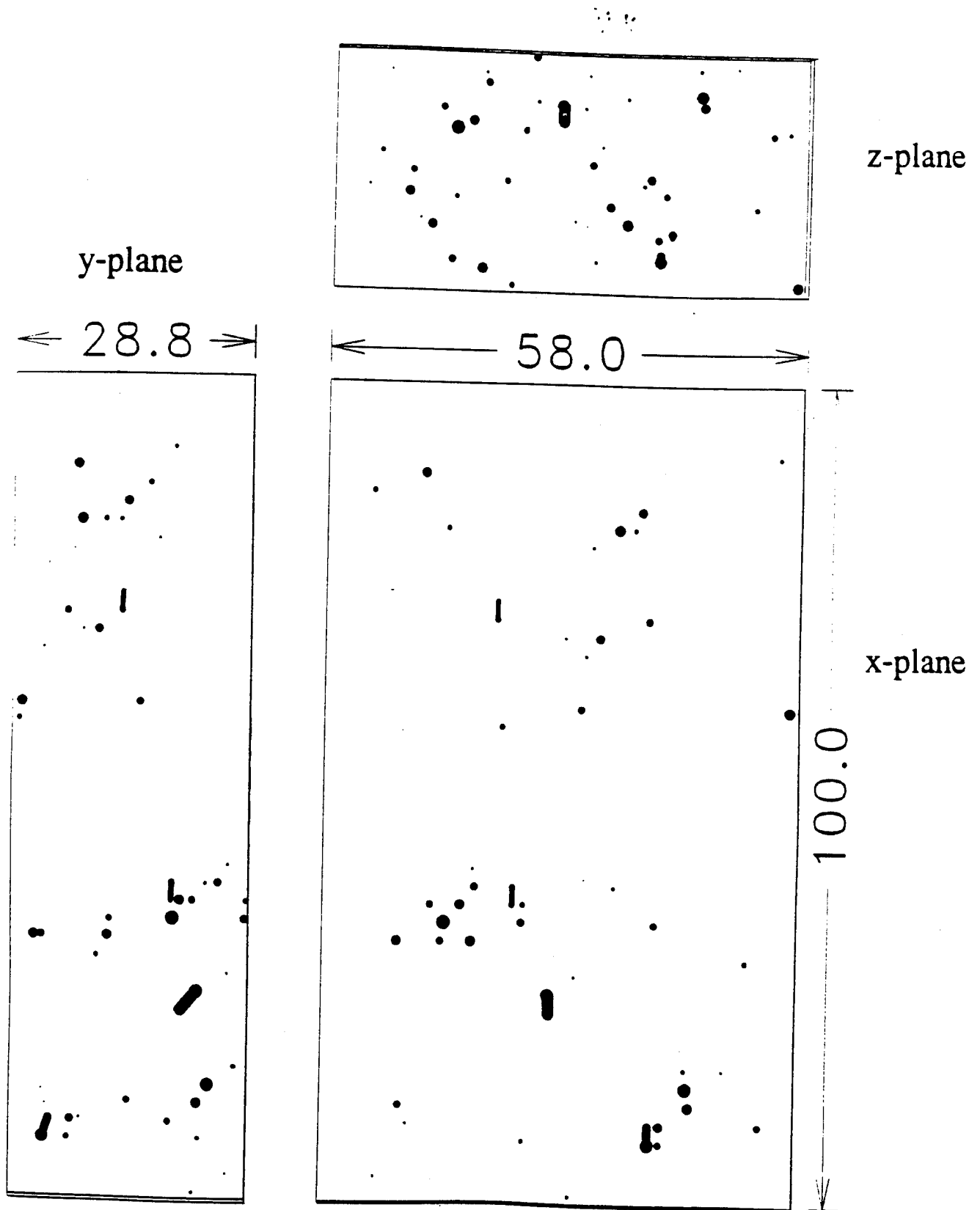
Figure 2

SANTA CRUZ - DATA REPORT - CARDER GROUP
PARTICLE SIZE DISTRIBUTIONS CORRESPONDING TO WATER BOTTLE SAMPLES
Differential Distribution, $dN/dD = kD^{-B}$ - units $\#/cm^3/cm$

NOTES:
  1) Distributions were highly variable temporally and spatially.
  2) Data presented is from a two meter bin centered at reference depth.
  3) Data is also presented for distinct layers (from c-meter profile).

DAY	DEPTH	k x 10⁻⁴	B
7/24	2	6	3.72
	7	32	3.24
	15	34	3.41
	1 to 10	26	3.33
	11 to 15	30	3.28
7/25	1	54	2.90
	3	80	2.91
	5	213	2.67
	7	113	2.93
	12	33	3.20
	1 to 7	141	2.82
	8 to 14	61	3.08
7/26	3	416	2.59
	10	84	2.91
	1 to 7	199	2.82
	8 to 14	70	2.96
	> 14	53	3.08
7/28	3	175	2.77
	7	50	2.96
	12	18	3.15
	0 to 6	133	2.85
	7 to 12	35	3.04
7/30	2	74	2.58
	5	2	3.60
	15	21	3.07
	40	49	2.91
	< 20	25	3.08
	> 20	54	2.83
7/31	5	4	3.28
	15	36	3.39
	20	65	3.12
	0 to 10	11	3.40
	11 to 20	39	3.30

SHAPE PARAMETERS FOR THE HYPERBOLIC SIZE DISTRIBUTION

7/30/93 am dc#2

k (# cm^ (B-1) cm^ (-3))

B (dimensionless)

z (m)
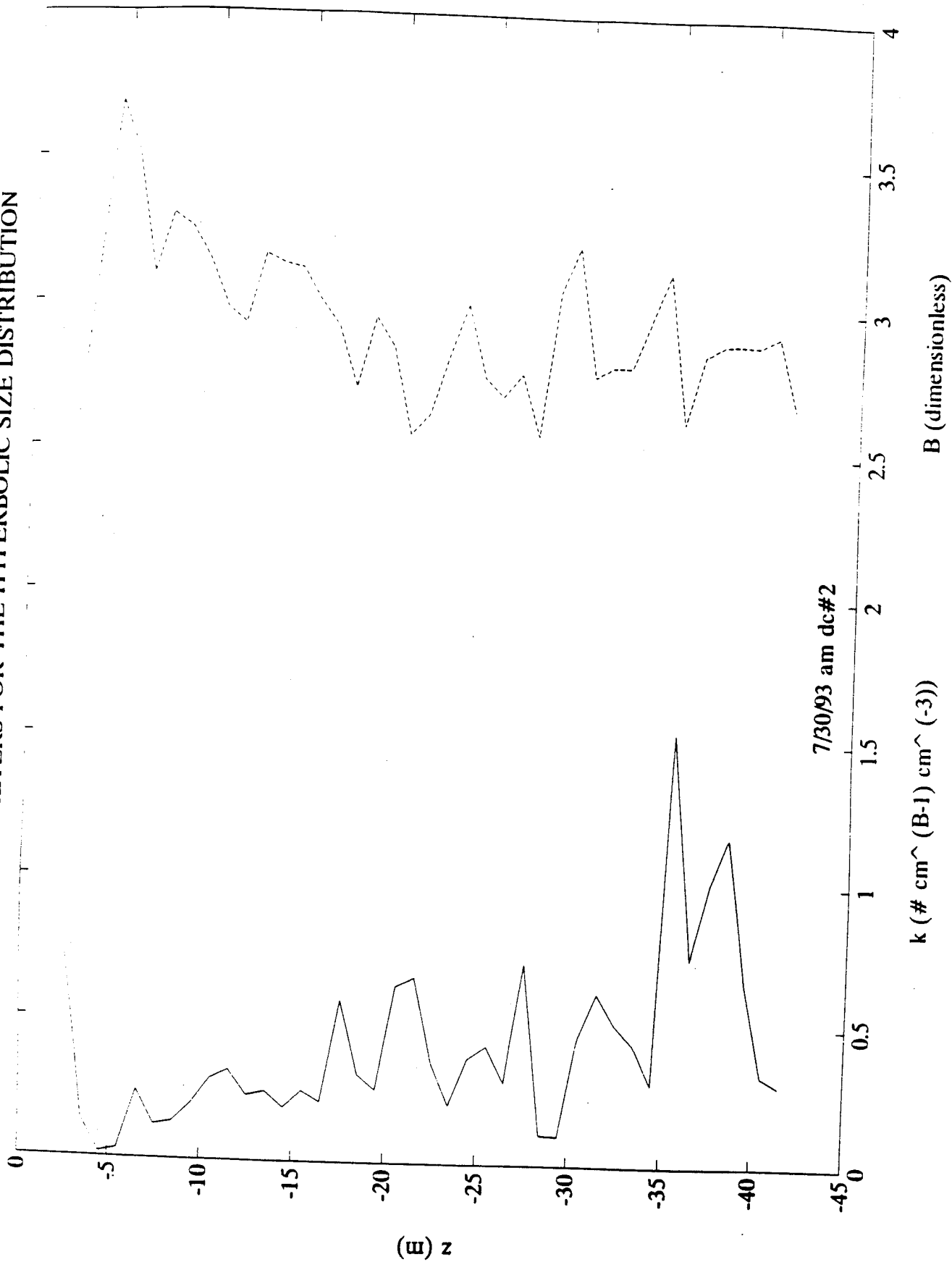
Carder Group Data Report
SIGMA Monterey Bay Field Experiment
Figure 3

LARGE PARTICLE VOLUME CONCENTRATION - MONTEREY BAY 7/30/94

> 0.5 mm

0.1-0.5 mm

Volume Concentration (ppm)

z (m)

−80 ppm

−20 ppm

Z (m)

41.5

2.5

0.01

0.05

0.1

0.2

ESD (µm)

Carder Group Data Report
SIGMA Monterey Bay Field Experiment
Figure 5

MEAN BEAN ATTENUATION, c (m^{-1}) - Shallow Station - 5 meter depth bins

TIME is hours after 7/23/93 noon

TIME	0-5 m	5-10 m	10-15 m
0	1.383	1.208	0.828
20	1.621	1.575	1.422
24	1.633	1.379	0.841
44	1.805	1.217	0.748
68	1.898	1.350	1.235
72	2.043	1.714	1.495
116	1.414	0.586	0.515
120	1.506	0.757	0.757
188	1.135	0.987	1.048
AVERAGE	1.604	1.197	0.938

Carder Group Data Report
SIGMA Monterey Bay Field Experiment
Table 3

ATTENUATION TIME SERIES, SHALLOW STATION, SANTA CRUZ

0-5 m

5-10 m

10-15 m

Beam Attenuation, c (m^-1)
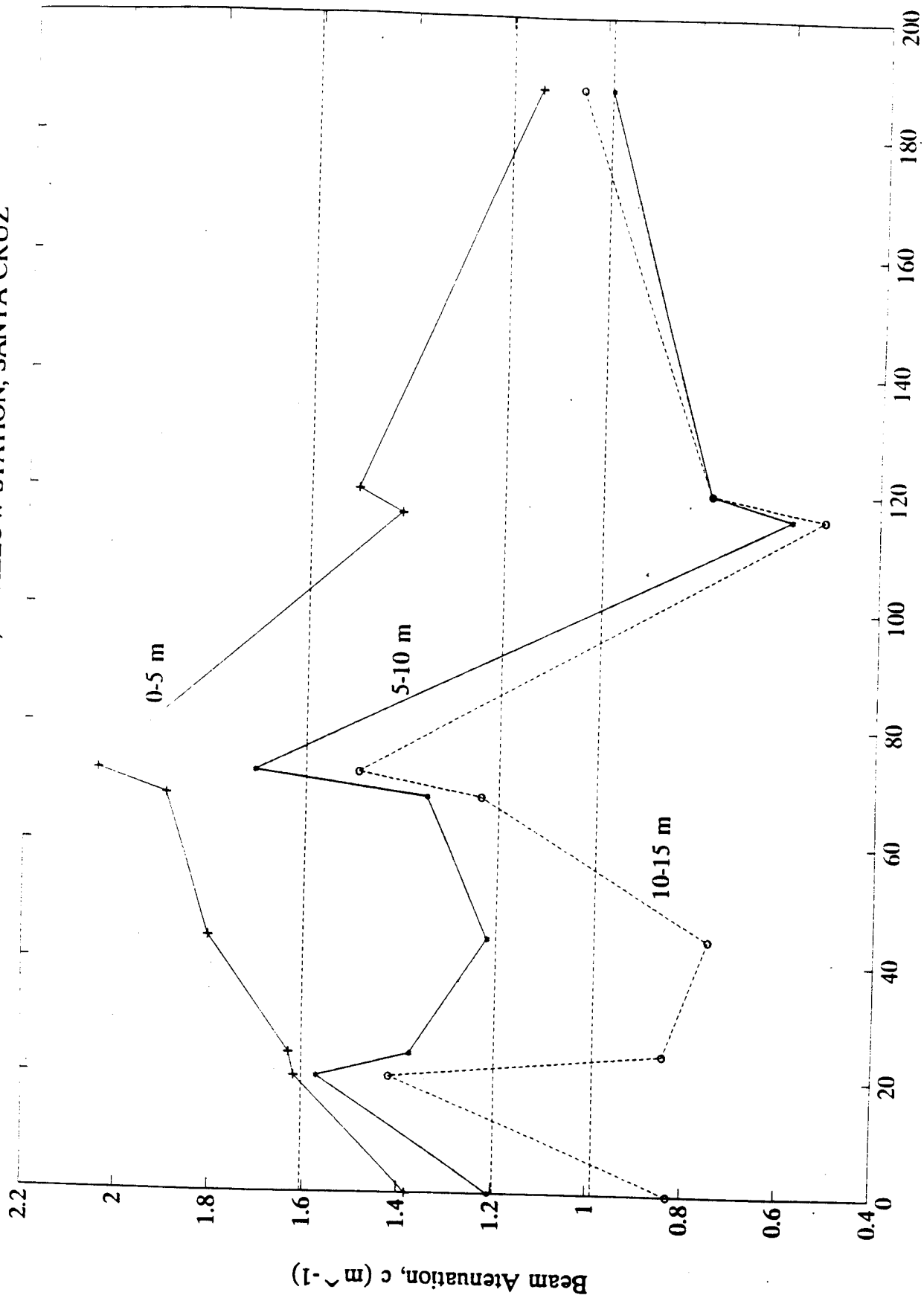
Time (hours after 7/28/93 noon)

Carder Group Data Report
SIGMA Monterey Bay Field Experiment
Figure 6

BEAM ATTENUATION COEFFICIENT PROFILES, SHALLOW STATION

z (m^-1)

Beam Attenuation Coefficient, c (m^ -1)

7/25
7/26
7/24
7/23
7/28
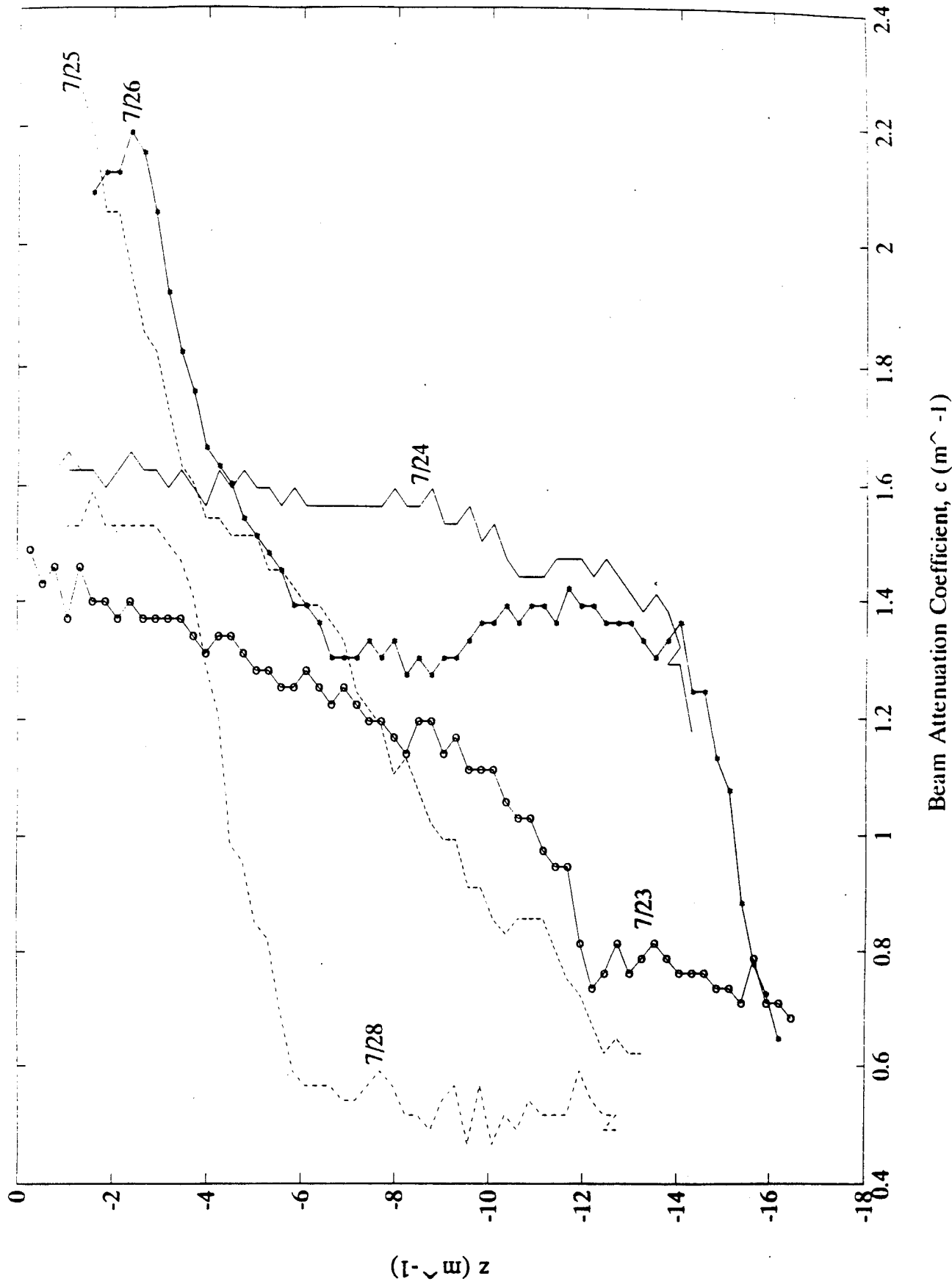
THE SHAPE PARAMETER, k, and THE BEAM ATTENUATION COEFFICIENT, c

k (# cm^ (B-1) dm^ (-3)), c (m^ (-1))

7/30/93 am dc#2

Carder Group Data Report
SIGMA Monterey Bay Field Experiment
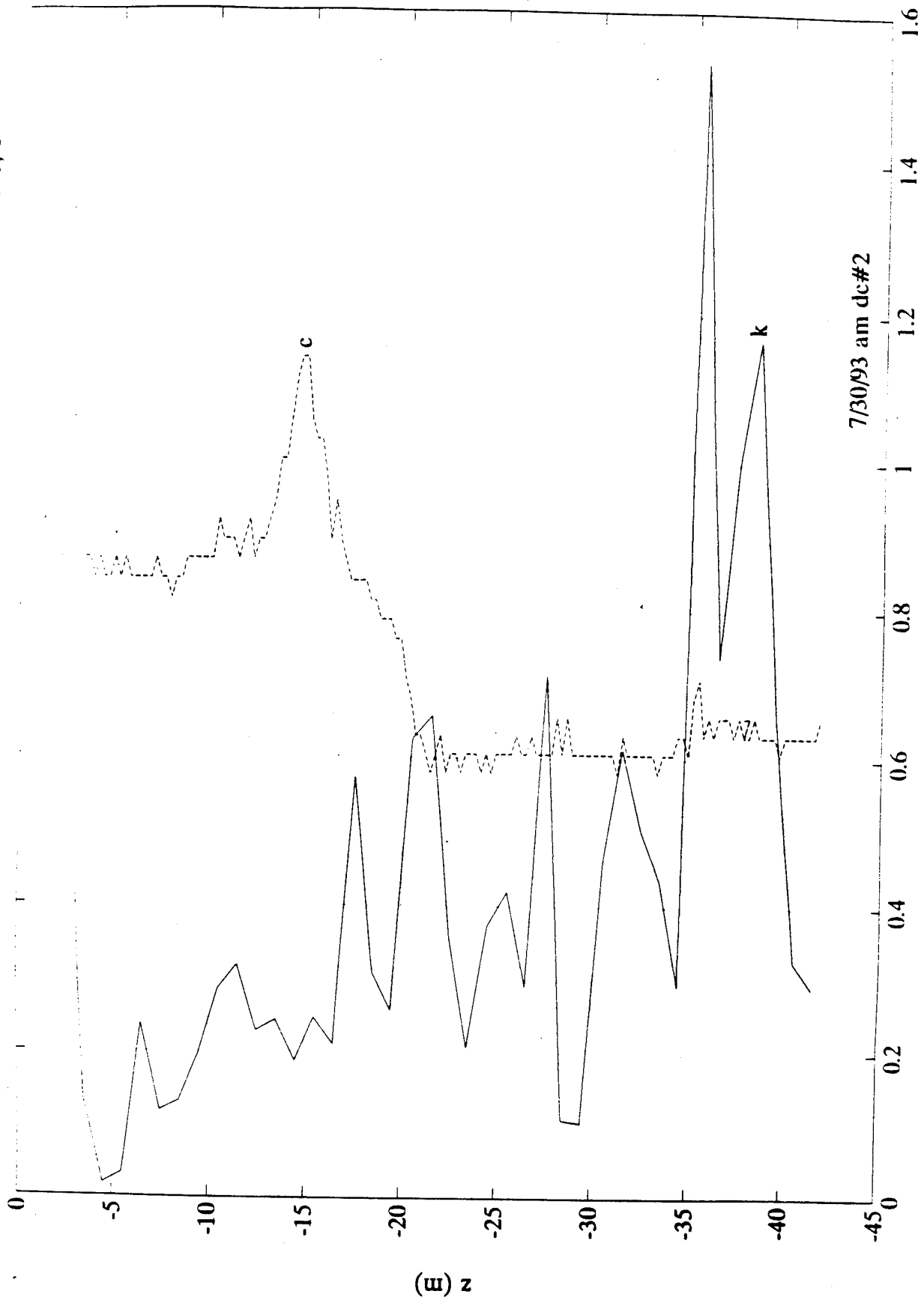
BEAM ATTENUATION COEFFICIENT PROFILES, TWO DEEPER STATIONS
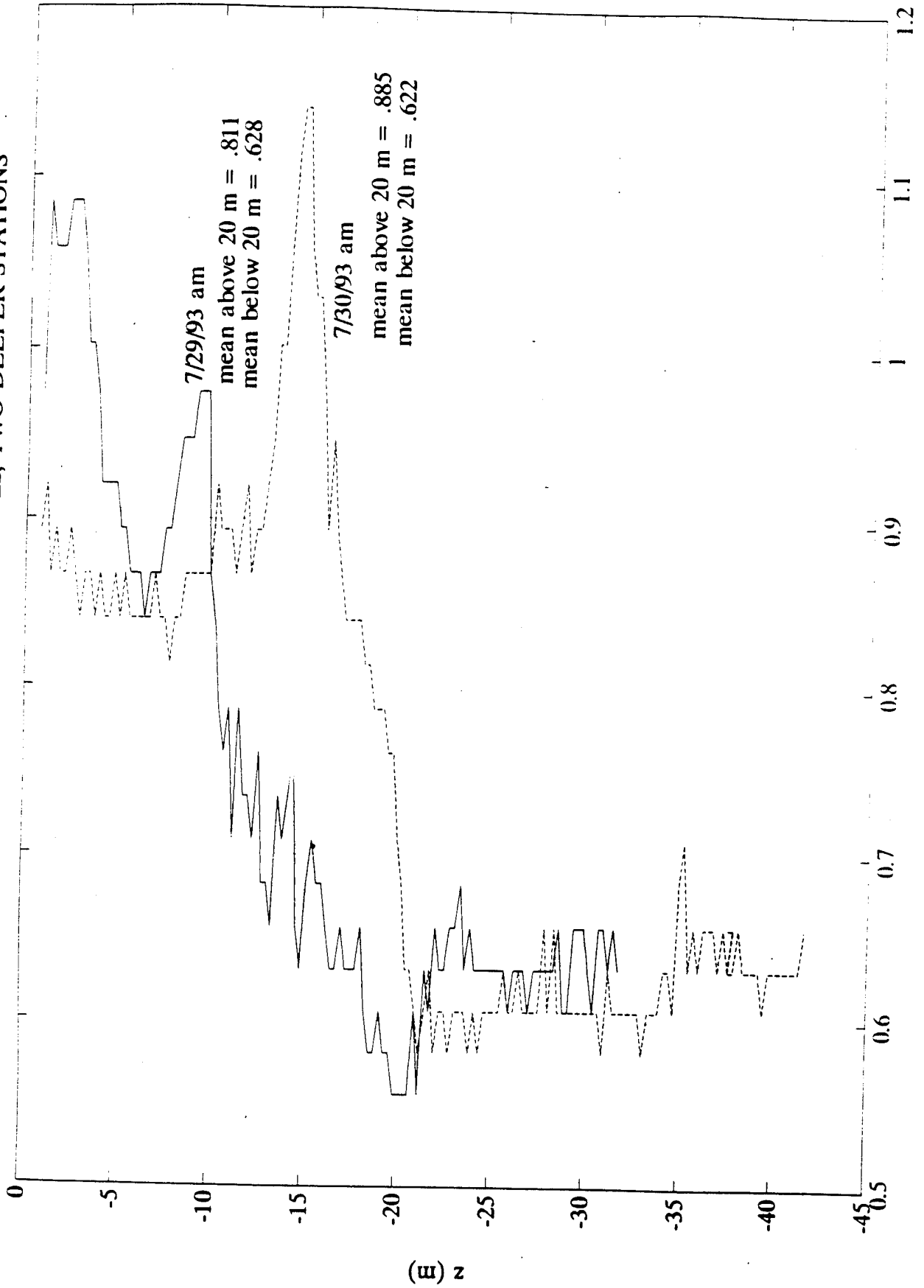
7/29/93 am
mean above 20 m = .811
mean below 20 m = .628

7/30/93 am
mean above 20 m = .885
mean below 20 m = .622

z (m)

Beam Attenuation Coefficient, c (m^ -1)

Carder Group Data Report
SIGMA Monterey Bay Field Experiment

Santa Cruz – Spectral Absorption
7/24/93, total

a (m^-1)

(1 mg/m~3 assumed)

lamda (nm)

Sample Depth (m)
— 2 - - 7 -- 15

Carder Group Data Report
SIGMA Monterey Bay Field Experiment
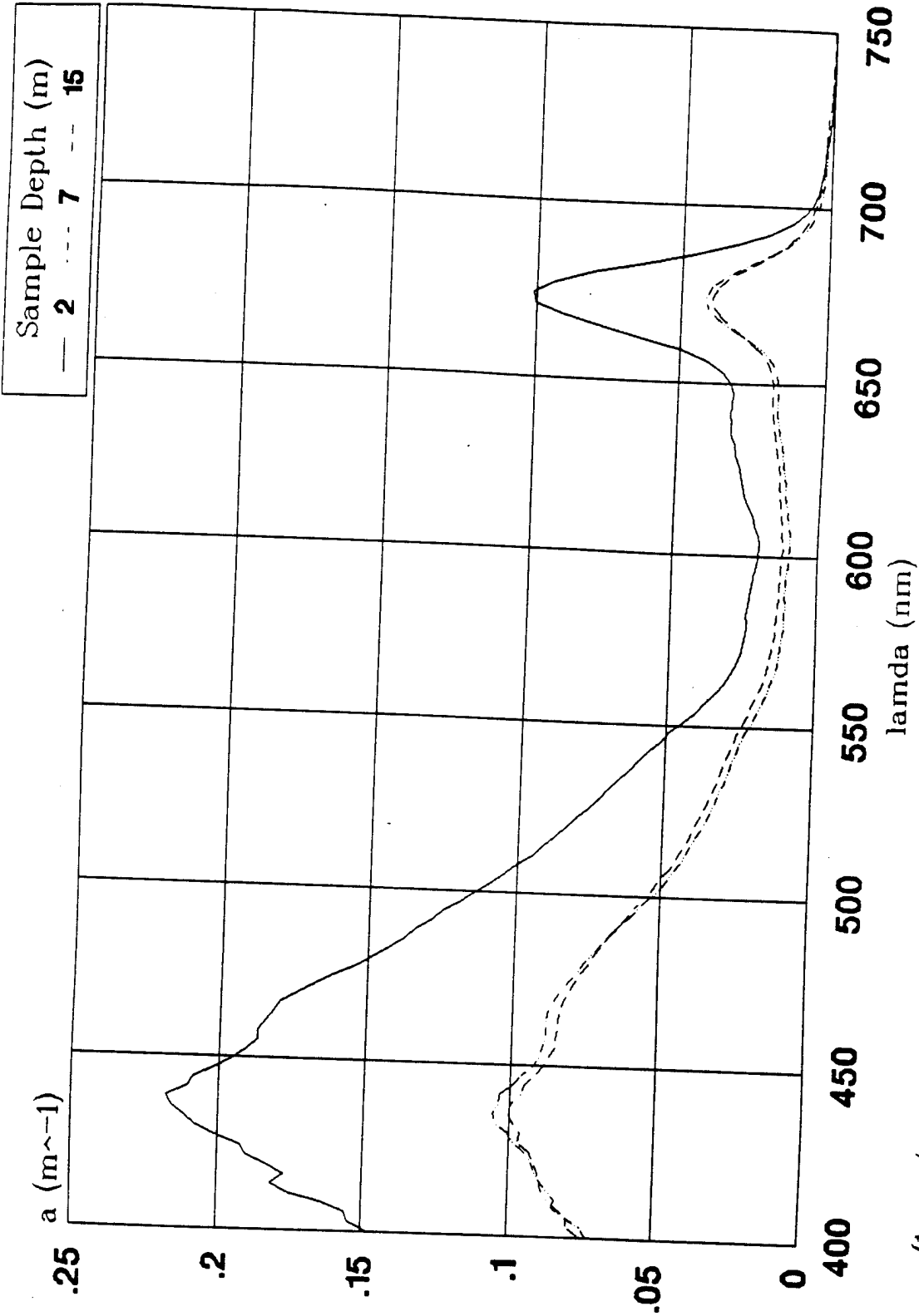
Santa Cruz – Spectral Absorption
7/24/93, detritus

a (m~-1)

(1 mg/m~3 assumed)

Sample Depth (m)
— 2   -- 7   -- 15

lamda (nm)
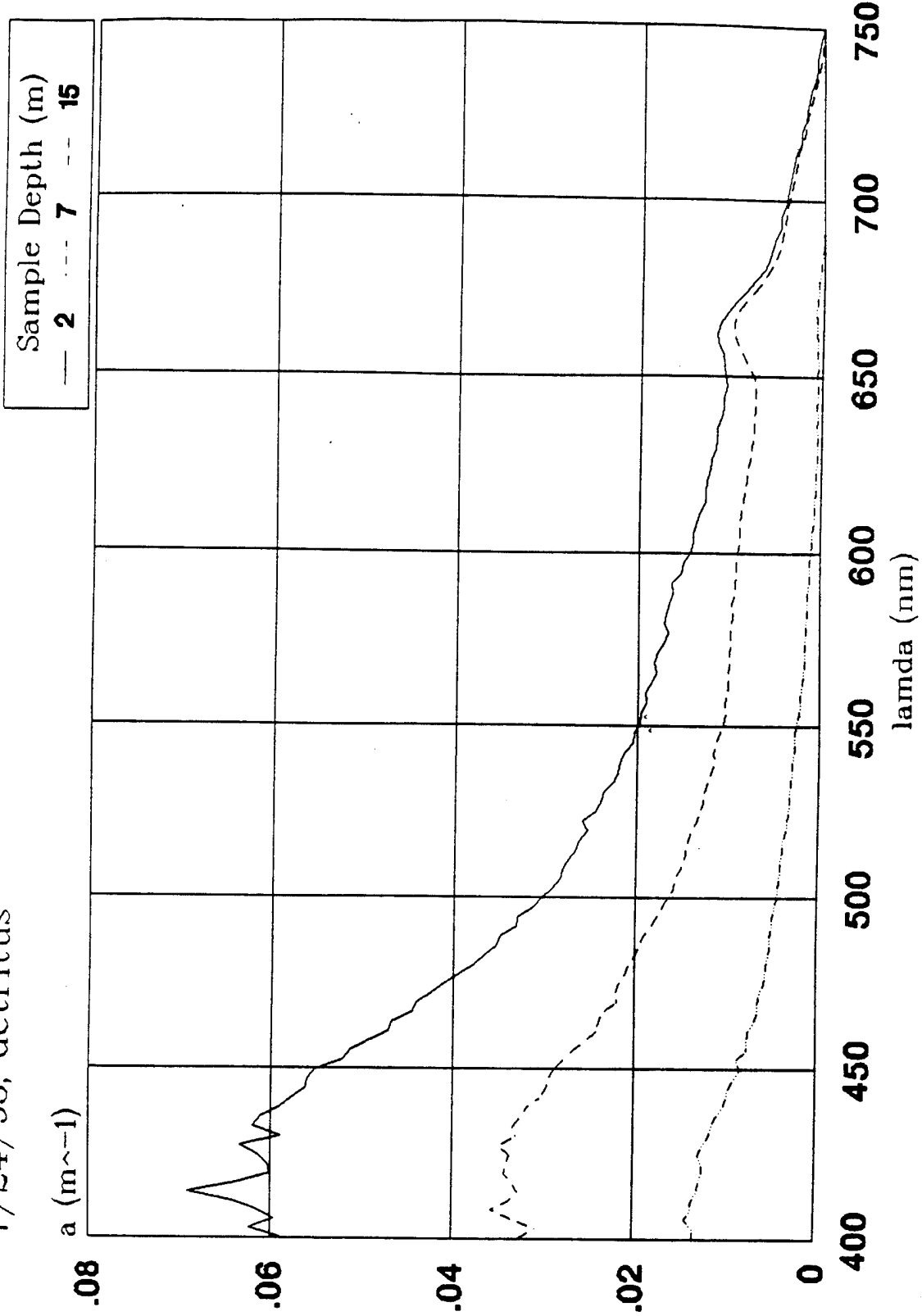
Santa Cruz – Spectral Absorption
7/24/93, pigments
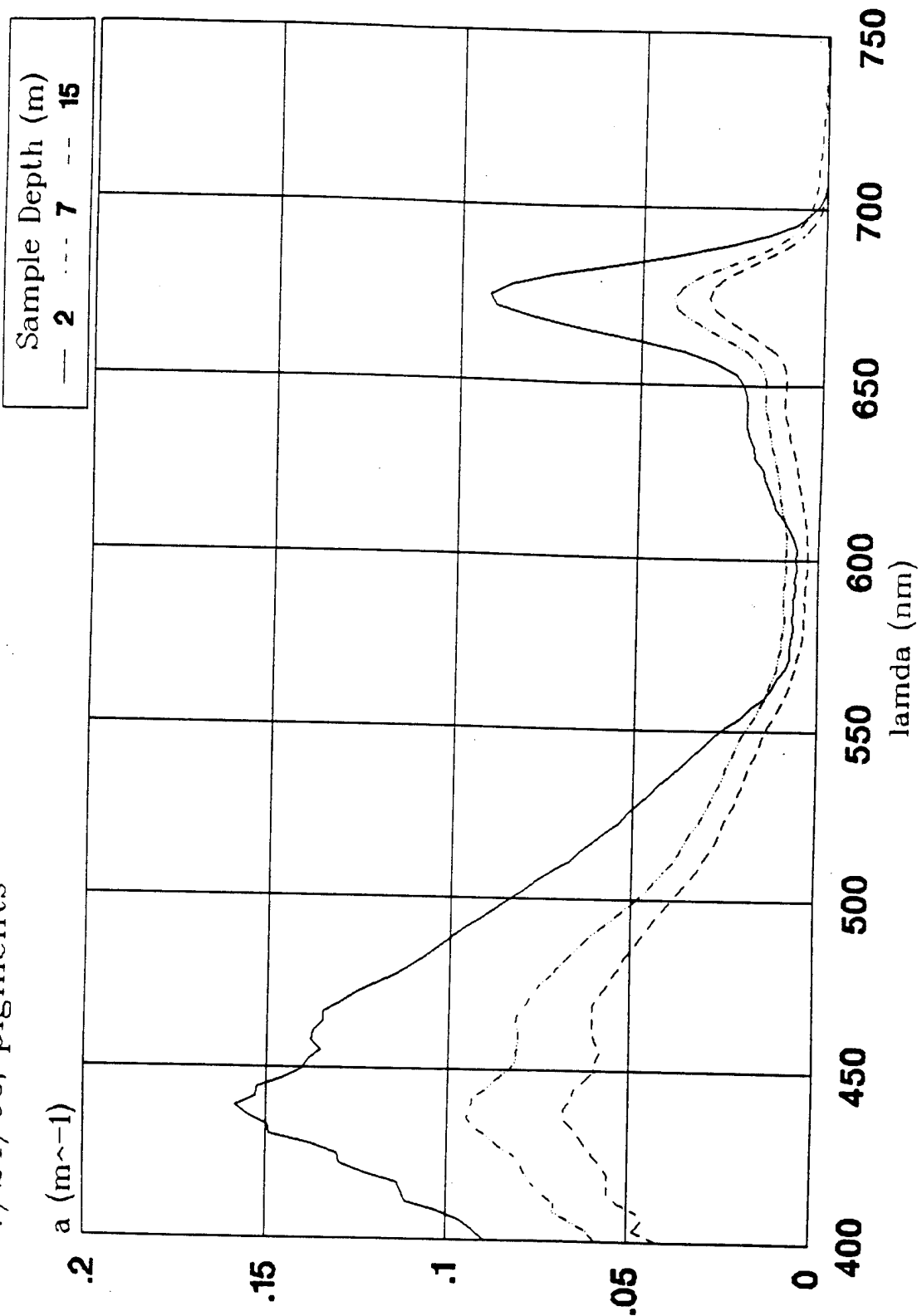
Sample Depth (m)
— 2   - · - 7   - - 15

a (m~-1)

lamda (nm)

(1 mg/m~3 assumed)

Santa Cruz, Spectral Absorption
7/31/93, total

depth (m)
— 5   - - 15   - · - 20

a (m~-1)

.12
.11
.1
.09
.08
.07
.06
.05
.04
.03
.02
.01
0

400   450   500   550   600   650   700   750

lamda (nm)
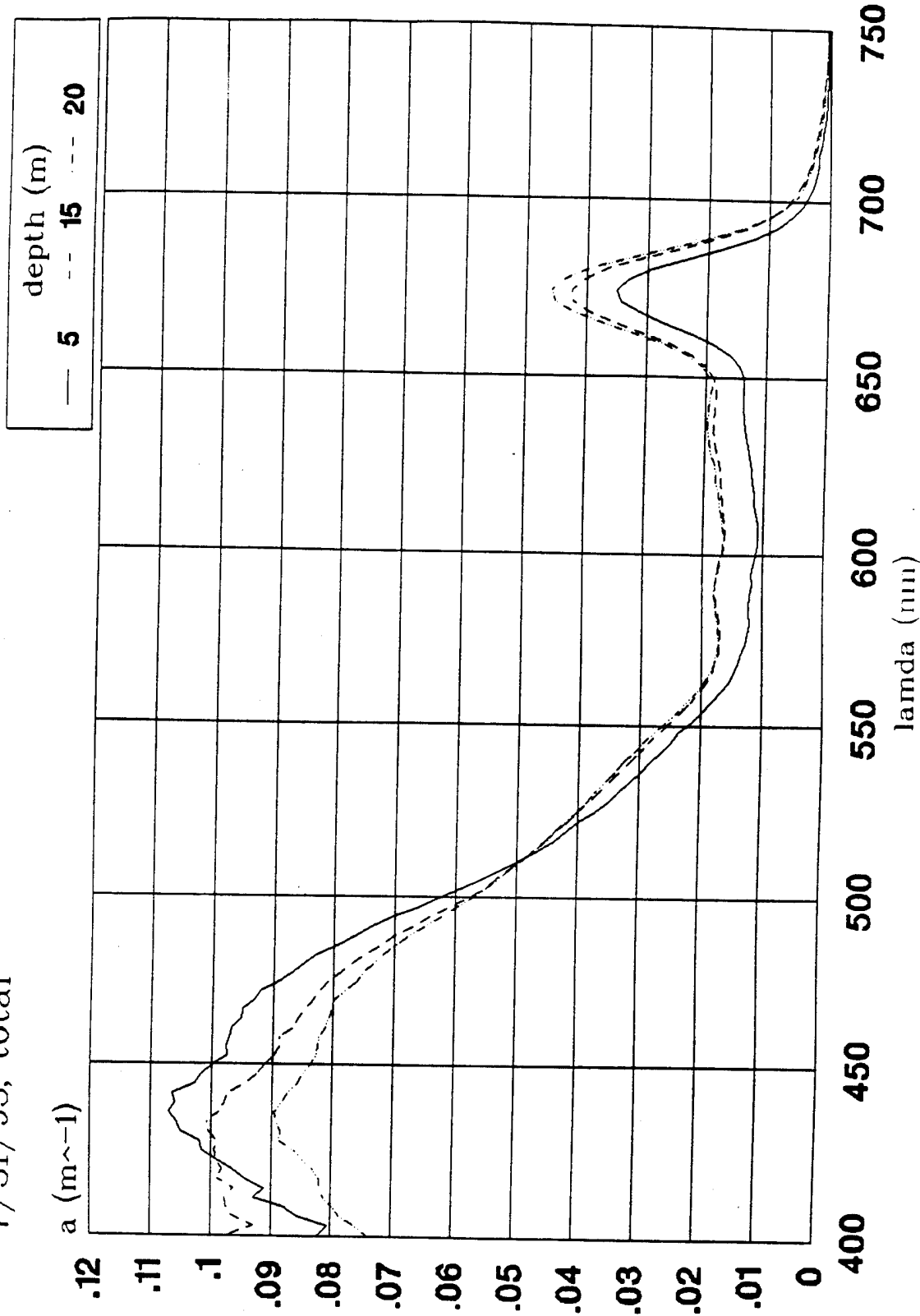
(1 mg/m~3 assumed)

Santa Cruz, Spectral Absorption
7/31/93, detritus

depth (m)
— 5   — · — 15   — · · 20

a (m~-1)

.05

.04

.03

.02

.01

0

400   450   500   550   600   650   700   750

lamda (nm)

(1 mg/m~3 assumed)

Carder Group Data Report
SIGMA Monterey Bay Field Experiment
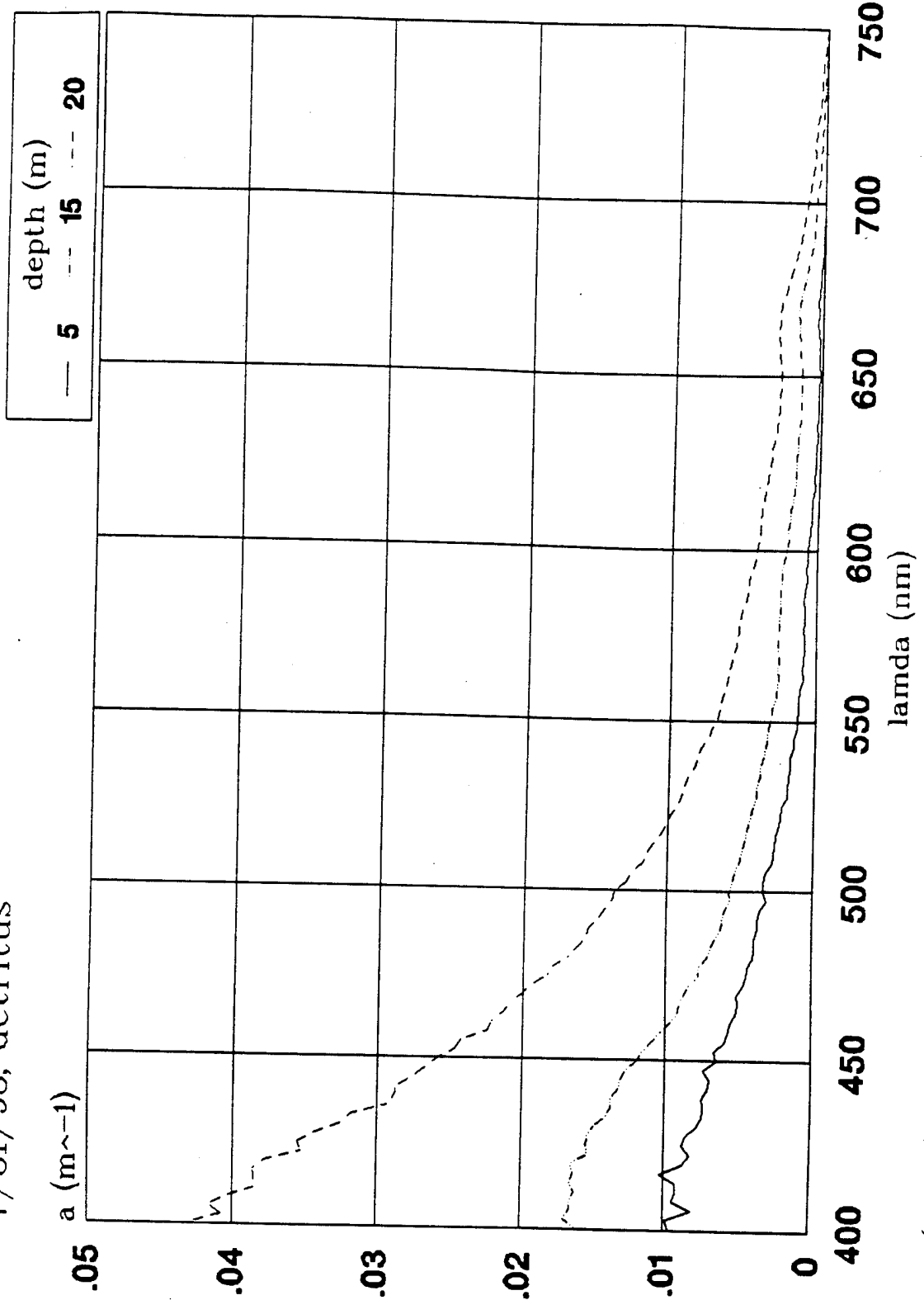
Santa Cruz, Spectral Absorption
7/31/93, pigment
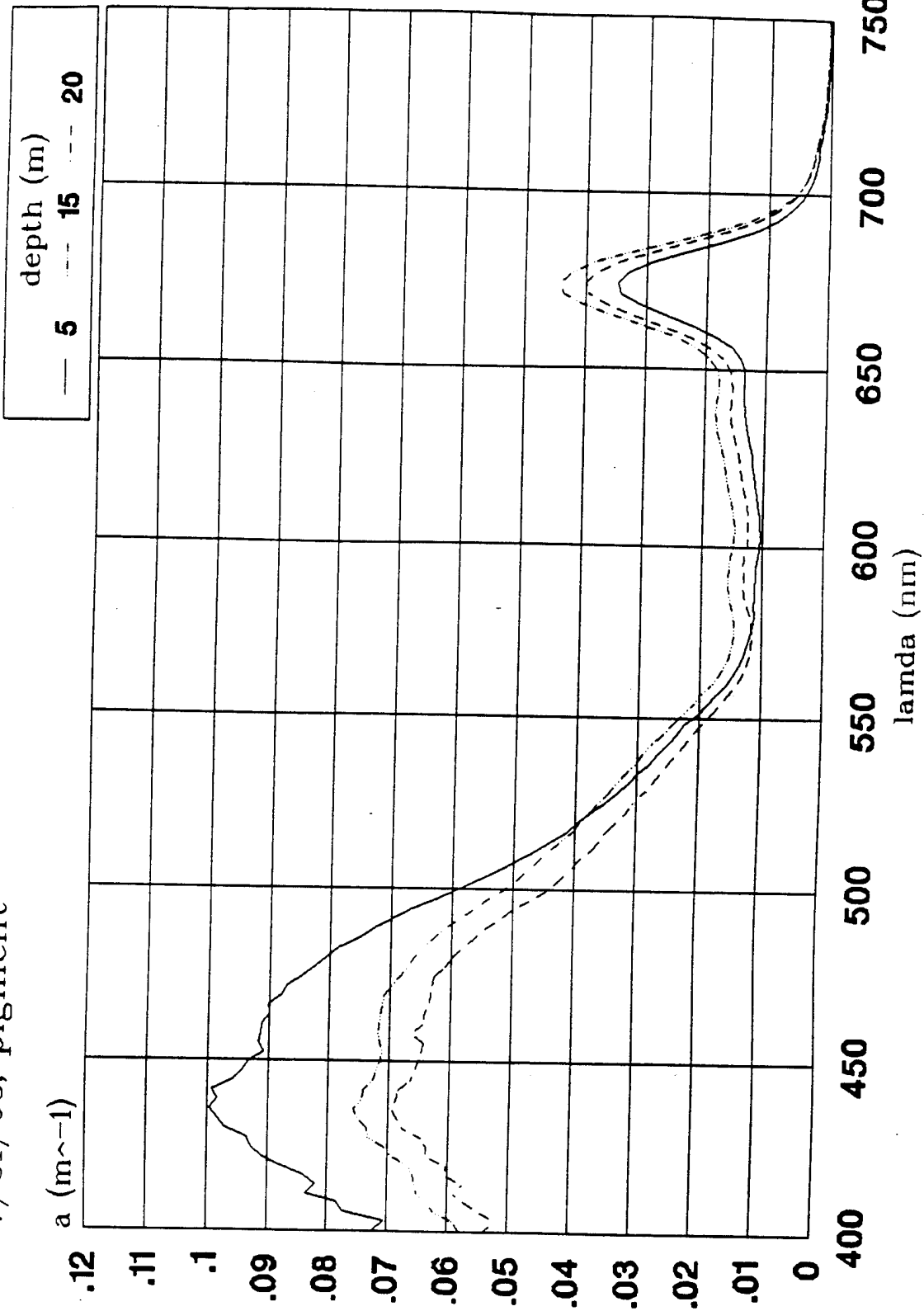
(1 mg/m~3 assumed)

Santa Cruz – Pigment Absorption Spectra
Shallow Station Surface Water (7–10 m)

Date (all 7–10 m)
-□- 7/24 -▽- 7/25 -△- 7/26 + 7/28

a(p) (m–1)

lamda (nm)

Carder Group Data Report
SIGMA Monterey Bay Field Experiment
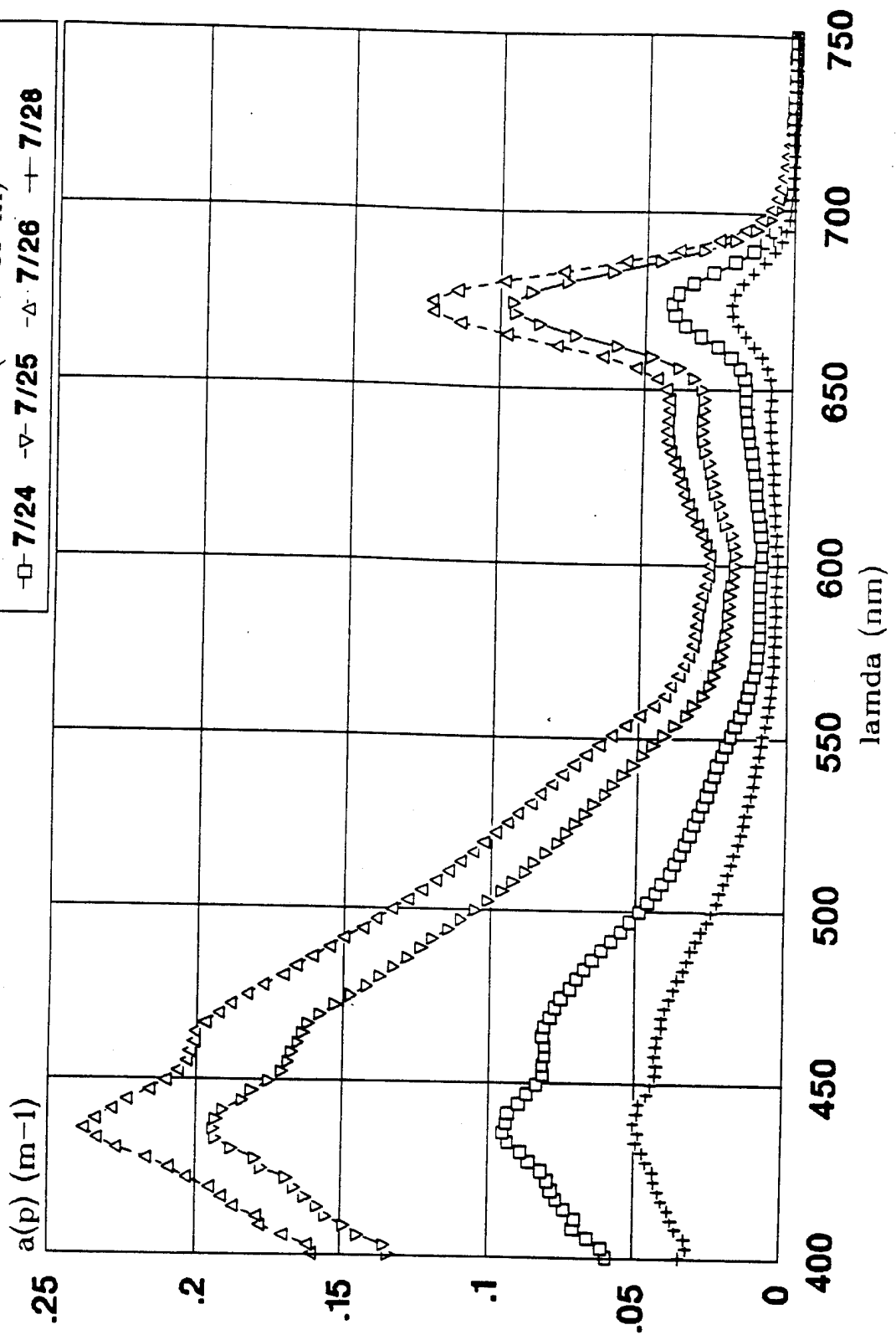
Santa Cruz – Pigment Absorption Spectra
Shallow Station Surface Water (7–10 m)
(Normalized at 674 nm)

Date (all 7–10 m)
-□- 7/24 -▽- 7/25 -△- 7/26 -+- 7/28

a(p) (m-1)

lamda (nm)

MAPPER Particle Size Spectra for Different Depth Layers

Particle Size (cm)

Particle Counts (cm^-1 cm^-3)

REDUCE BY 10

MAPPER Particle Size Spectrum (ESP vs ESD)

SIGMA Monterey Bay
(Averaged over depth)
7/29 1100 hours (DC3)

ESP

ESD

Particle Size (cm)

Particle Counts (cm^-1 cm^-3)

REDUCE BY 10 !

MAPPER Particle Size Spectrum (ESP vs ESD)

SIGMA Monterey Bay
(Averaged over depth)
7/29 1100 hours (DC3)

MAPPER Particle Size Spectrum

7/30 0900 hours (DC2)

7/29 1100 hours (DC3)

SIGMA Monterey Bay
(Averaged over depth)

7/29/93: 2-32m
7/30/93: 2-42m

ESP

Particle Size (cm)

Particle Counts (cm^{-1} cm^{-3})

REDucE BY 10.'

MAPPER Particle Size Spectrum

Particle Counts (cm^{-1} cm^{-3})

10^4

10^3

10^2

10^1

10^0

10^{-1}

7/30 0900 hours (DC2)

10^{-2}

SIGMA Monterey Bay
(Averaged over depth)

7/29/93: 2-32m
7/30/93: 2-42m

10^{-3}

7/29 1100 hours (DC3)

ESP

10^{-4}

10^{-2} 10^{-1} 10^0 10^1

Particle Size (cm)

MAPPER Particle Size Spectra for Three Depth Layers

o = <10 m
+ = 10-20 m
x = >20 m

SIGMA Monterey Bay
7/29/94 1100 hours (DC3)

Y-axis: Particle Counts (cm^{-1} cm^{-3})

X-axis: Particle Size (cm-ESP)

REDUCE ALL CONCENTRATIONS BY 10!

MAPPER Particle Size Spectra for Three Depth Layers
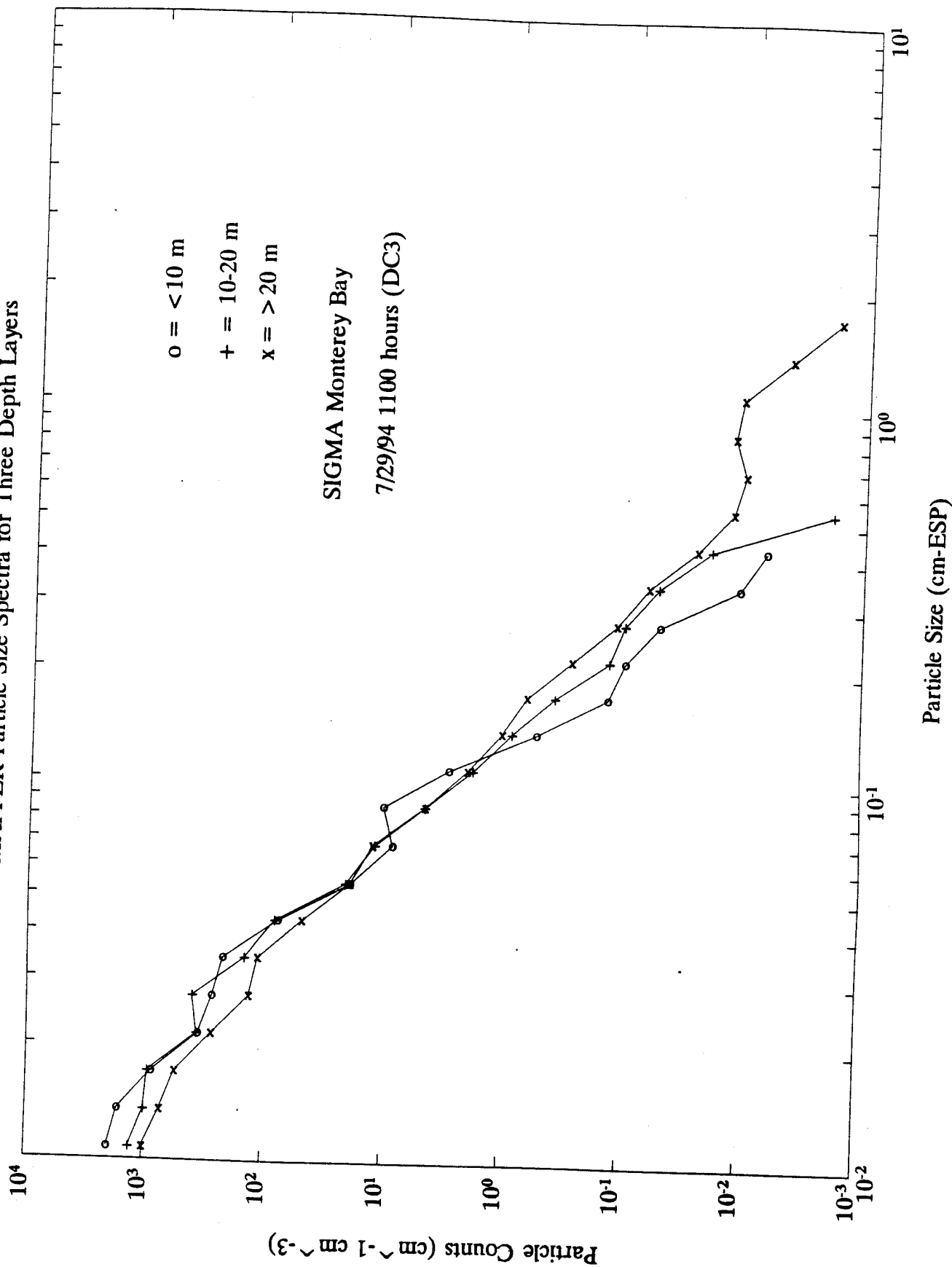
o = <10 m

+ = 10-20 m

x = >20 m

SIGMA Monterey Bay

7/29/94 1100 hours (DC3)

Particle Size (cm-ESP)

Particle Counts (cm^{-1} cm^{-3})

MAPPER Particle Size Spectra for Four Depth Layers

o = <10 m
+ = 10-20 m
x = 20-30 m
* = >30 m

SIGMA Monterey Bay

7/30 0900 hours (DC2)

Particle Counts (cm^ -1 cm^ -3)

Particle Size (cm-ESP)

MAPPER Particle Size Spectra for Four Depth Layers

o = <10 m
+ = 10-20 m
x = 20-30 m
* = >30 m

SIGMA Monterey Bay

7/30 0900 hours (DC2)

Particle Size (cm-ESP)

Particle Counts (cm^-1 cm^-3)
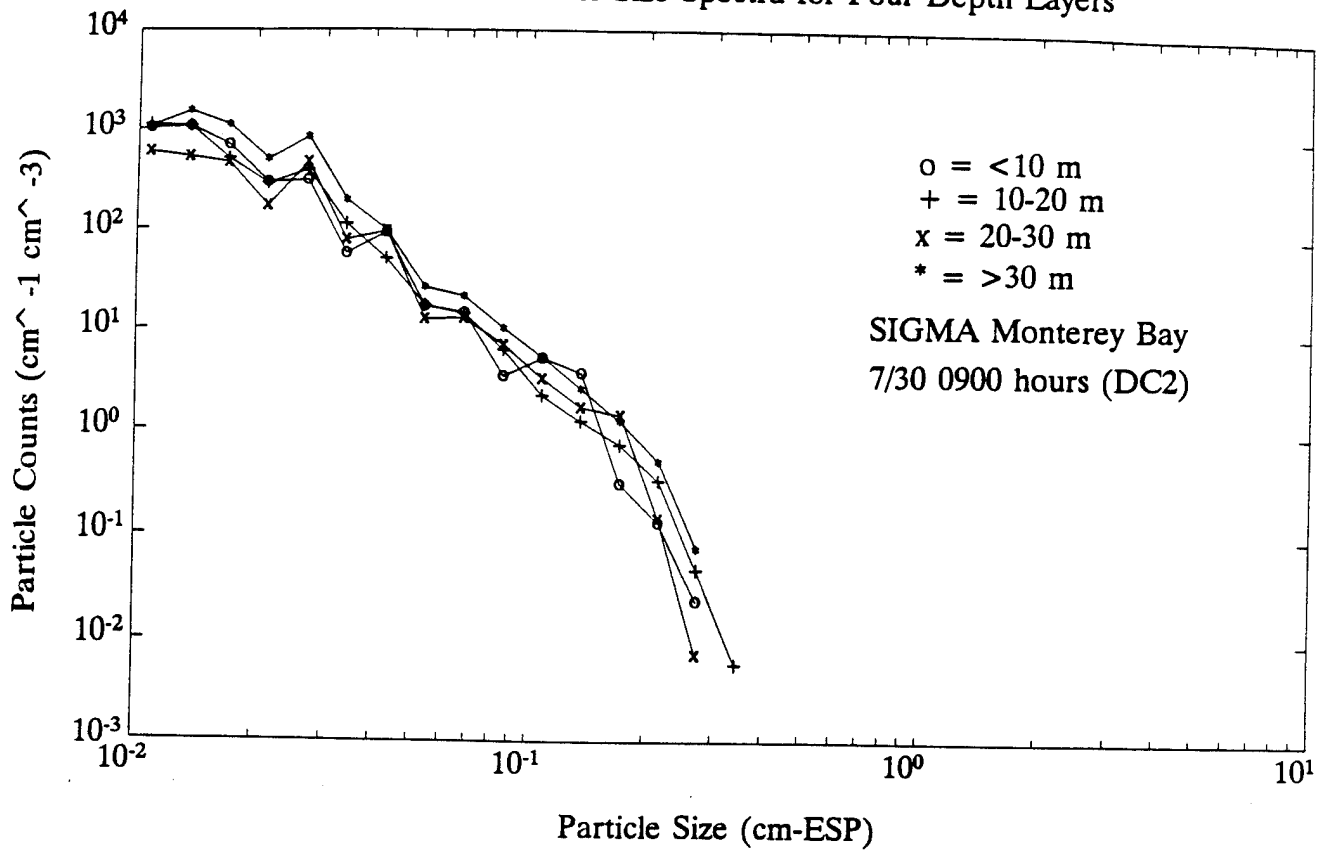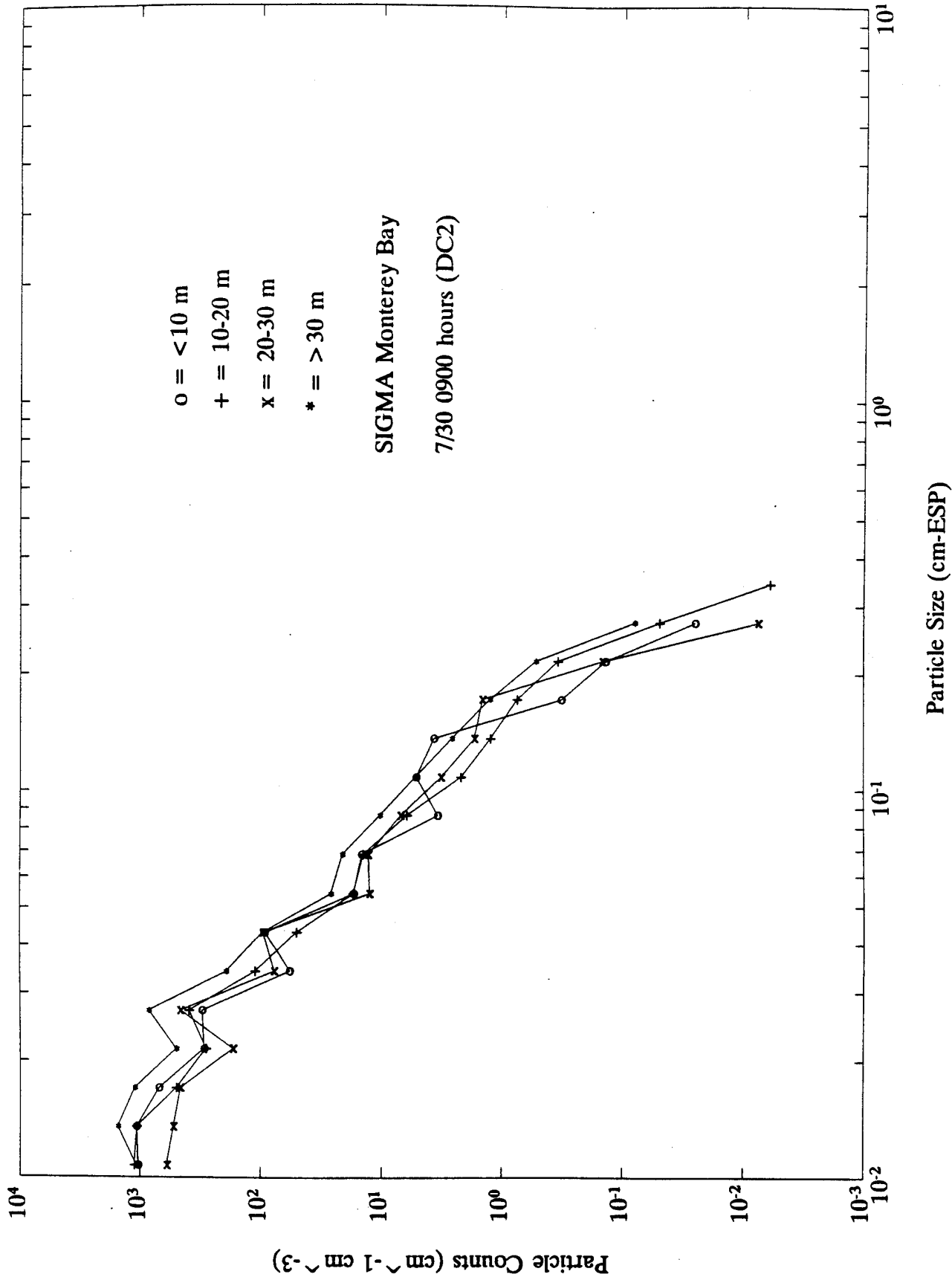
Reprinted from

Ocean Optics XI

20–22 July 1992
San Diego, California

SPIE

P

PROCEEDINGS
SERIES

Volume 1750

Structured Visible Diode Laser Illumination for Quantitative Underwater Imaging

David K. Costello
Kendall L. Carder
Weilin Hou

Department of Marine Science
University of South Florida
140 7th Avenue South
St. Petersburg, FL 33701-5016

ABSTRACT

Knowledge of the marine particle volume concentration is critical to many oceanographic research efforts. A description of particle volume concentration is most often estimated by assuming particle volumes based on a particle size distribution. This requires the enumeration (ideally, in situ) of a statistically significant number of particles across the size spectrum. This becomes increasingly difficult as one approaches the large-particle end of the size distribution because of the low concentrations of large particles found in most waters. However, even though number concentrations are generally low, the volume flux of large particles and their effect on the underwater light field may be significant.

The Marine Aggregated Particle Profiling and Enumerating Rover (MAPPER) is an instrument under development to help address the difficulties associated with the enumeration and analysis of large marine particles. MAPPER will utilize visible diode lasers (670 nm) to produce a structured-light sheet (SLS) coincident with the image planes of video imaging systems of various resolutions. This contribution focuses on the development of the diode laser SLS, on the sheet/system characterization required to make possible the retrieval of quantitative, individual-particle information, and on the unique information offered by imaging in an SLS as opposed to other structured-light volumes. The deviation of the implemented sheet from the "ideal" sheet is presented as are the first field data acquired by deploying the SLS module on a remotely operated vehicle testbed.

1. INTRODUCTION

The term "marine snow" was first used to describe large, aggregated marine particles in 1953[1]. Since that time, it has been realized that marine particle aggregation is ubiquitous and might be of significant, if not crucial, importance in understanding particle mass flux, primary productivity, the spectral quality of the underwater light field, and, hence, ocean color as sensed from airborne/spaceborne platforms[2,3,4,5,6]. The study of these particles is problematic because the friable nature of the aggregations essentially precludes their physical capture and transport from capture depth for subsequent study. *In situ* investigations utilizing optical techniques (non-contact) minimize particle alteration/disruption. The *in situ* imaging of marine particles, however, shares many of the signal-to-noise difficulties of underwater imaging in general. Natural and traditional artificial illumination, for example, allow light scattered from illuminated particles outside the imaging volume, reducing the image contrast. Sizing and classification of small-particle images (magnification approaching 1 or more) have additional difficulties associated with a limited depth-of-field and the resulting noise from illuminated but unfocused targets in the field of view. Moreover, target sizing and classification are uncertain without individual target range information. Structured-light, controlling the illuminated volume, helps to ameliorate these difficulties and makes possible the retrieval of otherwise unavailable information. A new instrument, the Marine Aggregated Particle Profiling and Enumerating Rover (MAPPER), is under development to help address the difficulties associated with enumeration, analysis, and the quantification of the optical properties of marine particles from tens of micrometers to several centimeters major dimension. This work is pragmatic because it is known, for example, that very small marine particles (less than 1 μm diameter) dominate backscattering in the open ocean and that total light scattering is dominated by particles less than 10 μm diameter[7]. However, the effects of the presence of large particles on the underwater light field is currently unknown and may be significant[8].

To enable the enumeration and analysis of large marine particles, MAPPER employs visible laser-diode illumination with line-generator optics to produce a thin light sheet at the system focal plane. This structured-light sheet (SLS) and long-pass optical filters are utilized to minimize noise associated with diffuse ambient illumination since significant red ambient illumination is lost below 5 m depth. The MAPPER instrument and data reduction approach is described elsewhere[4], this contribution focuses on the development of the structured-light sheet and the system characterization required to make possible the retrieval of quantitative, individual-particle information.

2. LIGHT SHEET MODULE

The MAPPER SLS module consists of a 10mW laser diode with line-generator optics (Melles Griot Electro-Optics Division, Boulder, CO) mounted at each corner of a square, and projecting a fan of light toward the center of the square. The intersection of all four light-fans thus define a bounded volume of area $A = L^2$ cm^2 (where L is a side of the square), thickness T cm (width of the 1/e^2 intensity level measured orthogonal to the light plane) and volume T*A cm^3.

In this configuration (square), opposing laser diode pairs help to compensate for the 1/r (2-dimensional) geometrical attenuation of beam power. These laser diodes were selected because of their small size, output power stability (+/- 1%), low power consumption (60 mA, +5 VDC), and the visible wavelength (670 nm) near the wavelength (660 nm) commonly utilized in oceanographic transmissometers. The line generators expand the beam in one dimension only to produce a nominal 1/e^2 fan thickness of 1 mm.

2.1 Structured light in Utopia

The "perfect" SLS would be a 2-dimensional step function, an evenly illuminated square of light the dimensions of which were continuously variable in order to optimize the imaging of a wide range of target sizes. There would also be no power losses in the optics or in light propagation and the geometry of the volume would not be affected by the medium. In reality, however, and in accordance with Snell's law, a 70° half-angle fan must be produced in air to yield a 45° half-angle fan in water. At this large half-angle, output power losses within the line generators are significant and reduce the output for each laser to about 4 mW yielding 16 mW available in the sheet. Additional power is lost, in reality, to attenuation by water, dissolved material, and particles. The diffuse attenuation coefficient k at 670 nm for the cleanest ocean water, for example, is 0.43 m^{-1} [9]. A further departure from the utopian SLS is that a laser diode produces a light fan that also has a Gaussian intensity distribution in the polar co-ordinates which define the beam spread. Accepting the Gaussian nature of laser diode illumination, an "ideal" Gaussian SLS for underwater deployment would have a 1/e^2 intensity (13.5% of peak intensity) at the 70° half-angle in the plane defined by the fan. A more realistic 2% of peak intensity was finally realized at the 70° half-angle.

2.2 Structured light in Florida

The calculated, in-water, intensity distribution for one of our laser diodes is shown in Fig. 1. The figure was generated from 200 measurements made in air using a Newport 840 power meter. The measurements were made in a grid spanning approximately a 180° from the laser projector. Measuring power flux beyond the required (in air) full fan angle of 140° was necessary to allow a distance-weighted interpolation algorithm to mathematically warp the intensity distribution into the shape that would result in water. The matrix describing this distribution can then be rotated at multiples of 90° and placed at the corners of squares (or other geometries) of different sizes. The sum the four rotated matrices is the 4-projector, non-attenuated, SLS intensity distribution that can be expected in this configuration. An attenuation coefficient can then be chosen and the SLS intensity distribution for different waters can be approximated. The intensity distribution for a 25 cm square SLS in the clean ocean waters (c = 0.5 m^{-1}) is shown in Fig. 2a and for a much higher attenuation (c = 4.0 m^{-1}) in Fig. 2b.

As illustrated in Fig. 2, attenuation in the medium helps flatten out the intensity peak which results from the central convergence of the four Gaussian fans. In practice, it is desirable to image particles as far as is practical from the laser projectors in order to minimize potential effects from induced turbulence. This results in the utilization of the central portion of the SLS appropriate to the operational field-of-view (FOV). This central portion (corrected for attenuation) can be transformed into an intensity image which can be used to correct acquired real images for differences in the SLS intensity.

With modern image processing boards and digital signal processors, this correction can be done in real time. Although this correction effectively reduces the dynamic range of the resulting image by a factor equal to the dynamic range of the intensity-correction image, the result is otherwise the equivalent of imagery obtained in the utopian SLS discussed above. Additionally, since the SLS intensity is now corrected, introducing an element of known reflectance (eg. Spectralon, Labsphere Inc.) within the FOV allows the direct determination of individual particle scattering at 90°, $\beta(90°)$.
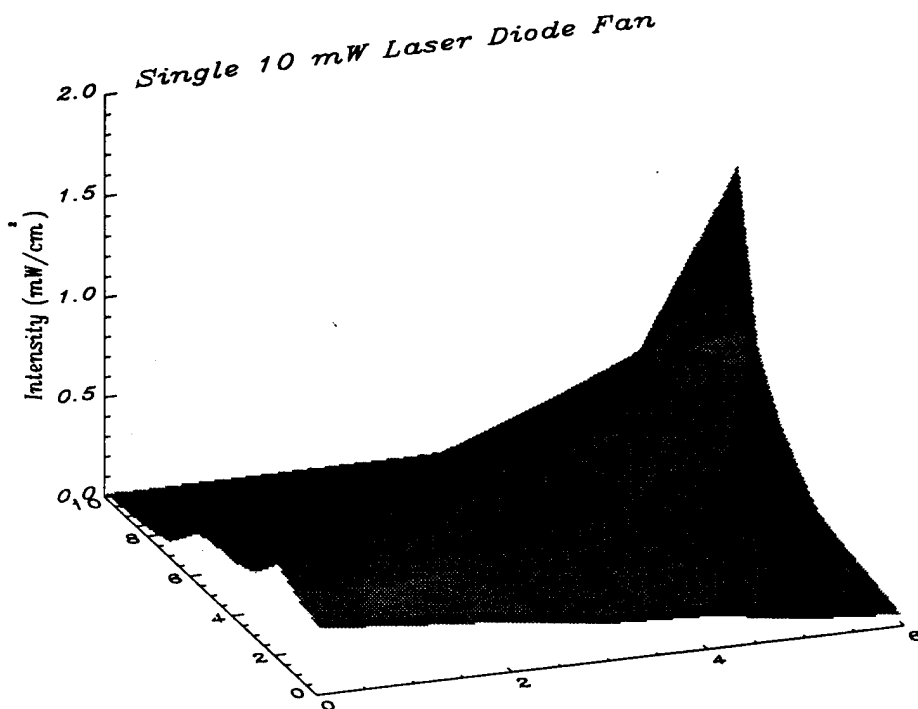
Figure 1. The calculated, in-water intensity distribution for a 10 mW structured-light fan. See text for discussion.
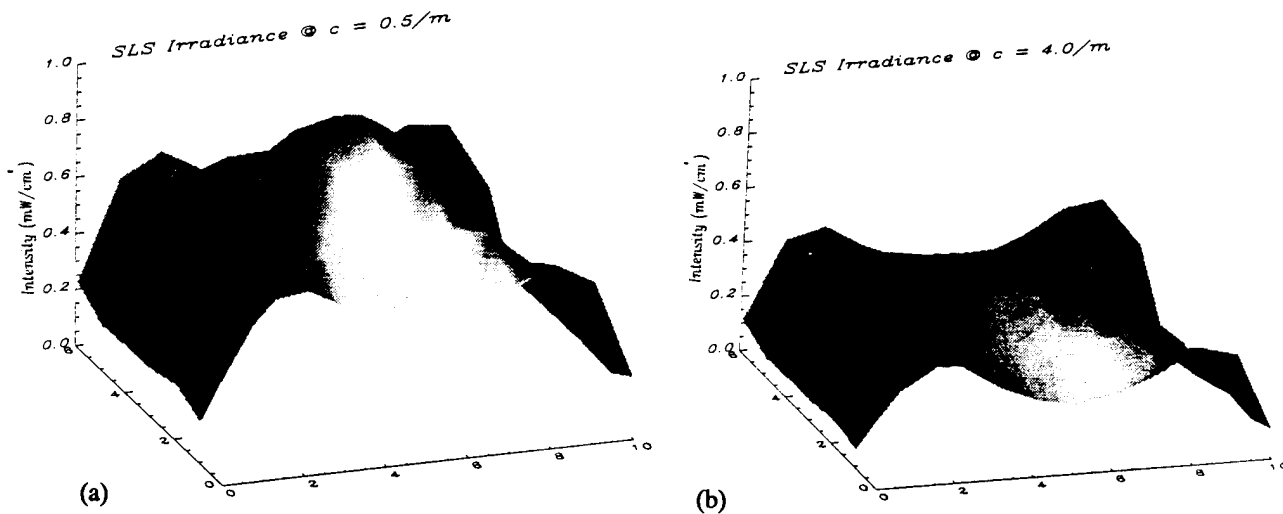
Figure 2. Computed intensity distributions for the SLS with attenuation coefficient c = 0.5 m^{-1} (a), and 4.0 m^{-1} (b).

3. SLS DEPLOYMENT

The SLS module was deployed in June 1992 in Tampa Bay mounted on a small Remotely Operated Vehicle (ROV). The objectives of the deployment were to test the laser projector housings and alignment mounts, to evaluate ROV maneuverability in this configuration, and, primarily, to secure a video record of *in situ* SLS imagery for automated video-data reduction. A hyperstereo mirror module (HMM) was also mounted on the ROV in order to obtain 3-dimensional particle information to compare with the SLS imagery.

3.1 Configuration

The field-of-view of the ROV camera included the SLS and a hyperstereo mirror module mounted on the ROV faceplate. The HMM uses 2 mirrors to divide the video image into 3 segments, a left-mirror view, a central view, and a right-mirror view (see Figure 3). This configuration provides two or three, 2-dimensional projections of the 3-dimensional particles in each frame as a particle passes through the hyperstereo volume. A 0.5 second particle traverse, for example, would generate, depending on the particle path through the HMM, between 30 and 45 different projections. This suite of different projections allows an accurate 3-dimensional determination of particle size, shape, and volume. This HMM ability is of special importance in interpreting SLS imagery of particles whose dimension along the optical axis exceeds the thickness of the sheet.
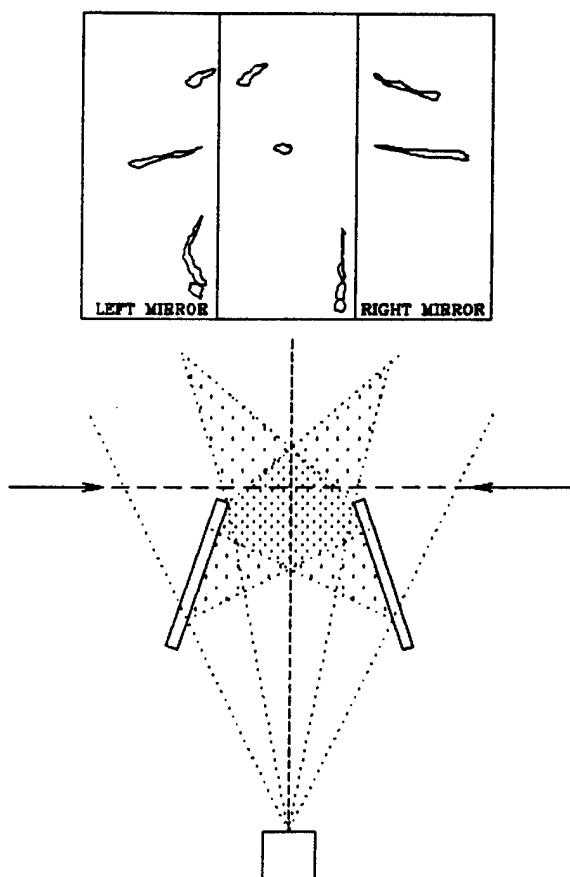
Figure 3. (Bottom) Schematic of a cross section of the HMM volume (plane view) showing mirror placement and resulting star-shaped, stereo-view volume. Arrows show placement of the SLS. (Top) Cartoon of an HMM image depicting the triple projections of two particles in the 3-view central area of the HMM volume and the double projections (the lowermost) which would result from a particle in the 2-view triangle at the upper right.

The presence of very large particles during this study was anticipated since an ROV/HMM time series at the study site in support of the second Tampa Bay experiment (TAMBAX II) found an abundance of marine snow of several centimeters length and millimeters in diameter[10]. In these circumstances, the SLS image is a 2-dimensional cross-section of the 3-dimensional particle. When the local current velocities exceed T (cm) X sampling rate (Hertz) (3 cm/sec for T = 0.1 cm at RS-170 video rates), the sample volume is not a continuum and the dimensions of most large particles cannot be determined. Since marine snow settling velocities w_{MS} are small (-0.2 > w_{MS} > O.3 cm/sec, mean=0.05 cm/sec)[12], tracking a particle through the center of the mirror module volume also allows the determination of a local current velocity record (which, then, defines the integrated sample volume). At very low local current velocities, differential particle settling can be observed. The time, ROV depth, and temperature at depth are available at the surface and encoded in the vertical blanking interval of the RS-170 video signal which is then recorded on S-VHS video tape. These environmental parameters are then integrated with the video data on a frame-by frame basis.

3.2 Methods

The primary objective of this deployment was to obtain *in situ* SLS imagery to test an automated, video data-reduction system. A short (20 min ≈ 7.5 Gbytes) video record was secured. This includes 13 minutes where the ROV was trimmed negatively buoyant, manuevered so that the tidal current was flowing along the ROV optical axis (through the SLS), and set on the bottom (7 m depth) with the optical axis 0.25 m above bottom. This configuration allows comparison with Wells and Shanks[12], one of the few shallow-water marine snow studies available.

The SLS was operating throughout the time on bottom, and the ROV navigation flood lights were intermittantly switched on to utilize the HMM 3-D capability. The on-bottom imagery for the SLS alone totaled 8.6 minutes (15,500 frames, 3 GBytes data, 63 liters volume). During later laboratory analysis, the video tape was advanced frame-by-frame under automated computer control and the imagery was digitized at 512Hx400V 8-bit pixels/frame. A 200Hx200V pixel window representing a 6.4 cm square was defined in the central portion of each frame (SLS imagery only) yielding a nominal pixel resolution of 320μm (H and V). The total intensity within the window (sum of all pixel grey-scale values) was computed and a target detection/sizing algorithm was applied. The algorithm utilized a pixel-intensity threshold and a 4-pixel, minimum-area criteria. This four-pixel criteria eliminates noise associated with highly reflective single-pixel (or sub-pixel) targets and insures that the targets accepted have a dimension > 500 μm, the accepted size definition for marine snow.

4. RESULTS

For particles > 20 μm diameter, the most important optical parameter for light propagation in the sea is the optical cross-sectional area (OCSA). For example, a particle's OCSA for attenuation is the product of its geometric cross-sectional area (GCSA) and its attenuation efficiency factor Q_c. The GCSA size-distribution for the particles detected in 6000 continuous frames (3.33 minutes) is shown in Figure 4. Since the local current velocity along the optical axis was 7 cm/sec (computed using the HMM), integrating this curve would only yield an accurate target count if no particles were present larger then 2.3 mm in the dimension along the optical axis. Such particles would occupy the SLS for more than one frame-period (33 msec) and be counted more than once. Although the 3-D mirror module imagery showed that a significant number of particles were present with a dimension > 1 cm, their long axis was more closely aligned with the gravitational vector than with the optical axis, and a very small percentage occupied the SLS for more than one frame. Noting this, target frequency vs. time (total number of targets detected per second) for the Fig. 4 data is shown in Fig 5. To compute actual particle numbers/unit volume, the instaneous sample volumes would need to be contiguous, and multiple counts of individual targets would have to be subtracted from target frequency to yield particle frequency.

This time series of target frequency does, however, have utility as an indicator of particle temporal distribution. Spatial distributions of marine snow have proven difficult to quantify and, hence, it is undetermined if there is some quantifiable degree of "patchiness" in a distribution. Wells and Shanks[12] hypothesized from photographs and transmissometer data that marine snow can have a patchy spatial distribution and may be advected in "waves". The data displayed in Fig. 5 show that this marine snow was certainly patchy. Preliminary power spectrum analysis of the data did not, however, indicate any dominant frequencies.
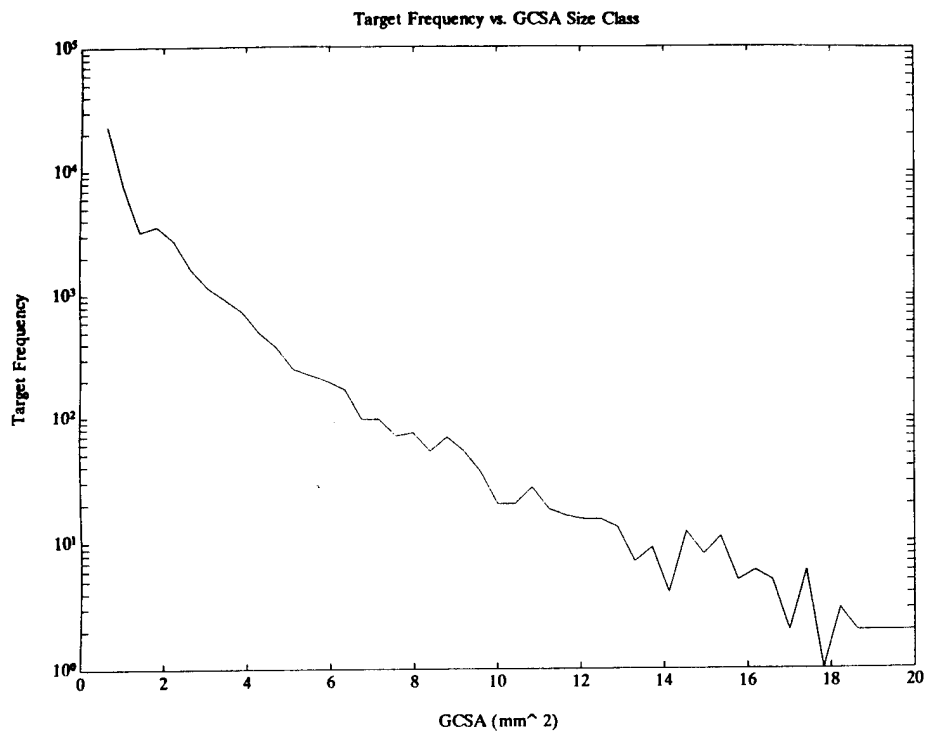
Target Frequency vs. GCSA Size Class

Figure 4. GCSA size distribution for particles detected in 6000 consecutive frames. See text for discussion.
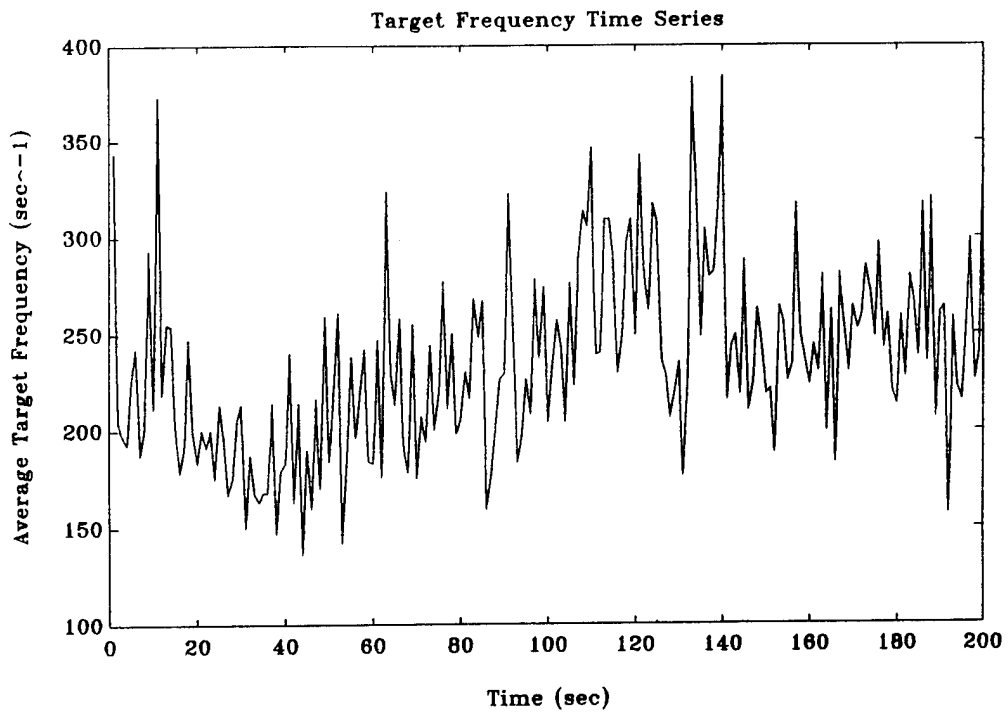
Target Frequency Time Series

Figure 5. Target frequency vs. time for the same data set as Fig. 4. (6000 continuous frames).

5. DISCUSSION

Difficulties in the determination of marine particle properties (size, shape, volume, optical characteristics, etc.) across a representative size spectrum are numerous. Particles range from sub-micrometers to centimeters in size, for example, and are subject to chemical, biological, and physical transformations when the analysis process involves contact, concentration, or confinement. An additional difficulty is that the spatial distribution usually cannot be determined on scales appropriate to particle size. Furthermore, marine aggregates are, by definition, composed of smaller particles and, thus, affect the numbers and distribution of the entire particle size spectrum.

Optical techniques can ameliorate some of these difficulties but must contend with the problems associated with light propagation in a particle-laden, fluid medium. Many forms of structured illumination have been devised to improve the signal-to-noise ratio of marine optical systems. The collimated beam of a trasmissometer, for example, defines a volume and allows a measure of bulk attenuation to be made. For underwater imaging, structured-light geometries help improve the contrast transfer function and can provide otherwise unavailable range information. As the dimension of the structured-light volume along the optical axis increases, the volume imaged increases but the range information becomes more ambiguous. Conversely, as this dimension decreases, the range information becomes more precise but the size of the particles which can be contained within the volume decreases. In fact, the utility and information content of structured-light imagery changes as a function of particle size with respect to thickness T.

For particles small compared to T, the image is equivalent to a 2-D photograph except that the particle image projection can be sized within the accuracy of the range information available. Also, since the illuminated volume is fixed, an accurate particle count per unit volume can be made and the particle volume per unit volume V_p/V_w can be estimated within the accuracy allowed by the sizing and the assumption of volumes of revolution or some other technique. If the particle dimension along the axis exceeds T, the image is the GCSA of the particle and V_p/V_w can be estimated but a particle count per unit volume cannot be made. This GCSA has special utility, for example, since the attenuation efficiency factor Q_c for large particles equals 2 (Van de Hulst, 1957)[13], one can estimate the particle OCSA for attenuation. If the particle GCSA is determined accurately and if the choice, $Q_c=2$, is correct for the particles in the imagery, then the SLS imagery can be converted into large-particle transmissometry. For example, using $Q_c=2$, and the average total particle GCSA for these data of 0.28% of the SLS window, the average OCSA is 0.56% of the window. One can then treat the SLS as a transmissometer of 1 mm pathlength and arrive at a large-particle attenuation coefficient $c_{lp} = 5.6$ m^{-1}. Total attenuation would also include attenuation by small particles, dissolved material, and the water and, presumably, be much higher. For comparison, Carder, et al.[14] measured total attenuation minus water attenuation at 660 nm ($c_t - c_w$) of 5.3 m^{-1} for Bayboro Harbor in Tampa Bay.

The accuracy of the extrapolation largely depends on the GSCA measurement. This measurement is primarily a function of the pixel-intensity threshold value utilized during post-deployment image processing. In practice, the threshold value is chosen to eliminate image noise arising from gain-amplified, sensor dark current, sub-pixel-sized targets, and particles at the edge of the SLS and/or indirectly illuminated by light scattered from targets within the sheet. An examination of the combined HMM/SLS imagery to look for indirect particle illumination was conducted. Although it was detected, the intensity levels observed fell below the threshold value for the SLS image processing and, therefore, did not bias the GCSA measurements. However, more laboratory work with marine snow surrogates is required and more *in situ* imagery with higher S/N ratios need to be obtained and examined to quantify this phenomenon.

6. SUMMARY

A structured-light-sheet module utilizing visable laser diode illumination for the analysis of large marine particles has been developed and deployed. A hyperstereo mirror module was deployed in conjunction with the SLS module in order to allow intercomparison of imagery. Each module offers advantages and drawbacks.

The HMM is a single camera system which allows unambiguous determination of particle position, size, shape, and volume. Local current velocity, which defines the time-series sample volume, can also be estimated by tracking a particle through the HMM volume. The primary disadvantages of HMM imagery are two-fold. First, the relatively large depth-of-

field and FOV required allows imaging of particles outside the stereo volume. This introduces noise which lowers image contrast and increases image complexity. This complexity is the second drawback of HMM imagery. Each of the many projections of a particle passing through the HMM image-space is from a unique viewing angle and most differ in magnification. The pixel map representing this space, therefore, consists of three, convolved, 3-dimensional arrays. Although the determination of particle position in 3-space is straightforward (as, for example, is required in velocity calculations), the development of algorithms for automated target detection and shape determination is a significant task.

On the other hand, ease of target detection and sizing is a primary advantage of SLS imaging. Even though the pixel map represents 3-dimensional space, one dimension is fixed by the geometry of the SLS and automated image processing is readily implemented. This processing facility is enhanced by the high-contrast nature of SLS images and provides for the determination of the number-frequency distribution of particle GCSA. This GCSA distribution makes possible the estimation of large-particle attenuation c_{lp}. Other compelling advantages are that a fully parameterized SLS system (ie. S/N ratio maximized with the sheet intensity fully mapped and monitored via a reference of known reflectance) will allow an estimate of $\beta(90°)$ for the individual targets while the signal in the imagery below threshold intensity will be porportional to $\beta(90°)$ per unit volume for particles below the resolution of the imaging system.

The primary disadvantage of SLS imaging is that particles which exceed the thickness of the sheet in the dimension along the optical axis cannot be sized if the sample volumes are not contiguous. In these conditions, even though an unambiguous GCSA size distribution could be determined, any particle size distribution derived from the imagery would, invariably, under-represent the large particles. Some consideration should be given, however, to the fact that, since these large particles are generally non-spherical, any size-distribution derived from a single projection of these 3-dimensional particles would also, invariably, under-represent the large sizes.

Another constraint in SLS imagery is that accurate measurements are largely dependent on the choice of an appropriate pixel-intensity threshold in the processing of the imagery. Additional field work with higher S/N ratio systems and laboratory work with marine snow surrogates is required and is underway.

In short, the information content of SLS imagery is limited by constraints inherent to the technique. The strength of the technique, however, is that this information is otherwise unavailable. Finally, the combination of SLS imagery and HMM imagery should prove to be a synergistic tool for marine particle research.

7. ACKNOWLEDGEMENTS

REFERENCES CITED

1. Suzuki, N. and K. Kato (1953) Studies on suspended materials. Marine snow in the sea. I. Sources of marine snow. Bulletin of the Faculty of Fisheries of Hokkaido University, 4, 132-135.
2. Alldredge, A. L. and M. W. Silver (1988) Characteristics, dynamics and significance of marine snow. Progress in Oceanography, 20, 41-82.
3. Alldredge, A. and E. O. Hartwig, editors (1986) Aggregate Dynamics in the Sea Workshop Report, Office of Naval Research, Asilomar, Pacific Grove, Ca. 211 pp.
4. Costello, D.K., K.L. Carder and R.G. Steward. (1991) Development of the Marine Aggregated Particle Profiling and Enumerating Rover (MAPPER). Underwater Imaging, Photography, and Visibility, Richard W. Spinrad, Editor, Proc. SPIE 1537, 161-172.
5. Carder, K. L. and D. K. Costello, Optical effects of Large Particles. Ocean Optics. K.L. Carder, M.J. Perry, and R.W. Spinrad, editors, Oxford University Press, New York, N.Y. In press.
6. Baker, E.T. and J.W. Lavelle (1984) The effect of particle size on the light attenuation coefficient of natural suspensions. J. Geophys. Res. 89, 8197-8203.
7. Stramski, D. and D. A. Kiefer (1991) Light scattering by microorganisms in the open ocean. Prog. Oceanog. 28, 343-383.

8. Carder, K. L. and D. K. Costello, Optical effects of Large Particles. <u>Ocean Optics</u>. K.L. Carder, M.J. Perry, and R.W. Spinrad, editors, Oxford University Press, New York, N.Y. In press.

9. Smith. R. C. and K. S. Baker (1981) Optical properties of the clearest natural waters (200-800 nm). <u>Applied Optics</u> 20,(2), 177-184.

10. Costello, D.K., W. Hou, K.L. Carder, R.G. Steward and B. B. Preston (In prep.) 3-dimensional determination of the size, shape, and volume of estuarine marine snow.

11. Riebesell, U. (1992) The formation of large marine snow and its sustained residence in surface waters. <u>Limnol. Oceanogr.</u> 37(1), 63-76.

12. Wells, J.T. and A. L. Shanks (1987) Observations and geological significance of marine snow in a shallow-water, partially enclosed marine embayment. <u>J. Geophys. Res.</u> 92, 13,185-13,190

13. Van de Hulst, H. C. (1957) <u>Light Scattering by Small Particles</u>. John Wiley, New York.

14. K. L. Carder, R. G. Steward, T. G. Peacock, P. R. Payne, and W. Peck (1988) Spectral transmissometer and radiometer: design and initial results. <u>Ocean Optics IX</u>, Marvin A. Blizard, Editor, Proc. SPIE 925, 189-195.

Reprinted from

Underwater Imaging, Photography, and Visibility

23 July 1991
San Diego, California

P

Volume 1537

Development of the Marine Aggregated Particle Profiling and Enumerating Rover (MAPPER)

David K. Costello
Kendall L. Carder
Robert G. Steward

University of South Florida, Marine Science Department
St. Petersburg, FL 33701-5016

ABSTRACT

The *in situ* imaging of marine particles shares many of the signal-to-noise difficulties of underwater imaging in general. Natural and traditional artificial illumination, for example, allow light scattered from particles outside the imaging volume, reducing the image contrast. Sizing and classification of small-particle images (magnification approaching 1 or more) have additional difficulties associated with a limited depth-of-field and the resulting noise from illuminated but unfocused targets in the field of view. Moreover, target sizing and classification are uncertain without individual target range information. The new marine particle imaging instrument to be discussed employs diode laser illumination (675 nm) with line-generator optics to produce a thin light sheet at the system focal plane. This light sheet and narrow-band, optical filters are utilized to minimize noise associated with diffuse ambient illumination since significant red ambient illumination is lost below 5 m depth. It also removes the uncertainty involved in the determination of the 3-dimensional position and size of a target in a 2-dimensional image. An additional problem inherent in marine particle research is that the size of the particles of interest ranges over several orders of magnitude (micrometers to centimeters diameter). The instrument addresses this problem of scale with coincident video imaging systems of high and low spatial resolution. Shape-generated feature vectors and particle optical attributes are extracted from digitized particle images and utilized in an automatic particle classification scheme. The strategy is multidimensional and incorporates a pattern recognition algorithm rooted in the theory of moment invariants.

1. INTRODUCTION

The effort to understand the effects of past and ongoing human activity on our planet's climate is of increasing interest. Part of this effort is the study of the role of the world's oceans in the planet's environment. Ocean primary productivity is of central interest and a synoptic view of the ocean system is most easily acquired using airborne or spaceborne platforms. Hence, considerable effort has been put forth in developing optical models to interpret a remotely sensed radiometric signal. Up to 90% of the total radiance received by a remote platform for even cloud-free scenes is due to the intervening atmosphere[1]. Figure 1 depicts potential components of the remainder of the signal, the water-leaving radiance. In much of the world's open-water ocean the water-leaving radiance is primarily backscatter from water molecules and the small (< 10 μm dia.) particles present. Interpretation of the signal is driven by differential absorption by the small-particle pigments, eg. chlorophyll. Signal interpretation algorithms are calibrated by comparing the remotely sensed data with *in situ* measurements of the water properties and constituents. It is of importance here that these measurements are generally acquired with radiometric, that is, non-imaging instruments. Optical model closure is obtained if we can describe the measured light environment by combining these elementary measurements of the optical properties of the medium with radiative transfer theory. If we can accurately deduce the concentration of various constituents from a combination of measures of the submarine light field and inverse model calculations, we effect model inversion. An invertable optical model must, then, include every component which can make a significant contribution to the remotely sensed water-leaving radiance.

Model closure and model inversion both become more tenuous when the following phenomena are present:

1) Transpectral or inelastic scattering such as fluorescence[2,3,4,,5,6] or water Raman scattering[7,8,9]; or

2) Particles that are large relative to the measurement volume for instruments such as c-meters, light-scattering photometers, fluorometers, and absorption meters which are used to provide input to radiative transfer models.

The transpectral phenomena affecting model closure are being actively pursued as a research topic. However, the effects of large particles on model closure and model inversion have been less vigorously studied. As depicted in Figure 1, large particles, when present, would make a direct scattering contribution to the light field. Some large particles could also affect the spectral characteristics of the light field through pigment absorption and narrow-band fluorescence, bioluminescence, and perhaps exhibit broadband fluorescence from dissolved organic material (DOM) associated with a particle microenvironment. The instrument and data reduction methodology to be described are designed to assist in the enumeration and classification of large marine particles and their *in situ* optical properties.
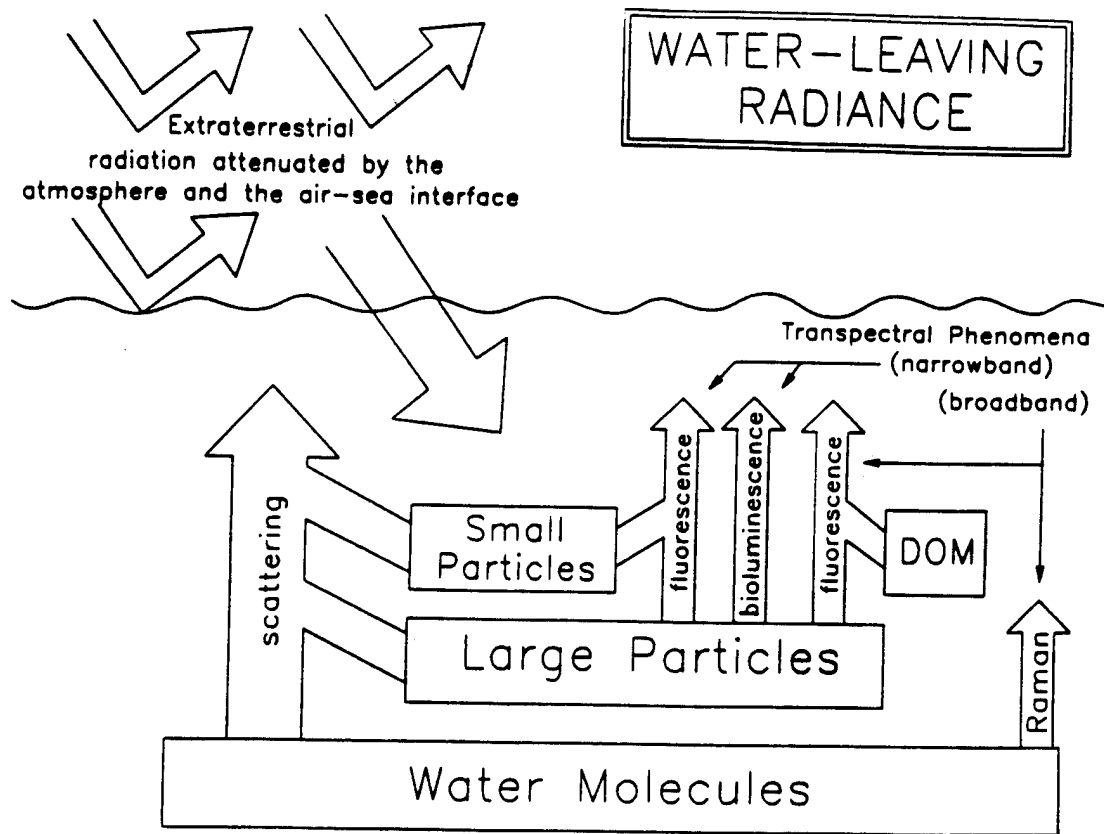
Figure 1. Potential components of water-leaving radiance. See text for discussion.

2. BACKGROUND

A difficulty inherent in addressing the effect of large particles on the light field results from the difference in the scales of measurement typical for the water's apparent optical properties (AOP's) and its inherent optical properties (IOP's). The AOP's are dependent on the geometry of the light field and derive from measures of the light field associated with water volumes of order one to hundreds of cubic meters. The IOP's, in contrast, are independent of the geometry of the light field[10] and derive from very local measurements, with sample volumes ranging from of order cubic millimeters to cubic centimeters.

The effect of large particles on AOP's is a function of their concentration relative to smaller particles and, therefore, will vary geographically. High concentrations of large particles are generally associated with near-shore or near-bottom environments. However, significant concentrations of optically "large" particles can be found in the open ocean. In the oligotrophic north central Pacific gyre (26°W, 155°N), Betzer et al.[11] found an influx of optically large (due to size and high relative index of refraction) eolian particles which amounted to some 10,000 particles m^{-2} day^{-1}. Although the concentrations from such an influx would likely affect a remotely sensed signal which is dependent on the backscattering coefficient b_b, it is estimated that a typical c-meter with a one meter pathlength, for example, may measure in these waters a significant perturbation in its background signal due to such eolian particles only 1 to 2 % of the time. A typical scattering meter, because of its small sample volume, would have a probability approaching zero of detecting these particles. Hence an optically significant portion of the particle population could go essentially undetected.

The question then arises whether these "rare event" large particles are indeed optically significant enough to attempt to measure. Assuming a constant particle volume per seawater volume per log size class[12] allows one to envision the potential contribution. With this assumption, particle numbers diminish by a factor of 10^3 for each larger log-size class. However, even though particle numbers are reduced by a factor of 10^3, individual particle cross-sectional area, a significant optical parameter[13], increases by a factor of 10^2 per log size class. This results in a reduction of total particle cross-sectional area per increasing log-size class of only one order of magnitude. Additionally, the particles in the larger size-class may have optical effects disporportionate to their spherical-equivalent, cross-sectional areas. Larger marine particles, especially large aggregates or marine snow[14] tend to be more complex in shape than smaller particles. This greater degree of complexity would tend to increase the ratio of surface area to volume and change the shape of the volume scattering function $\beta(\theta)$. For example, in microwave analog experiments Greenburg et al.[15] found that a "roughened" sphere versus a smooth sphere demonstrated enhanced scattering in all orientations. Furthermore, Zerull and Weiss[16] found, in a comparison of scattering intensities at angles greater than 10 degrees, that "fluffy" particles scattered nearly an order of magnitude more effectively than smooth particles. This would be especially important the for backscattering and reflectance measurements important for remote sensing applications. Hence, despite the reduction of particle numbers by a factor of 10^3 in increasing log-size class and the reduction of total cross-sectional area by an order of magnitude, the optical contribution to attenuation c through scattering b of, for example, the 10-100 μm diameter and the 100-1000 μm diameter size classes could approach the same order of magnitude if "fluffy", marine snow types of aggregates were present in the larger size class.

Under such circumstances, the optical contribution from neither class would generally be adequately measured by a scattering meter, while the latter class would not be adequately measured by a c-meter. Furthermore, because of the nature of these types of instrumentation, there would be zero probability of identifying the large particles, a valuable step when performing model inversions. This would also be the case even for regions having high concentrations of large particles. Hence, even though traditional *in situ* optical instrumentation may adequately measure the numerically and, generally, optically dominate marine particle classes, the pursuit of model closure and inversion suggests the development of new approaches, especially when considering environments containing large aggregates and animals effecting patchy, schooling types of behavior.

3. NEW INSTRUMENTATION

It is unlikely that existing IOP instrumentation can be easily "scaled up" because of physical limitations, technical considerations, and the critical resultant loss of resolution in measuring the dominant smaller sized particles. This would also not assist in the desired identification of the larger particles. Imaging the large particles, whether it be through photography, holography, video, or some other method, would assist in particle identification and enumeration and allow the measurement and/or inference of particle optical properties. For example, to first order, the attenuation due to large simple particles can be estimated if the large-particle size distribution is known since for large particles the attenuation efficiency factor $Q_c \approx 2$ (Van de Hulst)[13]. An advantage of continuous, sequential imaging (ie. video) is that it provides for the behavioral classifications of swimming versus settling and allows the determination of swimming speed for the former and settling speed for the later. For settling particles, if the size and settling speed are known, the dynamic density (which should have some correlation with optical density) can be inferred by inverting the appropriate, shape dependent, Stoke's settling equation[17,18].

An inherent difficulty in any imaging approach, however, lies in the reduction of massive amounts of information (the images) in order to extract useful data (the particle attributes). A scattering meter or a c-meter, for example, will have two discrete "numbers" corresponding to an instantaneous sample volume (the signal and the reference) while a modest 2-dimensional video image, digitized in an image processing environment at a typical 512 x 512 x 1 pixels (low resolution compared to photography and very low resolution compared to 3-dimensional holography) will have over 250,000 "numbers" corresponding to an instantaneous sample volume. At normal video frame rates (30 frames/sec) this generates nearly one-half billion "numbers" per minute. Thus, any attempt to extract a body of statistically meaningful information from an image data base must necessarily work in an automated image processing/analysis environment. One approach is discussed later.

Many researchers are involved in the acquisition of image-based data at many different scales. For example, Hammer et al.[19] describe a system for a 3-dimensional (time-multiplexed stereo video) study of fish schooling. Carder et al.[17] and Costello et al.[18] describe holographic systems for the study of eolian particles. Honjo et al.[20] and Asper[21] describe photographic systems for investigating marine snow. Various aspects of these and other efforts are discussed in Alldredge and Silver[14]. To date, the only selective, intelligent *in situ* particle observation/collection has been performed by humans utilizing equipment ranging from diving gear to Remotely Operated Vehicles (ROVs) and deep-diving, manned submersibles. This is simply because Autonomous Underwater Vehicles (AUVs) optimized for particle research do not, as yet, exist.

We are in the process of modifying a small ROV for large-particle observation and selective collection to act as a test bed for a first-generation AUV, dubbed the Marine Aggregated Particle Profiling and Enumerating Rover (MAPPER). MAPPER will be a "semi-smart" machine (ie. programmable and able to respond to external stimuli) and a step toward an eventual artificially intelligent AUV.

3.1. Sample volume

The evolution of high-powered, small-sized visable diode lasers allowed the development of the MAPPER sample volume as a light-sheet configuration (hence, 90° scattering). Elements of materials of known reflectance (Spectralon, Labsphere Inc.) and a traditional c-meter are embedded within the light sheet. The light sheet is at the focal plane in the field-of-view of the large-field video camera. The focal plane of a second, higher magnification video camera system is embedded within the larger image volume to evaluate particles as small as 50 μm diameter. In the lower resolution, large-area camera field, the pixel resolution is 500 μm. The light sheet is produced by positioning a 10 mW diode laser with line-generator optics at each corner of a square oriented orthogonally to the imaging axis and at the system focal plane. This yields an evenly illuminated light sheet since opposing diode laser pairs compensate for the 1/r (2-dimensional) light spread. This configuration also establishes the 3-dimensional position of targets. Furthermore, the use of narrow-band, optical filters centered about the Gallium Aluminum Arsenide diode laser wavelength (675 nm) precludes the loss of image contrast due to ambient light scatter from particles outside the imaging volume since significant red ambient illumination is lost below 5 m depth. The degradation of the power output from a 10 mW GaAlAs diode laser (LaserMax Inc.) powered only by four "AA" batteries during a 10 hour test is shown in Figure 2. Although the slope of the power output reduction (about one percent per hour) proved highly linear, change in the wavelength of the output was not monitored. GaAlAs diode lasers typically have a wavelength dependence to changes in temperature (0.3-0.4 nm/°C) and a smaller dependence on change in drive current (0.025 nm/mA)[22]. It is important, then, to chose narrow-band optical filters appropriate to the anticipated operational wavelength range.

An additional problem inherent in marine particle research is that the size of the particles of interest ranges over several orders of magnitude (micrometers to centimeters diameter). The instrument addresses this problem of scale with coincident video imaging systems of high and low spatial resolution. Figure 3 shows a cartoon of a large particle in the coincident c-meter and large-field video camera sample volumes. In this scenario, the c-meter would measure some unknown combination of increased/decreased attenuation relative to the small-particle, background level due to a mix of the following mechanisms: 1) absorption, 2) scattering out of the beam, and 3) enhanced scattering in the near-forward direction within the acceptance angle of the instrument that should have contributed to attenuation if this were an "ideal" c-meter. The video image would record the intensity of the 90° side-scatter from the particle (relative to the reference reflector), the size and shape of the particle, and any textural intensity variations caused by particle internal or surface structure. This will enable not only the enumeration of particles by size and shape but also allows an *in situ* multi-instrument investigation of the optical properties of individual, large particles.
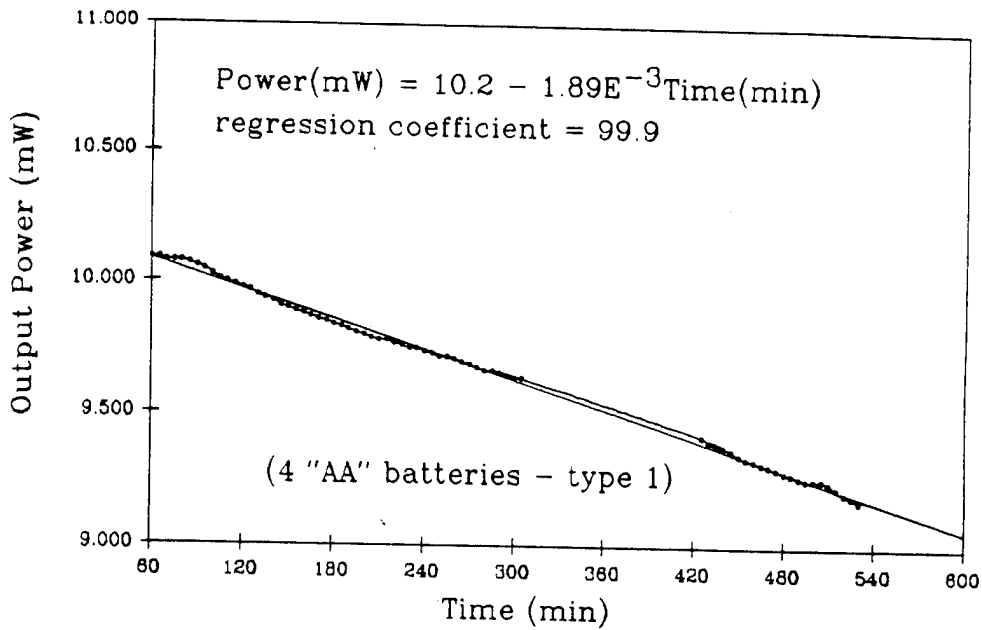
$$\text{Power(mW)} = 10.2 - 1.89E^{-3}\text{Time(min)}$$

regression coefficient = 99.9

(4 "AA" batteries - type 1)

Figure 2. Output power vs. Time for a 10 mW GaAlAs diode laser powered by four "AA" batteries.
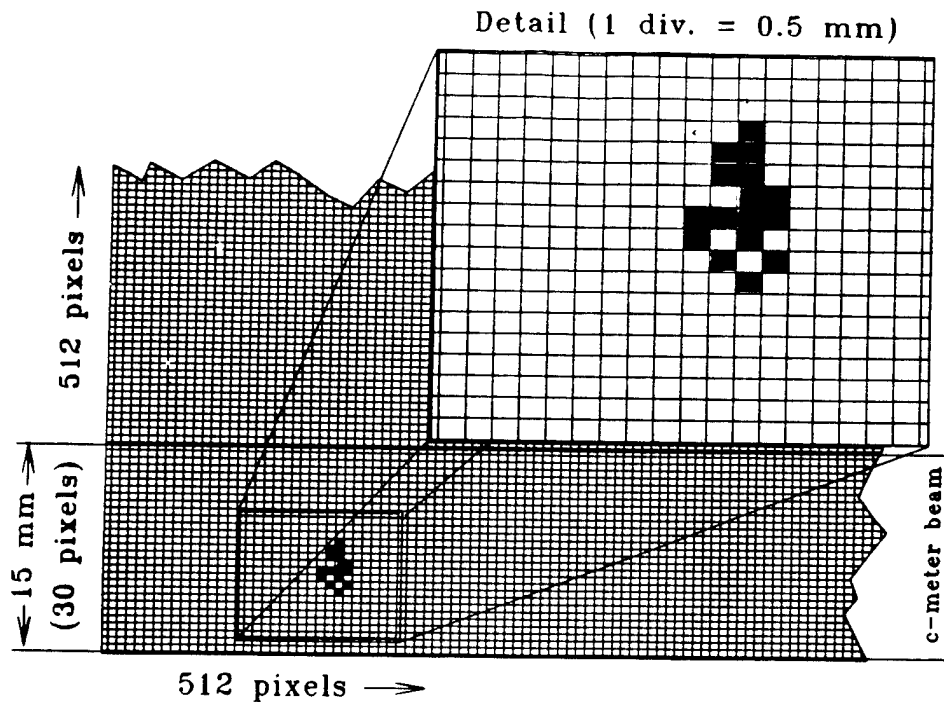

Detail (1 div. = 0.5 mm)

Figure 3. MAPPER sample scenario. See text for discussion.

     Instrument sample volume is actually a function of the thickness of the light sheet since the video frame acquisition is set (33 msec). To image a water volume, then, one needs to translate the instrument at a speed no greater than 30 times the thickness of the light sheet per second. With a field-of-view of 24 cm by 18 cm (conforming to the 4:3 ratio of NTSC video), this translates into a 78 liter/min sample volume and 3 cm/sec translation velocity for each millimeter of thickness of the light sheet. By defocusing the diode laser collimating optics and exploiting the inherent beam asymmetry, we have produced sheets varying in thickness from less than 1 mm to more than 1 cm.

3.2. Control and instrumentation

Instrument control and data collection is integrated on a single-board computer (Pisces Design) capable of encoding environmental data in the vertical blanking period of the video signal. This method of data storage is not only convenient but also insures that environmental parameters and the status of instrument systems are recorded on each image acquired. The board provides a real-time clock/alarm, 12 digital input/output discrete control pins, 8 analog input channels, 2 pulse width modulated outputs and an RS-232 port. The unit currently installed in our ROV testbed is configured with sensors for temperature and pressure. A fluxgate compass, an altimeter, an acoustic pinger/release, and buoyancy/attitude control circuitry will be added for deployment in MAPPER. System development utilizing the ROV testbed is enhanced by the ability to monitor and control the remote board on the ROV through a deck unit via bidirectional communications multiplexed with the existing ROV video signal.

3.3. Deployment configurations

Since MAPPER is an autonomous untethered instrument, a variety of deployment configurations are possible as shown in Figure 4. Phase I configuration is a free-fall instrument which would sample during descent and ascent. Phase II configuration is a moored instrument with instrument attitude control systems utilized to maintain the desired vertical or horizontal orientaion. The Phase III configuration is as an AUV capable of, for example, identifying a feature (eg. thermocline) during descent, sampling beneath the feature for one-half its deployment then ascending to sample above the feature. MAPPER could also be programmed to descend to a height above the bottom and transect at that altitude in order to investigate resuspension of large particles.
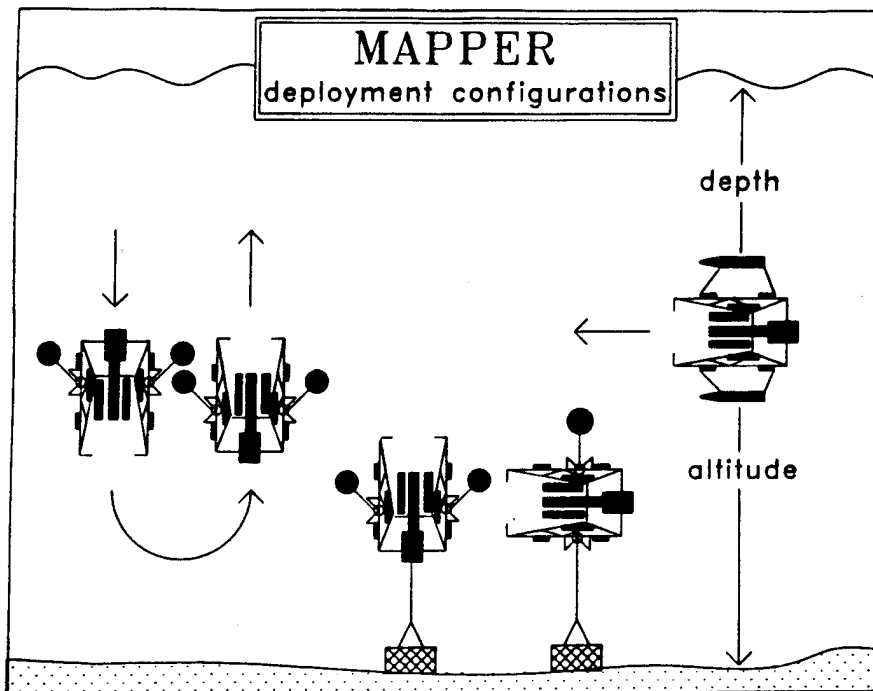
Figure 4. MAPPER deployment configurations. See text for discussion.

4. DATA REDUCTION

Another intrinsic difficulty which must be addressed by any effort aimed at generating a database from which statistically reasonable modelling can be attempted is data reduction. And, as is intuitive, the higher the dimensionality of the data the more formidable is the data reduction. Our video particle imagery will constitute a 4-Dimensional database (3-Space and time) which can best be reduced in the digital domain. Figure 5 shows our multiple-image digital/video image analysis and processing system which will be utilized in this effort. The system allows up to four synchronous video images

to be retrieved with field-rate precision (1/60 sec.), folded into a single image, and overlayed with the recorded data that is associated with that moment in time (eg. depth, distance from bottom, temperature, salinity, etc.). The images can be automatically digitized, operated on with point and area digital processing algorithms and analyzed for the presence of a "target". Targets can then be automatically sized and classified using the method of moment invariants. The resultant database will not only enumerate large particles as a function of size and shape, but also as a function of volume, settling speed, and dynamic density while also recording depth, salinity, temperature, and up to five other deployment variables available for video encryption.
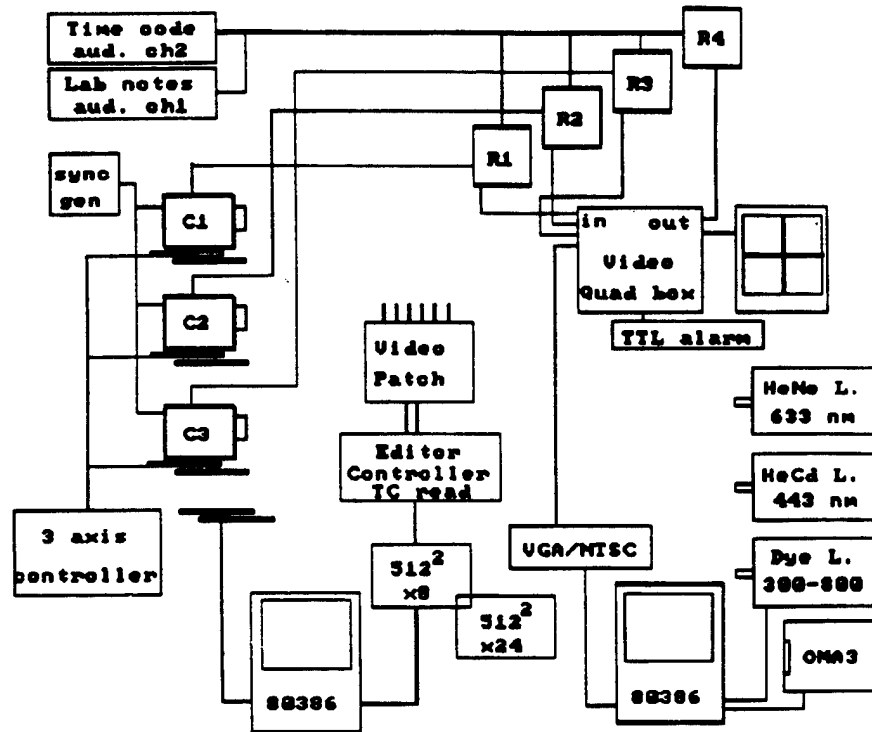
Figure 5. MAPPER video systems. The system allows the real-time integration of four video sources onto one video tape (Recorder R4) for subsequent analysis. Three of the inputs are from cameras C1, C2, C3 and 1 from the microcomputer output of an Optical Multi-channel Analyser III (OMA3). The original high-resolution video is timecoded and recorded on recorders R1, R2, R3. These recorders act as video sources for the reduction of field data. Another microcomputer digitizes images and controls a micropositioner. GaAlAs diode, HeNe, HeCd and a gateable Dye laser illumination are available.

4.1. Pattern recognition

The inevitable artificially intelligent AUV of the future will require that particle imagery be reduced in near real-time for selective particle capture to be efficiently implemented. Due to the diversity which marine particles exhibit, the image analysis approach must quickly provide a high degree of information. One method that we have been investigating follows.

To describe the distribution of radiance from a particle within an x - y field (i.e. an image), we utilize the method of moment invariants. The two-dimensional (i + j)th order moments of a density distribution function $\rho(x,y)$ are defined in terms of Riemann integrals (proper, bounded) as[23]

$$m_{ij} = \int_{-\infty}^{\infty} \int_{-\infty}^{\infty} x^i y^j \rho(x,y) \, dxdy \qquad i,j = 1,2,3... \qquad (2)$$

The low-order ordinary moments are especially useful to the extent that m_{10}/m_{00}, m_{01}/m_{00} locate the (x, y) coordinate position for the centroid of the image intensity distribution. Sequential centroid locations, then, can be used in a first-order classification scheme for particles since inanimate particle centroid trajectories would follow the gravitational vector at a constant velocity (settling) relative to water motion, while animated particles could demonstate non-nadir and/or accelerated velocities (swimming).

For this approach to be useful in pattern recognition strategies, however, the sample-space vectors generated must be invariant with object position and/or orientation within the image field. Translational invariance can be achieved by the determination of object centroid (from the first and zero order ordinary moments) and then the ordinary moments can be recalculated with the origin of the coordinate field coincident with the object image centroid. This first step toward both translational and rotational invariance, however, can be achieved (and computational time minimized) by transforming the ordinary moments (m_{ij}) into central moments (μ_{ij}), moments relative to the centroid of the object image. Using the notation of Hu[23]:

$$\mu_{00} = m_{00} = \mu \qquad (3)$$

$$\mu_{10} = \mu_{01} = 0 \qquad (4)$$

$$\mu_{20} = m_{20} - \mu\bar{x}^2 \qquad (5)$$

$$\mu_{11} = m_{11} - \mu\bar{x}\bar{y} \qquad (6)$$

$$\mu_{02} = m_{02} - \mu\bar{y}^2 \qquad (7)$$

$$\mu_{30} = m_{30} - 3m_{20}\bar{x} + 2\mu\bar{x}^3 \qquad (8)$$

$$\mu_{21} = m_{21} - m_{20}\bar{y} - 2m_{11}\bar{x} + 2\mu\bar{x}^2\bar{y} \qquad (9)$$

$$\mu_{12} = m_{12} - m_{02}\bar{x} - 2m_{11}\bar{y} + 2\mu\bar{x}\bar{y}^2 \qquad (10)$$

$$\mu_{03} = m_{03} - 3m_{02}\bar{y} + 2\mu\bar{y}^3 \qquad (11)$$

where $\bar{x} = m_{10}/m_{00}$, $\bar{y} = m_{01}/m_{00}$.

It is notable that the first-order central moments μ_{10}, μ_{01} are equal to zero under this tranformation. This follows intuitively since the first order "spread" of an object relative to any axis of a coordinate system drawn through its centroid would center about the origin.

These central moments can then be utilized to produce moment functions which possess the desired invariance with rotation and translation. Seven such functions were first formulated by Hu[23] and are presented here following the form of Dudani et al.[24]:

$$M_1 = (\mu_{20} + \mu_{02}) \qquad (12)$$

$$M_2 = (\mu_{20} - \mu_{02})^2 + 4\mu_{11}^2 \qquad (13)$$

$$M_3 = (\mu_{30} - 3\mu_{12})^2 + (3\mu_{21} - \mu_{03})^2 \qquad (14)$$

$$M_4 = (\mu_{30} + \mu_{12})^2 + (\mu_{21} + \mu_{03})^2 \qquad (15)$$

$$M_5 = (\mu_{30} - 3\mu_{12})(\mu_{30} + \mu_{12})$$

$$\cdot [(\mu_{30} + \mu_{12})^2 - 3(\mu_{21} + \mu_{03})^2]$$

$$+ (3\mu_{21} - \mu_{03})(\mu_{21} + \mu_{03})$$

$$\cdot [3(\mu_{30} + \mu_{12})^2 - (\mu_{21} + \mu_{03})^2] \tag{16}$$

$$M_6 = (\mu_{20} - \mu_{02})[(\mu_{30} + \mu_{12})^2 - (\mu_{21} + \mu_{03})^2]$$

$$+ 4\mu_{11}(\mu_{30} + \mu_{12})(\mu_{21} + \mu_{03}) \tag{17}$$

$$M_7 = (3\mu_{21} - \mu_{03})(\mu_{30} + \mu_{12})$$

$$\cdot [(\mu_3 + \mu_{12})^2 - 3(\mu_{21} + \mu_{03})^2]$$

$$- (\mu_{30} - 3\mu_{12})(\mu_{21} + \mu_{03})$$

$$\cdot [3(\mu_{30} - \mu_{12})^2 - (\mu_{21} + \mu_{03})^2] \tag{18}$$

It is interesting to note that M_7 is a psuedo-invariant function which undergoes a sign change under reflection and, hence, would be useful for recognition of a mirror-image of a cataloged pattern. M_7 would recognize the "front or back" of a cataloged pattern and would also be useful for recognition of spatial features such as a right-hand versus a left-hand spiral structure.

Size invariance is more subtle, however, since for the purposes of estimating particle volume, the knowledge of the discrete size of a target particle is not only desirable but necessary. With discrete size and settling speed information particle dynamic density can be calculated through the inversion of the appropriate (shape dependent) Stoke's settling equation. Since the sample space will necessarily be 3 dimensional, however, the apparent size (solid angle) of an object will change with a change in position along the axis between the particle and the sensor (optical axis). What is required is "apparent size" invariance, with retention of discrete size information.

The desired "apparent size" invariance can be effected, however, by normalizing M_1 through M_7 in the manner proposed by Dudani[24]. Here, the radius of gyration of an object is defined as:

$$r = (\mu_{20} + \mu_{02})^{1/2} \tag{19}$$

and
$$r \cdot B = \text{constant} \tag{20}$$

(where μ_{20} and μ_{02} are second order central moments and B is the axial distance of the object from the sensor) since the radius of gyration of an object would be directly porportional to the mean image diameter and inversely porportional to the distance of the object along the optical axis. Then:

$$M_1' = (\mu_{20} + \mu_{02})^{1/2} \cdot B = r \cdot B \tag{21}$$

$$M_2' = M_2/r^4 \tag{22}$$

$$M_3' = M_3/r^6 \tag{23}$$

$$M_4' = M_4/r^6 \tag{24}$$

$$M_5' = M5/r^{12} \tag{25}$$

$$M_6' = M_6/r^8 \tag{26}$$

$$M_7' = M_7/r^{12} \tag{27}$$

Although M_2' through M_7' are now independent of object distance, this normalization method requires a priori knowledge of B for the utilization of M_1'. In our deployment configuration B will be the focal length of the imaging system, and hence will be known.

The rotational, translational, and size invariance of the computer code generated to implement equations 2-27 was tested by the analysis of a computer-generated binary "object", alphanumeric characters, and the images of marine animals and aggregates recorded in situ in a sediment trap in the subtropical North-central Pacific were analyzed. The methodology used in recording the images is discussed in Costello et al.[18]. A discussion of the various tests are presented in Carder and Costello[25] In order to "classify" these images, the pattern recognition algorithm must generate classification parameters (feature vectors) which are similar on an intragroup and dissimilar on an intergroup basis. Twelve factors each are available by operating on the target silhouette (low frequency information), target outline (high frequency information), and the full 8-bit image of the target which includes a contribution from any interior structure. The twelve factors are as follows: the zero order central moment (image power); the seven normalized Invariant Moment Functions (equations 21 through 27) as first formulated by Hu[23] with the size normalization as proposed by Dudani[24]; and the following four moment-generated elliptical classification factors as developed by Teague[26].

$$\alpha = ((\mu_{20} + \mu_{02} + ((\mu_{20} - \mu_{02})^2 + 4\mu_{11}^2)^{1/2})2/\mu_{00})^{1/2} \tag{28}$$

$$\zeta = ((\mu_{20} + \mu_{02} - ((\mu_{20} - \mu_{02})^2 + 4\mu_{11}^2)^{1/2})2/\mu_{00})^{1/2} \tag{29}$$

$$\Gamma = (1/2)\tan^{-1}(2\mu_{11}(\mu_{20} - \mu_{02})^{-1}) \tag{30}$$

$$F = \mu_{00}/\pi\alpha\zeta \tag{31}$$

These factors characterize any image as a constant intensity ellipse with intensity F inside and zero outside, defined major axis α, minor axis ζ, and angular orientation Γ within the 2-dimensional coordinate field. The method is also computationally attractive since it requires the computation of moments to only second order.

To our knowledge this approach to the combination of shape recognition factors is unique in that it utilizes highly shape-discriminate factors (the moment invariant functions) as well as factors which emphasize general shape and optical image power (the elliptical factors). Although further work with additional in situ images is required, it appears that the method can adequately address the shape-diverse and the shape-amorphous nature of marine particles. Because of the computationally intensive nature of machine vision and pattern recognition, further work with additional in situ images is also required for the determination of the value and utility of the information content specific to each of the 36 available classification dimensions. However, the method has proven invariant to target translation, rotation, and "apparent" size and has successfully classified (separated) computer generated test patterns, alphanumeric characters, and images of marine particles acquired in situ. Further, image power can be related to $\beta(90°)$, image size can be used to determine the large-particle ends of size distributions, and size and shape can be used to estimate c values for comparison with c-meter perturbations.

5. SUMMARY

One of the research areas which requires further exploration in the effort toward marine optical model closure and inversion is the effect of large particles on the underwater light field. The temporally and spatially variable concentration (and, hence, optical effect) of large particles demands an understanding of not only the size and number but also the optical nature of the individual particles. The macroscopic size of the particles allows their study on an individual basis once they are located and imaged. This requires the development of new, large-volume, in situ instrumentation to augment traditional small-particle methods. The large volume of data required to understand the temporal and spatial distributions of various particle classes demands an automated classification and analysis method.

We are developing a new instrument, MAPPER, to enumerate and image individual particles at rapid sampling rates (on the order of hundreds of liters per minute). The instrument employs diode laser illumination (675 nm) with line-generator optics to produce a thin light sheet at the system focal plane. This light sheet and narrow-band, optical filters are utilized to minimize noise associated with diffuse ambient illumination since significant red ambient illumination is lost below 5 m depth. It also removes the uncertainty involved in the determination of the 3-dimensional position and size of a target in a 2-dimensional image. An additional problem inherent in marine particle research is that the size of the particles of interest ranges over several orders of magnitude (micrometers to centimeters diameter). The instrument addresses this problem of scale with coincident video imaging systems of high and low spatial resolution.

To address the large quantity of imagery expected, a classification and analysis scheme based on the method of moment invariants has been developed and presented. Any pattern recognition/classification method is most effective when the particles under analysis exhibit a high degree of intraclass similarity and interclass diversity. However, some types of marine particles (eg. marine snow and other aggregates) would be generally amorphous to traditional classification schemes. A variation of the method[26] has also been incorporated which will have utility in the study of these generally amorphous types of particles. The utility of this approach for the classification of aggregated particles lies in the retention of the ability to discriminate between the dominate aggregate shapes (chain, comet, elliptical, spherical, etc.) with the quantification of individual particle or sidescattering. Since remote sensing reflectance R_{rs} is highly backscattering-dependent, and the backscattering and sidescattering coefficients are similar[27], MAPPER data will enhance the interpretation of R_{rs}. This information, when combined with large-particle classification and enumeration constitutes a requisite step toward optical model closure and inversion for a significant part of the world ocean.

6. Aknowledgements

REFERENCES CITED

1. Gordon, H.R., D.K. Clark, J.W. Brown, O.B. Brown, R.H. Evans, and W.W. Broenkow (1983) Phytoplankton pigment concentration in the Middle Atlantic Bight: Comparison of ship determinations and CZCS estimates. Appl. Opt. 22: 20-36.

2. Gordon, H.R. (1979) Diffuse reflectance of the ocean: The theory of its augmentation by chlorophyll a fluorescence at 685 nm. Appl. Opt. 18. 1161-1166.

3. Carder, K.L., and R.G. Steward (1985) A remote sensing reflectance model of a red tide dinoflagellate off West Florida. Limnol. Oceanogr. 30(2): 286-298.

4. Mitchell, B.G. and D.A. Kiefer (1988) Variability in pigment specific fluorescence and absorption spectra in the northeastern Pacific Ocean. Deep-Sea Res. 35. 665-689.

5. Spitzer, D. and R.W.J. Dirks (1985) Contamination of the reflectance of natural waters by solar-induced fluorescence of dissolved organic matter. Appl. Opt. 24(4): 444-445.

6. Hawes, S.K., and K.L. Carder (1990) Fluorescence quantum yields of marine humic and fulvic acids: application for in situ determination. EOS 71(2): 136.

7. Marhall, B.R., and R.C. Smith (1990) Raman scattering and in-water ocean optical properties. Appl. Opt. 29(1): 71-84.

8. Stavn, R.H. (1990) Raman scattering effects at the shorter visible wavelengths in clear ocean waters. Ocean Optics XI SPIE 1302.

9. Peacock, T.G., K.L. Carder, C.O. Davis , and R.G. Steward (1990) Effects of fluorescence and water Raman scattering on models of remote sensing reflectance. Ocean Optics XI SPIE

10. Preisendorfer, R.W. (1961) Application of radiative transfer theory to light measurements in the sea, UGGI Monogr. no.10 (Symp. on Radiant Energy in the Sea), 11-30.

11. Betzer, P. R., K. L. Carder, R. A. Duce, J. T. Merrill, N. W. Tindale, M. Uematsu, D. K. Costello, R. W. Young, R. A. Feely, J. A. Breland, R. E. Bernstein and A. M. Greco (1988) Long-range transport of giant mineral aerosol particles. Nature, 336, 54-56.

12. Sheldon, R.W., A. Prakash, and W.H. Sutcliffe, Jr. (1972) The size distribution of particles in the ocean. Limnol. Oceanogr. 27(3). 327-340.

13. Van de Hulst, H. C. (1957) Light Scattering by Small Particles. John Wiley, New York.

14. Alldredge, A. L. and M. W. Silver (1988) Characteristics, dynamics and significance of marine snow. Progress in Oceanography, 20, 41-82.

15. Greenberg, J.M., R.T. Wang, and L. Bangs (1971) Extinction by rough particles and the use of Mie theory. Nature Phys. Sci. 230. 110-112.

16. Zerull, R.H. and K. Weiss (1974) Scattering properties of irregular dielectric and absorbing particles, in Atmospheric Aerosols: Their Optical Properties and Effect. Optical Society of America.

17. Carder, K. L., D. K. Costello, and R. G. Steward (1986) State of the art instrumentation for measuring ocean aggregates. Aggregate Dynamics in the Sea Workshop Report. E. Hartwig and A. Alldregde, editors, Office of Naval Research, Asilomar, Pacific Grove, Ca. 131-181.

18. Costello, D. K., K. L. Carder, P. R. Betzer, and R.W. Young (1989) In-situ holographic imaging of settling particles: Applications for Individual Particle Dynamics and Oceanic Flux Measurements. Deep-Sea Res, 36, 1595-1605.

19. Hamner, W., E. Kristof, and A. Chandler (1987) 3-D video and computer analysis of fish schooling. IEEE Oceans 87 Proceedings, 3. 1232-1233.

20. Honjo, S., K.W. Doherty, Y.C. Agrawal, and V. Asper (1984) Direct optical assessment of large amorphous aggregates (marine snow) in the deep oceans. Deep-Sea Res. 31, 67-76.

21. Asper, V. L. (1987) Measuring the flux and sinking speed of marine snow aggregates. Deep-Sea Research, 34, 1-17.

22. Optics Guide 5, Melles Griot, Irvine, CA. 20-11.

23. Hu, M. (1962) Visual Pattern Recognition by Moment Invariants. IRE Trans. Inf. Theory, IT-8, 179.

24. Dudani, S.A., K.A. Breeding, and R.B. McGee. (1977) Aircraft identification by moment invariants. IEEE Trans. Comput. C-26, 39-45.

25. Carder, K. L. and D. K. Costello, Optical effects of Large Particles. Ocean Optics. K.L. Carder, M.J. Perry, and R.W. Spinrad, editors, Oxford University Press, New York, N.Y. In press.

26. Teague, M.R. (1980) Image analysis via the the general theory of moments. J. Opt. Soc. Am., v. 70, n. 8.

27. Petzold, T.J. (1972) Volume scattering functions for selected ocean waters. SIO Ref. 72-78.

INSTRUMENTS AND METHODS

In situ holographic imaging of settling particles: applications for individual particle dynamics and oceanic flux measurements

D. K. Costello,* K. L. Carder,* P. R. Betzer* and R. W. Young*

Abstract—A new dual-axis holographic imaging system provides a means for estimating *in situ* the sizes, shapes, settling rates and densities of both individual particles and aggregates. The optical system, which is an integral part of a free-drifting sediment trap (collection area = 0.66 m^2), utilizes two independent imaging systems with HeNe laser illumination to record holographically the particles moving through the collection cup from two orthogonal perspectives. Mass accumulation is monitered in all cups by the upward-looking holographic imaging system and sequential imaging of particles using the horizontal system provides settling speed determinations. The configuration is flexible and can be programmed to collect as many as 500 far-field (Fraunhoffer) holographic records (250 for each axis). In addition, up to six sequential samples of particulate matter can be collected over periods ranging from as little as 3 h (30 min per sample) to as long as 6 days (1 day per sample). An isotonic high-viscosity medium (viscosity = 5.2 cp, density = 1.12 g ml^{-1}) has been utilized in some sample cups to discriminate against organic material and to maximize the probability that large particles are slowed sufficiently to allow for sequential holographic imaging.

Four free-drifting, holographically equipped sediment traps have been utilized on three cruises to the North Pacific Ocean where repeated deployments were made between 37 and 907 m. While analysis of the more than 4000 holograms is incomplete, the holographically determined dynamic densities for individual particles include high-density material of eolian origin (density $\cong$ 2.6 – 5.2 g ml^{-1}) and also lower density organic material (density $\cong$ 1.12 – 1.21 g ml^{-1}). Such optically enhanced sediment traps provide a means of directly recording particle settling dynamics and may also provide insight into biological activity within sediment traps.

INTRODUCTION

The importance of understanding the dynamics of particles within the oceans and their effect on biochemical processes is described by Fowler and Knauer (1986), Alldredge and Silver (1988), Betzer *et al.* (1988) and Karl *et al.* (1984). The accurate measurement of the nature and flux of particles within the ocean, however, is made complex by a myriad of diverse particle sources and sinks and, most importantly, by transformations (e.g. aggregation, disaggregation, repackaging and dissolution) which change particle shapes, alter chemical reaction rates and also modify settling characteristics.

Although natural processes continuously modify oceanic particulate materials, additional transformations are introduced by sampling techniques. That is, most methods of

*Department of Marine Science, University of South Florida, 140 Seventh Avenue South, St. Petersburg, FL 33701, U.S.A.

collecting particles involve their capture in either water bottles, in sediment traps or by *in situ* pumping. All of these approaches can disrupt friable aggregates, provide increased opportunities for aggregate formation, and/or lead to dissolution of soluble materials such as celestite, aragonite, calcite, etc. All of the above distort particle size distributions and result in inaccurate estimates of water column residence times. Further, dissolution of labile phases also can affect our understanding of chemical cycling in the ocean (BETZER *et al.*, 1984a; BYRNE *et al.*, 1984; BERNSTEIN *et al.*, 1987). Finally, organisms can actively enter (swim into) the collection cups of sediment traps where they can contribute to the estimated downward flux of material and also modify the composition and size distribution of collected material (HONJO *et al.*, 1982; HARBISON and GILMER, 1986). Thus the development of accurate particle dynamics/particle transformation models for the ocean is a major challenge and is related in large part to the development of methods that can, with minimal disruption, assess particle characteristics *in situ*.

To date, optical methods that measure particles freely in the water (e.g. JOHNSON and WANGERSKY, 1985) or within settling tubes or sediment traps that attempt to minimize the fluid flow relative to the measurement system (e.g. ASPER, 1987; CARDER *et al.*, 1982, 1986b) seem to have the fewest inherent disadvantages. The latter approaches provide a measure of particle settling speed as well as images of individual particles, while the first method yields particle images and/or scattering characteristics. Also, fluid flow relative to the trap further constrains the type of trapping system that could successfully provide accurate measures of friable materials (BUTMAN, 1986).

While *in situ* optical methods provide some obvious advantages, most use a fractional magnification factor ($\ll 1.0$) to increase the depth of field (CARDER *et al.*, 1986a). This approach may be adequate for large particles (e.g. diameter >100 µm), but in the case of the more abundant smaller particles, it is much more limiting. The increased magnification required to image the finer particle fraction reduces the depth of field to a very narrow range and thus decreases the probability that a particle of interest will be in focus. Holographic methods, however, have a large depth of field (THOMPSON *et al.*, 1967) and provide a means of simultaneously recording the precise location and size of particles in an illuminated volume. Further, with appropriately timed sequential holograms, one not only can determine individual particle settling velocity, but also (by optimizing programmable system functions) observe other phenomena such as dissolution or particle–particle interactions.

This paper provides documentation of the design and initial performance of a holographic imaging system developed to study the flux and fate of atmospherically delivered material in the upper kilometer of the Pacific Ocean.

SYSTEM OVERVIEW

The systems described here were deployed on three cruises at a study site in the subtropical North Pacific gyre (26°N; 155°W). Due to the paucity of eolian particles, a two-axis imaging system (horizontal and vertical views) was augmented with a cone-shaped concentrator (described by BETZER *et al.*, 1984b). The cone has a relatively large cross-sectional collection area (0.66 m²) and a frustrum angle of 15°. This conical concentrator (cone collection area/area of entrance to sample cup = 830), along with a six-cup sample system, provided for the collection of discrete samples for chemical and mineral analysis over variable collection periods.

From an optical perspective, a cone provides a means of concentrating mineral particles so that a relatively small volume (7 cm^3) can be monitored holographically to record particle fluxes, settling rates and individual densities. In our optically enhanced trapping system, the bottom of each collection cup also serves as the optical window for the vertically oriented holographic imaging system. In order to avoid excessive occlusion of these optical windows by the accumulated sample, cup exchange in the multiple-cup sampling system can be programmed from as short as 30 min to as long as 24 h.

Details of the optical/mechanical systems integral to the laser-equipped, free-drifting sediment trap are reported by COSTELLO (1988). Briefly, the traps approach 3 m in height, weigh 350 kg and are 110 kg negatively buoyant in seawater (Fig. 1). The optical and sample cup systems are rigidly attached to the fiberglass concentrator cone and form an assembly which "floats" within a stainless steel reinforced, polyvinyl chloride (PVC) exoskeleton.

The controller/timer system, a hybrid electronic unit, utilizes cascaded 556 IC timer chips. Time between exposures in both the vertical and the horizontal imaging systems is independently programmable from as short as 15 s to as long as 28.8 min. Therefore, the entire holographic image record for each axis (250 exposures per axis) can cover a period as short as 1.1 h to as long as 5 days. The residence time for each individual sample cup is also programmable anywhere from 0.5 h to 1 day. Thus the total collection period for the six-cup system is essentially continuously variable from 3 h to 6 days. While this system provides only a short-term record of the particle suites moving through the ocean, the "snap shots" are made on time scales appropriate for the study of processes that influence particle fluxes in the ocean system, such as primary production, dissolution, diel migration, air–sea interactions, atmospheric input events and benthic storms. To prevent either sample contamination or loss, each cup is sealed prior to and after its individual collection period. System activation also can be programmed to be delayed from 0 to 24 h, which provides for flushing during descent to deployment depth with an open cone (no cup in receiving position) and allows system equilibration with the deployment environment before sampling begins.

The usual deployment strategy is to program the horizontal imaging system to record a hologram of the sample volume every minute (optimized to record multiple sequential images of settling particles in the first cup) with the vertical system synchronized to fire every sixth horizontal frame (optimized to observe mass accumulation for the duration of a six-cup, 24 h deployment). Once sampling is initiated, particles that enter the first sample cup encounter an isotonic, high viscosity aqueous medium. This 6% dextran in 24% sucrose solution with 2% formalin has a density of 1.12 g ml^{-1} and a viscosity of 5.2 cp at 20°C, which slows mineral particle velocities about six-fold. The reduction in settling velocity aids in meeting the holographic stability requirement for particle motion during the exposure period (particle movement <0.1 particle diameter per period: THOMPSON *et al.*, 1967) and improves the opportunity to secure multiple sequential views of a particle by the horizontal imaging system. It also insures that most particles of interest ($d < 150$ µm for a particle density of 2.65 g ml^{-1}) meet the low Reynolds number requirement (Re < 0.1) to allow the direct application of Stokes' equations (LERMAN, 1979). In addition, the density of the medium prevents light organic material from settling into the cup. [For comparison the density gradient utilized in the VERTEX studies is a NaCl solution with a density of 1.07 g ml^{-1} (KNAUER *et al.* 1979).] Also, if a swimmer enters the sample cup, it entrains the lower density (and, hence, lower index of
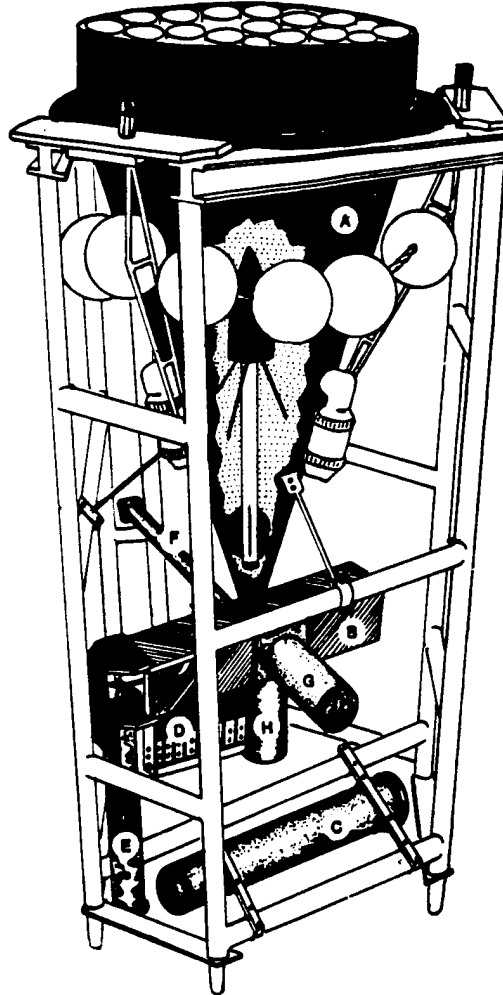
Fig. 1. Schematic of a sediment trap equipped with horizontal and vertical axis holographic camera systems. At the apex of the inverted conical concentrator (A) is the six-cup viewing and sampling assembly (B). The timer/battery pack (C) controls the timing sequence of cups, laser on/off cycles, and camera firing. Motive force for advancing the cup assembly through sequentially fired registration pins (D) is provided by a lead weight in the long acrylic tube (E) vertically attached to the trap frame. The horizontal laser housing (F), horizontal camera housing (G), and the vertical camera housing (H) are shown. The vertical laser housing assembly is shown in the cutaway cone section.

refraction) seawater into the sample cup medium (CARDER *et al.*, 1986a). The resulting "density trails" are readily observed holographically and indicate that particle dynamics calculations are inappropriate at that time. Also indicative of swimming effects are particle acceleration and/or non-vertical particle trajectories.

In order to allow organic material (specifically fecal pellets and aggregates) to reach the cup bottom where mass accumulation was recorded by the vertical imaging system, the remaining five sample cups were filled with a high salinity (45 ppt; $\rho = 1.03 \text{ g ml}^{-1}$)

media with 2% formalin. Holographic records (discussed later) graphically show that the 45 ppt poisoned seawater did not deter organisms from moving through these cups.

HOLOGRAPHIC SYSTEMS

A schematic of the holographic imaging system utilized in the laser-equipped traps is shown in Fig. 2. The 1.0 mm diameter HeNe laser beam is focused through a spatial filter, expanded and collimated to 1.4 cm diameter. The beam then passes through the sample volume where any particles present scatter the beam and contribute to the diffraction field. The intensity distribution is then magnified ($\times$ 2.83) and then recorded on high speed, 35 mm Kodak So-253 holographic film.

The horizontal imaging system was designed to provide accurate particle settling speeds as well as particle size and shape characteristics. Assuming that a given particle is recorded on two successive holograms made 1 min apart and utilizing the diameter of the HeNe laser beam (1.4 cm), settling speeds of up to 0.023 cm s^{-1} in the viscous medium (5.2 cp) can be measured. This is equivalent to 0.12 cm s^{-1} in seawater, or the fall velocity of a 38 μm diameter quartz sphere. If, however, we use the shortest programm-
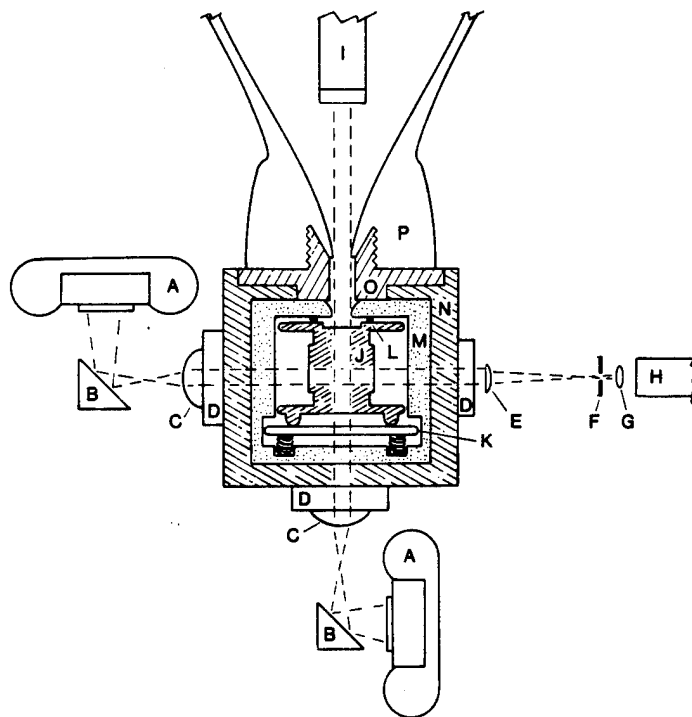
Fig. 2. Schematic drawing for holographic imaging systems and sample cup assembly. Pressure housings are removed for clarity. Drawing not to scale. Components include: A, lenseless 35 mm camera with 250 exposure filmback; B, front-surface mirror; C, plano-convex lens; D, fused quartz window; E, plano-convex lens; F, 50 μm pinhole; G, aspheric lens; H, horizontal HeNe laser; I, vertical HeNe laser with optics as in horizontal system; J, sample cup assembly (cross-section); K, spring-loaded plate; L, O-ring seals; M, transition box; N, exterior (fixed) box; O, mounting flange; P, conical concentrator.

able time between exposures (15 s), the fall velocity for a quartz sphere of 76 μm diameter can be recorded. Obviously, much larger materials can be recorded successfully on sequential holograms if their settling rates are less than the figures cited above.

The optical object plane in both the vertical and the horizontal systems is positioned directly interior to the sample window. This provides a means of rapidly assessing mass accumulation rates on the bottom of each cup at sea. That is, the film from the vertical system can be developed and examined, without holographic reconstruction, within an hour of system retrieval. Of course, in the absence of excessive field aberration from the accumulated material, holographic recording of particles higher in the vertical beam also occurs and their images subsequently can be reconstructed holographically.

The holographic systems were designed to record 12 μm diameter or larger SiO_2 spherical particles located at the far wall of the sample volume (128 mm from the camera port). In the Fraunhoffer regime, zeros of the particle scattering intensity distribution pattern occur at $z = 3.832, 7.016, 10.173...$ (VAN DE HULST, 1957). In this case, $z = \pi r \phi / \lambda$, where r is particle radius, λ is illumination wavelength in the medium, and ϕ is the angle (radians) off the axis of light propagation. Assuming a minimum of three rings as a requirement for adequate holographic reconstruction, z equals 10.173 (corresponding to the third intensity minimum or third dark ring in the diffraction pattern) and the resulting scattering angle ϕ for a 12 μm diameter particle is 0.17 radians. This angle is accomodated by an aperture of at least 44 mm diameter at the camera port some 128 mm from the particle. The camera port apertures are 47 mm diameter and, since the angle of propagation of the diffraction field is inversely related to particle radius, are also able to gather adequate diffraction field information for particles that are larger and/or closer.

The holographic reconstruction system is outlined in Fig. 3. A spatially filtered/ expanded/collimated HeNe laser beam illuminates the holographic transparency and, in order to reverse lens aberrations, the diffracted pattern continues through the same 47 mm diameter plano-convex lens (with orientation reversed) used in hologram con-
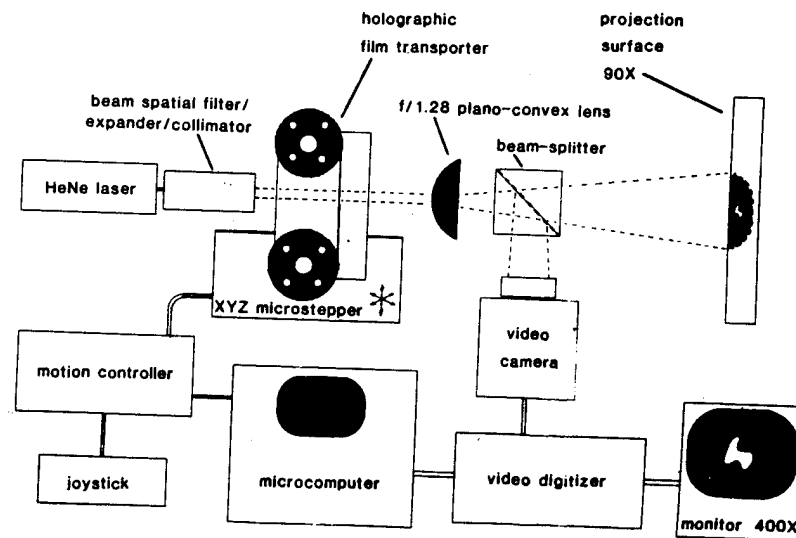
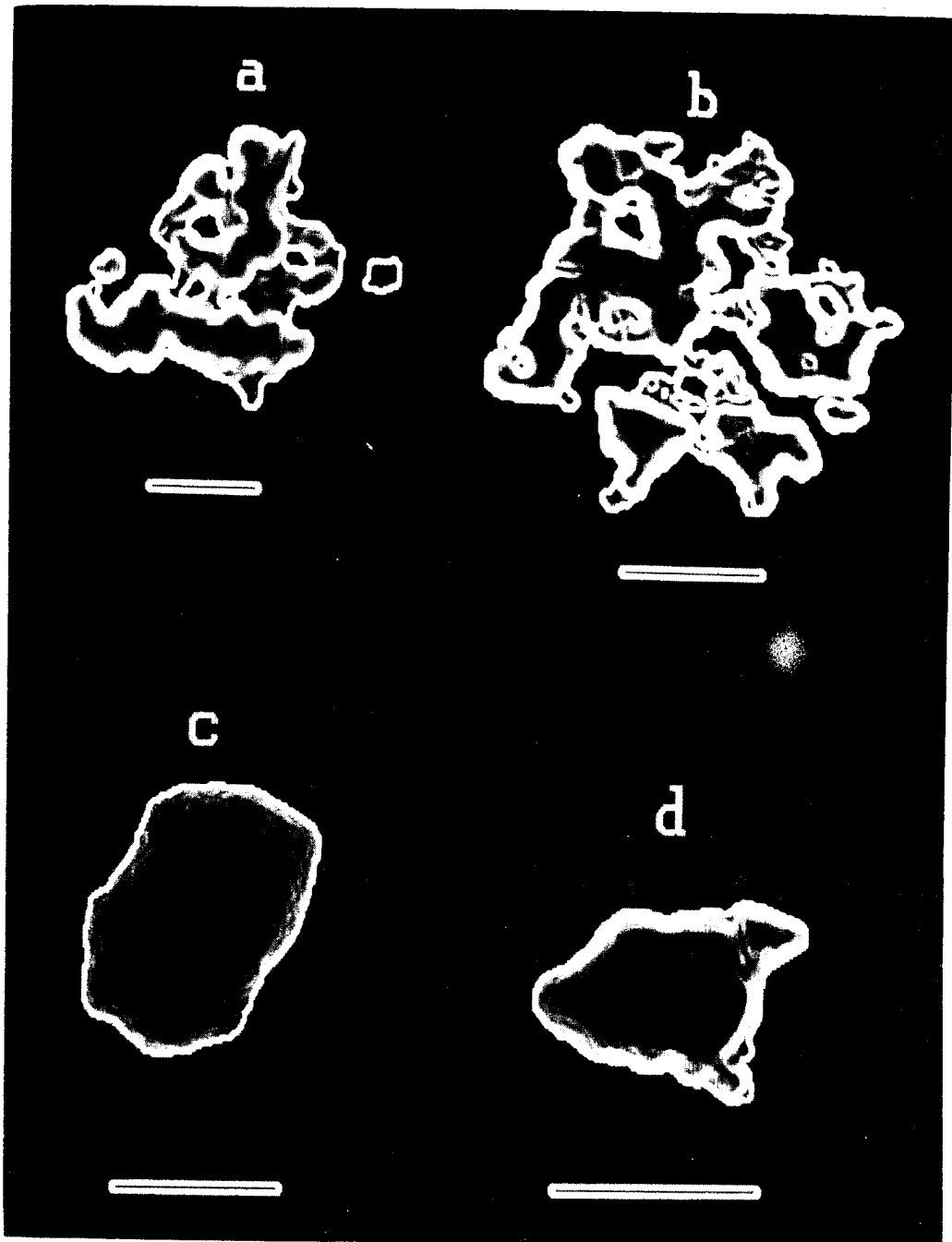Fig. 3. Holographic image reconstruction system.

Fig. 4. Photographs of digitally processed images of holographically reconstructed particles. The size bar in each image represents 20 μm. (a, b) Aggregates with dynamic density of 1.12 g ml^{-1}. (c) Quartz: 2.61 g ml^{-1}. (d) Heavy mineral: 5.1 g ml^{-1}
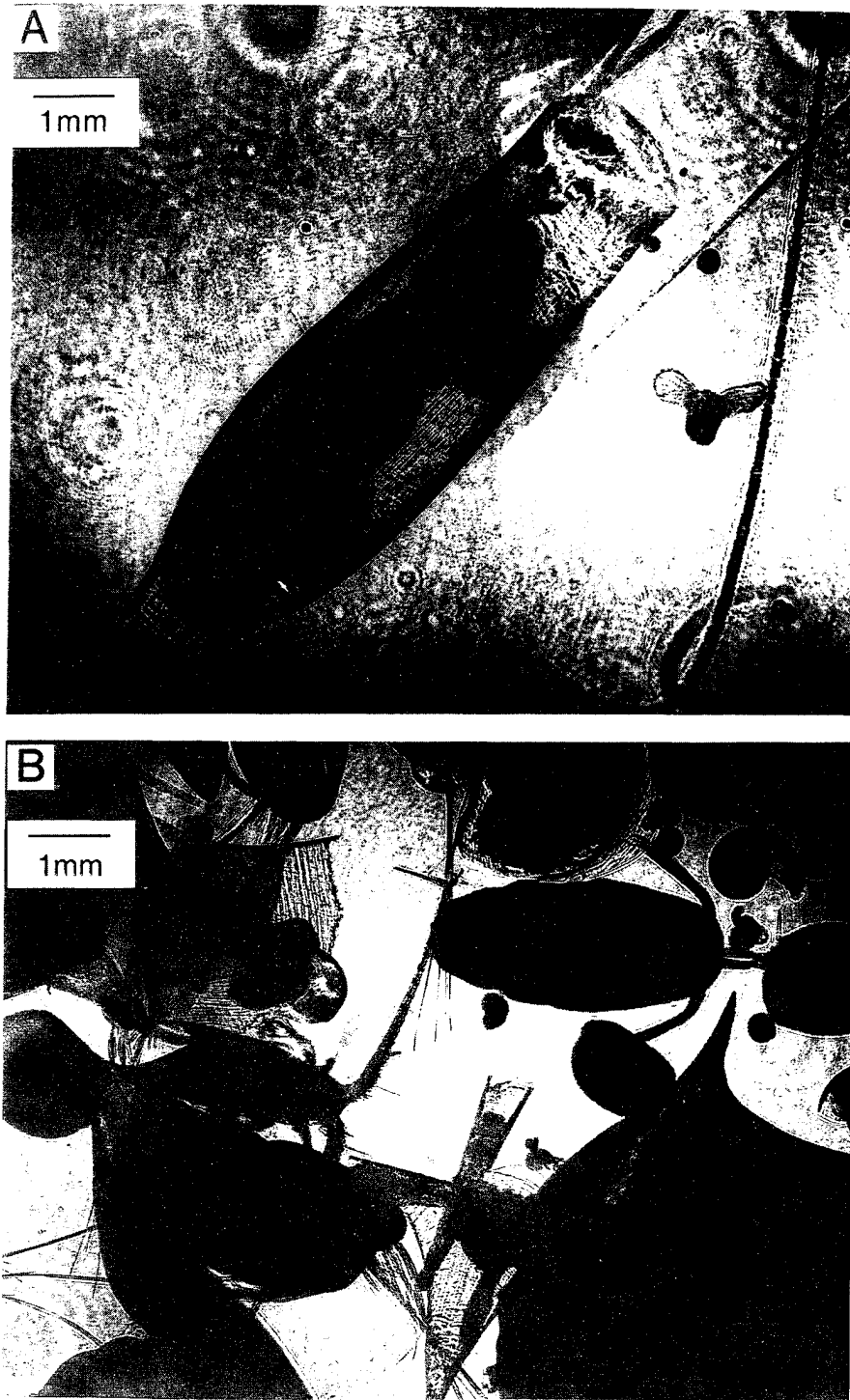
Fig. 5. Photographic prints made from holographic negatives recorded, respectively, at 1630 h on 10 April 1987 (A) and 0325 h on 11 April 1987 (B) at 37 m depth in the North Pacific Ocean. The printing process utilized the object image plane of the vertical holographic imaging system. Concentric diffraction rings which are particularly apparent in (A) result from settling particles which have yet to reach the bottom of the sampler (focal plane). The large pteropod in (A) is *Cuvierina columnella*, the smaller a swimming *Limacina* species. There are pteropods, heteropods, and copepods in (B). The pteropods include *Clio pyramidata*, *Limacina* species and a juvenile *Diacria trispinosa*. The heteropods are *Atlantid* species. In both (A) and (B) growth striations are clearly evident on the pteropod shells.

struction. The detailed methodology and equations for specifying the position and size of each particle in the reconstruction process are reported elsewhere (COSTELLO, 1988).

PERFORMANCE AND DISCUSSION

The laser traps developed for sampling eolian material in the water column have been utilized on 28 deployments to a maximum depth of 907 m on three cruises in the North Pacific Ocean to: (1) collect multiple physical samples of particulate material settling through the upper kilometer; and (2) holographically record *in situ* images and settling velocities of oceanic particles. The size and shape information present in sequential images provides a means of applying the appropriate (shape-dependent) Stokes' settling equation to estimate the dynamic densities of particles (LERMAN, 1979). The use of a viscous fluid in the sample cup extends, by a factor of six, the valid range (due to Reynolds number limitations) of mineral particle settling velocities to which Stokes' settling equations can be applied.

In more conventional forms of microscopy, the very shallow depth of field associated with high magnification places a severe constraint on the detection of particle edges. Although this constraint is relaxed through holographic microscopy, there is a substantial amount of holographic noise (laser speckle and diffraction rings from other particles) inherent in the image which itself constrains precise edge detection during image reconstruction. By capturing the holographic images in a computer video frame buffer, it is possible to perform operations in the digital domain which suppress noise and enhance particle edges. However, well-known edge detection filters (e.g. Robert's cross-operator, Sobel operator, and the Laplacian convolution) are very sensitive to the high-contrast noise inherent in a holographic image (laser speckle) since they utilize only locally limited information (an $N \times N$ pixel neighborhood, for example, with N typically ranging from 2 to 7). Image noise can be reduced through the averaging and/or differencing of multiple image fields, pixel averaging (median filter) within an image field, or the application of intensity weighting functions (determined by parameters from the image intensity histogram) which suppress noise and maximize the probability that a particle edge will be enhanced (HAUSSMAN and LAUTERBORN, 1980). Once noise is suppressed, we have found that an efficient edge detection algorithm for our holographic images is to threshold the image at an intensity level indicated by the maximum intensity gradient between target and background. The threshold level is determined through a series of intensity profile transects through the particle. All pixels with intensity values below threshold level are then set to zero while any pixel above threshold level remains unchanged. Selected photographs of reconstructed holographic images of particles settling through the high viscosity medium which have been digitally processed are shown in Fig. 4 (horizontal imaging system). Image noise (e.g. laser speckle) was first reduced with a pixel averaging median filter operating within a 3×3 neighborhood and then thresholded as described above. A Sobel filter was then applied which enhances all intensity gradients. The nominal classification of particle type is based on dynamic density (as determined from particle settling speed and shape parameters) as well as particle appearance. Scanning electron microscopy coupled with energy-dispersive X-ray analysis (SEM/EDAX) confirms that the mineral particles collected fall into density categories consistent with those determined holographically for particles of similar size (e.g. CARDER *et al.*, 1986a).

The vertical imaging system, while holographically functional, is most useful for its enhanced depth of field near the photographic image plane which allows high resolution recording of mass accumulation in the sample cups. The system provides considerable flexibility as the sampling intervals for both the optical and the particle collection systems can be adjusted over wide ranges. This flexibility in the optical system allows the assessment of mass accumulation rates over extremely short time scales (i.e. minutes) within an hour of trap recovery. System flexibility also makes it possible to: (1) capture images of labile particles (i.e. acantharian skeletons/cysts, pteropods, etc.); (2) record the effects of particle–particle interactions; and (3) examine biological modifications of collected materials during the sampling process.

Examples of images acquired by the vertical imaging system of larger organisms are shown in Fig. 5. The images are photographic prints of holographic transparencies taken of sample cups with the 45 ppt seawater/2% formalin medium. These images were made by exploiting the placement of the optical object plane of the vertical imaging system (see earlier discussion). They provide a valuable arrival record for the collected organisms and some insight into biological activity in the sample cups. For example, the *Cuvierina columnella* (Fig. 5A), *Clio pyramidata* (Fig. 5B) and even the juvenile *Diacria trispinosa* (Fig. 5B) all have clearly discernable growth striations on their shells. Further, the *Limacina* sp. (Fig. 5A) had its "wings" extended and apparently was swimming about the 45 ppt poisoned environment of the collection cup while the sampling was in progress. This type of data is not provided by traditional trapping systems which are not optically enhanced. Given the importance of biological activity (production, predation, migration, etc.) and related sampling problems in the upper 200 m of the ocean, holographically equipped systems may provide an initial means of assessing the number and type of "swimmers" in sediment traps and the extent to which their feeding modifies collected material. Finally, despite the lower signal-to-noise ratio associated with imaging organic-rich material, the soft parts within the shell of several pteropods are clearly evident in Fig. 5A and B as are the extended wings of the *Limacina* sp. in Fig. 5A. Thus, studies of photographic sequences made with the vertical imaging system should provide some insights into biological involvement while sampling with sediment trap systems.

However, while our ability to capture holographic images *in situ* has been demonstrated and our ability to enhance image quality is evolving, there are several data reduction considerations that remain problematic. Foremost is the density of the visual information acquired by the system. For example, the 4000 holograms which were acquired on three cruises to the North Pacific Ocean contain on the order of 10^8 observable data planes. An ancillary consideration is the four-dimensional (3-space and time) nature of the data. This, combined with the rigorous optical/mechanical requirements for registration during holographic reconstruction, complicates particle identification and co-registration of orthigonal views. Finally, a biophysical difficulty associated with the reduction of holographic data is the relatively rapid eye strain (due to laser speckle) that results when one is searching a holographic projection of the sample space for particles. In an attempt to alleviate the above difficulties we are in the early stages of incorporating machine vision and pattern recognition logic into an automated image analysis system.

However, even though system complexity and the inordinately large volume of holographic data generated by the system present notable difficulties requiring further attention, the inherent optical advantages of holography can provide unambiguous

particle imagery *in situ*. Utilization (on widely programmable time scales) of this holographic capability will enhance efforts to understand both the production rates and fates of particulates in the oceanic system.

REFERENCES

ALLDREDGE A. L. and M. W. SILVER (1988) Characteristics, dynamics and significance of marine snow. *Progress in Oceanography*, **20**, 41–82.

ASPER V. L. (1987) Measuring the flux and sinking speed of marine snow aggregates. *Deep-Sea Research*, **34**, 1–17.

BERNSTEIN R. E., P. R. BETZER, R. A. FREELY, R. H. BYRNE, M. F. LAMB and A. F. MICHAELS (1987) Acantharian fluxes and strontium to chlorinity ratios in the north Pacific Ocean. *Science*, **237**, 1490–1494.

BETZER P. R., R. H. BYRNE, J. G. ACKER, R. R. JOLLEY and R. A. FEELY (1984a) The oceanic carbonate system: a reassessment of biogenic controls. *Science*, **226**, 1074–1077.

BETZER P. R., W. J. SHOWERS, E. A. LAWS, C. D. WINN, G. R. DITULLIO and P. M. KROOPNICK (1984b) Primary productivity and fluxes on a transect of the equator at 153°W in the Pacific Ocean. *Deep-Sea Research*, **31**, 1–11.

BETZER P. R., K. L. CARDER, R. A. DUCE, J. T. MERRILL, N. W. TINDALE, M. UEMATSU, D. K. COSTELLO, R. W. YOUNG, R. A. FEELY, J. A. BRELAND, R. E. BERNSTEIN and A. M. GRECO (1988) Long-range transport of giant mineral aerosol particles. *Nature*, **336**, 54–56.

BUTMAN C. A. (1986) Sediment trap biases in turbulent flows: Results from a laboratory flume study. *Journal of Marine Research*, **44**, 645–693.

BYRNE R. H., J. G. ACKER, P. R. BETZER, R. A. FEELY and M. H. CATES (1984) Water column dissolution of aragonite in the Pacific Ocean. *Nature*, **312**, 321–326.

CARDER K. L., R. G. STEWARD and P. R. BETZER (1982) *In-situ* holographic measurements of the sizes and settling rates of oceanic particulates. *Journal of Geophysical Research*, **87**, 5681–5685.

CARDER K. L., D. K. COSTELLO and R. G. STEWARD (1986a) State of the art instrumentation for measuring ocean aggregates. In: *Aggregate dynamics in the sea, Workshop Report*, E. HARTWIG and A. ALLDREDGE, editors, Office of Naval Research, Asilomar, Pacific Grove, CA, pp. 131–181.

CARDER K. L., R. G. STEWARD, P. R. BETZER, D. L. JOHNSON and J. M. PROSPERO (1986b) Dynamics and composition of particles from an eolian input event to the Sargasso Sea. *Journal of Geophysical Research*, **91**, 1055–1066.

COSTELLO D. K. (1988) Multiple-sample sediment trap with holographic imaging capability: design and function of the ADIOS laser trap. Master's thesis, University of South Florida, 40 pp.

FOWLER S. W. and G. A. KNAUER (1986) Role of large particles in the transport of elements and organic compounds through the oceanic water column. *Progress in Oceanography*, **16**, 147–194.

HARBISON G. R. and R. W. GILMER (1986) Effects of animal behaviour on sediment trap collection: Implications for the calculation of aragonite fluxes. *Deep-Sea Research*, **33**, 1017–1024.

HAUSSMANN G. and W. LAUTERBORN (1980) Determination of size and position of fast moving gas bubbles in liquids by digital 3-D image processing of hologram reconstructions. *Applied Optics*, **19**, 3529–3535.

HONJO S., S. J. MANGANINI and J. J. COLE (1982) Sedimentation of biogenic matter in the deep ocean. *Deep-Sea Research*, **29**, 609–625.

JOHNSON B. D. and P. J. WANGERSKY (1985) A recording backscatter meter and camera system for examination of the distribution and morphology of macroaggregates. *Deep-Sea Research*, **32**, 1143–1150.

KARL D. M., G. A. KNAUER, J. H. MARTIN and B. B. WARD (1984) Bacterial chemolithotrophy in association with sinking particles. *Nature*, **309**, 54–56.

KNAUER G. A., J. H. MARTIN and K. W. BRULAND (1979) Fluxes of particulate carbon, nitrogen and phosphorous in the upper water column of the northeast Pacific Ocean. *Deep-Sea Research*, **26**, 97–108.

LERMAN A. (1979) *Geochemical processes: water and sediment environments*. Wiley-Interscience, New York, 481 pp.

THOMPSON B. J., J. H. WARD and W. R. ZINKY (1967) Applications of hologram techniques for particle size analysis. *Applied Optics*, **6**, 519–526.

VAN DE HULST H. C. (1957) *Light scattering by small particles*. John Wiley, New York, 470 pp.

COLD IRIS

Classification of Oceanic Light Disruptors

using an

Intelligent Remote Imaging System

ANNUAL REPORT

to the Office of Naval Research

Phase I - Year 2

October 1, 1988 - September 30, 1989
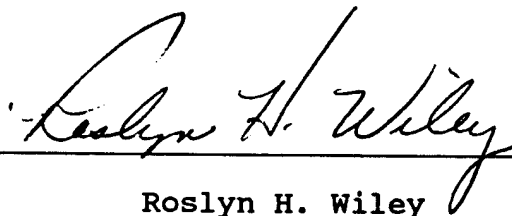

submitted by:

David K. Costello

Kendall L. Carder

and

Robert G. Steward

University of South Florida

Marine Science Department

Roslyn H. Wiley

Program Director, Sponsored Research

University of South Florida

TABLE OF CONTENTS

SYNOPSIS

A major objective of COLD IRIS Phase I has been the development of a machine vision system capable of pattern recognition and classification. Our operational hypothesis is that a planar image can be uniquely represented by a set of real numbers determined through the method of moment invariants[1,2,3]. It is required that these functions be invariant to object translation, rotation, and position in a 3-dimensional sample space. This hypothesis proved valid for computer generated test "objects" during year one (10/87 - 9/88)[4]. The method was further tested in this program year (10/88 - 9/89) using high resoluton images of marine zooplankton from our holographic image library[5,6,7]. The method successfully "recognized" (separated) eight groups of organisms in a multi-dimensional sample space[8].

Additionally, modules for automatic target detection/sizing and 2-dimensional Fast Fourier Transforms (FFTs) have been incorporated into the image processing environment and a methodology for particle edge detection in the presence of holographic background noise (diffraction patterns and laser speckle) has been developed[7].

The project has been enhanced through the acquisition of the following hardware with University funding:

1. Optical Multichannel Analyser (OMA 3) with image intensifier, pulse amplifier, and fast pulser (EG&G);

2. Tunable Dye Laser (LaserScience);

3. "SCAMP" Remotely Operated Vehicle-ROV (Hydrobotics).

FOURTH QUARTER EFFORTS

Our main goal for this fourth quarter is the acquisition and integration of components into a configuration approaching the laboratory particle imaging/analysis system depicted in Figure 1. This will enable work in the following primary areas:

1. Automatic target ranging using stereo video (Epipolar Line Technique[9]);

2. Automatic target ranging with a single video sensor,and;

3. The generation of an amplitute map of the forward scattering function for particles of known sizes and differing relative indices of refraction to develop and test a refractive index classification strategy.

Ancillary fourth quarter investigations involve:

1. Correlation of computed dynamic mass density[10] with observed optical density[11];

2. Initial investigation of Laser Stimulated Fluorescence using the newly acquired OMA-3 and tunable dye laser;

3. Quantification of the signal-to-noise ratio (S/N) for forward/back scattering for differing laboratory configurations, and;

4. Continued investigation into the incorporation of artificial intelligence into our Pattern Recognition strategy.
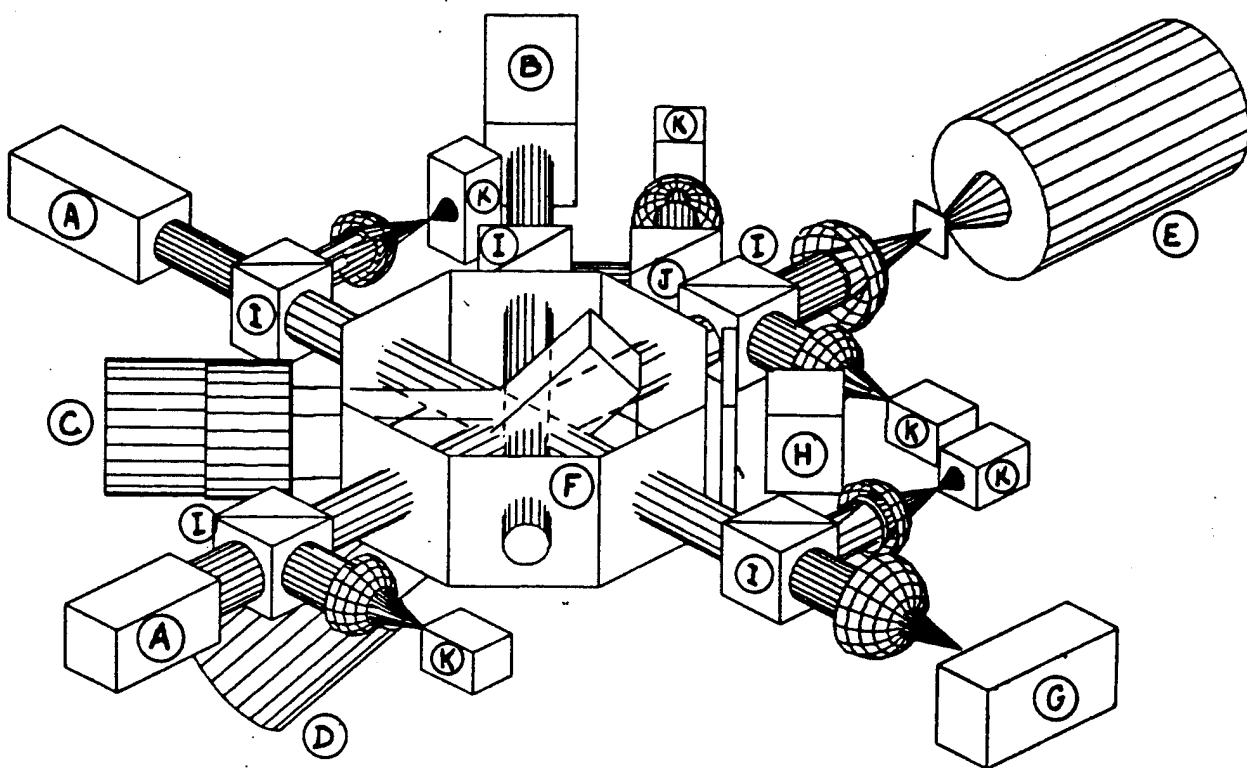
Figure 1. Laboratory particle imaging/analysis system:
A. HeNe lasers; B. HeCd or Tuneable Dye laser; C. Primary video camera; D. Video range camera; E. Dark-field video camera; F. Octagonal sample chamber; G. Holographic camera; H. OMA-3 with narrow bandpass filter; I. Beamsplitters; J. 90° prism (TIR mode); K. Photocells.

IMAGE ACQUISITION AND PROCESSING

In conventional microscopy, the very shallow depth of field associated with high magnification places a severe constraint on the detection of particle edges. We are, therfore, attempting to

develop automatic target ranging (autofocus) strategies for in situ particle imaging. In our laboratory work with holographic images, however, although this shallow depth of field restraint is considerably relaxed, there is a substantial amount of holographic noise (laser speckle and diffraction rings from other particles) inherent in the image which itself constrains precise edge detection during image reconstruction. By capturing the holographic images in a computer video frame buffer, it is possible to perform operations in the digital domain which suppress noise and enhance particle edges. However, well-known edge detection filters (e.g. Robert's cross-operator, Sobel operator, and the Laplacian convolution) are very sensitive to the high-contrast noise inherent in a holographic image (laser speckle) since they utilize only locally limited information (an $N \times N$ pixel neighborhood, for example, with N typically ranging from 2 to 9). Image noise can be reduced through the averaging and/or differencing of multiple image fields, pixel averaging (median filter) within an image field, or the application of intensity weighting functions (determined by parameters from the image intensity histogram) which suppress noise and maximize the probability that a particle edge will be enhanced[12]. Once noise is suppressed, we have found that an efficient edge detection algorithm for our holographic images is to threshold the image at an intensity level indicated by the maximum intensity gradient between target and background. The threshold level is determined through a series of intensity profile transects through the

particle.

An example of effective noise reduction is shown in Figure 2. These are real-time images using HeNe laser illumination and dark-field optics. The upper two quadrants are individual images (frames) of the sample space separated in time with the upper left image taken before and the upper right image after the introduction of 20 micrometer diameter latex test spheres into the test chamber. It is not readily apparent whether the test spheres have entered the field of view shown in the upper right. However, the result of the differencing operation on the two fields (defined as the absolute value of a pixel-by-pixel subtraction between fields) is shown in the lower right (after contrast stretch) and two targets are apparent. One particle is nearly in focus and the other more out-of-focus as indicated by its accompanying diffraction rings.
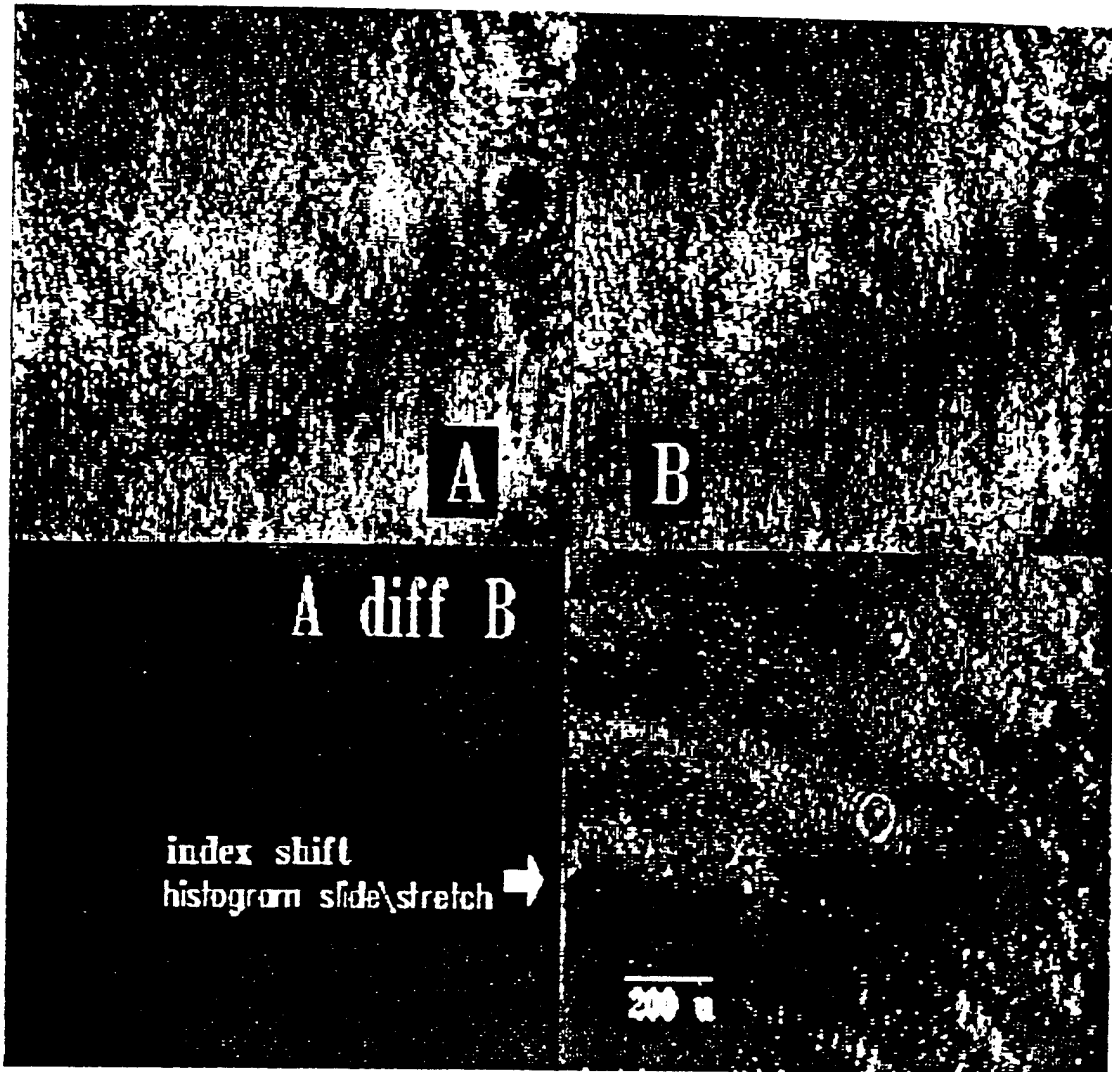
Figure 2. Pixel-by-pixel differencing to reveal targets obscured by field noise (see text for discussion).

TARGET DETECTION AND SIZING

Automatic video target detection strategies must necessarily rely on the detection of pixels which contrast in intensity from their neighbors sufficiently to surpass some defined threshold. Factors to consider include whether the threshold is

weighted by target contrast to a constant or a variable (adaptive) background, measured by single-pixel contrast or by the contrast gradient along a specified number of pixels, and by how wide a "gap" (pixels which, individually, do not meet threshold conditions, usually due to noise) the algorithm will extrapolate across in determining whether a threshold condition is met. This ability to integrate across a gap (closing tolerance) is also critical in specifying whether two adjacent targets are actually one target. This is of most importance when testing minimum-valid-size and maximum-valid-size detection parameters to eliminate erroneous targets.

A target detection module (ImageMeasure/IP) has been incorporated into our imaging environment which adequately addresses the above by placing all detection parameters under user command. Utilization of the module in the laboratory will indicate which parameter configuration has the most utility for a field instrument in which near-real-time considerations demand a streamlined algorithm. Following detection, target area, perimeter, several shape parameters, and centroid X and Y coordinates are generated in the module and can be incorporated into the pattern recognition classification strategy.

2-DIMENSIONAL FAST FOURIER TRANSFORM

A two-dimensional Fast Fourier Transform (FFT) module has been integrated into the imaging environment which will provide for the analysis and modification of images in the spatial frequency

domain. Although the module will have utility in filtering image field noise, the primary value will be the FFT's analog to a lens in analyzing placement of the light field-stop for use in the spatial filtering of collimated light for dark-field imaging applications. Perturbations in the beam direction may result, for example, from temperature fluctuations in a deployment environment. This then, would cause asymmetry of the focused light field with respect to the circular spatial filter stop. The resulting dark-field image would have irregular intensity patterns due to more low frequency filtering in some directions then in others. The effect on image analysis must be known and correctable if dark-field applications are to have utility.

PATTERN RECOGNITION

The pattern recognition (PR) algorithm (previously verified with computer generated "images") was further tested with images of 18 marine organisms shown in Figure 3 (one group of four, five pairs, and four individuals). To effectively "classify" these images, the PR algorithm must generate classification parameters (feature vectors) which are similar on an intragroup and dissimilar on an intergroup basis. Furthermore, an effective algorithm for in situ pattern recognition (where image location, orientation, and size cannot be controlled) must be invariant for image translation, rotation, and apparent size. The PR algorithm we have developed is based on the method of moment invariants and can generate 36 invariant classification factors which act as
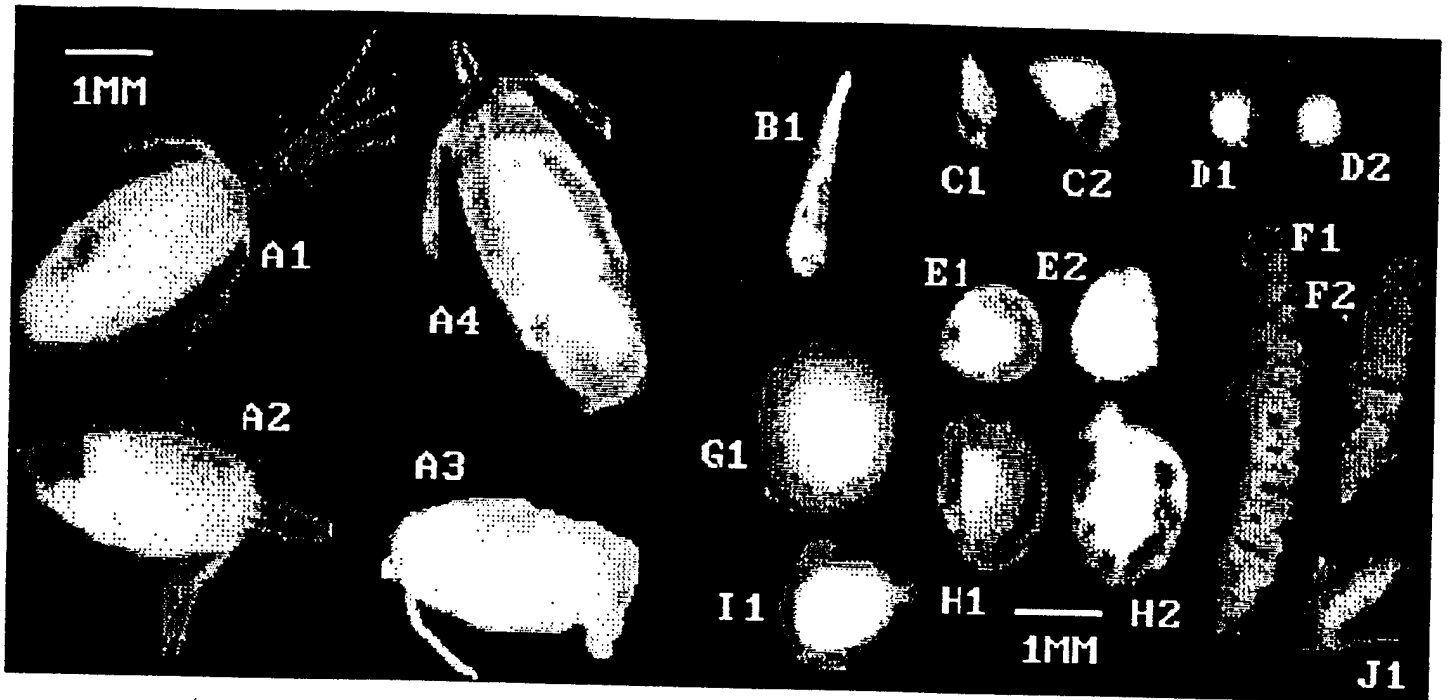
Figure 3.   Pattern Recognition strategy test images.

vectors in a multi-dimensional classification space.   Twelve factors each are generated by operating on the target silhouette (low frequency information), target outline (high frequency information), and the target's full 8-bit image which will include a contribution from any interior structure.   The twelve factors are: the zero order central moment (image power); the seven Invariant Moment Functions as first developed by Hu[1] with the size normalization first proposed by Dudani[2]; and five moment-generated elliptical classification factors as developed by Teague[3] which characterize any image as a constant intensity ellipse with defined major axis, minor axis, and orientation within the coordinate field.

The algorithm not only successfully classified members of a group (or pair) as associated with each other but not with other groups, it also placed the four individuals in discreet areas of classification space. The multi-dimensional classification strategy is depicted in Figure 4.

A year three priority will be the analysis of the relevant information content of the different feature vectors in order to maximize the information gain while minimizing computational demands.
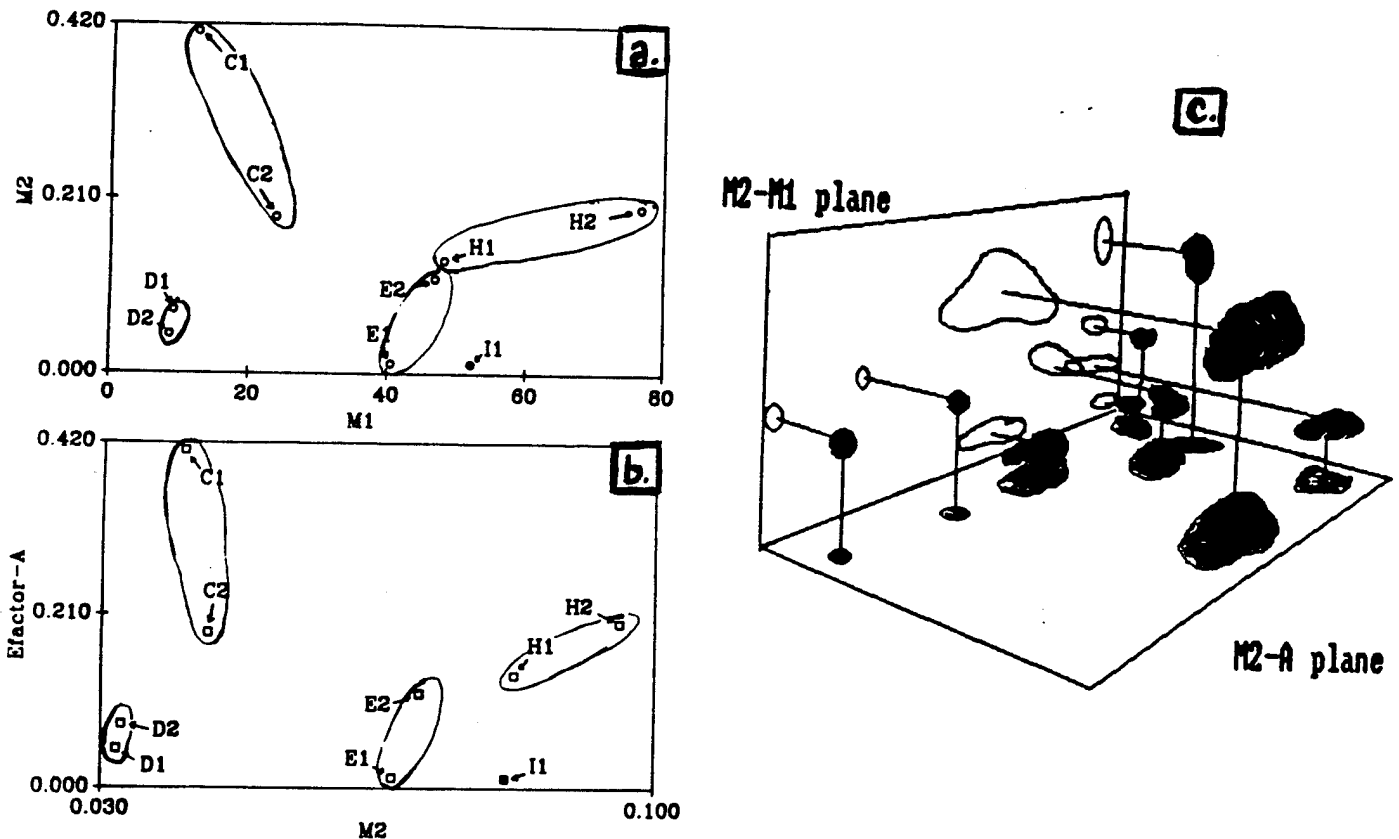

Figure 4. Pattern Recognition classification strategy.
a) Hu Invariant Functions M1 vs. M2.   b) Teague elliptical factor A vs M2. c) Cartoon depicting feature vector separation in a multi-dimensional classification space.

ARTIFICIAL INTELLIGENCE

As the field of Artificial Intelligence (AI) develops and grows, so do the prospects for successful incorporation of an AI system into this project. We currently feel that a Neural Network System will be more appropriate (and more powerful) than the previously envisioned Expert System. To that end, a Neural Network simulator (California Scientific) has been secured and its implementation is being investigated. If the Neural Network approach proves viable, a hardware network may be secured in year three.

REFERENCES

1. Hu, M. 1962. Visual Pattern Recognition by Moment Invariants. IRE Trans. Inf. Theory, IT-8, 179

2. Dudani, S.A., K.A. Breeding, and R.B. McGee. 1977. Aircraft identification by moment invariants. IEEE Trans. Comput. C-26, 39-45.

3. Teague, M.R. 1980. Image analysis via the the general theory of moments. J. Opt. Soc. Am., v. 70, n. 8.

4. Costello, D.K., R.W. Young, K.L. Carder and P.R. Betzer. 1986. Multiple-sample sediment traps with in situ holographic imaging of settling particles. EOS 67, 899

5. Carder, K.L., D.K. Costello, and R.G. Steward. 1986. State of the art instrumentation for measuring ocean aggregates. Aggregate Dynamics in the Sea Workshop Report, E. Hartwig and A. Alldredge (eds). Office of Naval R e s e a r c h , Asilomar Ca. 131-181.

6. Costello, D. K. 1988. Multiple-sample sediment trap with holographic imaging capability: design and function of the ADIOS laser trap. Master's thesis, University of South Florida. 40 pp.

7. Costello, D. K., K. L. Carder, P. R. Betzer, and R.W. Young. 1989. In-situ holographic imaging of settling particles:Applications for Individual Particle Dynamics and Oceanic Flux Measurements. Deep-Sea Res. In press.

8. Costello, D.K., K.L. Carder, and R.G. Steward. 1988. Computer enhancement of in situ holographic images with preliminary algorithms for marine particle pattern recognition. EOS, 69, 1124.

9. Nguyen, T. V. 1989. Three-Dimensional Robotic Vision System. NASA Tech Briefs. June. Marshall Space Flight Center

10. Carder, K. L., R. G. Steward, P. R. Betzer, D. L. Johnson and J. M. Prospero. 1986. Dynamics and composition of particles from an eolian input event to the Sargasso Sea, Journal of Geophysical Research, 91 (D1), 1055-1066.

11. Carder, K. L., P. R. Betzer and D. W. Eggiman. 1974. Physical, chemical, and optical measures of suspended-particle concentrations: Their intercomparison and application to the west African shelf. In Suspended Solids In Water. R. J. Gibbs, ed. Plenum, N. Y.

THE HYDRAULIC EQUIVALENCE OF MICA[1]

LARRY J. DOYLE, KENDALL L. CARDER, AND ROBERT G. STEWARD

Department of Marine Science
University of South Florida
104 Seventh Avenue South
St. Petersburg, Florida 33701

ABSTRACT: Settling experiments performed on silt- to fine-sand-sized mica flakes with a holographic micro-velocimeter revealed that mica is the hydraulic equivalent of quartz spheres having diameters a factor of 4 to 12 times smaller. Mica in the very fine to fine-sand sizes has been traditionally used by sedimentologists to delineate areas of deposition or nondeposition and potential winnowing of fines, and is here found to be the hydraulic equivalent of silt-sized particles but not of clay.

Experiments also showed that mica flakes tend to settle at orientations which are neither perpendicular nor parallel to the gravitational vector and tend to generally maintain their orientation throughout. Equations for the settling of a disc in Lerman and others (1974) and that developed by Komar and Reimers (1978) are shown to be mathematically similar for the coarse-silt to fine-sand ranges of discs and are adequate predictors of settling rates of mica flakes. A comparison of the hydraulic equivalency of quartz spheres to coarse-silt- through fine-sand-sized mica flakes is presented.

INTRODUCTION

Because it cleaves into flaky particles, sand-sized mica is a mineral group in which shape should obviously affect settling charateristics and, in fact, has often been considered to be the hydraulic equivalent of silt and clay. Neihesel (1965) noted the close association between sand-sized mica and the clay fraction of Georgia estuaries, an association also recognized by Pamerancblum (1966) off Israel. Doyle and others (1968) used the abundance of mica in the 125- to 250-μm size fraction to delineate areas of the southeastern United States continental margin that might be undergoing winnowing or deposition of fines, a process which otherwise would be masked by the dominance of reworked Pleistocene sands. A similar approach was used by Adegobe and Stanley (1972) on the Niger Shelf. Doyle and others (1979) and Park and Pilkey (1981) discuss the significance of mica content to the depositional and erosional systems of the whole continental margin of the Eastern United States.

Despite its intuitive widespread use as a hydraulic analog of finer sized sediments, no quantitative evaluation of the sedimentologic characteristics of mica has yet been undertaken. The purpose of this paper is to determine as far as possible the hydraulic characteristics of mica flakes and how these characteristics compare with those predicted from settling equations in the literature.

APPROACH

Our approach is to utilize a modified holographic micro-velocimeter developed and described by Carder (1978) and Carder and Meyers (1979). Figure 1 shows the system used. Transmission holograms are simultaneously collected along the vertical and horizontal axes of a settling cuvette. A reference point in the cuvette is also recorded on each vertical and horizontal hologram to allow translation between the two axes. Sequential frames at accurately timed intervals (from 0.5 to 3.0 seconds depending on the particle size) record the settling velocity and orientation as well as particle size and shape. The images are reconstructed by placing the hologram back into the laser path and refocusing on particles in any of the infinite number of focal planes in the settling cuvette. This system offers the advantage of using actual sedimentary particles in the sand- to clay-size ranges, thus obviating any errors that may be inherent in scale modeling systems.

Mica samples were chosen from sediment cores from the Eastern United States continental slope (Doyle and others, 1979). Silt- to fine-sand-sized mica flakes were added to a small

FIG. 1.—Holographic micro-velocimeter setup used to measure the settling velocity of the mica flakes.

quantity of filtered distilled water to obtain a slurry. A drop of slurry was picked up on a fine brush and the drop barely touched to the top of the miniscus of the distilled filtered water in the cuvette, thereby introducing mica flakes into the measuring apparatus. Other methods of sample introduction, including use of an eye dropper, were tried, but they tended to set up convection within the cuvette.

Resulting settling velocities were then compared with the theoretical settling rates generated from the equations of Lerman and others (1974) and Komar and Reimers (1978). In the calculations of settling rates a density for mica of 2.9 g/cm^3 was used, midway in the normal range for biotite and muscovite. Examination of the mica by standard optical techniques showed that the mica fraction in the cores was composed of muscovite and a lesser amount of biotite. Finally, we compared the measured settling rates of the mica with those for quartz spheres.

SHAPES AS A FACTOR OF GRAIN SETTLING

Shape has been recognized as an important factor in the analysis of sediments by hydraulic methods (principally settling tube) for over 100 years. Gibbs and others (1971), Lerman and others (1974), Komar and Reimers (1978), and Brezina (1979) have summarized the development of thinking concerning the hydraulic importance of shape and have contributed to the formulation of equations for settling velocity that take grain shape into account. In a series of recent articles Baba and Komar (1981a and b) have begun to examine shape effects of various types of natural particles.

Lerman and others (1974) modified the equations for the settling of a disc of "no thickness" in the Stoke's range, developed by Lamb (1932), Payne and Pell (1960), and Brenner (1964), by adding a term for disc thickness. The resulting formulae for the two major orientations of fall are:

$$U = \frac{g(\rho_s - \rho) \, q_h r^2}{3.396 \, \mu} \text{ (edgewise)} \quad (1)$$

$$U = \frac{g(\rho_s - \rho) \, q_h r^2}{5.1 \, \mu} \text{ (broadside)}, \quad (2)$$

where U = settling speed; r = disc radius; h = thickness; q_h = h/r; μ = dynamic viscosity of water; ρ_s = particle density; ρ = density of water; and g = acceleration due to gravity (981 cm/sec^2).

Komar and Reimers (1978) approached the effect of shape on settling velocity by scale modeling with pebbles in a glycerine settling medium. the results being equivalent to quartz sand and silt in water. They found experimentally that the Corey Shape Factor (CSF) introduced by Corey (1949), Malaika (1949), McNown and Malaika (1950), and McNown and others (1951) gave the best prediction of shape effects for the pebbles they used in their experiment. Based upon their experimental results, Komar and Reimers (1978) developed an empirical formula for settling velocity in the Stoke's range, taking into account shape effect:

$$U = \frac{1}{18 \, \mu} \frac{1}{f(CFS)} (\rho_s - \rho) \, gD_n^2, \quad (3)$$

where $D_n = (hD_iD_l)^{1/3}$; D_i = intermediate axis particle diameter; D_l = principal axis particle diameter; CSF = h/ $\sqrt{D_iD_l}$; h = small axis particle diameter; f(CSF) = 0.946(CSF)$^{-0.378}$ when 0.4 ≤ CSF ≤ 0.8; and f(CSF) = 2.18 − 2.09 (CSF) when CSF ≤ 0.4.

They further found that they could extend the range of the grain sizes following Stoke's settling to Reynolds numbers of up to 0.10 or for particles of up to 100 μm, and they were able to empirically extend their data to cover grain sizes up through pebbles. For particles like mica where h is small relative to D_i and D_l, CSF is ≤0.4 and the general equation (3) becomes:

$$U = (1/18 \, \mu) \frac{1}{[2.18 - 2.09 \, (h/\sqrt{D_iD_1})]}$$
$$\cdot (\rho_s - \rho) \, g(hD_iD_1)^{2/3} \quad (4)$$

The particle thickness h may be expressed as a ratio with respect to D, that is, D/100, D/50, D/25 . . . D/χ, and therefore in the ranges in which we are working, the equations of Lerman and others (1974) and equation (3) are similar. For example, let $D_i = D_1 = \bar{D}$, $\chi = \bar{D}/h = 2r/h$, and $q_h = h/r$. Then equation (4) becomes:

$$U = \frac{1}{18\mu} \frac{1}{\left(2.18 - 2.09 \dfrac{1}{\chi}\right)}$$
$$\cdot (\rho_s - \rho)g \left(\frac{\bar{D}^3}{\chi}\right)^{2/3}$$

$$U = \frac{1}{\left(2.18 - 2.09 \dfrac{1}{\chi}\right) \chi^{2/3}}$$
$$\cdot \underbrace{\frac{1}{18\mu} (\rho_s - \rho) \, g\bar{D}^2}. \quad (5)$$
$$\text{Stoke's Formula}$$

Our measurements of h for mica flakes yielded a range of h $\approx$ 0.007D − 0.05 D. For $\chi = \bar{D}/h = 1/0.01 = 100$, and substituting in (5), we obtain:

$$U = 0.021 \frac{1}{18\mu} (\rho_s - \rho) \, g\bar{D}^2.$$

Lerman's formulae are of the general form

$$U = \frac{g(\rho_s - \rho) \, q_h r^2}{c\mu},$$

where c = 3.396 to 5.1. Substituting as before we obtain

$$U = \frac{g(\rho_s - \rho) \, D^2}{2c\mu x}.$$

Multiplying by 18/18 yields

$$U = \frac{18}{2c\chi} \underbrace{\frac{1}{18\mu} (\rho_s - \rho) \, gD^2}.$$
$$\text{Stoke's Formula}$$

For Lerman's formula to be equivalent to Ko-

mar and Reimers at $\chi = 100$ we can set

$$\frac{18}{2c\chi} = 0.021$$

$$c = \frac{18}{2(100)(0.021)}$$

$$c = 4.28.$$

This value lies between Lerman's two values of 3.396 and 5.1, and therefore values derived from the two sets of formulae will be close to each other over the ranges we are examining.

Assuming $D_i = D_1 = \bar{D}$ (where $\bar{D}$ is an average diameter) is an idealized case which all mica flakes do not meet. Any deviation from $D_i = D_1$ will obviously cause some deviation in the calculation of μ. When $D_i = D_1$, the parameter $\chi = D/h$ becomes the shape parameter directly related to the Corey shape factor.

THE HYDRAULIC EQUIVALENCY OF MICA

In our experiments mica flakes seldom settled either exactly broadside or edgewise. They usually assumed an orientation between the two extremes, neither perpendicular nor parallel to the gravitational vector which they maintained throughout. Stringham et al. (1969) also showed that particles settling at low Reynolds numbers maintain their initial orientation which need not be perpendicular to the settling direction.

Figure 2 shows the experimentally determined settling velocities of mica flakes plotted on the family of curves of Lerman and others (1974) and Komar and Reimers (1978) for thicknesses of D/200, D/50, D/20, and D/10. Komar and Reimer's (1978) equation begins to diverge from those of Lerman (1974) only at thicknesses of D/20 and greater. The thicknesss/D ratios of 32 mica grains from a split of the slope sediment used for the settling velocity experiment were determined by scattering some quartz beach sand on an SEM stub and then sprinkling the mica-rich slope sample over it. Some of the mica flakes landed on edge and we were thus able to measure thickness-to-D ratios. Thicknesses ranged from 0.7 percent of D to 5 percent of D, with the average at 2 percent and a standard deviation of 1.15 percent. Figure 2 also shows that most of the velocities of mica flakes that we measured fall within the envelope created by the theoretical curves. Scatter at the coarser end is probably mostly the result of variation in thickness,
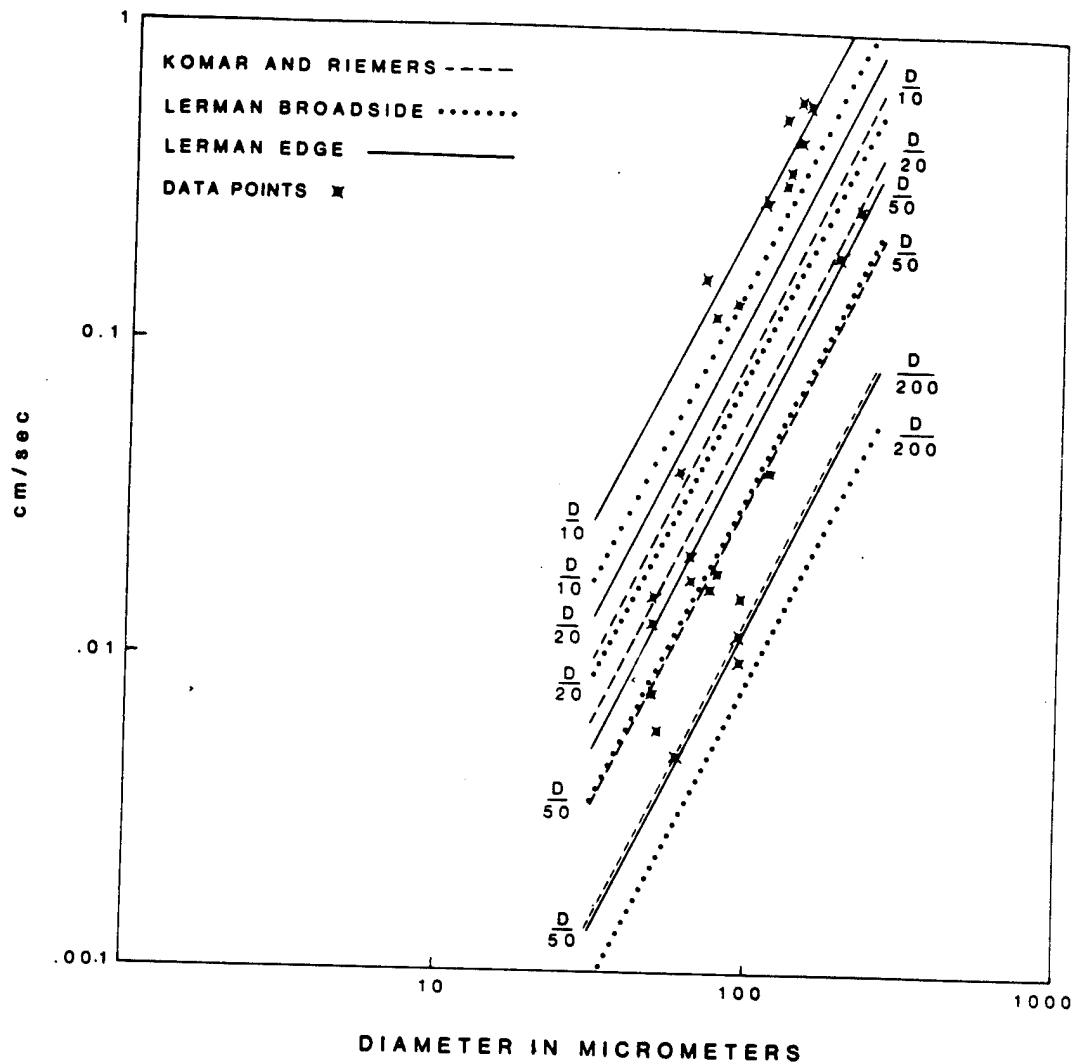
DIAMETER IN MICROMETERS

FIG. 2.—Lerman and others (1974) equations for the settling of discs both broadside and edgewise plotted along with that of Komar and Reimers (1978) for thickness of D/200, D/50, D/20, and D/10. Note that the equations yield values which are very close to each other at thicknesses of D/50 or less, thicknesses most prevalent for mica flakes. X's are values of mica flakes we measured.

symmetry (for example, $D_i \neq D_j$) and settling orientation, because some particles in this size range are beginning to exceed the Stoke's low Reynolds number constraint on the Stoke's equation.

At the coarser end of the scale, particles fall closer to the equations of Lerman and others (1974) than to that of Komar and Reimers (1978). Figure 3 shows the diameter of spherical quartz particles of density of 2.65 which would settle at rates of the variously sized mica flakes determined from the equations of Ler-

man and others (1974) for h = D/200, D/50, and D/20. Our experiments show that mica ranging in diameter from 62 μm to 250μm, with a thickness of no more than 5 percent of the sieve diameter, is the hydraulic equivalent of 5-μm to 82-μm quartz spheres. Very fine, sand-sized mica, then, is the hydraulic equivalent of silt-sized quartz spheres whereas fine-sand-sized mica is the equivalent of silt- to very fine sand-sized spheres. Coarse-silt-sized mica flakes are the equivalent of fine, and very fine quartz silts.
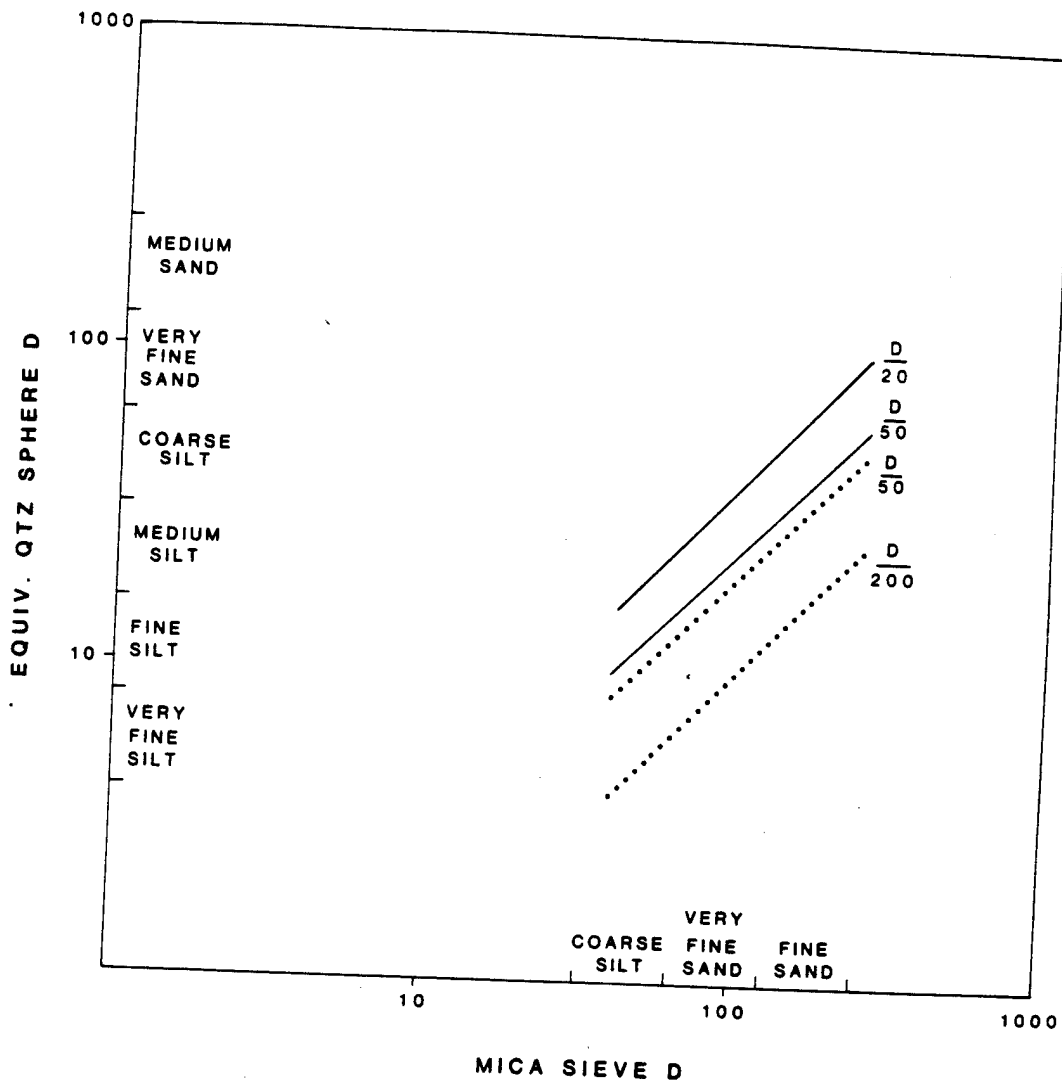
FIG. 3.—The hydraulic equivalency of mica to quartz spheres. Mica sizes are coarse slit to fine sand, and thicknesses are D/200, D/50, and D/20.

CONCLUSIONS

1) The equations for determining settling velocity of a disc presented by Lerman and others (1974) and that developed by Komar and Reimers (1978) for particles where the Corey Shape Factor ≤ 0.4 are similar for thicknesses of D/50 or less.

2) Experiments on fine-sand- to coarse-silt-sized mica flakes using a holographic micro-velocimeter showed that grains most often do *not* orient themselves perpendicular to the flow field as they settle but that they tend to settle at some orientation between broadside and edgewise.

3) Mica in the coarse-silt, very fine sand, and fine-sand sizes is the hydraulic equivalent of silt- and very fine sand-sized quartz spheres according to the relationships shown in Figures 2 and 3.

Contrary to previous assumptions, mica in the coarse-silt to fine-sand sizes is not the hydraulic equivalent of clay.

critically reviewed some of the manuscript. The authors wish to acknowledge the especially thorough review of Paul Komar who pointed out a more elegant comparison between the equation of Komar and Reimers and the equations of Lerman than we had originally presented and which we have incorporated into this paper.

REFERENCES

ADEGOBE, O. S., AND STANLEY, D. J., 1972. Mica and shell as indicators of energy level and depositional regime on the Nigerian shelf: Marine Geology, v. 13, p. M61–66.

BABA, J., AND KOMAR, P. D., 1981. Settling velocities of irregular grains at low Reynolds numbers: Jour. Sed Petrology, v. 51, p. 121–128.

BABA, J., AND KOMAR, P. D., 1981. Measurements and analysis of settling velocities of natural quartz sand grains: Jour. Sed. Petrology, v. 51, p. 631–640.

BRENNER, H., 1964, The Stoke's resistance of a slightly deformed sphere: Chem. Eng. Sci. 19, p. 519–539.

BREZINA, J. 1979, Particle size and settling rate distributions of sand-sized materials: Second European Symposium on Particle Characterization, Nuremberg, September 24–26, 1979, 44 p.

CARDER, K. L., 1978, A holographic micro-velocimeter for use in studying ocean particle dynamics: SPIE Vol. 160 Ocean Optics V, p. 63–66.

CARDER, K. L., AND MEYERS, D. J., 1979, New optical techniques for particle studies in the bottom boundary layer: SPIE vol. 208 Ocean Optics VI, p. 151–158.

COREY, A. T., 1949. Influence of shape on the fall velocity of sand grains. [unpub. Masters thesis]: Colorado A&M College, 102 p.

DOYLE, L. J., CLEARY, W. J., AND PILKEY, O. H., 1968, Mica: its use in determining shelf-depositional regimes: Marine Geology, v. 6, p. 381–389.

DOYLE, L. J., PILKEY, O. H., AND WOO, C. C., 1979 Sedimentation on the Eastern United States continental slope,

in Doyle, L. J., and Pilkey O. H., eds., Geology of Continental Slopes: Soc. Econ. Paleontologists Mineralogists Spec. Pub. no. 27, p. 119–129.

GIBBS, R. J., MATTHEWS, M. D., AND LINK, D. A., 1971, The relationship between sphere size and settling velocity: Jour. Sed. Petrology, v. 41, p. 7–18.

KOMAR, P. D., AND REIMERS, C. E., 1978, Grain shape effects on settling rates: Jour. Geology, v. 86, p. 193–209.

LAMB, H., 1932 (1945), Hydrodynamics (Sixth edition): New York, Dover.

LERMAN, A., LAL, D., AND DACEY, M. F., 1974, Stoke's settling and chemical reactivity of suspended particles in natural waters. *in* Gibbs, R. J., ed., Suspended Solids in water: New York, Plenum Press, p. 17–47.

MALAIKA, J., 1949, Effect of shape of particles on their settling velocity, [unpub. Ph.D. dissertation]: State Univ. Iowa. 64 p.

McNOWN, J. S., and MALAIKA, J., 1950, Effects of particle shape on settling velocity at low Reynolds numbers: Trans. American Geophysical Union, v. 31, p. M74–82.

McNOWN, J. S., MALAIKA, J., AND PRAMANIK, H., 1951, Particle shape and settling velocity: Proc. Intern. Assoc. Hydr. Res., fourth meeting, Bombay, India, p. 511–522.

NEIHEISEL, J., 1965, Source and distribution of sediments at Brunswick Harbor and vicinity Georgia: U. S. Army Coastal Engineering Res. Center Tech. Memo. 12, 21 p.

PAMERANCBLUM, M., 1966, The distribution of heavy minerals and their hydraulic equivalents in sediments of the Mediterranean continental shelf off Israel: Jour. Sed. Petrology, v. 36, p. 162–174.

PAYNE, L. E., and PELL, W. H., 1960, The Stokes' flow problem for a class of axially symmetric bodies: Jour. Fluid Mech., v. 7, p. 529–549.

PARK, Y. A., AND PILKEY, O. H., 1981, Detrital mica: environmental significance of roundness and grain surface textures: Jour. Sed. Petrology, v. 51, p. 113–120.

STRINGHAM, G. E., SIMONS, D. B., GUY, H. P., 1969, The behavior of large particles falling in quiescent liquids: U.S. Geological Survey Prof. Paper 562-C, 36 p.

Image analysis techniques for holograms of dynamic oceanic particles

Paul R. Payne, Kendall L. Carder, and Robert G. Steward

A holographic image analysis system has been developed to measure position, velocity, size, and shape of microscopic particles settling in 3-D space. Images of particles recorded sequentially on individual holographic frames are reconstructed using an in-line far-field configuration, registered in 3-D space, and particle displacements (velocities) between sequential frames are determined. Particle settling velocity is calculated using elapsed time between frames. Digitized video signals of the reconstructed holographic images are processed to determine particle size, shape, and area to facilitate identification by shape from frame to frame and to calculate particle specific gravities. A cataloging system was developed to provide efficient data management.

I. Introduction

Measurements of size, shape, and density are critical factors in the study of particle dynamics and settling characteristics of marine hydrosols. Micrographic holography has been widely used in aerosol studies[1] and holographic movie cameras have been developed for studying zooplankton feeding behavior in ocean waters.[2] Using a similar holographic technique, the size and settling behavior of aggregates resulting from mixing riverine water with seawater has been determined in the laboratory[3] and the effect of particle shape on the settling velocities of primary hydrosols (unaggregated) has also been investigated.[4,5]

Carder et al.[6] have developed an in situ holographic microvelocimeter for the study of microscopic particles suspended in seawater. This device records the image of each particle in 3-D space on a series of successive holograms with respect to time. Horizontal and vertical dimensions and cross-sectional area have been used to determine particle density using the Stokes theorem.[3] Edge coordinates are useful for particle identification (e.g., Zernike moments) and analysis of shape on particle rotation and settling speed.[4] During these studies,

a great number of samples must be analyzed in order to provide sufficient statistics for determining particle population characteristics of shape and size as well as settling velocity, trajectory, orientation, and oscillations. Such measurements can be facilitated by use of a computer-controlled image analysis system to improve the accuracy and reduce the number of man-hours in analyzing holographic particle data.

II. Problem Definition

A measurement technique was needed to determine the position, size, shape, orientation, and velocity of microscopic particles moving in 3-D space. The marine particles of interest in the study[6] cited above typically ranged from 5 to 250 μm in diameter, which necessitated the use of microscopic techniques for any detailed size or shape analysis. Since oceanic particle densities may vary from ~1.03 to 5.2 g/mliter and typical settling velocities may range from <0.0001 to 1.0 cm/sec, a variety of frame or sample periods from <1 sec to as much as 1 min may be necessary in order to provide short-term velocity measurement accuracy. In addition, the duration or exposure time for the position measurement should be <1/500 sec in order to maintain sufficient positional accuracy and prevent hologram smearing. Therefore, a relatively high-speed microscopic technique was developed[6] to record the images of multiple particles as they settled in 3-D space. To deal with the enormous data volume generated in applying these techniques (more than 50 particles/hologram), an automated method for reconstructing and analyzing the particle data has been developed. Edge coordinates are recorded when needed for particle identification and for analysis of the particle shape effects on particle rotation.

Paul Payne is with Aztec Computer Engineering, 6805 Circle Creek Drive, Pinellas Park, Florida 33565; the other authors are with University of South Florida, Department of Marine Science, St. Petersburg, Florida 33701.
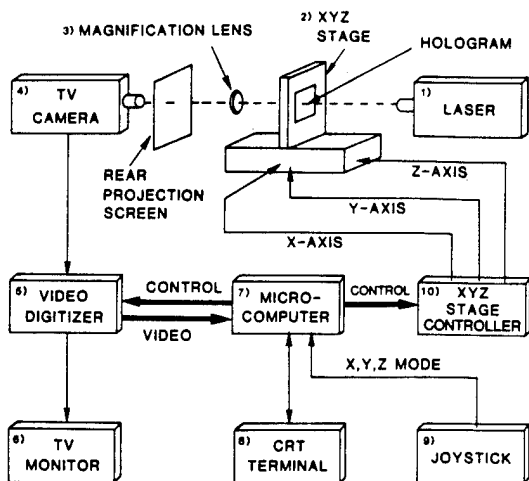
Fig. 1. Holographic image analysis system block diagram.

III. System Description

A functional block diagram of the holographic image analysis system is shown in Fig. 1. The major components and functions are: (1) a laser to reconstruct the holographic image, (2) a mechanical stage to position the hologram in 3-D space, (3) a magnification lens and rear projection screen on which to reconstruct the particle image, (4) a TV camera to produce a video signal of the image, (5) a video digitizer to convert the video signal into digital data, (6) a TV monitor to display the particle image, (7) a microcomputer with disk storage for processing and storing input data from the video digitizer and controlling the position of the mechanical stage, (8) an interactive terminal to enable operator control of the system, (9) a joystick for manual control of the frame position, and (10) the XYZ drive controller to move the holographic frame in the laser beam. Table I presents a list of the equipment which comprises the system.

The system is designed to perform the following functions: (1) determine the position of a particle with respect to a 3-D frame reference, (2) determine the width, height, cross-sectional area, and perimeter of a particle using a scanning algorithm, (3) determine the

Table I. Holographic Image Analysis System Equipment

Item	Description	Manufacturer	Model
1	Laser, 15-mW He–Ne	Spectra-Physics	124B
2	XYZ axes table	Aerotech, XY: Z:	ATS-303 ATS-416
3	28- or 50-mm lens	Nikon	
4	TV camera, high resolution	Dage	650
5	Video digitizer	Colorado video	270A
6	TV monitor	Panasonic	WV 5300
7	Microcomputer, Z-80, dual disk	Cromemco	Z-2D
8	CRT terminal	Soroc	IQ 120
9	Joystick	Cromemco	JS-1W
10	XYZ drive controller	Aerotech	EC-2

cross-sectional area, perimeter, and edge coordinates of the particle using a tracking algorithm, (4) enable particle identification from frame to frame by displaying the particle position and edge points (shape) from the previous holographic frame on the current frame, and (5) calculate the velocity, average diameter, and particle density from the recorded data for each particle.

IV. Technical Discussion

Successive holograms of settling particles were recorded *in situ* on negative holographic transparency film using the particle velocimeter described in Ref. 6 with 4× magnification. The film was processed using standard photographic techniques and mounted on individual frames. Each holographic frame was positioned in a laser beam to reconstruct a 2-D profile of each particle in the direct transmission mode with an additional magnification of 25–40, depending on the particle size. With this particular setup we have measured particles down to 10-μm diam (see Ref. 3). Increased magnification onto the holographic film is required to measure smaller particles.

The image of each particle was successively focused on the rear projection screen by moving the holographic frame in the Z axis. The projected scene was viewed with a TV camera and converted into a digitized video signal. The holographic frame was then moved in the X and Y axes to bring the focused image of each particle into the center of the TV monitor screen. The position of the frame and the size, shape, and orientation of each particle were analyzed and recorded by the computer. As images of the same particles in subsequent frames were cataloged, a matrix of settling velocity and lateral motion characteristics was generated for each particle. The statistical distribution of settling velocity with respect to particle size, shape, and orientation provided an accurate determination of particle density and ultimately permitted a general particle classification (e.g., organic, mineral, heavy mineral), based largely on density.

A. Particle Position and Velocity

Particle settling velocity using the system described in Fig. 1 was determined by measuring the position of each particle in 3-D space at two or more different sample times. A typical particle configuration is shown in Fig. 2. Prior to cataloging any particle images from a frame, an accurate and repeatable reference is established for a point common to all frames. The reference point in a frame is centered on the TV monitor by moving the frame in the X, Y, and Z axes under computer control with a joystick. The image of each particle in the frame is then subsequently moved to the center of the monitor with the joystick and its position recorded. Size and orientation parameters are determined using the particle scanning and edge-tracking algorithms described below. Once recorded, the particle data from a previous frame can be retrieved and the XYZ stage driven to that position under computer control to enhance location and identification of that
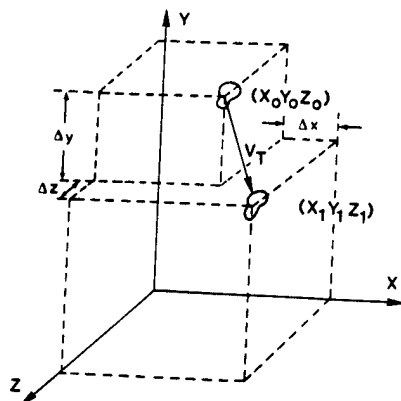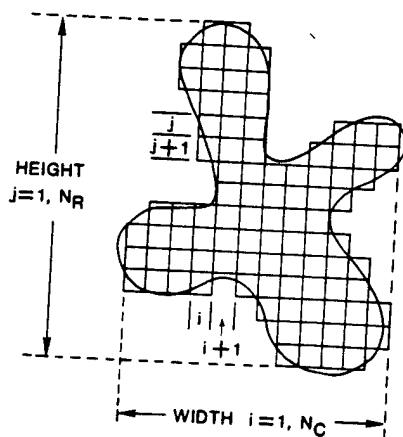
Fig. 2. Particle moving in 3-D space.

Fig. 3. Scanning algorithm processes pixels above threshold for area and perimeter.

oped a multipass technique[8] which processes a full video frame of data to obtain edge coordinates of very complex shapes. However, this method would be far more complex and time-consuming than necessary for determination of area and perimeter in most of our applications. Also, it is rare for more than one particle image to be found in a given focal plane.

Therefore, we have chosen an image scanning technique which uses a simplified edge detection process that is based on a comparison of the pixel intensity with a threshold adjusted for the average intensity between the particle and background to determine particle area and perimeter. Pixels at each transition across the threshold are accumulated as the perimeter of the particle, while pixels above the threshold are accumulated as its area.

C. Particle Area Scan Technique

The particle scanning algorithm developed for this system is based on a simplified single-pass edge detection process. The surface area and edge perimeter of each particle are determined by comparing the video intensity of each pixel to a selected threshold value. The technique consists of processing a series of vertical scans which horizontally cover the image as depicted in Fig. 3. The horizontal (equatorial) and vertical (polar) axes of the particle are determined by manually adjusting a vertically scanning cursor to the edges of the particle when the algorithm is first executed for each measurement. This limits the region under investigation to the immediate environment of the particle and eliminates the generally out-of-focus neighboring particles from consideration.

Beginning on the left side, the particle is scanned from top to bottom in synchronism with the TV raster. The video intensity (0–255) of each pixel is compared to a threshold value corresponding to the intensity at the particle edge. If the pixel intensity is greater than the threshold, the pixel area is assigned a unit value and the column area is incremented. Otherwise, its value is zero. If the pixel area value is different from that of the last pixel, the horizontal perimeter is incremented. When the vertical scan is complete, the difference between areas of current and previous columns is added to the vertical perimeter. The scan is then incremented to the right and the process repeated until the entire particle has been scanned. The selected scan consists of N_r rows vertically and N_c columns horizontally. The total area of the particle is the sum of all column areas scaled as shown in Eq. (1). Since the shape of each pixel is not square, the vertical component must be scaled to provide an accurate measurement of the area and perimeter. Or simply,

if $V_{p(i,j)} > V_t$ then $A_{p(i,j)} = 1$,

if $V_{p(i,j)} < V_t$ then $A_{p(i,j)} = 0$,

$$\text{Area} = F_x * F_y * \sum_{i=1}^{N_c} \left[\sum_{j=1}^{N_r} A_p(i,j) \right], \quad (1)$$

particle on a subsequent frame. When the entry of data for all frames has been completed, the distance each particle has traveled between successive frames is determined and the individual velocities calculated.

B. Particle Area and Perimeter

Determination of the projected cross-sectional area of a particle can be derived from the reconstructed image by counting the number of pixels inside the particle boundary. In a similar manner, the perimeter of the particle can be derived from the number of pixels along the edge. One of the major problems with a noisy image is detection of the pixels which represent the edge. Yakimovsky discussed an edge detection technique[7] based on maximizing the likelihood ratio with a simple single-pass region-growing algorithm. This ratio is a comparison of the intensities of neighboring pixels within the same object to neighboring pixels within two different objects. The boundary decision is based on comparing the ratio with a predefined threshold and accumulating those neighborhoods which are considered to be within a single object into one contiguous region. McKee and Aggarwal have devel-

where i and j are the pixel column and row,

> V_p is the video amplitude of pixel (i,j),
> V_t is the preselected video threshold,
> N_c is the number of scanned columns,
> N_r is the number of scanned rows,
> F_x is the horizontal scale factor, and
> F_y is the vertical scale factor.

The error introduced by the quantization of area should converge toward zero and become negligible as the size of the particle increases.

The vertical component of the perimeter (P_v) is the difference between the number of pixels above the threshold in one column compared with the number in the previous column. The horizontal component (P_h) is the sum of all transitions across the threshold occurring in each column. The horizontal and vertical components are scaled by F_x and F_y, respectively, and combined to form the particle perimeter as shown in Eq. (2). If $V_p(i,j)$ is not equal to $V_p(i,j + 1)$, the incremental horizontal component $H_p(i,j) = 1$, otherwise $H_p(i,j) = 0$:

$$\text{perimeter} = (F_x * P_h) + (F_y * P_v), \qquad (2)$$

where

$$P_h = \underset{i = 1}{\overset{N_c}{\text{sum}}} \left[\underset{j = 1}{\overset{N_r}{\text{sum}}} H_p(i,j) \right],$$

$$P_v = \underset{i = 1}{\overset{N_c}{\text{sum}}} \left[\underset{j = 1}{\overset{N_r}{\text{sum}}} A_p(i,j) - \underset{j = 1}{\overset{N_r}{\text{sum}}} A_p(i - 1,j) \right].$$

The major error in this method is highly dependent on the orientation of any edge segment with respect to the scanning axis. Although straight edges orthogonal to the scan will yield good measurements of perimeter, those same straight edges oriented diagonally to the scan axis can degrade the perimeter measurement by as much as 30% [1-SQRT (1/2)]. Therefore, a different method of determining perimeter which will be insensitive to particle orientation was required. Also, variations in the pixel intensity around the particle perimeter with respect to the threshold level increase measurement uncertainty. A dynamic threshold which can adapt to varying particle and background video intensities will improve this condition. Such a technique is implemented in an edge-tracking routine described below that provides data for determination of particle shape and orientation.

D. Particle Shape and Orientation

Boundary definition using direction and curvature chains has been described by Eccles et al.[9] These techniques generally describe an image boundary in terms of a 1-D list of angles starting from an origin on the image edge and incrementing uniformly around the boundary. Freeman has described another method for determining shape by defining critical points around the boundary.[10] These points include discontinuities

ENLARGED SCAN PATTERN

WHERE $N_s = 20$

FIGURE REPRESENTS $\frac{\Delta X}{\Delta Y} = 0.75$

⊙ SCAN START NUMBER
▣ SCAN END NUMBER AND ORIGIN OF NEXT SCAN PATTERN
⟶ TRACKED EDGE
⟶ PARTICLE EDGE

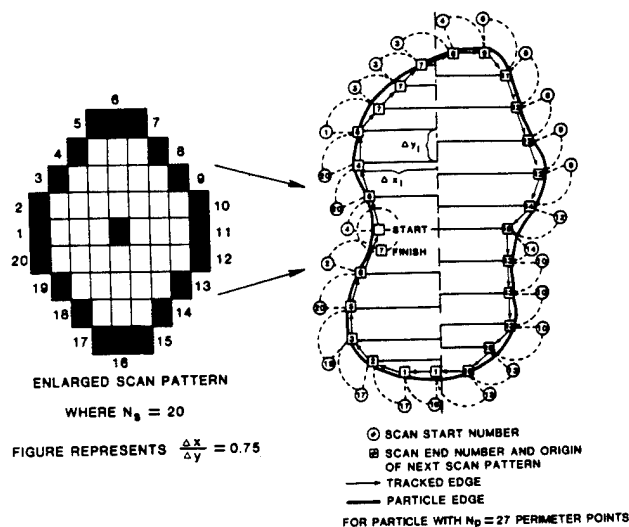FOR PARTICLE WITH $N_p = 27$ PERIMETER POINTS

Fig. 4. Tracking algorithm.

in curvature, points of inflection, curvature maxima, intersections, and points of tangency. Fourier transforms have been used as digital filters to smooth the digitized boundaries of planar objects. Pavlidis discusses several algorithms using Fourier transform coefficients to define detailed shape characteristics.[11] Teague has developed similar shape analysis techniques using Zernike moments.[12]

We have chosen a boundary chain technique to determine particle shape and orientation which is similar to the method described by Eccles.[9] The edge-tracking algorithm, described below, determines the boundary between the particle and background by examining a small region of pixels along the particle edge. Edge detection is based on the intensity gradient between neighboring pixels rather than the simple threshold technique used in the particle scanning algorithm described above. As each new point along the particle edge is determined, the tracking pattern is then centered on that point and the new neighborhood is explored. This process continues until the particle has been fully circumnavigated. A more detailed discussion is given below.

E. Particle Edge-Tracking Technique

The particle edge-tracking algorithm provides the capability to classify particle size, shape, and orientation for applications dealing with particle settling dynamics. The edge-tracking algorithm scans across the particle edge in a series of small circular patterns where i is one of the N_p scans around the particle edge and j is one of the N_s points in a scan as shown in Fig. 4. The point j in the scan for which the pixel intensity $V(i,j)$ exceeds the previous pixel intensity $V(i,j - 1)$ by a threshold value V_t is defined as the edge for the current scan pattern i and is used as the center of the next scan pattern $(i + 1)$. This process continues until the scan returns to the neighborhood of the starting point. The scan radius R_s, number of points per scan N_s, and threshold value V_t, can be manually selected, depending on the particle size and shape.
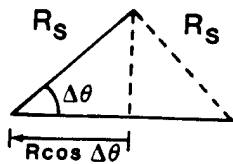
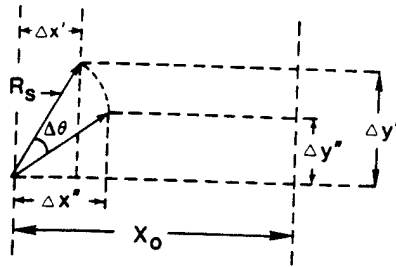Fig. 5. Radial error due to $\Delta\theta$ affecting perimeter accuracy.

Fig. 6. Angular error affecting area accuracy.

Fig. 7. Video amplitude across the edge of a high contrast (top) and low contrast (bottom) particle.

The perimeter of each particle is measured by accumulating the radial distance of each threshold transition around the particle edge until the circumnavigation of the particle is complete. Since the shape of each pixel is not square, both vertical and horizontal components must be scaled accordingly, by F_y and F_x, respectively, to provide an accurate measurement of the distance around the particle. The algorithm for this function is

$$\text{perimeter} = \sum_{i=1}^{N_p} [(F_y * T_y)^2 + (F_x * T_x)^2]^{1/2}, \qquad (3)$$

where $T_y = R_s \sin$,
$\quad T_x = R_s \cos$,
$\quad R_s$ = scan radius, and
$\quad N_p$ = number of threshold transition points along the edge.

The area of each particle is determined by accumulating the trapezoidal area defined by each new transition as shown in Fig. 4. The distance x_i between the particle edge and a vertical reference line at the center of the screen is determined for each transition point and multiplied by the vertical distance dy_i between two successive edges. The entire area of the particle is determined by successively adding or subtracting each incremental area depending on the vertical direction until the particle has been completely encircled as described by

$$\text{area} = \left(\frac{1}{2} \sum_{i=1}^{N_p} (x_i + x_{i+1}) * dy_i * F_y/F_x \right). \qquad (4)$$

Particle identification from frame to frame is achieved by displaying the edge pixels of a selected particle on the next frame and comparing it with the shapes of the new particles for correlation.

F. Algorithm Error Analysis

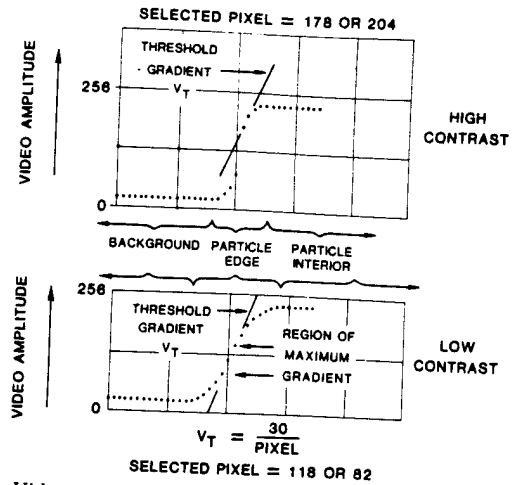The inherent error in the tracking process consists of radial and angular components, as shown in Figs. 5 and 6, respectively. These errors are functions of the number of scan points (N_s) and the scan radius (R_s), as shown in

$$\text{radial error} = R_s * [1 - \cos(2\pi/N_s)]/2,$$

$$\text{Angular error} = +/-2\pi/N_s. \qquad (5)$$

The error in determining the perimeter of a smooth boundary will produce a small positive error (e.g., 2.5% for $N_s = 20$) as shown in Eq. (6). However, the algorithm may exhibit a large negative error for figures with sharp corners because of truncation produced by the discrete scan process. The difference between the actual and measured area for large, smooth particles should be small but may become negative for particles with sharp corners, Eq. (7):

$$\text{perimeter error} = +N_p * R_s(1 - \cos 2\pi/N_s), \qquad (6)$$

$$\text{area error} = +/-(N_p * R_s * \sin 2\pi/N_2)/2. \qquad (7)$$

Area and perimeter measurements will also vary as a function of the video intensity threshold value for the scan mode and as a function of the video intensity gradient threshold value for the tracking mode. The video amplitude across the edge of an image with varying contrasts is shown in Fig. 7. The effects due to variation of the threshold values on measurements of a high-contrast, white-on-black square (2 cm/side) are summarized in Table II. In generating these data the video threshold intensity for the scan mode was set at values from 23% to 74% of the intensity difference between the square and the background, whereas the intensity gradient threshold (intensity difference/pixel) for the tracking algorithm was varied from 8% to 32% of the total intensity difference between the square and the

Table II. Effects of Variation of Video Threshold Intensity (Scan) and Intensity Gradient (Track); Variation is Represented by ±1 Standard Deviation as well as the Total Range of Deviation

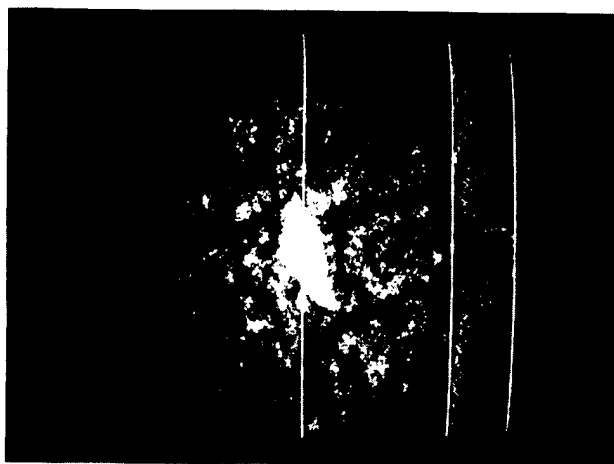| Area (pixels)		Perimeter (pixels)	
Scan	Track	Scan	Track
2165.6 ± 4.0%	2058.1 ± 1.3%	185.6 ± 4.7	180.4 ± 1.7%
11% Range	4% Range	15% Range	5.5% Range

Fig. 8. Photograph of video image of hologram of mica flake. The video amplitude of each pixel along the central white line is shown by the relative scale on the right-hand side of the screen. The length and width of this particle were 41 and 19 μm, respectively.

background. A negative threshold gradient (i.e., a bright-to-dark transition) was used to determine the edge in this particular application.

The range of threshold effects is smaller for the tracking mode than the scanning mode because the maximum video intensity gradient, generally found about halfway between the intensities of the image and the background (see Fig. 7), cannot be exceeded without the algorithm losing track of the particle edge. The threshold intensity gradient value for the tracking program is generally selected to be smaller than the smallest normal edge gradient (bottom curve in Fig. 7) found along the particle edge. This insures that oblique approaches to the edge do not reduce the measured intensity gradient below that of the threshold. This reduced threshold value causes the tracking program for the high-contrast part of the particle (upper curve, Fig. 7) to, in effect, underestimate the size of the particle for a white-on-black image and overestimate the size of a particle for a black-on-white image, especially for particles of varying contrast along the edges. For the white square on black background image addressed in Table II, this resulted in particle size estimates that were $\frac{1}{2}$ to $1\frac{1}{2}$ pixels lower per edge transition (see upper curve in Fig. 7), depending on the video threshold intensity gradient selected or a 1.2 to 3.6% underestimate of the length of each side. This underestimate would be offset to some extent by the radial error effect on the perimeter as described by Eq. (6).

V. Performance Evaluation

The performance of the scan and track algorithms was evaluated using white-on-black geometrical figures (square, equilateral triangle, and circle) of controlled size and shape. The figures are typical in projected size onto the TV screen of magnified holograms of 50–150-μm particles. They do not push the limits of resolution of the system since our primary objective was to test the performance of various image analysis algorithms as a function target size and shape. The standards for comparison were accurate to within $\frac{1}{2}$ to 1 pixel/side or to about ±2.5% for the small figures and ±1.25% for the large. The results of the comparisons are shown in Table III. Digitization error appears to have produced a greater effect on accuracy of the small figures with complex shapes compared with the larger ones. A digitization error of 1 pixel/edge can result in errors as large as ±3.6% for the small and ±2.0% for the large triangle measurements. However, this effect should approach zero as the shapes become larger and smoother.

For the tracking program, most errors did not exceed the accuracy limits of the standard measurement. Digitization errors, together with the uncertainties in the standards, can account for the differences between the measured and standard sizes; inclusion of the potential of radial, corner-truncation, and threshold intensity/threshold intensity gradient errors insures that the maximum tracking error measured (3.98%) falls within potential error limits.

For the scan program, all the areas measured were within expected error limits, although the triangle and circle perimeter errors were larger. The perimeter errors for the squares were quite low as the edges of each square were aligned with the vertical and horizontal axes of the TV camera. Perimeters in the scan mode can be exaggerated by as much as $1 - \sqrt{2}/2$ for lines sloping 45° to the vertical. The largest manifestation of this serrated-edge effect was found for the circle, with more than a +14% error.

VI. Application to Holograms

The application of these techniques was demonstrated by reexamining *in situ* transmission holograms of mica flakes collected during the settling experiment reported in Ref. 5. Because the mica flakes are very thin and tend to settle at some angle to the focal plane, only one side can be in sharp focus at any time. Therefore, a slightly defocused (lower contrast) image was analyzed (Fig. 8). This lower contrast image is

Table III. Perimeter and Area Measurement Accuracies of the Scanning and Tracking Algorithms for Some Standard Geometrical Shapes

Shape	Size (cm)	Track Area % Error	Track Perimeter % Error	Scan Area % Error	Scan Perimeter % Error
Square	3.0	0.38	−0.47	0.50	+1.4
Square	2.0	0.98	0.17	+2.89	+3.2
Triangle	4.0	−3.00	−2.90	−0.56	6.89
Triangle	2.2	+3.98	+1.83	−0.80	+4.23
Circle	4.0	−0.90	0.62	+3.14	+14.45
Circle	2.2	−0.88	2.97	+0.66	+9.36

Table IV. Holographic Image Analysis Measurements of Falling Mica Flakes Using the Scanning and Tracking Algorithms (Pixels)

Sample	Scanning Area	Scanning Perimeter	Threshold	Tracking Area	Tracking Perimeter	Threshold gradient	General shape	Longest dimension (μm)
1	498	127	134	500	135	26	Elliptical	41
2	107	40	113	101	42	30	Elliptical	14
3	485	118	100	501	106	30	Elliptical	42

typical of the type collected from irregularly shaped particles commonly found in seawater.

A comparison between the tracking and scanning algorithm data (Table IV) shows that the areas generated are within ~6% of each other for these mica holograms. However, the elliptical image of the third measurement resulted in a perimeter that was 11% higher for the scanning than for the tracking algorithm. The long axis of this image was diagonal to the screen axes, and the scanning algorithm overestimated the perimeter by serrating the diagonally oriented edges.

VII. Summary

The holographic microvelocimeter has proven to be an invaluable tool in studying the settling dynamics of particles in both marine and laboratory environments. The reduction of data from this instrument has been semiautomated using a microcomputer to control two phases of the analysis and provide data storage and retrieval. During the first phase of the analysis a precision translation stage is controlled to bring a sequence of holographic frames into register for the 3-D measurement of particle displacement between frames. Control of this stage is of the order of ±0.0002 cm with even greater accuracies in particle settling velocities being achieved by increasing the hologram exposure interval.

The second phase of the analysis is the measurement of the size, shape, and perimeter of the digitized video image of suspended particles within the hologram. Two techniques have been developed to measure the area and perimeter of an image. Both methods have been tested with standard geometric as well as holographic images and are accurate to within 4–6%. The first method utilizes a scanning algorithm based on absolute video intensity for edge detection. Although the algorithm is quite fast and is able to scan the area and perimeter of a particle in a single pass, accuracy is compromised for very noisy low-contrast particles or for particles with long diagonal edges. The second method uses a tracking algorithm based on video intensity gradient for edge detection. This technique not only provides accurate area and perimeter measurements but also produces detailed edge coordinates which can be used for complex shape identification. Although this system has been applied to the study of particle settling dynamics, the techniques developed could also be applied to other pattern recognition and image analysis problems.

References

1. R. A. Briones, L. O. Heflinger, and R. F. Wuerker, Appl. Opt. 17, 944 (1978).
2. L. O. Heflinger, G. L. Stewart, and C. R. Booth, Appl. Opt. 17, 951 (1978).
3. K. L. Carder, Opt. Eng. 18, 524 (1979).
4. K. L. Carder and D. J. Meyers, Proc. Soc. Photo-Opt. Instrum. Engl. 208, 151 (1979).
5. L. J. Doyle, K. L. Carder, and R. G. Steward, J. Sediment. Petrol. 53, 2 (1983).
6. K. L. Carder, R. G. Steward, and P. R. Betzer, J. Geophys. Res. 87, 5681 (1982).
7. Y. Yakimovsky, Fourth International Joint Conference on Artificial Intelligence (1974).
8. J. W. McKee and J. K. Aggarwal, Pattern Recognition 7, 25 (1975).
9. M. J. Eccles, M. P. C. McQueen, and D. Rosen, Pattern Recognition 9, 31 (1977).
10. H. Freeman, Pattern Recognition 10, 159 (1978).
11. T. Pavlidis, IEEE Trans. Pattern Anal. Machine Intell. PAMI-2, 301 (1980).
12. M. R. Teague, J. Opt. Soc. Am. 70, 920 (1980).